

Universidade do Minho
Escola de Engenharia

Fábio Quintas Cruz

Innovative structural systems for durable and resilient artificial reefs and other geometrically complex marine constructions

July 2026

Innovative structural systems for durable and resilient artificial reefs and other geometrically complex marine

Fábio Quintas Cruz

UMinho | 2026

Fundação
para a Ciência
e a Tecnologia

Universidade do Minho
Escola de Engenharia

Fábio Quintas Cruz

Innovative structural systems for durable and resilient artificial reefs and other geometrically complex marine constructions

Doctoral thesis

Civil engineering

Work performed under the supervision of:
Eduardo Nuno Borges Pereira
Maria Isabel Brito Valente

July 2026

Copyright and Terms of Use for Third Party Work.

This dissertation reports on academic work that can be used by third parties as long as the internationally accepted standards and good practices are respected concerning copyright and related rights.

This work can thereafter be used under the terms established in the license below.

Readers needing authorization conditions not provided for in the indicated licensing should contact the author through the RepositóriUM of the University of Minho

License granted to users of this work:



Atribuição-NãoComercial-SemDerivações
CC BY-NC-ND

https://creativecommons.org/licenses/by-nc-nd/4.0/

To my family

ACKNOWLEDGMENTS

The research has been carried out at the Civil Engineering Department of University of Minho, Portugal, under the supervision of Professor Eduardo Nuno Borges Pereira and Professora Maria Isabel Brito Valente. This work was financially supported by the Portuguese Foundation for the Science and Technology (FCT) under the grant number SFRH/BD/137220/2018, which is gratefully acknowledged. Additionally, this work was also incorporated in a research project "NEXT-SEA: Next Generation Monitoring of Coastal Systems in a Scenario of Global Change", NORTE-01-0145-FEDER-000032, financed by Comissão de Coordenação e Desenvolvimento Regional do Norte (CCDR-N) and Fundo Europeu de Desenvolvimento Regional (FEDER).

First and foremost, I would like to express my profound gratitude to Professor Eduardo Pereira for the friendship, their invaluable guidance, support, encouragement, and scientific insights. I would also like to acknowledge for all the support and assistance provided by Professor Isabel Valente, whose contributions were instrumental in the realisation of this research. Their mentorship has been fundamental in shaping this research.

I sincerely thank the staff of the Civil Engineering Department at the University of Minho, with special appreciation for the Structural Laboratory team, particularly António Matos, Marco Peixoto, and Carlos Jesus from the LMC Laboratory. I also acknowledge ISISE for providing the necessary facilities and resources for this research. My gratitude extends to Professor Tiago Miranda for reviewing the scientific articles and to Professors Nuno Dourado and Miguel Araujo from the Mechanical Engineering Department for their support in specimen preparation for microscope analysis. Lastly, I thank Hilti for supplying the HIT RE 500 V4.

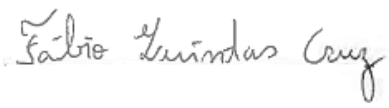
I would like to thank friends and colleagues that I had the pleasure to meet during these PhD years: João Almeida, Rita Neves, Filipa Monteiro, Dmytro Maslov, and so many others.... Finally, I would like to dedicate this work to my family and to my soulmate, Catarina. Your love and support have been invaluable, making this PhD adventure possible. I am forever grateful to you.

STATEMENT OF INTEGRITY

I hereby declare having conducted this academic work with integrity. I confirm that I have not used plagiarism or any form of undue use of information or falsification of results along the process leading to its elaboration.

I further declare that I have fully acknowledged the Code of Ethical Conduct of the University of Minho.

University of Minho, July 15, 2026



Fábio quintas Cruz

ABSTRACT

Multifunctional Artificial Reefs (MFARs) are essential components for marine strategies. As they evolve in complexity toward scalable and modular forms (MMFARs), well-documented engineering approaches become increasingly critical. This work focuses on the engineering approach for structural design, development and characterization of MMFARs.

The research discusses artificial reef development, covering regulations, design, materials, construction, and structural principles for marine applications. A structural design methodology is proposed and demonstrated through a case study involving reinforced concrete (RC) and steel–concrete composite (CS) systems, hydrodynamics, analytical and numerical modelling, enabling the optimisation of MMFARs. Given the modularity of MMFARs, this research emphasizes the development and characterization of structural connections, contributing to the efficiency of construction systems. The study evaluates also MMFAR units made of RC and engineered cementitious composites (ECC), showing RC units outperform ECC in load capacity, stiffness, and deformation, with distinct failure modes. The bond behaviour between concrete and galvanized steel tubes is examined through pushout tests, including concrete pin connectors and long-term seawater exposure. Results indicate that initial bond degradation may be counterbalanced by long-term strength gains associated with corrosion product development at the interface. Hydrodynamic performance is analysed through flume tests assessing scour and flow effects around small-scale reef prototypes.

By integrating advanced engineering techniques, this research contributes to the development framework of MMFARs. The results enable both RC and CS solutions, with CS offering higher flexural strength and greater design flexibility, and enhanced connection performance, though at higher cost. The work addresses previous reliance on empirical or geometric criteria by providing a systematic, technically grounded approach that integrates structural analysis, hydrodynamics, design loads, and performance criteria. This framework supports more robust, efficient, and replicable modular reef designs, opening new possibilities for flexible configurations and long-term performance assessment.

KEYWORDS: Experimental characterization; Multifunctional Modular Artificial Reefs; Steel–concrete composite systems; Structural connections; Structural design methodology.

RESUMO

Os Recifes Artificiais Multifuncionais (MFARs) são componentes essenciais para as estratégias marinhas. À medida que evoluem em complexidade para formas escaláveis e modulares (MMFARs), abordagens de engenharia bem documentadas tornam-se cada vez mais críticas. Este trabalho apresenta um quadro de engenharia para o projeto estrutural, desenvolvimento e caracterização de MMFARs.

A investigação discute o desenvolvimento de recifes artificiais, incluindo regulamentação, geometrias, materiais, construção e projeto marítimo. É proposta uma metodologia de projeto estrutural, demonstrada por um estudo de caso envolvendo estruturas de betão armado (BA) e compósitos aço-betão, considerando hidrodinâmica e modelação analítica e numérica para otimização dos MMFARs. Dada a modularidade dos MMFARs, o estudo enfatiza o desenvolvimento e a caracterização de ligações estruturais, contribuindo para melhorar a eficiência dos sistemas construtivos. Avalia-se igualmente unidades MMFAR em BA e em compósitos cimentícios de engenharia (ECC), mostrando que as unidades de BA superam as de ECC em capacidade resistente, rigidez e deformação, com modos de rotura distintos. O comportamento de aderência entre o betão e tubos de aço galvanizado é analisado através de ensaios de pushout, incluindo conectores de betão e exposição prolongada à água do mar. Os resultados indicam que a degradação inicial da aderência pode ser compensada por ganhos de resistência a longo prazo devido à corrosão na interface. O desempenho hidrodinâmico é analisado em canal hidráulico, avaliando erosão localizada e efeitos do escoamento em protótipos de MMFAR em escala reduzida.

Ao integrar técnicas avançadas de engenharia, este trabalho contribui para o desenvolvimento dos MMFARs, permitindo soluções em BA e compósitos aço-betão, sendo que os compósitos oferecem maior resistência à flexão, flexibilidade de projeto e melhor desempenho das ligações, embora a custo mais elevado. O trabalho substitui a dependência de critérios empíricos ou geométricos por uma abordagem sistemática e técnica, integrando análise estrutural, hidrodinâmica, ações de projeto e critérios de desempenho, apoiando projetos modulares mais robustos, eficientes e replicáveis, e permitindo novas configurações flexíveis e avaliação de desempenho a longo prazo.

KEYWORDS: Caracterização experimental; Recifes artificiais modulares multifuncionais; Sistemas compósitos aço–betão; Ligações estruturais; Metodologia de projeto estrutural.

TABLE OF CONTENTS

ACKNOWLEDGMENTS ..... **iv**

ABSTRACT ..... **vi**

RESUMO ..... **vii**

TABLE OF CONTENTS ..... **viii**

LIST OF TABLES ..... **xi**

LIST OF FIGURES ..... **xiii**

LIST OF ABBREVIATIONS AND SYMBOLS ..... **xx**

1. INTRODUCTION **1**

1.1. MOTIVATION 1

1.2. OBJECTIVES AND RESEARCH METHODOLOGY 3

1.3. OUTLINE OF THE THESIS 5

1.4. PUBLICATIONS 6

1.5. REFERENCES 8

2. ARTIFICIAL REEFS: DESIGN, MATERIALS AND APPLICATIONS **10**

2.1. DEFINING ARTIFICIAL REEFS 10

2.2. SINGLE-PURPOSE AND MULTIFUNCTIONAL ARTIFICIAL REEFS 11

2.3. HISTORICAL PERSPECTIVE 13

2.4. REGULATIONS ON ARTIFICIAL REEFS 16

2.5. PLANNING PHASES 17

2.6. DESIGN CRITERIA 19

2.7. MATERIALS 20

2.8. STRUCTURES AND CONSTRUCTION 24

2.8.1. Small-scale 24

2.8.2. Complexity-added 27

2.8.3. Large-scale 31
2.8.4. Very large-scale and emerging approaches 33
2.9. FINAL CONSIDERATIONS 36
2.10. REFERENCES 38
3. STRUCTURAL DESIGN OF GEOMETRICALLY COMPLEX ARTIFICIAL REEFS 49
3.1. CONCEPTION WITH PARAMETRIC DESIGN 49
3.2. STANDARDS AND GUIDELINES 52
3.3. DESIGN METHODS AND ANALYSIS 55
3.4. ACTIONS AND EFFECTS 63
3.4.1. Dead load 64
3.4.2. Tidal effects and currents 64
3.4.3. Waves 67
3.4.4. Marine growth 75
3.4.5. Earthquakes 75
3.4.6. Accidental Actions 76
3.4.7. Sea ice and snow 76
3.4.8. Temperature 76
3.5. ANALYTICAL MODELS FOR HYDRODINAMIC LOADING 77
3.6. DURABILITY 83
3.7. FINAL CONSIDERATIONS 86
3.8. REFERENCES 87
4. SUMMARY OF APPENDED PAPERS 101
4.2. PAPER I 102
4.3. PAPER II 103
4.4. PAPER III 104

4.5. PAPER IV 105
4.6. PAPER V 106
4.7. PAPER VI 106
5. CONCLUSIONS AND FUTURE WORK 108
5.1. CONCLUSIONS 108
5.1.1. Artificial reefs construction and structural design – state of the art 108
5.1.2. Engineering and structural systems approach for MMFARs 110
5.1.3. MMFAR connections 111
5.1.4. Bond Behaviour and Durability 112
5.1.5. Hydrodynamic and scour of small-scale prototype 114
5.1.6. Real-scale reef module prototype for MMFAR 115
5.2. FUTURE WORK 115
6. ENGINEERING-DRIVEN APPROACH FOR THE STRUCTURAL DESIGN OF GEOMETRICALLY COMPLEX MODULAR ARTIFICAL REEFS 119
7. DEVELOPMENT AND CHARACTERIZATION OF STRUCTURAL CONNECTIONS FOR MODULAR ARTIFICIAL REEFS 165
8. EXPERIMENTAL CHARACTERIZATION OF BOND BETWEEN CONCRETE AND HDG STEEL TUBES FOR MIXED STEEL-CONCRETE STRUCTURES 203
9. LONG-TERM BEHAVIOUR OF BOND BETWEEN HDG STEEL AND CONCRETE FOR MIXED STEEL-CONCRETE MARINE STRUCTURES 234
10. CONSTRUCTION AND CHARACTERIZATION OF STRUCTURAL UNIT FOR MODULAR ARTIFICIAL REEFS 276
11. EXPERIMENTAL CHARACTERIZATION OF THE SCOUR OF INNOVATIVE ARTIFICIAL REEF PROTOTYPES USING HYDRAULIC FLUME AND PHOTOGRAMMETRY 305

LIST OF TABLES

Table 2.1: Examples of regulations covering or influencing ARs design. 17

Table 3.1: European standards for the design, sizing and verification of structures. 52

Table 3.2: Reference standards and regulations for the design of marine structures. 54

Table 3.3: Types and methods of engineering approaches contributing to structural design of ARs. 57

Table 3.4: Typically wave parameters [96,97]. 68

Table 3.5: Formulas for Airy theory [93]. 71

Table 3.6: Water depth criteria and wavelength [93]. 71

Table 3.7: Formulas for Stokes' second-order wave theory [93]. 73

Table 3.8: Examples of estimated maximum thickness of marine growth for different locations, based on [11,89,97,110]. 75

Table 3.9: Typical values of hydrodynamic coefficients. 82

Table 3.10: Examples of protection systems for steel and concrete marine structures. 85

Table I.1: Wave height and period for different sea conditions [58–61]. 129

Table I.2: 1st and 2nd order components of stokes wave theory [62,63]. 131

Table I.3: Results in terms of the maximum efforts obtained for different load combinations. 133

Table I.4: Axial strength of the cross-section according to the structural system. 136

Table I.5: Shear strength of the cross-section according to the structural system. 137

Table I.6: Flexural first cracking strength (M_{cr}), ultimate strength (M_{Rd}) and minimum reinforcement ($A_{s,min}$) of the cross-section for both RC and CS structural systems. 139

Table I.7: Parametric analysis of RC alternatives. 162

Table I.8: Parametric analysis of CS alternatives. 164

Table II.1: Experimental program. 173

Table II.2: Materials composition for 1 dm^3 of ECC. 174

Table II.3: Results of the mechanical properties of the concrete and ECC. 177

Table II.4: Characteristics of steel according to technical document or experimental testing. 178

Table II.5: Main results obtained from the experimental tests. 184

Table III.1: Variables and specimens tested in the experimental program. 207

Table III.2: Concrete composition. 208

Table III.3: Slump flow and mechanical properties of concrete mixtures 1 to 4. 210

Table III.4: Main pushout experimental results obtained for each mixture and series (average values). 216
Table IV.1: Variables and specimens tested. 239
Table IV.2: Results obtained in concrete characterization at 7, 28, 90, 190 and 500 days..... 244
Table IV.3: Steel characteristics. 244
Table IV.4: Main pushout experimental results obtained for each group and series (average values). 250
Table IV.5: Average results of depth of carbonatation and chlorites at 7, 28, 90, 190 and 500 days. 259
Table IV.6: Parameters of seawater according to the pushout test dates. 274
Table V.1: Materials composition for 1 m^3 of concrete. 280
Table V.2: Materials composition for 1 m^3 of ECC..... 281
Table V.3: Results of the mechanical properties of the concrete and ECC. 281
Table V.4: Main results obtained from the experimental tests. 291
Table VI.1: Tests performed, running time and experiments measurements. 310

LIST OF FIGURES

Figure 2.1: AR components hierarchy [8]. 11

Figure 2.2: General location of ARs in (a) World [24] and (b) Europe [9]. 15

Figure 2.3 - Global distribution of artificial marine reef research. The size of each circle represents the number of papers published by each country, with larger circles indicating greater research output. Only countries with at least two publications are marked. The gradient colours show the strength of collaboration between countries, with thicker, darker lines (dark orange) indicating stronger cooperation and thinner, lighter lines (yellow) indicating weaker collaboration. The colour gradient reflects collaboration strength, ranging from low to high (0 to 61), from [25]. 16

Figure 2.4: Project design criteria scheme, adapted from [6,26]. 20

Figure 2.5: Geographic distribution of research studies categorized by the materials employed in ARs development [24]. 21

Figure 2.6: Materials used in AR construction, adapted from [35]. 22

Figure 2.7: Types and characteristics of small-scale and low-complexity ARs structures. 26

Figure 2.8: Types and characteristics of complex ARs. 28

Figure 2.9: Examples of complex 3D printed reef structures. 30

Figure 2.10: Examples of large ARs. 32

Figure 2.11: Examples of extraordinarily large AR structures. 34

Figure 2.12: Mega projects involving ARs technology. 35

Figure 3.1: Workflow of the design process using parametric modelling [3]. 51

Figure 3.2: Hierarchy of standards and reference standards in the field of marine structures, adapted from [6,8]. 53

Figure 3.3: Example of a hydraulic flume experimental setup using PIV and ADV systems [42]. .. 58

Figure 3.4: Pullout test: (a) rebar embedded in concrete prism. Adapted from [129]; b) Typical analytical bond stress-slip relationship (monotonic loading). Adapted from [128]. 60

Figure 3.5: Beam test schemes (a) RILEM [70] and (b) alternative scheme [64]. 60

Figure 3.6: Pushout tests (a) designed for concrete-steel tube slices [72], (b) for CFST cross-sections [73] and (c) typical axial compressive behaviour of CFST stub column [74]. 61

Figure 3.7: Examples of connection tests setups: (a) flange-plate connections for circular or square hollow sections [77], (b) cruciform beam-column specimen [78] and (c) for steel beam-column connection [79]. 62

Figure 3.8: Regions of Applicability of Wave Theory [11,92]. 70

Figure 3.9: Classification of wave theories according to Keulegan (1950) [91]. 72

Figure 3.10: Wave force regimes and limits of application for small vs. large structure [112]..... 78

Figure 3.11: Fluid particles velocities and acceleration directions at every location [90]. 79

Figure 3.12: Damage to structures exposed to the marine environment: (a) steel corrosion of a marine structure and (b) damaged submerged concrete [125–127]. 84

Figure I.1: Design flowchart..... 124

Figure I.2: Geometric design using novel approaches and design processes for the 3D network of individual modules of the MMFAR (adapted from [57]). 125

Figure I.3: Structural systems: (a) RC unit with four galvanized steel rebars interconnected using external rods by welding, (b) CS unit based on the use of four galvanized steel tubes with holes along the length, interconnected using external rods by welding, (c) RC with three central galvanized steel rebars interconnected at the centre of the unit by welding or tying and (d) CS based on the use of three central galvanized steel tube profiles with holes along the length, interconnected by welding at the intersection..... 127

Figure I.4: 3D model of MFMAR with the connectors system. 128

Figure I.5: (a) Geographical location of the Littoral North Marine Park in Esposende, Portugal; (b) detailed bathymetry distribution, and (c) zone with acceptable MMFAR depth [45]. 129

Figure I.6: MMFAR structure: (a) 3D model, (b) numerical bar model (c) forces applied to the numerical bar model. The marks “a, b, c and d” show the visual correspondence between the elements of the 3D model and the bar model. 130

Figure I.7: Location of the maximum stresses in the numerical model. 132

Figure I.8: Representative cross section of the alternative structural systems: (a) RC structure and (b) CS structure. 135

Figure I.9: Schematics representing the simplified strains and stresses at ULS in flexure for (a) RC and (b) CS cross-sections..... 138

Figure I.10: Flexural strength, $M_{pl,Rd}$, *versus* concrete strength for various structural combinations for cross-section types (a) RC, and (b) CS..... 142

Figure I.11: Tensile (above) and compressive (below) axial strength, $N_{pl,Rd}$, *versus* concrete strength for cross-section types (a) RC and (b) CS..... 143

Figure I.12: Shear strength (V_{Rd}) versus concrete strength for cross-section types (a) RC and (b) CS. 146

Figure I.13: Correlation between the minimum (D_{min}) and maximum (D_{max}) cross-section diameters and the flexural strength, $M_{pl,Rd}$, as a function of concrete compressive strength, f_c, and reinforcement configuration (approach 1). 148
Figure I.14: Correlation between the minimum (D_{min}) and maximum (D_{max}) cross-section diameters and the flexural strength, $M_{pl,Rd}$, as a function of concrete compressive strength, f_c, and reinforcement configurations (approach 2). 149
Figure I.15: (a) RC structure with polar array of compression steel reinforcement and (b) CS structure. 150
Figure I.16: Correlation between reef module weight and cost for CS and optimized RC configurations. 152
Figure II.1: Examples of connections for (a) ARs and (b) other marines structures. [67,78,221,224,231–233]. 168
Figure II.2: Modular MFAR geometry with structural combinations and related connection systems: (a) CS, (b) ECC and (c) RC modules. 169
Figure II.3: Geometric design of (a) CS connection with steel clamp (SC) and (b) CS connection with SC covered with an KTP filled with ECC (b) (side and cross section views). 171
Figure II.4: Geometric design of (a) RC connection with epoxy, steel hasp & bar couplers, (b) ECC connections with epoxy & steel hasp (b) ECC adhesive connection (side and cross section views). 172
Figure II.5: Specimens preparation for concreting: (a-d) wood mould and detail of the foam piece at the base and top for connection, (d) concreting phase and (e, f) demould and storage. 175
Figure II.6: Connections preparation: (a) tube hole, (b-e) epoxy, steel hasp and rebar couplers application, (f, g) SC assembly and SG application, (h, i) general view and frame positioning. 176
Figure II.7: Preparation and application of the KPTs connection sleeve: (a) sleeve production, (b) KPT with valves attached, (c) KTPs system placement and (d) ECC injection. 177
Figure II.8: General test configuration and instrumentation: (a) CS_90° (back and top view), (b) CS_0° (back view), (c) RC_$H_{steel}B_CE$_0° (back view) [dimensions in millimetres]. 179
Figure II.9: Experimental responses of load force *versus* displacement at mid-span. 180
Figure II.10: Moment *versus* curvature at mid-span without (a) and with (b) the KTPs system. . 182
Figure II.11: Failure modes of the RC_$H_{steel}B_CE$_0°. 186
Figure II.12: Failure modes of the RC_$H_{steel}IB_CE$_180° 186
Figure II.13: Failure modes of the CS_SC_0° 187

Figure II.14: Failure modes of the CS_SC_90°. 188
Figure II.15: Failure modes of the CS_SC&KTPsECC_0°. 189
Figure II.16: Failure mode of the CS_SC&KTPsECC_90°. 190
Figure II.17: Failure modes of the ECC_H_{steel}E_0°. 190
Figure II.18: Failure modes of the ECC_0°. 191
Figure II.19: Strain on steel parts: (a) hasp of RC_$H_{steel}B_c$E and ECC_H_{steel}E, (b) steel clamp of CS_SC and (c) steel clamp of CS_SC&KTPsECC. 193
Figure II.20: Correlation between (a) F_{max} vs d_{ult} and (b) E_i vs δ_{ult}. 195
Figure III.1: Specimen's preparation. 209
Figure III.2: HDG steel uniaxial stress-strain curves and properties. 211
Figure III.3: Experimental setup and instrumentation adopted for pushout tests. 212
Figure III.4: Typical responses in terms of F_l-s_l and F_l-$s_{f:}$ (a) M02_LB50_01 and (b) M02_LB100_01. 213
Figure III.5: F_l-s_l experimental responses: (a) M01, (b) M02, (c) M03 and (d) M04. 214
Figure III.6: Average pushout force versus loaded end slip (*Fl-sl*) responses computed for all specimens tested: (a) LB50, (b) LB75, (c) LB100 and (d) LB100 vs LB100_H40. 218
Figure III.7: Failure modes: (a) D, (b) DC and (c) S. 220
Figure III.8: Influence of the concrete strength, M01 to M04 (a), and LB (b), on the average value of $F_{l,max}$ within each series. 221
Figure III.9: Influence of the f_{cm} and LB, on the average values of τ_{max} (a, b, e, f), and τmax (b, d), within each series. 224
Figure III.10: Influence of the type of concrete and LB, on the average values of the energy dissipated during pushout testing, G_f (a, b), and Gf (c,d), within each series. 226
Figure III.11: Influence of the type of concrete, M01 to M04, and of LB, on the average values of F_r, (a, b) and $F_r/F_{l,max}$ (c,d), within each series. 228
Figure IV.1: Specimens preparations: (1) cleaning the steel tubes; (2) overview of the moulds and materials and detail of the foam-steel union; (3) adjustment and levelling of the tube in the mould; (4) mould positioned for casting and (5/6) demoulding of the specimens. 241
Figure IV.2: Preparation of the specimens for exposure in the climatic chamber and immersion in the seawater tank: (a) specimens after demoulding; (b,c) details of the silicone application and waterproofing measures; (d) specimens in the climatic chamber; (e) specimens immerse in the seawater tank and (f) seawater monitoring system. 243

Figure IV.3: Experimental setup and instrumentation adopted for pushout tests: (a) global scheme; (b) perspective image of the specimen during testing. 245
Figure IV.4: Preparation of the samples for FEG/SEM (EDS) analysis. 246
Figure IV.5: Curves of the pushout force versus relative vertical displacement at 28 days. 247
Figure IV.6: Curves of the pushout force versus relative vertical displacement for each. 248
Figure IV.7: Average pushout force versus loaded end slip (F_r-s_l) responses computed for all specimens tested. 253
Figure IV.8: Typical FM: (a) pushout debonding failure, (b) pushout debonding failure with crack. 255
Figure IV.9: Detail of the steel ITZ in the specimen's exposure to SW with different exposition times. 255
Figure IV.10: Influence of the bond length, LB on the average values of the τ_{max} (a, b) and τmax (b, d), within the exposure condition (CC or SW). 257
Figure IV.11: Influence of exposure conditions (CC and SW) and exposure times (90, 190 and 500 days) on the average values of (a) maximum shear strength and (b) normalized maximum shear strength within each LB. 258
Figure IV.12: Representative test of carbonation and chlorites on the pushout specimens CC_28d. 259
Figure IV.13: Representative pushout specimens for carbonation and chlorites tests according exposure condition (CC and SW) and age (90, 190 and 500 days). 260
Figure IV.14: Cross-section SEM images for both exposure condition over time. 262
Figure IV.15: HDG steel ITZ SEM images for both exposure condition over time. 264
Figure IV.16: Concrete ITZ SEM micrographs for both exposure condition over-time. 267
Figure IV.17: Continuous measurements of seawater parameters from the built monitoring system: (a) seawater temperature, pH and salinity and (b) Total Dissolved Solids (TDS) and Oxydation Reduction Potential. 275
Figure V.1: Construction techniques used for artificial reefs constructions: (a) traditional wood formwork [20], (b) steel formwork [21], (c) manufactured GFRP moulds [22], (d) silicon moulds [23], (e) concrete 3D printer [24] and (f) clay 3D printer [13]. 278
Figure V.2: MMFAR with possible construction systems. 280
Figure V.3: Reef modules prototypes constructed with different scales: 1:13 (left), 1:3.6 (centre) and real scale 1:1 (right). 282

Figure V.4: Production of the smallest-scale unit reef prototype in cement paste at 1:13 scale.. 282
Figure V.5: Production of the small-scale unit reef prototype in cement paste at 1:3.6 scale. 283
Figure V.6: Prototype construction phases: 3D printing, assembling, concreting, demoulding. .. 284
Figure V.7: MMFAR numerical model, defined with beam elements..... 285
Figure V.8: Numerical model of reef module with unitary load to support experimental test setup. 286
Figure V.9: General test configuration and instrumentation of the artificial reef module, perspective view. 287
Figure V.10: Identification of maximum internal forces in MMFAR for abnormal extreme condition. 288
Figure V.11: Shear force and bending moment distribution in the reef module for unitary load. 289
Figure V.12: Experimental responses obtained in terms of load force versus displacement at mid-span..... 290
Figure V.13: Representation of the Ki and Ki′ in the experimental response of (a) RC module and (b) ECC module. 291
Figure V.14: Failure mode of the RCs reef module. 293
Figure V.15: Failure mode of the ECC reef module. 294
Figure V.16: Load factor considering the experimental responses. 295
Figure V. 17: Forces and moment distribution in MMFAR for an extreme scenario in terms of axial force (N), shear force (V), bending moment (M) and torsional moment (T). 304
Figure VI.1: Assembled small-scale prototype of the modular artificial reef with the dimensions of 15×15×15 cm and individual prototype units of 5 cm. 311
Figure VI.2: ADV testing locations for the two stages of testing: (a) without the structure, stage 1, (b) before structure, stage 3 and (c) after structure, stage 3. Note: (1) is the flow chamber, (2) is the holder of the measurement sensor above the flow chamber, (3) is the sensor, (4) is the sensor holding pole, (5) is the PMFAR. W_d is the water depth in the chamber (W_d=25cm), S_d is the sensor depth, and $L_d$is the distance between the artificial reef and the sensor (L_d=30cm). 313
Figure VI.3: Test A: (a) start, (b) final, (c) 2D photography and (d) reconstructed digital 3D model. Note: due some technical problems it was not possible to accurately reconstruct the digital models. 315
Figure VI.4: Test B: (a) time-lapse: start, (b) time-lapse: final and (c) reconstructed digital 3D model, digital elevation model and elevation map in meters. Note: the image of the DEM model is viewed

from the bottom plane (excavation zones: 1, 2, 3, 6, 8, 9, 10 and 11; deposition zones: 4, 5, 7 and 12). 316
Figure VI.5: Test C: (a) time lapse-start, (b) time lapse-final and (c) reconstructed digital 3D model, digital elevation model and elevation map in meters. 317
Figure VI.6: Test D: (a) time-lapse: start, (b) time-lapse: final and (c) reconstructed digital 3D model, digital elevation model and elevation map in meters. 318
Figure VI.7: Velocity magnitude profiles and average velocity in the y and z-direction without PMFAR (a) upstream, position@9 and (b) downstream position@17. 320
Figure VI.8: Velocity magnitude profiles and average velocity in the y and z-direction with PMFAR: (a) upstream, position@9 and (b) downstream position@17. 320
Figure VI.9: Velocity magnitude (above) and average velocity in the y and z-direction (below) time series data with PMFAR at downstream position@17 during the scour process for all tests. 323

LIST OF ABBREVIATIONS AND SYMBOLS

Abbreviations

AAM	Alkali-activated materials
ABS	American Bureau of Shipping
AC	Alumina cement
ADV	Acoustic doppler velocimeters
AGA	American Galvanizers Association
$AgNO_3$ 0.1N	Silver nitrate solution
Al	Aluminum
ALS	Accidental limite state
AM	Additive manufacturing
API	American Petroleum Institute
AR	Artificial reef
Au	Gold
BFRP	Basalt fibre reinforced polymer
C	Carbon
Ca	Calcium
$Ca(OH)_2$	Calcium hydroxides
$Ca[Zn(OH)_3]_2 \cdot 2H_2O$	CHZ-calcium hydroxyzincate
CaCl	Calcium chloride
$CaCO_3$	Calcium carbonates
CC	Climatic chamber
CEN	European Committee for Standardization
CFD	Computational fluid dynamics
CFST	Concrete-filled steel tubular
CoV	Coefficient of variation
CS	Composite steel-concrete systems
CS	Cross-section
D	Pushout debonding
DC	Pushout debonding with thin crack development

DEC-UM	Civil Engineering Department of the University of Minho
DEM	Digital elevation model
DNV	Det Norske Veritas
DOM	Orthomosaic model
EARRN	European Artificial Reef Research Network
ECC	Engineering cementitious composite
EMU	Erosion mitigation units
EN	European standard
FAO	Food and Agriculture Organization
Fe	Iron
FEA	Finite element analysis
FEG-SEM/EDS	Field emission gun - scanning electron microscopy
FEM	Finite element methods
FM	Failure modes
FPSOs	Floating production, storage, and offloading
FRP	Fibre reinforced polymer
FSI	Fluid-structure interaction
GFRP	Glass fibre reinforced polymer
H_3BO_3	Boric acid
HDG	Hot-dip galvanized
HR	Relative humidity
IH	Hydrographic Institute
ISO	International Organization for Standardization
ITZ	Interface transitional zone
K	Potassium
KCl	Potassium chloride
KTP	Knitted textile preforms
KTPsECC	knitted textile preform filled with ECC
LAT	Lowest astrological tide
LB	Bond length
LCA	Life cycle analysis
LDV	Laser doppler velocimetry

LEST	Laboratory of Structures
LVDT	Linear variable differential transducers
MAR	Modular artificial reef
MARS	Modular artificial reef structure
MFAR	Multifunctional artificial reef
Mg	Magnesium
$MgCl_2$	Magnesium chloride
MHHW	Mean higher high water
MKPC	Magnesium potassium phosphate cement
MMFAR	Multifunctional modular artificial reef
MNPC	Magnesium ammonium phosphate cement
MPA	Marine protected area
Na_2SO_4	Sodium sulphate
NaCl	Sodium chloride
$NaHCO_3$	Sodium bicarbonate sodium
NOAA	National Oceanic and Atmospheric Administration
NORSOK	Norwegian Petroleum Industry
O	Oxygen
OAR	Offshore artificial reef
OBS	Ocean brick system
ORP	Oxidation reduction potential
PIV	Particle image velocimetry
PL	Plasticizer
PMFAR	Small-scale multifunctional artificial reef prototype
PVA	Polyvinyl alcohol fibre
RC	Reinforced concrete
REU	Reef enhancement units
S	Splitting of the concrete block
SAC	Silica-alumina cement
SC	Steel clamp
SG	Strain gauges
Si	Silica

SLS	Service limite state
SP	Superplasticizer
$SrCl_2$	Strontium chloride
SW	Seawater
SWL	Still water level
TDS	Total dissolved solids
ULS	Ultimate limite state
USA	United States of America
Zn	Zinc
$Zn(OH)_2$	Zinc hydroxide
ZnO	Zinc oxide

Symbols

A	Effective dimension of the cross-sectional area
A	Elongation
a	Distance from the centroid of the reinforcement to the geometric centre of the section
A_a	Steel profile area
A_c	Concrete area
A_s or A_{sl}	Steel reinforcement area
$A_{s,min}$	Minimum cross-sectional area of reinforcement
A_{cc}	Cross sectional area of concrete in compression
A_s	Cross sectional area of reinforcement
$A_{s,eff}$	Real reinforcement area
$A_{s,pl}$	Theoretical required reinforcement area (ULS)
$A_{s,satur}$	Saturation reinforcement area
A_{sc}	Cross sectional area of steel in compression
A_{st}	Cross sectional area of steel in tension
b_w	Width or cross-section diameter
c	Phase velocity
C_D	Hydrodynamic drag coefficient
C_M	Hydrodynamic inertia coefficient

$C_{Rd,c}$	Coefficient of shear strength of concrete
D	Effective element diameter
D	Diameter of the circular cross-section
d	Water depth
d	Effective section height
d	Effective depth of a cross-section
dF	Local action vector per unit length acting normal to the axis of the member
dF_D	Drag action per unit length acting normal to the axis of the member in the plane of the member axis
dF_I	Inertia action per unit length acting normal to the axis of the member in the plane of the member axis
D_{max}	Maximum viable diameter of the cross-section
D_{min}	minimum viable diameter of the cross-section
d_o	Reference depth for wind-generated current
E_c	Modulus of elasticity of concrete
E_{corr}	Corrosion potential
E_i	Dissipated energy for $0.8F_{max}$
E_s	Modulus of elasticity of steel
E_w	Characteristic environmental event
$E_{w,e}$	Abnormal extreme environmental condition
$E_{w,storm}$	Typical storm environmental condition
$E_{w,máxstorm}$	Extreme storm environmental condition
E_{wcm}	Environmental actions including waves, currents and marine growth
F	Vertical load
F_c	Concrete compressive force
F_l	Pushout force
$F_{l,max}$	maximum pushout load
F_{max}	Maximum force
F_r	Residual pushout force
$F_r/F_{l,max}$	Force ratio
F_s	Steel tensile force of the RC cross-section
F_{sc}	Steel compressive force

F_{st}	Steel tensile force of the CS cross-section
f_{cd}	Design value of concrete compressive strength
f_{ck}	Characteristic compressive cylinder strength of concrete at 28 days
f_{ctm}	Mean value of axial tensile strength of concrete
f_s	Structural vibration frequency
f_{sd}	Yield stress of the longitudinal reinforcement
f_{yd}	Design yield strength of reinforcement
f_{yk}	Characteristic yield strength of reinforcement
g	Acceleration of gravity
G_f	Energy dissipated
H	Wave Height
H ; W_d	Height of water flow in the hydraulic flume
$H_{1/10}$	Average wave height of the highest 10% of waves
$H_{1/3}$	Average height of the highest one-third of waves
$H_{2\%}$	Wave height exceeded by 2% of waves
H_s	Significant wave height
h	Surface elevation
h	Effective strength
h and l	Effective height of the compression zone
k	Wind speed coefficient
k	Wave number
k	Shear factor
k_1	Shear behaviour coefficient
k_a	Diffraction parameter
KC	Keulegan-Carpenter number
K_i	Stiffness in different phases of the curve
l	Geometric ratio of longitudinal reinforcement
L or λ	Wavelength
L_0	Deep-water wavelength
L_d	Distance between the artificial reef and the sensor
M	Bending moment
M_{2-2}	Maximum flexural stress in 2-2

$M_{3\text{-}3}$	Maximum flexural stress in 3-3
M_{max}	Maximum bending moment
M_{Rd}	Flexural strength
M_{ult}	Ultimate bending moment
N	Axial force
N^+ and N^-	Maximum axial stress
N_{Ed}	Design value of the applied axial force (tension or compression)
$N_{pl,Rd,comp}$	Normal compressive strength
$N_{pl,Rd,trac}$	Normal tensile strength
Ø	Diameter of a reinforcing bar
$Ø_{eff}$	Real reinforcement bar diameter
$Ø_{satur}$	Saturation reinforcement bar diameter
R or r	Radius of the concrete circular section; Radius of the steel tube
R_{eH}	Upper yield strength if yield phenomenon
R_m	Tensile strength
R_p	Polarization resistance
$R_{p,\eta}$	Upper yield strength if yield phenomenon is not present
s	Wave slope
s	Slip
s	Density of the bottom material
s_{cp}	Compressive stress of concrete due to normal forces
S_d	ADV sensor depth
s_f	Free end slip
s_l	Loaded end slip
$s_{l,max}$	Displacement of the tube at the loaded end section corresponding to $F_{l,max}$
T	Wave period
T	Torsional moment
t	Time
t	Average growth thickness
t	Wall tube thickness
T_p	Average period or peak period
U	Water flow velocity in the hydraulic flume

$U_{1hour,\ 10m}$	1-hour sustained wind speed at a height of 10 m above sea level
U_c	Critical average velocity
U_r	Maximum global displacement
V	Displaced volume of the member per unit length
V	Shear force
V_{2-2}	Maximum shear stress in 2-2
V_{3-3}	Maximum shear stress in 3-3
$V_c(z)$	Total current
$V_{c,circ}$	Circulational currents
$V_{c,tide}$	Tidal currents
$V_{c,wind}$	Wind-generated currents
V_{Rd}	Shear strength
$V_{Rd,c}$	Design shear strength of the member without shear reinforcement
$V_{Rd,sl}$	Design "shear" strength of the longitudinal reinforcement
w	Wave angular frequency
x	Neutral axis depth
$Y_{CM,\ CC}$	Centroid of concrete internal forces in the section (in compression)
$Y_{CM,sc}$	Centroid of steel internal forces in the section (in compression)
$Y_{CM,st}$	Centroid of steel internal forces in the section (in tension)
Z; Z_c; Z_{sc}	Lever arm of internal forces
z	Distance from the SWL measured positively upward
u	Water horizontal velocity
v	Water vertical velocity
$\dot{u}$	Water horizontal acceleration
$\dot{v}$	Water vertical acceleration
$\overline{y_g}$	Distance from the centroid of the section to the outermost fibre
α	Exponent
α	Young's Modulus ratio
α_{cc}	Reduction factor for concrete strength, used in ULS
β	Angle of the compressed steel section
γ_c	Partial factor for concrete

δ	Steel contribution ratio
δ_{max}	Mid-span displacement at F_{max}
δ_{ult}	Ultimate mid-span displacement
$\mathcal{E}_c$	Compressive strain in the concrete
$\mathcal{E}_{c2}$	Concrete strain
$\mathcal{E}_{cu}$	Ultimate compressive strain in the concrete
$\mathcal{E}_s ; \mathcal{E}_{st} ; \mathcal{E}_{sc}$	Strain of steel reinforcement (tension or compression)
$\bar{G}_f$	Normalized energy dissipated
η	Wave profile
θ	Angle of the compressed concrete section
θ_{max}	Maximum rotation moment corresponding to M_{max}
θ_{ult}	Ultimate rotation (referring to the rupture of the specimen or the excessive deformation that led to the interruption of the test)
$\bar{I}_x$	Equivalent moment of inertia of the section
μ	Ductility factor
ξ	Iribarren number
p	Dynamic pressure
ρ or ρ_w	Water density
σ_D	sediment geometric standard deviation
σ_s	Steel stress
τ	Shear stress
τ	Bond shear stress
τ_{max}	Maximum shear stress
$\bar{\tau}_{max}$	Normalized shear strength
χ	Rotation
ψ_c	Shields coefficient
ω^2	Dispersion relationship

CHAPTER 1

INTRODUCTION

This chapter sets the background of the research, objectives, research scope, methodology, outlines of the thesis and research publications.

1.1. MOTIVATION

The ocean is the largest ecosystem in our planet. It regulates climate variability, sustains global chain and water cycle, supports economic activity and energy production, and underpins the health and well-being of billions of people. Most of the world's population lives in coastal areas and our dependence on marine ecosystem services continues to grow [1]. For centuries, the ocean was regarded as an almost inexhaustible and self-regulating component of the Earth system, capable of absorbing pressures arising from fisheries expansion, resource exploitation, agriculture, and maritime transport [2–4]. However, according to the first World Ocean Assessment, published in 2016, *'the ocean is being seriously degraded, with changes and losses in the structure, function and benefits of marine systems*' [2,5]. At the same time, global warming is emerging as a pervasive threat to the stability of ecosystems worldwide [6]. These developments highlight the urgency of advancing scientific knowledge and developing innovative approaches for the sustainable management of the ocean [1,2,5].

Humanity's connection to aquatic environments has always been profound. Oceans, seas and rivers have shaped cultural development, enabled communication and trade, and provided essential resources. However, they have also served as pathways for disease, environmental disruption and

biological invasions [7]. Until the mid-twentieth century, this relationship was largely symbiotic, as marine systems could absorb or reverse most human impacts [2,7]. In recent decades, however, rapid socio-economic development has placed unprecedented pressure on coastal zones, accelerating the degradation of water and ecological resources. The cumulative and often unregulated exploitation of these systems now threatens environmental sustainability at a planetary scale [7]. Achieving a new balance between development and environmental protection requires a revised philosophy of coastal and ocean engineering — one that integrates efficiency, safety and environmental stewardship, while explicitly accounting for the stochastic nature of marine processes and the uncertainties inherent to environmental events [7].

In recognition of these global challenges, the United Nations declared 2021–2030 the "*International Decade of Oceanography for Sustainable Development*" [7]. Under UNESCO's coordination, the initiative aims to expand scientific research, improve observation systems, strengthen capacity building, enhance maritime spatial planning and reduce risks to coastal regions [5]. Audrey Azoulay, while UN Director-General, recalled that oceans are "the most powerful regulators of climate" and warned of persistent knowledge gaps in the area. In Azoulay's words "*the ocean is a new frontier - it covers 71% of planet earth and only less than 5% has been explored*" [8]. Marine and coastal biodiversity supports over 3 billion people`s livelihood, absorbs one third of anthropogenic CO_2 and mitigates many of the impacts of climate change [2,5]. According to UNESCO Intergovernmental Oceanographic Commission (IOC) estimates, only 0.04% to 4% of general research and development investment is directed to oceanographic research [2,5]. In this scenario, UNESCO intends to strengthen and encourage research in an area with high exploration and research costs. The International Decade of Oceanography will help achieve the 14th Sustainable Development Goal, which is focused on the conservation and sustainable use of oceans, seas and marine resources [5].

In light of the alarming trajectory threatening the planet's sustainable development, developing coastal and maritime solutions that promote ecological restoration, enhance survival rates and support sustainable human activities has become imperative. Innovative marine infrastructures—including offshore wind farms, ports, and emerging concepts such as floating islands and energy islands —are receiving growing global attention.

Multifunctional artificial reefs (MFARs) stand out among these innovations, offering ecological, socio-economic and technical benefits [9–11]. Previous experience has demonstrated that these structures can offer significant ecological, socio-economic, and technical benefits [9,10,12,13]. However,

artificial reef technology face substantial challenges related to structural complexity, engineering approaches, durability, hydrodynamic behaviour, environmental interactions, operational logistics, renewable energy integration and the need for bioreceptive, resilient and environmentally friendly constructions [13–17].

1.2. OBJECTIVES AND RESEARCH METHODOLOGY

The main objective of the present work is to contribute to the development of structural systems for innovative multifunctional modular artificial reef systems capable of supporting the rehabilitation of marine ecosystems, while also enabling recreational activities, tourism, and environmental monitoring.

The design of innovative MMFARs presents significant challenges due to the need to reconcile complex geometrical configurations, modularity, material selection, and ecological objectives. Establishing a clear relationship between structural design, material properties, and the expected ecological benefits is particularly difficult, as is adopting an engineering-based approach that accounts for site-specific conditions, intended functions, and environmental variability, including long-term impacts such as climate change. Additional challenges include the lack of standardised design guidelines for artificials reefs, the necessity of ensuring environmental safety and sustainability, and the requirement for geometries that promote habitat creation and long-term durability. Addressing these challenges demands an integrated methodology that combines structural analysis, material characterization, and ecological considerations, enabling the development of MMFAR systems that are resilient, environmentally compatible, and capable of supporting both ecosystem restoration and multifunctional human use.

In order to address the current technological challenges identified, the following research questions should be answered:

- Which structural design strategies or procedures may be followed for an integrated and effective design MMFARs, considering the local implementation conditions and the design requirements?
- Which procedures may be followed to identify what is the most suitable structural systems for modular artificial reefs, considering stability, durability, hydrodynamic performance, assembling constrains, and adaptability to various marine environments?

- Is it feasible to develop and adopt efficient and reliable structural connection systems for modularity, particularly regarding the underwater assembly process and the structural performance requirements in the marine context?
- Which processes are most compatible with underwater operations, particularly when the process involves the assembly of parts and modules?
- Can the adoption of galvanized steel reinforcement contribute to cost-effective composite steel–concrete marine structures, considering short- and long-term performance and durability requirements in aggressive marine environments, as well as its effect on bonding behaviour between concrete and galvanized steel?
- Are there any particularly effective manufacturing methods and construction techniques that are best suited to fabricate MMFAR modules, envisioning simplicity, economy, versatility and sustainability?

In order to answer the research questions, specific objectives or tasks where proposed that included the following:

- Establish a systematic engineering-driven structural design methodology for geometrically complex MMFARs, demonstrated through a case study that integrates the structural system definition, site conditions, structural model and cross-sections design.
- Perform parametric and cost-effectiveness studies for structural optimisation of the studied solutions.
- Investigate new structural connection systems for MMFARs with complex geometries and evaluate their structural performance and construction feasibility through experimental studies.
- Investigate the bond behaviour between different concrete compositions and hot-dip galvanised (HDG) smooth steel tubes in composite steel–concrete structures, including the influence of mechanical connectors and steel surface conditions.
- Study the long-term bond behaviour between concrete and hot-dip galvanised (HDG) steel tubes under different environmental conditions (seawater immersion and controlled atmospheric environment), assessing the influence of bond length and exposure time (28, 90, 180, and 500 days) on bond strength.

- Investigate and construct MMFAR units, exploring the use of alternative manufacturing and construction methods, such as 3D-printed moulds.
- Characterise the MMFAR modules with respect to strength, stiffness, ductility, and failure modes, while evaluating their technical and economic feasibility.
- Assess hydrodynamic behaviour and the scour phenomenon of a small-scale artificial reef prototype on a non-cohesive sediment bed using 3D photogrammetry for accurate post-scour analysis.

The contributions of this research align directly with the priorities defined in the United Nations' 2030 Agenda for Sustainable Development [9], with relevance to Sustainable Development Goals 9, 13, and 14.

1.3. OUTLINE OF THE THESIS

The content of this work, which is presented as a collection of papers published or submitted to peer-review international journals, is organized in five chapters and appended papers, as follows:

- **Chapter 1** provides a general introduction and motivation to the research topic, describes the general objectives and overall methodology, publications, and finally presents an outline of the work developed.
- **Chapter 2**. provides a comprehensive review of artificial reef structures, covering their historical development, classification, planning methodologies and design principles. It examines the planning and design phases, addressing key criteria for project development and material selection. Additionally, the chapter delves into the structural and construction aspects of artificial reefs, categorizing them based on size and complexity added. The chapter concludes with final considerations on the future of artificial reef.
- **Chapter 3** provides a detailed examination of the fundamentals of structural design for marine structures, with a particular focus on geometrically complex artificial reefs. It addresses key topics including the parametric design process, relevant regulatory frameworks, structural design methods and analysis, and design loadings. The chapter further explores hydrodynamic loading models and durability challenges, offering a comprehensive understanding of the critical factors that influence the structural integrity and long-term performance of artificial reefs.

- **Chapter 4** presents a brief summary of the papers that constitute this PhD thesis. Four of these papers have been already published in scientific journals (Q1), while fifth has been submitted for publication, and a sixth paper has been published in the proceedings of a peer-reviewed international conference.
- **Chapter 5** summarizes the main conclusions of the developed work and presents recommendations for future work.
- **Appended Papers** are presented as:

PAPER I	Engineering-Driven Approach for the Structural Design of Geometrically Complex Modular Artificial Reefs
PAPER II	Development and characterization of structural connections for modular artificial reefs
PAPER III	Experimental characterization of bond between concrete and HDG steel tubes for mixed steel-concrete structures.
PAPER IV	Long-term effect of seawater on bond performance between HDG steel and concrete for hybrid concrete-steel marine constructions
PAPER V	Construction and characterization of a structural unit for modular artificial reefs.
PAPER VI	Experimental characterization of the scour of innovative artificial reef prototypes using hydraulic flume and photogrammetry

1.4. PUBLICATIONS

Several papers have been published in peer-reviewed ISI indexed journals or international conference proceedings in the course of the development of this research work. These publications are listed as follows:

i. International Peer-Reviewed Journals

- **Cruz F**, Valente IB, Miranda T, Pereira, EB. Long-term effect of seawater on bond performance between HDG steel and concrete for hybrid concrete-steel marine constructions [Submitted, December 2025];
- **Cruz F**, Valente IB, Miranda T, Pereira EB. Construction and characterization of a structural unit for modular artificial reefs. Structures 2025;81:110154. https://doi.org/10.1016/j.istruc.2025.110154. Impact factor: 4.3;

- **Cruz F**, Valente IB, Maslov D, Miranda T, Pereira EB. Engineering-driven approach for the structural design of geometrically complex modular artificial reefs. Appl Sci 2025;15:5907. https://doi.org/10.3390/app15115907. Impact factor: 2.5;
- **Cruz F**, Valente IB, Monteiro F, Maslov D, Miranda T, Pereira EB. Development and characterization of structural connections for modular artificial reefs. Ocean Eng 2025;320:120311. https://doi.org/10.1016/j.oceaneng.2025.120311. Impact factor: 4.6;
- Maslov D, **Cruz F**, Pinheiro M, Miranda T, Valente IB, Ferreira V, Pereira E. Functional conception of biomimetic artificial reefs using parametric design and modular construction. J Mar Sci Eng 2024;12:1682. https://doi.org/10.3390/jmse12091682. Impact factor: 2.8;
- **Cruz F**, Valente IB, Almeida J, Neves A, Pereira E. Experimental characterization of bond between concrete and HDG steel tubes for mixed steel-concrete structures. Mater Struct 2024;57:89. https://doi.org/10.1617/s11527-024-02352-8. Impact factor: 4.0;
- Maslov, D., Pereira, E., Duarte, D., Miranda, T., Ferreira, V., Tieppo, M., **Cruz, F**., Johnson, J. Numerical analysis of the flow field and cross section design implications in a multifunctional artificial reef. Ocean Eng 2023;272:113817. https://doi.org/10.1016/j.oceaneng.2023.113817. Impact factor: 5.5;

ii. International Conference proceedings

- Monteiro FB, Pereira E, Almeida J, **Cruz F**, Barajas D, Zille A, Martins MS, Miranda T. Knitted textile KTPs for instrumented underwater building systems. OCEANS 2023 MTS/IEEE Limerick. 2023. https://doi.org/10.1109/OCEANSLimerick52467.2023.10244591;
- **Cruz F**, Pereira E, Lima M, Johnson J, Duarte D, Valente IB, et al. Experimental characterization of the scour of innovative artificial reef prototypes using hydraulic flume and photogrammetry. OCEANS 2019 MTS/IEEE Marseille, IEEE; 2019, p. 1–10. https://doi.org/10.1109/OCEANSE.2019.8867581;
- Maslov D, Johnson J, Pereira E, Duarte D, Miranda T, Lima M, **Cruz F**, Valente I, Pinheiro M. Experimental testing and CFD modelling for prototype design of innovative artificial reef structures. OCEANS 2019 MTS/IEEE Marseille; 2019. p. 1–7. https://doi.org/10.1109/OCEANSE.2019.8867383;

- **Cruz F**, Pereira E, Valente IB, Tiago M, Maslov D, Pinheiro M. Structural design of an innovative multifunctional artificial reef. OCEANS 2018 MTS/IEEE Charleston, Charleston: IEEE; 2018, p. 1–7. https://doi.org/10.1109/OCEANS.2018.8604587;
- Maslov D, Pereira E, Miranda T, Valente M, **Cruz F**, Pinheiro M. Innovative monitoring strategies for multifunctional artificial reefs. OCEANS 2018 MTS/IEEE Charleston. 2018:1–8. https://doi.org/10.1109/OCEANS.2018.8604656;

iii. Posters and Bulletins

- **Cruz F**, Pereira E, Valente IB, Tiago M, Maslov D, Pinheiro M. Structural design of an innovative multifunctional artificial reef. OCEANS 2018 MTS/IEEE Charleston, Charleston: IEEE; 2018, p. 1–7. https://doi.org/10.1109/OCEANS.2018.8604587;
- Maslov D., Johnson J, Pereira E, Duarte D, Miranda T, Lima MMCL, Valente IB, **Cruz F,** Pinheiro M. "Study on laminar and turbulent openfoam flow solvers based on hydraulic flumes test with artificial reef prototype experimental data". In 3rd FOAM@Iberia Meeting, Porto, Portugal, 11-12 June 2018, pp 33;

1.5. REFERENCES

[1] Pörtner HO, Roberts DC, Masson-Delmotte V, Zhai P, Tignor M, Poloczanska E, et al., editors. The Ocean and Cryosphere in a Changing Climate. Cambridge, UK: Cambridge University Press; 2019.

[2] Valdés L. Global Ocean Science Report: The Current Status of Ocean Science Around the World. Paris, France: UNESCO Publishing; 2017.

[3] European Commission. Marine Strategy Framework Directive. 2018.

[4] Commission of the European Communities. Thematic Strategy on the Protection and Conservation of the Marine Environment. Brussels, Belgium; 2005

[5] UNESCO. United Nations Decade of Ocean Science for Sustainable Development (2021-2030) 2017. Paris, France: UNESCO; 2017.

[6] Kerry JT, Baird AH, Connolly SR, Dietzel A, Eakin CM, Heron SF, et al. Global warming transforms coral reef assemblages. Nature 2018;556:492–496. https://doi.org/10.1038/s41586-018-0041-2.

[7] Kim YC, editor. Handbook of Coastal and Ocean Engineering. Singapore: World Scientific; 2010.

[8] UNESCO. Sustainable Development Goals 2017. https://www.un.org/sustainabledevelopment/sustainable-development-goals/.

[9] Ng K, Phillips MR, Calado H, Borges P, Veloso-Gomes F. Seeking harmony in coastal development for small islands: Exploring multifunctional artificial reefs for São Miguel Island, the Azores. Appl Geogr 2013;44:99–111. https://doi.org/10.1016/j.apgeog.2013.07.013.

[10] López I, Tinoco H, Aragonés L, García-Barba J. The multifunctional artificial reef and its role in the defence of the Mediterranean coast. Sci Total Environ 2016;550:910–923. https://doi.org/10.1016/j.scitotenv.2016.01.180.

[11] Ng K, Thomas T, Phillips MR, Calado H, Borges P, Veloso-Gomes F. Multifunctional artificial reefs for small islands: An evaluation of amenity and opportunity for São Miguel Island, the Azores. Prog Phys Geogr 2015;39:220–257. https://doi.org/10.1177/0309133314567581.

[12] Dafforn KA, Glasby TM, Airoldi L, Rivero NK, Mayer-Pinto M, Johnston EL, et al. Marine urbanization: An ecological framework for designing multifunctional artificial structures. Front Ecol Environ 2015;13:82–90. https://doi.org/10.1890/140050.

[13] Lee MO, Otake S, Kim JK. Transition of artificial reefs (ARs) research and its prospects. Ocean Coast Manag 2018;154:55–65. https://doi.org/10.1016/j.ocecoaman.2018.01.010.

[14] Broomfield JP. Chapter 9 Galvanized Steel Reinforcement in Concrete: A Consultant's Perspective. 2004.

[15] Reeds KA, Smith JA, Suthers IM, Johnston EL. An ecological halo surrounding a large offshore artificial reef: Sediments, infauna, and fish foraging. Mar Environ Res 2018;141:30–38. https://doi.org/10.1016/j.marenvres.2018.07.011.

[16] Mendonça A, Neves MG, Fortes CJ, Carmo JSA, Moura T. Hydrodynamics around an artificial surfing reef at Leirosa, Portugal. J Waterw Port Coast Ocean Eng 2012;138:226–235. https://doi.org/10.1061/(ASCE)WW.1943-5460.0000128.

[17] Soon C, Ng L, Chou LM. Artificial reefs as a reef restoration strategy in sediment-affected environments: Insights from long-term monitoring. Aquat Conserv Mar Freshw Ecosyst 2017;27:976–985. https://doi.org/10.1002/aqc.2755.

CHAPTER 2

ARTIFICIAL REEFS: DESIGN, MATERIALS AND APPLICATIONS

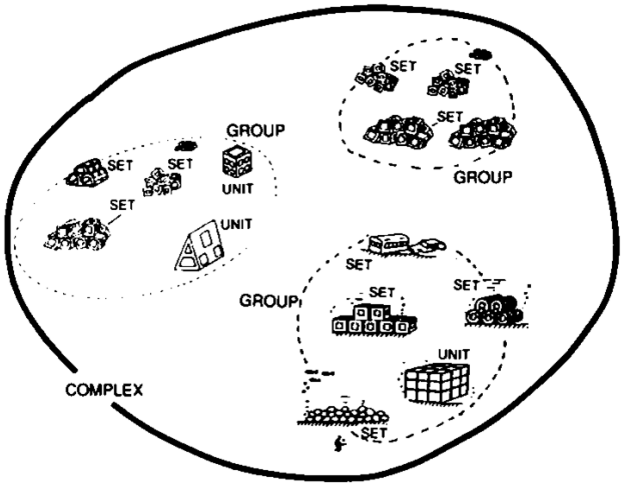
This chapter analyses the literature on artificial reef (AR) structures, addressing their historical evolution, planning, design, materials used and construction techniques, and regulatory aspects. It discusses the importance of ARs in coastal and environmental engineering, highlighting their role in marine conservation, biodiversity enhancement, and sustainable ocean management. Despite being conceptually introduced as early as 1640, ARs have seen significant technological and functional advancements in the past 30 years. The increasing need for multifunctional and adaptive solutions has led to a surge in research and governmental initiatives promoting AR deployments as a marine protection strategy. The chapter covers the classification of ARs into single-purpose and multifunctional structures, analysing their design criteria, geometry, and material selection. Additionally, it reviews the regulatory framework governing AR implementation and the planning phases required for effective deployment. A special focus is given to the materials and structural system types used in AR constructions, discussing their durability, structural performance, and environmental impact.

2.1. DEFINING ARTIFICIAL REEFS

There are numerous factors influencing the definition of an AR, including social, cultural, economic, environmental and regional. However, a generic and unambiguous definition is generally adopted by several scientific conventions, protocols and guidelines [1–6]:

"*An artificial reef is a submerged structure deliberately constructed or placed on the seabed to emulate some functions of a natural reef such as protecting, regenerating, concentrating, and/or enhancing populations of living marine resources. Objectives of an artificial reef may also include the protection, restoration and regeneration of aquatic habitats, and the promotion of research, recreational opportunities, and educational use of the area. The term does not include submerged structures deliberately placed to perform functions not related to those of a natural reef - such as breakwaters, mooring, cables, pipelines, marine research devices or platforms - even if they incidentally imitate some functions of a natural reef*".

Alternatively, Bohnsack and Sutherland (1985) propose a classification system that categorises ARs according to their location in the water column, namely as bottom, mid-water or surface AR. In this case, the authors integrate the oil and gas rigs and oceanic installations in a fourth category, since they exhibit similar characteristics to the reef categories mentioned above [7]. **Figure 2.1** shows the standard terminology adopted to distinguish the different components of an AR [8].



Reef unit or module - *the smallest element of an AR. The units can be placed individually on the seabed or assembled*;

Reef set - *structure composed by several assembled reef units;*

Reef group - *area with a group of modules and/or reef sets;*

Reef complex – *two or more reef groups.*

Figure 2.1: AR components hierarchy [8].

2.2. SINGLE-PURPOSE AND MULTIFUNCTIONAL ARTIFICIAL REEFS

Artificial reefs are increasingly recognised as an essential component of coastal engineering and ecosystem restoration plans to mitigate the impacts of human activities. It is globally accepted that they are very attractive systems and can generate ecological, socioeconomic and technical benefits [7,9–11]. As a globally utilized engineering technology, AR serve diverse marine management purposes [1–4,6,12], such as:

(i) protecting sensitive habitats from fishing activities;

(ii) restoring depleted habitats;

(iii) mitigating habitat loss;

(iv) enhancing biodiversity;

(v) improving populations of aquatic organisms by providing shelter for juvenile and immature individuals, as well as for adults during delicate life stages (e.g. moulting season for crustaceans);

(vi) providing new substrates for algae and mollusc culture;

(vii) absorption of excess organic matter produced by aquaculture, thereby reducing the environmental impact of this activity;

(viii) enhancing professional and recreational fisheries;

(ix) providing a mean to manage coastal activities and reduce conflicts;

(x) research and educational activities, such as diving;

(xi) creating potential networks of marine protected areas (MPA) to manage the life cycles of fish.

Initially, the implementation of AR was oriented towards a single purpose, namely the provision of substrates that facilitated the rapid development of marine biota. Consequently, they were used to diversify marine fauna and enhance fisheries by attracting and concentrating wildlife. In some cases, they were built to improve spawning conditions and protect juvenile populations [7,11]. Some have also been used to reduce shoreline erosion, avoid trawling in certain areas, restrict sea lanes, reduce fishing pressure, mitigate the negative impacts of certain activities on habitats or for recreational use [7,10]. Thus, considering the function-specific criteria, single-purpose AR can be divided into four categories: (1) protection, (2) production, (3) recreational and (4) restoration ARs [3].

In recent years, there has been an increased interest in multifunctional artificial reefs (MFAR), which aim to serve multiple purposes simultaneously [11,13]. These reefs can also adopt a modular construction approach (MMFAR). This enables the optimisation of benefits and the minimisation of costs associated with their development and construction, with the integration of expertise from a variety of disciplines, including engineering, biology, ecology, economics and sociology [3,11,13]. To date, there are few examples of objectively and fully designed multifunctional systems that meet current needs and future challenges [10,11]. Its main features may include the possibility of simultaneous rehabilitation and restoration of marine ecosystems in areas damaged by natural and

anthropogenic factors, habitat protection, coastal protection, energy production, support for recreational activities and environmental monitoring [11,13–16].

In the future, the development of AR is expected to evolve from a multifunctional perspective [11]. According to the UN Food and Agriculture Organization (FAO), coastal countries should invest in this technology to better conserve and exploit marine resources. Most countries should therefore be actively using at least some of the functions of ARs.

2.3. HISTORICAL PERSPECTIVE

ARs date back to the 1550s, when Mediterranean fishermen unintentionally created habitats by leaving behind rocks used to anchor tuna nets [11]. Similar practices emerged worldwide, namely in Japan in the 1640s. In the USA, the earliest records date back to 1880, when fishermen repurposed sunken huts as fishing reefs [11].

- **Development of Modern Artificial Reefs**

The modern concept of AR appeared in Japan, during the early 20th century, and later spread to the USA and Europe [7,11,17]. Japan invested heavily in research and development, creating sophisticated reef structures, while in the USA, early ARs were largely community driven, built with scrap materials and minimal government funding. The introduction of the National Artificial Reef Plan in 1985 marked a turning point, leading to more systematic development in USA. In Europe, ARs were not widely used until the second half of the 20th century (e.g. 1950) [2,7,11,18].

- **Artificial Reef Development by Region**

Japan's ARs were engineered using durable, prefabricated materials and strategically placed in both shallow and deep waters for commercial purposes [7]. In 1976, the government launched a six-year improvement plan, investing $250 million in reef projects, including $65.2 million for research. A second six-year plan, initiated in 1982, doubled the funding, solidifying Japan's status as a global leader in AR technology [11].

In the USA, most reefs were built by private organizations, local governments, or individuals on limited budgets, primarily for recreational fishing [7]. The first designed ARs were constructed in the Gulf of Mexico in 1954, followed by a pilot monitoring program in Southern California [11].

In Europe, ARs are primarily found in four regions: the Mediterranean Sea, the Black Sea, the Baltic Sea and the OSPAR Maritime Area (including the Arctic Waters, the Greater North Sea, the Celtic Seas, the Bay of Biscay and the Iberian Coast, and the Wider Atlantic) [1,2]. Initially, ARs projects were localised and lacked national or international coordination [9]. This changed in 1991 when Italian scientists formed a national AR group, followed by Spain in 1998, leading to the creation of the Association of Mediterranean Artificial Reef Scientists. In 1995, the European Artificial Reef Research Network (EARRN) was established under the European Commission's Agriculture and Agro-Industrial Research (AIR) Programme, to promote scientific collaboration [9].

The Mediterranean Sea hosts the highest concentration of ARs, primarily used for fisheries management and preventing illegal trawling [18]. Monaco pioneered ARs for marine conservation in the late 1960s [9]. Since then, ARs have been officially licensed and deployed in multiple European countries, including Finland, France, Greece, Spain, Italy, Portugal, Malta, Poland, Israel, Romania, and the UK [9]. Norway has shown particular interest in the rigs-to-reefs concept, repurposing decommissioned oil rigs as ARs [9].

In Portugal, AR development began in 1989 [11]. Notable projects include multifunctional reefs in São Miguel, Azores [15,19], studies on the biological colonization of the Aguda coastal protection structure [20,21], the Nazaré AR [22], the Faro/Antão AR [23], and the artificial surfing reef at Leirosa [16].

Over the years, knowledge has been disseminated, and the AR technology has been successfully applied on Asia, with the installation of ARs in several countries between 1970 and 1991 like China, Thailand, Korea, Malaysia, Singapore, Philippines and Cambodia as well as in Australia in Port Phillip Bay in 1965 [11].

The construction of ARs has been a pervasive phenomenon at a global scale, with a multitude of objectives being pursued, ranging from the attraction and facilitation of fish capture to the promotion of tourism. **Figure 2.2** presents a general location of ARs around the world (a) and in Europe (b).

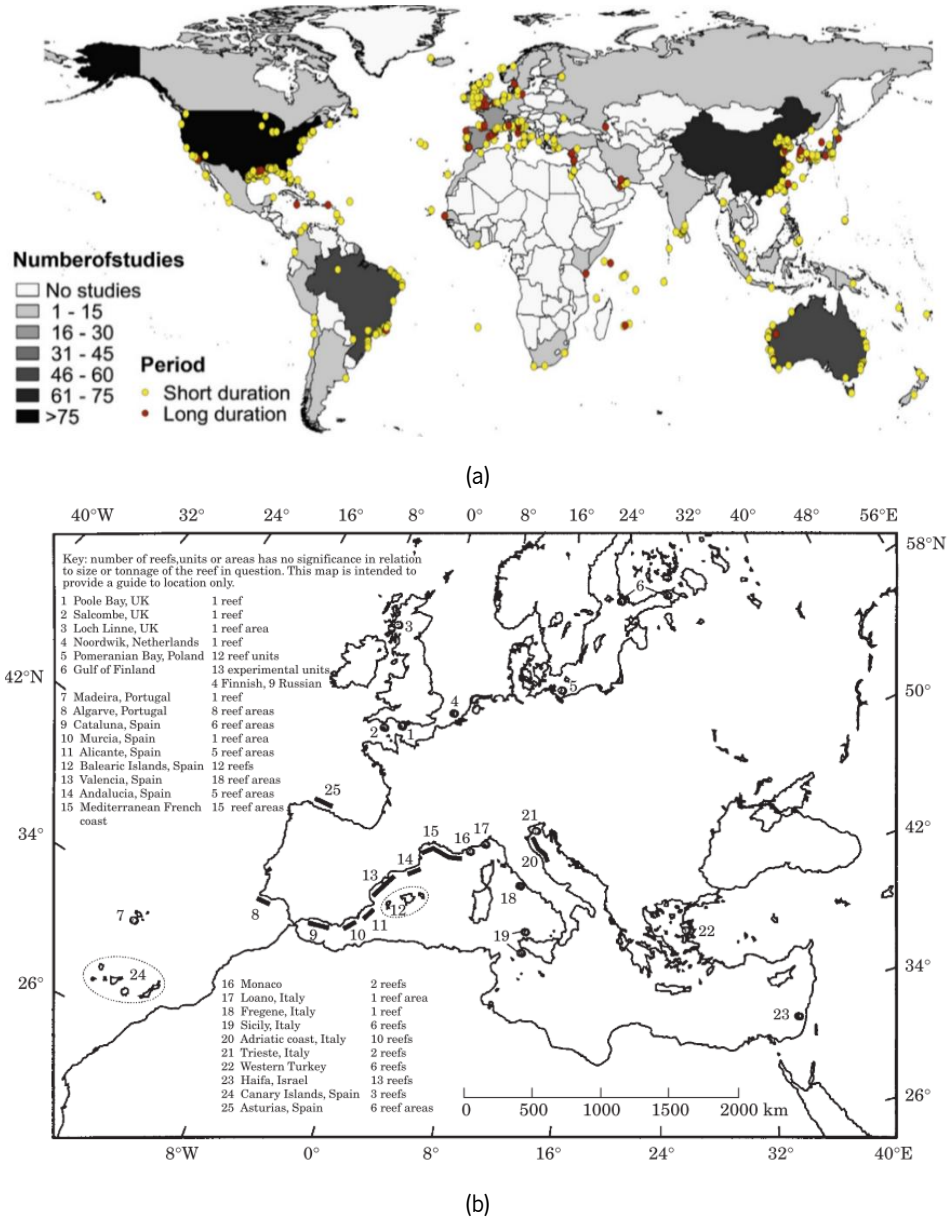


Figure 2.2: General location of ARs in (a) World [24] and (b) Europe [9].

In addition to these developments, there has been a significant increase in the number of research publications dealing with the subject of marine ARs. A recent study deepened the analysis of reef studies between 1996 and 2024, revealing a marked increase in global development and research efforts directed towards advancing the field of AR research, as illustrated in **Figure 2.3** [25]. The research underscores the importance of collaborative work endeavours among countries to ensure the effective integration of ARs in the preservation of marine ecosystems and the sustainable utilisation of ocean resources [25].

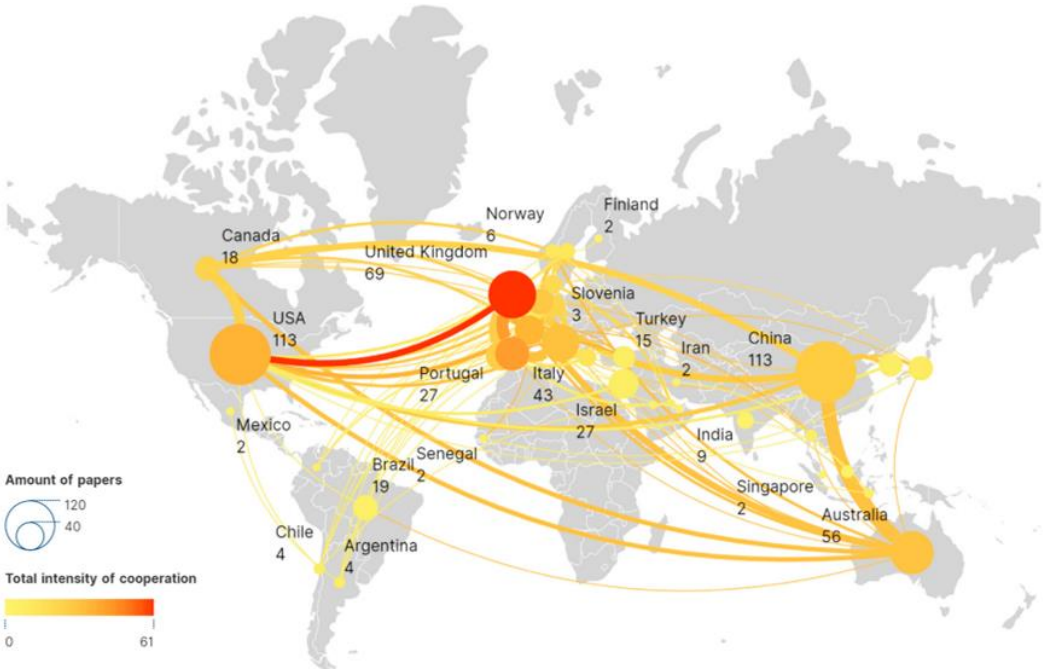


Figure 2.3 - Global distribution of artificial marine reef research. The size of each circle represents the number of papers published by each country, with larger circles indicating greater research output. Only countries with at least two publications are marked. The gradient colours show the strength of collaboration between countries, with thicker, darker lines (dark orange) indicating stronger cooperation and thinner, lighter lines (yellow) indicating weaker collaboration. The colour gradient reflects collaboration strength, ranging from low to high (0 to 61), from [25].

2.4. REGULATIONS ON ARTIFICIAL REEFS

The interest in AR technology has become increasingly common in various parts of the world due to its benefits. However, due to the potential environmental impacts that these reefs may cause, there are a number of regulations and guidelines in place to ensure their ecological safety and effectiveness. As part of these regulatory efforts, the development and placement of artificial reefs is covered by several national and international marine environmental conventions, including the Conventions of London, of OSPAR, of Barcelona, of Helsinki, of Basel and of Bucharest. These conventions have also developed specific guidelines for the construction and management of ARs. **Table 2.1** highlights some of the key regulations on ARs.

Table 2.1: Examples of regulations covering or influencing ARs design.

Name	Year	Promoter
Marine Strategy Framework Directive 2008/56/EC;	2025	UN
Updated Guidelines Regulating the Placement of Artificial Reefs at Sea;	2019	
Practical Guidelines for the use of artificial reefs in the Mediterranean and the Black sea (amended);	2019	
Guidelines on Artificial Reefs in relation to Living Marine Resources;		
Assessment of construction or placement of artificial reefs;	2013	
Guidelines for the Placement of Artificial Reefs;		
Methodological Guidelines for Artificial Reefs Placement (Spain);	2009	
Marine Works (Environmental Impact Assessment) Regulations (UK);	2009	
Guidelines for the placement at sea of matter for purpose other than the Mere disposal (construction of	2008	
artificial reefs);	2005	
Basic Policy on the Improvement of Fishing Ports and Fishing	2022	Japan
Grounds (amended);		
Guideline for Designing Artificial Reefs (amended);	2017	
Standards for Planning for the Improvement of Artificial Reefs;	2000	
Regulations for the Evaluation of Artificial Reef Project;	1999	
Guidelines for the Artificial Reefs with Obsolete Ship and Vessels;	1982	
Fishing Ports and Fishing Grounds Improvement Law;	1950	
Coastal Artificial Reef Planning Guide;	1998	USA
Guidelines for Marine Artificial Reef Materials. 2nd Ed	2005	
National Artificial Reef Plan: Guidelines for Siting, Construction, Development, and Assessment of	2007	
Artificial Reefs;	2011	
Guidelines and management practices for artificial reef siting, use, construction, and anchoring in	2013	
Southeast Florida;	2009	
A Guide to Fishing and Diving New Jersey Reefs (amended)		
Environment Protection and Biodiversity Conservation Act 1999 *(amended)*;	2024	Australia
National artificial reef guidelines	2023	
Environment Protection (Sea Dumping) Act 1981 (amended)	2016	
Sea Installations Act 1987 *(amended)*	2014	
National regulation on construction and management of artificial reefs, 1988 (amended);	2004	South Korea
Canadian Environmental Protection Act, 1999 (amended);	2023	Canada
Clean-Up Guideline for Ocean Disposal of Vessels;	2011	

2.5. PLANNING PHASES

The successful construction of an AR is determined by the planning of its pre-construction, construction and post-construction phases [3]. This process must consider the effective cooperation between numerous maritime stakeholders and does not end with its placement at sea. It's therefore

crucial to have a management plan that accurately describes aspects such as the objectives and functions of the reef, its target users, its pre-installation planning, its lifelong management, the methods that can be used to evaluate its effectiveness and environmental impact, and the measures that can be taken to minimise its negative environmental impact [3,4,26].

Pre-construction is defined as the set of activities carried out prior to the construction of the structure. At this stage, the interest in building is assumed and presented to the competent authorities. The objectives of the project are identified and the ecosystem in which the structure will be implemented is evaluated, taking into account the short and long term positive and negative impacts (for ARs, approximately 30 years timespan is considered reasonable). Alternative ideas and solutions are developed, analysed and discussed to enhance the main objectives and mitigate the potential negative impacts of the structure. According to the "Practical guidelines for the use of ARs in the Mediterranean and the Black Sea: studies and reviews", the following questions need to be considered before making any commitment to the planning and development of ARs [2,3,27]:

a) "**Is the concept of the AR realistic**?" Aimed at addressing if the construction of an AR is valid and feasible in a particular area.

b) "**How will the new reef and the natural ecosystem interact**?" Anticipating the impact of the new AR on the ecosystem and ecological processes before implementation. It involves assessing local, social, and economic conditions, engaging potential users, setting goals, and calculating investment and ecological/social return periods to evaluate reef performance.

c) "**What are the potential alternatives to reefs construction which may produce similar environmental, social and economic outcomes? What would be the likely situation if the reefs were not built?** To assess whether the AR is an effective alternative to other solutions.

This phase will allow to identify the location of the structure and proceed with its geometric and structural development. Site selection should consider the physical characteristics of the proposed site (depth, sea floor properties, currents, wave characteristics), the marine ecosystem (distribution, feeding, reproduction) and the purpose of the reef [3]. Thereby, it is important to obtain a complete environmental and biological characterization of the prospective location [26]. It is also important to select the correct materials to prevent marine pollution, and to develop the design of the AR based on

technical and ecological specifications. Ensuring the structural integrity of the reef units is critical, as an unstable structure will not perform as expected.

The **construction phase** includes all activities related to construction and deployment at sea. The areas for storage, preparation, loading and installation must be clearly identified and easily accessible by land and sea. The assembly and/or deployment area must be demarcated and signalled by buoys to avoid hazards to navigation and other marine activities. The competent maritime and judicial authorities must be informed of the location and time of the work development. After completion of the installation works, the final position and orientation of the structure, as well as the minimum navigation depths at the lowest astrological tide (LAT) shall be verified by direct (e.g. divers) and indirect (e.g. side-scan sonar or multibeam echosounder) techniques. National and regional hydrographic authorities should be informed of the characteristics of the artificial structure (e.g. location, geometry, safe navigation depth) in order to update the navigational charts (e.g. warning to mariners) [2,3,27].

The **post-construction** phase concerns the management and monitoring of the reef over its lifetime. To optimise the benefits of reefs to all users and reduce conflicts between them, it is essential to regularly evaluate the effectiveness of the structure through a scientific monitoring and management programme [3,26]. Monitoring can be carried out by direct observation, cabled cameras, remotely operated vehicles with cameras and/or remote sensing. Environmental, biological and structural monitoring will allow the performance of the AR to be assessed in terms of structural, ecological and socio-economic performance. In addition, monitoring will allow for the assessment of the cost effectiveness of AR construction and maintenance, thus allowing for future improvements in AR development methods and technology [2,3,27].

2.6. DESIGN CRITERIA

The design of an AR is essential and should occur in the pre-construction phase, as it establishes the foundation for the reef's success. A well-planned design is driven by the reef's specific goals, ensuring the best cost-benefit relationship while addressing technical, environmental, and economic considerations [28]. The design must consider general and specific criteria, all of which must align with the reef's intended purpose and the oceanographic conditions at the site, as outlined next. Legal and technical criteria are fundamental, as they provide the framework for meeting regulatory

requirements, aligning with national legislation and international obligations, while optimizing the reef's functionality and environmental compatibility based on technical aspects.

One of the most important aspects of the AR planning process is the design, which includes selecting materials and defining the structural system for a certain location. These factors ensure the reef achieves its objectives while being technically, economically, and environmentally adequate. **Figure 2.4** illustrates the main project design considerations according to the guidelines presented in section **2.4**.

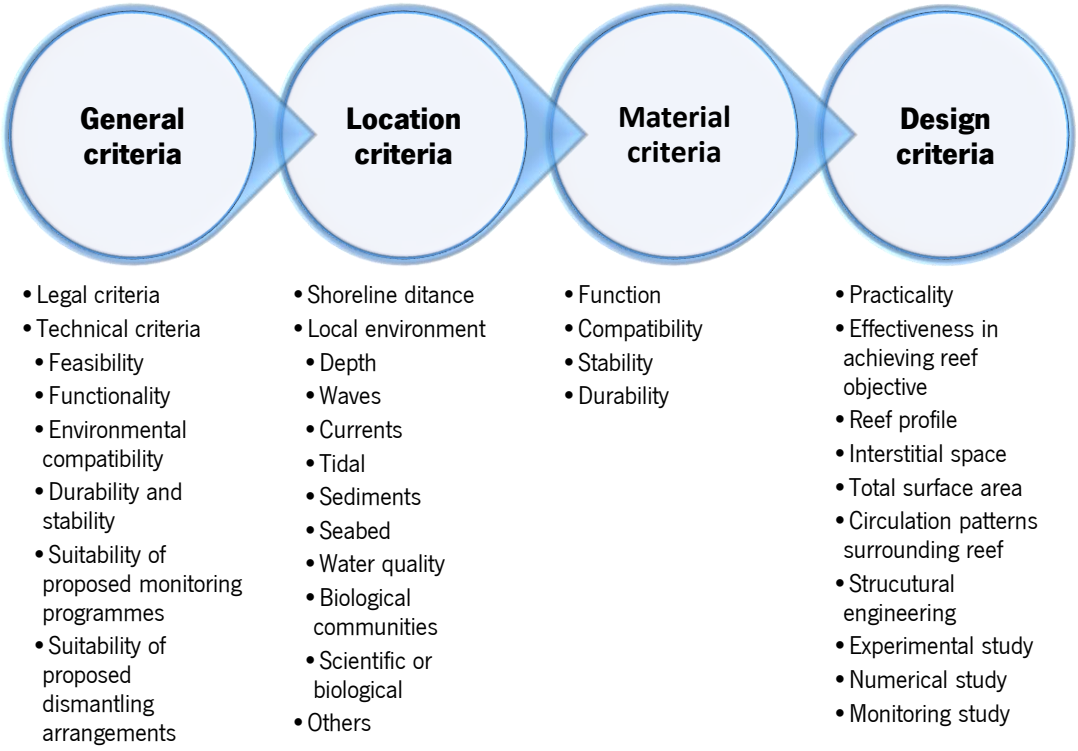


Figure 2.4: Project design criteria scheme, adapted from [6,26].

2.7. MATERIALS

The construction of ARs involves the strategic selection of materials to foster biodiversity and ecosystem stability. To facilitate effective biotic development, these structures must be composed of stable, durable and environmentally suitable materials [14]. It is imperative to utilise inert materials, defined as those that do not pollute the environment through leaching, physical or chemical weathering, or adverse biological activity [1]. Materials that are susceptible to breakage or that contain toxic substances such as fats, oils or chemicals, including tributyltin, a component of anti-fouling

paints, should not be used in the construction of ARs [29]. The materials intended to be used in the construction of the structure must be inspected and approved prior to the installation [29]. The cost-effectiveness of materials should also be considered.

A variety of materials have been utilised in the construction of ARs, encompassing both natural and synthetic. Natural materials include wood, shells and rocks, the latter being the most durable. These materials are usually scattered or stacked on the seabed or even incorporated into structural frames. The most widely used artificial material on a global scale is concrete, due to its versatility, cost-effectiveness, and suitability as one of the preferred materials for use as a colonization substrate [1–3], as illustrated in **Figure 2.5** and **Figure 2.6**. Other materials commonly used include iron, steel, plastics [1,3,30] and waste materials. Additionally, materials such as fibreglass, wood, ceramics, ferro-cement, and electrodeposition of elements naturally found in seawater have also been employed in AR construction [31]. However, some studies have shown problems with the use of wood, fibreglass and rubber tires [32]. According to Soon et al (2017), fibreglass is much lighter and easy to transport and deploy, however it has a shorter lifetime (≈ 20 years) and requires more frequent structural integrity evaluations when compared to concrete [14].

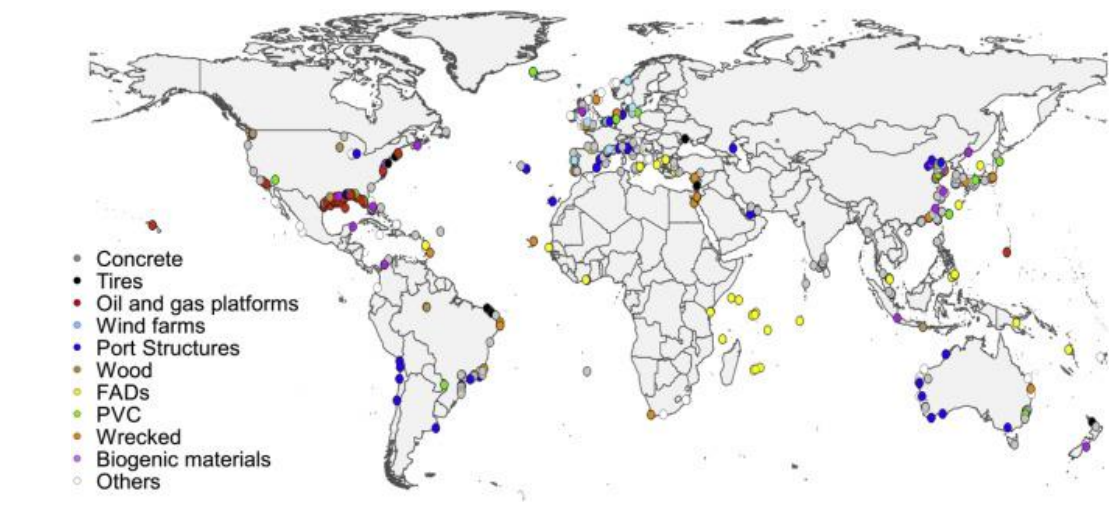


Figure 2.5: Geographic distribution of research studies categorized by the materials employed in ARs development [24].

Waste materials such as decommissioned ships, aircrafts, old vehicles, railway tracks, tires, demolition debris, and obsolete offshore platform components continue to serve as structures of opportunity for ARs (**Figure 2.5** and **Figure 2.6**) [2,3,33,34]. Some of these, while generally inexpensive and abundant, have been found to gradually deteriorate and cause water pollution, particularly in the case of rubber tires. A significant example is the disaster at Osborne Reef, where millions of tyres

deteriorated on the seabed [32]. Due to the potential environmental risks of waste materials, Mediterranean and Black Sea countries strictly regulate their use through national legislation in accordance with international conventions and protocols to prevent dumping at sea [2,11,31]. According to the OSPAR Convention, materials classified as waste or otherwise prohibited for sea disposal (e.g tires, asbestos) must not be used in the construction of artificial reefs [2, 28]. Prefabricated ARs may incorporate waste-derived materials, such as coal ash or ash from incinerator mixed with cement; however, their use must be evaluated in accordance with the "Revised Specific Guidelines for Assessment of Inert, Inorganic Geological Material" established under the London Convention [6].

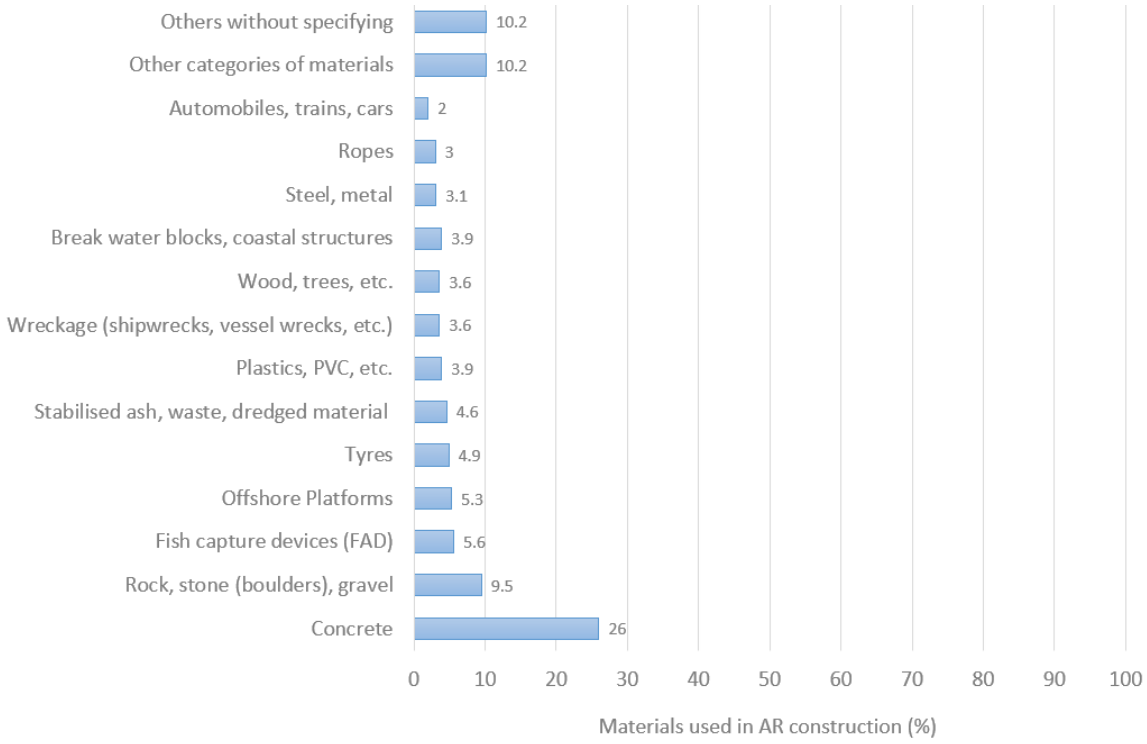


Figure 2.6: Materials used in AR construction, adapted from [35].

Furthermore, it is important to consider the mechanical resistance and durability requirements of materials when subjected to the highly aggressive marine environment, which poses unique challenges due to its chemical and physical action. Stable and suitable materials with a minimum durability of 30 years should be selected for the structure [3,14]. The OSPAR Commission recommends that the specific weight of the materials should be at least twice the one of seawater, therefore requiring the use of bulky materials. In cases when such materials are not viable for the construction of the reef, the structures must be securely anchored to the seabed [1,2].

The texture of the materials also plays a crucial role in their proneness to biotic colonisation. In shallow waters, the presence of rough surfaces or cavities facilitates the settlement of reef organisms, although in deep waters this is less significant [6]. Different materials may be better suited to specific communities of benthic organisms. These benthic organisms will, in turn, attract and enable the local colonisation of particular species of fish. [3]. Rough surface texture has already been identified as relevant for promoting colonization [3]. Fitzhardinge and Bailey-Brock (1989) investigated the development of benthic communities on coral rock and on materials commonly used in AR construction—such as concrete, painted metal, and car tires—at two sites off Oahu (Kaneohe Bay and Kahala, Hawaii). Their study showed that both concrete and coral rock, characterized by irregular and rough surfaces, supported higher levels of colonization [36]. In contrast, the smoother surfaces of metal and tire plates exhibited lower colonization rates [36]. These findings suggest that substrate texture plays a key role in benthic community development, and that concrete is an appropriate material for AR construction due to its surface roughness and similarity to natural coral substrates [36,37]. In another study, Bombace et al. (1997) also observed greater abundance of benthic species in concrete and plywood when compared to fibreglass or aluminium [37].

In recent years, sustainability has become a key priority in the construction sector, driving the search for eco-efficient materials [38]. Considering that concrete remains the most widely used material, research on ARs has increasingly focused on developing alternative binders and aggregates that minimize environmental impact while maintaining or enhancing bioreceptive and structural performance [38,39]. Numerous studies have investigated the use of low-clinker or alternative binders, as well as the replacement of natural aggregates with recycled materials or industrial by-products [40–42]. Materials such as fluorogypsum, steel and blast furnace slag concrete, and sulphoaluminate cement have demonstrated promising results for AR applications [41,43,44]. Moreover, innovative binder systems combining geopolymer and cement-based matrices with recycled sands have been explored to improve durability, compatibility with marine environments, and the overall sustainability of AR structures [38,45]. In addition, other studies have proposed a concrete composition incorporating sulphoaluminate cement, marine sand, and seawater, demonstrating improved workability, mechanical performance, and compatibility with the marine environment compared to conventional concrete, thus confirming its feasibility for artificial reef applications [46].

2.8. STRUCTURES AND CONSTRUCTION

The growing interest in artificial reefs has triggered the development of several reef units of different shapes, sizes, weights, spatial heterogeneity and configurations [3,6]. Reef units range from simple stone or prismatic blocks placed on the seabed to sophisticated and modular structures designed in complex three-dimensional spatial networks [7,9,14,37,47,48]. Most of the units are designed to provide a good water recirculation, current diversion and creating upwelling to enhance marine colonization [49,50]. It should be noted that the surface and geometry complexity of the AR structure results in a higher diversity of marine life [6,51]. In addition, the stability and durability of the structure depends, among other things, on the relationship between shape, size, weight, profile, surface area and type of seabed [52]. In general, the ARs were deployed at depths of 10 to 35 m [53,54]. This section is dedicated to the analysis of structural systems and construction processes most recently adopted in the development of artificial reefs, organising the discussion according to their gradual evolution in terms of both scale and complexity. It examines the challenges that have emerged over time, initially focusing primarily on scale, and later on the geometric and complexity-related characteristics of individual units, niches, or AR clusters developed up to the present day.

2.8.1. Small-scale

Small-scale ARs are defined here by their simplicity, compact size (up to approximately 3 meters) and ease of deployment. Despite that, these structures can fulfil diverse ecological and management purposes. **Figure 2.7** presents examples of low-complexity and small-scale AR structures, encompassing artificial cavities in intertidal rocks, modular units with diverse geometries (e.g., prisms, domes), and “small” structures of opportunity such as sunken tanks, tires, and vehicles [14,18,55]. In general, the reef modules are usually individually produced on land using moulded concrete and then transported by water to the deployment area, allowing for adaptation to local conditions [49].

Waste-based structures of opportunity, including obsolete vessels and vehicles, are still employed under strict legal control to avoid sea dumping with hydrocarbons, anti-fouling and heavy metal pollutants [7,11,30,56,57]. The dismantling and cleaning of these structures of opportunity significantly increase costs. The tyre reefs have been shown to release toxic pollutants and metal fragments, leading to contamination and consequently to reduced biological colonization and a short lifespan of only about three years [3,58,59].



Variable size and weight
Natural rock
Dredged rocks, USA [60]



9.27×3.63×2.74 m ; 52 tons
Steel
Sunken tank M60, USA [61]



2 million of tires
Rubber
Osborne tyre reef, USA [30]



0.25-0.33×0.66-0.91 m ; 73 - 209 kg
Concrete
Cube module [62]



1×1×0.25 m
Reinforced concrete
Octo-reefs, Turkey [63]



1×1×1 m
Concrete
Cubic prism, Thailand [64]



4000 blocks (×30 groups); 6000 tons
Concrete blocks: ≈ 0.39 ×0.20×0.20 m
Concrete with coal-ash and quarry dust
Block, France [1]



≈2 to 6 m ;
Steel

Biorock, Indonesia [65]



≈2.0×1.6 m ;
Concretre and steel

Tecnoreef™ modules, Italy [66]



2.4 m (height) ;
Concrete and steel
Kheops [3]



2×2×2 m ; 10.4 m³
Reinforced concrete
Comin, France [67]



2.4×2.4×1.6 m; 5.5 tons
Reinforced concrete, steel and PVC
Anti-trawling module, Spain [1]



≈0.46×0.30 m ; 18-27 kg , 0.012 m^3
≈1.83×1.46 m ; 1818-2727 kg , 0.99 m^3
Fibre reinforced marine concrete
ReefBall, Curacao [68]



500 underwater sculptures over
420 m^2; 120 tons
Concrete, stainless steel and basalt
MUSA, Mexico [69]



0.70×0.50 m ;
18-27 kg
Fibreglass and calcium carbonate
REU, Singapore [14]

Figure 2.7: Types and characteristics of small-scale and low-complexity ARs structures.

For example, Biorock® technology employs submerged steel frameworks through which low-voltage direct currents stimulate mineral deposition, accelerating coral growth and enhancing local biodiversity [70,71]. Similarly, concrete units such as ReefBall™ (with approximately 750 000 units installed in the oceans as part of 5 000 projects across 70 countries) [72] or Tecnoreef™ plates have been deployed worldwide for ecosystem restoration [66], promoting fish aggregation and stabilizing sediments in shallow waters [73]. However, localized settlement and scour were observed within a few months after construction [73], highlighting the importance of considering hydrodynamic interactions between the modules and the seabed.

In contrast, anti-trawling reefs are specifically designed to deter illegal fishing rather than enhance colonization [1,53]. They consist of compact, plain concrete blocks with protruding steel girders and cross-shaped bases, deployed over long stretches of seabed to prevent bottom trawling [1,53]. Studies using side-scan sonar to monitor the structural and functional quality of ARs have demonstrated that these units can rapidly reduce illegal fishing pressure and provide opportunities for ecological settlement when appropriate [1].

Small modules facilitate large-scale production and cost-effectiveness [64]. Nevertheless, despite their measurable ecological and social benefits, such structures lack the large-scale morphological complexity and natural aesthetics of coral reefs, which may constrain their capacity to support diverse marine communities and limit their appeal for tourism-oriented initiatives [25]. Recognizing these limitations, the technology of ARs has evolved substantially over the past two decades, as growing interest from government agencies and public–private partnerships has driven the design and construction of larger and more geometrically complex structures, thereby requiring the adoption of engineering-based approaches from the earliest design stages.

2.8.2. Complexity-added

The development of increasingly complex structures has significantly transformed AR technology. This transformation has been fuelled by advances in fabrication techniques and the enhanced capabilities of digital and parametric 3D design tools. Research findings indicate a growing trend towards the utilisation of modular systems, eco-friendly materials and 3D printing technologies [25,74], as shown in **Figure 2.8**.

Reflecting these technological advancements, several units were developed and deployed, including the fish cave, fish box, abalone habitat, Arabic marine pyramid, and lobster habitat reefs modules (**Figure 2.8**) [75,76]. According to the designer, these AR modules, constructed from steel or reinforced concrete, were specifically engineered to withstand local wave, current, and sediment conditions, including cyclonic events, with an expected service life of at least 40 years [75]. These structures have been utilised in the construction of large-scale AR complexes in Australia, Asia, and the Middle East, with the primary objective of enhancing fishery productivity by increasing local biomass. More recently, the Gulf's largest AR project was completed near Al Suwaiq, integrating these modules across a 20×7 km area with 4 280 reef units, commissioned by the Ministry of Agriculture, Fisheries, and Water Resources of the Sultanate of Oman [75,77]. The projects have been monitored, and the results have generally indicated a substantial increase in biodiversity and biomass [75]. Since 2003, approximately 18 325 AR units, have been deployed along the Omani coast at a total cost of 9 830 000 euros, with 14 410 units specifically deployed in Al-Batinah [77].

The Ocean Brick System (OBS) is a modular construction technology that played a central role in the development of the Tamar AR [76,78]. Deployed in 2006 near the Gulf of Eilat MPA—an area characterized by two natural reefs and intense diving activity—the OBS consists of sophisticated hollow concrete precast modules (10 m × 10 m × 10 m) (**Figure 2.8**). These interlocking units form a highly versatile framework for artificial reefs and other marine infrastructures [76,78]. The mechanical performance of the OBS system was assessed using Finite Element Method (FEM) analysis, while wave load and stability were verified through hydraulic experiments and Computational Fluid Dynamics (CFD) models [76,78–81]. A recent study showed that the Tamar AR helped to preserve natural reefs by attracting divers, reducing pressure, and minimizing human damage [76].



4 m × 4 m × 5 m; 27 tons
Reinforced concrete
Reef temple [82]



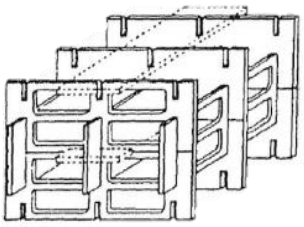
5 m × 3.85 m × 3 m
Concrete, steel
Steel basket [55]



5 m × 5 m × 5 m ; 125 m³ ; 10 tons
Reinforced concrete
Fish box reef [75]



6 m;
Concrete
Arab pyramid [75]



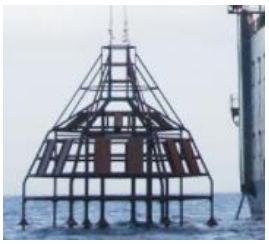
6 m × 6 m × 4 m; 158.4 m³
Concrete
Bonna reef [55]



6.2 m × 5.2 m × 5.4 m; 174 m³
≈40 tons; Concrete
Open concrete frame [83]



10 m × 10 m × 10 m /unit ; 110 tons /unit ; Concrete, steel
Tamar AR [84]



11 m × 11 m × 4 m; 14.4 tons
Steel
Fish reef [75]

Figure 2.8: Types and characteristics of complex ARs.

3D printing based on building materials also contributed to the evolution of ARs. This construction technique enables the creation of more irregular, complex, and organically shaped designs that closely resemble natural coral morphologies, which are difficult to achieve through conventional fabrication methods due to technical and economic constraints.

The world's first 3D-printed reef was implemented in the Reef Arabia project in 2012. This was achieved using the binder jetting process (a technique in which a liquid binder selectively joins powder particles layer by layer) with a D-Shape printer and a patented, non-toxic sandstone material. The resulting structures were 1 meter high and 498 kg in weight and were deployed to promote marine biodiversity in Bahrain waters [85].

Boskalis developed 3D-printed ARs (2017) and installed six reef modules in the Monaco Larvotto Reserve using the binder jetting process, with dolomite sand combined with sand and clay as a binder. Each structure measured approximately 2 m x 2 m x 1 m, weighed around 2.5 tons, and took about 13 hours to print. The modules were placed on the seabed in a triangular formation at a depth of 27 meters, supporting the creation of seven different habitats [86].

Seaboost, XtreeE and Vicat developed the X-reef (2 m x 2 m x 1.3 m, 2.5 tonnes) by 3D printing using concrete and local sand. It was first deployed in the Calanques Natural Park in 2017, and in a second

application 32 medium-sized structures (1.1 m x 0.9 m x 1.1 m, 1.5 tonnes) were installed in Cap d'Agde, France, in 2019. Designed in collaboration with biologists, these eco-engineered reefs featured organic morphology and textured surfaces to enhance marine biodiversity, as well as act as a barrier to trawling and replace old anchor surface marker buoys [87–90].

The modularity and scalability of the Modular Artificial Reef Structure (MARS) technology, developed by Reef Design Lab since 2013 [91], enabled the design of configurable reef systems that can be tailored to diverse marine environments. MARS was used to install the world's largest 3D-printed reef in the Maldives (2018). Designed to restore coral populations, combat bleaching, and create ecosystems [91], each 18 kg module was made from eco-friendly ceramics reinforced with concrete and steel. This modular approach required interlocking connection systems, allowing individual modules to be assembled manually by divers without heavy equipment. These innovations demonstrate how modular engineering and advanced manufacturing techniques enhance scalability, adaptability, and ecological functionality in artificial reef construction. The team also developed other projects like EMU (erosion mitigation units), artificial fish and oyster habitats modules, Nautilus Reef Sculpture, living seawalls, lightweight fish habitats in steel and more recently MARS II [91].

The combination of alternative ceramic-based materials and a gravity-assisted 3D paste extrusion process was employed in the construction of the underwater-assembled ceramic reef unit modules for the X-Coral project [32]. Specifically, a commercially available clay body (Goerg&Schneider Body 0311), composed primarily of silica (68.2%) and characterized by a high iron oxide content (6.5%), no chamotte, and 20% factory-level humidity, was processed using the Gravity-Stimulated Printing Design (GSPD) method with a large Paste-Based Extrusion (PBE) 3D printer. This synergy allowed precise control over structural geometry, porosity, and mechanical stability. The prototypes consist of 87 modules with a self-locking design, installed at two depths (15 and 23 meters) in the Red Sea, Israel. Each reef measured 3 meters in height and 1 meter in width and weighted approximately 100 kg. These reefs were designed to attract fish and facilitate coral growth by promoting the settlement of planula larvae settlement, thereby supporting coral reef restoration [32,74].



Figure 2.9: Examples of complex 3D printed reef structures.

Various binder formulations and fabrication techniques were explored within the AR 3D Printing for Atlantic Area (3DPARE) project, a collaborative initiative involving research institutes from Portugal, Spain, France, and the UK [92]. More than 100 mortar mixes combining geopolymer and cement-based binders with recycled sands were tested, achieving compressive strengths of up to 45 MPa. These mixes were used to produce 36 reef units, each weighing approximately 1 tonne and measuring 1 meter in width, which were deployed to promote marine biodiversity. Findings revealed that structures manufactured with CEM III type cement supported higher biological colonization compared to those made with geopolymer-based formulations, confirming the effectiveness of the materials and manufacturing approaches adopted [38,45].

In 2020, Archireefs [93], in collaboration with the University of Hong Kong, introduced the world's first 3D-printed reef tile made from red terracotta clay using the Direct Ink Writing (DIW) printing technique, in which layers are sequentially deposited. A total of 128 modular reef tiles, each with a diameter of 600 mm, were produced, dried in a controlled environment until completely bone dry, and subsequently fired in a kiln at 1125 °C. These biomimetic structures were deployed over a 40 m^2 area in Hong Kong waters. According to the authors, monitoring campaigns demonstrated high organism survivorship after three years—approximately four times higher than traditional methods—enhancing biodiversity by 40% and supporting marine restoration and blue carbon initiatives [93,95,96]. These were also employed in Abu Dhabi.

The *coral carbonated* is a research project (2021) using 3D printing with calcium carbonate (patent pending) to create structures that support coral growth and marine life. Manufactured through binder jetting process, it aims to regenerate ecosystems by providing a substrate for marine organisms to thrive [94,97]. Coral polyps naturally capture CO_2 from seawater, converting it into calcium carbonate ($CaCO_3$) to form their skeletons. This project mimics that process via 3D printing, producing biocompatible $CaCO_3$ substrates that support marine life and could potentially be sourced through carbon sequestration to accelerate coral settlement [94,97].

2.8.3. Large-scale

The most notable examples of large-scale ARs include the Cable Station and Narrowneck Reefs in Australia [98], along with the Mount Reef in New Zealand, and the Bournemouth surf reef in United Kingdom, all designed to improve surfing conditions (**Figure 2.10**).

The Cable Station reef, constructed in 1999, is a granite reef with 80 meters cross-shore by 90 meters longshore. Prior to its placement, and after its construction, a series of studies were conducted including two experimental design studies, three numerical surfability studies, one beach response study, one environmental study that assessed the biotic diversity of the local habitats, and lastly a post-construction performance study. These studies concluded that the performance of the reef exceeded initial expectations [99–101].

The Narrowneck reef, built in 2000 off the Gold Coast, Australia, used geotextile sandbags to prevent beach erosion and enhance surfing [101]. Consisting of 332 sand containers (up to 20m long, 5m

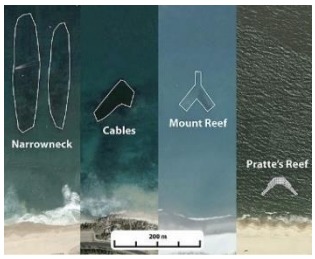
wide, and 160 - 300 tons), it spanned 400 × 200 meters and was the largest multi-purpose reef at the time [101,102]. Environmental assessments and modelling included the use of the refraction model WBEND, a sediment transport model POL3DD and 2DBeach, aiming at optimizing its design [103,104]. Monitoring conducted between 2000 and 2004 showed shoreline expansion of 40 meters windward and 30 meters leeward [101]. Nevertheless, its isolated effect cannot be accurately quantified due to the prior sand nourishment of over one million cubic metres. In addition to enhancing the conditions for surfing, the project also had a beneficial effect on local biodiversity, as evidenced by the presence of diverse marine species on the reef [101,105].

The construction of the Boscombe reef began in 2008 and it was the first AR deliberately designed for improving surfing conditions in Europe. The structure is composed of 70 meters long, 2 meters high and 6 meters wide geotextile sandbags and includes a geo-mat, to prevent sinking. However, the reef did not succeed in producing consistently surfable waves, which were often unstable and potentially hazardous [106].

The world's largest non-purpose built AR was created in 2006 by sinking the naval aircraft carrier USS Oriskany off the coast of Pensacola, Florida. The structure, which measures 277 meters in length, 48 meters in breadth, and weighs 40 000 tons, is referred to as "The Great Carrier Reef" (**Figure 2.10**) [107]. The Ocean Revival project, initiated in 2011, sought to establish Europe's largest AR along the Algarve coastline in Portugal, followed a similar approach by submerging four Portuguese warships, with the objective of promoting the region's aquatic tourism sector [108].



Narrowneck [109] **and other surf ARs scale** [110]





Boscombe reef [111]



Aircraft carrier USS Oriskany [107]



Portuguese warship [112]

Figure 2.10: Examples of large ARs.

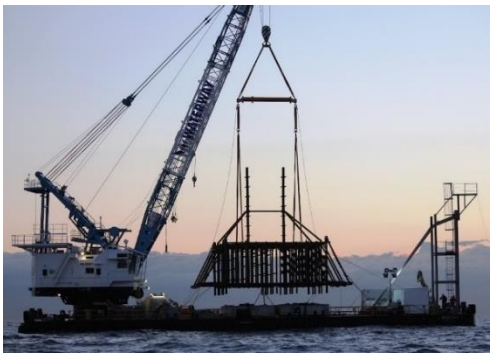
2.8.4. Very large-scale and emerging approaches

Very large and complexity-added AR systems are increasingly being integrated into coastal masterplans, reflecting the convergence of ecological, design and socio-economic objectives. These extraordinarily large ARs demonstrate the potential of artificial reefs for large-scale marine conservation, providing habitats that support biodiversity while also contributing to coastal protection, fisheries management, and ecotourism. Characterized by their substantial dimensions, such structures often involve the combination of diverse materials, modules and construction techniques. The following examples highlight recent developments in large and complex artificial reef structures, as well as emerging trends in ambitious reef projects, illustrating how AR technology and these extensive interventions are expanding the possibilities for sustainable marine conservation.

The Terrace House Reef was developed by JTC and NParks in 2018 as Singapore's largest AR project to enhance marine ecosystems and strengthen coastal conservation efforts (**Figure 2.11**). Eight structures were installed at Sisters' Islands Marine Park, adding 500 m^2 of reef habitat to support marine biodiversity. The partially modular design extends through the entire water column, mimicking a natural reef while ensuring durability for up to 100 years with minimal maintenance [113].

The Recif'lab massive AR, developed in 2021 by Seaboost and CyBe, is a 7-meter-high 3D-printed concrete structure designed to reduce diving pressure on coralligenous habitats (**Figure 2.11**). Made of 26 elements and weighing over 20 000 kg, it is part of a broader eco-design strategy that includes port nurseries and moorings. The reef was printed in under 30 hours, showcasing the efficiency and scalability of 3D concrete printing for marine conservation [90,114].

Several offshore artificial reefs (OARs) have been developed, particularly around Australia. These projects include large pyramid reefs and steel pinnacle reef towers (**Figure 2.11**). Notable examples include the Shoalhaven, Port Macquarie, Southern Sydney "JD," NSW Sydney offshore ARs, as well as the Merimbula, Newcastle, Wollongong, Tweed, Eurobodalla, Forster, and Terrigal OARs—some of the largest and most ambitious projects undertaken. Developed by Subcon Blue Solutions and promoted by the Australian Government, these initiatives highlight the extraordinary scale of such projects. For instance, the Forster OARs (2023) stand out with dimensions of 16 m × 16 m × 12 m, weighting 90 tons and occupying a total volume of 2100 m^3, constructed using steel [82,115].



12 m × 15 m × 12 m ; 42 tons; 700 m³; steel

Sydney OARs, 2011 [115]



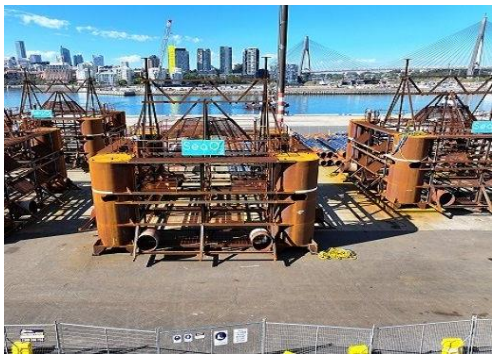
≈11 m × 6 m × 10 m ; >80 tons; concrete, fibreglass, steel, stone

Terrace house reef, 2018 [113]



8 m × 6 m × 7 m ; >20 tons, concrete, steel; 3D print

Recif'lab massive AR, 2021 [114]



16 m × 16 m × 12 m ; 90 tons ; 2100 m3 ; steel

Forster OARs, 2023 [115]

Figure 2.11: Examples of extraordinarily large AR structures.

A number of other mega-scale projects have been initiated with the aim of constructing extensive reef complexes. Examples of such projects include the Neptune Memorial Reef, the Poseidon Memorial Reef and the UAE and Dubai reef projects.

The Neptune Memorial Reef, initiated in 2007, and the Poseidon Memorial Reef, launched in 2024, are located off the coast of Key Biscayne, Florida, at a depth of 12 meters [116]. These underwater installations function as ARs and underwater columbariums, officially certified as memorial sites for the interment of cremated human remains (**Figure 2.12**). Both projects are composed of modular constructions, covering approximately 65 000 m² and 10 000 m² of ocean floor, respectively. According to the promoter, the Neptune Memorial Reef was engineered to withstand the strongest storm in a century, reflecting a design emphasis on long-term resilience. The materials selected for the Poseidon Memorial Reef encompass marble statues and custom bronze statues, limestone coral boulders, marine-friendly concrete, and steel; all selected for their durability and compatibility with marine ecosystems. A 2012 survey conducted at Neptune identified 195 coral colonies and 14 species, and a total of 56 different species of fish were also recorded [116]. A recent study conducted

by the Department of Environmental Resource Management reported that marine life around the reef increased from zero to thousands in just a few years [117]. It should be noted, however, that the information presented here is primarily derived from non-scientific or publicly available sources and should therefore be interpreted with caution.

The Fujairah Cultured Coral Reef Gardens, launched in 2020 by United Arab Emirates, intended to cover around 200 000 m^2 an ocean floor area off the east coast involving the cultivation of 1.5 million coral colonies over a five-year period [118]. More recently, in 2024, the large-scale project "Dubai Reefs" has been launched, which aims to create the world's largest AR, covering 200 km^2 and providing a habitat for over 1 billion corals and 100 million of mangrove trees. In addition, the project intends to integrate renewable energy, regenerative ocean farming and innovative blue infrastructures. Wave and tidal energy provide a continuous, carbon-free power source for the floating platforms. Regenerative ocean farming including kelp, seaweed, and oyster cultivation—supports habitat restoration, carbon sequestration, and sustainable protein production. Floating infrastructures also function as wildlife sanctuaries, research hubs, and food security systems, enhancing marine and coastal resilience [119,120]. The project began with the manufacture of the first 1 000 purpose-built reef modules, and by 2027 a total of 20 000 reef modules are expected to be deployed in the study area. These include reef shade, Arab marine pyramid, X-Reef, fish cube, fish cave and ocean castle units, ranging in size from 1.5 to 4.5 meters [119,120].



Neptune Memorial Reef™ [116]



Dubai reefs (virtual design) [119,120]

Figure 2.12: Mega projects involving ARs technology.

2.9. FINAL CONSIDERATIONS

ARs have proven to be valuable tools for enhancing marine ecosystems, supporting biodiversity, and providing additional benefits such as recreational opportunities and coastal protection. However, their successful design and implementation come with significant challenges, particularly in relation to materials, structural design, regulatory frameworks, and existing knowledge gaps. These aspects must be carefully considered to ensure that ARs are not only effective but also sustainable and environmentally responsible.

Challenges in Artificial Reef Design

The construction of ARs faces increasing complexity as durability and functionality requirements grow. As ARs evolve to incorporate scalable multifunctional modular designs, the need for a robust connection system to integrate modules into a 3D arrangement becomes crucial, ensuring both durability and structural performance in the harsh and unpredictable marine environment. Key challenges in AR design include durability demands, the selection and development of materials with bioreceptive properties to promote the growth of marine biota and structural/stability demands.

Structural design approaches often lack a comprehensive framework that spans from early stages, involving primary analytical and numerical methodologies, to advanced phases with real-scale experiments and simulations, the latter being more widely disseminated. While the literature addresses functional aspects like geometric design and hydrodynamic performance, research on structural design remains limited and poorly shared, hindering broader integration and trust in global implementations. Additionally, understanding fluid-flow interactions and the bonding mechanisms between materials under both short- and long-term exposure conditions to harsh marine environment remains a critical challenge.

Regulatory and Policy Considerations

The regulatory framework surrounding ARs is another important aspect of their successful implementation. Legal criteria, such as national legislation and international agreements like the London Convention and Protocol, guide the selection of materials and the overall design process. However, the regulatory landscape can be complex, and varying policies across regions may pose challenges in ensuring consistent standards for reef construction. It is essential that ARs adhere to local regulations, as well as broader environmental policies, to prevent unintended ecological consequences and ensure that they contribute positively to marine ecosystems. As the demand for

ARs grows, the need for clearer and amended standardized guidelines at both the national and international levels become increasingly important.

Knowledge Gaps and Research Needs

Despite the significant progress in AR development, numerous gaps in the knowledge persist and need to be addressed to optimize their design and functionality. From the engineering point of view, systematic approaches to the development and design of these solutions are scarce. Aspects such as structural behaviour, adhesion between cement, ceramics, metals, composites, and other materials, as well as interactions with natural organisms and colonization layers, and overall durability, should be thoroughly investigated through laboratory experiments, numerical simulations, and full-scale physical tests. Research into the long-term impacts of ARs on marine biodiversity, water quality, and surrounding ecosystems is still limited. While many ARs have shown positive effects in terms of providing habitat for fish and other marine species, it is crucial to conduct more extensive studies to better understand their ecological role and ensure their positive effect over time. Additionally, data on the effectiveness of various reef designs and materials in different environments is still scarce, which makes it difficult to predict the outcomes of new reef projects.

Trends and Future Directions

Looking forward, there are several emerging trends that are likely to shape the future of AR development. Advances in technology and materials science offer the potential for more sustainable and effective reef structures. For example, the use of environmentally friendly materials, such as specially designed concrete or eco-friendly ceramics, is nowadays seen as a way to reduce the environmental impact of ARs. Furthermore, the integration of advanced monitoring systems, such as underwater sensors and remote sensing technologies, allows for real-time data collection and assessment of reef health, providing valuable insights into their performance. Another promising trend is the use of ARs as part of integrated coastal management strategies. Future developments may focus on creating multi-functional reefs that serve a variety of purposes, including ocean research, renewable energy generation, mitigation of the impact of other marine infrastructures, and supporting marine monitoring, alongside the more traditional purposes of enhancing biodiversity and providing habitats for marine life. Moving forward, it is crucial to balance innovation with environmental responsibility, ensuring that ARs contribute to the long-term health and resilience of marine ecosystems.

2.10. REFERENCES

[1] OSPAR Commission. Assessment of construction or placement of artificial reefs. London: OSPAR Commission; 2009.

[2] OSPAR Commission. OSPAR guidelines on artificial reefs in relation to living marine resources. London: OSPAR Commission; 2013.

[3] Fabi G, Giuseppe Scarcella, Alessandra Spagnolo SAB, Charbonnel E, Goutayer JJ, Haddad N, And AL, et al. Pratical guidelines for the use of artificial reefs in the Mediterranean and the Black Sea; 2015.

[4] UNEP-MAP. Guidelines for the placement at sea of matter for purpose other than the Mere disposal (Construction of artificial reefs). Athens: UNEP/MAP; 2005.

[5] Directorate-General for Natural Resources, Safety and Maritime Services (DGRM). Marine Strategy Framework Directive – Parte C: Análise económica e social, subdivisão dos Açores. Lisbon: DGRM; 2020.

[6] London Convention and Protocol/UNEP. Guidelines for the placement of artificial reefs. London: International Maritime Organization; 2009.

[7] Bohnsack JA, Sutherland DL. Artificial reef research: a review with recommendations for future priorities. Bull Mar Sci 1985;37:11–39.

[8] Grove RS, Sonu CJ. Review of Japanese fisheries reef technology. Report 83-RD-137. Vicksburg, MS: US Army Engineer Waterways Experiment Station; 1983.

[9] Jensen A. Artificial reefs of Europe: perspective and future. ICES J Mar Sci 2002;59:S3–S13. https://doi.org/10.1006/jmsc.2002.1298.

[10] Evans AJ, Garrod B, Firth LB, Hawkins SJ, Morris-Webb ES, Goudge H, et al. Stakeholder priorities for multi-functional coastal defence developments and steps to effective implementation. Mar Policy 2017;75:143–155. https://doi.org/10.1016/j.marpol.2016.10.006.

[11] Lee MO, Otake S, Kim JK. Transition of artificial reefs (ARs) research and its prospects. Ocean Coast Manag 2018;154:55–65. https://doi.org/10.1016/j.ocecoaman.2018.01.010.

[12] Cruz F, Pereira E, Valente IB, Tiago M, Maslov D, Pinheiro M. Structural design of an innovative multifunctional artificial reef. OCEANS 2018 MTS/IEEE Charleston, Charleston: IEEE; 2018, p. 1–7. https://doi.org/10.1109/OCEANS.2018.8604587.

[13] López I, Tinoco H, Aragonés L, García-Barba J. The multifunctional artificial reef and its role in the defence of the Mediterranean coast. Sci Total Environ 2016;550:910–923. https://doi.org/10.1016/j.scitotenv.2016.01.180.

[14] Soon C, Ng L, Chou LM. Artificial reefs as a reef restoration strategy in sediment-affected environments: Insights from long-term monitoring. Aquat Conserv 2017;27:976–985. https://doi.org/10.1002/aqc.2755.

[15] Ng K, Thomas T, Phillips MR, Calado H, Borges P, Veloso-Gomes F. Multifunctional artificial reefs for small islands: An evaluation of amenity and opportunity for São Miguel Island, the Azores. Prog Phys Geogr 2015;39:220–257. https://doi.org/10.1177/0309133314567581.

[16] Mendonça A, Neves MG, Fortes CJ, et al. Hydrodynamics around an artificial surfing reef at Leirosa, Portugal. J Waterw Port Coast Ocean Eng 2012;138:226–235. https://doi.org/10.1061/(ASCE)WW.1943-5460.0000128.

[17] Thierry JM. Artificial reefs in Japan: A general outline. *Aquac Eng* 1988;7:321–348.

[18] Fabi G, Spagnolo A, Bellan-Santini D, Charbonnel E, Çiçek BA, García JJG, et al. Overview on artificial reefs in Europe. Braz J Oceanogr 2011;59:155–166.

[19] Ng K, Phillips MR, Calado H, Borges P, Veloso-Gomes F. Seeking harmony in coastal development for small islands: Exploring multifunctional artificial reefs for São Miguel Island, the Azores. Appl Geogr 2013;44:99–111. https://doi.org/10.1016/j.apgeog.2013.07.013.

[20] Santos J. Impactos e colonização biológica de uma estrutura de defesa costeira: O quebramar da Aguda [Master's thesis]. Porto: Faculdade de Engenharia da Universidade do Porto; 2008.

[21] Santos J, Weber M, Veloso-Gomes F. Concepção, construção, implantação e monitorização de recifes artificiais de betão com incorporação de lamas orgânicas. J Integr Coast Zone Manag 2010;10:23–48.

[22] Ramos J, Lino PG, Himes-Cornell A, Santos MN. Local fishermen's perceptions of the usefulness of artificial reef ecosystem services in Portugal. PeerJ 2019;7:e6206. https://doi.org/10.7717/peerj.6206.

[23] Leitão F, Santos MN, Erzini K, Monteiro CC. Fish assemblages and rapid colonization after enlargement of an artificial reef off the Algarve coast (southern Portugal). Mar Ecol 2008;29:435–448. https://doi.org/10.1111/j.1439-0485.2008.00253.x.

[24] Silva J, Rosental I, Love M. Overview and trends of ecological and socioeconomic research on artificial reefs. Mar Environ Res 2019;145:81–96. https://doi.org/10.1016/j.marenvres.2019.01.010.

[25] Bao H, Nikolaeva A, Xia J. Evolution trends and future prospects in artificial marine reef research: A 28-year bibliometric analysis. Sustainability 2025;17:184. https://doi.org/10.3390/su17010184.

[26] National Oceanic and Atmospheric Administration (NOAA). National Artificial Reef Plan (as amended): Guidelines for siting, construction, development, and assessment of artificial reefs. Silver Spring, MD: NOAA; 2007.

[27] General Fisheries Commission for the Mediterranean (GFCM). Practical guidelines for artificial reefs in the Mediterranean and Black Sea. Rome: GFCM.

[28] Diplock J. Artificial reefs – Design and monitoring standards workshops – Fisheries Research and Development Corporation Project 2010/400. Canberra: Fisheries Research and Development Corporation; 2010.

[29] Great Barrier Reef Marine Park Authority. Guidelines for the management of artificial reefs in Great Barrier Reef Marine Park. Townsville: Great Barrier Reef Marine Park Authority; 2011.

[30] Florisson JH, Rowland AJ, Matthews AC, Tweedley JR, Campbell LL. The application, needs, costs and benefits of habitat enhancement structures in Western Australia and cost-effective monitoring methods. Perth: Department of Primary Industries and Regional Development; 2018.

[31] Aguilera A, Broitman BR, Thiel M. Artificial breakwaters as garbage bins: Structural complexity enhances anthropogenic litter accumulation in marine intertidal habitats. Environ Pollut 2016;214:737–747. https://doi.org/10.1016/j.envpol.2016.04.058.

[32] Berman O, Zavadsky A, Drimer N, Shashar N, Wang G, Tarazi E. A pure ceramic 3D printed artificial reef: Stability and response. J Clean Prod 2025;523:146380. https://doi.org/10.1016/j.jclepro.2025.146380.

[33] Pham LT, Huang JY. 3D printed artificial coral reefs: Design and manufacture. Low-Carbon Mater Green Constr 2024;4. https://doi.org/10.1007/s44242-024-00056-4.

[34] Suzdaleva AL, Beznosov VN. Artificial reef: Status, life cycle, and environmental impact assessment. Power Technol Eng 2021;55:558–561. https://doi.org/10.1007/s10749-021-01397-x.

[35] Carral L, Alvarez-Feal JC, Tarrío-Saavedra J. Social interest in developing a green modular artificial reef structure in concrete for the ecosystems of the Galician rías. J Clean Prod 2018;172:1881–1898. https://doi.org/10.1016/j.jclepro.2017.11.252.

[36] Fitzhardinge RC, Bailey-Brock JH. Colonization of artificial reef materials by coral and other sessile organisms. Bull Mar Sci 1989;44:567–579.

[37] Baine M. Artificial reefs: A review of their design, application, management and performance. Ocean Coast Manag 2001;44:241–259.

[38] Yoris-Nobile AI, Slebi-Acevedo CJ, Lizasoain-Arteaga E, Indacoechea-Vega I, Blanco-Fernández E, Castro-Fresno D, et al. Artificial reefs built by 3D printing: Systematisation in the design, material selection and fabrication. Constr Build Mater 2023;362:129766. https://doi.org/10.1016/j.conbuildmat.2022.129766.

[39] Veeger M, Ottelé M. Making bioreceptive concrete: Formulation and testing of bioreceptive concrete mixtures. J Build Eng 2021;44:102545. https://doi.org/10.1016/j.jobe.2021.102545.

[40] Farf GM, Sempere-Valverde J, Ostal E. Substratum type affects recruitment and development of marine assemblages over artificial substrata: A case study in the Alboran Sea. Estuar Coast Shelf Sci 2018;204:56–65. https://doi.org/10.1016/j.ecss.2018.02.017.

[41] Huang X, Wang Z, Liu Y, Hu W, Ni W. On the use of blast furnace slag and steel slag in the preparation of green artificial reef concrete. Constr Build Mater 2016;112:241–246. https://doi.org/10.1016/j.conbuildmat.2016.02.088.

[42] Nashira N, Leclerc J, Pinochet J, Oyarzo-Vera C, Brante A. Incorporating industrial by-products within concrete has limited effects on the assembly of marine sessile communities. J Environ Manage 2025;395.

[43] Bigdeli Y, Barbato M, Lofton CD, Gutierrez-Wing MT, et al. Mechanical properties and performance under laboratory and field conditions of a lightweight fluorogypsum-based blend for economic artificial-reef construction. J Mater Civ Eng 2020;32. https://doi.org/10.1061/(ASCE)MT.1943-5533.0003240.

[44] Xu Q, Ji T, Yang Z, Ye Y. Preliminary investigation of artificial reef concrete with sulphoaluminate cement, marine sand and sea water. Constr Build Mater 2019;211:837–846. https://doi.org/10.1016/j.conbuildmat.2019.03.272.

[45] Ly O, Yoris-Nobile AI, Sebaibi N, Blanco-Fernández E, Boutouil M, Castro-Fresno D, et al. Optimisation of 3D printed concrete for artificial reefs: Biofouling and mechanical analysis. Constr Build Mater 2021;272:121649. https://doi.org/10.1016/j.conbuildmat.2020.121649

[46] Chen C, Ji T, Zhuang Y, Lin X. Workability, mechanical properties and affinity of artificial reef concrete. Constr Build Mater 2015;98:227–236. https://doi.org/10.1016/j.conbuildmat.2015.05.109.

[47] Sherman RL, Gilliam DS, Spieler RE. Artificial reef design: Void space, complexity and attractants. ICES J Mar Sci 2002;59:S196–S200. https://doi.org/10.1006/jmsc.2001.1163.

[48] Limlunjakorn T. The designing of 3D-printed modular artificial reefs through design thinking framework: A case study in Koh Khai, Chumphon Province, Thailand. Discover Sustainability 2025;6. https://doi.org/10.1007/s43621-025-01691-y.

[49] O'Leary E, Hubbard T, O'Leary D. Artificial Reefs Feasibility Study. 2001.

[50] Maslov D, Pereira E, Duarte D, Miranda T, Ferreira V, Tieppo M, et al. Numerical analysis of the flow field and cross section design implications in a multifunctional artificial reef. Ocean Eng 2023;272:113817. https://doi.org/10.1016/j.oceaneng.2023.113817.

[51] Galdo L, Carballo R. Numerical and experimental analysis of the velocity field inside an artificial reef: Application to the Ares-Betanzos estuary. J Mar Sci Eng 2022;10:1827. https://doi.org/10.3390/jmse10121827.

[52] Wang F, Feng Y, Liu S, Chen Y, Ding J. Artificial fish reef site evaluation based on multi-source high-resolution acoustic images. J Mar Sci Eng 2025;13:309. https://doi.org/10.3390/jmse13020309.

[53] Jensen A, Collins KJ, Lockwood APM, editors. Artificial reefs in European seas. Dordrecht: Springer; 2000. https://doi.org/10.1007/978-94-011-4215-1.

[54] Tessier A, Dalias N, Lenfant P. Expectations of professional and recreational users of artificial reefs in the Gulf of Lion, France. J Appl Ichthyol 2015;31:60–73. https://doi.org/10.1111/jai.12951.

[55] Tessier A, Francour P, Charbonnel E, Dalias N, Bodilis P, Seaman W, et al. Assessment of French artificial reefs: Due to limitations of research, trends may be misleading. Hydrobiologia 2015;753:1–29. https://doi.org/10.1007/s10750-015-2213-5.

[56] Ilieva I, Jouvet L, Seidelin L, Best BD, Aldabet S, da Silva R, et al. A global database of intentionally deployed wrecks to serve as artificial reefs. Data Brief 2019;23:103732. https://doi.org/10.1016/j.dib.2018.12.023.

[57] Schulze A, Erdner DL, Grimes CJ, Holstein DM, Miglietta MP. Artificial reefs in the northern Gulf of Mexico: Community ecology amid the "ocean sprawl." Front Mar Sci 2020;7:447. https://doi.org/10.3389/fmars.2020.00447.

[58] The Joint Artificial Reef Technical Committee of the Atlantic and Gulf States Marine Fisheries Commissions. Coastal artificial reef planning guide. Washington, DC: Atlantic States Marine Fisheries Commission and Gulf States Marine Fisheries Commission; 1998.

[59] Artificial Reef Subcommittees of the Atlantic and Gulf States Marine Fisheries Commissions. Guidelines for marine artificial reef materials. Washington, DC: Atlantic States Marine Fisheries Commission and Gulf States Marine Fisheries Commission; 2004.

[60] New Jersey Artificial Reef Program. New Jersey artificial reefs. 2000. Available from: http://njscuba.net/reefs/misc_materials.php. Accessed February 20, 2019.

[61] Maduro Dive Staff. Scuba tanks. Available from: https://www.madurodive.com/2014/02/13/scuba-tanks/. Accessed November 10, 2025.

[62] Reef Ball Foundation. Reef Ball Foundation. Available from: https://www.reefball.org. Accessed January 10, 2019.

[63] Ulaş A, Lök A, Ozan Düzbastılar F, Özgül A, Metin C. A new artificial reef design for octopus (Octopus vulgaris Cuvier, 1797) in the Aegean Sea and preliminary results. Braz J Oceanogr 2011;59:21–25. https://doi.org/10.1590/S1679-87592011000500004.

[64] Matus IV, Alves JL, Vaz-Pires P. Artificial reefs through additive manufacturing: A review of their design, purposes and fabrication process for marine restoration and management. Rapid Prototyp J 2024;30:87–122. https://doi.org/10.1108/RPJ-07-2023-0222.

[65] Oldfield M. Divers swim past a Biorock structure, Gili Trawangan, Lombok, Indonesia. Matthew Oldfield Photography; 2009. Available from: https://matthewoldfield.photoshelter.com/image/I000097eUIHQnmRI. Accessed February 2, 2019.

[66] Tecnoreef S.R.L. Tecnoreef® module. Available from: http://www.tecnoreef.it/index-en.html. Accessed October 15, 2025.

[67] RHOMBI. Reef Home Biodiversity. Available from: https://rhombi.earth.

[68] Dovala JC. ReefBall Curaçao. 2006. Available from: http://www.reefball.com/map/curacao.htm.

[69] deCaires Taylor J. Underwater Sculpture. Available from: https://www.underwatersculpture.com. Accessed January 8, 2019.

[70] Vogler V. A new framework for artificial coral reef design. J Digit Landsc Archit 2022;2022:524–537. https://doi.org/10.14627/537724050.

[71] Biorock. Biorock technology. 2017. Available from: http://www.biorock.org/. Accessed February 10, 2019.

[72] Leftheriotis GA, Sibetheros IA, Dimas AA. Large-eddy simulation of the turbulent oscillatory flow around an artificial reef. Ocean Eng 2025;318:120142. https://doi.org/10.1016/j.oceaneng.2024.120142.

[73] Sordini P. Confronto tra l'applicazione della GIZC nella difesa della costa in Italia e in Spagna: Evoluzione morfo-batometrica di un tratto di costa ravennate difeso da reef artificiali [Master's thesis]. 2011.

[74] Berman O, Weizman M, Oren A, Neri R, Parnas H, Shashar N, et al. Design and application of a novel 3D printing method for bio-inspired artificial reefs. Ecol Eng 2023;188:106892. https://doi.org/10.1016/j.ecoleng.2023.106892.

[75] Haejoo Group. Haejoo Group projects. Available from: https://haejoo.com/category/projects/. Accessed March 20, 2025.

[76] Belhassen Y, Rousseau M, Tynyakov J, Shashar N. Evaluating the attractiveness and effectiveness of artificial coral reefs as a recreational ecosystem service. J Environ Manage 2017;203:448–456. https://doi.org/10.1016/j.jenvman.2017.08.020.

[77] Al S, Al H, Dutta S. Contribution of artificial reefs on fisheries productivity in the Sultanate of Oman from the fishermen perspective. Ocean Coast Manag 2024;254:107201. https://doi.org/10.1016/j.ocecoaman.2024.107201.

[78] OceanBrick Group. Ocean Brick System (OBS). 2015. Available from: http://www.oceanbricks.com/. Accessed February 15, 2019.

[79] Bollineni H, Wang X, Toblas J. Numerical investigation of an Ocean Brick System. Fluids 2025;10:231. https://doi.org/10.3390/fluids10090231.

[80] Pfoertner S, Oumeraci H, Kudella M, Kortenhaus A, Braunschweig TU. Wave loads and stability of new foundation structure for offshore wind turbines made of Ocean Brick System (OBS). In: Coasts, Marine Structures and Breakwaters: Adapting to Change. Proceedings of the 9th International Conference organised by the Institution of Civil Engineers. Edinburgh; 2009.

[81] Oumeraci H, Pfoertner S, Kudella M, Kortenhaus A. Ocean Brick System (OBS) as a foundation structure for offshore wind turbines: An experimental study of wave loads and stability. In: Coasts, Marine Structures and Breakwaters: Adapting to Change. Proceedings of the 9th International Conference organised by the Institution of Civil Engineers. Edinburgh; 2010. p. 1–12.

[82] Subcon – Blue Solutions. Reef pyramid. Available from: https://www.subcon.com/portfolio/reef-pyramid/. Accessed March 20, 2021.

[83] Valéry P. Les « habitats artificiels »: Élément de stratégie pour une gestion intégrée des zones côtières? Essai de méthodologie d'aménagement [PhD thesis]. Montpellier: Université Paul-Valéry Montpellier III; 2008.

[84] Linden B. Tamar artificial reef. 2024. Available from: https://submersed.wordpress.com/. Accessed October 25, 2024.

[85] Reef Arabia. Reef Arabia. Available from: https://reefarabia.com/. Accessed March 12, 2025.

[86] Lescinski J, Kramer A. Boskalis Horizons: Revolutionary ReefVival. 2017. Available from: https://magazine.boskalis.com/issue05/revolutionary-reefvival. Accessed March 11, 2025.

[87] XtreeE. XtreeE. Available from: https://www.xtreee.com/. Accessed March 11, 2025.

[88] Matus I. Estudo da aplicação da impressão 3D na produção de substratos que fomentam a propagação de corais [Master's thesis, in Portuguese]. Porto: Faculdade de Belas Artes da Universidade do Porto; 2020.

[89] VICAT. Vicat's concrete 3D ink buoys up marine biodiversity. Available from: https://www.vicat.com/news/vicats-concrete-3d-ink-buoys-marine-biodiversity. Accessed March 11, 2025.

[90] SEABOOST. 3D-printed ecological mooring systems (Recif'Lab – Marine Protected Area of Agde, France). 2019. Available from: https://www.seaboost.fr/en/reciflab-ecological-restoration-of-marine-infrastructures-of-the-agde-coast/. Accessed March 11, 2025.

[91] Reef Design Lab. Reef Design Lab. 2019. Available from: https://www.reefdesignlab.com. Accessed February 10, 2019.

[92] 3D PARE – Artificial Reef 3D Printing for Atlantic Area. 3D PARE. Available from: https://www.giteco.unican.es/proyectos/3dpare/index.html. Accessed October 1, 2025.

[93] Archireef. Archireef. Available from: https://archireef.co/. Accessed March 10, 2025.

[94] Schofield A. Coral Carbonate 3D Printed. Available from: https://www.oplusi.com/coral-carbonate. Accessed March 11, 2025.

[95] Lange C, Ratoi L, Co DLIM. Rethinking artificial reef structures through a robotic 3D clay printing method. In: RE: Anthropocene, Design in the Age of Humans. Proceedings of the 25th International Conference on Computer-Aided Architectural Design Research in Asia. Vol. 2; 2020. p. 463–472.

[96] Souza E. Rethinking artificial reef structures through 3D clay printing. 2020.

[97] Dezeen. Coral skeletons crafted from 3D-printed calcium carbonate could restore damaged reefs. 2020. Available from: https://www.dezeen.com/2020/08/06/coral-carbonate-reef-skeletons-objects-ideograms/. Accessed March 11, 2025.

[98] Ranasinghe R, Evans P, Hacking NJ. Multi-functional artificial surf breaks: A review. 2001.

[99] ten Voorde M. Contribution to the design of multi-functional artificial reefs [PhD thesis]. Coimbra: University of Coimbra; 2009.

[100] Pattiaratchi C. Design studies for an artificial surfing reef: Cable Station, Western Australia. 1999.

[101] Jackson LA, Corbett BB. Review of existing multi-functional artificial reefs. In: Australasian Conference on Coasts and Ports. Melbourne, Australia; 2007. p. 1–6.

[102] Black K. Artificial surfing reefs for erosion control and amenity: Theory and application. J Coast Res 2001;SI 29:1–14.

[103] Turner L, Leyden VM, Cox RJ, Jackson LA, McGrath JE. Physical model study of the Gold Coast artificial reef. J Coast Res 2001;SI 29:131–146.

[104] Black K, Mead S. Design of the Gold Coast reef for surfing, public amenity and coastal protection: Surfing aspects. J Coast Res 2001;SI 29:115–130.

[105] Jackson A, Tomlinson R, Corbett B, Strauss D. Long-term performance of a submerged coastal control structure: A case study of the Narrowneck multifunctional artificial reef. Coast Eng Proc 2012;1(33):1–13.

[106] Rendle EJ. The environmental, social and economic impacts of an artificial surf reef: The UK experience [PhD thesis]. Plymouth: University of Plymouth; 2016.

[107] Florida Department of State. USS Oriskany. Available from: http://www.floridapanhandledivetrail.com/oriskany.html. Accessed October 1, 2025.

[108] Directorate-General for Natural Resources, Safety and Maritime Services (DGRM). Marine Strategy Framework Directive – Part C. Lisbon: DGRM; 2020.

[109] Griffith Centre for Coastal Management. How Narrowneck copied nature. Available from: https://boatgoldcoast.com.au/how-narrowneck-copied-nature/. Accessed November 10, 2025.

[110] Raised Water Research. Surfing reefs. Available from: https://raisedwaterresearch.com/. Accessed November 10, 2025.

[111] Borrero JC, Mead S. Stability considerations and case studies of submerged structures constructed from large, sand-filled geotextile containers. Coast Eng Proc 2011;1(32):60. https://doi.org/10.9753/icce.v32.structures.60.

[112] Ocean Revival. Underwater park by sinking four navy warships. Available from: http://www.oceanrevival.org. Accessed April 13, 2025.

[113] JTC. Singapore's largest artificial reef project to be piloted at Sisters' Islands Marine Park to enhance marine biodiversity. Available from: https://www.jtc.gov.sg/news-and-publications/press-releases/Pages/20180517(PR1).aspx. Accessed March 28, 2021.

[114] CyBe Construction. Artificial reef. Available from: https://cybe.eu/cases/artificial-reef/. Accessed March 12, 2025.

[115] State of New South Wales. Artificial reefs. Available from: https://www.dpi.nsw.gov.au/fishing/recreational/resources/artificial-reef. Accessed March 12, 2025.

[116] SCI Shared Resources, LLC. Neptune Memorial Reef™. Available from: https://www.nmreef.com/. Accessed July 1, 2025.

[117] SCI Shared Resources, LLC. Trident Society – Memorial Reef. Available from: https://www.tridentsociety.com/memorial-reef. Accessed November 10, 2025.

[118] United Arab Emirates Ministry of Climate Change and Environment (MOCCAE). MOCCAE News: Ministry of Climate Change and Environment and Fujairah Adventures launch Fujairah Cultured Coral Reef Gardens Project. 2019. Available from: https://www.moccae.gov.ae/en/media-center/news/13/4/2019/-التغير-المناخي-والبيئة-ومركز-الفجيرة-للمغامرات-يطلقا-مشروع-حدائق-الفجيرة-للشعاب-المرجانية-المستزرعة.aspx. Accessed May 1, 2021.

[119] URB. Dubai Reefs. Available from: https://urb.ae/projects/dubaireefs/. Accessed March 12, 2025.

[120] Dubai Department of Economy and Tourism. Supporting marine life with Dubai Reef. Available from: https://www.dubaidet.gov.ae/en/dubai-can/dubai-reef. Accessed March 12, 2025.

CHAPTER 3

STRUCTURAL DESIGN OF GEOMETRICALLY COMPLEX ARTIFICIAL REEFS

This chapter covers the structural design and analysis of marine structures, with a focus on applications to complex artificial reefs. The section discusses recent approaches such as parametric design and its role in defining structural geometry, exploring alternatives and optimizing geometrically complex artificial reef structures. *Additionally, it explores the regulatory framework, identifying the most relevant design guidelines and standards applicable to marine engineering and, consequently, to ARs. The design methods and analysis section discusses structural modelling approaches, numerical simulations, and empirical validation techniques. Design loadings are analysed, highlighting the main effects on artificial reefs and the hydrodynamic models governing fluid-structure interactions. Furthermore, the chapter highlights durability challenges in marine structures, emphasizing corrosion, material degradation, and long-term performance under harsh environmental conditions. The experimental characterization section reviews efforts to improve the study of artificial reefs, and the behaviour of materials and structural systems suitable for these structures. The final considerations summarize findings and future research directions.*

3.1. CONCEPTION WITH PARAMETRIC DESIGN

Parametric design is a process that uses advanced parametric modelling techniques to define and optimize a project's geometry and structural form through iterative exploration of design alternatives. It focuses on developing structures based on defined parameters and performance criteria, while

parametric modelling refers to the digital tools and methods that enable this process by generating and adjusting the geometry according to variable inputs [1]. Initially used by architects to create complex 3D models, this method has been adopted by structural engineers in recent years. Parametric modelling allows rapid modification of a model's geometry by changing dimensional values, saving time, especially in early design stages [2]. The main advantage is that when one parameter is altered, the others automatically adjust accordingly, thereby eliminating the need for redrawing the entire model. This process is also highly beneficial in promoting creativity and the development of innovative solutions, because the iterative creative process becomes more agile and intuitive. **Figure 3.1** presents the generic workflow for parametric modelling-based design, as originally proposed in [3]. The diagram summarizes the main stages of the process, from the initial geometry definition to structural analysis and final design of buildings. It highlights the iterative nature of parametric modelling-based design, where geometry, structural system selection, and analytical and numerical results are continuously interconnected. This approach is especially important for projects involving complex or non-standard geometries, as conventional design methods require significantly more time to accommodate design changes. The workflow emphasizes the role of parametric modelling in translating conceptual geometries into structurally rationalized configurations. Structural analysis tools are then used to assess the response of the system and inform subsequent design adjustments. Geometry modifications may be required as a result of performance criteria or external constraints imposed during the design process. In the case of complex artificial reef constructions, geometry is often driven by ecological, hydrodynamic, structural and fabrication considerations. As a result, multiple iterations are necessary to balance structural stability with environmental performance. Therefore, the presented workflow provides a methodological framework that is easily transferable to the case of structural development of ARs subjected to marine loading conditions.

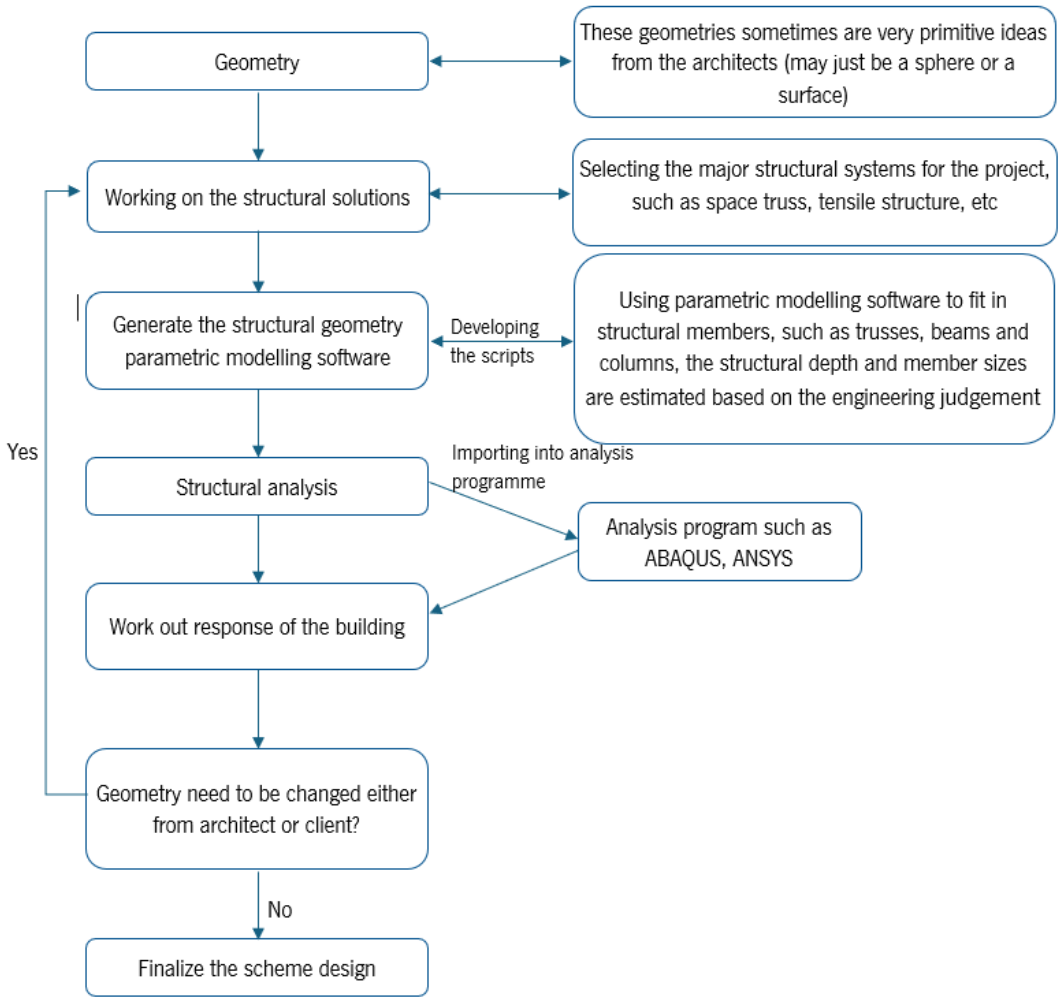


Figure 3.1: Workflow of the design process using parametric modelling [3].

There is a growing number of CAD tools incorporating parametric modelling functions, enabling engineers to develop structural designs with components that can meet the project´s requests. Some leading industry tools are [3]:

- **Rhino**, is a 3D drafting software by Robert McNeel & Associates, used for creating, editing, analysing and rendering NURBS curves, surfaces, solids, point clouds, and polygon meshes. It features the Grasshopper plug-in, which enables parametric modelling, making it useful during the changing phases of scheme design.
- **SolidWorks,** launched in 1995 and acquired by Dassault Systems in 1997, SolidWorks is a low-cost parametric modelling software mainly used in mechanical design and the plastics industry.

- **Revit**: developed by Autodesk, Revit is widely used in architecture, structural engineering, and construction. It offers parametric modelling features, particularly for building design and BIM (Building Information Modelling).
- **AutoCAD -** developed by Autodesk, is a widely used 3D CAD software in architecture, engineering, and design. The latest version includes parametric modelling features, easier to access from the main menu.
- **CATIA -** developed by Dassault Systems in the 1970s, CATIA is a sophisticated software widely used in the aerospace, automotive, and shipbuilding industries.
- **Bentley MicroStation** - developed by Bentley Systems, is a major CAD software for architectural and engineering design. Its latest version includes parametric modelling features.

In the process of designing the artificial reef, it is imperative to acknowledge the profound interconnection between structural design and architectural shape. The utilisation of parametric optimisation techniques assumes paramount importance in facilitating the exploration of diverse design alternatives through rigorous testing and prototyping. In this context, Rhino with Grasshopper is particularly well-suited for generating highly complex and experimental forms, providing greater flexibility and freedom in designing natural-looking structures such as artificial reefs.

3.2. STANDARDS AND GUIDELINES

The design of maritime structures, particularly MMFARs, requires careful consideration of the relevant standards and recommendations applicable in the country of implementation from the viewpoint of safety. In Portugal, structural design follows the Eurocodes, developed by the European Committee for Standardization (CEN) to unify criteria for calculation, design, and construction in the European Union (EU). Within the European standards framework, the Eurocodes are a specific set of standards, from NP EN 1990 to NP EN 1999, dedicated to structural design and safety (**Table 3.1**) [4].

Table 3.1: European standards for the design, sizing and verification of structures.

European Committee for Standardization (CEN)	
Eurocode 0 (NP EN 1990)	Basis of structural design;
Eurocode 1 (NP EN 1991)	Actions on structures;
Eurocode 2 (NP EN 1992)	Design of concrete structures;
Eurocode 3 (NP EN 1993)	Design of steel structures;
Eurocode 4 (NP EN 1994)	Design of composite steel and concrete structures;
Eurocode 7 (NP EN 1997)	Geotechnical design;
Eurocode 8 (NP EN 1998)	Design of structures for earthquake resistance;

Note: Eurocodes 5, 6 and 9 refer to the design of wood, masonry and aluminium structures, respectively.

Despite the fact that the Eurocodes provide a comprehensive set of standards for the design of buildings and civil engineering structures, their application is limited when it comes to special marine structures. As highlighted by NP EN 1990, there is a possible need for complementary standards or recommendations beyond the Eurocodes, particularly for projects involving innovative constructions, materials or techniques. Similarly, as stated in NP EN 1991, which covers common structural actions, there is a lack of detailed guidance on aerodynamic and hydrodynamic forces affecting maritime structures. Consequently, there is the need for additional standards and recommendations to address the specific loading demands on these structures.

Given its technological advancements and global socio-economic significance, the oil and gas industry is governed by numerous technical standards, covering topics from site studies to decommissioning of structures. These are developed by national and international certification entities, standardization organizations, and industry-leading associations. **Figure 3.2** illustrates the hierarchy of standards and reference frameworks in the field of marine and offshore structures [5–7]. At the top are government organizations that set laws and regulations, followed by standards from international, regional, and national organizations, and industry-specific standards created by businesses. These entities work together to ensure consistency. To prevent conflicts between ISO and CEN standards, the Vienna Agreement was signed allowing the adoption of ISO standards within the EU [5].

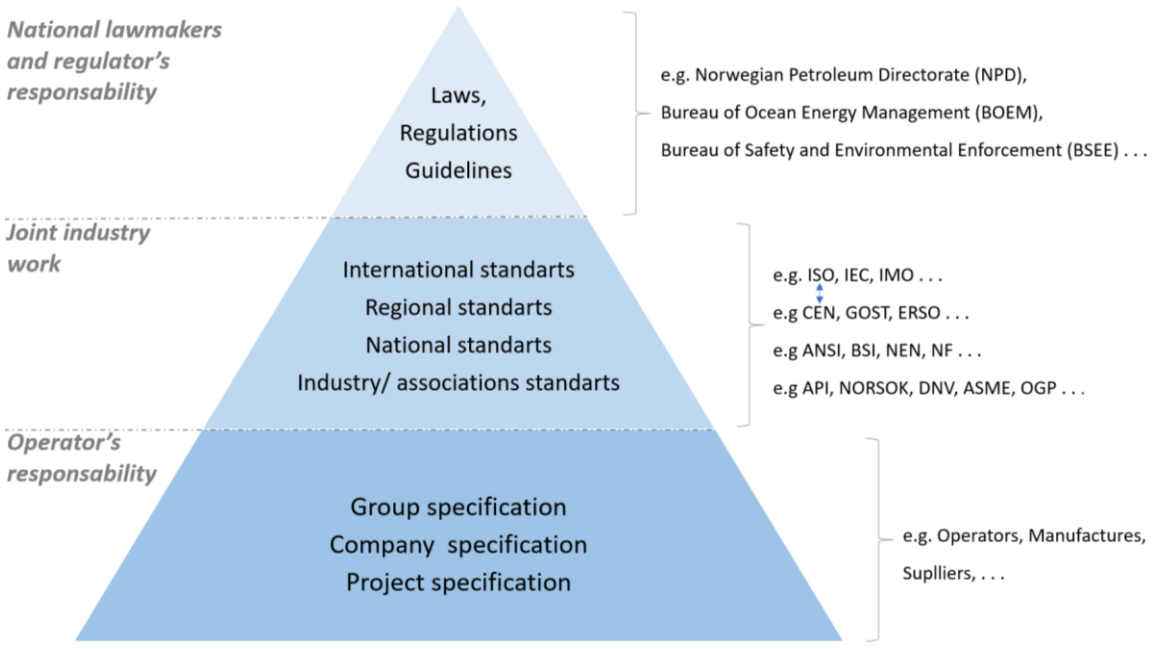


Figure 3.2: Hierarchy of standards and reference standards in the field of marine structures, adapted from [6,8].

As illustrated in **Table 3.2**, a number of recommended standards have been established for marine structures. The baseline knowledge contained within these documents can be utilised and/or adapted appropriately for use in other marine structures, such as multifunctional artificial reefs, in accordance with the technical requirements of the project.

Table 3.2: Reference standards and regulations for the design of marine structures.

International Organization for Standardization (ISO)	
ISO 19900	General requirements for offshore structures;
ISO 19901-1	Part 1: Metocean design and operating considerations;
ISO 19901-2	Part 2: Seismic design procedures and criteria;
ISO 19902	Fixed steel offshore structures;
ISO 19903	Fixed Concrete structures
ISO 19904-1	Floating Structures
ISO 19906	Additional requirements of Arctic Structures
American Petroleum Institute (API)*	
API RP 2A-WSD	Recommended Practice for Planning, Designing and Constructing Fixed Offshore Platforms;
API RP 2FPS	Recommended Practice for Planning, Designing, and Constructing Floating Production System;
API RP 2SK	Recommended Practice for Design and Analysis of Station keeping Systems for Floating Structures;
Det Norske Veritas (DNV)	
DNV-OS-C101:	Design of Offshore Steel Structures, General (LRFD Method);
DNV-OS-C401	Fabrication and Testing of Offshore Structures;
DNV-RP-C205:	Recommended Practice for Environmental Conditions and Environmental Loads;
DNV Report No. 95-3203	Guideline for Offshore Structural Reliability: Application to Jacket Platforms;
DNV Technical Report n° 677	Comparison of API, ISO, and Norsok offshore structural standards;
Norwegian petroleum industry (Norsok)	
NORSOK N-001	Integrity of offshores structures;
NORSOK N-003	Actions and actions effects, Edition 2;
NORSOK N-004	Design of steel structures. Rev. 2;
NORSOK M-120	Material data sheets for structural steel;
American Bureau of Shipping (ABS)	
ABS Guide	Guidance notes on Accidental Load Analysis and Design for Offshore Structures;

*Artificial reef structure designed according to [9]

3.3. DESIGN METHODS AND ANALYSIS

A structure consists of interconnected elements designed to support and transfer loads efficiently. The development of man-made structures has often been inspired by nature, with natural principles being adapted to engineering. A notable example is the human skeleton, which functions similarly to reinforcement elements in construction, providing support and resilience. Likewise, structural design is essential, allowing the construction to withstand applied loads throughout its service life, avoiding the risk of catastrophic failure, while also minimizing maintenance and repair costs.
While some structures follow conventional and mostly well-defined design approaches, others present additional challenges due to their complexity, including irregular geometry, large or asymmetric spans, specific design constraints and complex loading interactions, as seen in the construction of innovative modular ARs and other marine structures [3,10].

The development of maritime structures is a very complex, time consuming and often expensive multidisciplinary process. It is crucial to consider various operational aspects, such as function, location, orientation, water depth, equipment, and materials, as well as general planning, including design criteria and relevant standards. Environmental factors, such as meteorological and oceanographic data, and the type of foundation substrate (e.g., seafloor instability, scour), must also be considered, as they directly influence the structure's stability. The durability and toxicity of materials, construction methods, available resources, and the costs associated with maritime operations are also fundamental aspects [11,12].

The design of ARs has historically been primarily reliant on empirical methods and subjective assessments, and in some cases, it was simply materialized by sinking structures without the adoption of a defined design process [13]. In fact, over the past decades, ARs design and fabrication strategies aimed at habitat regeneration have primarily focused on increasing construction scale and achieving higher levels of morphological complexity [14]. The study of ARs has involved a wide range of engineering approaches that combine analytical, experimental, and numerical methods, thereby contributing to a more comprehensive understanding of AR design. These approaches can be broadly classified and discussed as follows:

- **Analytical methods** are fundamental for understanding the structural behaviour of ARs under different loading conditions and interactions with the marine environment. These methods involve the use of mathematical equations that describe the forces, deformations,

and stresses within the structures. Despite their simplicity and applicability in more conventional situations, analytical methods have limitations when it comes to complex geometry or dynamic conditions, which are common in the design of ARs.

- **Experimental methods** play a vital role in the development of complex structures, such as artificial reefs, providing valuable insights into the real behaviour of structures under simulated conditions. These models are often used to validate the results of analytical and numerical approaches, as well as to provide data on the performance of the structure in real or controlled physical conditions. In the specific case of marine structures, a distinction is made between hydraulic and mechanical tests. Among these, reduced-scale physical models enable controlled testing in simulated marine environments, such as water tanks or hydraulic flumes. On the other hand, materials and structural testing is essential for evaluating the mechanical properties, durability, and long-term performance of materials and structural systems, providing insights into both short- and long-term structural behaviour under different loading patterns and exposure conditions.
- **Numerical methods** provide valuable insights into the behaviour of both the structure and the surrounding fluid environment. The main numerical methods includes (i) Finite Element Analysis (FEA), to assess the structural integrity and response under various loading conditions, analysing stress, deformation, and stability; (ii) Computational Fluid Dynamics (CFD) to simulate the flow behaviour of water around construction, evaluating hydrodynamic forces such as pressure, velocity, and cavitation effects; (iii) Fluid-Structure Interaction (FSI) to simulate the interaction between the structural module and fluid, helping to assess the structure dynamic response to varying flow conditions and predict its stability and performance and (iv) Hydro and morphodynamics modelling tools and CFD methods to study the effects of water movement and sediment deposition on the stability over time.

Table 3.3 summarizes approaches and methods that contribute to the structural design of ARs, reveals that only a limited number of studies have investigated structural design aspects.

Table 3.3: Types and methods of engineering approaches contributing to structural design of ARs.

Type	Analysis & Methods		Goal	References
Analytical	Hydrodynamic models	Ocean mechanics, Morrison's equation (small structures); Froude-Krylov force and Diffraction theory (large structures)	Determine hydrodynamic external forces	[9,13–18]
	Static equilibrium analysis	Structural mechanics principles; Force balance equations; Free-body diagrams; Cross-section study	Determine internal forces based on equilibrium equations	[9,13,15,17]
	Elasticity theory	Stress-strain relationships; Differential equations of elasticity	Assess stress and deformation under external loads	[13,19]
	Flexibility and stiffness analysis	Matrix stiffness method; Moment distribution method; Energy methods	Evaluate the structural response considering flexibility and rigidity	-
	Others: Fatigue, Impact analysis	S-N Curves; Miner's Rule; Fatigue Crack Growth Models; Response Spectrum Analysis; Time History Analysis; Modal Analysis	Access fatigue, cyclic load, impact	[15]
Experimental	Fluid-Structural modelling with scaled model	Hydrodynamic tests in hydraulic flume integrating particle image velocimetry, acoustic doppler velocimetry and pressure sensors	Analyse flow field, hydrodynamic loads, and fluid–structure interaction, including unit stability and scour	[14,15,20–30]
	Testing of materials and structures	Micro and macro-scale structural characterization	Analyse strength, deformability, failure, durability, fatigue, bond behaviour	[14,31–34]
Numerical	Finite Element Analysis (FEA)	Finite Element Methods (FEM)	Evaluate loading response, strength, stress, deformation	[13,18,19,31,35]
	Hydro- and Morphodynamic	Hydrodynamics of wave propagation and balance; Navier-Stokes equation; Finite Difference Method	Sediment transport and morphology, flow and wave propagation	[9,24,25,36,37]
	Computational Fluid Dynamics (CFD)	Finite (Volume or Difference or Element) methods; Smoothed-particle hydrodynamics; Lattice Boltzmann method; Discrete Particle Method; Volume of Fluid; Large Eddy Simulation; Reynolds-Averaged Navier-Stokes	Simulate fluid flow, access hydrodynamic coefficients, optimize designs, analyse turbulence and interactions.	[15,17,18,21,22,30–32,35,36,38–40]
	Fluid-Structure Interaction (FSI)	Coupling FEA-CFD simulations (one way or two way)	Assess structural response, predict fluid dynamics, stability and performance	[18,31,32,35,41]

Despite this diversity, the majority of previous research has been strongly oriented toward physical experimentation and multiphysics numerical modelling [42–47], primarily addressing the influence of

geometric configuration on the flow field from a biological perspective [15,43–45,48,49]. Most of the studies focus primarily on reef stability (overturning) and scour phenomena, often using hydraulic flumes experiments with scaled models [50]. Many ARs studies have evaluated the hydrodynamic and morphodynamic performance of artificial reef structures, including variations in upwelling and eddy currents promoted by these structures [22,24,25,42–44,49,51], vortex and turbulence features around ARs [42,44,45], sediment suspension and transport [118], as well as local erosion mechanism [20,27]. Flow pattern has mostly been investigated using several measurement techniques, including Particle Image Velocimetry (PIV) [43,45,46], Laser Doppler velocimetry (LDV) [47] and Acoustic Doppler Velocimeters (ADV) [43,46] enabling a detailed analysis of flow field and interactions between the structure and the surrounding fluid (**Figure 3.3**). PIV is limited in breaking waves due to bubble scattering, making it valid only in the submerged region. LDV was used to measure the aerated region, but it only provides single-point measurements [47]. Hydrodynamic forces and pressure distributions can be obtained using dynamic piezoelectric pressure transducers or pressure sensors distributed throughout the structure [26,53,54]. Additionally, photogrammetry has proven to be an effective image-processing technique for capturing scour patterns after experimental testing [20]. To ensure that laboratory results might represent real conditions, dimensional analysis and scaling effects, including geometric, kinematic dynamic similarities, as well as fluid and sediment properties [55] are considered. Relevant dimensionless numbers are Froude (inertial force/gravity force), Reynolds (inertial force/viscous force), Weber (inertial force/surface tension force), Cauchy (inertial force/elastic force) and Euler (pressure force/inertial force) numbers. Shields number and the first two numbers commonly describe the erosion around structures.

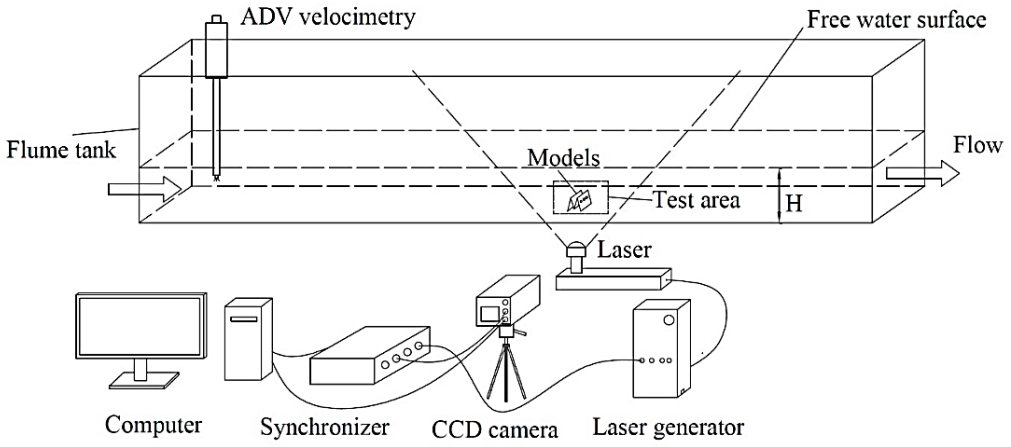


Figure 3.3: Example of a hydraulic flume experimental setup using PIV and ADV systems [42].

In addition, numerical approaches have been employed, including CFD for estimating hydrodynamic coefficients essential to calculate hydrodynamic loads in ARs structures. Finite Element Analysis are also used for evaluating stress distribution within the reef units, as shown in **Table 3.3**. Furthermore, a few works have conducted material testing, typically in instances where novel materials or materials compositions are employed, with a view to evaluating their mechanical properties. Nevertheless, investigations explicitly focused on structural design principles, mechanical performance, and long-term durability assessment remain limited, and have rarely been investigated or experimentally validated [14].

In this context, experimental investigation of materials and components represents a crucial step in the design and validation of engineered solutions. Among mechanical characterizations, composite materials and mixed structural systems offer technical advantages to the development of the next generation of ARs, as well as modular construction systems. In this case, particular attention is given to (a) the bond behaviour between materials and (b) the performance of connection systems between AR modules, as both influence structural integrity and load transfer mechanisms. These two aspects are analysed below:

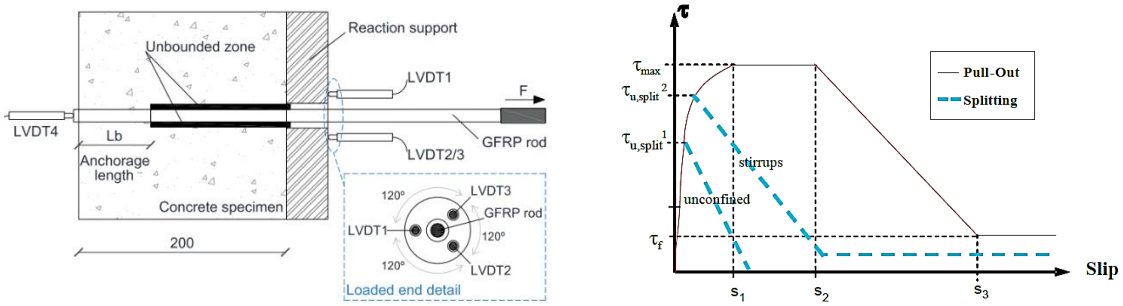
a. Mixed structural systems

Mixed structural systems take advantage of the best properties of different materials that are combined in strong and durable structural systems. Understanding the bond mechanisms that govern the interface transitional zone (ITZ) between the materials is essential. In the case of the current research, special attention was given to reinforced concrete and composite steel-concrete structures due to their favourable combination between structural performance, durability, cost-effectiveness and compatibility with the marine environment.

Understanding the bond mechanisms that govern the interface transitional zone (ITZ) between reinforced concrete and composite steel-concrete structures is fundamental to model the structural behaviour and perform the structural design optimisation, especially when coatings are used and may influence bond performance [56–58]. Bond is a complex interaction dependent on chemical adherence, friction, geometric interlocking mechanisms [59], coating thickness [57,60–62], materials composition, mechanical properties [59,63] and the surface condition of the reinforcement [59]. The bond stress-slip relationship can be assessed experimentally by performing direct pushout or pullout tests, and indirectly via beam tests [64].

- Pullout tests

Pullout tests are mostly used for the characterization of the bond behaviour between reinforcement rebars and concrete [65]. The test specimen consists of a rebar embedded in a concrete prism with a predefined anchorage length. A tensile normal force is applied along the rebar axis, and the relative displacement between the materials is measured while the concrete block remains fixed to a reaction frame, as presented in **Figure 3.4**(a). The typical analytical load vs slip response presented in Model Code 2010 is also presented in **Figure 3.4**(b) [66].

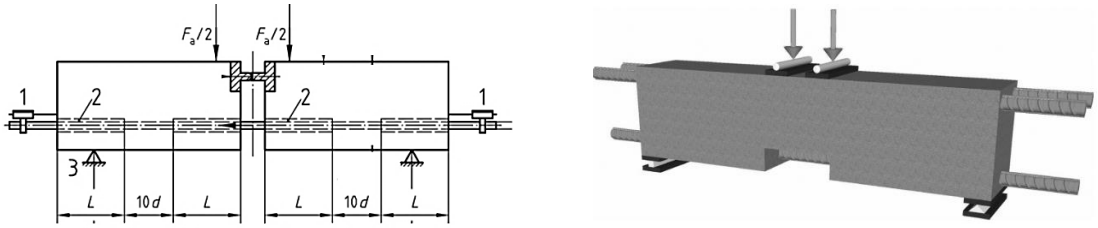


(a) (b)

Figure 3.4: Pullout test: (a) rebar embedded in concrete prism. Adapted from [129]; b) Typical analytical bond stress-slip relationship (monotonic loading). Adapted from [128].

- Beam tests

Bond tests could also be conducted using reinforced concrete beams in accordance with the RILEM specifications [65,68,69]. It comprises two parallelepiped blocks that are connected by a hinge in the compression zone, with a steel rebar positioned at the bottom, as illustrated in **Figure 3.5**. The beam is subjected to bending by the application of two equal and symmetrical forces to the top face. This loading induces tension in the rebar, resulting in its protrusion from the block faces. The relative displacement between the rebar and the concrete is measured.



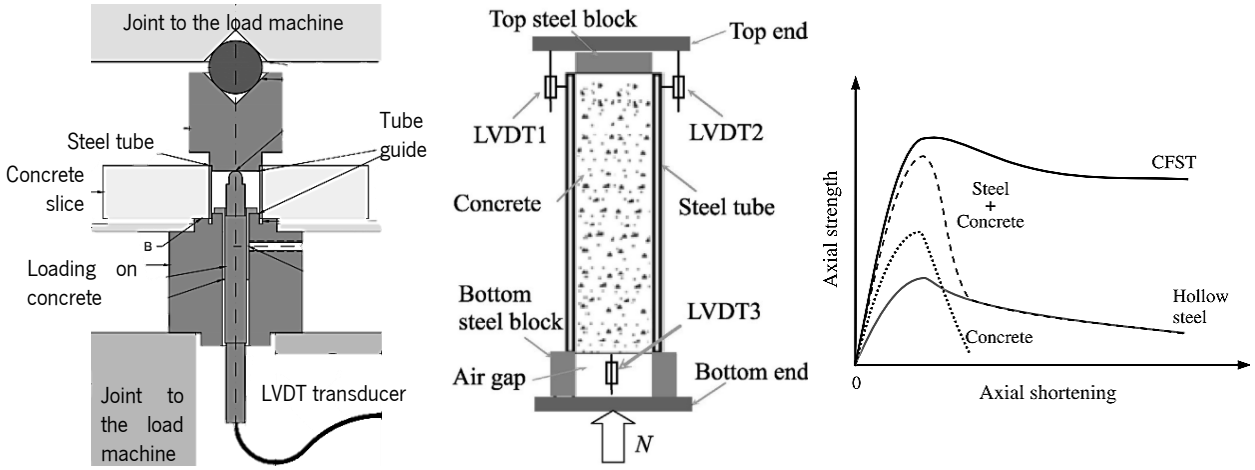
1 - Slip measuring devices
2 - Unbonded length (tubes to prevent bond)
3 - Supports

(a) (b)

Figure 3.5: Beam test schemes (a) RILEM [70] and (b) alternative scheme [64].

- Pushout tests

Pushout tests are commonly used to characterize the bond behaviour in steel-concrete composite structures, particularly in concrete-filled steel tubular (CFST) cross sections, where O shapes, H-shaped or I-shaped profiles can be used in combination with concrete [71]. The pushout test consists of applying an axial load to push the concrete out of a concrete-filled steel tube, as shown in **Figure 3.6**. During the process, the load and the displacement between the materials is measured, evaluating the bond strength between the two materials.



(a) (b) (c)

Figure 3.6: Pushout tests (a) designed for concrete-steel tube slices [72], (b) for CFST cross-sections [73] and (c) typical axial compressive behaviour of CFST stub column [74].

b. Mechanical behaviour of connection systems

The mechanical characterisation of connections is fundamental for understanding the behaviour of modular systems, including artificial reefs. Although various types of connectors have been studied in conventional marine structures, limited research has been reported on the test setups and experimental performance of connections in modular artificial reefs [75]. The mechanical behaviour of connection systems depends on the type of connection and its functionality, with different designs developed to meet specific load, deformation, and durability requirements [75]. Rigid connections provide high strength and minimal rotation, while articulated connections allow for greater flexibility [76].

Given the particular interest in connections that exploit the internal metallic reinforcement of the AR module, with a focus on demountable connection systems, typical experimental setups for the study of bolted connections between metallic components are presented below. Flange-plate connections

were tested using beams spliced at the centre and subjected to four-point loading over a 2 m span. The setup ensured pure bending at the connection, with synchronized jacks applying load **Figure 3.7**(a). Bolt force variations were monitored using gauged bolts [77]. Cruciform beam-column specimens were tested upside down with pin-supported beam ends **Figure 3.7**(b). A vertical load induced reactions at the beam ends, allowing moment calculation based on the lever arm. A 500 kN universal testing machine applied displacement-controlled loading until failure [78]. Steel beam-column connections underwent cyclic loading until failure **Figure 3.7**(c). Instrumentation measured applied forces, displacements, and strains to define the moment-rotation curve and analyse the connection's deformation behaviour [79].



Figure 3.7: Examples of connection tests setups: (a) flange-plate connections for circular or square hollow sections [77], (b) cruciform beam-column specimen [78] and (c) for steel beam-column connection [79].

Overall, engineering-based methodologies that combine analytical reasoning, simple numerical modelling, and experimental studies as central elements of the structural design process remain succinctly scarce. This limitation may hinder the development of geometrically complex, modular, and multifunctional artificial reef systems, which demand more rigorous and oriented design strategies. Moreover, there is currently no specific international or national legislation governing AR stability or

deterioration. Instead, the guidelines on ARs presented before (see **Table 2.1**) emphasize the importance of evaluating stability and structural integrity before deployment, highlighting that these structures must maintain their integrity under the influence of waves, currents, erosion, and anthropogenic activities without compromising environmental safety [14]. In this context, there is a growing recognition of the importance of integrating structural analysis with geometric-functional design to ensure their stability and ecological and flow effectiveness [12,14,36]. This is particularly relevant when aiming to develop increasingly complex constructions, which highlight the need for dedicated structural analysis methods.

3.4. ACTIONS AND EFFECTS

Artificial reefs can be found at different depths [15,80], ranging from shallow subtidal waters [16,17,81] to offshore zones [82]. They may be positioned on the seabed [80,83], suspended within the water column [84], or configured as floating structures [15,85]. Note that floating AR introduce additional complexity due to interactions among buoyancy, mooring, and fishing net systems [15]. The sit-bottom ARs have been found installed on sandy [32,86–88] or bedrock [32,81] seabed, but substrate type is critical, as reefs placed on soft sediments such as clay are more prone to failure due to sedimentation and erosion, highlighting the importance of careful site selection and structural adaptation to local hydrodynamic conditions [15]. The selection of AR type and deployment position must account for environmental challenges such as substrate composition, ocean floor stability, hydrodynamic forces, and other hydrodynamic conditions, all of which influence the ARs. In this context, ARs may have been exposed to the principal actions, categorized as follows [3,89,90]:

- **Dead**: self-weight, hydrostatic pressure.
- **Live**: actions whose magnitude changes in time.
- **Environmental**: hydrodynamic, marine growth, ice, earthquake, etc.
- **Accidental**: abnormal events, impact, dropped objects.
- **Deformation**: temperature, settlement of foundations.
- **Temporary**: transportation and lifting loads, installation.

The environmental actions are among the most important when designing marine structures or managing other coastal activities [91]. Although the quantification of environmental exposure

parameters is a rather complex process due to the time and space nonlinearity, their accurate characterization is fundamental to ensure the structural integrity and long-term performance of marine structures. Therefore, it is very important to use historical site data and/or appropriate mathematical prediction models. The number and complexity of actions on marine structures are considerable, encompassing hydrodynamic, hydrostatic, and other environmental and operational effects. In the present study, particular attention is given to hydrodynamic actions due to their predominant influence on the behaviour of underwater structures such as MMFARs. Whenever possible, the evaluation of these actions should be supported by technical standards and design recommendations [92–98].

3.4.1. Dead load

Gravity or dead loads are the permanent static forces such as the weight of the structure and any permanent equipment. In the case of ARs technology, the weight of the modules and the connection system must be considered, taking into account the dimensions and materials involved. Hydrostatic forces acting on the structure and buoyancy must also be considered. According to OSPAR guideline, the reef units should at least double the specific gravity of seawater or be securely anchored to the seabed [99]. Considering that seawater has a density of approximately 1025 kg/m^3, the reef material should therefore have a density of about 2050 kg/m^3 to meet this requirement. Common concrete, with a density ranging from 2300 to 2500 kg/m^3, fulfils this criterion. Consequently, solid concrete blocks generally do not require additional anchoring. For example, the weight of the OBS-structure (10 × 10 × 10 meters) under buoyancy is around 110 tons per module [100].

3.4.2. Tidal effects and currents

A tide is a cyclic rise and fall of sea levels caused by the Earth's rotation and the gravitational pull of the Moon and Sun [89,101,102]. Tidal effects create large-scale flow patterns that vary in speed, with periodicity and amplitude influenced by local conditions. According to NOAA (2019), there are three main tidal cycle patterns: (i) Diurnal – one high and one low tide per lunar day (e.g., Gulf of Mexico); (ii) Semidiurnal – two equal high and low tides per lunar day (e.g., Portugal); (iii) Mixed semidiurnal – two high and two low tides per lunar day, but of different heights (e.g., west coast of North America). Tide tables, showing the times and heights of high and low water, are based on harmonic analysis of

maregraphic observations over time in the harbour [89,101,102]. The accuracy of forecasts depends on the length of the observation period. In the case of the Portuguese Hydrographic Institute (IH) an observation period of at least one year was used for most ports in the Tide Table [101,102].

Ocean currents driven by variations in salinity, density, temperature, pressure, wave height, and tides, are a significant environmental factor in marine structure design. These generate significant loads, particularly in coastal zones, and must be considered during design, construction, and operation [91,97]. The current velocity should be added vectorially to the horizontal water particle velocity. While current effects are often neglected in direct calculations, they are accounted for indirectly by increasing wave height by 5%-10% [96]. Currents contribute to mooring drift, drag and lift forces, structural vibrations, and seafloor scouring, especially in cohesionless soils [96]. The scour around AR has been evaluated [15,20,27].

Ocean currents are categorized as follows [96,97]: (i) **wind-generated currents** ($V_{c,wind}$) arise from wind and atmospheric pressure changes, reaching up to 3% of the one-hour wind speed during tropical storms [11]; (ii) **tidal currents** ($V_{c,tide}$) result from planetary motions, typically weak in deep waters (<0.3 m/s) but stronger on broad shelves and narrow inlets (up to 3 m/s) [11]; (iii) **circulational currents** ($V_{c,circ}$) include large-scale flows like the Gulf Stream and Loop Current (1–2 m/s), which can form eddies exceeding main current speeds [11]; (iv) **loop and eddy currents** extend deep into the water column; (v) **soliton currents** arise from internal waves due to density differences and also penetrate deeply; and (vi) **longshore currents** run parallel to the shore, driven by wave angles [11].

Understanding the local current regime is a critical aspect in the design and assessment of ARs structures since current is among the most important factors affecting reef stability and performance [16,39]. Current velocity vector varies with depth and time, and the total current, $V_c(z)$, is given by the vector sum of its components [93]. Although currents are mostly turbulent, they are often approximated as averaged flows [93]. However, site-specific metocean data, particularly detailed current distributions and velocity profiles, are frequently limited or unavailable, presenting a challenge for accurate hydrodynamic analysis. Accurate knowledge of these currents is essential for determining hydrodynamic forces on the reef and for deriving hydrodynamic coefficients in numerical and

experimental models, ensuring that designs remain stable and effective under site-specific conditions [9,14].

A recent study investigated a three-layer "Puzzle Reef" deployed at the new seafloor observatory (OBSEA) (20 meters depth, NW Mediterranean Sea), where an Acoustic Doppler Current Profiler (ADCP) was used to continuously measure current speed and direction across the water column (cells spaced 1 meter each) [9]. The reef modules were designed to withstand currents up to 0.98 m/s without additional anchoring [9]. Numerical simulations considering current velocities from 0.1 to 1 m/s and different seabed types demonstrated general structural stability, although partial collapses occurred during extreme current events in October and November 2023 [9]. Maximum recorded current components reached 0.91–0.94 m/s, included components of 0.81–0.92 m/s (eastward), 0.61–0.64 m/s (northward), and 0.07–0.12 m/s (upward), emphasizing the critical role of site-specific current measurements in artificial reef design [9].

Another recent work examined 3D-printed ceramic AR, showing depth significantly affects post-deployment stability, with greater displacement at 15 meters (compared to 23 meters) due to local environmental conditions, including Northern Red Sea currents (up to 0.4 m/s) and seasonal storms influence structural behaviour. Physical experiments quantified hydrodynamic forces on reef modules to analyse hydrodynamic load, enabling the calculation of drag and inertia coefficients [14]. As a separate reference, a typical total current of 1 m/s is commonly used in the North Sea [11].

The cited work highlights the importance of current action in hydrodynamic studies, emphasizing that real measurements should be used whenever possible prior to the development phase, as also recommended by the standards and guidelines presented in Section 3.2. However, when direct field data is unavailable, analytical models can be used to estimate design current profiles [60,63,66,70]. In this context, the variation in shallow water of tidal current velocity with the depth may be modelled assuming unidirectional current according to **Eq. (3.1)** [60]. The variation of wind-generated current may be represented either by a linear profile from $z = -d_o$ to the still water level (SWL) (**Eq. (3.2)**) or by a slab profile (**Eq. (3.3)**), with the profile producing the highest loads for the specific application being applied [60]. Below the SWL ($z < d_o$), wind-generated currents can be considered negligible, i.e., $V_{c,wind}\ (z) = 0$ [96].

$V_{c,tide}\,(z)$	$V_{c,tide}\,(0)\left(\frac{d+z}{d}\right)^{\propto}$, $for\ z \le 0$	**(3.1)**
$V_{c,wind}\,(z)$	$V_{c,wind}\,(0)\left(\frac{d_0+z}{d_0}\right)$, $for - d_0 \le z \le 0$	**(3.2)**
	$V_{c,wind}\,(0)$, $for - d_0 < z < 0$	**(3.3)**
$V_{c,wind}\,(0)$	$k\,(U_{1hour,10m})$, deepwater	**(3.4)**

Where, z is the distance from the SWL measured positively upward, $V_{c,tide}(0)$ is the tidal current velocity at the SWL, $V_{c,wind}(0)$ is the wind-generated current velocity at the SWL, d is the water depth to SWL (taken as positive), d_o is the reference depth for wind-generated current and α is the exponent, typically $\alpha=1/7$.

In deep water along an open coastline, wind-generated current velocities at the SWL may be estimated, in the absence of current data, using **Eq. (3.4)**, where k=0.015–0.03k and ($U_{1hour,\ 10m}$) is the 1-hour sustained wind speed at a height of 10 meters above sea level.

3.4.3. Waves

Wave effects are critical in marine structures and must be carefully accounted for in the structural design. Understanding the wave regime is a critical aspect for the design and assessment of AR structures, as wave action is one of the main factors influencing hydrodynamic forces and AR stability, which vary with water depth, and consequently affect reef stability depending on the AR position. In fact, some works have studied the influence of water depth on the hydrodynamic forces acting on ARs by simulating regular and irregular waves, showing that the forces increase as water depth decreases, with the effect being most pronounced in ultra-shallow water [16]. The authors concluded that the influence of water depth on hydrodynamic forces is closely related to the ratio of water depth to reef height. Long-term hydrodynamic forces tend to increase as this ratio decreases, reaching approximately 10% higher than in deep water when the ratio is around 4.0. However, when the ratio exceeds 6.0, water depth has little effect on the hydrodynamic forces, as the reef is sufficiently submerged for wave interaction to be limited [16]. In this context, appropriate wave theory and prediction methods should be adopted, considering the characteristics of the structure and its position [98,103]. Ocean waves are irregular and random in shape, height, length, and speed, with a real sea

state being best represented by a random wave model [70]. Site-specific wave conditions, defined by parameters in **Table 3.4**, should be considered for accurate design and analysis.

Table 3.4: Typically wave parameters [96,97].

Parameter	Symbol	Significance
Wave Height	H	distance between its crest and trough. In deep water, wave height is often described by the Rayleigh distribution. It is common to consider the significant wave height parameter (H_s), representing the average height of the highest one-third of waves, $H_{1/3}$. In shallow water, the Rayleigh distribution is not applicable, and different distributions or parameters, such as $H_{2\%}$ or $H_{1/10}$, are used.
Wave Period	T	Wave period is the time a wave takes to travel one wavelength and can be defined as the average period or peak period (T_p), the latter being the inverse of the frequency with the highest wave energy
Wavelength	L or λ	distance between successive crests
Phase velocity	C	the propagation velocity of the wave form
Surface elevation	η	the surface elevation z = η (x, y, t) is the distance between the still water level and the wave surface
Water depth	d	distance between seabed and the SWL
Wave number	k	spatial frequency of a wave
Wave angular frequency	ω	rate at which a wave oscillates
Wave direction	-	direction from which waves approach a specific location
Wave slope	s	relationship between wave height and wavelength
Iribarren number	ξ	describes the wave action on a sloping beach, slope or structure
Wave energy spectrum	-	defines the distribution of wave energy across frequencies to predict wave behaviour. Common models include the **Pierson-Moskowitz** (for fully developed seas), **JONSWAP** (for growing seas), and **Bretschneider** (for swell conditions)

Wave theories

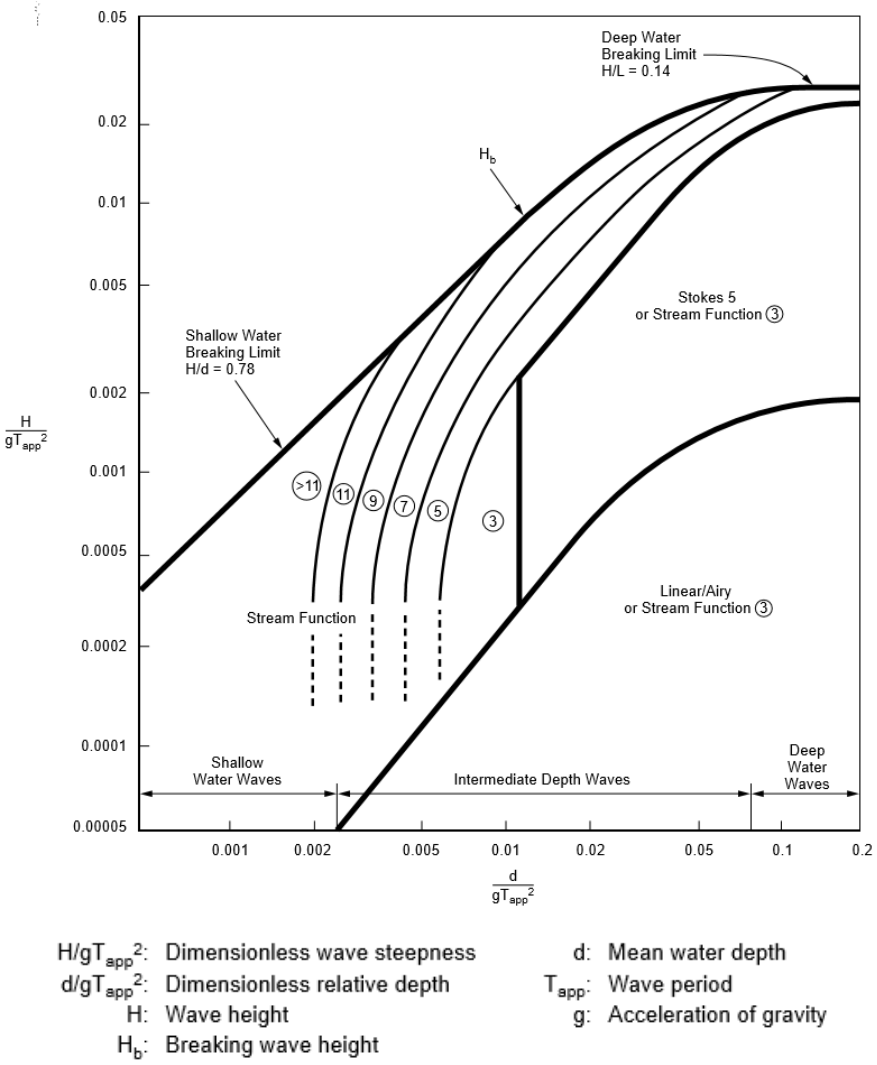
The mathematical description of seawater-wave phenomena is complex and difficult due to nonlinearities, three-dimensional characteristics and apparent random behaviour [60]. In this context, several theories have been developed, which are generally classified into small amplitude and finite amplitude wave theories [93]. The most common small amplitude wave theory is the Airy theory or Linear wave theory. Finite amplitude wave theories include the second to fifth-order Stokes theory, solitary wave theory, cnoidal theory, and stream function theory [96]. For engineering applications, including ARs, the most commonly used theories are the Airy, second-order and, in some cases, the fifth-order Stokes theories, as discussed below.

In a study of the interaction between waves and a hollow cube weighing 0.84 t, as well as a water pipe weighing 0.13 t — both with practical applications for ARs in shallow waters — linear wave theory was used to compute the horizontal water particle velocity [17]. Another investigation on porous artificial reefs employed linear wave theory to obtain wave kinematics during physical modelling experiments

in a wave flume, analysing wave transformation across both porous and impermeable artificial reefs under various regular wave conditions and submergence depths [104]. In the early stages of an MFAR experimental campaign, linear wave theory was also adopted to define water-level boundary conditions for numerical modelling, ensuring clean and reliable wave propagation in the flume [25]. However, the system was later transitioned from linear to second-order Stokes theory, implemented in the wave paddle control software to represent nonlinear wave behaviour [25]. Nevertheless, limitations of this approach became evident when the selected wave conditions exceeded the theory's range of validity, highlighting the importance of accurate boundary condition specification. Consequently, the fifth-order Stokes theory was considered to improve simulation accuracy under stronger nonlinear wave regimes [25].

Stokes' wave theory was also applied in an engineering-driven approach for the structural design of modular artificial reefs [13]. Additionally, the results obtained with the OBS modular system, with practical applications for modular ARs, showed good agreement with Stokes' second-order wave theory and with numerical tests carried out in the Numerical Wave Tank [105,106]; a rough approximation based on linear wave theory was also employed to estimate the order of magnitude of the measured forces [105,106]. Other numerical studies of flow around AR geometries modelled the inflow as unidirectional, based on the wave-induced velocity distribution derived from Stokes' wave theory [80,107].

As observed, the choice of wave theory is crucial for accurately capturing wave-structure interactions. **Figure 3.8** illustrates the applicable regions for different wave theories [93,103]. The fundamental wave parameters are used to define three non-dimensional parameters that determine the validity range of various wave theories: i) the wave steepness ($H/(gT^2)$), ii) the relative depth ($d/(gT^2)$) and iii) the Ursell number ($(H\lambda^2)/d^3$) [93,97].



H/gT_{app}^2: Dimensionless wave steepness
d/gT_{app}^2: Dimensionless relative depth
H: Wave height
H_b: Breaking wave height
d: Mean water depth
T_{app}: Wave period
g: Acceleration of gravity

Figure 3.8: Regions of Applicability of Wave Theory [11,92].

❖ Linear or Airy wave theory

The linear or Airy wave theory, developed by Airy in 1845, is the simplest and most widely used wave theory [92]. Often referred to as first-order Stokes or sinusoidal wave theory, it describes small amplitude waves with linear approximations. Based on the assumption that wave height is smaller than the wavelength or water depth, it linearizes the free surface boundary condition [92]. This theory provides accurate predictions for kinematic and dynamic properties of surface waves, making it suitable for most practical applications, especially for small wave steepness. **Table 3.5** presents the Airy wave theory formulas and **Table 3.6** shows the deepwater criteria and corresponding wavelength.

Table 3.5: Formulas for Airy theory [93].

Quantity	Finite depth	Deep water
Dispersion Relationship, ω^2	$\mathrm{gk}\tanh\mathrm{kd}$	gk
Wave profile, η	$\frac{\mathrm{H}}{2}\cos[\mathrm{k}(\mathrm{x}-\mathrm{ct})]$	$\frac{\mathrm{H}}{2}\cos[\mathrm{k}(\mathrm{x}-\mathrm{ct})]$
Horizontal velocity, u	$\frac{\mathrm{gkH}}{2\omega}\frac{\cosh[\mathrm{k}(\mathrm{y}+\mathrm{d})]}{\cosh\mathrm{kd}}\cos[\mathrm{k}(\mathrm{x}-\mathrm{ct})]$	$\frac{\mathrm{gkH}}{2\omega}\exp(\mathrm{ky})\cos[\mathrm{k}(\mathrm{x}-\mathrm{ct})]$
Vertical velocity, v	$\frac{\mathrm{gkH}}{2\omega}\frac{\sinh[\mathrm{k}(\mathrm{y}+\mathrm{d})]}{\cosh\mathrm{kd}}\sin[\mathrm{k}(\mathrm{x}-\mathrm{ct})]$	$\frac{\mathrm{gkH}}{2\omega}\exp(\mathrm{ky})\cos[\mathrm{k}(\mathrm{x}-\mathrm{ct})]$
Horizontal acceleration, $\dot{u}$	$\frac{\mathrm{gkH}}{2}\frac{\cosh[\mathrm{k}(\mathrm{y}+\mathrm{d})]}{\cosh\mathrm{kd}}\sin[\mathrm{k}(\mathrm{x}-\mathrm{ct})]$	$\frac{\mathrm{gkH}}{2}\exp(\mathrm{ky})\cos[\mathrm{k}(\mathrm{x}-\mathrm{ct})]$
Vertical acceleration, $\dot{v}$	$\frac{\mathrm{gkH}}{2}\frac{\sinh[\mathrm{k}(\mathrm{y}+\mathrm{d})]}{\cosh\mathrm{kd}}\cos[\mathrm{k}(\mathrm{x}-\mathrm{ct})]$	$\frac{\mathrm{gkH}}{2}\exp(\mathrm{ky})\cos[\mathrm{k}(\mathrm{x}-\mathrm{ct})]$
Dynamic pressure, p	$\mathrm{pg}\frac{\mathrm{H}}{2}\frac{\cosh[\mathrm{k}(\mathrm{y}+\mathrm{d})]}{\cosh\mathrm{kd}}\cos[\mathrm{k}(\mathrm{x}-\mathrm{ct})]$	$\mathrm{pg}\frac{\mathrm{H}}{2}\exp(\mathrm{ky})\cos[\mathrm{k}(\mathrm{x}-\mathrm{ct})]$

where t – time; g – gravity; $c=\frac{\omega}{k}=\frac{L}{T}$; ω=2π/T; k=2π/L; y = H/2

Table 3.6: Water depth criteria and wavelength [93].

Water depth	Criteria	tanh kd	Wavelength
Deep water	d/L ≥ 1/2	1	$L_0=\frac{gT^2}{2\pi}$
Shallow water	d/L ≤ 1/20	kd	$L=T\sqrt{gd}$
Intermediate water	1/20 < d/L < 1/2	-	$L=L_0\left[\tanh\left(\frac{2\pi d}{L_0}\right)\right]^{1/2}$

❖ Nonlinear wave theory – 2nd and 5th order Stokes theories

As the amplitude of the wave increases, the wave becomes non-linear. To accurately represent the motion of the wave, it is necessary to retain higher-order terms, especially when the wave amplitude is large [91]. Therefore, finite amplitude wave theories, such as the second to fifth-order Stokes theories, must be applied. These theories offer a more rigorous approximation, as the higher the order, the higher the limiting wave height for which the theory remains valid [91]. This method is considered valid for $H/d \leq (kd)^2$, for $(kd)<1$ and $H/L \leq 1$ [92]. **Figure 3.9** illustrates the classification of different wave types and their shapes based on the ratio of water depth (d) to wavelength (L).

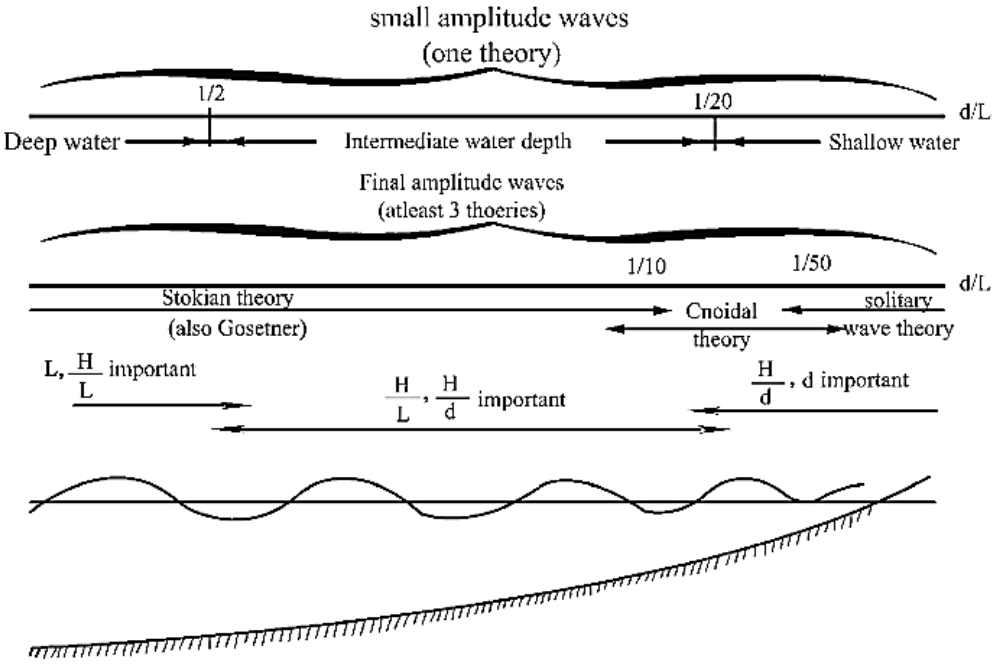


Figure 3.9: Classification of wave theories according to Keulegan (1950) [91].

Stokes' second-order theory is a mathematical model that determines two kinematic parameters. The second parameter has a lower magnitude and twice the specified wave frequency (see **Table 3.7**). The addition of this latter component alters the wave profile, making it more representative of the most prevalent wave type in the ocean, which is characterised by peaked crests and shallowest troughs. However, it should be noted that Stokes' second-order theory is only applicable when wave steepness is of the order of 0.1 [93]. In deep waters, the ratio d/L exceeds 0.5 and tanh kd is close to 1, so there is minimal contribution of the second-order component [93].

Table 3.7: Formulas for Stokes' second-order wave theory [93].

Quantity	1st order component	2nd order component
Dispersion Relationship, c^2	$\frac{g}{k}\tanh kd$	$\frac{g}{k}\tanh kd$
Wave profile, η	$\frac{H}{2}\cos(kx - \omega t)$	$\frac{\pi H^2}{8L}\frac{\cosh kd}{\sinh^3 kd}[2 + cosh\ 2kd]\cos 2(kx - \omega t)$
Horizontal velocity, u	$\frac{\pi H}{T}\frac{\cosh ks}{\sinh kd}\cos(kx - \omega t)$	$\frac{3}{4c}\left(\frac{\pi H}{T}\right)^2\frac{\cosh 2ks}{\sinh^4 kd}\cos 2(kx - \omega t)$
Vertical velocity, v	$\frac{\pi H}{T}\frac{\sinh ks}{\sinh kd}sin(kx - \omega t)$	$\frac{3}{4c}\left(\frac{\pi H}{T}\right)^2\frac{\sinh 2ks}{\sinh^4 kd}\sin 2(kx - \omega t)$
Horizontal acceleration, $\dot{u}$	$\frac{2\pi^2 H}{T^2}\frac{\cosh ks}{\sinh kd}sin(kx - \omega t)$	$\frac{3\pi}{2L}\left(\frac{\pi H}{T}\right)^2\frac{\cosh 2ks}{\sinh^4 kd}\sin 2(kx - \omega t)$
Vertical acceleration, $\dot{v}$	$\frac{2\pi^2 H}{T^2}\frac{\sinh ks}{\sinh kd}cos(kx - \omega t)$	$\frac{3\pi}{4L}\left(\frac{\pi H}{T}\right)^2\frac{\sinh 2ks}{\sinh^4 kd}\cos 2(kx - \omega t)$
Dynamic pressure, p	$pg\frac{H}{2}\frac{\cosh ky}{\cosh kd}\cos[k(x - ct)]$	$\frac{3}{4}pg\frac{\pi H^2}{L}\frac{1}{\sinh 2kd}\left[\frac{\cosh 2ks}{\sinh^2 kd} - \frac{1}{3}\right]\cos 2(kx - \omega t) - \frac{1}{4}pg\frac{\pi H^2}{L}\frac{1}{\sinh kd}[\cosh 2ks - 1]$

where $s = y + d$

Conversely, in the context of deep-water high waves, it is recommended to employ the Stokes' fifth-order theory. This encompasses five parameters, each exhibiting a lower magnitude and higher frequency compared to the preceding parameter. This configuration provides a more reliable representation of the wave profile [93]. The horizontal velocity is represented by a five-term series, as depicted in **Eq. (3.5)**:

$$u = \sum_{n=1}^{5} u_n\ \cosh\ nks \cos n(\ kx - \omega t) \qquad \textbf{(3.5)}$$

It is evident that higher-frequency wave components undergo rapid decay with depth, rendering their effects negligible in deeper waters. Consequently, even when employing Stokes' fifth-order theory, non-linear effects are significant only in proximity to the free surface [93]. Far from the mean water level, the waves behave more like the linear wave [93]. This enables numerous submerged structures in deep water to be designed using Airy wave theory without significant inaccuracies. However, it is important to note that the steeper crests and shallower troughs of fifth-order waves can have a significant impact on superstructure loads, airgap considerations, and floating structure motion [93].

- **Stream function theory**

Stream Function Theory is a highly accurate numerical approach for modelling finite amplitude waves, particularly in intermediate and shallow waters. Unlike Stokes' theories, which use a series expansion approach, Stream Function Theory (regular or irregular) employs a numerical iterative method to solve the governing equations while satisfying boundary conditions exactly [93]. This theory provides a more precise representation of wave kinematics and dynamics, making it especially useful for engineering applications involving steep waves and complex wave-structure interactions. Its use is especially recommended when detailed data on the free surface over time is available and widely used in numerical modelling.

Ocean wave prediction models

The description of wave conditions may be achieved through the utilisation of deterministic design wave methods or stochastic methods that employ wave spectra [97].

Deterministic methods are effective and simple when there is a clear understanding of wave conditions, such as a specific design wave with defined height and period. They are used to calculate the structural response to regular or "quasi-regular" waves, whose parameters can be predicted by statistical methods [97]. However, they do not account for the variability of wave conditions nor accurately represent complex spectral distributions. To predict the response of quasi-static structures, deterministic regular wave theories are sufficient [97].

Stochastic methods are more suitable for modelling dynamic behaviour of structures, such as floating structures, as they account for the variability and uncertainty of wave conditions over time. These methods use wave spectra, like Pierson-Moskowitz or JONSWAP, to represent the energy distribution of waves and the probability of different wave conditions occurring. By simulating the structure's response to a wave distribution over an extended period, this approach offers more realistic modelling, providing a more accurate prediction of the structure's performance over time and under varying sea conditions. However, stochastic methods are more complex, requiring increased time, computational resources, and detailed statistical data for simulations [97].

3.4.4. Marine growth

Marine growth is predominantly observed on submerged structural components, increasing the thickness and surface roughness, resulting in a rise in mass and element diameter. This amplifies drag forces and lowers natural frequencies due to the added non-structural mass [96,108]. Since ARs structures are intentionally designed to be colonised, marine growth must be accounted for by increasing member dimensions and selecting the appropriate drag and inertia coefficients based on classifying elements as hydrodynamically "smooth" or "rough" depending on expected accumulation [96]. As previously mentioned, the study of the hydrodynamic coefficients may be done with experimental testing [9,14,39]. Structural members are considered smooth above the mean higher high water (MHHW) or below 45 meters, where marine growth is minimal, and rough in the zone between these depths [11,96]. The effective element diameter (cross-sectional width for non-circular cylinders, or prisms) considers the "clean" outer diameter (D_c) and the average growth thickness (t), given by $D = D_c + 2t$. In the absence of site-specific information, the values provided by DNV-RP-C205 [97], NORSOK N-003 [89], ISO 19901-1 [109], and API RP 2A-WSD [11] can be used as indicative values for marine growth thickness, as shown in **Table 3.8**. For elements with circular cross-sections, the drag coefficient is influenced by the relative roughness (e), defined as the ratio of the average peak-to-valley height of hard growth organisms (k) to the diameter (D), as $e = k/D$ [11].

Table 3.8: Examples of estimated maximum thickness of marine growth for different locations, based on [11,89,97,110].

Water depth	**Location**				
	North-west Europe	United Kingdom	Gulf of Mexico	US Coast of California	West coast of Africa
+2 m	0 mm (56-59°N) 0 mm (59-72°N)	-	-	200 mm (range depth not specified)	30 mm
+2 to -40 m	100 mm (56-59°N) 60 mm (59-72°N)	200 mm (hard)[1] 70 mm (soft)[2] 300 mm (soft)[3]	-38 mm[4]		100 mm
-40 m	50 mm (56-59°N) 30 mm (59-72°N)	10 mm (hard)[3] 300 mm (soft)[3]			100 mm

[1]from 0 to -30 m; [2] from 0 to -15 m; [3]from -30 to seafloor; [4]from MHHW to -50 m.

3.4.5. Earthquakes

ARs structures in seismic regions must be designed considering seismic action, based on detailed site investigations, including seismic and tectonic characterization, seismic exposure assessment, and the

definition of design ground motion [108]. In areas with low seismic activity (<0.05 g), environmental load design generally provides sufficient structural safety. For seismic activity between 0.05–0.1 g, seismic behaviour should be verified, particularly for installations such as piping and facilities, using dynamic analysis methods like spectrum or time history analysis [108]. Additional requirements are provided by ISO 19901-2 [108].

3.4.6. Accidental Actions

Accidental actions are defined as events which, although unlikely, have the potential to cause structural collapse if not properly considered. Such events may include collisions, dropped objects, explosions, fires and abnormal waves. Detailed guidance is given in *Guidance Notes on Accidental Load Analysis and Design for Offshore Structures* [111]. In the context of artificial reefs, the main concern is the abnormal wave or debris or objects impacts.

3.4.7. Sea ice and snow

Snow accumulation should be considered when relevant and combined with other environmental conditions. Ice loads are crucial for structures in Alaska [96]. Structural design must account for sea ice and icebergs, considering their type, thickness, drift speed, direction, and interaction with environmental actions. Long-term statistics of these factors are also essential. Detailed guidance is provided by ISO 19906 [108].

3.4.8. Temperature

Sea and air temperatures may be relevant in structural design, as they are deemed to be significant factors in material selection due to their potential impact on the characteristics of the materials. Furthermore, it is imperative to take into account the prediction of temperature variations over the anticipated lifetime of the structure [108].

3.5. ANALYTICAL MODELS FOR HYDRODINAMIC LOADING

Estimating hydrodynamic loads is complex due to the main actions involved. Specifically, estimating wave forces on marine structures is challenging due to a number of factors, including non-linearity in water motion, wave variability, turbulence, wave-interactions, and dynamic effects [91]. Wave force equations describe unsteady, non-uniform flow with non-deterministic dynamic effects [112]. Consequently, the selection of an appropriate wave theory and hydrodynamic coefficients is imperative to ensure the alignment between theoretical assumptions and experimental data [91].

Wave forces on a structure might be obtained using different methods based on its size, classified as small or large according to the Keulegan-Carpenter number (KC) - a parameter that relates water particle excursion to structure diameter - and the diffraction parameter (k_a) which compares the structure diameter with the incident wavelength scale. These classifications depend on factors like the element diameter (D) and fluid parameters including wave period (T), wavelength (L), and water particle velocity (u) (**Figure 3.10**) [91,113]. The Morison equation is used to determine wave forces on small structures with members having $D/L < 0.2$ or $KC > 6$ and $k_a < 0.5$, as the structure does not significantly alter the incident wave [112,113]. For larger members, where D/H ratios are large and KC values are very small, more complex theories, such as Froude-Krilov force, wave diffraction force or linear diffraction theory ($D/L > 0.2$; $k_a > 0.5$) should be considered since these structures cause a large amount of scattering or diffraction of the incident wave [112,113]. Thus, since the length scale of an AR is generally smaller than the wavelength the Morison equation can be used, as reported in several studies [14,114–116]. Although the Morison equation does not consider the interaction of the structure to the fluid, it is efficient and accurate for calculating wave forces, but unsuitable for large reef bodies or AR groups [15]. Miao and Xie (2007) analysed the distribution of flow and wave forces on floating artificial reefs with a cylindrical rigid frame using static theory and the Morison equation [16].

In general, the wave forces acting on the structure depend on several independent parameters. **Eq. (3.6) and**. **Eq. (3.7)** identifies the important non-dimension parameters that contribute to the forces on a structure [113],

$$f = \psi(t, T, D, K, f_s, L, u_0, \rho, v) \quad \textbf{(3.6)}$$

$$\frac{f}{\rho u_0^2 D} = \psi\left(\frac{t}{T}, \frac{u_0 T}{D}, \frac{u_0 D}{\nu}, \frac{\pi D}{L}, \frac{K}{D}, \frac{U}{f_s D}\right) \quad \textbf{(3.7)}$$

- $\frac{U}{f_s D}$ → Reduced velocity (V_R)
- $\frac{K}{D}$ → Relative roughness parameter (e)
- $\frac{\pi D}{L}$ → Diffraction Parameter (k_a)
- $\frac{u_0 D}{\nu}$ → Reynolds number (Re)
- $\frac{u_0 T}{D}$ → Keulegan-Carpenter number (KC)

which involves time (t), mass density of water (ρ), wave period (T), water particle velocity amplitude (u_o), kinematic viscosity of water (ν), surface roughness parameter (K), member diameter (D), wavelength (L), current velocity (U) and structure vibration frequency (f_s).

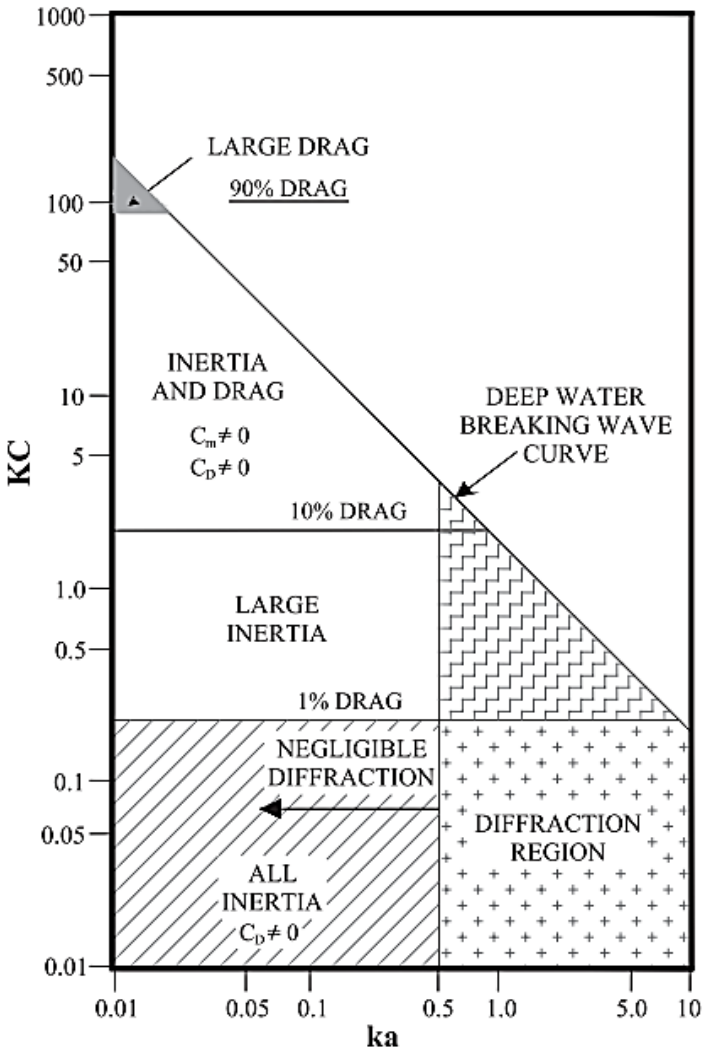


Figure 3.10: Wave force regimes and limits of application for small vs. large structure [112].

Figure 3.11 illustrates the fluid particles' velocities and acceleration directions at each location. These parameters are fundamental for the calculation of the wave forces on structures, as both inertial and drag forces are directly dependent on them [90].

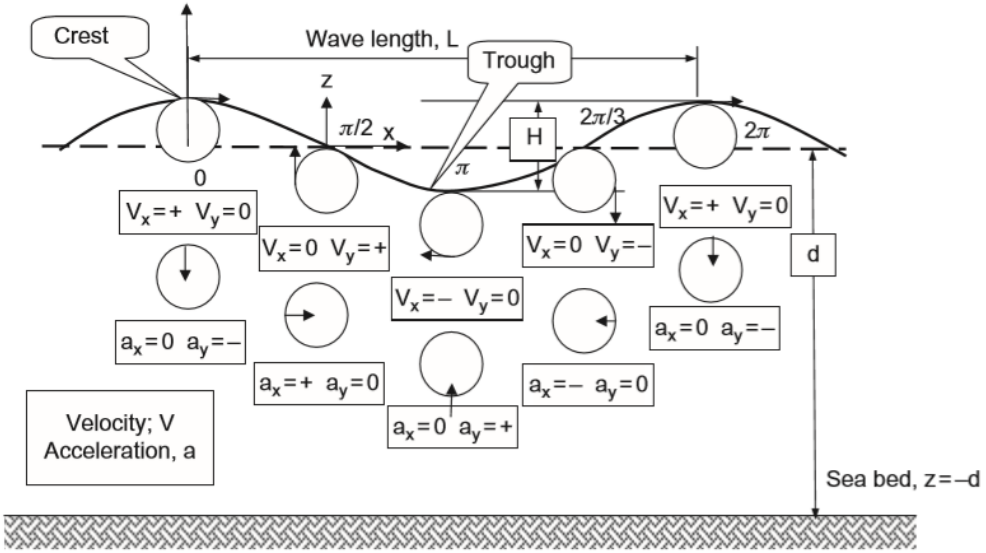


Figure 3.11: Fluid particles velocities and acceleration directions at every location [90].

- **Morison formulation**

The Morison equation is a semi-empirical equation widely used in fluid dynamics to estimate wave and current loads in the design of marine structures, including ARs. Initially introduced to calculate horizontal wave force on a vertical cylinder, the equation has been adapted for use in other structures such as pipelines and risers [91].

The hydrodynamic force is computed as the sum of two components: drag force, which depends on water orbital particle velocity, and inertia force, which is related to water particle acceleration as shown in **Eq. (3.8)** [91,117]. When ocean current is present, the total water particle velocity is adjusted by adding the wave particle velocity to the current velocity. If the current is inline, the velocities are simply added to determine the total velocity. The combined effects of water particle velocity and acceleration yield the horizontal force on a vertical element (dz) of the structure at a given level (z) due to regular waves [108,117]:

$$dF = dF_D + dF_I \quad \textbf{(3.8)}$$

$$dF_D = C_D \times \frac{1}{2} \times \rho \times A \times u|u|dz$$

$$dF_I = C_M \times \rho \times V \times \frac{\partial u}{\partial t} dz$$

Where,

- dF is the local action vector per unit length acting normal to the axis of the member [N/m];
- dF_D is the vector for the drag action per unit length acting normal to the axis of the member in the plane of the member axis [N/m];
- dF_I is the vector for the inertia action per unit length acting normal to the axis of the member in the plane of the member axis [N/m];
- z is the level measured from the still water level and z axis point upward;
- C_D is the hydrodynamic drag coefficient [-];
- ρ_w is the mass density of water [kg/m^3];
- A is the is the effective dimension of the cross-sectional area normal to the member axis per unit length (= D for circular cylinders) [m];
- V is the displaced volume of the member per unit length (= $\pi D^2/4$ for circular cylinders) [m^2];
- D is the effective diameter of a member (a circular cylinder), including marine growth [m];
- u is the component of the local water particle velocity vector (due to waves and/or current) normal to the axis of the member [m/s];
- |u| is the modulus (the absolute value) of u [m/s];
- C_M is the hydrodynamic inertia coefficient;
- $\frac{\partial u}{\partial t}$ is the component of the local water particle acceleration vector normal to the axis of the member (m/s^2).

As shown, the drag force and inertia force depend on the drag and inertial coefficients, respectively. In the case of wave plus current load, the drag coefficient must consider the combined effect of the actions [11,113]. Hydrodynamic coefficients can be determined experimentally through laboratory tests or field measurements [118]. However, in the case of ARs, these coefficients are often difficult to obtain due to the complex geometry and flow conditions associated with such structures, and therefore they are typically estimated [116] or derived from engineering judgment. It should be noted that, over time, C_D increases as biological growth occurs on the AR surface, increasing roughness and leading to higher drag forces. C_M, depends on the added mass experienced by the structure when

water accelerates. It is generally expressed as $C_M = 1 + k_m$, where k_m is the added mass term. For the modular artificial reef (MOSES) composed of interlocking blocks [116], the adopted values of $C_D$and C_M were based on geometric similarity to the reefs studied by Koudstaal & van Rijn (2020), as reported in their experiments (**Table 3.9**) [116]. For reefs with a circular cross-section, $k_m = 1$, giving $C_M = 2$. However, when a reef is placed directly on the seabed, proximity to the boundary increases the added mass, and k_m becomes 2, resulting in $C_M = 3$ (**Table 3.9**) [116]. Woo et al. (2014) [39] investigated the drag coefficients of 24 representative artificial reefs used in South Korea, developing a practical methodology to estimate these values based on geometric characteristics such as wall area, height, and orientation relative to the flow. The investigation grouped the ARs in six types: box, tunnel, arch, dome, leg, and complex types, and representative examples of each type are shown in **Table 3.9**. The dimensions, porosity, permeability and the flow angle were also discussed [39]. This study provides valuable reference data for the hydrodynamic design and analysis of new artificial reefs, offering a reliable basis for comparison with other ARs. In the absence of specific data, it is common practice to use typical values reported in standards and guidelines for regular structural members, as shown in **Table 3.9**.

The forces predicted by the Morison equation provide an engineering approximation [11,118]. However, according to API [11], the equation does not account for certain effects, including the convective acceleration component in the inertia force calculation, slam forces, and axial Froude-Krylov forces [11]. Additionally, it ignores the lift force (transverse to the flow direction) generated by waves in steady flow [118].

Once the forces acting on the structure are evaluated and quantified, it is essential to combine them according to relevant standards and recommendations. The principles for actions combination are outlined in ISO 19900, while NORSOK N-003 provides a detailed and specific methodology for combining actions of different values.

Table 3.9: Typical values of hydrodynamic coefficients.

Type	Dimension [m]	C_D	C_M	References
Smooth, unshielded circular cylinders	-	0.65	1.6	[119]
Rough, unshielded circular cylinders	-	1.05	1.2	[119]
Modular AR (MOSES)	2.0×2.0×1.0	2.0	2.0 to 3.0	[116]
X-coral AR (unit A+B)	≈ 0.4×0.3×0.3	0.8 to 0.9*	6.5 to 7.0	[14]
Korean AR01 (Box – only edges)	2.0×2.0×2.0	1.51	-	[39]
Korean AR03 (Box – intricate hollow)	3.0×3.0×3.0	2.11	-	
Korean AR08 (tunnel – pyramidal shape)	2.2×2.2×1.4	0.83	-	[39]
Korean AR07 (tunnel – square, hollow)	3.0×3.0×2.4	1.17	-	
Korean AR10 (arch – double)	2.4×2.9×1.4	0.95	-	[39]
Korean AR11 (arch – hedgehog)	3.4×5.0×2.8	1.24	-	
Korean AR12 (dome – similar to reefball)	4.1×4.1×2.1	0.62	-	[39]
Korean AR13 (dome – pyramidal)	3.3×3.3×2.2	0.95	-	
Korean AR17 (leg – cross)	3.0×3.0×0.5	0.70	-	[39]
Korean AR16 (leg – W)	2.0×2.4×1.5	1.26	-	
Korean AR18 (complex – boxes)	3.0×2.0×2.6	1.27	-	[39]
Korean AR20 (complex – intricate boxes)	12.0×12.0×8.0	2.47	-	
Korean AR19 (complex – frames, plates)	4.9×4.9×4.0	2.56		

*Includes the supporting pole structure (12 mm steel rods).

- **Froude-Krylov force**

The main difference between Froude-Krylov forces and the Morison equation lies in how they account for the interaction between waves and structure. The Froude–Krylov pressure forces represent the pressure exerted by the incident wave on a structure, without considering the disturbance that the structure causes in the surrounding flow field [112,118]. They are derived directly from the unperturbed wave pressure distribution, as described by wave potential theory [112,118]. Froude-Krylov forces are particularly relevant when the structural dimension is large relative to the wavelength, where wave diffraction effects are significant as found for semi-submersible platforms, vessels, floating production storage and offloading, large monopiles and SPARs [112,118]. Despite its limitations, applying force coefficients can account for wave diffraction effects, making this method useful for moderate-sized structures with simple contours.

- **Wave diffraction force**

When the relative characteristic dimension of a structure is large compared to the wavelength of the incident wave, diffraction effects become significant. This leads to the scattering of the incident wave around the structure (D/L>0.2), altering the wave pattern and creating complex hydrodynamic forces [112,118]. The linear diffraction theory assumes small wave amplitudes and linear superposition, simplifying the calculation of forces acting on structures like semi-submersible platforms, FPSOs, or large monopiles [112,118]. The key considerations in solving the linear diffraction problem include the wave diffraction parameter ka, and the need to consider both the incident and diffracted waves when calculating forces [112,118]. The theory provides a mathematical framework to predict the wave-induced forces on the structure without fully accounting for the nonlinearities that occur in more extreme conditions. Although the theory offers a simplified approach, it is essential for accurately determining the dynamic response and stability of large offshore structures in realistic wave environments [112,118].

3.6. DURABILITY

Marine structures are subjected to harsh environmental conditions, including constant exposure to saltwater, humidity, environmental action, and temperature variations [64,120–122]. These factors accelerate physical, chemical, and microbiological deterioration, leading to severe durability problems such as material degradation, corrosion and fatigue failure as evidenced in **Figure 3.12** [64,120–122].

Durability problems in ARs often arise from material degradation, insufficient maintenance, and incompatibility between the reef structure and its surrounding environment, which can result in pollution and the failure to achieve ecological objectives. Although materials such as durable concrete and steel cages are designed for long service life, reefs constructed with less stable materials—such as tires—can release pollutants, as exemplified by the Osborne Reef disaster. Even durable structures are susceptible to degradation or failure without proper long-term management [14,123]. Consequently, these challenges contribute to reduced service life, increased maintenance costs, structural failures, and undesirable environmental impacts [124]. The durability, potential toxicity, and environmental impacts are therefore recognized as critical factors in ARs, yet they have been rarely investigated in detail [14,120,123].



(a) (b)

Figure 3.12: Damage to structures exposed to the marine environment: (a) steel corrosion of a marine structure and (b) damaged submerged concrete [125–127].

Steel structures and structural systems designed to combine advanced coated steel and adequate concrete are favoured due to their excellent resistance to marine environments as the concrete and coatings protect against external damage, reducing the need for regular maintenance. Despite alternatives like stainless steel and FRP, steel remains essential in construction because it is cost-effective, easy to process, and mechanically versatile. To mitigate durability challenges, various methods are employed, from design and materials strength considerations to protective coating systems [122]. Cathodic protection is frequently used in submerged and tidal zones, alongside coating systems [93].

Coating systems may consist of multiple layers, combining organic/inorganic (or both), metallic and non-metallic coatings. Metallic coatings, typically made of zinc, aluminium, and alloys, provide corrosion protection to steel through galvanic action and barriers. In recent decades, various organic-based coatings, such as anti-fouling paints [122,128,129] epoxy, special mixed coating, and hybrid sol-gel materials [63,122,130], have been developed to enhance protection and durability. **Table 3.10** presents various types of protection systems, as well as the potential release of toxic substances into the ocean if the protection system deteriorates, along with possible structural concerns.

Table 3.10: Examples of protection systems for steel and concrete marine structures.

Protection systems	Type	Toxic ocean products risk[1]	Structural concerns	References
Design and materials specifications	-	-	-	[131]
Marine and anti-fouling paints (e.g epoxy prime, epoxypoliamide, polyurethane, self-polishing, copolymers)	Organic non-metallic coating	High	-	[122,128, 129]
Acrylic coatings	Organic non-metallic coating	High	Less durable	[132]
Epoxy based coatings	Organic non-metallic coating	High	Low mechanical resistance Pone to damage Affect bond strength	[64,130, 131]
Zinc-Rich epoxy coating	Organic non-metallic coating	High	Affect bond strength	[63,122]
Zinc coating (e.g. HDG)	Inorganic metallic coating, cathodic protection	No problematic	Affect bond strength	[121,132, 134]
Zinc coating w/ epoxy coating	Mixed coating	High	Affect bond strength	[56]
Metallic coating with paint	Duplex system	High	-	[122]
Anodic/cathodic anodes (e.g zinc, magnesium, aluminum)	Potential change, anodic/cathodic protection	Low	-	[135]
Organic-inorganic sol-gel coatings (e.g epoxy-silica-zirconia sol-gel)	Special mixed coating	Moderate	Affect bond strength	[63,122, 130]
Modified Polysiloxane coatings	Special mixed coating	Moderate	-	[136]
Methacrylate surface coating	Organic non-metallic coating	High	Affect bond strength	[137]
Supplementary cementitious materials (e.g slag, fly ash, metakaolin silica fume)	Mineral admixtures	Low	Influence chloride threshold Increase surface scaling Might affect bond strength	[131, 137–139]
Alternative binders (e.g AC, SAC, AAM, MKPC, MNPC)[2]	Inorganic binder material	Low	Might affect bond strength	[134,137]
Chemical additives (e.g chromates)	Corrosion inhibitors in concrete mixture	High	Affect bond strength	[60,64]

[1]concerns the potential release of toxic substances if the protective system deteriorates, considering the components involved and the risk of generating microplastics and other harmful substances

[2]Alumina cement (AC), silica-alumina cement (SAC), alkali-activated materials (AAM) (e.g geopolymer), magnesium potassium phosphate cement (MKPC), magnesium ammonium phosphate cement (MNPC).

As shown, organic and hybrid coatings (e.g. paints, epoxy, methacrylate, polysiloxanes) are of particular concern when considering marine pollution due to their degradation into microplastics and the release of solvents and toxic polymeric bases. In contrast, metallic and cementitious coatings pose a lower risk since they do not contribute to direct plastic debris, but may suffer leaching. However, despite their advantages, protective coatings can influence the bond behaviour between the reinforcement element and concrete, potentially affecting short and long-term structural integrity. Research findings indicate that, following 250 days of exposure to seawater, steel reinforcement may experience a reduction in bond strength of up to 10%, while GFRP reinforcement may exhibit a loss of up to 20% [140,141].

Therefore, selecting appropriate protective systems and optimizing structural designs are crucial to ensuring long-term durability, cost-effectiveness, and sustainability in marine engineering.

3.7. FINAL CONSIDERATIONS

This chapter addressed the principles and methodologies involved in parametric design, structural analysis, and regulatory framework for marine structures, with a particular focus on single and multipurpose modular artificial reefs (MMFAR). The integration of parametric modelling tools, such as Rhino and Grasshopper, has been emphasized as a crucial approach for optimizing the structural and geometric aspects of artificial reefs, facilitating iterative design processes and enhancing flexibility.

The discussion on regulatory frameworks highlighted the importance of international and national standards, particularly the Eurocodes, while also acknowledging their limitations in addressing the specific challenges of marine structures. Complementary standards and industry guidelines remain essential to ensure the structural integrity and performance of these constructions under complex environmental conditions.

Various design methods and analytical, experimental, and numerical approaches were examined, showcasing the multidisciplinary nature of artificial reef structure development. The integration of Finite Element Analysis (FEA), Computational Fluid Dynamics (CFD), and Fluid-Structure Interaction (FSI) techniques was identified as fundamental for evaluating structural behaviour, hydrodynamic forces, and long-term stability. Experimental techniques, such as hydraulic flume testing, bond tests, mechanical characterization were reviewed to demonstrate their role in structural performance and design.

The chapter also addressed critical design considerations, including load assessment, hydrodynamic forces and durability challenges, emphasizing the significance of corrosion protection strategies and material selection in harsh marine environments. Additionally, the complexity of the underwater environment, along with unpredictable factors such as climate change and sea condition variability, presents significant challenges for the structural analysis of modular reefs. For quick and well-defined wave conditions, deterministic methods are suitable. For more comprehensive and realistic analyses, considering variability and long-term risks, stochastic methods are preferable.

Overall, this chapter underscores the necessity of a holistic and integrated approach in the design of next generation marine structures, combining parametric modelling, structural analysis, experimental

validation, and regulatory compliance to achieve efficient, durable and sustainable artificial reef systems.

3.8. REFERENCES

[1] Azanaw GM. Material efficiency through mechanics: A systematic review of advanced structural modeling for load-optimized building design. Int J Inventive Eng Sci 2025;12:8–18. https://doi.org/10.35940/ijies.g1106.12060625.

[2] Martín-Mariscal A, Fernández-Rodríguez JF, Picardo A, Peralta E. Grasshopper algorithmic modelling: Parametric design for product platform customisation. Appl Sci 2025;15:6243. https://doi.org/10.3390/app15116243.

[3] Fu F. Design and analysis of tall and complex structures. Oxford: Butterworth-Heinemann; 2018.

[4] European Commission. Eurocodes: Building the future. Available from: https://eurocodes.jrc.ec.europa.eu/. Accessed October 6, 2019.

[5] International Association of Oil & Gas Producers (OGP). Position paper on the development and use of international standards. London: OGP; 2010.

[6] International Association of Oil & Gas Producers (OGP). Regulators' use of standards. London: OGP; 2010.

[7] CEN, ISO. Guidelines for the implementation of the Agreement on Technical Cooperation between ISO and CEN (the Vienna Agreement). Brussels: CEN; Geneva: ISO; 2014.

[8] Manco T. Avaliação comparativa da regulamentação para estruturas offshore (API, ISO, NORSOK, EC3) [Master's thesis]. 2013.

[9] Francescangeli M, Toma DM, Mendizabal V, Carandell M, Martinez E, Martin D, et al. Artificial reef based ecosystem design and monitoring. Ecol Eng 2025;221:107752. https://doi.org/10.1016/j.ecoleng.2025.107752.

[10] Fu F. Advanced modelling techniques in structural design. Oxford: Wiley-Blackwell; 2015.

[11] American Petroleum Institute (API). API Recommended Practice 2A-WSD: Recommended practice for planning, designing and constructing fixed offshore platforms—Working stress design. Washington, DC: API; 2003.

[12] Kim YC. Handbook of Coastal and Ocean Engineering. Singapore: World Scientific; 2010.

[13] Cruz F, Valente IB, Maslov D, Miranda T, Pereira EB. Engineering-driven approach for the structural design of geometrically complex modular artificial reefs. Appl Sci 2025;15:5907. https://doi.org/10.3390/app15115907.

[14] Berman O, Zavadsky A, Drimer N, Shashar N, Wang G, Tarazi E. A pure ceramic 3D printed artificial reef: Stability and response. J Clean Prod 2025;523:146380. https://doi.org/10.1016/j.jclepro.2025.146380.

[15] Pan Y, Tong H, Wei D, Xiao W, Xue D. Review of structure types and new development prospects of artificial reefs in China. Front Mar Sci 2022;9:853452. https://doi.org/10.3389/fmars.2022.853452.

[16] Miao ZQ, Xie YH. Effects of water depth on hydrodynamic force of artificial reef. J Hydrodyn 2007;19:372–377. https://doi.org/10.1016/S1001-6058(07)60072-9.

[17] Düzbastılar FO, Şentürk U. Determining the weights of two types of artificial reefs required to resist wave action in different water depths and bottom slopes. Ocean Eng 2009;36:900–913. https://doi.org/10.1016/j.oceaneng.2009.06.008.

[18] Cruz F, Pereira E, Valente IB, Tiago M, Maslov D, Pinheiro M. Structural design of an innovative multifunctional artificial reef. Oceans 2018 MTS/IEEE Charleston, IEEE; 2018, p. 1–7. https://doi.org/10.1109/OCEANS.2018.8604587.

[19] Kertorahardjo SP, Vincent H, Duta PH. Structure analysis on artificial reefs. Appl Mech Mater 2018;874:27–34. https://doi.org/10.4028/www.scientific.net/AMM.874.27.

[20] Cruz F, Pereira E, Lima M, Johnson J, Duarte D, Valente IB, et al. Experimental characterization of the scour of innovative artificial reef prototypes using hydraulic flume and photogrammetry. OCEANS 2019 MTS/IEEE Marseille, IEEE; 2019, p. 1–10. https://doi.org/10.1109/OCEANSE.2019.8867581.

[21] Galdo L, Carballo R. Numerical and experimental analysis of the velocity field inside an artificial reef: Application to the Ares-Betanzos estuary. J Mar Sci Eng 2022;10:1827. https://doi.org/10.3390/jmse10121827.

[22] Maslov D, Johnson J, Pereira E, Duarte D, Miranda T, Lima M, Cruz F, Valente I, Pinheiro M. Experimental testing and CFD modelling for prototype design of innovative artificial reef structures. OCEANS 2019 MTS/IEEE Marseille; 2019. p. 1–7. https://doi.org/10.1109/OCEANSE.2019.8867383.

[23] Vieira BFV, Pinho JLS, Barros JAO, Antunes do Carmo JS. Hydrodynamics and morphodynamics performance assessment of three coastal protection structures. J Mar Sci Eng 2020;8:175. https://doi.org/10.3390/jmse8030175.

[24] Neves MG, Fortes CJ. Numerical study of hydrodynamics around an artificial surf reef for São Pedro do Estoril, Portugal. J Coast Res 2009;SI 56:1163–1167.

[25] Kroon MEN. Design method for multi-functional artificial reefs in a coastal environment: Integrating ecological and coastal protection [Master's thesis]. 2016.

[26] Xu L, Gao S, Wang D, Barltrop N. Shallow water breaking wave loads on vertical cylinders. Adv Mater Res 2013;694–697:659–664. https://doi.org/10.4028/www.scientific.net/AMR.694-697.659.

[27] Kimura H, Ingsrisawang V, Ban M. Study on local scour of cylindrical artificial fish reefs. J Fish Eng 1994;31:33–40. https://doi.org/10.18903/fisheng.31.1_33.

[28] Yun DH, Kim YT. Experimental study on settlement and scour characteristics of artificial reef with different reinforcement type and soil type. Geotext Geomembranes 2018;46:448–454. https://doi.org/10.1016/j.geotexmem.2018.04.005.

[29] Düzbastılar FO, Lök A, Ulaş A, Metin C. Recent developments on artificial reef applications in Turkey: Hydraulic experiments. Bull Mar Sci 2006;78:195–202.

[30] Ji Z, Li Z, Hu L. Characteristics from a hydrodynamic model of a trapezoidal artificial reef. Chinese J Oceanol Limnol 2014;32:1329–1338. https://doi.org/10.1007/s00343-014-3298-9.

[31] Galdo MIL, Guerreiro MJR, Vigo JL, Rodríguez IA, Lorenzo RV, Couce JCC, et al. Definition of an artificial reef unit through hydrodynamic and structural (CFD and FEM) models: Application

to the Ares-Betanzos estuary. J Mar Sci Eng 2022;10:230. https://doi.org/10.3390/jmse10020230.

[32] Yoris-Nobile AI, Slebi-Acevedo CJ, Lizasoain-Arteaga E, Indacoechea-Vega I, Blanco-Fernández E, Castro-Fresno D, et al. Artificial reefs built by 3D printing: Systematisation in the design, material selection and fabrication. Constr Build Mater 2023;362:129766. https://doi.org/10.1016/j.conbuildmat.2022.129766.

[33] Cruz F, Valente IB, Miranda T, Pereira EB. Construction and characterization of a structural unit for modular artificial reefs. Structures 2025;81:110154. https://doi.org/10.1016/j.istruc.2025.110154.

[34] Chen C, Ji T, Zhuang Y, Lin X. Workability, mechanical properties and affinity of artificial reef concrete. Constr Build Mater 2015;98:227–236. https://doi.org/10.1016/j.conbuildmat.2015.05.109.

[35] Han S, Jung S, Na WB. Estimation of seabed settlement during initial installation of a box-type artificial reef considering different seabed soil compositions and incident angles. Ocean Eng 2020;218:108269. https://doi.org/10.1016/j.oceaneng.2020.108269.

[36] Xue D, Wang C, Huang T, Pan Y, Zhang N, Zhang L. Flow field effects and physical stability of pyramidal artificial reef with different slope angles. Ocean Eng 2023;283:115059. https://doi.org/10.1016/j.oceaneng.2023.115059.

[37] Mendonça A, Neves MG, Fortes CJ, et al. Hydrodynamics around an artificial surfing reef at Leirosa, Portugal. J Waterw Port Coast Ocean Eng 2012;138:226–235. https://doi.org/10.1061/(ASCE)WW.1943-5460.0000128.

[38] Kim D, Woo J, Na WB, Yoon HS. Flow and structural response characteristics of a box-type artificial reef. J Korean Soc Coast Ocean Eng 2014;26:113–119. https://doi.org/10.9765/KSCOE.2014.26.3.113.

[39] Woo J, Kim D, Yoon HS, Na WB. Characterizing Korean general artificial reefs by drag coefficients. Ocean Eng 2014;82:105–114. https://doi.org/10.1016/j.oceaneng.2014.02.025.

[40] Yu J, Li DB, Wang DB. Digital design of artificial reef with computational fluid dynamics and topology optimization. In: Proceedings of the International Conference; vol. 1. Singapore: Springer Nature Singapore; 2024. https://doi.org/10.1007/978-981-96-3433-0.

[41] Tavakoli S, Singh M, Hosseinzadeh S, Hu Z, Shao Y, Wang S, et al. A review of flexible fluid-structure interactions in the ocean: Progress, challenges, and future directions. Ocean Eng 2025;342:122545. https://doi.org/10.1016/j.oceaneng.2025.122545.

[42] Shu A, Qin J, Rubinato M, Sun T, Wang M, Wang S, et al. An experimental investigation of turbulence features induced by typical artificial M-shaped unit reefs. Appl Sci 2021;11:1393. https://doi.org/10.3390/app11041393.

[43] Jiao L, Zhao YX, Gu PH, Gu CT. Numerical simulation and PIV experimental study of the effect of flow fields around tube artificial reefs. Ocean Eng 2017;140:96–104. https://doi.org/10.1016/j.oceaneng.2017.02.016.

[44] Liu Y, Zhao Y, Dong G, Guan C, Cui Y. A study of the flow field characteristics around star-shaped artificial reefs. J Fluids Struct 2013;39:27–40. https://doi.org/10.1016/j.jfluidstructs.2013.02.018.

[45] Kim D, Jung S, Na WB. Evaluation of turbulence models for estimating the wake region of artificial reefs using particle image velocimetry and computational fluid dynamics. Ocean Eng 2021;223:108673. https://doi.org/10.1016/j.oceaneng.2021.108673.

[46] Liu Y, Guan C, Zhao Y, Cui Y, Dong G. Numerical simulation and PIV study of unsteady flow around hollow cube artificial reef with free water. Eng Appl Comput Fluid Mech 2012;6:206–220. https://doi.org/10.1080/19942060.2012.11015440.

[47] Chang C, Lan Y. Experimental and numerical studies on wave transformation over artificial reefs. Coast Eng Proc 2011;1(32):17. https://doi.org/10.9753/icce.v32.waves.17.

[48] Jiang Z, Liang Z, Zhu L, Guo Z, Tang Y. Effect of hole diameter of rotary-shaped artificial reef on flow field. Ocean Eng 2020;197:106917. https://doi.org/10.1016/j.oceaneng.2020.106917.

[49] Liu Y, Dong G, Zhao Y. The investigation of the hydrodynamics of an artificial reef. In: Aquaculture and the Environment; 2007.

[50] Rubinato M, Heyworth J, Hart J. Protecting coastlines from flooding in a changing climate: A preliminary experimental study to investigate a sustainable approach. Water 2020;12:2471. https://doi.org/10.3390/w12092471.

[51] Wang G, Wan R, Wang X, Zhao F, Lan X, Cheng H. Study on the influence of cut-opening ratio, cut-opening shape, and cut-opening number on the flow field of a cubic artificial reef. Ocean Eng 2018;162:341–352. https://doi.org/10.1016/j.oceaneng.2018.05.007.

[52] Pomeroy AWM, Lowe RJ, van Dongeren AR, Ghisalberti M, Bodde W, Roelvink D. Spectral wave-driven sediment transport across a fringing reef. Coast Eng 2015;98:78–94. https://doi.org/10.1016/j.coastaleng.2015.01.005.

[53] El Malki A, Nême A, Scolan YM. Experimental investigation of hydrodynamic loads and pressure distribution during a pyramid water entry. J Fluids Struct 2015;54:925–935. https://doi.org/10.1016/j.jfluidstructs.2015.01.018.

[54] Vested MH, Carstensen S, Christensen ED. Experimental study of wave force distribution on a monopile structure. In: Proceedings of the ASME 37th International Conference on Ocean, Offshore and Arctic Engineering (OMAE 2018); 2018. p. 1–8.

[55] Lima MMCL. Estudo experimental da erosão localizada na proximidade de pilares de pontes. Guimarães: Universidade do Minho; 2008.

[56] Camões A, Cruz P, Sá JM. Avaliação da aderência ao betão de varões de aço galvanizado ou com revestimento epoxídico. In: BE2008 – Encontro Nacional de Betão Estrutural. Guimarães; 2008. p. 1–10.

[57] Pokorný P, Chobotský T, Prodanovic N, Steinerová V, Hurtig K. Bond strength and corrosion protection properties of hot-dip galvanized prestressing reinforcement in normal-strength concrete. J Compos Sci 2024;8:407. https://doi.org/10.3390/jcs8100407.

[58] Hamad BS, Mike JA. Bond strength of hot-dip galvanized reinforcement in normal-strength concrete structures. Constr Build Mater 2005;19:275–283. https://doi.org/10.1016/j.conbuildmat.2004.07.008.

[59] Cruz F, Valente I, Almeida J, Neves A, Pereira E. Experimental characterization of bond between concrete and HDG steel tubes for mixed steel-concrete structures. Mater Struct 2024;57:235. https://doi.org/10.1617/s11527-024-02352-8.

[60] Korkeakoulu T. Service life of hot-dip galvanised reinforcement bars in carbonated and chloride-contaminated concrete. 2009.

[61] Andrade MC, Macias A. Galvanized reinforcements in concrete. In: Surface Coatings—2. Berlin: Springer; 1988. p. 137–182.

[62] Bellezze T, Malavolta M, Quaranta A, Ruffini N, Roventi G. Corrosion behaviour in concrete of three differently galvanized steel bars. Cem Concr Compos 2006;28:246–255. https://doi.org/10.1016/j.cemconcomp.2006.01.011.

[63] Afshar A, Jahandari S, Rasekh H, Shariati M, Afshar A, Shokrgozar A. Corrosion resistance evaluation of rebars with various primers and coatings in concrete modified with different additives. Constr Build Mater 2020;262:120034. https://doi.org/10.1016/j.conbuildmat.2020.120034.

[64] Tej P, Kour M, Pokorný P. Evaluation of the impact of corrosion of hot-dip galvanized reinforcement on bond strength with concrete: A review. Constr Build Mater 2017;132:271–289. https://doi.org/10.1016/j.conbuildmat.2016.11.096.

[65] Dybel P, Kucharska M, Golewski GL, Singh K, Singh S. Properties of a bond between the steel reinforcement and the new generation concretes: A review. IOP Conf Ser Mater Sci Eng 2019;603:042057. https://doi.org/10.1088/1757-899X/603/4/042057.

[66] Comité Euro-International du Béton (CEB). CEB-FIP Model Code 1990. Bulletin d'Information No. 213/214. Lausanne: CEB; 1993.

[67] Soares S, Freitas N, Pereira E, Nepomuceno E, Pereira E, Sena-Cruz J. Assessment of GFRP bond behaviour for the design of sustainable reinforced seawater concrete structures. Constr Build Mater 2020;231:117277. https://doi.org/10.1016/j.conbuildmat.2019.117277.

[68] Hossain KMA, Ametrano D, Lachemi M. Bond strength of GFRP bars in ultra-high strength concrete using RILEM beam tests. J Build Eng 2017;10:69–79. https://doi.org/10.1016/j.jobe.2017.02.005.

[69] RILEM TC RC6. RC6 bond test for reinforcement steel. 2. Pull-out test. In: RILEM recommendations for the testing and use of construction materials. London: E & FN Spon; 1994. p. 218–220.

[70] Santos RMV. Avaliação da aderência aço-betão em elementos estruturais de betão armado [Master's thesis]. Aveiro: Universidade de Aveiro; 2012.

[71] Li YJ, Han LH, Xu W, Tao Z. Circular concrete-encased concrete-filled steel tube (CFST) stub columns subjected to axial compression. Mag Concr Res 2016;68:995–1010. https://doi.org/10.1680/jmacr.15.00359.

[72] Sanz B, Planas J, Sancho JM. Study of the loss of bond in reinforced concrete specimens with accelerated corrosion by means of push-out tests. Constr Build Mater 2018;160:598–609. https://doi.org/10.1016/j.conbuildmat.2017.11.093.

[73] Lyu WQ, Han LH. Investigation on bond strength between recycled aggregate concrete (RAC) and steel tube in RAC-filled steel tubes. J Constr Steel Res 2019;155:438–459. https://doi.org/10.1016/j.jcsr.2018.12.028.

[74] Han LH, Li W, Bjorhovde R. Developments and advanced applications of concrete-filled steel tubular (CFST) structures: Members. J Constr Steel Res 2014;100:211–228. https://doi.org/10.1016/j.jcsr.2014.04.016.

[75] Cruz F, Valente IB, Monteiro F, Maslov D, Miranda T, Pereira EB. Development and characterization of structural connections for modular artificial reefs. Ocean Eng 2025;320:120311. https://doi.org/10.1016/j.oceaneng.2025.120311.

[76] Jiang D, Tan KH, Wang CM, Dai J. Research and development in connector systems for very large floating structures. Ocean Eng 2021;232:109150. https://doi.org/10.1016/j.oceaneng.2021.109150.

[77] Wang YQ, Zong L, Shi YJ. Bending behavior and design model of bolted flange-plate connection. J Constr Steel Res 2013;84:1–16. https://doi.org/10.1016/j.jcsr.2013.01.012.

[78] Shehab BA, Ekmekyapar T. Joint behaviour of through steel beam to composite column connections: Experimental study. Mar Struct 2021;76:102921. https://doi.org/10.1016/j.marstruc.2020.102921.

[79] Nogueiro P. Comportamento cíclico de ligações metálicas [PhD thesis]. Coimbra: Universidade de Coimbra; 2009.

[80] Leftheriotis GA, Sibetheros IA, Dimas AA. Large-eddy simulation of the turbulent oscillatory flow around an artificial reef. Ocean Eng 2025;318:120142. https://doi.org/10.1016/j.oceaneng.2024.120142.

[81] Ng K, Phillips MR, Calado H, Borges P, Veloso-Gomes F. Seeking harmony in coastal development for small islands: Exploring multifunctional artificial reefs for São Miguel Island, the Azores. Appl Geogr 2013;44:99–111. https://doi.org/10.1016/j.apgeog.2013.07.013.

[82] NSW Government. Artificial reefs. Available from: https://www.dpi.nsw.gov.au/fishing/recreational/resources/artificial-reef. Accessed March 12, 2025.

[83] Dini E, Nuzzolese M, Cafaro F, Lernia A, Gadaleta A, Sollecito F. Subsidence of artificial reefs with bamboo foundations on a soft seabed. Appl Sci 2024;14:720. https://doi.org/10.3390/app14020720.

[84] Bohnsack JA, Sutherland DL. Artificial reef research: A review with recommendations for future priorities. Bull Mar Sci 1985;37:11–39.

[85] URB. Dubai Reefs. Available from: https://urb.ae/projects/dubaireefs/. Accessed March 12, 2025.

[86] Matus IV, Alves JL, Vaz-Pires P. Artificial reefs through additive manufacturing: A review of their design, purposes and fabrication process for marine restoration and management. Rapid Prototyp J 2024;30:87–122. https://doi.org/10.1108/RPJ-07-2023-0222.

[87] Soon C, Ng L, Chou LM. Artificial reefs as a reef restoration strategy in sediment-affected environments: Insights from long-term monitoring. Aquat Conserv 2017;27:976–985. https://doi.org/10.1002/aqc.2755.

[88] Belhassen Y, Rousseau M, Tynyakov J, Shashar N. Evaluating the attractiveness and effectiveness of artificial coral reefs as a recreational ecosystem service. J Environ Manage 2017;203:448–456. https://doi.org/10.1016/j.jenvman.2017.08.020.

[89] NORSOK. NORSOK Standard N-003: Actions and action effects. Lysaker: Standards Norway; 2007.

[90] El-Reedy MA. Marine structural design calculations. Oxford: Elsevier; 2015.

[91] Sundar V. Ocean wave mechanics: Applications in marine structures. 1st ed. Boca Raton, FL: CRC Press; 2017.

[92] Chakrabarti SK. Hydrodynamics of offshore structures. 1st ed. Southampton: WIT Press; 1987.

[93] Chakrabarti SK. Ocean environment. In: Handbook of offshore engineering. 1st ed. Oxford: Elsevier; 2005. p. 79–106.

[94] Sorensen RM. Basic coastal engineering. 3rd ed. New York: Springer; 2005.

[95] Newman JN. Marine hydrodynamics. 40th anniversary ed. Cambridge, MA: MIT Press; 2017.

[96] El-Reedy MA. Offshore structures: Design, construction and maintenance. Oxford: Gulf Professional Publishing; 2012.

[97] Det Norske Veritas (DNV). DNV-RP-C205: Environmental conditions and environmental loads. Høvik: Det Norske Veritas; 2010.

[98] International Organization for Standardization (ISO). ISO 19900:2012. Petroleum and natural gas industries—General requirements for offshore structures. Geneva: ISO; 2012.

[99] OSPAR Commission. OSPAR guidelines on artificial reefs in relation to living marine resources. London: OSPAR Commission; 2013.

[100] Oumeraci H, Pfoertner S, Kudella M, Kortenhaus A. Ocean Brick System (OBS) as a foundation structure for offshore wind turbines: An experimental study for wave loads and stability. In: Coasts, Marine Structures and Breakwaters: Adapting to Change. Proceedings of the 9th International Conference Organised by the Institution of Civil Engineers. Edinburgh, UK; 2010. p. 1–12.

[101] Instituto Hidrográfico. Capítulo 3: Informação suplementar sobre marés. Lisboa: Instituto Hidrográfico; 2020. (In Portuguese).

[102] Instituto Hidrográfico. Capítulo 1: Generalidades. Lisboa: Instituto Hidrográfico; 2020. (In Portuguese).

[103] Fu F. Design of offshore structures. In: Fu F, editor. Design and analysis of tall and complex structures. 1st ed. Oxford: Butterworth-Heinemann; 2018. p. 345–394. https://doi.org/10.1016/B978-0-08-101018-1.00008-3.

[104] Huang J, Lowe RJ, Ghisalberti M, Hansen JE. Wave transformation across impermeable and porous artificial reefs. Coast Eng 2024;189:104488. https://doi.org/10.1016/j.coastaleng.2024.104488.

[105] Bollineni H, Wang X, Tobias J. Numerical investigation of an Ocean Brick System. Fluids 2025;10:231. https://doi.org/10.3390/fluids10090231.

[106] Bollineni H. Numerical investigation of an Ocean Brick System [Master's thesis]. West Lafayette, IN: Purdue University; 2024.

[107] Maslov D, Pereira E, Duarte D, Miranda T, Ferreira V, Tieppo M, et al. Numerical analysis of the flow field and cross section design implications in a multifunctional artificial reef. Ocean Eng 2023;272:113817. https://doi.org/10.1016/j.oceaneng.2023.113817.

[108] International Organization for Standardization (ISO). ISO/DIS 19900. Petroleum and natural gas industries—General requirements for offshore structures. Geneva: ISO; 2012.

[109] International Organization for Standardization (ISO). ISO/DIS 19901-1. Petroleum and natural gas industries—Specific requirements for offshore structures—Part 1: Metocean design and operating considerations. Geneva: ISO; 2013.

[110] International Organization for Standardization (ISO). BS EN ISO 19901-1:2005. Petroleum and natural gas industries—Specific requirements for offshore structures—Part 1: Metocean design and operating considerations. London: British Standards Institution; 2005.

[111] American Bureau of Shipping (ABS). Guidance notes on accidental load analysis and design for offshore structures. Houston, TX: ABS; 2013.

[112] Sundar V. Ocean wave mechanics. Chichester: John Wiley & Sons; 2016.

[113] Chakrabarti SK. Loads and responses. In: Handbook of offshore engineering. Vol. I. 1st ed. Oxford: Elsevier; 2005. p. 133–161.

[114] Huang J, Lowe RJ, Ghisalberti M, Hansen JE, Altomare C. Numerical study of wave-structure interactions with porous artificial reefs using smoothed particle hydrodynamics. Coast Eng 2026;203:104871. https://doi.org/10.1016/j.coastaleng.2025.104871.

[115] Carral L, Lamas MI, Barros JJC, López I, Carballo R. Proposed conceptual framework to design artificial reefs based on particular ecosystem ecology traits. Biology (Basel) 2022;11:680. https://doi.org/10.3390/biology11050680.

[116] Diederen C. Experimental wave flume study: The stability of an artificial reef [Master's thesis]. 2022.

[117] Chakrabarti SK. Handbook of offshore engineering. Vol. I. 1st ed. Oxford: Elsevier; 2005.

[118] Chakrabarti SK. Loads and responses. In: Handbook of offshore engineering. Vol. I. 1st ed. Oxford: Elsevier; 2005. p. 133–161.

[119] International Organization for Standardization (ISO). ISO 19902:2007. Petroleum and natural gas industries—Fixed steel offshore structures. Geneva: ISO; 2007.

[120] Baine M. Artificial reefs: A review of their design, application, management and performance. Ocean Coast Manag 2001;44:241–259.

[121] Molina FJ, Cruz MA, Alonso A, Montes EH, Cecilio L. Galvanized steel in concrete: More durable structures maintaining the bond length. J Mater Civ Eng 2017;29:04017012. https://doi.org/10.1061/(ASCE)MT.1943-5533.0001903.

[122] Price SJ, Figueira RB. Corrosion protection systems and fatigue corrosion in offshore and marine structures: Current status and future perspectives. Coatings 2017;7:25. https://doi.org/10.3390/coatings7020025.

[123] Suzdaleva AL, Beznosov VN. Artificial reef: Status, life cycle, and environmental impact assessment. Power Technol Eng 2021;55:558–561. https://doi.org/10.1007/s10749-021-01397-x.

[124] Melchers RE, Chaves IA. Durable steel-reinforced concrete structures for marine environments. Boca Raton, FL: CRC Press; 2021.

[125] GATE Inc. Corrosion on offshore structures. Available from: https://www.gateinc.com/oil-gas-engineering-services/materials-corrosion/. Accessed November 7, 2018.

[126] Axiom NDT Ltd. Offshore corrosion on the Tartan Alpha. Available from: http://www.axiomndt.co.uk/services/derrick-services/attachment/18-offshore-corrosion-on-the-tartan-alpha/. Accessed November 7, 2018.

[127] LYON Associates, Sea Engineering. Underwater inspection of Delap and Uliga Dock. Republic of the Marshall Islands Port Authority; 2015. Available from: http://rmipa.com/delap-and-uliga-docks-inspection/. Accessed November 7, 2018.

[128] Dafforn KA, Glasby TM, Airoldi L, Rivero NK, Mayer-Pinto M, Johnston EL, et al. Marine urbanization: An ecological framework for designing multifunctional artificial structures. Front Ecol Environ 2015;13:82–90. https://doi.org/10.1890/140050.

[129] Niaounakis M. The problem of marine plastic debris. In: Management of marine plastic debris. Oxford: Elsevier; 2017. p. 1–55. https://doi.org/10.1016/B978-0-323-44354-8.00001-X.

[130] Pokorný P, Pernicová R, Tej P, Kolísko J. Changes of bond strength properties of hot-dip galvanized plain bars with cement paste after 1 year of curing. Constr Build Mater 2019;226:920–931. https://doi.org/10.1016/j.conbuildmat.2019.07.147.

[131] Shi X, Xie N, Fortune K, Gong J. Durability of steel reinforced concrete in chloride environments: An overview. Constr Build Mater 2012;30:125–138. https://doi.org/10.1016/j.conbuildmat.2011.12.038.

[132] Rodrigues MPMC, Costa MRN, Mendes AM. Effectiveness of surface coatings to protect reinforced concrete in marine environments. Mater Struct 2000;33:618–626.

[133] Pokorný P, Kouřil M, Stoulil J, Bouška P, Simon P, Juránek P. Problems and normative evaluation of bond-strength tests for coated reinforcement and concrete. Mater Tehnol 2015;49:847–856. https://doi.org/10.17222/mit.2014.227.

[134] Zhang Z, Yao X, Wang H. Potential application of geopolymers as protection coatings for marine concrete. III. Field experiment. Appl Clay Sci 2012;67–68:57–60. https://doi.org/10.1016/j.clay.2012.05.008.

[135] Persson D, Thierry D, Karlsson O. Corrosion and corrosion products of hot-dip galvanized steel during long-term atmospheric exposure at different sites world-wide. Corros Sci 2017;126:152–165. https://doi.org/10.1016/j.corsci.2017.06.025.

[136] Figueira RB, Silva CJR. Corrosion of hot-dip galvanized steel reinforcement. Corros Prot Mater 2014;33:51–61.

[137] Yi Y, Zhu D, Guo S, Zhang Z, Shi C. A review on the deterioration and approaches to enhance the durability of concrete in the marine environment. Cem Concr Compos 2020;113:103695. https://doi.org/10.1016/j.cemconcomp.2020.103695.

[138] Mo EG, Thomas MDA, Fahim A. Performance of high-volume fly ash concrete in marine environment. Cem Concr Res 2017;102:127–135. https://doi.org/10.1016/j.cemconres.2017.09.008.

[139] Mo EG, Thomas MDA. Performance of 25-year-old silica fume and fly ash lightweight concrete blocks in a harsh marine environment. Cem Concr Res 2018;113:65–73. https://doi.org/10.1016/j.cemconres.2018.07.004.

[140] Kazemi H, Yekrangnia M, Shakiba M, Bazli M, Vatani Oskouei A. Bond-slip behaviour between GFRP/steel bars and seawater concrete after exposure to environmental conditions. Eng Struct 2022;268:114796. https://doi.org/10.1016/j.engstruct.2022.114796.

[141] Kazemi H, Yekrangnia M, Shakiba M, Bazli M, Vatani Oskouei A. Bond durability between anchored GFRP bar and seawater concrete under offshore environmental conditions. Mater Struct 2023;56:174. https://doi.org/10.1617/s11527-023-02153-5.

CHAPTER 4

SUMMARY OF APPENDED PAPERS

This chapter provides a synopsis of the papers that constitute this PhD thesis. The papers are presented in a sequence that reflects the contribution of the research to the objectives., ***PAPER I****, presented an engineering-driven approach for the structural design of MMFARs, exploring the structural behaviour of reinforced concrete (RC) and composite steel-concrete systems (CS).* ***PAPER II*** *focuses on the development and experimental characterization of various structural connection systems for modular artificial reefs constructed in RC, CS an ECC (Engineering Cementitious Composite). While PAPER II examines connections at a structural level,* ***PAPER III*** *shifts the focus to the bond behaviour between concrete and HDG steel tubes, a fundamental aspect of composite steel-concrete reef structures, identifying key factors that enhance or weaken adhesion. Pushout tests were performed to investigate bond strength, failure mechanisms, and the role of factors such as concrete strength, bond length and surface conditions. Expanding on this theme,* ***PAPER IV*** *explores the long-term effects of seawater exposure on the bond between HDG steel tube and concrete. By analysing specimens exposed to a controlled environment (climatic chamber) and to seawater for up to 500 days, the study provided insights into bond strength degradation and the formation of corrosion-related crystalline phases.* ***PAPER V*** *focuses on the real-scale construction prototype and mechanical characterization of modular reef units, comparing RC and ECC solutions, and demonstrating the benefits of 3D printing for mould fabrication.* ***PAPER VI*** *analyses the hydrodynamic behaviour and local scour effects around small-scale MMFAR prototypes through hydraulic flume experiments and photogrammetry surveys.*

4.2. PAPER I

- Cruz, F., Valente, I. B., Maslov, D., Miranda, T., & Pereira, E. B. **Engineering-Driven Approach for the Structural Design of a Modular Artificial Reef Structure**. Applied Sciences, 15(11), 5907. https://doi.org/https://doi.org/10.3390/app15115907. Impact factor: 2.5

Modular Artificial reefs constructions play a crucial role in marine ecosystem restoration and coastal engineering, contributing to biodiversity enhancement, fisheries management, and recreational activities. However, their structural design remains insufficiently standardized, often relying on empirical approaches with limited integration of engineering principles. The increasing complexity of artificial reef designs, particularly modular multifunctional artificial reefs (MMFARs), demands a rigorous methodology to ensure durability, resilience, and environmental compatibility in open-water conditions.

This study presents an engineering-driven approach for the structural design of MMFARs, focusing on reinforced concrete (RC) and composite steel-concrete systems (CS). The methodology integrates geometric design, material selection, hydrodynamic modelling, and numerical simulations to evaluate structural behaviour under various load conditions. A parametric study explores different material and structural configurations, assessing their feasibility and optimisation potential.

The results show that in RC structures, tensile behaviour limits reinforcement requirements, especially in variable cross-sections where the largest section dictates minimum reinforcement needs. Although flexural strength appears to be the limiting factor due to reduced cross-sectional dimensions, increasing reinforcement does not always improve performance. Optimizing reinforcement area, rather than solely increasing steel strength, is more effective for sections with reduced diameters. In contrast, CS structures offer greater design flexibility and higher axial and flexural strength, with material selection significantly influencing performance. Overall, CS structures demonstrate superior performance, particularly in resisting extreme actions, while RC solutions are more adaptable but constrained by geometric limitations. The study highlights the importance of systematic design optimisation and underscores the need for further research on fatigue and long-term deformations to ensure structural resilience in marine environments.

4.3. PAPER II

- Cruz F, Valente IB, Monteiro F, Maslov D, Miranda T, Pereira EB. **Development and characterization of structural connections for modular artificial reefs**. Ocean Eng 2025;320:120311. https://doi.org/10.1016/j.oceaneng.2025.120311.Impact factor: 4.6

Artificial reefs and other marine structures are gaining prominence in the fields of ecosystem restoration and coastal engineering. However, their success depends on efficient and durable connection systems that ensure structural performance and integrity in harsh marine environments. Existing solutions for artificial reefs often lack sufficient validation and characterization, posing challenges for their widespread use.

The objective of this study was to design and experimentally characterize structural connections systems for multifunctional modular artificial reefs (MMFARs). A variety of materials were investigated, including concrete, hot-dip galvanized steel (HDG), engineered cementitious composites (ECC), underwater epoxy and knitted textile preforms (KTPs). The research included an extensive experimental program, including bending tests to evaluate the strength, deformability, and failure mechanisms of various connection types. The analysis of these connections considered their structural efficiency, ease of construction, and durability, with parametric studies providing a deeper understanding of material behaviour under marine conditions.

The results show that CS connections with KTPs and ECC perform exceptionally well, offering high load-bearing capacity and energy dissipation, making them ideal for more energetic marine environments. While reinforced concrete (RC) connections are adaptable, they are constrained by geometric limitations and offer lower energy absorption. ECC connections exhibited impressive ductility, reducing crack formation and enhancing long-term durability. Pure adhesive connection provides a simple and user-friendly assembly process. However, mechanical testing shows that it has lower strength and deformability compared to other connection types. The study underscores the importance of systematic design optimisation, proper material selection, and further research into fatigue and long-term behaviour to ensure the structural resilience of modular artificial reefs.

4.4. PAPER III

- Cruz F, Valente I, Almeida J, Neves A, Pereira E. **Experimental characterization of bond between concrete and HDG steel tubes for mixed steel-concrete structures**. Mater Struct 2024;57:89. https://doi.org/10.1617/s11527-024-02352-8. Impact factor: 4.0

The bond between concrete and reinforcement materials is a key factor in the structural performance of reinforced concrete or composite steel-concrete structures. This is particularly relevant in aggressive environments such as marine and submerged conditions, where corrosion is a major concern. Hot-hip galvanized (HDG) steel has emerged as a promising solution due to its protective coating, which enhances durability. However, the bond behaviour between HDG steel and concrete remains insufficiently understood.

This study experimentally investigates the bond behaviour between HDG steel tubes and concrete by mean of pushout tests. The research focuses on the influence of different concrete mixtures, bond lengths and on the impact of concrete pin connectors, created by perforating the tube, as well as the effect of galvanic surface conditions. The results allowed to analyse failure mechanisms and load-end slip responses, based on key parameters such as maximum bond stress, dissipated energy, and residual pushout force.

The findings indicate that while bond length and concrete composition had limited impact on the overall response shape, they significantly influenced bond stress and energy dissipation. The presence of a concrete pin connector notably improved adhesion, enhancing the mechanical interlock between materials. Conversely, surface contamination significantly reduced bond strength, emphasizing the importance of handling and maintaining a clean HDG surface during construction.

4.5. PAPER IV

- Cruz F, Valente, IB, Miranda T, Pereira EB. **Long-term effect of seawater on bond performance between HDG steel and concrete for hybrid concrete-steel marine constructions** [Submitted].

The bond between concrete and galvanized steel is critical for the performance of composite structures, particularly in marine environments. While galvanized steel offers corrosion resistance, its long-term interaction with concrete remains insufficiently understood, especially regarding bond strength degradation over time. Previous studies suggest conflicting results on the effect of galvanized coatings in different exposure conditions. This study addresses the knowledge gap by investigating how bond length, exposure time, and environmental conditions impact the bond behaviour of HDG steel in steel-concrete composite structures.

This research experimentally examines the long-term bond behaviour between HDG steel tubes and concrete under controlled atmospheric conditions and seawater exposure. The study involved 63 pushout specimens with different bond lengths, subjected to different environmental conditions for up to 500 days. Bond strength was assessed through direct pushout tests, while Field Emission Gun - Scanning Electron Microscopy (FEG-SEM/EDS) analyses provided insights into the interface morphology and chemical composition of the interface transitional zone (ITZ). Additional carbonation and chloride penetration tests were also performed.

Results indicate that specimens exposed to seawater (SW) exhibited a significant reduction in bond strength compared to those in a controlled chamber (CC), with an average decrease of 14.3% and a maximum reduction of 32%. However, bond strength in seawater-exposed specimens increased gradually over time, likely due to the migration of zinc corrosion products into concrete pores, counteracting the effects of hydrogen evolution. The study also confirms that longer bond lengths improve load-bearing capacity but can lead to abrupt failure modes. Microstructural analysis identified the formation of corrosion-related crystalline phases at the ITZ, highlighting the impact of environmental exposure on long-term bond performance. These findings contribute to an open topic where further research is needed, emphasizing the importance of studying long-term degradation mechanisms in marine applications.

4.6. PAPER V

- Cruz F, Valente IB, Miranda T, Pereira EB. **Construction and characterization of a structural unit for modular artificial reefs**. Structures 2025;81:110154. https://doi.org/10.1016/j.istruc.2025.110154. Impact factor: 4.3

The use of modular systems, such as those developed in this study, provides a flexible and scalable solution that can be implemented in different marine environments. In addition, the use of innovative technologies such as 3D printing to create moulds provided an opportunity to overcome challenges associated with traditional industry costs.

This study focuses on the construction and performance evaluation of modular artificial reef units. Two structural systems were tested: reinforced concrete (RC) and engineered cementitious composite (ECC). The research aimed to understand the stiffness, strength and failure modes of these systems through experimental bending tests and material characterisation. The results showed that the RC unit had superior structural performance with higher load capacity and ductility compared to the ECC unit, which had better initial stiffness. The study also highlighted the use of 3D printing to produce low-cost moulds for the reef units. Future work should focus on durability testing and the investigation of self-healing mechanisms under submerged conditions.

4.7. PAPER VI

- Cruz F, Pereira E, Lima M, Johnson J, Duarte D, Valente IB, et al. **Experimental characterization of the scour of innovative artificial reef prototypes using hydraulic flume and photogrammetry**. OCEANS 2019 MTS/IEEE Marseille, IEEE; 2019, p. 1–10. https://doi.org/10.1109/OCEANSE.2019.8867581.

The increasing need to protect and restore marine ecosystems has led to the development of multifunctional artificial reefs, which support habitat rehabilitation, recreational activities, and scientific research. However, their stability and functionality can be affected by hydrodynamic behaviour and local scour. Experimental studies are a valuable tool to analyse fluid-structure interaction, allowing for design adaptations and minimizing adverse effects.

This study experimentally evaluates the local scour phenomenon and hydrodynamic behaviour of an innovative multifunctional modular artificial reef prototype. Using hydraulic flume tests and photogrammetry surveys, the research investigates how the structure interacts with sediment transport and water flow. Measurements of velocity profiles upstream and downstream of the MFAR, along with digital elevation models of the scour cavity, provide a detailed understanding of the sediment displacement process and structure stability.

The results demonstrate that local scour occurs primarily around the vertical support elements of the MFAR, leading to asymmetric dune formations downstream. The structure exhibited slight sinking and rotation, highlighting the potential risk of instability. Velocity measurements confirmed a reduction in flow speed downstream, indicating energy dissipation around the reef. Photogrammetry proved to be an effective technique for characterizing sediment displacement, enabling precise documentation of scour cavity evolution. The study underscores the importance of incorporating base plates or geogrids to enhance stability. Future research should focus on long-term erosion monitoring, numerical simulations, and the optimisation of artificial reef geometry to improve performance in real marine environments.

CHAPTER 5

CONCLUSIONS AND FUTURE WORK

This chapter aims to summarize the main results and contributions of the thesis, highlighting the innovations and advances achieved in the development of innovative structural systems for artificial reefs and other geometrically complex marine constructions. In addition, it outlines the directions for future work, which seek to overcome the identified limitations and explore new opportunities for research and practical application.

5.1. CONCLUSIONS

The thesis explored an integrated approach on the development of modular structural systems adapted to marine environments such as multifunctional modular artificial reefs (MMFAR), by combining parametric modelling methodologies, experimental tests, analytical calculations and numerical analysis. By integrating knowledge from structural engineering, hydrodynamic studies, and materials science, the thesis promoted a multidisciplinary effort to improve the structural design of such structures, with focus on their contribution to environmental sustainability and interaction with the ocean environment. Among the main contributions, the following may be highlighted:

5.1.1. Artificial reefs construction and structural design – state of the art

State-of-the-art analysis has enabled the mapping of existing knowledge on artificial reefs, identifying theories, methods, and solutions that are either well-developed or underdeveloped, detecting gaps and

opportunities for new research or innovations, and highlighting unexplored approaches, methodological limitations, and potential paths for future investigation.

- The analysis of artificial reefs highlights their evolution from simple, single-component structures to large, complex, modular, and multifunctional systems. This progression reflects both technological advancement and an increasing focus on environmental integration and structural resilience. While concrete has traditionally dominated AR construction, its prevalence is increasingly being challenged by bio-receptive and more sustainable material alternatives, driven by ecological considerations and stringent international regulatory frameworks governing marine interventions.
- Technological innovations, particularly in additive manufacturing, have enabled the creation of increasingly complex geometries, with 3D printing proving especially effective in producing the morphological complexity needed to enhance ecological performance. Despite these advancements, persistent knowledge gaps remain, especially regarding the long-term structural behaviour of AR systems and the lack of systematic, fully validated design guidelines to support standardised engineering practice. Addressing these gaps is critical to ensuring the structural reliability, ecological functionality, and operational lifespan of future artificial reef developments.
- The trajectory of AR technology is increasingly defined by sustainable engineering solutions that support coastal protection, habitat creation, and the broader resilience and management of marine ecosystems. The future of artificial reefs depends on technological innovation, such as 3D printing and advanced monitoring systems, and their integration as multifunctional solutions within integrated coastal management strategies. Balancing innovation with capable, optimised structural design is essential to safeguard marine ecosystem resilience.
- Analysis of parametric design principles, structural analysis, and regulatory frameworks for the development of multifunctional modular artificial reefs (MMFARs) further demonstrates their relevance. While the literature extensively addresses geometric design—including conceptual requirements and hydrodynamic or morphodynamic performance evaluated through numerical simulation and physical modelling—the primary analytical and numerical methodologies underpinning structural design remain significantly underdeveloped. Existing research on structural behaviour predominantly focuses on advanced fluid–structure interaction simulations, highlighting the need for more comprehensive approaches to support practical, standardised engineering design.

5.1.2. Engineering and structural systems approach for MMFARs

The approach aimed to address the gap identified in the state-of-the-art regarding AR structural design, raising awareness among designers about this critical aspect and stressing the importance of structural design, while also providing detailed guidance. An engineering-driven systematic methodology was proposed that prioritizes the structural design and optimisation of complex modular ARs made of concrete and steel. The methodology evaluates alternative structural configurations based on reinforced concrete (RC) and composite steel–concrete (CS) systems, as well as their cost-effectiveness, thereby enabling a comprehensive assessment of structural viability prior to prototyping, advanced numerical analyses, and full-scale experimental testing. This methodology comprises the following stages (i) **Structural and regulatory requirements:** establishment of design requirements, supported by the explicit justification of specific standards for marine structures, thus providing the standardisation benchmark missing in the literature; (ii) **Action quantification**: utilisation of standards for the reliable quantification of hydrodynamic actions and other loads, which are crucial elements for design of durable and resilient MMFARs for open waters and (iii) **Structural design and optimisation**: implementation of a parametric design, followed by numerical modelling and parametric studies to explore structural and material combinations, culminating in the optimisation of the cross-section and an assessment of cost-effectiveness.

Regarding the structural systems studied, a case study was developed, and the proposed methodology was employed to assess and optimize a modular artificial reef unit for open-water deployment, comparing RC and CS solutions under combined hydrodynamic and extreme loading, highlighting the following:

- **RC System**: fixed and reduced diameters impose a geometric limitation on cross-section optimisation. Tensile strength is the primary constraint, especially for RC with variable cross-sections, where minimum reinforcement is limited by the larger cross-section. This system experiences steel saturation, where increasing reinforcement does not significantly improve flexural strength, requiring increased section dimensions and its optimisation to ensure safety and ductility.
- **CS System**: the CS structure shows higher axial and flexural strength compared to RC, exhibiting sufficient robustness under flexural stresses without the need for high-strength concrete. The numerous combinations of materials and reinforcement geometries enable

better cross-section optimisation, allowing the structure to withstand extreme loads and achieve optimal structural efficiency.

- **Optimisation**: optimizing the RC cross-section for extreme load scenarios would increase its size by 23%, making the unit structure bulkier and heavier, whereas the CS solution requires no sectional enlargement.
- **Construction**: the RC unit was found to be easier to construct and adapt, while the CS unit is anticipated to present higher construction complexity.
- **Cost-effectiveness**: The most cost-effective RC solution (C90/105, S500, 1Ø25) offers lower costs (18.7€/unit) and optimal material efficiency but is heavier (≈159.8 kg) and +25% of volume increase. CS solutions maintain external geometry, are lighter (≈150 kg), but nearly double the cost (39.2€/unit for C30/37, S420, Ø76.1, tw = 4). If cost is secondary and geometry preservation is critical, CS excels in structural efficiency, low carbon footprint, and minimal ecological impact by using conventional concretes, while RC is more cost-effective and simpler but less efficient and alters the initial geometry.

The validation of this methodology demonstrates its applicability and reliability, with its main contribution lying in the application of standardised structural engineering knowledge to the Artificial Reef (AR) field, ensuring that future developments are grounded in transparent design and optimisation principles. This systematically engineered approach is crucial for guiding subsequent studies and increasing confidence in the efficient implementation of complex and modular ARs, particularly slender and framed structural systems, as it promotes the optimization of cross-sectional geometry and global structural configuration prior to advanced numerical analyses. Nevertheless, further analysis of axial–flexural stress interactions is still required to achieve a complete understanding of structural performance under in situ conditions. It should be noted, however, that the design of ARs composed of rubble mound structures, such as submerged breakwaters commonly employed to enhance surf conditions, requires a different design approach, as structural performance in these systems is governed by additional hydraulic and morphodynamic design criteria not addressed in this work.

5.1.3. MMFAR connections

Considering that modular construction requires the use of connections between modules, and that these may be one of the weakest parts of MMFAR structures, research introduced new concepts of connection systems for the integration of artificial reef modules, focusing on robust connections

involving the use of more traditional solutions such as concrete and steel tube profiles or rebars as reinforcement, and alternatives involving epoxies and composites such as Engineered Cementitious Composites - ECC or knitted textile preforms - KTP. The experimental program demonstrated that the proposed systems are effective, contributing to the overall stability of the structure.

- The most innovative system, combining steel connections with high-performance concrete and knitted textile preforms CS_SC&KTPsECC), exhibited the highest load-bearing capacity and ductility (F_{max} > 146.55 kN and E_i > 2195.62 kN·m·mrad), making it suitable for highly dynamic marine environments.
- Exhibiting moderate strength and deformability, the RC_H_{steel}B$_c$E composite achieved performance comparable to CS_SC connections; however, its substantially lower energy dissipation (a reduction of 88%) renders it better suited for deployment in stable, sheltered marine environments.
- Other systems displayed significantly lower resistance and brittle failure modes (ECC_E: F_{max} = 18.16 kN; E_i = 10.22 kN·m·mrad), making them unsuitable for application. Notably, adding an epoxy-bonded steel hasp to the connection significantly improved deformability (+693%) and strength (+67%).
- RC_H_{stee}IBcE connections faced engagement challenges, CS_SC was lightweight and easy to assemble underwater, KPT was practical onshore but ECC injection at sea requires careful planning, while ECC_E and ECC_H_{steel}E posed no significant assembly issues.
- In general, the experimental results confirmed the feasibility of the proposed solutions and emphasized the robustness of the developed connection systems.

5.1.4. Bond Behaviour and Durability

The study of the bond between concrete and smooth HDG steel tubes was conducted due to the interest the adoption of hot-dip galvanized steel as reinforcement of the structural system (CS), which tries to take advantage of galvanized steel as a cost-effective solution for improved durability. Moreover, it was observed that this topic approaches a highly sensitive and controversial area in the literature concerning the bond behaviour of galvanized steel and concrete. This motivated a thorough investigation to provide further insights and contribute to the existing knowledge base.

The research included an extensive experimental program comprising laboratory tests to evaluate the bond interaction between the two materials. Short-term studies at 28 days were conducted, showing a slight influence of concrete strength, surface contamination, and pin connectors on the experimental load-displacement responses obtained. Additionally, durability tests were performed to study the degradation mechanisms associated with exposure to aggressive marine conditions over 500 days. The results provided a better understanding of the effects of seawater exposure on the evolution of the bonding behaviour of this structural system.

Short-term:

- The global behaviour of the concrete–HDG steel interface was highly consistent across all tests, exhibiting a stiff initial response governed by chemical adhesion, followed by progressive interface degradation and a stable residual load plateau. This overall pattern was largely unaffected by the concrete mixture or the selected bond lengths.
- Concrete strength controlled the magnitude of the bond response: τ_{max} typically ranged between 1.1 and 2.0 MPa. Bond length had little effect on τ_{max}, indicating that the adopted embedment lengths were lower than the effective anchorage length.
- The condition of the HDG surface is highlighted, with bond reduced by 39.5% due to contamination, emphasizing the importance of rigorous cleaning and handling procedures.
- The introduction of concrete pins significantly increased τ_{max} (up to ~2.8 MPa). However, it also promoted brittle splitting failures, indicating that higher bond strengths could potentially be achieved if the specimen dimensions were larger.
- The test setup was validated as reliable and repeatable, providing a solid basis for future studies on long-term HDG–concrete bond performance under aggressive environments.

Long-term:

- Measured average τ_{max} average values ranged from 2.00 to 2.86 MPa for specimens immersed in seawater, compared with 2.71 to 3.34 MPa for specimens stored in a climatic chamber, confirming the influence of the exposure environment on bond behaviour.
- Specimens exposed to seawater exhibited an initial reduction in maximum bond strength (τ_{max}) of approximately 14% on average, with a maximum of -32% when compared with specimens cured under controlled atmospheric conditions.

- For long-term seawater exposure (500 days), a progressive recovery of bond strength was observed, with the reduction in τ_{max} decreasing to only 4–8% after 500 days, demonstrating improvement in bond performance over time.
- Time-dependent analysis revealed a gradual increase in τ_{max} of between 1% and 38% and for $\bar{\tau}_{\max}$ for seawater-exposed specimens between 90 and 500 days, possibly attributed to the progressive infilling of concrete porosity by zinc reaction products (e.g zinc oxide, zinc hydroxide and calcium zincate) and densification of the steel–concrete interface.
- The normalised bond strength ($\bar{\tau}_{\max)}$ remained relatively stable, with mean values of 0.84–0.89 for seawater-exposed specimens and 0.94–1.03 for specimens in controlled conditions, indicating overall structural consistency despite the aggressive marine environment.

5.1.5. Hydrodynamic and scour of small-scale prototype

The hydrodynamic effects of modular artificial reefs and the local scour phenomenon in non-cohesive sediments were studied using small-scale prototypes and flume tests in non-invasive experimental tests based on photogrammetry to characterise the scour cavity around the structure. Key findings from this study include:

- The influence of the structure on water flow was evaluated via velocity profiles obtained with ADVs (Acoustic Doppler Velocimeters) along the water column. Measurements before and after the structure showed that the presence of the construction reduces flow velocity with depth, indicating that the structure dissipates energy and slows the flow downstream.
- Although the structure is somewhat permeable, sand erosion observed at the front of the MFAR and deposition at the rear, indicated the risk of rotation or sinking, which could be mitigated with a baseplate or geogrid.
- Although sand saturation introduced challenges for the photogrammetric surveys, seabed sediments are naturally saturated under offshore conditions. Consequently, the results obtained under saturated conditions are expected to be more representative of the scour processes occurring in real marine environments.
- Photogrammetry proved to be effective, providing high-density data and accurate mapping of the sand bed.

5.1.6. Real-scale reef module prototype for MMFAR

- 3D printing significantly improved mould production efficiency, reducing costs by 98% and manufacturing time by 27%, while enabling complex geometries without the need for post-processing.
- The RC unit exhibited a 31.56% higher maximum load capacity, 120.44% greater deformations, and 180.33% higher stiffness compared to the ECC unit, which controls initial cracking but has lower overall structural performance.
- Both units performed adequately under service and extreme storm conditions (SLS and ULS) but failed under abnormal wave events (ALS), as stresses exceeded the concrete and reinforcement capacity.

5.2. FUTURE WORK

In addition to opportunities for further deepening the addressed aspects, the development of new research lines could enhance the practical application of artificial reefs and their integration into coastal management strategies. These future works will not only consolidate the advances achieved in this thesis but also open new research avenues for the development of innovative and sustainable structural solutions for marine ecosystems restoration, contributing to the protection and biodiversity of marine ecosystems. Among the main directions for future research, the following stand out:

5.2.1 Fluid-Structure modelling

Experimental Approach

Future research should include large-scale experimental tests that can recreate and simulate natural conditions by using hydraulic flume with wave maker to minimize scaling effects and better approximate real conditions. Particle Image Velocimetry (PIV) technique could be incorporated to capture detailed flow dynamics around the structures, providing valuable data for comparison with numerical simulations. Although the experiments were conducted in freshwater, the prototype is intended to operate in seawater. Therefore, future work should investigate the influence of seawater on the hydrodynamic response and scour development to assess the applicability of the present

findings to real offshore conditions. These insights will improve the understanding of wave-structure interactions and validate hydrodynamic performance.

Numerical Approach

The studies should be complemented with advanced fluid-structure interaction (FSI) simulations using Computational Fluid Dynamics (CFD) and Finite Element Method (FEM) models. These analyses will support the optimisation of structural configurations, evaluating the effects of wave loading, flow-induced forces and potential fatigue issues to improve the resilience and efficiency of artificial reef systems.

5.2.2 Module and MMFAR prototype tests

Future research should focus on extending the experimental programme of artificial reef units, including testing the most promising module to validate and refine its design. Impact and cyclic loading tests are essential to assess structural integrity under dynamic marine conditions, simulating wave action, objects collisions, and fatigue effects. These steps will strengthen the structural efficiency and sustainability of artificial reef solutions.

5.2.3 Optimisation of connection systems and fluid-connection interaction

Fluid-structure interaction:

Further investigations exploring the interaction between fluid and connection systems could lead to the development of even more efficient solutions, capable of coping with the dynamic response of the structures to intense waves and currents.

Performance and long-term tests:

The study of the dynamic performance of connections between modules is essential, as well as the fatigue behaviour in controlled laboratory tests. Subsequently, the connections studied should also be exposed to seawater, both under laboratory conditions and in situ, over an extended period, carrying out tests at different exposure periods. This will allow the better understanding of the degradation mechanisms, quantification of their effects on structural behaviour, as well as the evaluation of the disassembly process of a real structure.

5.2.5 MMFAR – seabed foundations strategies

Future research should focus on developing the foundation and supports of MMFAR structures to ensure stability, durability, and adaptability to different seabed conditions. Studies should address geotechnical requirements, considering soil-structure interaction, scour, and long-term settlement effects. Numerical simulations and experimental validations will be essential to optimize foundation design, accounting for hydrodynamic effects. Additionally, anchoring and stabilization solutions should be explored to increase structural safety, preventing scouring and ensure the effective integration of MMFARs into diverse marine environments.

5.2.4 New Materials and Technologies

Advanced Materials and Green Technologies:

Research into new materials, such as advanced composites with memory shape effects, recycled materials and others with bioactive properties could offer alternatives that reduce environmental impact and improve the structural performance of ARs.

3D Printing and Digital Manufacturing Technologies:

The use of 3D printing techniques for the fabrication of artificial reef modules could allow for greater customization, waste reduction, and a more agile construction process, integrating digital processes for design simulation and optimisation. This may include underwater 3d printing.

5.2.5 Monitoring and Digital Twins

Implementation of Monitoring Systems:

The integration of smart sensors and remote monitoring systems can contribute to the acquisition of environmental data and real-time information on structural performance and degradation effects, as well as on the ecosystems condition. This data will be crucial to adjust predictive models and implement structural maintenance strategies.

Implementation of Digital Twins:

The implementation of digital twins will be expected to significantly enhance the management of the monitored structures by coupling high-fidelity numerical models with real-time monitoring data. This approach will enable continuous updating of the structural condition and will improve the accuracy of behavioural predictions. Consequently, maintenance strategies will be able to evolve from reactive to condition-based, contributing to an extended service life. The use of digital twins will also reduce the need for direct inspections, allowing safer and more cost-effective operation of underwater and remote structures. Moreover, the integration of structural models with environmental data will enable a holistic analysis of structure–environment interactions. This next-generation framework will support the prediction of key performance indicators and long-term system performance under evolving operational and environmental conditions.

5.2.6 Life Cycle and Cost Analysis:

Although initial cost-effectiveness and resource use efficiency studies were conducted, further Life cycle analysis (LCA) and cost-benefit studies should be carried out to thoroughly address the economic, social and environmental impacts of the developed solutions. Sustainability should be viewed in a broad perspective, considering concepts such as ecosystems services and natural capital, where biodiversity and marine ecosystems health play a central role. The most recent methodologies can be adapted to the context of the current research and provide a consistent framework to support decision-making and policy, supporting large-scale implementation and public policies in an informed way.

PAPER I

ENGINEERING-DRIVEN APPROACH FOR THE STRUCTURAL DESIGN OF GEOMETRICALLY COMPLEX MODULAR ARTIFICAL REEFS

REFERENCE: Cruz F, Valente IB, Maslov D, Miranda T, Pereira EB. Engineering-driven approach for the structural design of geometrically complex modular artificial reefs. Appl Sci 2025;15:5907. https://doi.org/10.3390/app15115907. Impact factor: 2.5

ABSTRACT: Over the years, artificial reefs with diverse forms and functions have become increasingly important in maritime engineering and ecosystem restoration plans, with socio-economic and ecological impacts on marine ecosystems. However, due to the increasing complexity of designs and durability requirements, the current structural design approaches lack adequate documentation and standardization. This work addresses this challenge by detailing an engineering-driven approach for the structural design of artificial reef structures made of reinforced concrete or composite steel and concrete. This study establishes the premises for the structural design, followed by the quantification of actions based on standards and recommendations for marine structures. Hydrodynamic and numerical models were utilized to assess the effects of these actions on the structure. A cross-section organic design was then implemented, followed by a parametric study exploring various structural and material combinations for optimisation. This study validates the developed design methodology

combining hydrodynamic actions and strength analysis for complex modular artificial reef structures of 3 to 15 m size, specifically tailored for open waters. The results confirm the applicability and reliability of the developed design methodology, demonstrating its potential for guiding future numerical and experimental studies on modular artificial reef structures in open waters.

KEYWORDS: Modular multifunctional artificial reef; Structural design; Cross-section analysis; Numerical model; Parametric study; Optimisation.

1 INTRODUCTION

In recent years, there has been a growing interest in the development of marine infrastructures and technologies to harness maritime resources [1–6]. These efforts aim at supporting the expanding global population and promoting the sustainability of human activities [7–9]. Significant strides have been made, ranging from the creation of modular floating structures for energy generation and artificial energy islands, to the development of modular artificial reef structures dedicated to the protection and restoration of marine ecosystems [10–14]. In fact, artificial reefs (ARs) might contribute to multiple other purposes such as increasing fisheries yield [15], recreational dive tourism [16], improving surf conditions [17], coastal protection [2,18,19], and preventing bottom trawling [20]. Some authors have highlighted the importance of designing ARs specifically for the ecosystems projected to be enhanced [8,12]. However, according to the literature, the purpose for which artificial reefs have been created is seldom revealed [6].

Despite all the advantages, these innovative structures face numerous challenges characteristic of a new era of coastal and maritime engineering [21–23]. These challenges include structural complexity and durability requirements, complex hydrodynamic interactions with ocean currents, and suitability for sea operations. There is an urgent need for new approaches that not only address these problems effectively but also prioritize ecologically friendly solutions, bio-receptiveness, efficiency, and resilience. This is essential for fostering a sustainable and balanced relationship between human activities and the environment [4,21,24–28].

Over time, the design of ARs has predominantly relied on empirical methods, guided by subjective judgments and assessments. In some cases, this approach was limited to sinking structures without the adoption of a clear design process. However, growing interest in artificial reef technology led to

the development of several guidelines and recommendations [29–32], as well as frameworks for the development of purpose-oriented ARs. In general, these frameworks address functional aspects and provide a global view of the entire process and, to some extent, also address the structural design, albeit superficially. Recently, Vogler proposed a conceptual framework to design artificial reefs, which includes a design component that focuses mainly on geometric design, materials, and manufacturing [33,34]. Carral et al. (2022) proposed a new general and integrated conceptual framework to guide the design of AR units by adopting an ecosystem ecology perspective [35]. The flowchart is composed of three main parts: (i) marine ecosystem ecology model, (ii) AR-ecosystem index transformation, and (iii) the stability analysis. Although there is no detailed framework for the structural design, the general methodology highlights this aspect. The authors presented also a methodology based on geographic information systems (GISs) to determine the best area for installing ARs in a specific estuary considering the geomorphological, hydrodynamic, and bathymetric characteristics of the area, as well as the distance to the harbour and economic factors [36]. ARs designed for surfing show a robust and heavy morphology, similar to breakwaters, following similar design principles [17]. A preliminary design achieved step by step, making use of the theory and state of the art of multifunctional artificial reefs for surfing, was proposed by Voorde [17,26,37,38]. On the other hand, the geometry complexity of ARs is also an important aspect in other cases, and some works have found that increasing reef complexity has a significant and positive impact on fish species flourishing, density, and increased biomass [39,40]. Therefore, in recent years there has been a demand for modular, slender, and complex geometries for ARs. As a result, more sophisticated structures need to be designed based on engineering methods using analytical, numerical, and experimental analysis to produce structures capable of withstanding the harsh conditions typically encountered in marine environments.

The development of artificial reefs from an engineering, reliability, and feasibility standpoint remains relatively unexplored in the literature. Given the growing importance of these structures in the rehabilitation of marine ecosystems, it is essential to integrate clear and technically sound engineering methodologies. While aspects related to geometric design are well established—covering conceptual requirements [30,41–43], as well as hydrodynamic and morphodynamic performance using numerical simulation [18,44–52] and physical modelling [26,53,54]—the structural design based on primary analytical and numerical methodologies is still insufficiently addressed. Existing studies that explore structural behaviour typically focus on advanced fluid–structure interaction (FSI) simulations [49,55,56]. This may hinder the replication of such structures in different geographies and scenarios,

due to the lack of understanding of the overall relationships between general requirements including materials and action-effect relationships, and the design approach itself.

This work addresses this challenge by implementing an engineering-driven approach for the design of a geometrically complex and modular multifunctional artificial reef (MMFAR), allowing the safety verification and possibly the generalization of the methodology to other similar projects. The developed approach may also support subsequent stages of analysis based on CFD and FSI for detailed functional analysis.

2 MATERIALS AND METHODS

2.1. Engineering-Driven Methodology

In this study a systematic and engineering-driven approach was implemented having the structural design as the central process, based on analytical assumptions and simplified numerical models. The deployment site and the MMFAR requirements and functions were also considered as problem variables. Subsequent numerical analysis (CFD and FSI) and experimental characterization for detailed characterization of innovative materials and structural systems were also acknowledged. This approach is represented in **Figure I.1**, and in this research the focus is mostly on processes 1 to 5, directly related to the structural design, summarized as follows:

1. **Concept and geometric design:** in this stage, with the MMFAR objectives established, the process selects the site location and collects environmental data on physical and biological aspects. The design of shapes and dimensions is undertaken with the objective of meeting functional requirements. Stakeholders, including experts and the local community, participate actively.
2. **Constructive approach:** the development of cross-sections and 3D models is initiated. It considers materials, structural systems, constructive processes, and durability specifications. These aspects must prevent marine pollution and establish a support that meets technical and functional requirements. Logistics and construction techniques are also considered.
3. **Site location and sea conditions:** the analysis of the site location results in the identification of specific actions affecting the structure, such as dead, live, environmental and accidental. Environmental actions are among the most important. The actions and load

combinations follow the recommendations from ISO, API, DNV, and NORSOK [2–5]. Historical site data and prediction models are used to account for time and space variability.

4. **Structural model:** the effects of the loads are obtained from a simplified numerical simulation. For that, the numerical model is discretized in bar elements and a linear-elastic quasi-static analysis is performed. The materials, section properties, and supports are defined, along with load cases and combinations. The results are the axial (N), shear (V), flexural (M), and torsional (T) stresses for safety verifications.
5. **Cross-section design:** determines the load capacity based on material strength and cross-section dimensions, checking limit states to assess performance and feasibility. A parametric study explores various structural combinations in order to identify the promising solutions. This approach optimizes the cross-section, eliminates less promising options, and encourages new structural systems.

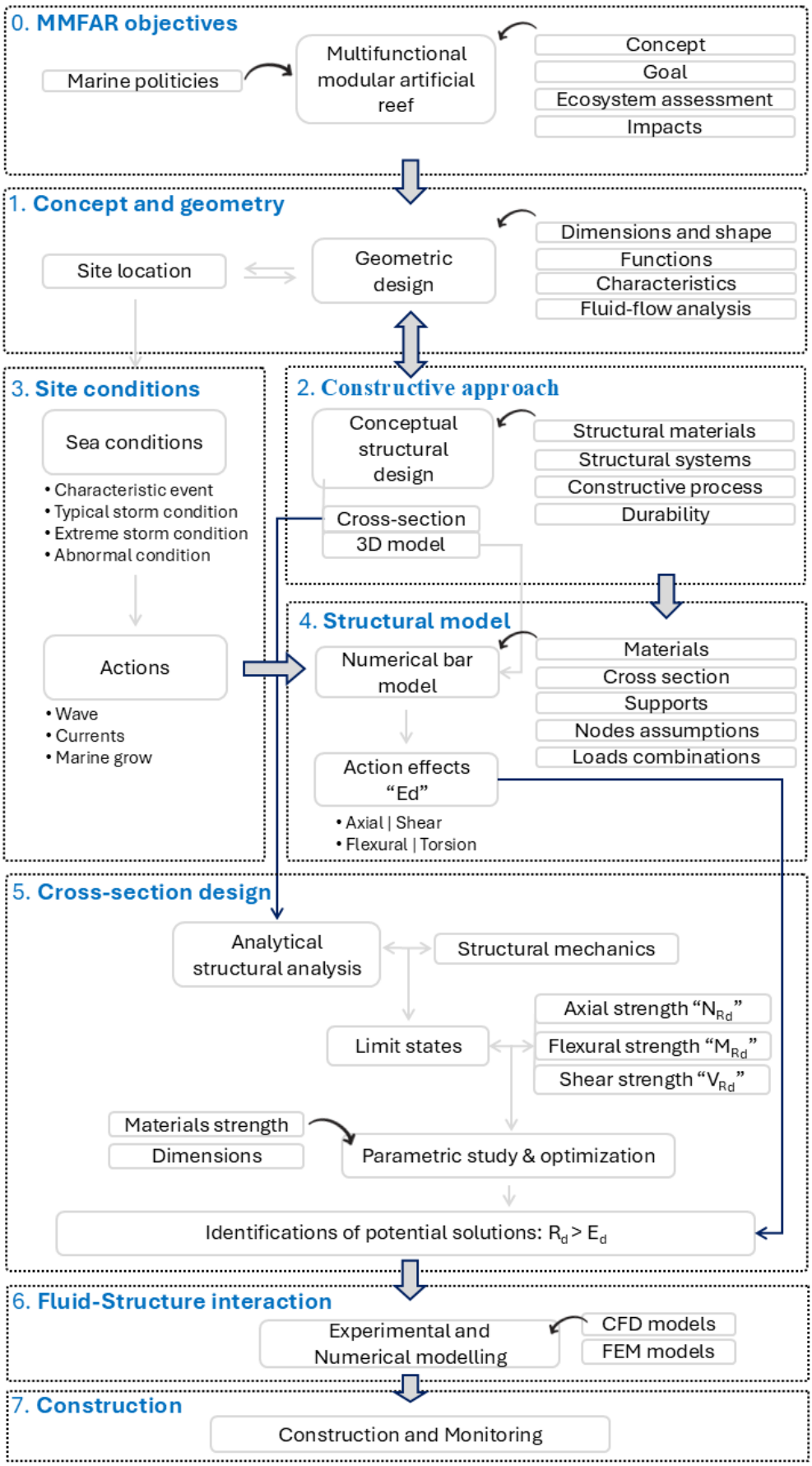


Figure I.1: Design flowchart.

2.2. Concept and Geometric Design

The concept of the MMFAR and the geometrical design were developed within the NEXTSEA project, as detailed by Maslov et al. (2024) [57]. The MMFAR was aimed at supporting marine restoration, enhancing fisheries, and promoting recreational diving [45,57]. In particular, the recovery of key species such as sea bass and seabream was targeted [57]. The geometric design considered also the marine protected area requirements, including site characteristics, bottom properties and habitats, and characteristics of the MMFAR resulting from its interaction with the flow, such as upwelling zones, velocities, and wake zones [45,57]. **Figure I.2** illustrates the evolution of the reef module geometry from module 1 to module 3. To ensure ease of transportation, the weight of each individual unit must not exceed 150 kg. The limb presents a variable cross-section, with a diameter of approximately 150 mm at the smallest section (at the connection end), increasing to around 196.5 mm at the junction with the central bulb. The modular units, united by connectors, allow various MMFAR configurations depending on the assembly scheme (niche, barrier, tunnel). The final assembled structures are reticulated, slender, and expandable, enabling the execution of various configurations from small niches to full reef barriers.

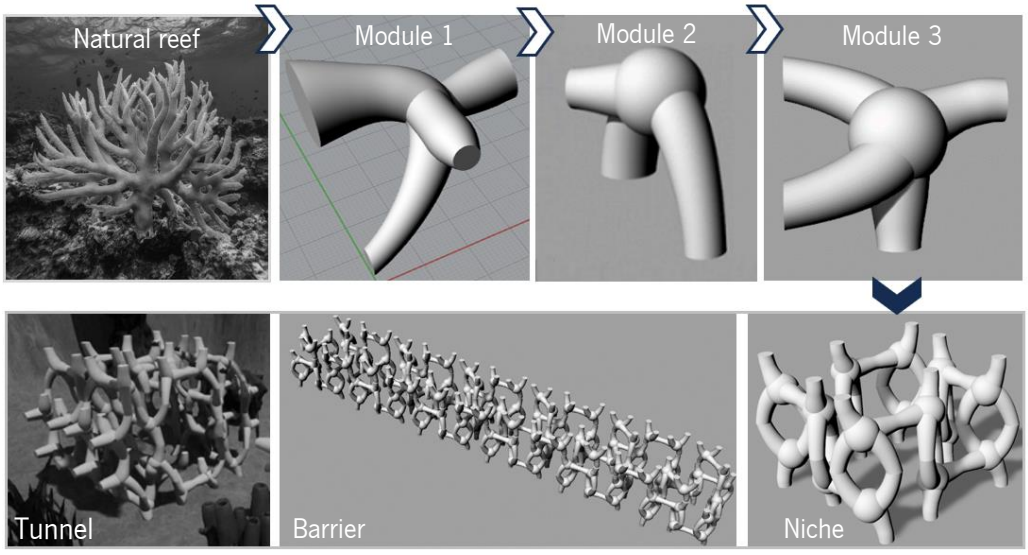


Figure I.2: Geometric design using novel approaches and design processes for the 3D network of individual modules of the MMFAR (adapted from [57]).

2.3. Constructive Approach

Considering the requirements and complex geometry of the MMFAR, it was necessary to design an efficient structural system to (i) allow adequate adjustment of the reinforcing elements within the module and ensure uniform cross-sectional stress distribution as well as a minimum nominal reinforcement cover; (ii) ensure continuity of the internal metallic reinforcement elements and between elements, to facilitate electrical conduction for added functionalities (e.g., self-healing techniques); and (iii) the need to adopt a modular and adaptable construction system to allow the practical and simple assemblage, compatible to underwater operations.

Algorithmic thinking using parametric modelling tools as well as structural design approaches was used for the iterative design and analysis, as shown subsequently. Concrete was chosen for its versatility and cost-effectiveness, as well as its proneness to serve as a colonizing substrate [41,43]. Its brittle nature was countered by the incorporation of ductile reinforcements, such as hot-dip galvanised (HDG) steel which is technically and financially attractive while offering high corrosion resistance. Other options may include self-healing cementitious composites and fibre-reinforced polymers, although the design of these materials was not addressed in this study.

In this sense, different structural systems for the reef module were proposed, as shown in **Figure I.3**: (i) a reinforced concrete structure approach (RC) based on the use of galvanized steel rebars along each limb of the unit (**Figure I.3**a,c), and (ii) a composite steel and concrete structure (CS) where a HDG steel tube was adopted, aligned with the geometric centroid of each limb (**Figure I.3**b,d). The tube was perforated to allow the concrete to flow and fill the inner part of the tube, increasing the bond between the materials and providing a dead weight to counteract buoyancy.

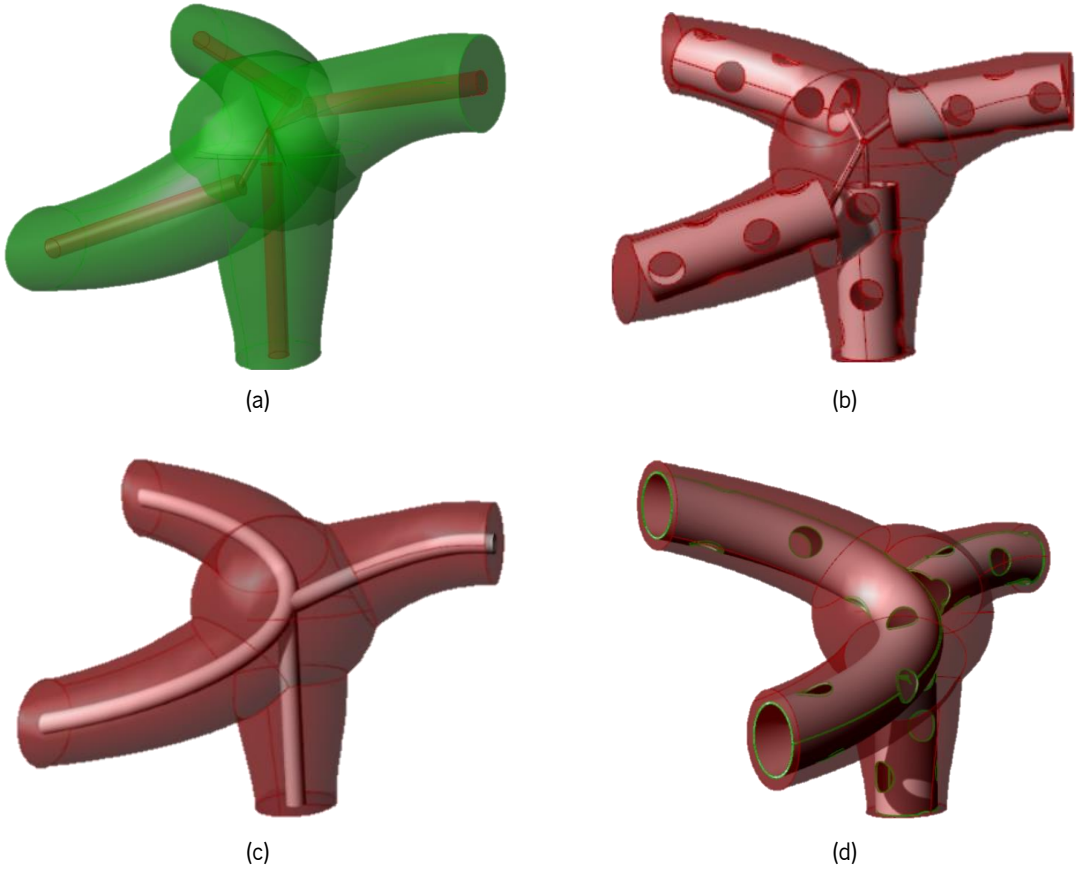


Figure I.3: Structural systems: (a) RC unit with four galvanized steel rebars interconnected using external rods by welding, (b) CS unit based on the use of four galvanized steel tubes with holes along the length, interconnected using external rods by welding, (c) RC with three central galvanized steel rebars interconnected at the centre of the unit by welding or tying and (d) CS based on the use of three central galvanized steel tube profiles with holes along the length, interconnected by welding at the intersection.

The adoption of straight reinforcement elements was tried; however, the accommodation of the reinforcement elements in the geometry was found to be hard, in particular trying to guarantee the minimum concrete cover. Curved reinforcement elements, although requiring additional forming procedures, were easier to adapt to the complex geometry of the module, ensuring better distribution of the reinforcement area along the cross-section and providing adequate reinforcement cover.

The extension of the tube or rebar beyond the edges of each module was considered to support the connection system, particularly favourable in the case of the solution adopting the steel tubes as shown in **Figure I.4**.

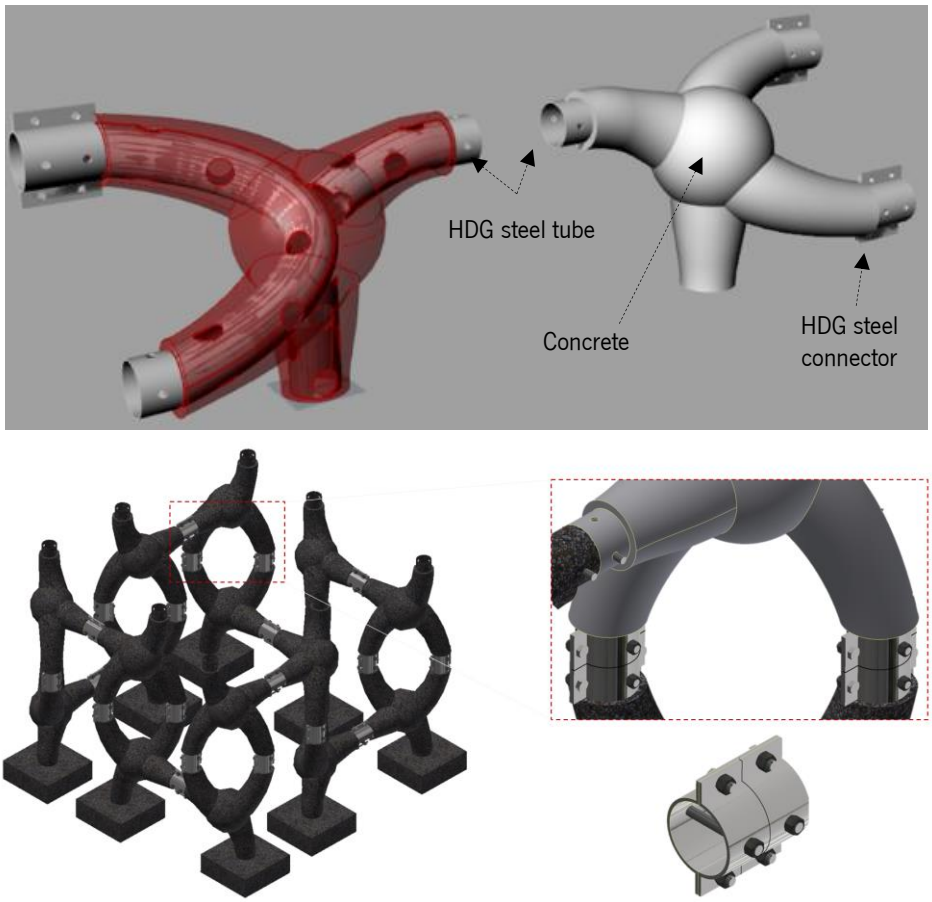


Figure I.4: 3D model of MFMAR with the connectors system.

2.4. Site Location and Sea Conditions

As a case study, the developed MMFAR was assumed to be deployed in a Marine Protected Area (MAP), in Esposende – Portugal. This site represents a promising location for the implementation of MMFAR for ecosystems restoration and protection, and for recreational or scientific diving. **Figure I.5** shows the geographical location of the Littoral North Marine Park, as well as the bathymetry in the area. The ideal installation depth of the MMFAR was defined as 20 meters, allowing recreational diving and avoiding the direct effect of high waves. The present study is related mainly to the structural design of an submerged structure; therefore in **Table I.1** the typical wave parameters in the area for different sea conditions of the study area are presented. Further details may be found in [58–61].

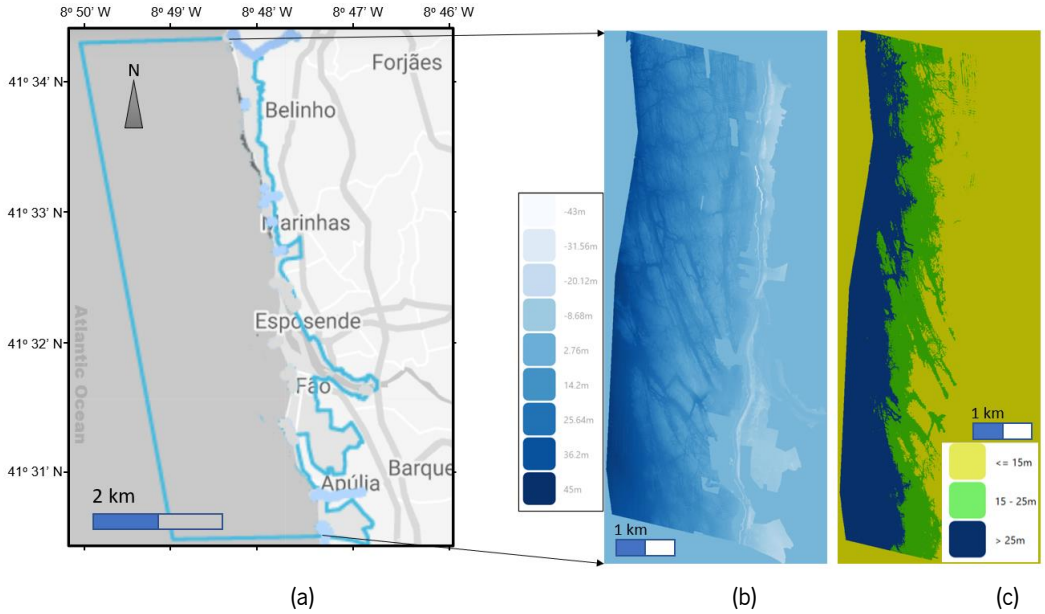


Figure I.5: (a) Geographical location of the Littoral North Marine Park in Esposende, Portugal; (b) detailed bathymetry distribution, and (c) zone with acceptable MMFAR depth [45].

Table I.1: Wave height and period for different sea conditions [58–61].

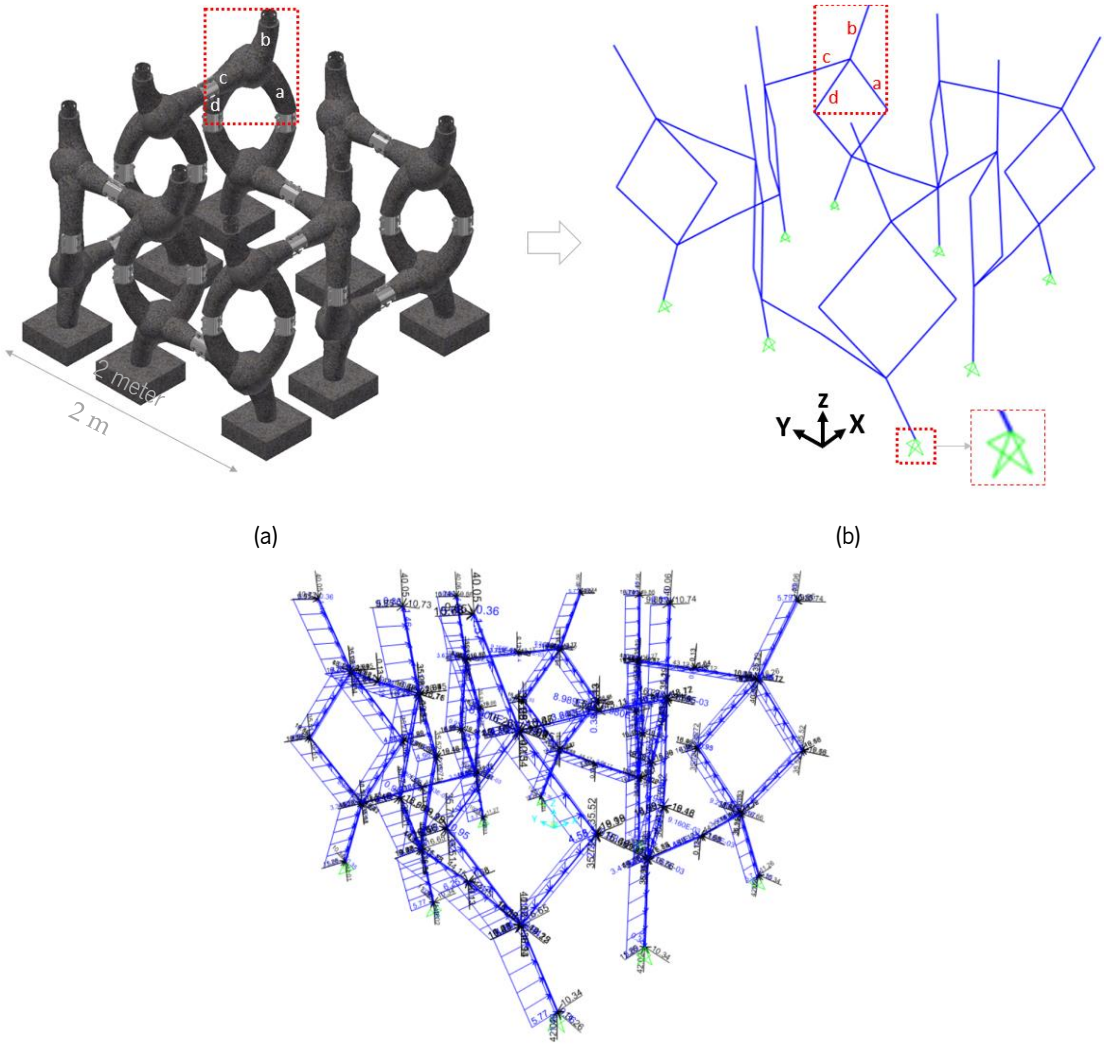
Characteristic Event E_w	Typical Storm Condition $E_{w,storm}$	Extreme Storm Condition $E_{w,máxstorm}$	Abnormal Extreme Condition $E_{w,e}$
H_s=2.20m T= 7.89s	$H_{S,storm}$ = 4m T= 10s	$H_{S,máxstorm}$ = 9m T= 14.6s	$H_{S,40}$ = 15.61m $T_{p,40}$ = 20s

2.5. Structural and Hydrodynamic Model

The research conducted considered the development of a MMFAR niche, whose structure was composed of 16 units, each of which occupied a cube with an edge of 65 cm (**Figure I.6**). With a width of approximately 2 by 2 meters, the structure represents a bottom projection area of 4.807 m², and a total volume of 1.76 m³ [57]. The full assemblage was numerically studied based on a reticulated model of bars to evaluate the stresses for the structural mechanics analysis. For that, a finite element tool, with a 3D graphical user interface object-oriented, was used for the linear static analysis of the structure. In this process, the 3D elements were transformed into bar elements connected by nodes. The connection zone was not considered by simplification, and the structure was treated as monolithic with a perfect continuity between modules. The base was restricted with double

supports, resembling real support conditions. Concrete and steel were considered for the sectional properties.

The structure was subjected to the self-weight and the hydrodynamic load (dF), which in turn was the result of the environmental actions (E) including waves (E_w), tidal currents (E_c) and marine growth (E_m). In this process, the fluid velocities and accelerations were resolved into drag (dF_D) and inertial forces (dF_I) and applied as distributed loads on the members of the numerical model. The velocities ($u_{wave;}$ $u_{current}$) and accelerations ($\partial u/\partial t$) of the fluid were calculated using the Stokes Wave Theory (**Table I.2**) [62,63]. The local current profile was combined vectorially with the wave kinematics to determine local fluid velocities and accelerations adopting the Morison (**Eq. (I. 1**)).



(a) (b)

(c)

Figure I.6: MMFAR structure: (a) 3D model, (b) numerical bar model (c) forces applied to the numerical bar model. The marks "a, b, c and d" show the visual correspondence between the elements of the 3D model and the bar model.

$$dF = dF_D + dF_I \quad [\text{N/m}];$$

$$dF_D = C_D \times \tfrac{1}{2} \times \rho \times D \times (u_{wave} + u_{current})^2\, dz \quad [\text{N/m}]; \qquad \textbf{(I. 1)}$$

$$dF_I = C_M \times \rho \times (\pi \times D^2)/4 \times (\partial u/\partial t)\, dt \quad [\text{N/m}];$$

In **Eq. (I. 1)**, ρ represents water density, dz the depth interval and D the diameter of the bar element. The hydrodynamic drag coefficient (C_D) and hydrodynamic inertia coefficient (C_M) were adopted following the recommendation of API [63,64]. The water current velocity profile ($u_{current}$) assumed a constant velocity of 1.2 m/s between the water surface level and half of the depth (z/2), and a constant velocity of 0.3 m/s between z/2 and the seabed. According to DNV-RP-C205, a value of 0.1 m was assumed for the marine growth [65]. Buoyant loads were also taken into account. The resulting forces were applied in x direction (d_{xx}). The load combinations followed the recommendations of ISO 19903:2006 [66]. The crest wave phase was considered since it corresponds to the maximum positive horizontal velocity and to zero horizontal acceleration. The vertical velocity is zero and the vertical acceleration is maximum (in negative value).

For the analysis the characteristic event, the typical storm condition and the extreme storm condition were considered. In addition, abnormal environmental extreme events were also considered as accidental loads.

Table I.2: 1st and 2nd order components of stokes wave theory [62,63].

Quantity	**1st order component**	**2nd order component**
Dispersion Relationship, c^2	$\frac{g}{k}\tanh kd$	$\frac{g}{k}\tanh kd$
Wave profile, η	$\frac{H}{2}\cos(kx - \omega t)$	$\frac{\pi H^2}{8L}\frac{\cosh kd}{\sinh^3 kd}[2 + cosh\ 2kd]\cos 2(kx - \omega t)$
Horizontal velocity, u	$\frac{\pi H}{T}\frac{\cosh ks}{\sinh kd}\cos(kx - \omega t)$	$\frac{3}{4c}\left(\frac{\pi H}{T}\right)^2\frac{\cosh 2ks}{\sinh^4 kd}\cos 2(kx - \omega t)$
Vertical velocity, v	$\frac{\pi H}{T}\frac{\sinh ks}{\sinh kd}sin(kx - \omega t)$	$\frac{3}{4c}\left(\frac{\pi H}{T}\right)^2\frac{\sinh 2ks}{\sinh^4 kd}\sin 2(kx - \omega t)$
Horizontal acceleration, $\dot{u}$	$\frac{2\pi^2 H}{T^2}\frac{\cosh ks}{\sinh kd}sin(kx - \omega t)$	$\frac{3\pi}{2L}\left(\frac{\pi H}{T}\right)^2\frac{\cosh 2ks}{\sinh^4 kd}\sin 2(kx - \omega t)$
Vertical acceleration, $\dot{v}$	$\frac{2\pi^2 H}{T^2}\frac{\sinh ks}{\sinh kd}cos(kx - \omega t)$	$\frac{3\pi}{4L}\left(\frac{\pi H}{T}\right)^2\frac{\sinh 2ks}{\sinh^4 kd}\cos 2(kx - \omega t)$
Dynamic pressure, p	$pg\frac{H}{2}\frac{\cosh ky}{\cosh kd}\cos[k(x - ct)]$	$\frac{3}{4}pg\frac{\pi H^2}{L}\frac{1}{\sinh 2kd}\left[\frac{\cosh 2ks}{\sinh^2 kd} - \frac{1}{3}\right]\cos 2(kx - \omega t) - \frac{1}{4}pg\frac{\pi H^2}{L}\frac{1}{\sinh kd}[\cosh 2ks - 1]$

c: wave celerity, g: gravitational acceleration, k: wave number ((k=2π/L), L: wavelength, d: water depth, H_w: wave height, η: wave profile (surface elevation of the water), ω: wave angular frequency (ω=2πf, where f is the wave frequency), T: wave period, x: horizontal coordinate, t: time, u: horizontal velocity of the fluid, v: vertical velocity of the fluid, ρ: fluid density, p: dynamic pressure.

2.6. Action and Effects

Table I.3 shows the results obtained for each of the load cases and load combinations, according to the limit states identified as the most severe, in terms of maximum axial (N), shear (V), flexural (M) and torsional (T) stresses. **Figure I.7** identifies the critical sections, i.e. the locations where the maximum stresses occur. As shown, the worst scenario is the abnormal extreme condition. In this context, the maximum deflection obtained was 1.789 mm, the maximum axial stress was -86.05 kN, the maximum flexural stresses were - 4.70 kN.m and 12.81 kN.m, the maximum negative and positive shear stresses were 36.43 kN and the maximum negative and positive torsional stresses were 1.94 kN.m.

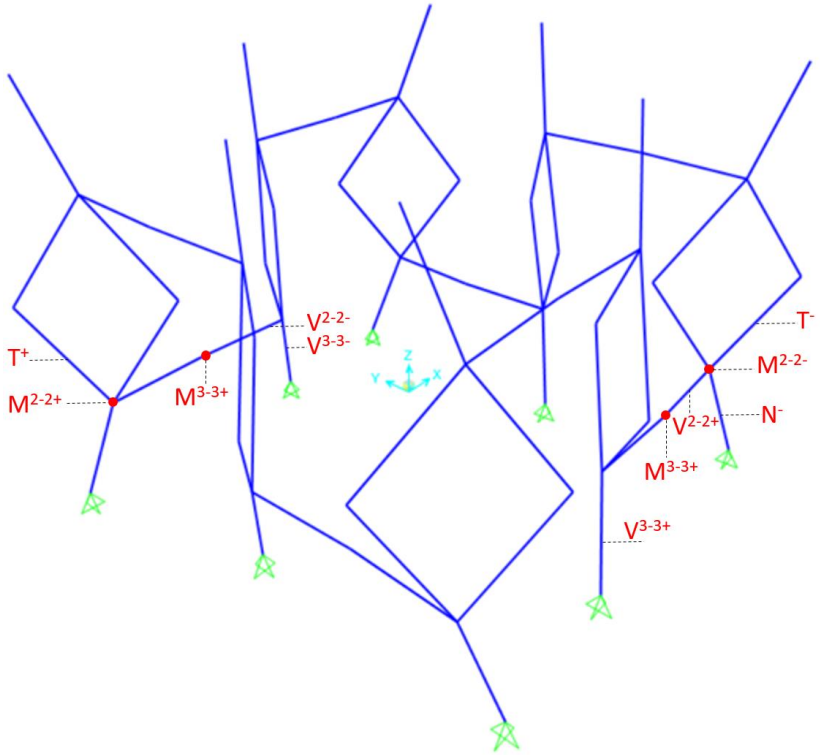


Figure I.7: Location of the maximum stresses in the numerical model.

Table I.3: Results in terms of the maximum efforts obtained for different load combinations.

Load combination	U_r [mm]	N^- [kN]	N^+ [kN]	$V_{2\text{-}2}^-$ [kN]	$V_{2\text{-}2}^+$ [kN]	$V_{3\text{-}3}^-$ [kN]	$V_{3\text{-}3}^+$ [kN]	$M_{2\text{-}2}^-$ [kNm]	$M_{2\text{-}2}^+$ [kNm]	$M_{3\text{-}3}^-$ [kNm]	$M_{3\text{-}3}^+$ [kNm]	T^- [kNm]	T^+ [kNm]
Type of support: double support													
LC1_ULS(A)_E_{wcm}_d_{xx}	0.090	-26.89	-	-1.17	1.00	-0.29	0.44	-0.15	0.13	-0.24	0.37	-0.08	0.06
LC2_ULS(B)_E_{wcm}_d_{xx}	0.143	-46.37	-	-1.62	1.38	-0.73	1.08	-0.37	0.25	-0.24	0.52	-0.11	0.08
LC3_ULS(A)_$E_{wcm,storm}$_d_{xx}	0.120	-28.32	-	-1.96	1.97	-0.51	0.81	-0.27	0.21	-0.47	0.61	-0.13	0.08
LC4_ULS(B)_$E_{wcm,storm}$_d_{xx}	0.215	-49.32	-	-3.22	3.33	-1.14	1.76	-0.59	0.38	-0.84	1.16	-0.20	0.15
LC5_ULS(A)_$E_{wcm,máxstorm}$_d_{xx}	0.421	-38.23	-	-8.53	8.53	-2.32	3.03	-1.07	1.02	-2.75	2.93	-0.44	0.43
LC6_ULS(B)_$E_{wcm,máxstorm}$_d_{xx}	0.789	-67.99	-	-15.43	15.51	-4.05	5.88	-2.00	1.89	-5.08	5.47	-0.81	0.81
LC7_ALS_E_{wcme}_d_{xx}	1.789	-86.05	-	-36.43	36.43	-11.14	12.65	-4.70	4.61	-12.46	12.81	-1.94	1.94

U_r – maximum global displacement; N – maximum axial stress; $V_{2\text{-}2}$ - maximum shear stress in 2-2; $V_{3\text{-}3}$ – maximum shear stress in 3-3; $M_{2\text{-}2}$ – maximum flexural stress in 2-2; $M_{3\text{-}3}$ – maximum flexural stress in 3-3; T – maximum torsional stress.

2.7. Design Considerations for Durability

According to NP-EN 1992-1-1 [67], the exposure class to be considered is XS2 (parts of permanently submerged marine structures), and according to NP-EN 1990 [68] the structural class 4 (S4) was considered, corresponding to a service life of at least 50 years. The durability of concrete structures depends on its composition and performance [67], and Annex E of NP-EN 1992-1-1 suggests that concrete for corrosion protection should comply with higher strength classes, C35/45 for exposure condition XS2. However, the National Annex for Portugal specifies C30/37* (or *C40/50 for CEM I or CEM II/A). According to NP-EN 206-1 Annex F [69], the recommended concrete composition includes a maximum w/c ratio of 0.45, minimum strength class C35/45, and a minimum cement dose of 320 kg/m^3. The concrete nominal cover (c_{nom}) of 50 mm was adopted, in accordance with the National Annex of NP-EN 1992-1-1 for Portugal.

2.8. Cross-Section Design

The cross-section design was conducted considering the two alternative structural systems studied, the RC and the CS, and adopting the organic sectional analysis based on the behaviour of the materials involved for ultimate limit states (ULSs).

Due to the geometric complexity and varying cross-sections of the members extending from the central core (sphere), the analysis focused on a typical cross-section that is geometrically representative (**Figure I.8**). The critical cross-section, selected for its likely impact on design limitations, was analysed to determine its axial, flexural, and shear strengths, based on the area, geometry, and material properties of both structural systems. A parametric study was conducted varying the strength class of both materials and tube dimensions. NP-EN 1992-1-1 [67] was used for the analysis of RC cross-section, and NP-EN 1994-1-1 was applied for the CS cross-section [70]. Following, the analytical methodology is presented, and a parametric study developed.

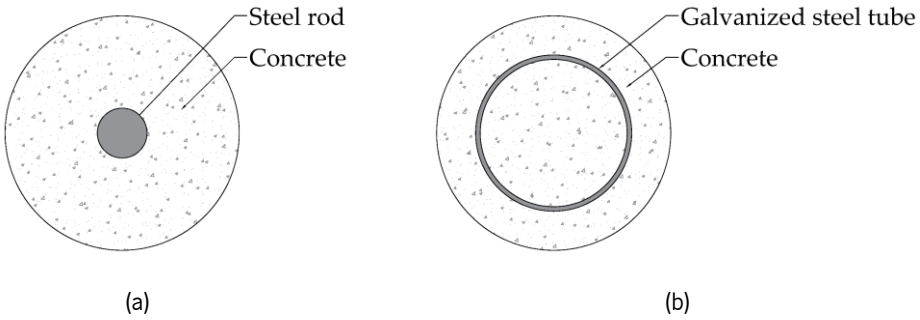


Figure I.8: Representative cross section of the alternative structural systems: (a) RC structure and (b) CS structure.

2.8.1. Axial Strength

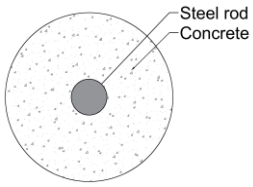
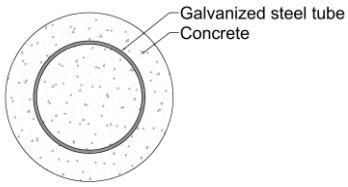
Considering that the most unfavourable scenario is the one where the entire section is under tension, the required amount of reinforcement in the cross section was obtained, ensuring that the stress in the reinforcement remains below the yield stress after concrete cracking, according to **Eq. (I. 2)**

Regarding the compressive strength ($N_{pl,Rd,comp}$), the contribution of both materials (concrete and steel) was considered. For the tensile strength ($N_{pl,Rd,trac}$), only the contribution of the steel was considered. $N_{pl,Rd,comp}$ and $N_{pl,Rd,trac}$ were obtained for smallest and largest cross-section areas, according to **Eq. (I. 3)** and **Eq. (I. 4)** (**Table I.4**), respectively.

Given that the cross-sections were subjected to approximately centred stresses, the average compressive strain was limited to $\mathcal{E}_{c2}$. Note that, in the case of class C45/55 concrete, then $\mathcal{E}_{c2} = 2\,‰$. Thus, by strain compatibility, $\mathcal{E}_s = 2‰$. Considering that the reinforcement exhibits elastic behaviour until yielding, the maximum tension to which the reinforcement can be subjected is given by $\sigma_s = E_s \times \mathcal{E}_s$.

Additionally, the steel contribution ratio (δ), which must lie between 0.2 and 0.9 in the case of the CS structures, was also a criterion. This is one of the aspects that differentiates the design of a RC structure from a CS structure.

Table I.4: Axial strength of the cross-section according to the structural system.

	RC	**CS**	
			
$A_{s,min}$	$f_{ctm} \times \left[A_c + \left(\frac{E_s}{E_c} - 1\right) \times A_{s,min}\right] = A_{s,min} \times f_{yk}$		**(I. 2)**
$N_{pl,Rd,trac}$	$f_{yd} \times A_s$	$N_{pl,Rd} = A_a f_{yd} + A_s f_{sd}$	**(I. 3)**
$N_{pl,Rd,comp}$	$(E_s \times \mathcal{E}_s) \times A_s + (A_c \times f_{cd})$	$A_a f_{yd} + \alpha_{cc} A_c f_{cd} + A_s f_{sd}$	**(I. 4)**

A_a – steel profile area; Ac – concrete area; As – steel reinforcement area;
E – modulus of elasticity (s–steel, c–concrete); ε – strain;
f_{ctm} – concrete tensile strength; f_{cd} – design value of concrete compressive strength;
f_{yk} – characteristic yield strength; f_{yd} – design yield strength of the structural steel;
f_{sd} – yield stress of the longitudinal reinforcement;
α_{cc} was equal to 1.0 (tubular steel section covered and filled with concrete).

2.8.2. Shear Strength

In the absence of specific transverse reinforcement in a given section, the effectiveness of the concrete's contribution to shear strength diminishes under higher loads. Consequently, the longitudinal reinforcement assumes an important function in the transfer of shear forces. This scenario is particularly relevant in cases where the implementation of shear reinforcement is either impracticable due to spatial constraints or challenging to execute, such as in narrow elements or sections with intricate geometries, as is the case of the MMFAR structure under study.

Thus, the shear strength, V_{Rd}, of the cross-section was obtained by considering the contributions of concrete and longitudinal reinforcement, based on NP-EN 1992-1-1 [67], as detailed in **Table I.5**. In this context, the smallest cross-section, located near the connection zone, was considered the critical cross-section, as it is where the maximum shear strength occurs, as indicated in **Figure I.7**

Table I.5: Shear strength of the cross-section according to the structural system.

V_{Rd}	$V_{Rd,c} + V_{Rd,sl}$	**(I. 5)**
$V_{Rd,c}$	$\left[C_{Rd,c} \cdot k(100 \cdot \rho_l \cdot f_{ck})^{1/3} + k_1 \cdot \sigma_{cp}\right] \cdot b_w \cdot d$	**(I. 6)**
$V_{Rd,sl}$	$A_{sl} \cdot f_{yd}$	**(I. 7)**

$V_{Rd,c}$ - design shear resistance of the member without shear reinforcement; **$V_{Rd,sl}$** - design "shear" strength of the longitudinal reinforcement, **$C_{Rd,c}$** - coefficient of shear strength of concrete ($0.18/\gamma_c$,with γ_c = 1.5), ρ_l- geometric ratio of longitudinal reinforcement ($A_{sl}/b_w d$), **b_w** – cross-section diameter, **d** – effective section height, **k_1** – shear behaviour coefficient, **k** = $1+\sqrt{(200/d)} \leq 2$, σ_{cp} - compressive stress of concrete due to normal forces ($N_{Ed}/A_c < 0{,}2 f_{cd}$), **$N_{Ed}$** - axial force in the cross-section due to loading, **Ac** - area of concrete cross section; ***A_{sl}*** – area of longitudinal steel reinforcement **f_{ck}** – characteristic compressive strength, **f_{cd}** - compressive failure stress of the concrete; **f_{yd}** – design yield strength of the structural steel;

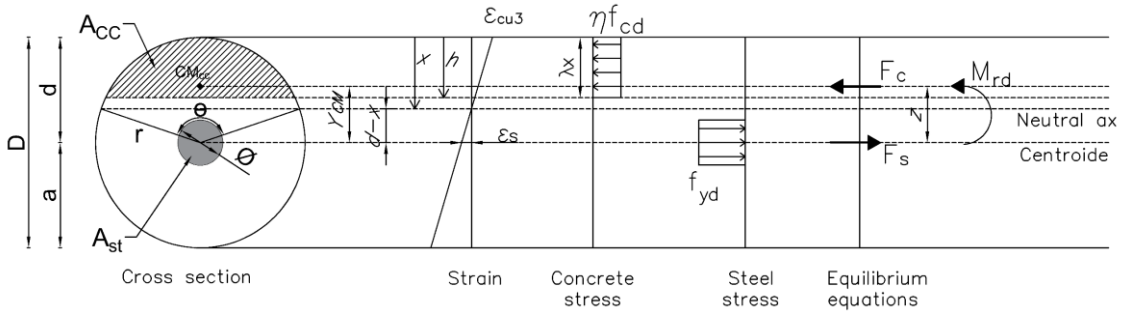
2.8.3. Flexural Strength

Considering the need to guarantee ductile failure, the minimum reinforcement A_{smin} was obtained according to **Eq. (I.9)**. The corresponding cracking flexural stresses (M_{cr}) was computed by **Eq. (I.8). Table I.6** shows the main equations and validation criteria related to the flexural behaviour of the cross-section for each structural system. **Figure I.9** shows the strains and stresses developed in both cross-section types assuming ULS and the simplified Bernoulli conditions for simple flexure.

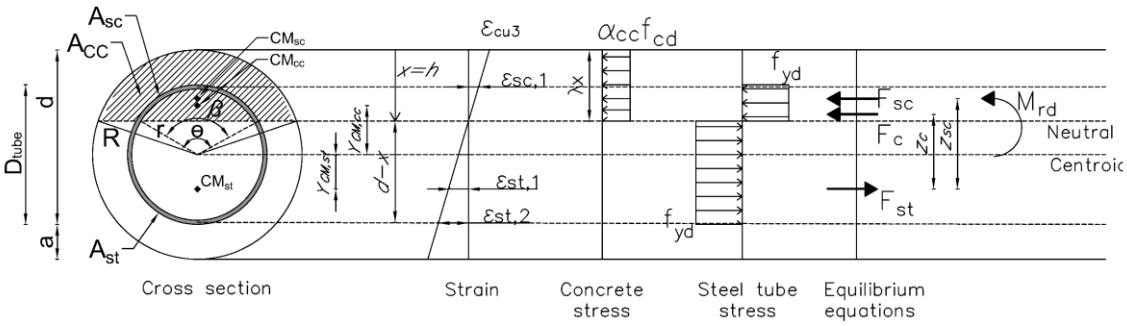
The approach consisted of determining the equilibrium of the cross-section stresses that maximizes the flexural strength to verify the safety condition, $M_{Rd} > M_{Ed}$. The problem was solved through the implementation of a flexural inverse analysis, which identified the critical cross-section as the one located in the proximity of the connection zone, since it shows simultaneously the minimum area and the maximum stress, as illustrated in **Figure I.7**.

The value of ε_s was adopted to ensure the plastic regime and the optimal position of the neutral axis could be calculated. For that, the rectangular stress block for the distribution of stresses in the concrete and an elastic-perfectly plastic diagram for steel (ε_{cu3}, $\varepsilon_{s=\infty}$, λ and η) were assumed. Subsequently, the required reinforcement to balance the tensile and compression forces in the cross-section was analysed and the M_{Rd} was calculated according to **Eq. (I.10**) and **Eq. (I.11**). The phenomenon of cross-section steel saturation was considered, whereby an increase in A_s does not necessarily result in a proportional increase in flexural strength due to cross-section limitations. The binary arms z, z_c and z_{sc} and the parameter that translates the geometric relationship between the concrete and steel cross sections and the position of the neutral axis θ and β are shown in

Table I.6. Design assuming reinforcement in the elastic regime should be avoided, as it risks uneconomical solutions and brittle failure.



(a)



(b)

Figure I.9: Schematics representing the simplified strains and stresses at ULS in flexure for (a) RC and (b) CS cross-sections.

Table I.6: Flexural first cracking strength (M_{cr}), ultimate strength (M_{Rd}) and minimum reinforcement ($A_{s,min}$) of the cross-section for both RC and CS structural systems.

	RC structure	CS structure	
M_{cr}	$M_{cr} = \frac{f_{ctm} \times \overline{I_x}}{\overline{y_g}} = \frac{f_{ctm} \times \frac{\pi D^4}{64}}{\frac{A_c \times \frac{D}{2} + (\alpha - 1)\, A_s \times a}{\pi \times r^2 + (\alpha - 1)\, A_s}}$		**(I.8)**
$A_{s,min}$	$A_{s,min} = \frac{A_{cc} \times \left[\frac{4\,r}{3}\left(\frac{\sin\left(\frac{\theta}{2}\right)^3}{\theta - \sin\theta}\right) - (d - x)\right]}{\alpha \times (d - x)}$		**(I.9)**
M_{Rd}	$F_c \times z$ ❖ $F_c = \left[r^2 \cos^{-1}\left(1 - \frac{h}{r}\right) - (r - h)\sqrt{2rh - h^2}\right]\eta f_{cd}$ ❖ $z = \frac{4\,r}{3}\left(\frac{\sin\left(\frac{\theta}{2}\right)^3}{\theta - \sin\theta}\right)$ ❖ $\theta = 2\cos^{-1}\left(\frac{r-x}{r}\right)$	$F_c \times z_c + F_{sc} \times z_{sc}$ ❖ $F_c = \left(\left[R^2 \cos^{-1}\left(1 - \frac{h}{R}\right) - (R - h)\sqrt{2rh - h^2}\right] - \left[2\cos^{-1}\left(\frac{R-h}{r}\right) rt\right]\right)\eta f_{cd}$ ❖ $F_{sc} = 2\cos^{-1}\left(\frac{R-h}{r}\right) rt \times f_{yd}$ ❖ $z_c = \frac{4\,R}{3}\left(\frac{\sin\left(\frac{\theta}{2}\right)^3}{\theta - \sin\theta}\right) + \left(\frac{r^2(\sin\beta - \sin(-\beta))}{r\,(2\pi - \beta)}\right)$ ❖ $z_{sc} = \frac{r \times \sin\left(\frac{\beta}{2}\right)}{\frac{\beta}{2}} + \left(\frac{r^2(\sin\beta - \sin(-\beta))}{r\,(2\pi - \beta)}\right)$ ❖ $\theta = 2\cos^{-1}\left(\frac{R-x}{R}\right)$ ❖ $\beta = 2\cos^{-1}\left(\frac{R-x}{r}\right)$	**(I.10)**
A_s	$A_s = \frac{F_c}{\sigma_s}$	$A_{st} = \frac{F_c + F_{sc}}{\sigma_s}$	**(I.11)**
Condition	ε_{cu3}=3.5 ‰ / ε_s = "∞" / λ=0.8 / η=0.9	ε_{cu3}=3.5 ‰ / ε_s = "∞" / λ=1.0 / η=0.85	
Validation	$\varepsilon_c = \varepsilon_{cu3}$ and $\varepsilon_{s,i} > \varepsilon_{yd}$		

M_{cr} – cracking flexural stress, **f_{ctm}** – mean concrete axial tensile strength, **$\overline{I_x}$** – equivalent moment of inertia of the section, **$\overline{y_g}$** – distance from the centroid of the section to the outermost fibre, **A_{cc}** – cross sectional area of concrete, **D** – diameter of the circular cross-section, **r** or **R** – radius of the concrete circular section, **t** – wall tube thickness, **E_i** – materials Young's Modulus, **α** – E_s/E_c, **a** - distance from the centroid of the reinforcement to the geometric centre of the section, **A_s** – cross sectional area of reinforcement**,** **A_{cc}** – compressive area of the concrete section, **A_{st}** – tensile area of the steel section**,** **θ** – angle of the compressed concrete section, **β** – angle of the compressed steel section , **r** – tube radius, **d** – effective depth of a cross-section, **x** – neutral axis depth, **h** and **λ** – effective height of the compression zone, **F_c** – concrete compressive force, **F_{sc}** – steel compressive force, **f_{cd}** – design compressive strength of concrete, **η** – effective strength, **f_{yd}** – design tensile strength of steel, **z** – lever arm of internal forces, **σ_S** – steel stress, **ε_{cu3}** – ultimate compressive strain in the concrete, **ε_s** – strain in the steel, **ε_c** – strain in the concrete.

3 RESULTS AND DISCUSSION

3.1. Parametric Study of RC and CS Design Without Cross-Sectional Diameters Modifications

The results of the parametric study conducted in terms of axial and flexural strength for both structural systems, where concrete and steel classes were varied, are shown in **Table I.7** (Appendix A) and **Table I.8** (Appendix B). **Figure I.10** and **Figure I.11** illustrate the correlation between the concrete compressive strength (f_c) and steel class and the obtained flexural ($M_{pl,Rd}$) and normal ($N_{pl,Rd}$) strengths based on **Table I.7** and **Table I.8**. The plotting colour-code in the graphs is combined with the reinforcement configuration according to steel class.

- ***RC cross-section:***

The reinforcement rebar (1ØD) was of conventional steel classes S400 and S500 used in civil construction, and threaded rods (1MD) of DIN 4.8, 5.8 and 8.8 steel class. The minimum concrete strength class was C30/37.

In terms of axial strength, it appears that the most unfavourable combination of materials for determining $A_{s,min}$ was concrete C90/105 and DIN 4.8 steel rebar. These require a minimum reinforcement of 5.02 cm^2, which can be fulfilled by a 30 mm threaded steel rod. As demonstrated, for all scenarios, the minimum reinforcement guaranteed that the compressive and tensile strengths ($N_{pl,Rd}$) (**Figure I.11**) clearly exceed the maximum axial stress N_{Ed} (–86.05 kN, refer to **Table I.3**) obtained from the numerical model.

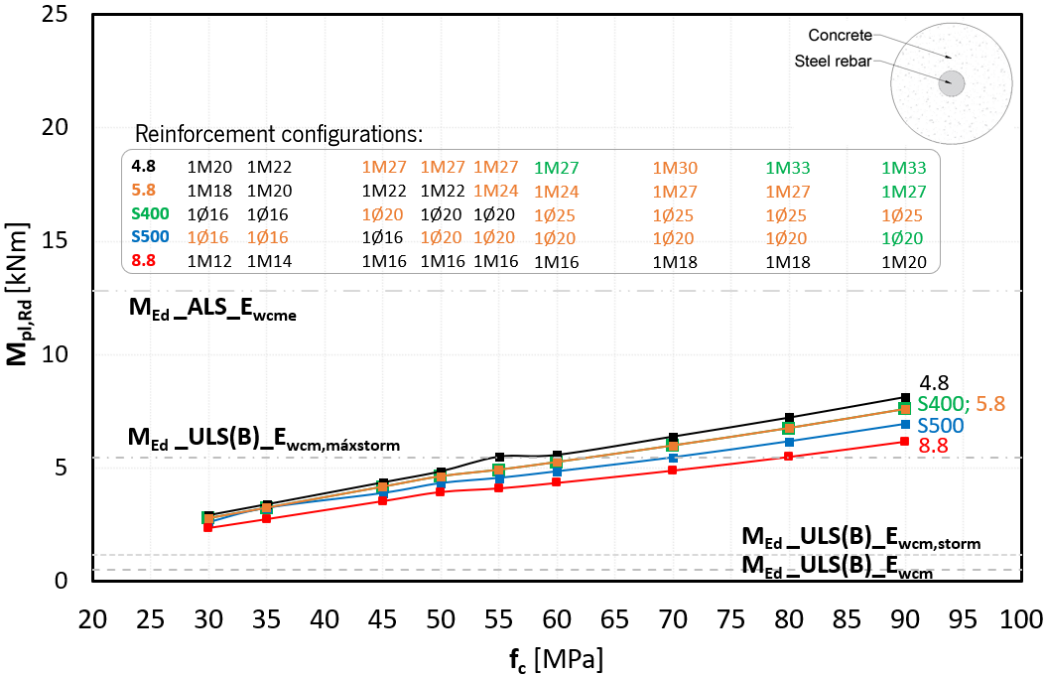
In terms of flexural strength, the minimum reinforcement could be fulfilled using 1Ø8 mm (M_{cr} = 1.65 kN·m). The obtained $A_{s,min}$ was in all cases below the A_s required for ULS. **Figure I.10** presents the flexural strength versus concrete strength for various structural combinations of RC cross-section. In general, the reinforced concrete critical cross-section showed limitations in terms of flexural strength, since it did not achieve safety for abnormal extreme conditions and, in some cases, extreme storm action (**Figure I.10**). The lowest flexural strength, $M_{pl,Rd}$ = 2.37 kN, was obtained for the combination of concrete class C30/37 and DIN 8.8 steel rebar, ensuring strength capacity only for the load combinations E_{wcm} and $E_{wcm,storm}$. The highest $M_{pl,Rd}$, 6.32 kN, was achieved for the concrete class C90/105 and DIN 4.8 steel rebar, meeting all requirements except the ALS_E_{wcme} load combination. As shown in **Figure I.10**(a), the $M_{pl,Rd}$ decreases as the steel strength

increases for the same class of concrete, as higher-strength steel reduces the saturation reinforcement area ($A_{s,satur}$) of the cross-section, reducing the lever arm of internal forces and decreasing the section's flexural strength. This trend is attributed to the restriction of the cross-section diameter to a minimum of 150 mm, imposed by the geometric design. This highlights the importance of balancing steel reinforcement layout with steel strength in small sections to optimize structural performance. The most promising combinations of materials were those that resulted in $A_{s,satur}$ (flexural) ≥ $A_{s,eff}$ (axial) and $Ø_{satur}$ (flexural) ≥ $Ø_{eff}$ (axial), identified in green shading in **Table I.7**. While the combinations identified in yellow coincide in diameter ($Ø_{eff} = Ø_{satur}$), these exhibit $A_{s,eff}$ >> $A_{s,satur}$, disrupting the cross-section equilibrium and preventing reinforcement yielding. In this case, it would be necessary to reconfigure and optimize the cross-section to accommodate the reinforcement imposed by $A_{s,min}$, as discussed in Sections 3.2 and 3.3.

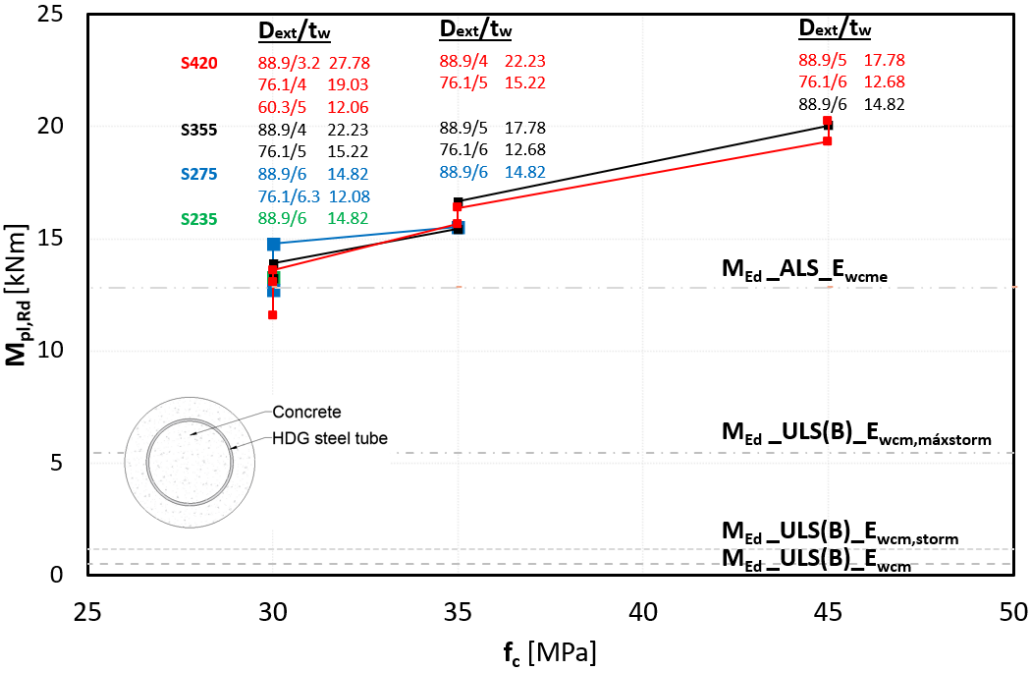
Regardless of the concrete class, it seems that the structural combinations showing the best compromise between the strength of the materials, the position of the neutral axis, and the normal and flexural strength, include the use of DIN 4.8, as evidenced by the highest $M_{pl,Rd}$ values shown in **Table I.7** and **Figure I.10**(a). In fact, the threaded rebar DIN 4.8 steel resulted in the most significant overlap between steel reinforcement diameters that satisfy both axial and flexural reinforcement requirements. For S500 steel, there is a central range in the graph where the effective steel area (A_s) remained constant, irrespective of the concrete strength (f_c), specifically within the range of f_c = 50 MPa to 90 MPa. This occurred due to a significant gap between $A_{s,pl}$ and $A_{s,eff}$, making the choice of S500 inefficient for lower concrete strength classes where $A_{s,pl}$ is significantly higher than $A_{s,eff}$. Furthermore, a higher concrete strength class results in the raise of the position of the neutral axis, increasing the $A_{s,pl}$ and respective M_{Rd}.

Summarizing, the results showed that the tensile behaviour of the cross-section limits the amount of reinforcement that must be provided in the cross-section. It was observed that the minimum reinforcement required for a RC element in tension with a variable cross-section (largest section being the most critical) is higher than the one obtained for flexure ($A_{s,satur}$) (smallest section being the most critical). However, the flexural strength of the section, although optimised internally, appears to be the limiting strength, primarily due to the reduced cross-sectional dimension. The results indicate that it may be more advantageous to optimize the reinforcement area rather than merely increasing the steel strength, particularly in the case of sections with reduced diameter.

This analysis shows that stronger materials do not always lead proportional structural gains, especially when geometric constraints and internal force distributions are significant.



(a)



(b)

Figure I.10: Flexural strength, $M_{pl,Rd}$, *versus* concrete strength for various structural combinations for cross-section types (a) RC, and (b) CS.

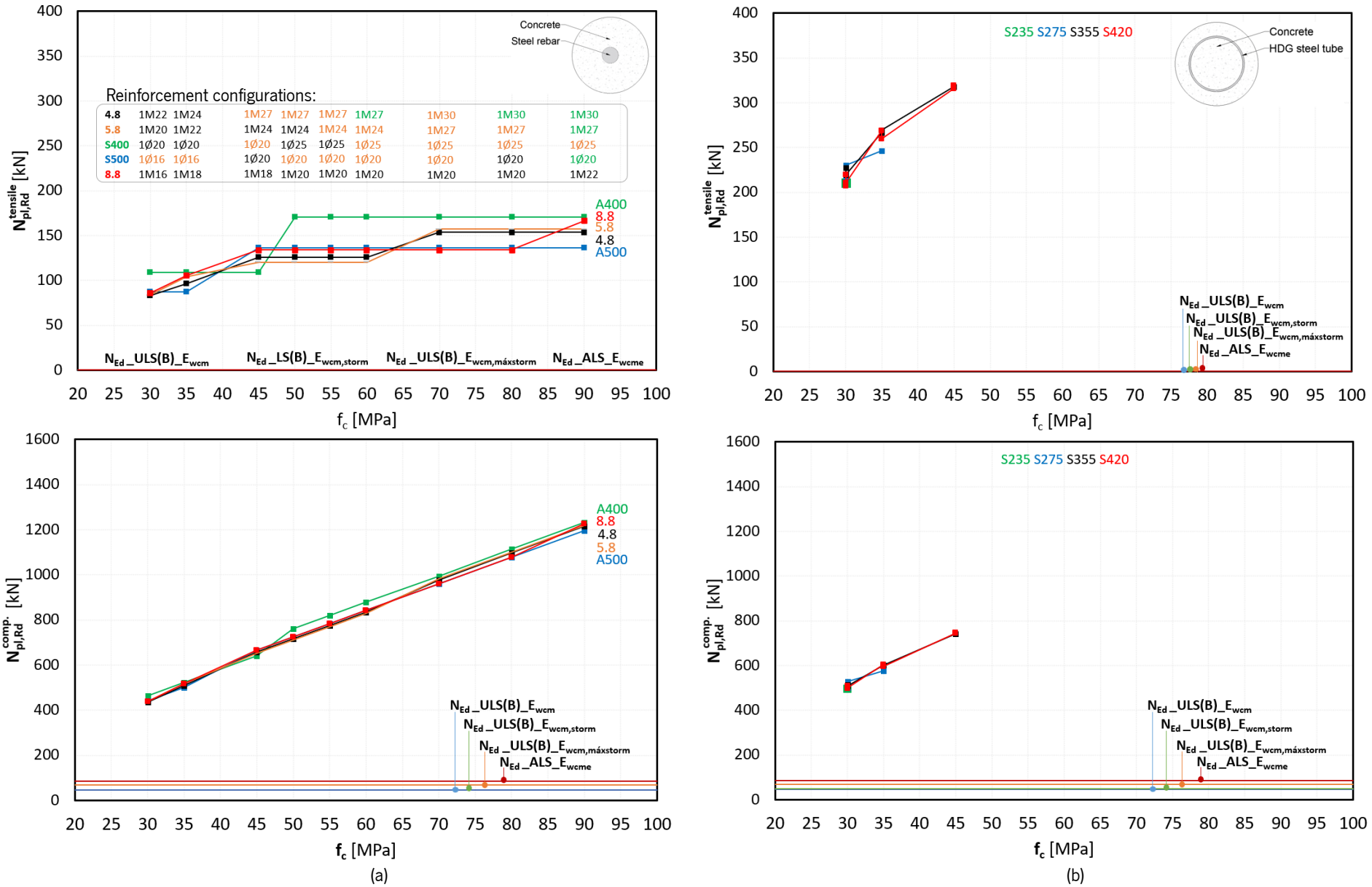


Figure I.11: Tensile (above) and compressive (below) axial strength, $N_{pl,Rd}$, *versus* concrete strength for cross-section types (a) RC and (b) CS.

❖ ***CS cross-section***

Tube diameters 60.3 mm, 76.1 mm, and 88.9 mm were selected to comply with the concrete cover and to offer a range of possible solutions for adapting the steel section to specific strength requirements. The minimum thickness of the tube wall was chosen to comply with the A_s, as well as to verify the requirement of a minimum contribution of steel (δ) for the non-perforated and perforated variants (two opposite holes with $D_{hole} = D_{ext}/2$). The minimum strength class for concrete was set to C30/37. In this case it was deemed unnecessary to expand the study to include high-strength concrete classes, as the combinations achieved with lower-strength concrete classes were found to be favourable. The minimum reinforcement was not a limitation when compared to the ULS analysis since $A_{s,min}$ (0.41 cm^2) was substantially lower when compared to $A_{s,pl}$.

In general, this structural solution easily achieved flexural strengths exceeding 12.81 kNm, ensuring compliance with the $M_{Rd}>M_{Ed}$ criterion, even for the lower-strength concretes and steel classes as shown in **Table I.8** and **Figure I.10**. As shown, for a given steel strength class and tube diameter, an increase in the concrete class resulted in a design that required a thicker tube, yielding an increase in $M_{pl,Rd}$. However, this increase was less relevant, since the material combinations analysed for lower-class concretes (e.g., C30/37) already met the safety criteria.

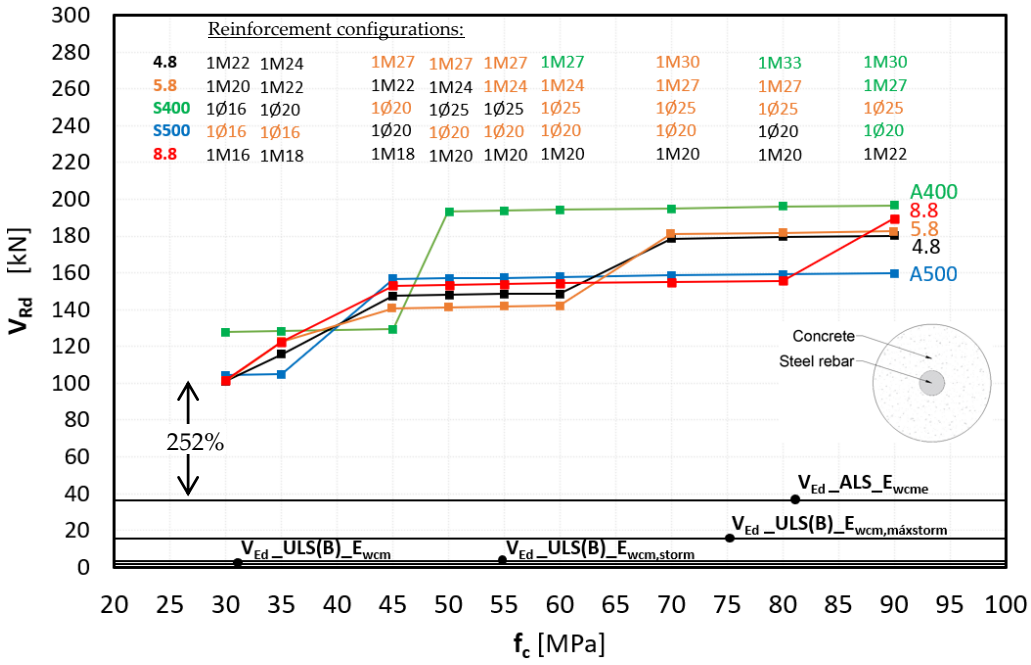
The geometric configuration that ensured the greatest nominal cover were associated to the tube with a diameter of 60.3 mm, which is important to prevent the corrosion caused by continuous exposure to seawater. However, in most cases, the adoption of this diameter and the maximum available thickness of 5 mm did not meet the required steel contribution ratio (δ). This criterion was only fulfilled when C30/37 concrete and S420 steel were combined. The parametric study showed that tube configurations with larger diameters (especially 88.9 mm) provided a greater number of efficient combinations, which is crucial for ensuring structural stability when the structure is subjected to significant horizontal forces. However, concrete cover in the connection region was small, and steel protection was reduced. Implementing additional protective measures or adjusting the section in this area should be considered.

The variety of structural solutions available for CS configuration resulted in a wider multitude of alternatives, withstanding the most extreme actions and ensuring optimal structural efficiency. A significant factor in this type of system is the D/t ratio, which directly impacts the $M_{pl,Rd}$. Additionally, the increase of f_c was linked to the need for increased t_w, thus ensuring harmonious integration of

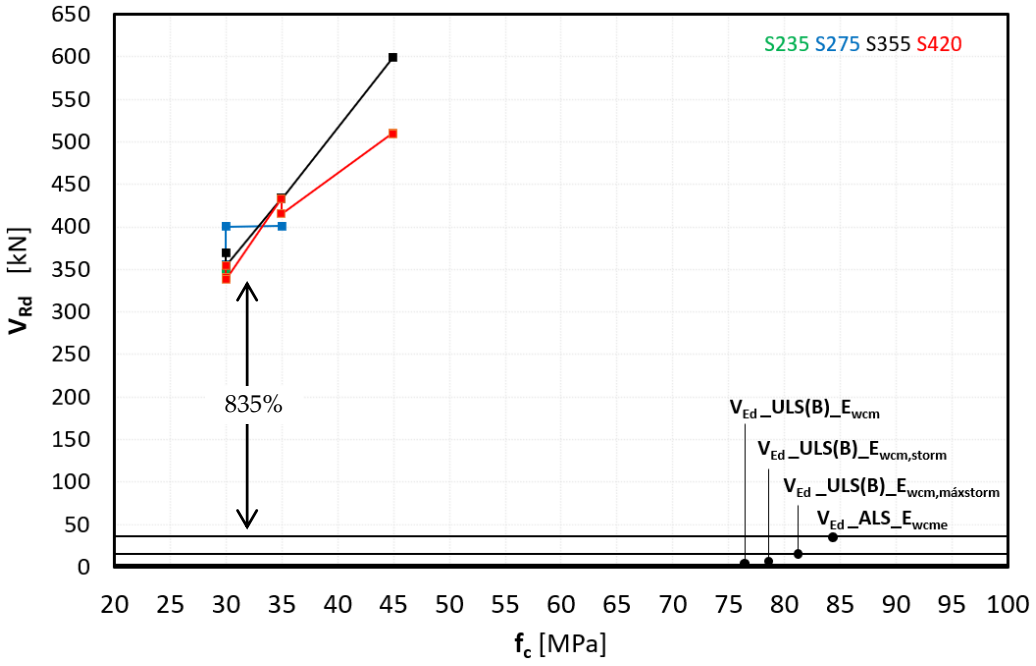
materials and sufficient sectional resilience. Nevertheless, to have the section classified as mixed concrete-steel according to NP-EN 1994-1-1 [67], for increased f_c the use of lower strength steels, such as S235, is not feasible.

The lowest $M_{pl,Rd}$ values were observed in sections comprising lower strength steels, such as S235, while the highest values were observed in sections comprising high-strength steels, such as S420. The highest steel classes (S355 and S420) resulted in the most efficient use of the full cross-section, providing greater strength and better efficiency in materials usage. Moreover, higher compressive strengths of concrete (f_c) resulted in higher normal plastic strengths ($N_{pl,Rd}$), with a nearly linear relationship (**Figure I.11**(b)).

Figure I.12 presents the shear strength of both structural systems obtained for the most critical scenarios. As observed, the shear strength clearly exceeded the applied shear stress, therefore ensuring shear safety.



(a)



(b)

Figure I.12: Shear strength (V_{Rd}) versus concrete strength for cross-section types (a) RC and (b) CS.

3.2. Optimisation of the RC cross-section

In the previous sections it has been shown that the majority of combinations designed to optimise the structural efficiency of the original geometry invariably result in a RC cross-section imbalance. This, in turn, compromises the structure's ability to withstand applied loads and increases the risk of obtaining failure modes where the reinforcement is in the elastic regime. In order to address this challenge, two optimisation approaches were explored, where the variation of the initial cross-section size was allowed. The first was aimed at minimising modifications to the cross-section, albeit with certain trade-offs. The second approach allowed the free resizing of the cross-section to meet the most demanding scenario. Considering the variable geometry of the cross-section, a minimum and maximum diameter will be defined for the smallest and largest cross-sections of the reef branch, respectively.

In **approach 1**, a diameter of 196.5 mm was considered to the cross-section, corresponding to the largest cross-section found the initial design. The $A_{s,min}$ was then calculated, and an initial solution was determined (1ØD). This resulted in a real steel area ($A_{s,real}$), which served as a reference for establishing a maximum limit for the section diameter (D_{max}). For the flexural analysis, which was critical when the smaller cross-section was considered, the minimum viable diameter (D_{min}) was calculated to ensure that $A_{s,pl}$ (flexural) matched $A_{s,real}$ (axial). For each configuration, the flexural ($M_{Pl,Rd}$) and axial ($N_{pl,Rd}$) strengths were obtained.

Figure I.13 presents the concrete and reinforcement combinations that meet the constraints of this approach for the RC cross-section. The upper graph illustrates the changes in minimum (D_{min}) and maximum (D_{max}) cross-sectional diameters correlated with different reinforcement configurations and concrete strengths. The lower graph displays the corresponding $M_{Pl,Rd}$ and M_{Ed}. The plotting colour-code in the graphs distinguished the steel class.

The results show that the alteration of the cross-section dimensions resulted in a significant improvement of $M_{pl,Rd}$. Most of the material combinations exceeded the requirements of the load combination ULS(B)_$E_{wcm,máxstorm}$ but none met the abnormal combination requirements, ALS_E_{wcme}.

A common trend across most combinations is the need to increase the diameter of the initial cross-section to optimize performance. The analysis identifies combinations that result in minimal changes (-7% to 7%) in the cross-sectional diameters, maintaining the original design's geometric effect. This reduction in material contributes to a more efficient and economical structural solution.

The maximum value found for D_{min} was 208 mm, occurring in the C35/45 + DIN 8.8 combination. This represents a 38.7% increase compared to the initial section (150 mm). On the other hand, the minimum value found for D_{min} was 140.19 mm, obtained for the C90/105 + 4.8 combination. D_{max} varied between 196.5 mm, for the C60/75 + DIN 5.8 combination, and 241.44 mm, for the C50/60 + S400 combination. The latter combination showed a 22.8% increase compared to the baseline design.

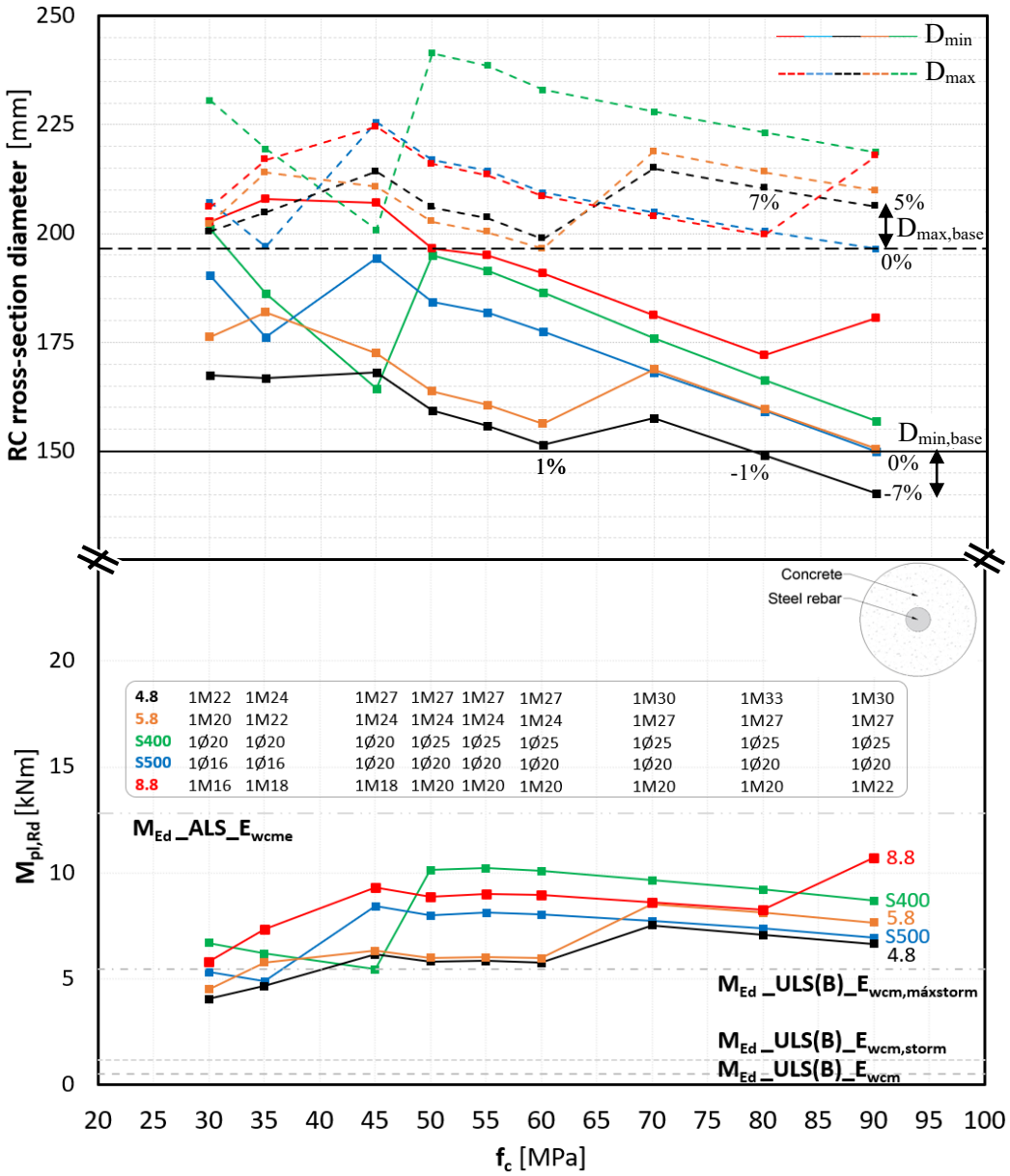


Figure I.13: Correlation between the minimum (D_{min}) and maximum (D_{max}) cross-section diameters and the flexural strength, $M_{pl,Rd}$, as a function of concrete compressive strength, f_c, and reinforcement configuration (approach 1).

In **approach 2**, a free optimisation was carried out to find the smallest cross-section and structural combination that guarantees the most challenging scenario.

For each combination of concrete and steel types, the reinforcement solution (1ØD) was imposed, and the minimum cross-section diameter (D_{min}) was found, ensuring that $A_{s,pl}$ matches $A_{s,real}$, while satisfying both axial and flexural strength criteria. Subsequently, the maximum diameter (D_{max}) was calculated considering that the minimum reinforcement area ($A_{s,min}$) determined by axial stresses did not exceed the real reinforcement area ($A_{s,real}$).

Figure I.14 illustrates the RC cross-section diameter obtained for each concrete strength class adopting the aforementioned procedure, showing the minimum and maximum section diameters and flexural strengths for different material combinations.

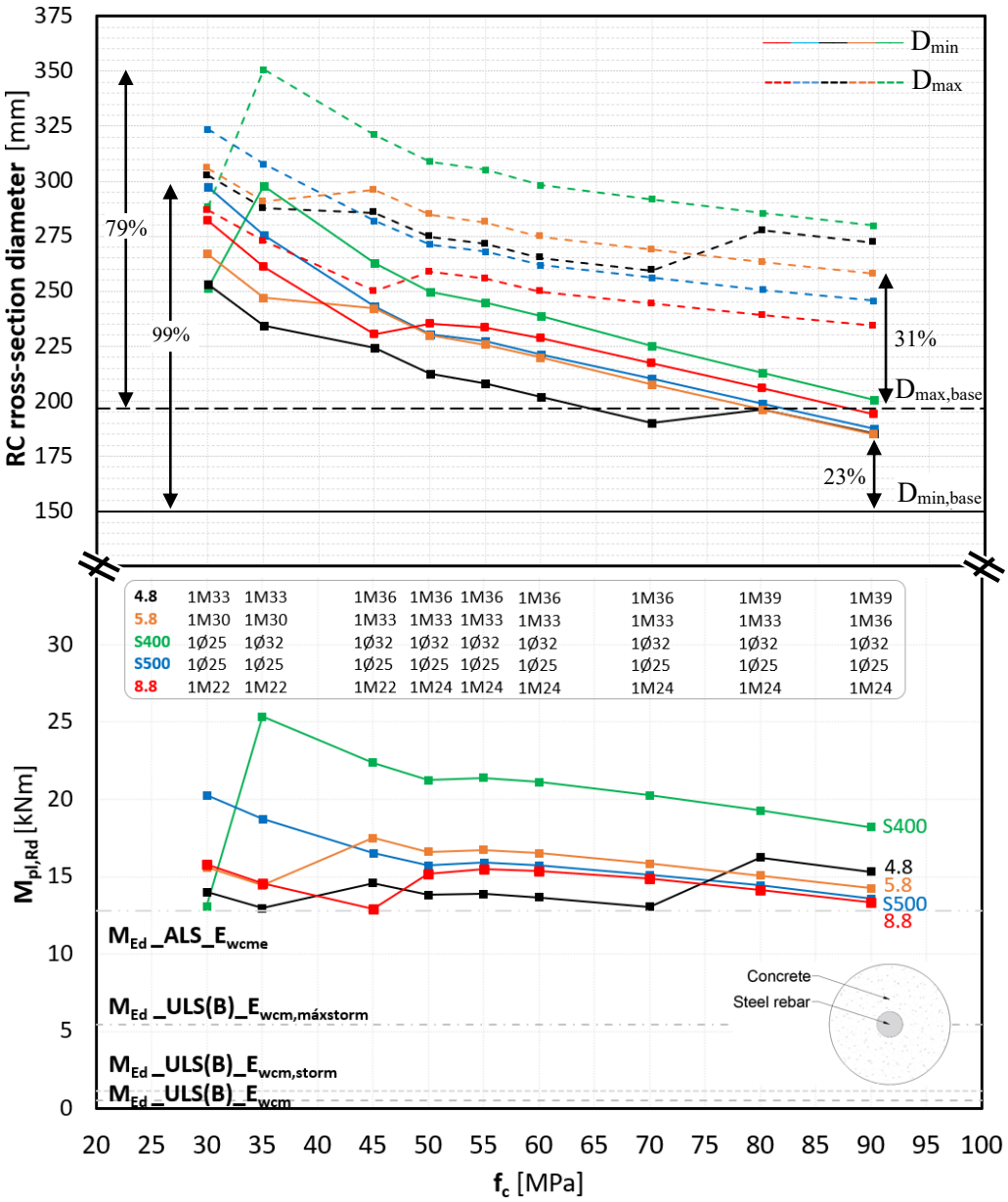


Figure I.14: Correlation between the minimum (D_{min}) and maximum (D_{max}) cross-section diameters and the flexural strength, $M_{pl,Rd}$, as a function of concrete compressive strength, f_c, and reinforcement configurations (approach 2).

The minimum diameter (D_{min}) required decreases with the increase in the concrete strength class. The influence of the concrete strength on the section size is significant, with increments ranging between 23% (for material combinations including high f_c) and 99% (for material combinations with lower f_c). The smallest admissible diameter was 185 mm, corresponding to the materials combination C90/105

+ DIN 5.8. The largest diameter was 298 mm for combination C35/45 + S400 and C30/37 + S500. Moreover, the obtained steel reinforcement in the new cross-section leads to a new maximum diameter for the element in order to comply with $A_{s,min}$ requirement, when subjected to a normal tensile stress. In this context, a minimum diameter of 234.32 mm (+19%) was found for the C90/105 + DIN 8.8 combination, and 350.76 mm (+79%) for the C35/45 + A400 combination. The combinations that best preserve the original dimensions, i.e., those requiring the smallest average diameter increase, correspond to higher concrete classes, namely C90/105 (S500, DIN 5.8, and 8.8), with average increases of 25%, 27%, and 24%, respectively.

3.3. RC Versus CS Cross-Sections

The RC unit was in general found to be easier to build and adapt, especially regarding rebar shaping. However, creating an effective and simple connection system between modules to ensure structural continuity can be challenging, as documented by [71]. While using a single rebar offers benefits such as better reinforcement cover and consistent mechanical strength across all loading directions, there are disadvantages that cannot be neglected. The small cross-sectional dimensions limit optimisation, especially under high flexural stresses, such as extreme storm or abnormal conditions. The close proximity of compression and tension forces reduces the torque arm and, consequently, flexural strength. Additionally, the original RC cross-section faces saturation of the steel, where increasing reinforcement does not significantly improve flexural strength. To avoid this, reinforcement ratios must be respected, steel distribution optimized, or section dimensions increased to ensure safety and ductility. In this context, using compression reinforcement in a polar array and a tubular profile with the appropriate diameter and thickness, as shown in **Figure I.15**, is advantageous.

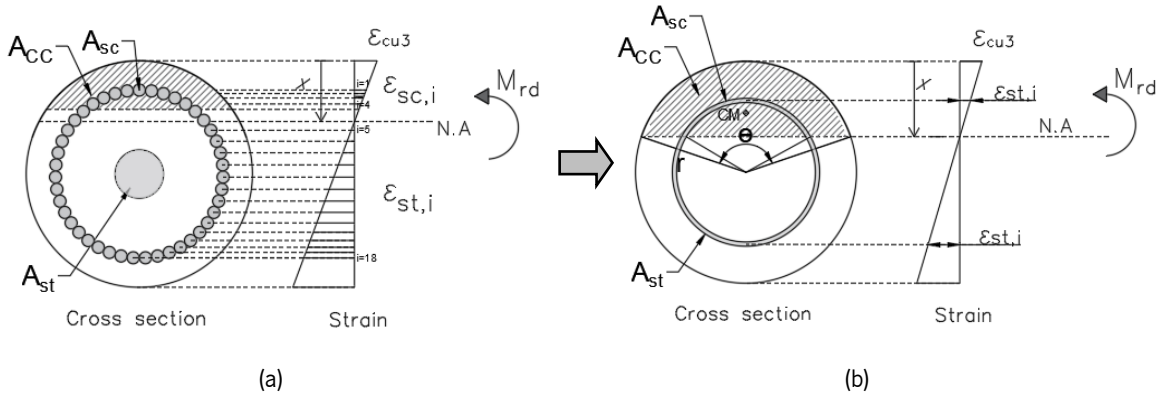


Figure I.15: (a) RC structure with polar array of compression steel reinforcement and (b) CS structure.

Although the CS solution is more complex to construct, it offers significant advantages in terms of structural behaviour due to its geometric flexibility and material strength. Additionally, the incorporation of bidirectional holes along the reinforcing tube improves material adherence and facilitates concrete filling, as suggested in [28]. The combination of materials allows for better optimisation of the cross-section, increasing structural efficiency, especially under bending conditions. This system also provides a practical solution for connecting modules as stated by [71]. However, the need for specific equipment to bend the steel tubes is a disadvantage in the construction process.

3.4. Cost-Effectiveness

Figure I.16 illustrates the correlation between the weight and cost of the reef module, based on the CS cross-section geometry and the optimized RC cross-section that ensures structural safety under the most demanding loading scenario. The analysis was conducted to assess the cost implications of strengthening the RC modules in comparison to the CS module, addressing concerns related to cost and construction feasibility. In the case of RC solution, only configurations resulting in a sectional increase of less than 35% in the critical area (D_{min}) were considered, and these were identified as the green zone in **Figure I.16**. In addition, the maximum dimension of the limb near the spherical zone was constrained to maintain the original geometric ratio between D_{max} and D_{min}, thereby ensuring consistency with the initial design morphology. This aimed to preserve the slenderness of the geometric form, as a bulkier structure could significantly alter the local hydrodynamic behaviour, potentially requiring further studies in that domain.

The analysis of the reinforced concrete (RC) and composite steel (CS) cross-sections reveals distinct trade-offs between weight, cost, and structural efficiency (**Figure I.16**). Most RC solutions have a weight of 160 kg, exceeding in 33% the initially desired 120 kg, which requires the use of medium equipment for handling the units. The cost of these RC solutions ranges from 18.7€ to 68.8€ per module. Conventional reinforcement results in lower costs, while the use of threaded bars significantly increases the unit cost. The RC combination with the best cost-construction feasibility ratio is the one using C90/105, S500, and 1Ø25, which has a weight of 159.8 kg and costs 18.7€ per unit. This solution offers an optimal balance between concrete usage and cost-efficiency, making it a more sustainable choice in terms of material optimisation.

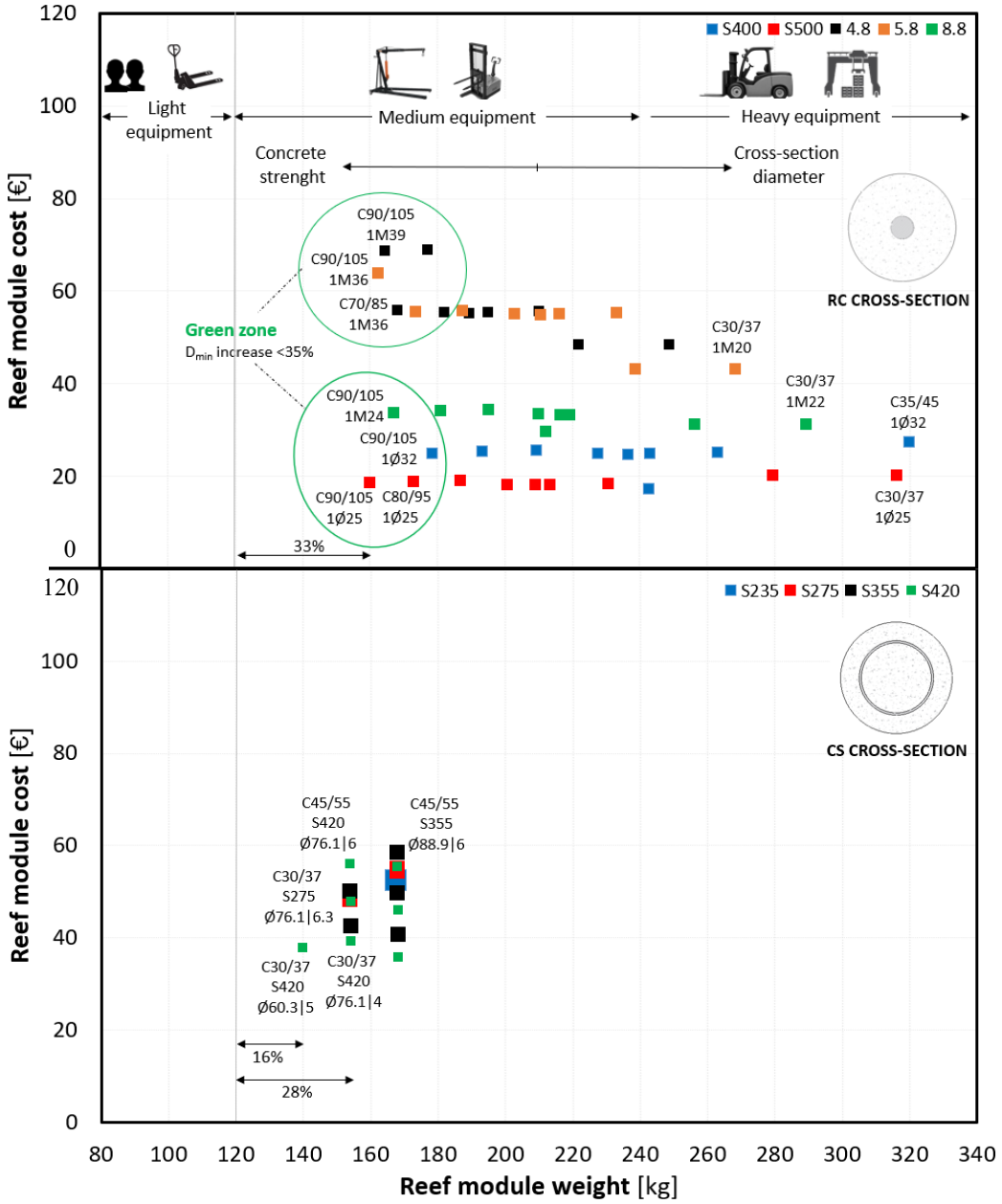


Figure I.16: Correlation between reef module weight and cost for CS and optimized RC configurations.

In comparison, CS solutions, which utilize a composite concrete and steel structure, present a lower increase in unit weight but come at a significantly higher cost (**Figure I.16**). The lowest cost for CS solutions is approximately double that of the RC unit. Several CS solutions, with weights around 150 kg, have costs ranging from 39.23€ per unit to 56€ per unit. A notable example is the combination of C30/37, S420, Ø76.1, and t_w 4, which weighs 154 kg and costs 39.23€ per unit. Whilst these CS solutions may exhibit a reduced weight relative to RC solutions, they necessitate a higher financial investment due to the materials employed. However, they can utilise lower-strength, more readily available concretes. The solution that results in the lowest possible weight for the CS cross-section uses the combination of C30/37, S420, Ø60.3, with a 5 mm thick wall, which achieves a weight of

139.72 kg (+16%) and costs 37.81€. However, it is important to note that this solution has a slightly lower $M_{pl,Rd}$ than required, meaning additional care is needed during application.

The cost-effectiveness analysis reveals that the optimized RC solution offers the most economical and structurally adequate configuration for the reef module. However, this comes at the expense of increased volumetry, which may alter local hydrodynamic behaviour and potentially impact biological colonization. If maintaining the original geometry is a priority—whether for ecological performance, fluid-structure interaction, or design constraints—the composite (CS) solution becomes the preferable alternative. Despite its higher unit cost, it provides a structurally efficient design while using lower-strength, cement-reduced concretes, contributing to lower carbon emissions and greater sustainability. Thus, the choice between RC and CS depends on project priorities: cost and simplicity favour RC, while environmental performance and geometric fidelity favour CS.

4 CONCLUSIONS

This work introduces the concept of different structural systems and presents a design methodology for developing and analysing modular and geometrically complex artificial reef structures. The study is based in a cross-sectional analytical approach based in the principles of structural mechanics supported by numerical analyses to evaluate actions and their effects on the structure.

By detailing the geometric design, structural conception, and relevant environmental actions, an approach was proposed for the evaluation of possible structural configurations. The analytical methodology, along with the parametric study, provided crucial insights into the performance and feasibility of different design configurations. In particular, and for the specific case of the cross-sections developed, the main findings were as follows:

- Reduced fixed diameters establish an important geometric limit for optimizing the cross-section of the RC type.
- Tensile strength emerged as the primary limiting factor, particularly in the RC type with variable cross-sections, where the minimum reinforcement was constrained by the larger section.
- Flexural strength was not a limiting factor for the CS structural solution, as the variety of structural combinations indicates sufficient robustness under flexural stresses.
- In terms of axial and flexural strength, the CS system provided significantly higher design strengths when compared to RC sections. Additionally, the CS structure did not require the use

of high-strength concrete, simplifying construction and potentially reducing costs and environmental impact.

- Shear strength was not a limiting factor for both structural solutions.
- Full optimisation of the cross-section to withstand the most demanding loading scenario would require a minimum size increase of 23%, making it bulky, heavier and less attractive.
- If cost is not a limiting factor and preserving the original geometry is a priority, the CS solution stands out for its high structural efficiency, reduced carbon footprint, and minimal impact on hydrodynamic and ecological performance.
- The methodology needs to include factors such as fatigue or long-term plastic deformation, which are crucial for structures exposed to high load cycles, like artificial reefs.

These findings emphasize the importance of a systematic engineering-driven analysis to the design and construction of artificial reefs, as it allows a comprehensive assessment of structural viability before advancing to prototyping and more complex numerical analyses. This stage enhances efficiency and ensures the most promising designs are pursued, optimizing resources and efforts. The design methodology has limitations due to the incomplete consideration of axial and flexural stresses interactions, which may affect performance and lead to an underestimation of the forces acting on the structure. This highlights the need for further analysis in future work to ensure robustness under real exposure conditions. Additionally, in situ monitoring strategies, such as wave height measurements, pressure sensors, strain gauges, accelerometers, or acoustic emission, need to be explored to assess real-time structural performance and detect signs of damage or degradation [72].

Given that marine structures are exposed to dynamic ocean loads over extended periods, future research will address the cumulative fatigue effects. This will require dedicated studies to characterize fatigue resistance as a function of the number of cycles and stress levels in critical sections, based either on the Model Code 90 framework or on experimental data. These investigations will build upon the structural insights developed in this initial study and aim to enhance the durability and reliability of the proposed modular reef system.

ACKNOWLEDGEMENTS

This work is financed by national funds through FCT – Foundation for Science and Technology, under grant agreement SFRH/BD/137220/2018 and SFRH/BD/129583/2017 attributed to the 1st and 3th

author, respectively. This work was partly financed by FCT/MCTES through national funds (PIDDAC) under the R&D Unit Institute for Sustainability and Innovation in Structural Engineering (ISISE), under reference UIDB/04029/2020 (doi.org/10.54499/UIDB/04029/2020), and under the Associate Laboratory Advanced Production and Intelligent Systems ARISE under reference LA/P/0112/2020. This work was partially funded by the research projects ‘‘NEXT-SEA: Next Generation Monitoring of Coastal Systems in a Scenario of Global Change”, NORTE-01-0145-FEDER-000032; “ASTRIIS – Atlantic Sustainability Through Remote and In-situ Integrated Solutions", POCI-01-0247-FEDER-046092, financed by FEDER funds; and “R2UTechnologies - modular systems”, PRR C644876810-00000019, funded by Plano de Recuperação e Resiliência.

REFERENCES

[1] Ng K, Phillips MR, Calado H, Borges P, Veloso-Gomes F. Seeking harmony in coastal development for small islands: Exploring multifunctional artificial reefs for São Miguel Island, the Azores. Appl Geogr 2013;44:99–111. https://doi.org/10.1016/j.apgeog.2013.07.013.

[2] López I, Tinoco H, Aragonés L, García-Barba J. The multifunctional artificial reef and its role in the defence of the Mediterranean coast. Sci Total Environ 2016;550:910–923. https://doi.org/10.1016/j.scitotenv.2016.01.180.

[3] Dafforn KA, Glasby TM, Airoldi L, Rivero NK, Mayer-Pinto M, Johnston EL, et al. Marine urbanization: An ecological framework for designing multifunctional artificial structures. Front Ecol Environ 2015;13:82–90. https://doi.org/10.1890/140050.

[4] Lee MO, Otake S, Kim JK. Transition of artificial reefs (ARs) research and its prospects. Ocean Coast Manag 2018;154:55–65. https://doi.org/10.1016/j.ocecoaman.2018.01.010.

[5] Pörtner HO, Roberts DC, Masson-Delmotte V, Zhai P, Tignor M, Poloczanska E, Mintenbeck K, et al. IPCC Special Report on the Ocean and Cryosphere in a Changing Climate. Geneva: Intergovernmental Panel on Climate Change; 2019.

[6] Bracho-Villavicencio C, Matthews-Cascon H, Rossi S. Artificial reefs around the world: A review of the state of the art and a meta-analysis of its effectiveness for the restoration of marine ecosystems. Environments 2023;10:121. https://doi.org/10.3390/environments10070121.

[7] Kim YC, editor. Handbook of Coastal and Ocean Engineering. Singapore: World Scientific; 2010.

[8] Ergin S, Soares CG. Sustainable Development and Innovations in Marine Technologies. Sustain. Dev. Innov. Mar. Technol. 2022, 9, 474. https://doi.org/10.1201/9781003358961.

[9] Carral L, Alvarez-Feal JC, Tarrío-Saavedra J. Social interest in developing a green modular artificial reef structure in concrete for the ecosystems of the Galician rías. J Clean Prod 2018;172:1881–1898. https://doi.org/10.1016/j.jclepro.2017.11.252.

[10] Ramos J, Lino PG, Himes-Cornell A, Santos MN. Local fishermen's perceptions of the usefulness of artificial reef ecosystem services in Portugal. PeerJ 2019;7. https://doi.org/10.7717/peerj.6206.

[11] Cruz F, Pereira E, Valente IB, Tiago M, Maslov D, Pinheiro M. Structural design of an innovative multifunctional artificial reef. Oceans 2018 MTS/IEEE Charleston, IEEE; 2018, p. 1–7. https://doi.org/10.1109/OCEANS.2018.8604587.

[12] Boakes Z, Hall AE, Ampou EE, Jones GCA, Suryaputra IGNA, Mahyuni LP, et al. Coral reef conservation in Bali in light of international best practice: A literature review. J Nat Conserv 2022;67:126190. https://doi.org/10.1016/j.jnc.2022.126190.

[13] Li Y, Ren N, Li X, Ou J. Hydrodynamic analysis of a novel modular floating structure system integrated with floating artificial reefs and wave energy converters. J Mar Sci Eng 2022;10:1091. https://doi.org/10.3390/jmse10081091.

[14] de Almeida JL. REEFS: An artificial reef for wave energy harnessing and shore protection—A new concept towards multipurpose sustainable solutions. Renew Energy 2017;114:817–829. https://doi.org/10.1016/j.renene.2017.07.076.

[15] Bohnsack JA, Sutherland DL. Artificial reef research: A review with recommendations for future priorities. Bull Mar Sci 1985;37:11–39.

[16] Kirkbride-Smith AE. The economic, social and conservation benefits of recreation-orientated artificial reefs [PhD thesis]. Hull, UK: University of Hull; 2014.

[17] Ten Voorde M. Contribution to the design of multi-functional artificial reefs [PhD thesis]. Coimbra, Portugal: University of Coimbra; 2009.

[18] Vieira BFV, Pinho JLS, Barros JAO, Antunes do Carmo JS. Hydrodynamics and morphodynamics performance assessment of three coastal protection structures. J Mar Sci Eng 2020;8:175. https://doi.org/10.3390/jmse8030175.

[19] Vieira, BFV. Engineering with Nature: An Innovative Solution for Coastal Erosion Protection. PhD Thesis in Civil Engineering. University of Minho. Guimarães, Portugal. https://hdl.handle.net/1822/79723, 2022.

[20] Fabi G, Spagnolo A, Bellan-Santini D, Çiçek BA, García JJG, Jensen AC, Kallianiotis A, Santos MN. Overview on artificial reefs in Europe. Braz J Oceanogr 2011;59:155–166.

[21] Silva J, Rosental I, Love M. Overview and trends of ecological and socioeconomic research on artificial reefs. Mar Environ Res 2019;145:81–96. https://doi.org/10.1016/j.marenvres.2019.01.010.

[22] Dini E, Nuzzolese M, Cafaro F, Lernia A, Gadaleta A, Sollecito F. Subsidence of artificial reefs with bamboo foundations on a soft seabed. Appl Sci 2024;14:720. https://doi.org/10.3390/app14020720.

[23] Wang F, Feng Y, Liu S, Chen Y, Ding J. Artificial fish reef site evaluation based on multi-source high-resolution acoustic images. J Mar Sci Eng 2025;13:309. https://doi.org/10.3390/jmse13020309.

[24] Broomfield JP. Galvanized steel reinforcement in concrete: A consultant's perspective. In: Corrosion of Steel in Concrete: Understanding, Investigation and Repair. Amsterdam: Elsevier Science; 2004. p. 188–208.

[25] Reeds KA, Smith JA, Suthers IM, Johnston EL. An ecological halo surrounding a large offshore artificial reef: Sediments, infauna, and fish foraging. Mar Environ Res 2018;141:30–38. https://doi.org/10.1016/j.marenvres.2018.07.011.

[26] Mendonça A, Neves MG, Mendonça A, Fortes CJ, Antunes do Carmo JS, Moura T. Hydrodynamics around an artificial surfing reef at Leirosa, Portugal. J Waterw Port Coast Ocean Eng 2012;138:226–235. https://doi.org/10.1061/(ASCE)WW.1943-5460.0000128.

[27] Soon C, Ng L, Chou LM. Artificial reefs as a reef restoration strategy in sediment-affected environments: Insights from long-term monitoring. Aquat Conserv Mar Freshw Ecosyst 2017;27:976–985. https://doi.org/10.1002/aqc.2755.

[28] Cruz F, Valente I, Almeida J, Neves A, Pereira E. Experimental characterization of bond between concrete and HDG steel tubes for mixed steel-concrete structures. Mater Struct 2024;57:89. https://doi.org/10.1617/s11527-024-02352-8.

[29] UNEP/MAP. Guidelines for the placement at sea of matter for purposes other than the mere disposal (construction of artificial reefs). Athens, Greece: UNEP/MAP; 2005.

[30] Fabi G, Scarcella G, Spagnolo A, Baines AS, Charbonnel E, Goutayer JJ, Haddad N, Altan L, Michel T. Practical guidelines for the use of artificial reefs in the Mediterranean and the Black Sea. Rome: Studies and Reviews, General Fisheries Commission for the Mediterranean; 2015.

[31] Great Barrier Reef Marine Park Authority. Guidelines for the management of artificial reefs in Great Barrier Reef Marine Park. Townsville, QLD, Australia: Great Barrier Reef Marine Park Authority; 2011.

[32] Florida Department of Environmental Protection. Guidelines and management practices for artificial reef siting, use, construction, and anchoring in Southeast Florida. Tallahassee, FL, USA: Florida Department of Environmental Protection; 2011.

[33] Vogler V. A new framework for artificial coral reef design. J Digit Landsc Archit 2022;7:524–537. https://doi.org/10.14627/537724050.

[34] Vogler V. A framework for artificial coral reef design: Integrating computational modelling and high precision monitoring strategies for artificial coral reefs—An ecosystem-aware approach [PhD thesis]. Weimar, Germany: Bauhaus-Universität Weimar; 2021.

[35] Carral L, Lamas MI, Barros JJC, López I, Carballo R. Proposed conceptual framework to design artificial reefs based on particular ecosystem ecology traits. Biology 2022;11:680. https://doi.org/10.3390/biology11050680.

[36] Carral L, Alvarez-Feal C, Rodríguez-Guerreiro MJ, Vargas A, Arean N, Carballo R. Methodology for positioning a group of green artificial reefs based on a database management system, applied in the estuary of Ares-Betanzos (NW Iberian Peninsula). J Clean Prod 2019;233:1047–1060. https://doi.org/10.1016/j.jclepro.2019.06.092.

[37] Antunes do Carmo JS, Neves MG, ten Voorde M. Designing a multifunctional artificial reef: Studies on the influence of parameters with most influence in the vertical plane. J Coast Conserv 2011;15:99–112. https://doi.org/10.1007/s11852-010-0124-1.

[38] Jackson A, Tomlinson R, Corbett B, Strauss D. Long-term performance of a submerged coastal control structure: A case study of the Narrowneck multifunctional artificial reef. Coast Eng Proc 2012;1:1–13.

[39] Charbonnel E, Serre C, Ruitton S, Harmelin JG, Jensen A. Effects of increased habitat complexity on fish assemblages associated with large artificial reef units (French Mediterranean coast). ICES J Mar Sci 2002;59–S213. https://doi.org/10.1006/jmsc.2002.1263.

[40] Pondella DJ, Claisse JT, Williams CM. Theory, practice, and design criteria for utilizing artificial reefs to increase production of marine fishes. Front Mar Sci 2022;9:983253. https://doi.org/10.3389/fmars.2022.983253.

[41] Stolk P, Markwell K, Jenkins JM. Artificial reefs as recreational scuba diving resources: A critical review of research. J Sustain Tour 2007;15:331–350.

[42] London Convention and Protocol, UNEP. London Convention and Protocol/UNEP guidelines for the placement of artificial reefs. London, UK: International Maritime Organization; 2009.

[43] OSPAR Commission. OSPAR guidelines on artificial reefs in relation to living marine resources. London, UK: OSPAR Commission; 2013.

[44] Maslov D, Johnson J, Pereira E, Duarte D, Miranda T, Lima M, Cruz F, Valente I, Pinheiro M. Experimental testing and CFD modelling for prototype design of innovative artificial reef structures. OCEANS 2019 MTS/IEEE Marseille; 2019. p. 1–7. https://doi.org/10.1109/OCEANSE.2019.8867383.

[45] Maslov D, Pereira E, Duarte D, Miranda T, Ferreira V, Tieppo M, Cruz F, Johnson J. Numerical analysis of the flow field and cross section design implications in a multifunctional artificial reef. Ocean Eng 2023;272:113817. https://doi.org/10.1016/j.oceaneng.2023.113817.

[46] Androulakis DN, Dounas CG, Banks AC, Magoulas AN, Margaris DP. An assessment of computational fluid dynamics as a tool to aid the design of the HCMR-Artificial-Reefs™ diving oasis in the Underwater Biotechnological Park of Crete. Sustainability 2020;12:4847. https://doi.org/10.3390/su12124847.

[47] Jiang Z, Liang Z, Zhu L, Guo Z, Tang Y. Effect of hole diameter of rotary-shaped artificial reef on flow field. Ocean Eng 2020;197:106917. https://doi.org/10.1016/j.oceaneng.2020.106917.

[48] Liu, Y.; Dong, G.; Zhao, Y. The Investigation of the Hydrodynamics of an Artificial Reef; INTECH Open Access Publisher: London, UK, 2007.

[49] Galdo MIL, Rodríguez-Guerreiro MJ, Vigo JL, Rodríguez IA, Lorenzo RV, Couce JCC, Couce LC. Definition of an artificial reef unit through hydrodynamic and structural (CFD and FEM) models: Application to the Ares-Betanzos estuary. J Mar Sci Eng 2022;10:230. https://doi.org/10.3390/jmse10020230.

[50] Xue D, Wang C, Huang T, Pan Y, Zhang N, Zhang L. Flow field effects and physical stability of pyramidal artificial reefs with different slope angles. Ocean Eng 2023;283:115059. https://doi.org/10.1016/j.oceaneng.2023.115059.

[51] Jang S, Jeong J, Lee S, Kim D. Identifying hydraulic characteristics related to fishery activities using numerical analysis and an automatic identification system of a fishing vessel. J Mar Sci Eng 2022;10:1619. https://doi.org/10.3390/jmse10111619.

[52] Shu A, Qin J, Rubinato M, Sun T, Wang M, Wang S, Wang L, Zhu J, Zhu F. An experimental investigation of turbulence features induced by typical artificial M-shaped unit reefs. Appl Sci 2021;11:1393. https://doi.org/10.3390/app11041393.

[53] Cruz F, Pereira E, Lima M, Johnson J, Duarte D, Valente IB, et al. Experimental characterization of the scour of innovative artificial reef prototypes using hydraulic flume and photogrammetry. OCEANS 2019 MTS/IEEE Marseille, IEEE; 2019, p. 1–10. https://doi.org/10.1109/OCEANSE.2019.8867581.

[54] Galdo L, Carballo R. Numerical and experimental analysis of the velocity field inside an artificial reef: Application to the Ares-Betanzos estuary. J Mar Sci Eng 2022;10:1827. https://doi.org/10.3390/jmse10121827.

[55] Kertorahardjo SP, Vincent H, Duta PH. Structure analysis on artificial reefs. Appl Mech Mater 2018;874:27–34. https://doi.org/10.4028/www.scientific.net/AMM.874.27.

[56] Jin L, Du L, Zhou Z, Bao X. Peak acceleration distribution on the surface of reef islands under the action of vertical ground motion. Appl Sci 2024;14:2515. https://doi.org/10.3390/app14062515.

[57] Maslov D, Cruz F, Pinheiro M, Miranda T, Valente IB, Ferreira V, Pereira E. Functional conception of biomimetic artificial reefs using parametric design and modular construction. J Mar Sci Eng 2024;12:1682. https://doi.org/10.3390/jmse12091682.

[58] Gomes AC, Pinho JLS, Granja HP. Caracterização da morfodinâmica de praias sob influência de cilindros geossintéticos: Caso de estudo da Praia de Ofir, Portugal. Rev Eletr Gestão Tecnol Ambient 2020;8:5. https://doi.org/10.9771/gesta.v8i1.36764.

[59] Loureiro E. Indicadores geomorfológicos e sedimentológicos na avaliação da tendência evolutiva da zona costeira (aplicação ao concelho de Esposende) [MSc thesis]. Braga, Portugal: Universidade do Minho; 2006.

[60] Mendes RPG. Energia das ondas: Desenvolvimento de uma tecnologia de geração (gerador tubular) [MSc thesis]. Covilhã, Portugal: Universidade da Beira Interior; 2011.

[61] Vieira BFV. Extreme wave value analysis under uncertainty of climate change scenarios off Iberian Peninsula coast. Ocean Eng 2021;229:109018. https://doi.org/10.1016/j.oceaneng.2021.109018.

[62] Sorensen RM. Basic Coastal Engineering. 3rd ed. Berlin/Heidelberg, Germany: Springer; 2006.

[63] American Petroleum Institute (API). API Recommended Practice 2A-WSD: Planning, Designing, and Constructing Fixed Offshore Platforms—Working Stress Design. 22nd ed. Washington, DC: American Petroleum Institute; 2014.

[64] Chakrabarti SK. Handbook of Offshore Engineering. Vol. I. Amsterdam: Elsevier; 2005.

[65] Det Norske Veritas (DNV). DNV-RP-C205: Environmental Conditions and Environmental Loads. Høvik, Norway: Det Norske Veritas; 2010.

[66] International Organization for Standardization (ISO). ISO 19903:2006. Petroleum and natural gas industries—Fixed steel offshore structures. Geneva, Switzerland: ISO; 2006.

[67] European Committee for Standardization (CEN). EN 1992-1-1: Eurocode 2: Design of concrete structures—Part 1-1: General rules and rules for buildings. Brussels, Belgium: CEN; 2004.

[68] European Committee for Standardization (CEN). EN 1990: Eurocode—Basis of structural design. Brussels, Belgium: CEN; 2013.

[69] European Committee for Standardization (CEN). NP EN 206-1: Concrete—Part 1: Specification, performance, production and conformity. Brussels, Belgium: CEN; 2005.

[70] European Committee for Standardization (CEN). EN 1994-1-1: Eurocode 4: Design of composite steel and concrete structures—Part 1-1: General rules and rules for buildings. Brussels, Belgium: CEN; 2004.

[71] Cruz F, Valente IB, Monteiro F, Maslov D, Miranda T, Pereira EB. Development and characterization of structural connections for modular artificial reefs. Ocean Eng 2025;320:120311. https://doi.org/10.1016/j.oceaneng.2025.120311.

[72] Maslov D, Pereira E, Miranda T, Valente M, Cruz F, Pinheiro M. Innovative monitoring strategies for multifunctional artificial reefs. OCEANS 2018 MTS/IEEE Charleston. 2018:1–8. https://doi.org/10.1109/OCEANS.2018.8604656.

APPENDIX A. RC Cross-Section

Table I.7: Parametric analysis of RC alternatives.

Materials (concrete + steel)	$A_{s,min}$			Tensile strength	Compressive strength		Flexural strength		M_{Ed}			
	$A_{s,req}$	$Ø_{eff}$	$A_{s,eff}$	$N_{pl,Rd}$	$N_{pl,Rd}$	$A_{s,satur}$	$M_{pl,Rd}$	$Ø_{satur}$	ULS(B)_ E_{wcm}	ULS(B)_ $E_{wcm,storm}$	ULS(B)_ $E_{wcm,máxstorm}$	ALS_ E_{wcme}
	[cm²]	[mm]	[cm²]	[kN]	[kN]	[cm²]	[kNm]	[mm]	[kNm]	[kNm]	[kNm]	[kNm]
C30/37 + S400	2.28	1Ø20	3.14	109.22	462.65	1.75	2.77	1Ø16	0.52	1.16	5.47	12.81
C30/37 + S500	1.81	1Ø16	2.01	87.39	440.82	1.25	2.60	1Ø16	0.52	1.16	5.47	12.81
C30/37+DIN 4.8	2.88	1M22	2.99	83.20	436.63	2.40	2.92	1M20	0.52	1.16	5.47	12.81
C30/37+DIN 5.8	2.28	1M20	2.41	83.83	437.26	1.75	2.77	1M18	0.52	1.16	5.47	12.81
C30/37+DIN 8.8	1.41	1M16	1.54	85.70	439.13	0.83	2.37	1M12	0.52	1.16	5.47	12.81
C35/45 + S400	2.52	1Ø20	3.14	109.22	521.55	2.01	3.23	1Ø16	0.52	1.16	5.47	12.81
C35/45 + S500	2.00	1Ø16	2.01	87.39	499.73	1.46	3.23	1Ø16	0.52	1.16	5.47	12.81
C35/45+DIN 4.8	3.19	1M24	3.46	96.28	508.61	2.80	3.40	1M22	0.52	1.16	5.47	12.81
C35/45+DIN 5.8	2.52	1M22	2.99	104.00	516.33	2.01	3.23	1M20	0.52	1.16	5.47	12.81
C35/45+DIN 8.8	1.55	1M18	1.89	105.18	517.52	0.98	2.76	1M14	0.52	1.16	5.47	12.81
C45/55 + S400	3.01	1Ø20	3.14	109.22	639.36	2.62	4.16	1Ø20	0.52	1.16	5.47	12.81
C45/55 + S500	2.39	1Ø20	3.14	136.52	666.67	1.87	3.89	1Ø16	0.52	1.16	5.47	12.81
C45/55+DIN 4.8	3.81	1M27	4.52	125.77	655.92	3.60	4.37	1M27	0.52	1.16	5.47	12.81
C45/55+DIN 5.8	3.01	1M24	3.46	120.35	650.49	2.62	4.16	1M22	0.52	1.16	5.47	12.81
C45/55+DIN 8.8	1.85	1M18	2.41	134.12	664.27	1.27	3.55	1M16	0.52	1.16	5.47	12.81
C50/60 + S400	3.26	1Ø25	4.91	170.78	759.83	2.91	4.62	1Ø20	0.52	1.16	5.47	12.81
C50/60 + S500	2.58	1Ø20	3.14	136.52	725.57	2.08	4.33	1Ø20	0.52	1.16	5.47	12.81
C50/60+DIN 4.8	4.12	1M27	4.52	125.77	714.82	4.00	4.86	1M27	0.52	1.16	5.47	12.81
C50/60+DIN 5.8	3.26	1M24	3.46	120.35	709.40	2.91	4.62	1M22	0.52	1.16	5.47	12.81
C50/60+DIN 8.8	2.00	1M20	2.41	134.12	723.17	1.41	3.95	1M16	0.52	1.16	5.47	12.81
C55/67 + S400	3.33	1Ø25	4.91	170.78	818.74	3.02	4.91	1Ø20	0.52	1.16	5.47	12.81

C55/67 + S500	2.64	1Ø20	3.14	136.52	784.48	2.14	4.56	1Ø20	0.52	1.16	5.47	12.81
C55/67+DIN 4.8	4.22	1M27	4.52	125.77	773.73	4.19	5.51	1M27	0.52	1.16	5.47	12.81
C55/67+DIN 5.8	3.33	1M24	3.46	120.35	768.30	3.02	4.91	1M24	0.52	1.16	5.47	12.81
C55/67+DIN 8.8	2.05	1M20	2.41	134.12	782.08	1.43	4.11	1Ø16	0.52	1.16	5.47	12.81
C60/75 + S400	3.49	1Ø25	4.91	170.78	877.64	3.18	5.25	1Ø25	0.52	1.16	5.47	12.81
C60/75 + S500	2.77	1Ø20	3.14	136.52	843.38	2.24	4.85	1Ø20	0.52	1.16	5.47	12.81
C60/75+DIN 4.8	4.42	1M27	4.52	125.77	832.63	4.43	5.59	1M27	0.52	1.16	5.47	12.81
C60/75+DIN 5.8	3.46	1M24	3.46	120.35	827.21	3.18	5.25	1M24	0.52	1.16	5.47	12.81
C60/75+DIN 8.8	2.15	1M20	2.41	134.12	840.98	1.49	4.35	1M16	0.52	1.16	5.47	12.81
C70/85 + S400	3.65	1Ø25	4.91	170.78	994.45	3.57	5.98	1Ø25	0.52	1.16	5.47	12.81
C70/85 + S500	2.89	1Ø20	3.14	136.52	961.19	2.50	5.47	1Ø20	0.52	1.16	5.47	12.81
C70/85+DIN 4.8	4.62	1M30	5.52	153.60	978.27	5.00	6.40	1M30	0.52	1.16	5.47	12.81
C70/85+DIN 5.8	3.65	1M27	4.52	157.22	981.89	3.57	5.98	1M27	0.52	1.16	5.47	12.81
C70/85+DIN 8.8	2.24	1M20	2.41	134.12	958.79	1.65	4.89	1M18	0.52	1.16	5.47	12.81
C80/95 + S400	3.81	1Ø25	4.91	170.78	1113.26	3.99	6.75	1Ø25	0.52	1.16	5.47	12.81
C80/95 + S500	3.02	1Ø20	3.14	136.52	1079.00	2.79	6.18	1Ø20	0.52	1.16	5.47	12.81
C80/95+DIN 4.8	4.82	1M30	5.52	153.60	1096.08	5.62	7.24	1M33	0.52	1.16	5.47	12.81
C80/95+DIN 5.8	3.81	1M27	4.52	157.22	1099.70	3.99	6.75	1M27	0.52	1.16	5.47	12.81
C80/95+DIN 8.8	2.34	1M20	2.41	134.12	1076.60	1.84	5.49	1M18	0.52	1.16	5.47	12.81
C90/105+ S400	3.97	1Ø25	4.91	170.78	1231.07	4.49	7.59	1Ø25	0.52	1.16	5.47	12.81
C90/105+ S500	3.14	1Ø20	3.14	136.52	1196.81	3.14	6.95	1Ø20	0.52	1.16	5.47	12.81
C90/105+DIN 4.8	5.02	1M30	5.52	153.60	1213.89	6.32	8.15	1M33	0.52	1.16	5.47	12.81
C90/105+DIN 5.8	3.97	1M27	4.52	157.22	1217.50	4.49	7.59	1M27	0.52	1.16	5.47	12.81
C90/105+DIN 8.8	2.44	1M22	2.99	166.40	1226.69	2.07	6.16	1M20	0.52	1.16	5.47	12.81

colour-code: $M_{Rd} > M_{Ed,ALS_Ewcme}$; $M_{Rd} < M_{Ed,ALS_Ewcme}$ | $A_{s,satur} \geq A_{s,eff}$; $Ø_{satur} \geq Ø_{eff}$ | $A_{s,satur} << A_{s,eff}$; $Ø_{eff} = Ø_{satur}$

APPENDIX B. CS Cross-Section

Table I.8: Parametric analysis of CS alternatives.

Materials (concrete + steel)	Steel tube		Steel ratio[1]	Compressive strength	Tensile strength	Flexural strength	M_{Ed}	Reef Unit Weight	Reef Unit Cost
	D_{ext}	t_w	$0.2<\delta<0.9$	$N_{pl,Rd,comp}$	$N_{pl,Rd,trac}$	M_{Rd}	ALS_E_{wcme}		
	[mm]	[mm]	[-]	[kN]	[kN]	[kN.m]	[kN.m]	[kg]	[€]
C30/37 S235	88.9	6	0.20	493.24	210.32	13.30	12.81	167.76	52.24
C30/37 S275	76.1	6.3	0.21	500.79	215.71	12.71	12.81	153.79	48.38
	88.9	6	0.23	529.04	230.19	14.77	12.81	167.76	54.47
C30/37 S355	76.1	5	0.22	515.20	227.30	13.28	12.81	153.93	42.55
	88.9	4	0.21	507.89	219.57	13.90	12.81	168.03	40.85
C30/37 S420	60.3	5	0.20	497.91	207.13	11.57	12.81	139.72	37.81
	76.1	4	0.21	509.91	219.73	13.09	12.81	154.05	39.23
	88.9	3.2	0.20	501.36	210.76	13.59	12.81	168.14	35.77
C35/45 S275	88.9	6	0.21	576.19	246.12	15.54	12.81	167.76	55.07
C35/45 S355	76.1	6	0.22	600.28	266.95	15.45	12.81	153.82	50.19
	88.9	5	0.22	600.78	269.61	16.66	12.81	167.89	49.76
C35/45 S420	76.1	5	0.22	604.80	268.92	15.64	12.81	153.93	47.91
	88.9	4	0.21	596.15	259.77	16.37	12.81	168.03	46.02
C45/55 S355	88.9	6	0.21	742.10	317.72	20.04	12.81	167.76	58.56
C45/55 S420	76.1	6	0.20	744.39	315.82	19.32	12.81	153.82	56.00
	88.9	5	0.21	747.33	318.98	20.24	12.81	167.89	55.51

[1] steel ratio for perforated section; colour-code: $M_{Rd} > M_{Ed,ALS_Ewcme}$; $M_{Rd} \approx M_{Ed,ALS_Ewcme}$; $M_{Rd} < M_{Ed,ALS_Ewcme}$

PAPER II

DEVELOPMENT AND CHARACTERIZATION OF STRUCTURAL CONNECTIONS FOR MODULAR ARTIFICIAL REEFS

REFERENCE: Cruz F, Valente IB, Monteiro F, Maslov D, Miranda T, Pereira EB. Development and characterization of structural connections for modular artificial reefs. Ocean Eng 2025;320:120311. https://doi.org/10.1016/j.oceaneng.2025.120311. Impact factor: 4.6

ABSTRACT: Artificial reefs and other marine structures are becoming relevant components of coastal engineering interventions and ecosystems restoration plans. Their construction and deployment, as well as durability, are challenging, and the available engineering solutions are limited and lack validation. Giving the need to address the increasing complexity of artificial reef designs and their durability requirements, this work focuses on the development and characterization of structural connections for modular artificial reef marine structures, with application to a case study. An extensive experimental program was conducted to assess their feasibility and performance, including the materials characterization and structural response. The materials and systems developed included hot-dip galvanized steel, engineered cementitious composites and knitted textiles in different layouts and combinations. The findings contribute to advancing the design of durable and efficient connections

for modular artificial reef structures, as well as for other similar emerging structural applications of submerged ocean constructions.

KEYWORDS: Modular artificial reefs; Connectors design; Concrete; Steel; Engineered cementitious composite; Epoxy; Experimental characterization.

1 INTRODUCTION

In recent years, there has been an increasing demand for marine infrastructures and technology, to take advantage of maritime resources [1,2]. Aiming at fostering the growing world population and promoting the sustainability of human activities, several progresses have been made, ranging from modular floating structures for electrical production, up to the development of artificial reefs with singular (AR) or multifunctional purposes (MFAR) for ecosystem management [3]. AR are man-made structures placed in aquatic environments to mimic some characteristics of natural reefs. They are used globally for multiple purposes, including protecting habitats, restoring ecosystems, enhancing biodiversity, fisheries and aquaculture, costal protection, enhancing surf conditions, prevent bottom trawling and promoting recreational activities [4,5]. Complex forms with irregular surfaces, cavities and rough materials enhance attachment opportunities for marine organisms [6]. AR have evolved from basic structures, such as sunken ships and singular units, to modular artificial reefs (MAR) designs with complex three-dimensional arrangements that facilitate marine colonization [7]. In fact, the development of scalable MAR adds complexity, requiring a connection system capable of integrating modules into a 3D arrangement, while also ensuring durability and good structural performance [8,9]. In this context, numerous connector designs have been developed, accompanied by research across various connector systems. **Figure II.1** illustrates examples of connections for MAR and other marine structures. Clamagirand (2001) describes connections for MAR as being achieved using metal tie-rods, tubes, or lock rings, facilitating the assembly of hexagonal plate and wall modules. Steel hinge and flexible male-female connectors have been developed for Coral Reef Arks (2024) to form geodesic dome structures and have been explored for modular floating structures [11,12]. Flexible steel hinged connections denoted high costs and damage in harsh conditions due to fatigue and durability issues [13]. Ding et al. (2020) investigated a chain-type floating platform with several semi-submersible modules connected by stainless-steel hinge connectors, highlighting the importance of connector strength and modular integration for scalable sea applications. The construction of ReefSystems (2024) was based on the use of concrete connectors with male-female

interlocking. However, these connectors lacked the robustness required for their intended purpose. MARS involved the use of ceramic clamping systems and stainless-steel bolts [15]. A linear steel anchor system was been used in ocean brick system [16]. An et al., (2023) concluded that bolted flange-plate connections are particularly valued for their ability to accommodate loads, facilitate assembly and disassembly when necessary. Experimental studies indicate that pre-tensioning bolts increase flexural capacity and energy absorption significantly than snug-tightened connections [18]. Wang et al., (2021) emphasized the need for preload management as temperature variations significantly impact bolt loads in subsea connections. Jiang, Tan, Wang, et al., (2021) presented a critical review on the research and development in connector systems for very large modular floating structures. It has been demonstrated that rigid connector systems provide stability with minimal motion and are well-suited for easy internal transport. However, they generate large connection forces, have complex configurations, and are difficult to decouple. In contrast, flexible connectors between modules can significantly reduce bending moments and simplify decoupling but may lead to larger motion amplitudes and complex system [11,21].

For design purposes, stable and suitable materials with a minimum durability of 30 years might be selected to build the modules and the connections [4,22]. It is essential to use inert materials that avoid environmental pollution from leaching, weathering, or harmful biological. In general, concrete is a versatile and cost-effective solution, being one of the preferred materials to be used as colonizing substrate activity [4,23]. Its brittle failure is compensated by adding ductile reinforcements, such as hot-dip galvanized or marine steel grade. These have the advantage of a high resistance to corrosion [24–26]. Other options include Cementitious Composites due to their self-healing capabilities and Fibre Reinforced Polymers (shorter lifespans) [27].

Extensive research studies have been conducted on connections for modular floating structures exploring alternative solutions along with their advantages and challenges [20]. However, limited research has been reported on the design and structural behaviour of connections for modular AR. To meet the demands of AR technology, this work aims to develop and characterize structural connections for modular MFAR structures with complex geometries and assess their construction feasibility. For that, an experimental programme was planned, based on bending tests and materials characterization, to study the construction and structural behaviour of the proposed connections. The design of the connections, the experimental programme, the test methods, as well as the main conclusions and insights are presented in detail.

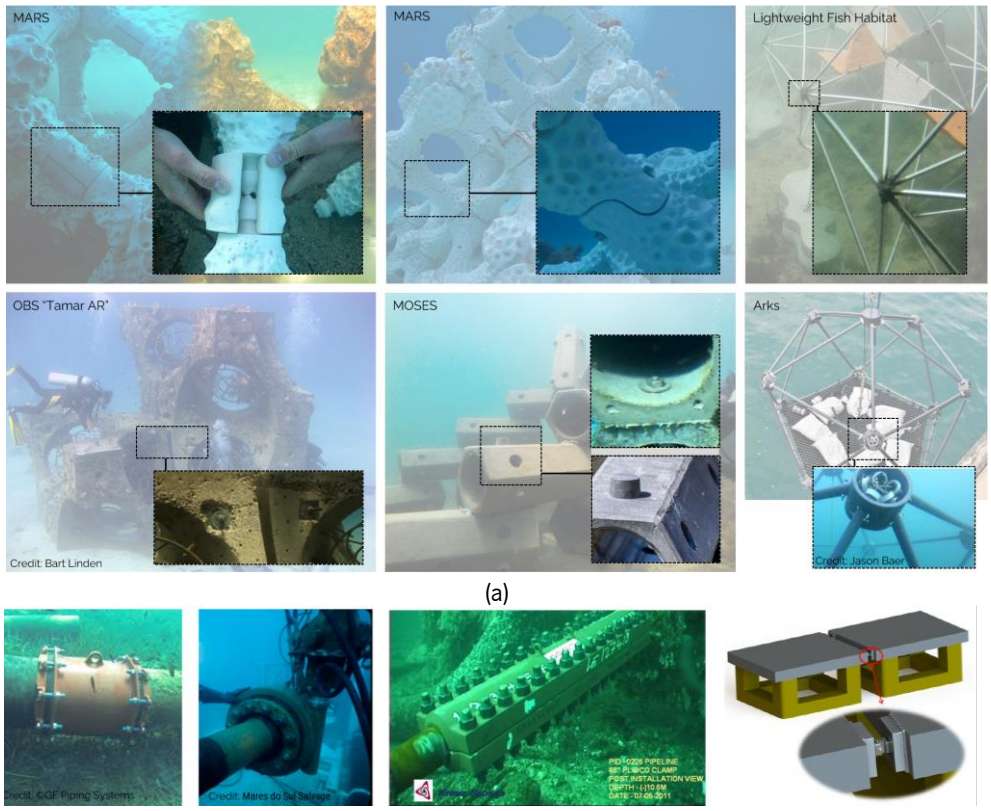
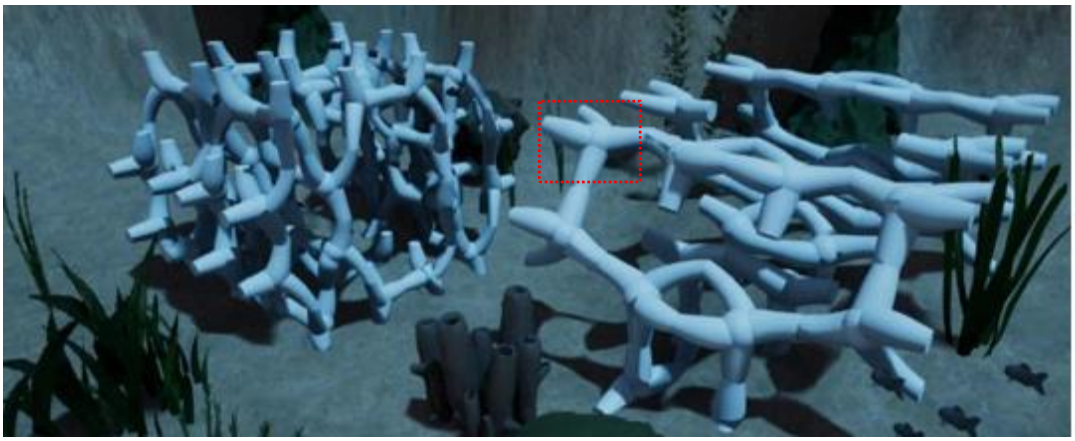


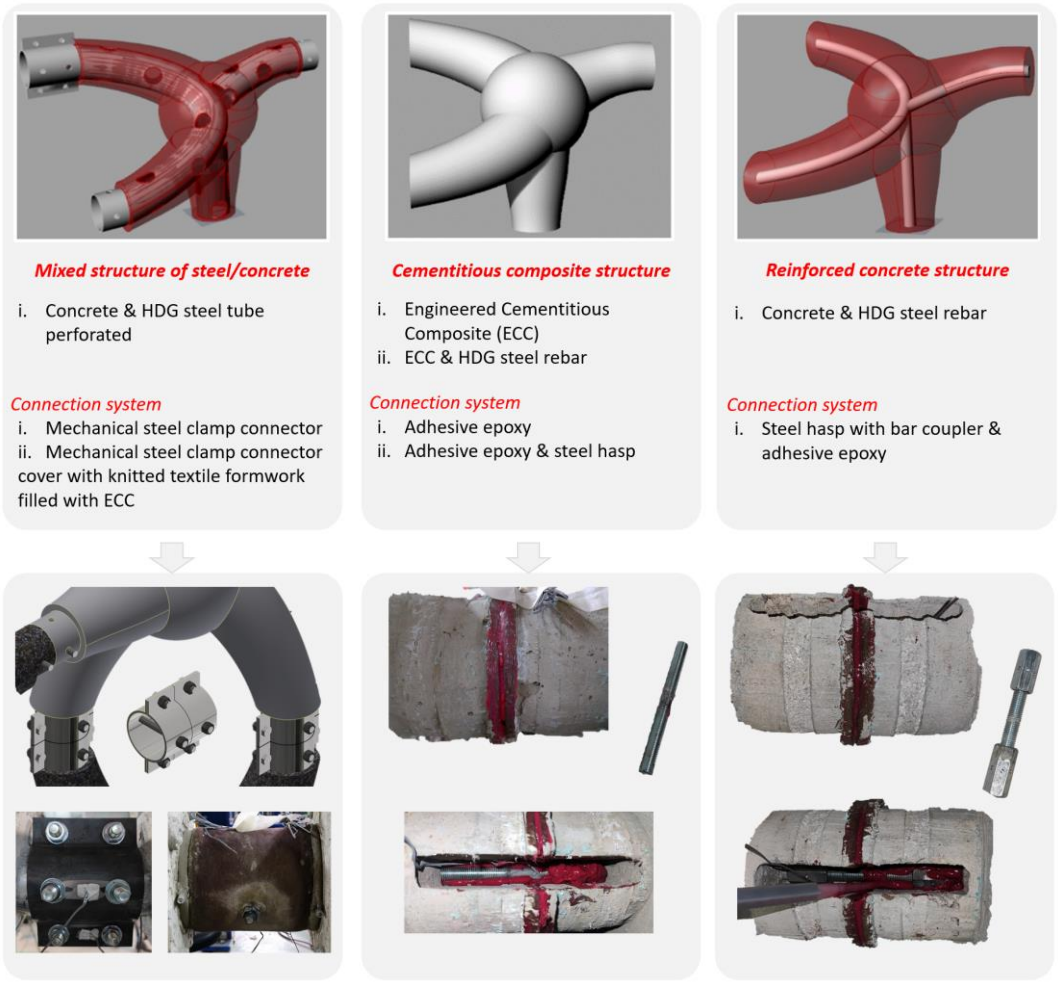
Figure II.1: Examples of connections for (a) ARs and (b) other marine structures [11,14–16,28–30].

2 DESIGN OF THE CONNECTION SYSTEMS

As part of the development of a modular MFAR, different connections were designed, tailored to the structural combinations deemed most suitable for the reef unit [7,27,32,33]. The structural systems considered for the development of the connectors were based on three main options: (i) a composite structure, CS, made of concrete and a galvanized steel tube aligned with the geometric centroid of each limb (**Figure II.2**(a)); (ii) an engineered cementitious composite, ECC, (**Figure II.2**(b)) and (iii) a reinforced concrete structure, RC, with a central rebar along each limb of the unit (**Figure II.2**(c)).

The geometries of the connection systems were defined considering the reef module geometry, the structural system, the lightweight and feasibility of underwater assembly and replacement of damaged modules by two divers, as well as the ability to maintain electrical conductivity between modules for self-healing mechanisms. The configuration of the connections for the reef units are presented in **Figure II.3** and **Figure II.4**, and the main aspects are subsequently discussed.





(a) (b) (c)

Figure II.2: Modular MFAR geometry with structural combinations and related connection systems: (a) CS, (b) ECC and (c) RC modules.

2.1. CS connections

The CS structure features a metallic bolted connector that utilizes the internal reinforcement extending from each limb of the reef unit (**Figure II.3**(a)). It consists of two steel half clamps embracing a holed tube connection, with each half having two tabs and a central body in contact with the tube. Six bolts secure the connection - two in each tab and two in the central zone for tightening. The possibility to cover the steel part with KTPs filled with an ECC adds an additional layer of protection against corrosion (**Figure II.3**(b)). The connector's design allows for effective load transfer between adjacent units, while its small size and weight facilitate easy on-site installation and disassembly for module replacement. on the bolts and tube were analysed to ensure that the connection withstands marine loads, considering various steel classes and bolt dimensions.

The metallic clamp connector is 130 mm long, 168 mm high, and 5 mm thick, with 80% contact with the tube's surface for better grip and positioning. The bolts are spaced 30 mm from the edge and 70 mm apart, allowing for positional adjustments and rotation. The 35 mm in height tabs were minimized to keep the connection compact. The design of the metallic connector was based on EN 1993-1-8 (2011). Numerical studies were also performed regarding the metallic connector [35].

2.2. RC connections

The RC unit connection (**Figure II.2**(c)) introduces a hybrid connection with mechanical and chemical components (**Figure II.4**(a)). HIT RE 500 V4 epoxy is combined with a steel hasp that connects to the unit's steel reinforcement via a bar coupler. After the mechanical coupling, the notch is filled with epoxy. Although the adhesive provides uniform load transfer of compressive and tensile forces between the units, the positioning of the steel elements in the centre of the cross section may reduce the efficiency of the steel hasp in transferring tensile stress for bending. The reduced working space at the notch for attaching the bar coupler, particularly in the case of poorly made moulds and errors in the positioning of the reinforcement, is a critical aspect to be considered. Additionally, the need for adhesive and its associated cost represent further drawbacks. The connection design was guided by rebar dimensions and available span, aiming to match the metallic connection's span to maintain equivalent axial, transverse, and moment efforts. The design of the fastenings-adhesive connector was based on EN 1992-4 (2018). A parametric study was conducted using Hilti® PROFIS Engineering software to estimate effective anchorage lengths by analysing tensile and shear stresses, various

loading conditions, materials strengths and concrete conditions. It led to a hasp with a length of 202 mm and a diameter of 16 mm (**Figure II.4**(a)).

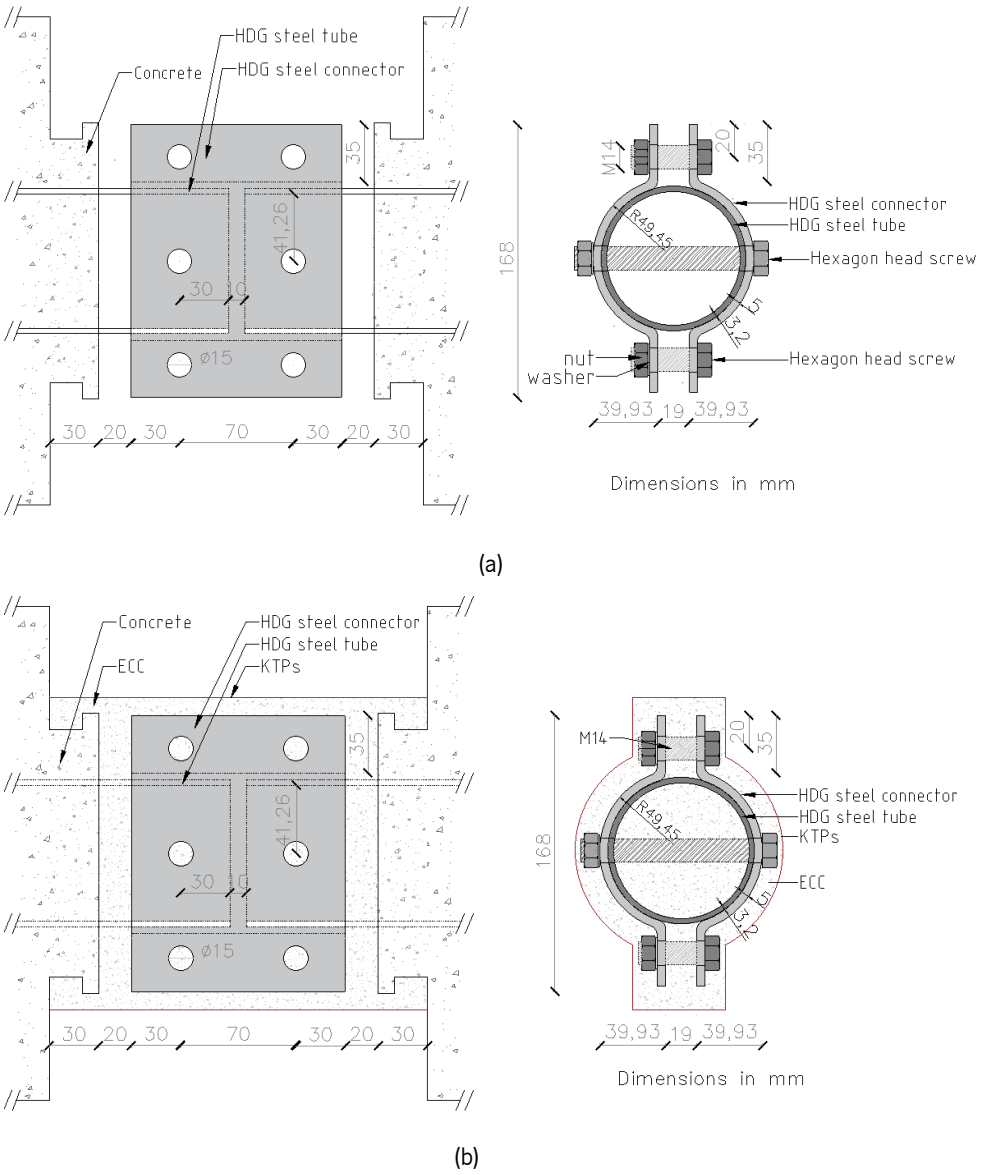


Figure II.3: Geometric design of (a) CS connection with steel clamp (SC) and (b) CS connection with SC covered with an KTP filled with ECC (b) (side and cross section views).

2.3. ECC connections

The connection of the ECC module (**Figure II.2**(b)) can be achieved through a hybrid or an adhesive connection. The hybrid connection adapts the design used in RC for ECC, given that there is no continuity between the internal reinforcement elements (PVA fibres) and the connection mechanism (**Figure II.4**(b)). In the adhesive connection, the bond is made exclusively with epoxy resin applied between the ends of the reef unit (**Figure II.4**(c)).

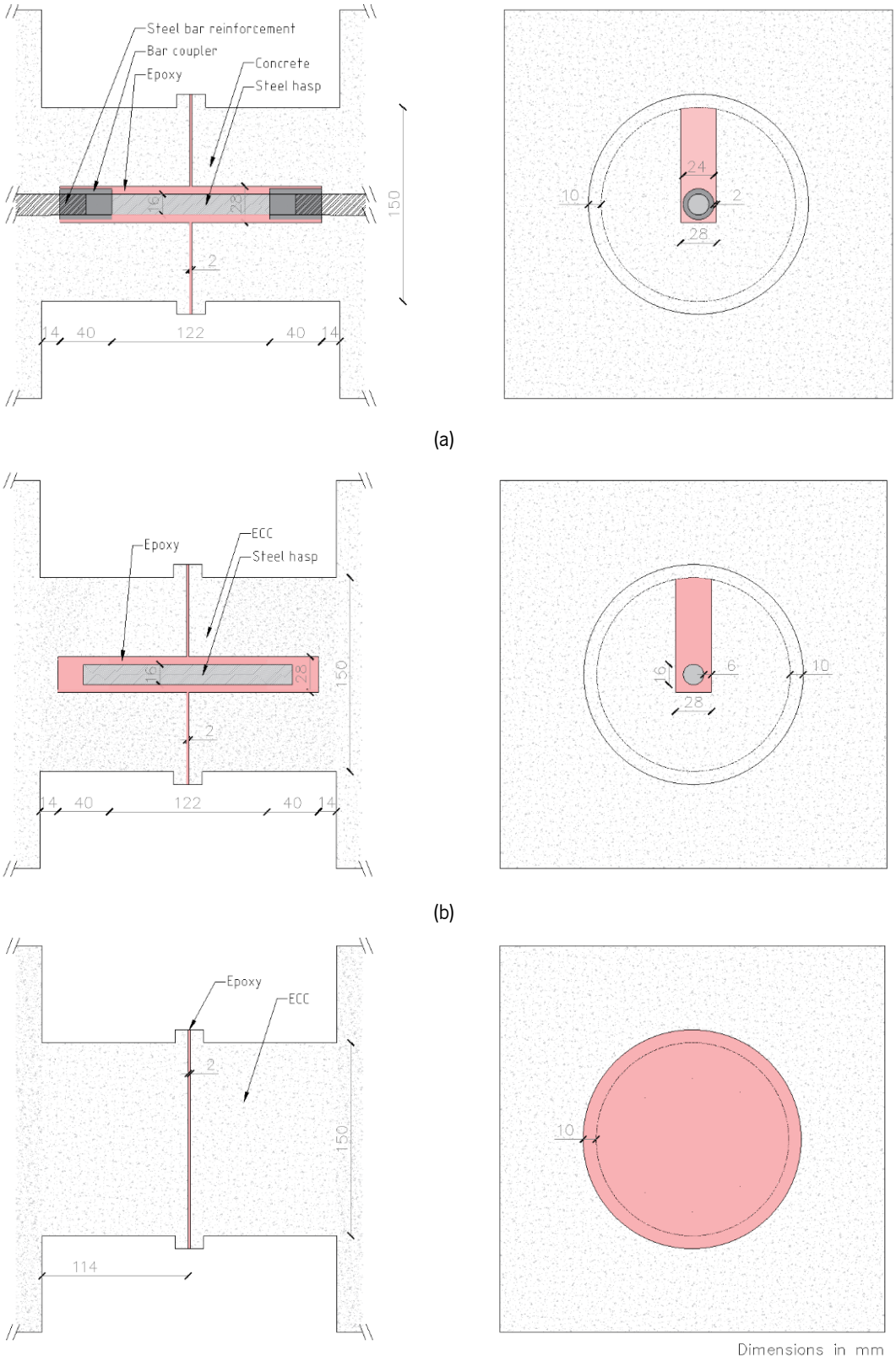


Figure II.4: Geometric design of (a) RC connection with epoxy, steel hasp & bar couplers, (b) ECC connections with epoxy & steel hasp (b) ECC adhesive connection (side and cross section views).

3 EXPERIMENTAL PROGRAM

An experimental program with bending tests was carried out to study the structural behaviour of the connection systems between modules. The main goal was to better understand the general functioning of the connections and evaluate their (i) construction; (ii) stiffness; (iii) strength; (iv) ductility and (v) failure modes.

In general, the programme was composed of 8 tests divided into three categories according to the structural configuration of the reef unit. The specimens made with concrete were cast in one batch, while the ECC units were concreted in another batch. These were distributed by groups according to structural systems and its type of connection. The test specimen's nomenclature is divided according to the structural system (CS – composite structure, RC – reinforced concrete structure, ECC – engineered cementitious composite); followed by the connection elements involved (SC – steel clamp, H_{steel} – steel hasp, Bc - bar coupler, E - epoxy, KTP_sECC – knitted textile preform filled with ECC); and the loading direction (0°, 90° or 180°), as shown in **Table II.1** Some of these were tested in two different loading directions: 0° and 90° in the case of composite structure, and 0° and 180° in the case of RC and ECC structure.

Table II.1: Experimental program.

Structural system for the reef unit	Connector components & type	Loading direction	Designation	Number of specimens
Steel-concrete composite structure	Steel clamp (mechanical)	0°	CS_SC_0°	1
		90°	CS_SC_90°	1
	Steel clamp protected with knitted textile filled with ECC (mechanical)	0°	CS_SC&KTP_sECC_0°	1
		90°	CS_SC&KTP_sECC_90°	1
Reinforced concrete structure	Steel hasp, bar coupler & epoxy (mixed)	0°	RC_$H_{steel}B_cE$_0°	1
		180°	RC_$H_{steel}B_cE$_180°	1
Engineered Cementitious Composites (ECC)	Epoxy (chemical)	-	ECC_E	1
	Epoxy & steel hasp (mixed)	0°	ECC_$H_{steel}E$_0°	1

3.1. Materials

Concrete and ECC were chosen for its high ductility and ability to adapt easily to complex geometries, its suitability for structures exposed to marine environments, and its good bio-receptivity. Epoxy "HIT RE 500 V4" was chosen for its versatility and its application in reinforcement systems, including underwater applications [116] . Galvanized steel was selected due to its excellent cost-durability balance. The KTP cotton is biodegradable and offers flexibility to be adapted to different shapes.

The type of concrete was selected to meet the requirements of structures exposed to marine environments, in accordance with EN 1992-1-1 (2004) and NP EN 206-1 (2005) with the following characteristics: strength class C30/37, maximum aggregate size of 14 mm, cement class CEM II 42.5, exposure class XC4 (P), chloride content class of 0.40, and consistency class S3. The ECC composition, developed by Pereira, (2012), is shown in **Table II.2**. The steel is available in the forms of (i) HDG steel tube, S195T, Ø88.9 mm × 3.2 mm, Zn 400 g/m²; (ii) threaded rod DIN 976-1, 4.8 Zn, M16; (iii) hexagon union DIN 6334 - M14 Zn (bar couplers); (iv) steel clamp connector with the curved surface produced by bending steel plate with 5mm; (v) hex head bolt M14×130 DIN 931 - 8.8 Zn; (vi) hexagon nut M14, DIN 934, class 8 Zn; and (vii) washer plate, DIN 125-A, M14 Zn. Two KTPs made from cotton, each with dimensions of 230 mm by 170 mm, were produced using the Shima Seiki® SSR112 14GG electronic knitting machine and designed with Apex4® CAD software. The KTPs feature three chambers: one at each end to form the tightening block, and a central one that embraces the steel part.

Table II.2: Materials composition for 1 dm³ of ECC.

Cement II AL 42,5R	Fly ash	Silica sand[1]	Limestone filler	Water	SP Sika 5501	VMA	PVA fibres[2]
461.01 g	691.51 g	161.35 g	161.35 g	341.20 g	26.10 g	1.21 g	26.00 g

[1] silica sand under 500 μm maximum aggregate size. [2] fibres with 8 mm length and 40 μm diameter.

3.2. Construction of the connections

The specimens for experimental testing are composed of two concrete cubes with 300×300×300 mm³ joined with a connection detail. Depending on the case, the specimens were reinforced with HDG steel tubes or steel rebars. No internal reinforcement was used in the units fabricated with ECC. **Figure II.5** presents some images related to the specimen's preparation. The HDG steel tubes were cleaned using a mild alkaline solution (10:1 water to cleaner) following the American Galvanizers Association

(2023) guidelines to remove organic contaminants without damaging the galvanized coating. A foam piece, matching the reinforcement diameter, was placed at the base to help position and prevent misalignment. Furthermore, an extruded polystyrene piece was constructed and attached to the wooden mould to form the nose and rim. For reinforcement with rebar, an additional foam piece was fabricated to create the negative space for inserting the hasp and epoxy at the top. Then, the tube and rebars were centred, and four bolts were used to adjust their position and vertical alignment before and during concreting. For the ECC specimens, only the complementary XPS mould with an adjusted height was needed. The specimens were concreted outdoors, vibrated for consolidation, and manually finished on the top surface. After casting, the specimens were sprayed with water and covered with plastic film. After demoulding, the specimens were placed in the climatic chamber at 55±2% of relative humidity (RH) and 20±1°C of temperature (T), until testing.

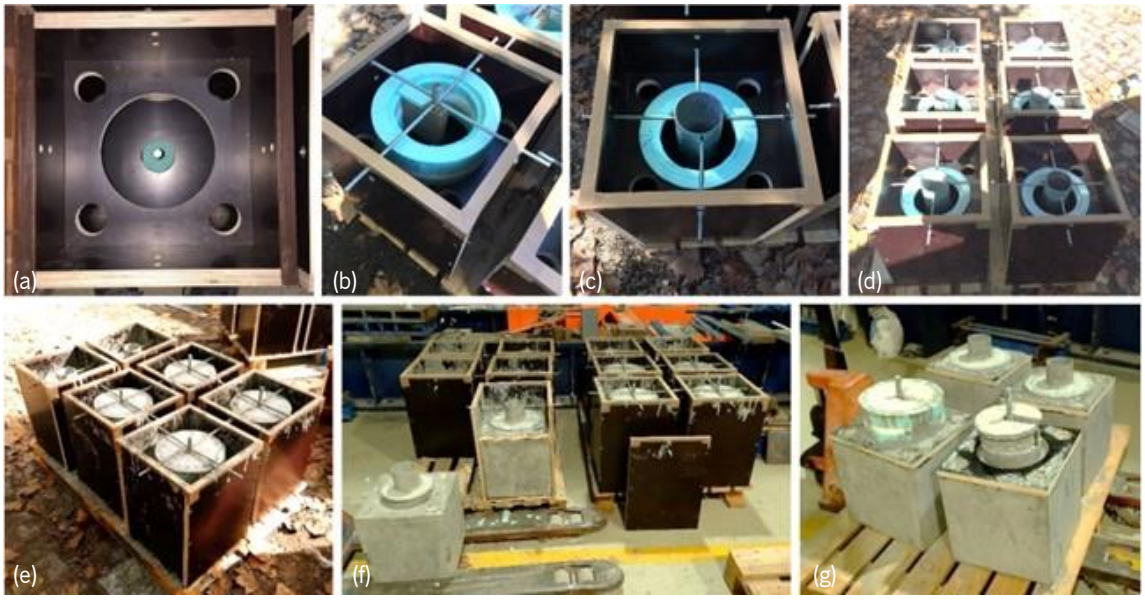


Figure II.5: Specimens preparation for concreting: (a-d) wood mould and detail of the foam piece at the base and top for connection, (d) concreting phase and (e, f) demould and storage.

Figure II.6 shows the preparation of the connection specimens for the mechanical test. In the case of CS specimens, the ends of the tubes were marked and holed. During this task, the block was supported to minimize the risk of vibration and consequent damage to the connection zone. Subsequently, some areas of the tube and the clamp were polished and cleaned for the application of unidirectional electrical strain gauges (SG). Afterwards, the connection was assembled, and the bolts were pre-tensioned with 70 kN.m and 90 kN.m torque, respectively. In the RC_H_{steel} and ECC_H_{steel} specimens, the application of SG to the steel hasps followed the same protocol. To assemble the

connection, the epoxy was first applied to the concrete tops of each module, and the two blocks were joined together. Then, the hasp with the bar couplers was inserted in the notch and connected to the end of the hub's reinforcing rod. Finally, the epoxy was applied evenly. The procedure to assemble the specimens in ECC followed a similar pattern, despite slight adaptations, as it did not involve the use of the bar coupler and one of the specimens only contemplated the top-top epoxy adhesive.

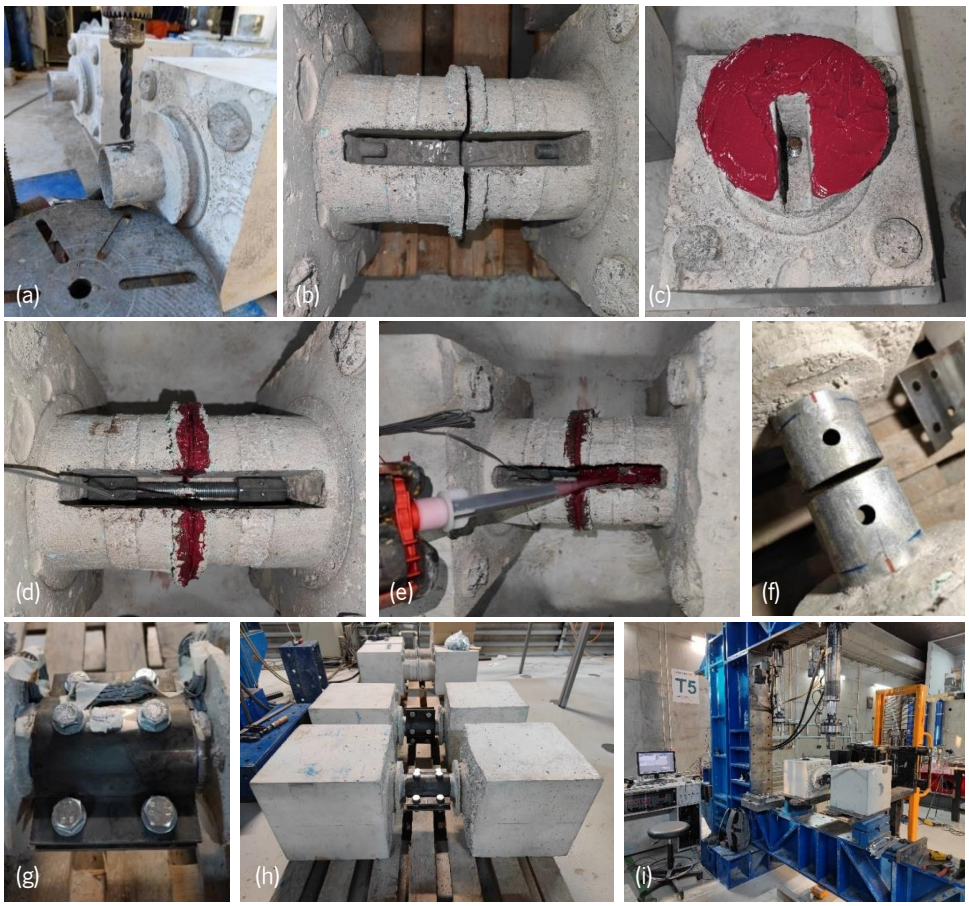


Figure II.6: Connections preparation: (a) tube hole, (b-e) epoxy, steel hasp and rebar couplers application, (f, g) SC assembly and SG application, (h, i) general view and frame positioning.

The KTPsECC were prepared by first placing the sleeve and passing the SG cables through the textile mesh. Then, the end and central chambers were filled with ECC using a cartridge gun connected to a valve attached to the KTP (**Figure II.7**).

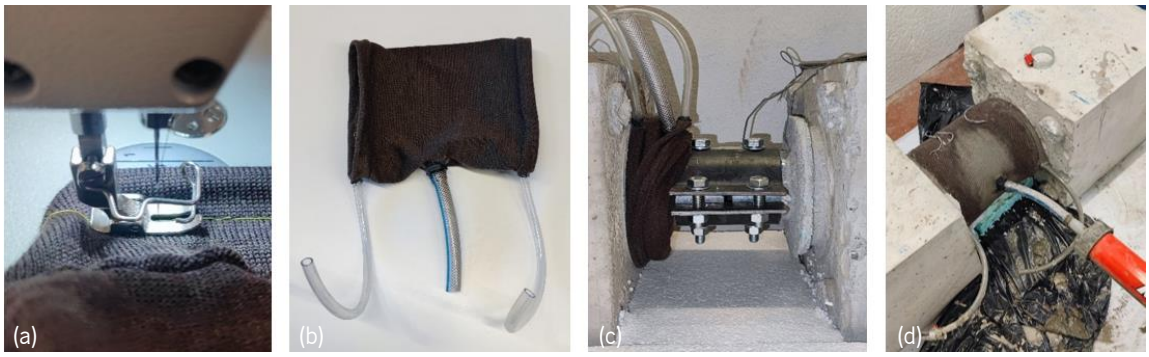


Figure II.7: Preparation and application of the KPTs connection sleeve: (a) sleeve production, (b) KPT with valves attached, (c) KTPs system placement and (d) ECC injection.

3.3. Testing methods

3.3.1. Materials tests

The fresh properties of concrete were accessed using the Abrams cone, following the European Standard EN 12350-2 (2009). The workability and consistency of ECC was assessed according to BS EN 12350-8 [42]. The compressive behaviour of concrete and ECC in the hardened state were evaluated by means of uniaxial compression tests in cylinders with 150 mm diameter and 300 mm in height and 60 mm of diameter and 120 mm height, respectively. Young's modulus (E_{cm}) and compressive strength (f_{cm}) were assessed according to EN 12390-13 (2013) and EN 12390-3 (2009), respectively. The tensile behaviour of the ECC mixture was characterized by direct tensile test in dogbone specimens, following the recommendations from Japan Society of Civil Engineers [45]. **Table II.3** presents the average results obtained for concrete and ECC characterization.

Table II.3: Results of the mechanical properties of the concrete and ECC.

	Slump class	E_{cm} [GPa]	f_{cm} [MPa]	E_{tm} [GPa]	f_{tm} [MPa]	$\varepsilon_{m,ftm}$ [%]
Concrete	S3	28.72 (5.42%)	40.15 (3.06%)	-	3.03[3] (3.05%)	<0.1[4]
ECC	280[1]/173[2]	9.04 (6.36%)	30.27 (2.36%)	20.08 (13.31%)	2.28 (9.60%)	1.33 (22.5%)

[1]mini slump without fibres; [2]mini slump with fibres; [3]estimated according to Eurocode 2; [4]typical reference value

The tests of the steel samples were performed in accordance with the ISO 6892-1 (2009). The applied tensile load and the strain in the longitudinal axis at middle height were measured. **Table II.4** presents the obtained average results as well as the technical specifications. The steel showed typical behaviour and material rupture. The epoxy, according to the technical specifications, has a compressive strength

of 82.7 MPa, a compressive modulus of 2.6 MPa, a tensile strength of 49.3 MPa at 7 days, an elongation at break of 1.1%, a tensile modulus of elasticity of 1.49 GPa and a bond strength around 10.8 MPa (2 days cure) or 11.7 MPa (14 days cure). The experimental characterization of 160 × 40 × 40 mm^3 specimens using a three-point bending test configuration indicated an average Young's modulus of 0.97 GPa, an extension of 4.00% and a flexural tensile strength of 39.3 MPa. In the compression test an average value of 106.6 MPa was obtained [47].

Table II.4: Characteristics of steel according to technical document or experimental testing.

	Grade [-]	E [GPa]	R_{eH} [MPa]	$R_{t,0.2}$ [MPa]	R_m [MPa]	A [%]	Zn coat [g/m²]
HDG steel tube							
Technical specifications	S195T	-	>289	-	>402	>29	402
Experimental characterization	-	199 [5%]	-	430.96 [3%]	508.7 [1%]	14.99 [%]	-
Steel from "SC" connector							
Technical specifications	S235	210	235	-	>360	>26	-
Threaded rod DIN 976-1 – 4.8 Zn (M16mm)							
Technical specifications	4.8	210	320	-	400	-	35.34

E is the modulus of elasticity; R_{eH} is the upper yield strength if yield phenomenon is present and $R_{t,0.2}$ is the upper yield strength if yield phenomenon is not present; R_m is the tensile strength and A is the elongation.

3.3.2. Connections tests

Figure II.8 illustrates the experimental setup used to characterize the mechanical behaviour of the connections under four-point flexural test. The specimens consisted of two connected concrete blocks, which were simply supported with a span of 730 mm and a pure bending region of 330 mm around the connection area (**Figure II.8**a).

These dimensions replicate the connection regions of the envisaged real size MFAR. The vertical load was applied using a servo-controlled actuator under displacement control, ensuring quasi-static monotonic loading up to failure. **Figure II.8** also details the instrumentation: three linear variable differential transducers (LVDT1 to LVDT3) with a stroke of ±25 mm to record the deflection along the longitudinal axis of the connection; four LVTD (1 to 4) with a stroke of ±50 mm to monitor the horizontal displacements between the internal faces of the concrete prisms; two LVDT with a stroke of ±2.5 mm to measure the slip between the steel tube or rebar and the concrete at the base; and 1 to 4 strain gauges (SG1 to SG4) type FLA-2-3-3L were used to measure strain in the steel elements.

The test protocol started with five loading cycles of 5 kN, followed by a monotonic test at an imposed deformation rate of 10 μm/s up to 10 mm of displacement. The following loading cycle was imposed at the displacement rate of 20 μm/s, until failure was reached. The applied force (F) was monitored using a load cell with a maximum measuring capacity of 100 kN (±0.12 kN; 0.05% F.S.).

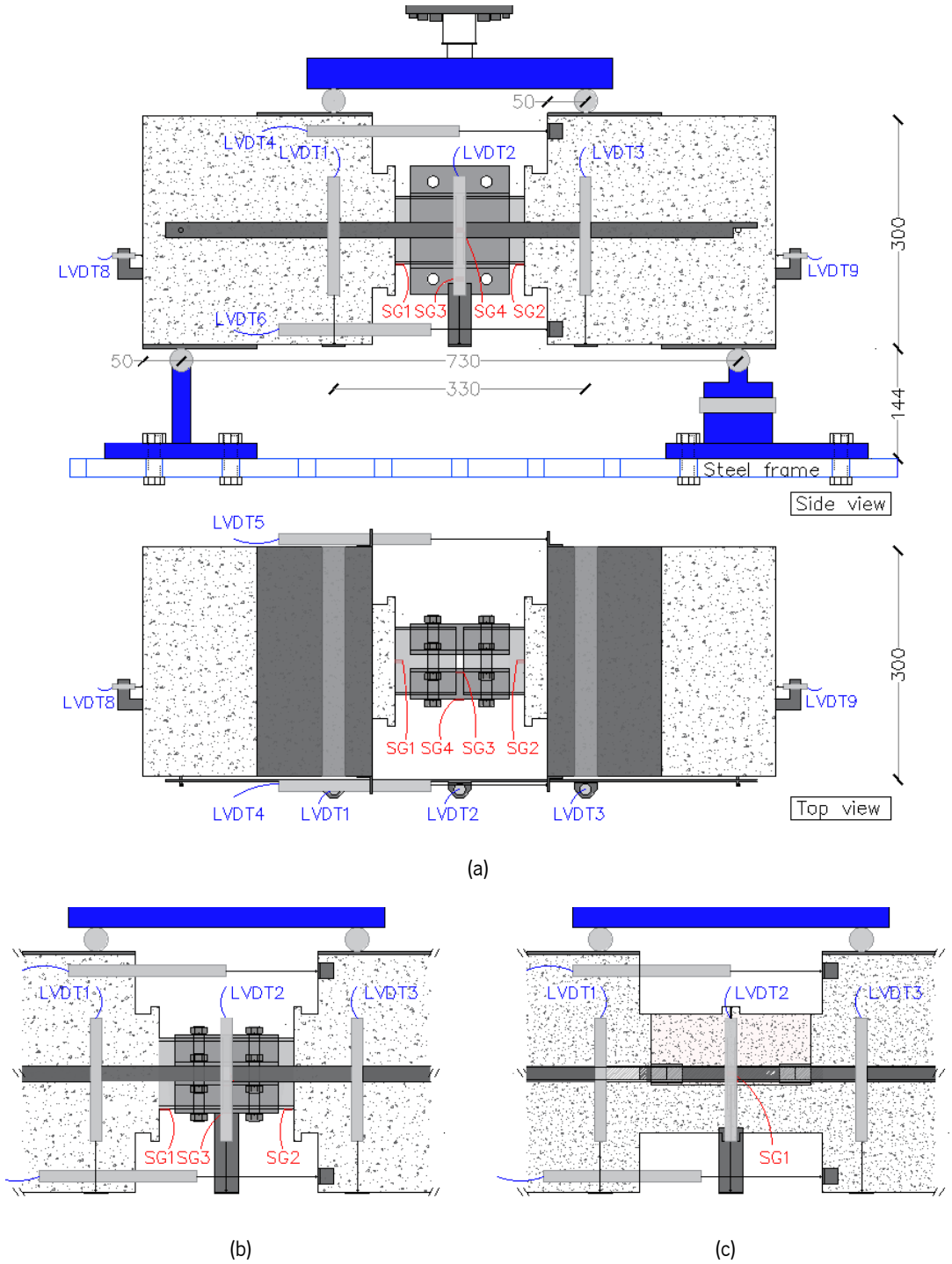


Figure II.8: General test configuration and instrumentation: (a) CS_90° (back and top view), (b) CS_0° (back view), (c) RC_$H_{steel}B_cE$_0° (back view) [dimensions in millimetres].

4 RESULTS

4.1. Overall monotonic behaviour

The behaviour of the connections was investigated and the main mechanical properties were determined, namely: initial and post-elastic stiffness, strength, yielding and ultimate rotation, and moment (M) versus rotation (χ) curve. The M-χ curve was calculate based on the load versus mid-span displacement curve (**Figure II.9**).

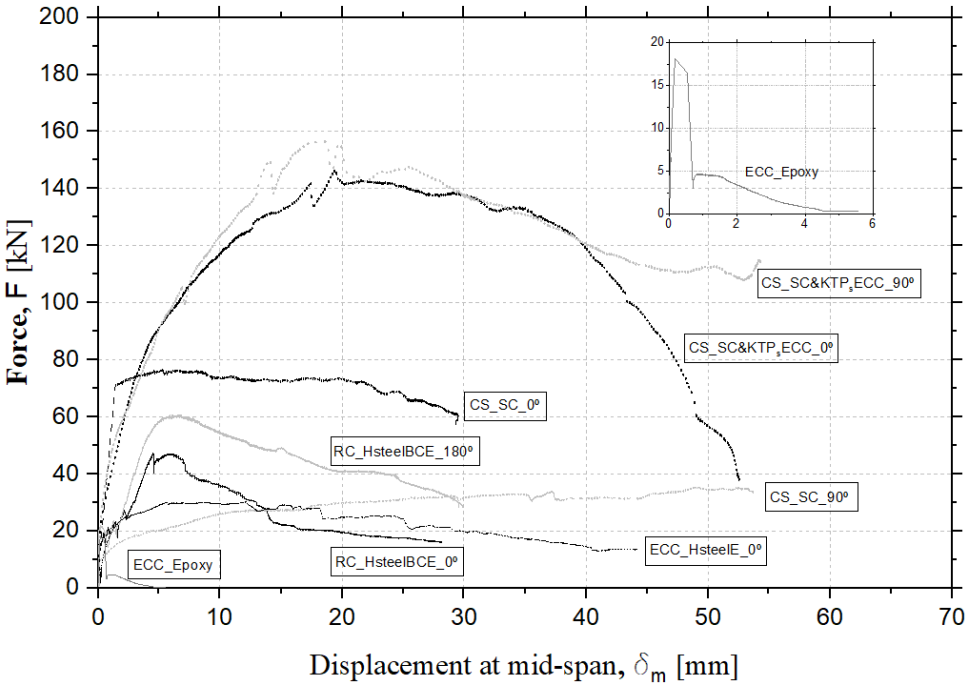


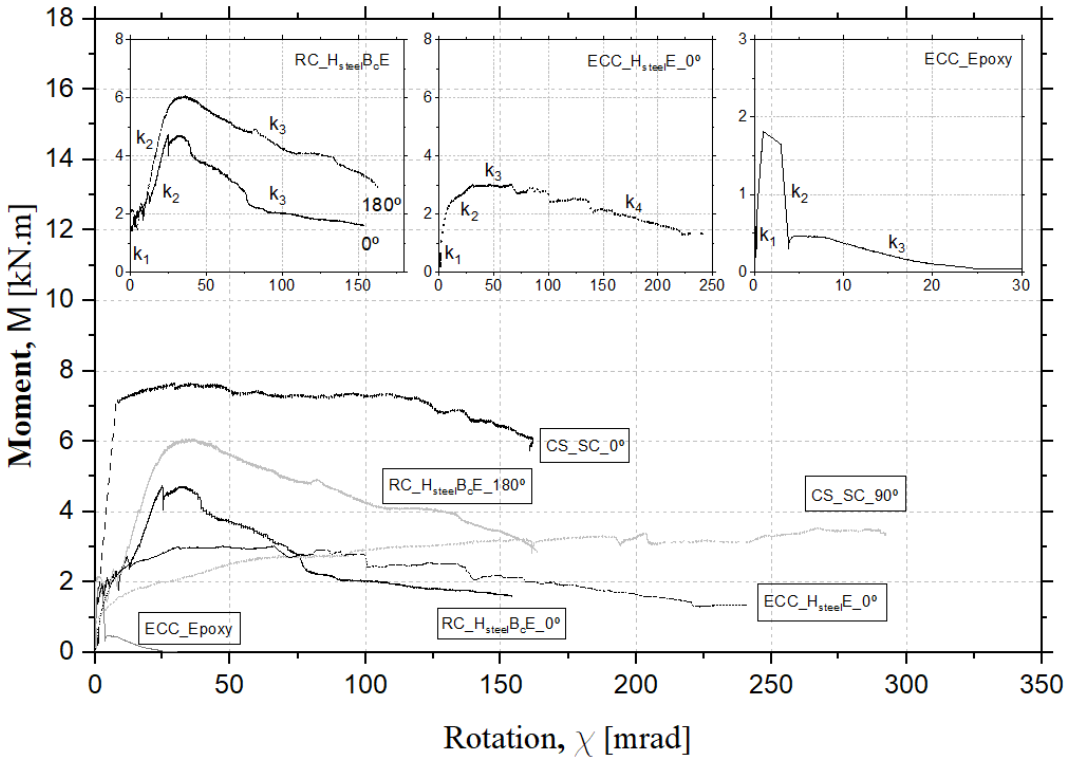
Figure II.9: Experimental responses of load force *versus* displacement at mid-span.

Figure II.10 shows the M-χ curves for each specimen tested, illustrating the influence of the connection types and loading direction. As observed in **Figure II.10**(a), the RC_$H_{steel}B_cE$ specimens tested at 0° and 180° present curves with very similar shape, although with some difference in the load values. The experimental response is essentially marked by four distinct phases, regardless of loading orientation. An initial phase of elastic behaviour with high stiffness, is followed by a phase of fluctuation on the applied force caused by progressive cracking of concrete. Subsequently, the specimens show a recovery of load capacity although with loss of stiffness due to damage on the connection, up to a maximum load value (pre-peak branch). Thereafter, the experimental response is characterized by a progressive reduction in the load capacity and loss of stiffness due to larger cracking and crushing of concrete and the plastification of the reinforcement until failure of the steel hasp (post-

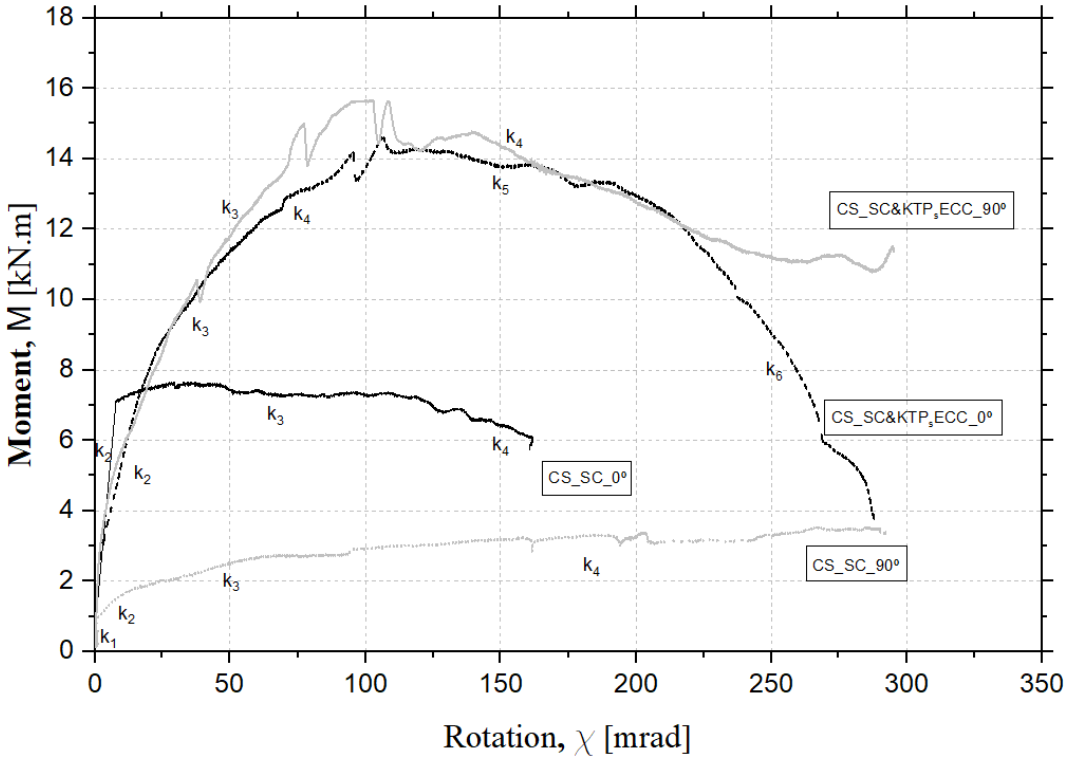
peak branch). The main difference between the responses of the two specimens is the higher value of the loading force when the wedge was facing downwards (RC_$H_{steel}B_cE$_180°).

The experimental curve of ECC_H_{steel}E_0° is marked by an elastic linear phase up to 15 kN, followed by non-linear phases with a slight loss of stiffness (cracking of the surrounding concrete in the connection zone) and increase in load capacity up to a peak value. After the peak, the response is characterized by a stable load plateau around 30 kN with increasing deflection, tailed by a gradual decrease of load capacity with increasing deformation. The ECC_H_{steel}E_0° exhibits a distinct experimental response from the RC_H_{steel}BCE_0°, demonstrating higher deformation capacity before failure but lower initial stiffness and load capacity. This behaviour can be attributed to the inexistence of continuity between the steel hasp and any reinforcement in the ECC_H_{steel}E_0°, unlike in the RC_H_{steel}BCE_0°. On the other hand, the behaviour of the ECC_H_{steel}E_0° system is significantly better than the ECC_Epoxy, highlighting the influence of the steel hasp and surrounding epoxy. In contrast, the ECC_Epoxy connection exhibits an experimental response significantly different from the others, both in form and in value. Its curve shows a "triangular" shape with an elastic linear branch with high stiffness up to a maximum force of 18.16 kN, followed by an abrupt loss of load capacity (**Figure II.10**(a)). Consequently, the structural behaviour of ECC_Epoxy is less recommended due to its lower load capacity and reduced ductility.

The CS_SC specimens show distinct behaviour compared to the RC_$H_{steel}B_cE$ specimens regarding the M-χ curve shape and load capacity. They also behave differently among themselves depending on the loading direction. Generally, both CS_SC specimens show three distinct phases in their experimental curves. Initially, they display elastic behaviour with high stiffness, similar for both specimens up to about 10 kN. Beyond this point, the CS_SC_0° exhibits non-linear behaviour, marked by significant deformation and a gradual increase in load capacity, tending towards stabilization. In contrast, the CS_SC_90° shows a steady increase in load capacity with low displacement until reaching peak force, accompanied by a slight loss of stiffness. After peaking, its response reveals a gradual reduction in load capacity until failure. The CS_SC_90° experiences a mid-span displacement at least fifteen times higher than that of the CS_SC_0°. The deformability of the RC_$H_{steel}B_cE$ is similar to that of the CS_SC_0° (**Figure II.10**(a)).



(a)



(b)

Figure II.10: Moment *versus* curvature at mid-span without (a) and with (b) the KTPs system.

The experimental responses obtained for CS_SC&KTP$_s$ECC tested at 0° and 90° present a very similar behaviour in terms of shape and load values (**Figure II.10**(b)). The use of KTPs filled with ECC

balances the mechanical behaviour of the connection system, attenuating differences that result from the loading direction. Initially, a similar linear elastic phase with high stiffness is observed up to a load value of approximately 24 kN. Until the peak force, the responses exhibit a non-linear behaviour, observing an increase in load capacity, with progressive loss of stiffness due to cracking and crushing of the ECC that surrounds the metallic connection (pre-peak branch). The post-peak phase is characterized by a reduction on the load carrying capacity and a loss of stiffness due to the progressive degradation of the connection system. The loss of stiffness is associated with the tearing of the internal tubular profile caused by the diametrical pressure by screw contact, by slippage between the ECC of the connection and the metallic connector, and by increased cracks. The CS_SC&KTP$_s$ECC structural system demonstrates a mechanical behaviour that is significantly superior to the one observed for CS_SC. It exhibits a higher load capacity, a more balanced mechanical response in terms of load and deformation, regardless of the loading direction (0° or 90°) and a higher residual load-bearing capacity after the peak, which is crucial for structures subjected to dynamic or cyclic loading.

Table II.5 summarizes the main experimental results obtained for each specimen. Based on the results, it is evident that the type of connection and the loading direction significantly influence the results obtained. The influence of loading direction is more noticeable in ECC_E and CS_SC specimens. In the first case, the connection mechanism is exclusively adhesive and, in the second, the rotation between the blocks depends highly on the direction of loading.

In the case of CS_SC specimens, while in the CS_SC_0° the rotation of the connection in the loading direction is restrained, in the CS_SC_90° it is close to free. This particularity represents an increase of about 116% in F_{max} and M_{max} values in CS_SC_0° specimen when compared to CS_SC_90°. In terms of M_{ult} e θ_{ult}, a difference of 80.4% and -72.3% was noted, respectively. Considering that specimen CS_SC_90° presents an almost "infinite" deformation load that approaches a plateau, leading to values close to maximum and ultimate support loads, the ductility factor has no physical expression. Therefore, for this case, the ductility factor of CS_SC_90° was calculated considering 70% of M_{max}, resulting in similar ductility factors for both specimens.

CS_SC&KTPsECC_0° and CS_SC&KTPsECC_90° connections present F_{max} and M_{max} values that are 91.3% and 342.4% higher than those obtained for CS_SC_0° and CS_SC_90°, respectively

Table II.5: Main results obtained from the experimental tests.

Name	F_{max} [kN]	δ_{max} [mm]	δ_{ult} [mm]	K_1 [kNm/rad]	K_2 [kNm/rad]	K_3 [kNm/rad]	K_4 [kNm/rad]	M_{max} [kNm/rad]	θ_{max} [rad]	M_u [kN.m]	θ_u [rad]	μ [-]	E_i [kNm.mrad]
RC_$H_{steel}B_cE$_0°	47.37	4.52	28.20	3916.01	119.23	-23.99	-	4.74	24.75	1.61	154.23	6.23	185.39
RC_$H_{steel}B_cE$_180°	60.74	6.57	29.92	4450.75	245.45	-24.17	-	6.07	35.99	2.83	163.58	4.55	388.33
CS_SC_0°	76.74	5.28	29.53	1317.23	839.90	3.13	-14.77	7.67	28.92	6.05	161.81	5.60	1607.54
CS_SC_90°	35.46	49.05	53.73	2396.38	75.24	20.32	2.34	3.55	267.17	3.36	292.33	6.03*	1380.33
CS_SC&KTPsECC_0°	146.55	19.43	52.56	1969.30	318.32	128.92	66.93**	14.66	106.46	3.79	287.98	2.71	2195.62
CS_SC&KTPsECC_90°	156.89	18.71	54.32	1833.14	218.36	102.36	-32.21	15.67	102.40	11.43	295.47	2.89	2642.75
ECC_E	18.16	0.18	5.58	1658.34	-1511.01	-23.56	-	1.82	0.99	0.04	30.58	31.00	10.22
ECC_$H_{steel}E$_0°	30.27	12.09	44.25	203.73	27.02	-0.02	-10.41	3.03	66.24	1.35	241.31	3.64	371.11

F_{max} - maximum force; δ_{max} - mid-span displacement at F_{max}; δ_{ult} - ultimate mid-span displacement; K_i - stiffness in different phases of the curve;
M_{ult} and θ_{ult} - ultimate bending moment and rotation (referring to the rupture of the specimen or the excessive deformation that led to the interruption of the test);
M_{max} and θ_{max} - maximum bending moment and corresponding rotation; μ - ductility factor ($\theta_{ult}/\theta_{max}$); E_i - dissipated energy for $0.8F_{max}$;
** The stiffnesses of the descending branch of CS_SC&KTPsECC_0° are K_5 = -13.90 kNm/rad and K_6 = -92.24 kNm/rad;
* μ referring to CS_SC_90° was calculated for 70% of M_{max};

The initial stiffness obtained (k_1) was similar for both specimens. In terms of θ_{ult}, the values for CS_SC_90º and CS_SC&KTPsECC_90º were similar. In turn, CS_SC&KTPsECC_0º presents a value that is 78% higher than CS_SC_0º. Regarding M_u and μ, it can be seen that the connector CS_SC&KTPsECC_90º presents a value 3.4 and 2.7 times higher than CS_SC_90º, respectively. On the contrary, when it comes to the loading direction of 0º, the CS_SC&KTPsECC_0º system presents a lower ductility factor (two times) compared to CS_SC_0º.

With regard to the connection RC_$H_{steel}B_cE$, the specimen tested with the epoxy wedge in the lower part (RC_$H_{steel}B_cE$_180º) reached values of F_{max} and M_{max} that are approximately 28.2% higher than the results measured in the specimen in which the wedge is in the upper part (RC_$H_{steel}B_cE$_0º). For δ_{max} and θ_{max}, the increase is 45.4%. It is also observed that the value of θ_{ult}, obtained for both specimens before failure, occurred for very similar values. In terms of M_u there is a difference of 75.8%. On the other hand, the RC_$H_{steel}B_cE$_180º specimen shows a ductility factor that is 27% lower than the RC_$H_{steel}B_cE$_0º, although it presents a higher dissipated energy (95.5%). The connection ECC_$H_{steel}E$_0º presents inferior values of M_{max} (1.56×), M_u (1.2×), μ (1.7×) e k_1 (19.22×) when compared to RC_$H_{steel}B_cE$_0º.

4.2. Failure modes

The failure modes (FM) vary significantly according to the connector type, as discussed below. In the case of RC_$H_{steel}B_cE$ type, the damaged zones are more evident due to cracking and crushing of the concrete adjacent to the connection. In the CS_SC, the damage occurs essentially at the level of the steel elements. The CS_SC&KTPsECC connectors, include the tearing of the KTPs, the formation of crushing zones, and sliding between materials. Next, the rupture that occurred for each tested system is individually discussed.

i. **RC_$H_{steel}B_cE$_0º**, the specimen shows initially transverse cracks in the tensile zone of the concrete near to the rim, for a load of 14 kN (**Figure II.11**). As the load increases, the crack propagates diagonally and thickens, indicating wedge formation. In the compression zone, longitudinal cracks appear first, followed by significant concrete crushing. The connection fails primarily due to concrete cracking and crushing, along with steel hasp plastification, resulting in a diagonal crack that intersects the adhesive.

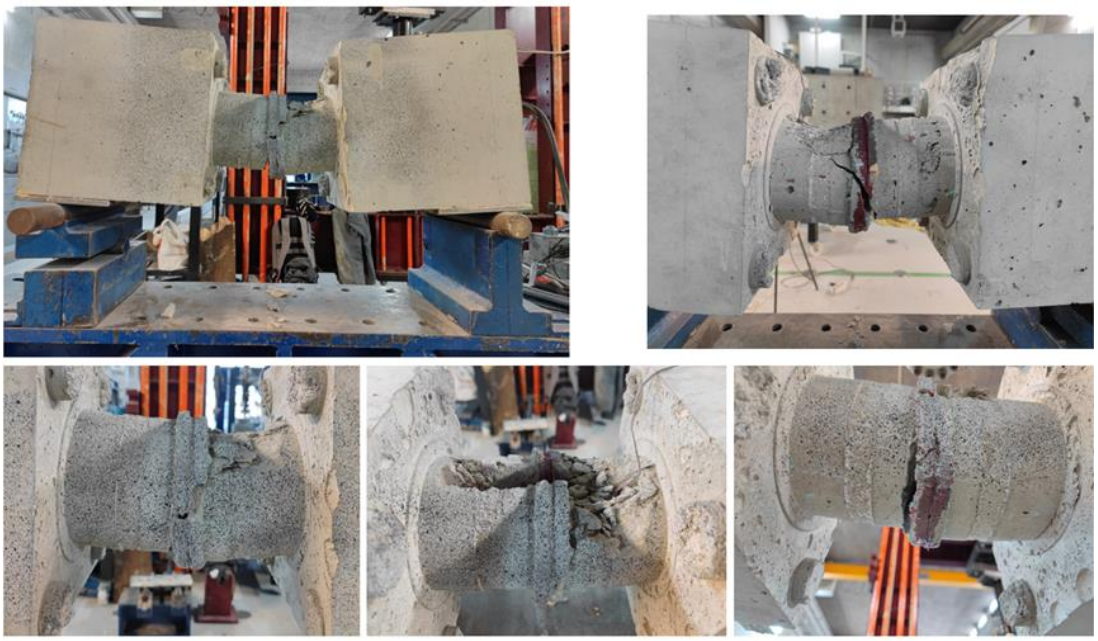


Figure II.11: Failure modes of the RC_$H_{steel}B_cE$_0°.

ii. **RC_$H_{steel}B_cE$_180º**, the damage and/or rupture mechanism followed a pattern similar to RC_$H_{steel}B_cE$_0° (**Figure II.12**). However, diagonal cracks were not observed at naked eye. In addition, the collapse developed quickly with plastification and rupture of the metallic hasp in the mid-span section, keeping the steel-epoxy-concrete adhesive zone intact.

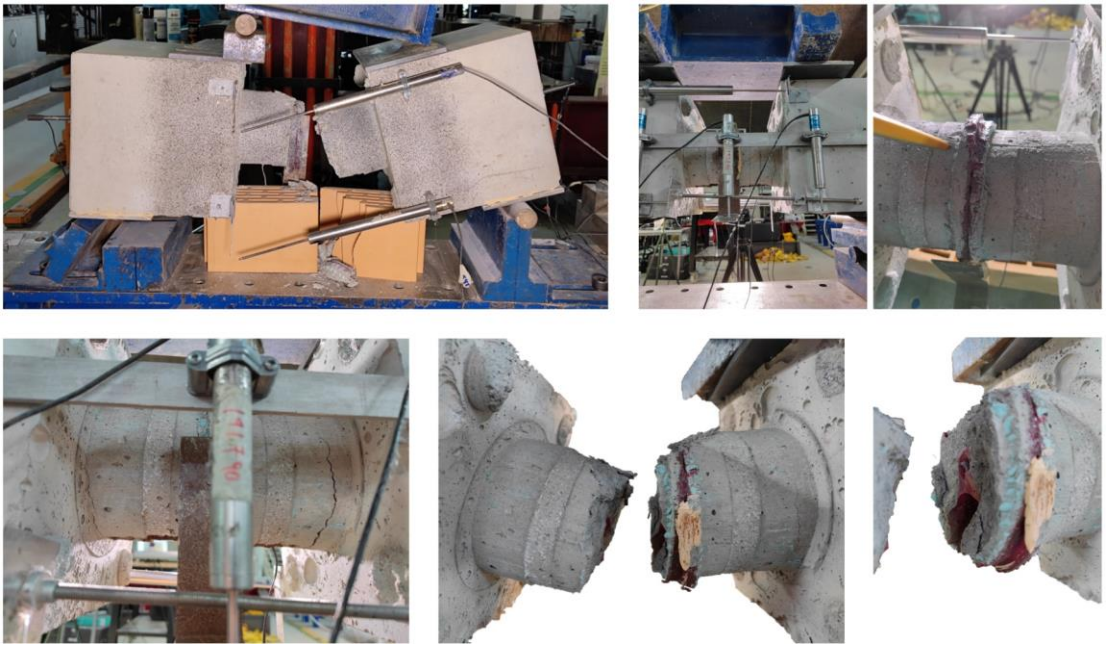


Figure II.12: Failure modes of the RC_$H_{steel}B_cE$_180°.

iii. **CS_SC_0º**, a pronounced deformation without mechanical collapse was observed (**Figure II.13**). The first signal was audible for a load of 65 kN, possibly due to adjustments in the metallic components slacks. The rotation between blocks is clear, with the ends of the tubes coming together in the upper area and spacing in the inner area. After disassembling the connection, it was noted that the tensioned end of the tubular profile had torn outwards by a factor of 1.7D. The bolts exerted diametral pressure on the connection holes, causing plastic deformation and eventual rupture. The same was observed in the compression zone, but on a smaller scale and in the opposite direction (inwards). A localized deformation of the perimeter was observed at the end of the profile, without significant visible deformation of the bolts to the naked eye.

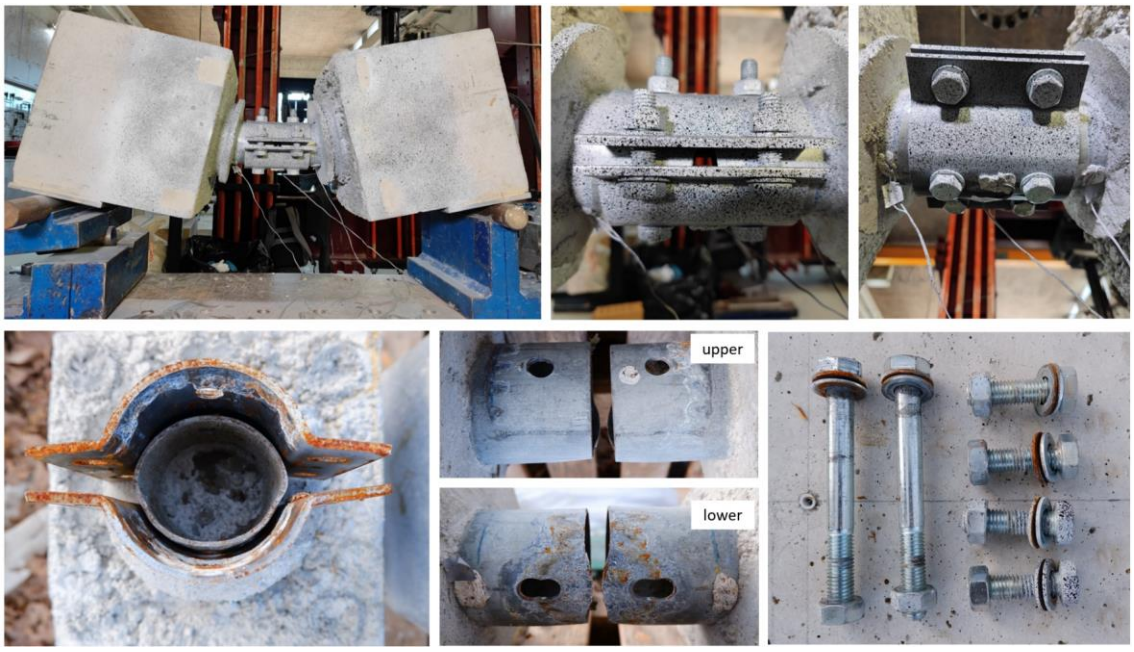


Figure II.13: Failure modes of the CS_SC_0°.

iv. **CS_SC_90º**, a significant deformation occurred without mechanical collapse or noticeable damage to the connection components (**Figure II.14**). The applied load caused large rotation of the blocks around the central bolts, which limited stress and structural damage to the steel parts. As the specimens deformed, the ends of the tubes separated in the tension zone and moved closer together in the compression zone. Although not observed, the tube contact in the compressed zone could lead to buckling, as indicated by localized perimeter deformation at the tube's upper end. The bolts exhibited no visible deformation (naked eye).

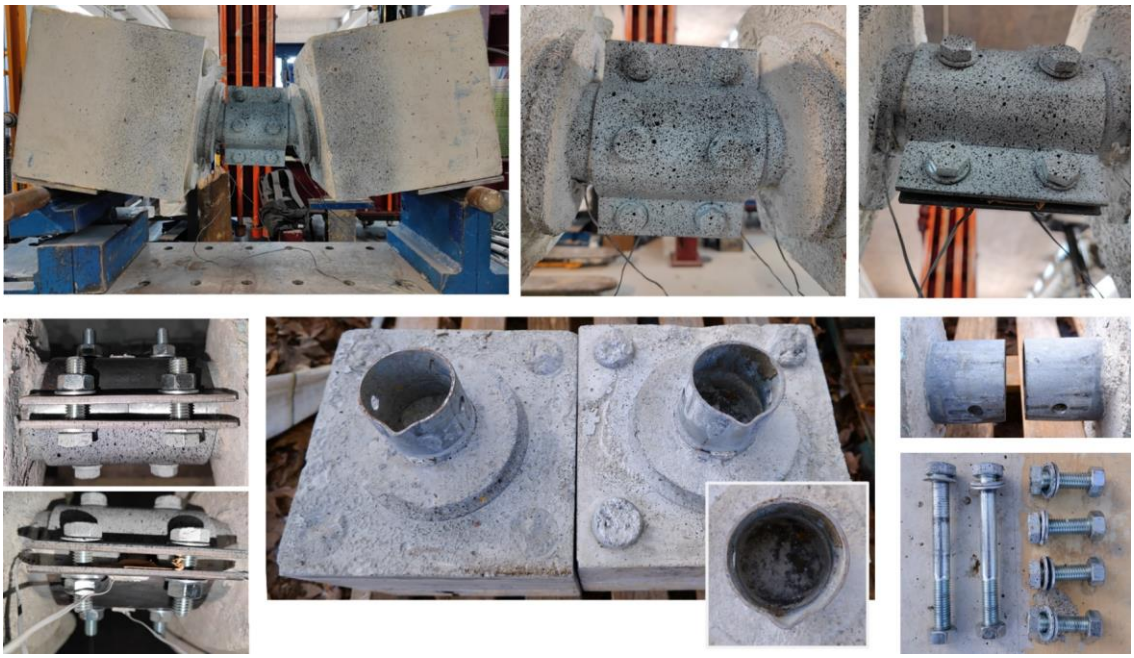


Figure II.14: Failure modes of the CS_SC_90°.

v. **CS_SC&KTPsECC_0º and CS_SC&KTPsECC_90º** exhibited similar ductile failure characterized by significant deformation without collapse (**Figure II.15** and **Figure II.16**). Tearing of the textile sleeve in the tensile zone and wrinkling of the KTPs in the compressed zone due to crushing of the ECC were observed. Slippage occurred between the tubular profile and the ECC confined by the KTPs, as the central ECC block maintained its position while the other blocks rotated. Upon disassembling the connections, the clamps and bolts were found to be structurally intact. However, a perimeter deformation of the tube near the connection area was observed. Additionally, the bolts induced high deformation in the tube due to the diametral bearing pressure at the hole, with CS_SC&KTPsECC_0° being more pronounced.



Figure II.15: Failure modes of the CS_SC&KTPsECC_0°.

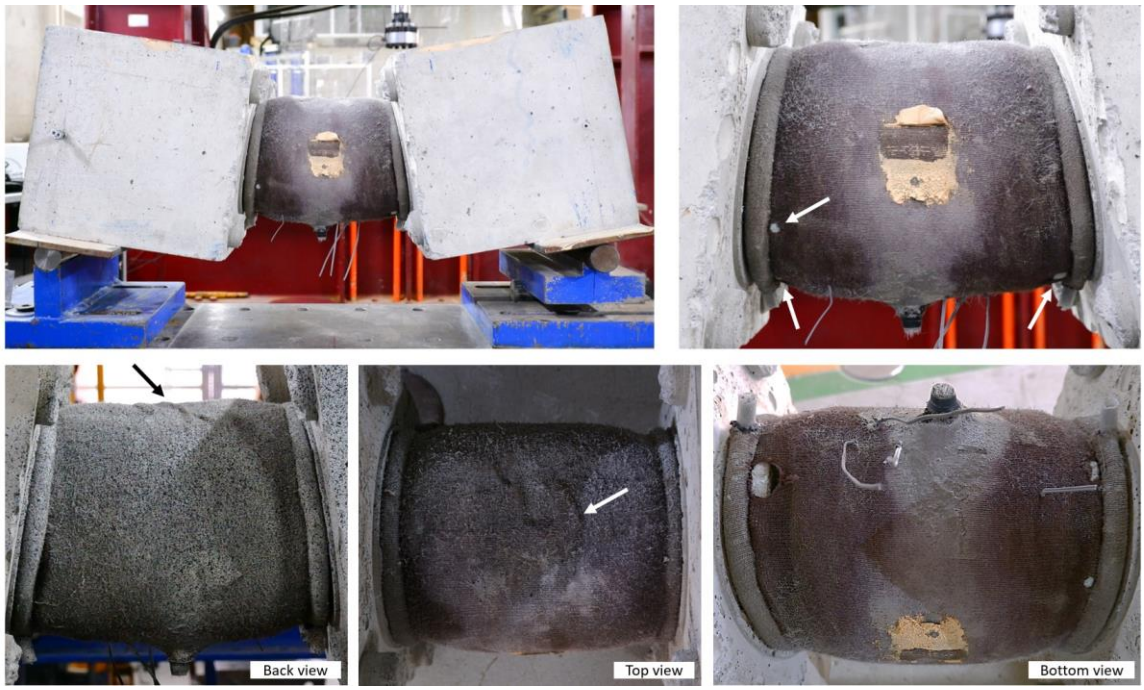




Figure II.16: Failure mode of the CS_SC&KTPsECC_90º.

vi. **ECC_H$_{steel}$E_0º**, showed a ductile failure (**Figure II.17**). Initial signs of damage occurred for a load of 16 kN, accompanied by audible "snaps" likely from ECC-adhesive detachment. As the load increases, a transversal crack between the adhesive and the ECC (peel off) can be observed in the lower part, which propagates with the increase of the load. In the compressed flange, the crushing of the ECC was observed, as well as a diagonal crack forming a wedge. Upon disassembly, the steel hasp remained intact, demonstrating good adhesion among materials.



Figure II.17: Failure modes of the ECC_H$_{steel}$E_0º.

vii. **ECC_E**, presented a brittle rupture which occurred at the level of the ECC -epoxy adhesive, as shown in **Figure II.18**. First, a small longitudinal crack caused by compression was observed in the upper part, as well as a transverse crack in the lower area (traction), that extended in the upward direction. The adhesive epoxy and the interface epoxy-ECC remained intact.

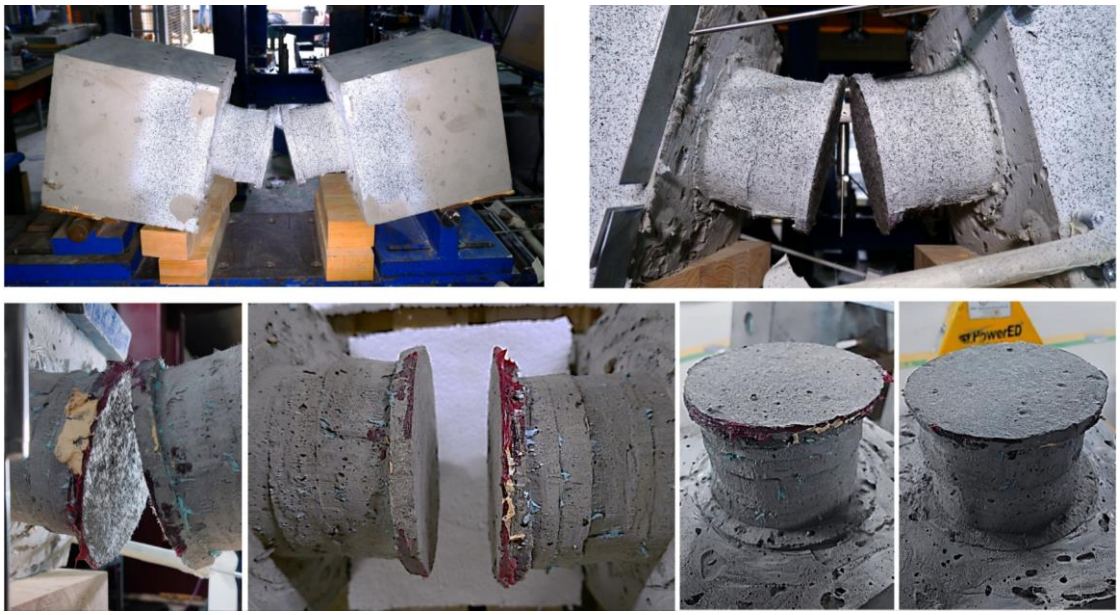


Figure II.18: Failure modes of the ECC_0°.

4.3. Deformability of components

The deformability of the steel components of the connections was studied based on data acquired by unidirectional electrical SG. **Figure II.19** shows the moment vs strain (M-με) experimental curves, grouped by connection type. The M-με responses of the RC_$H_{steel}B_cE$_0° and RC_$H_{steel}B_cE$_180° connections are similar up to a strain of 20 με, after which RC_H_{steel}BCE_180° shows increased deformation, indicating that the steel hasp was stressed even before reaching maximum load. This reflects the plasticization of the steel hasp culminating in its rupture and subsequent failure of the connection system. In contrast, the ECC_H_{steel}E_0° connection shows low strain values, which can be explained by an ineffective mobilization of the steel hasp, since it was not anchored to any reinforcement (**Figure II.19**(a)). For CS_SC_0°, the M-ε curves show higher strain values (ε_{max} of 810 με and ε_{ult} of 1756 με), while CS_SC_90° demonstrates lower strain due to its rotation about central bolts, reducing material stress (**Figure II.19**(b)). The CS_SC_0° strains are approximately 3.6 times higher than those of CS_SC_90°, likely due to the steel clamp's restriction on block rotation. This restriction forces the steel to deform more, leading to tube plasticization. In contrast, the CS_SC_90°

connection behaves more like a mechanism around the central bolts, reducing stress and resulting in lower strain values. The CS_SC connection reinforced with KTPs injected with ECC appears to enhance the utilization of the steel's capacity, particularly at 90° (**Figure II.19**(c)). In CS_SC&KTPsECC_0°, the maximum strain was 445 με in the left profile (SG1) followed by a reduction up to 8 με, at which point the SG stops working correctly. No significant deformation was noted in the right tube or steel clamp, with a maximum value of 55 με. For CS_SC&KTPsECC_90°, the maximum strains recorded were 2857 με (SG1) and 7710 με (SG2) in the left and right tubes before reaching F_{max}. The clamps exhibited a maximum deformation of 114 με after F_{max}.

5 DISCUSSION

5.1. Comparative analysis of connection strength and deformability

To better understand the behaviour as well as the advantages and limitations of each connection, the correlations between F_{max} *vs* δ_{ult} and between E_i *vs* δ_{ult} were studied (**Figure II.20**). The first analyses evidenced the relationship between the strength and deformability of the developed connection systems, with significant variability observed among them. The second relationship provides insights related to the capacity of the connections to absorb and dissipate energy throughout the loading cycle.

The ECC_E connection offers a straightforward, user-friendly assembly process, taking advantage of ECC's corrosion resistance and ductile mechanical properties, as shown in section 4.2 While ECC demonstrates ductility, mechanical testing of the connection reveals lower strength and deformability compared to other systems, with the F_{max} vs. δ_{ult} correlation positioned in the lower left quadrant. This limitation is partly attributed to the shallow bond depth of the adhesive connection and reduced matrix richness at the extremities, as noted in the failure mode description (**Figure II.18**). Recognizing these constraints, steel hasp were implemented in critical zones to bolster joint performance. Despite exhibiting the lowest deformability and strength among the systems evaluated, ECC_E offers benefits in durability and ease of application.

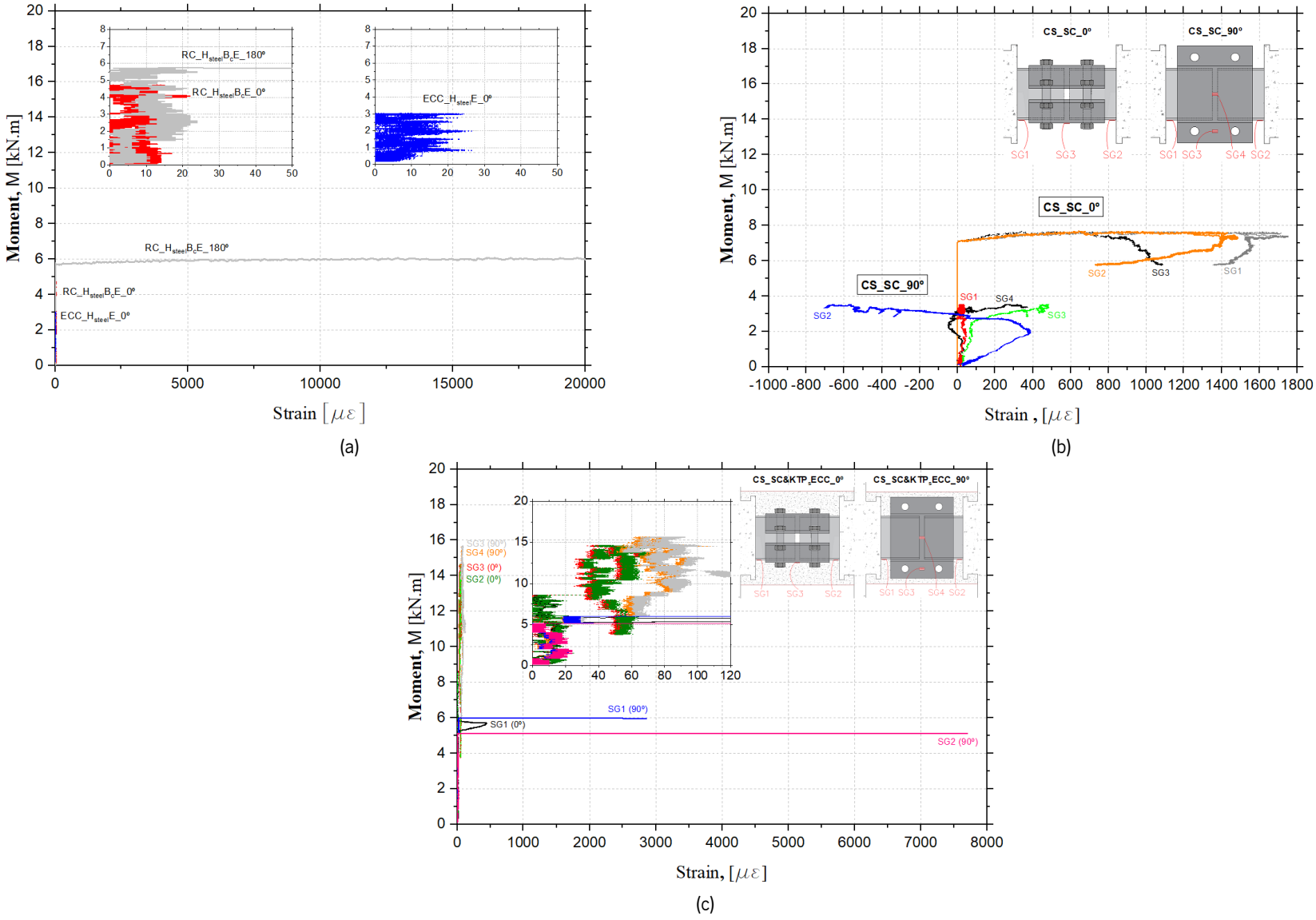
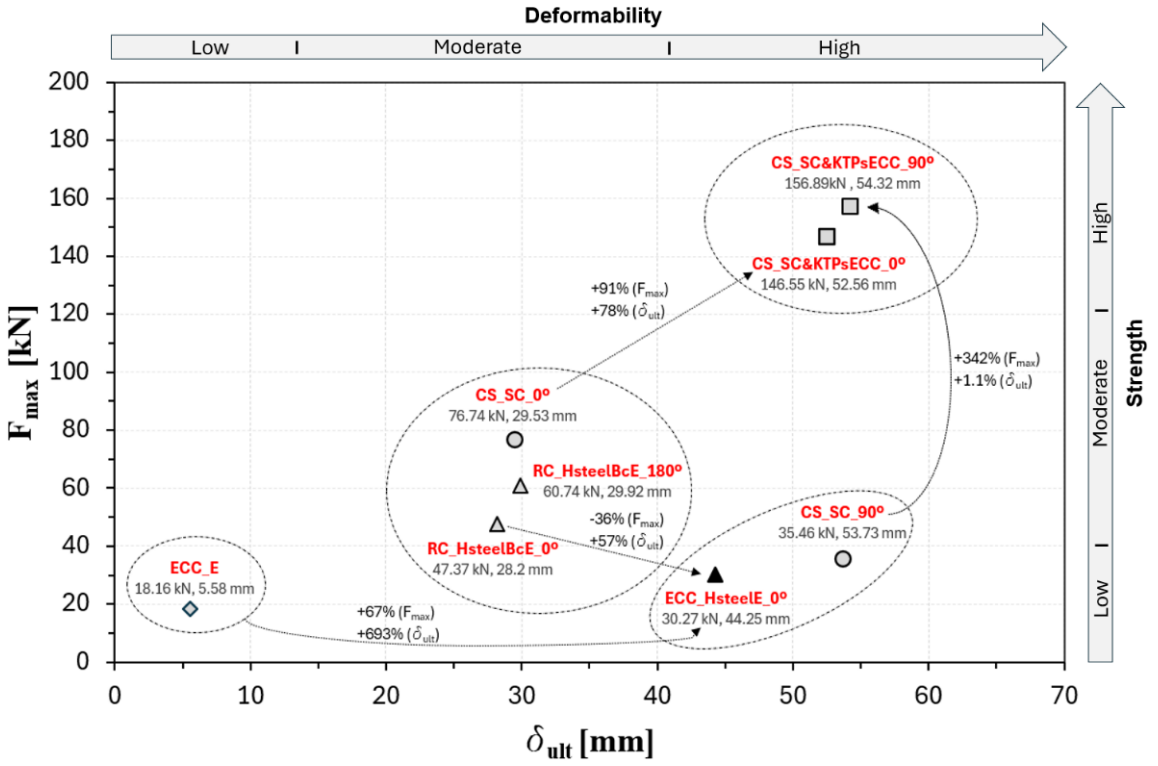


Figure II.19: Strain on steel parts: (a) hasp of RC_$H_{steel}B_cE$ and ECC_$H_{steel}E$, (b) steel clamp of CS_SC and (c) steel clamp of CS_SC&KTPsECC.

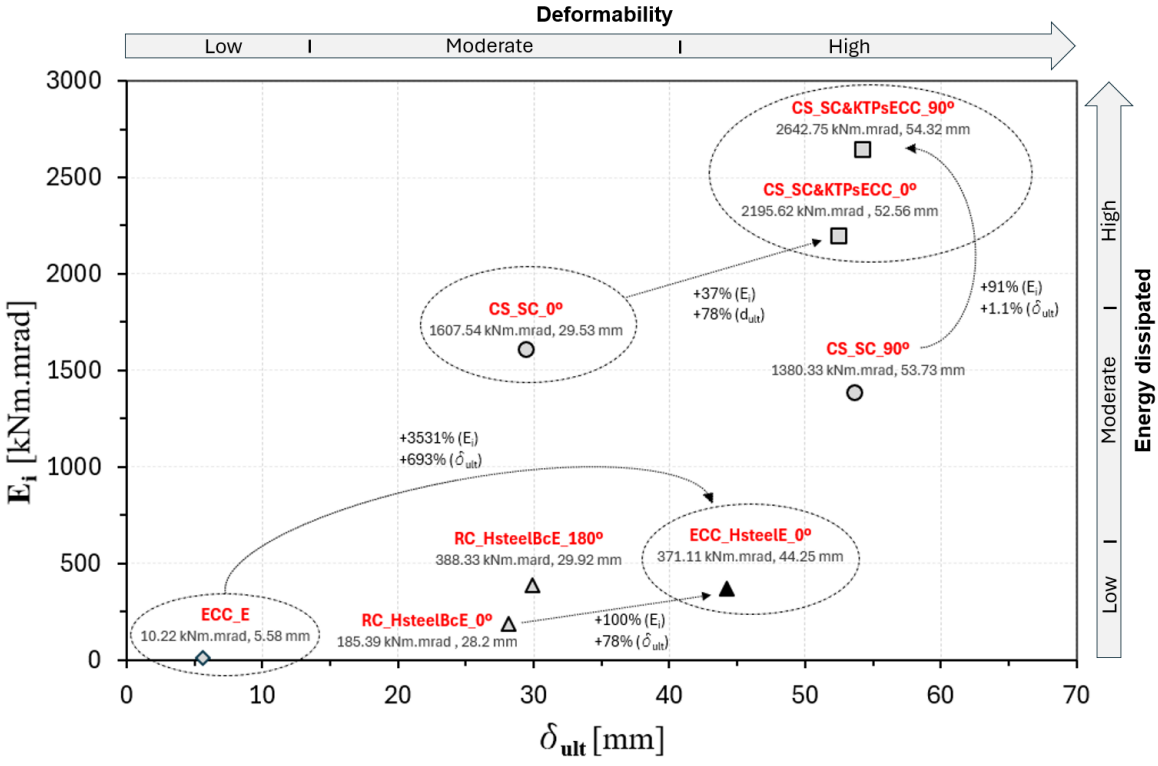
To partially address the limitations identified in the previous design, the ECC_H_{steel}E_0° connection introduces a macroscopic reinforcement element (steel hasp) to the ECC_E bonded connection. This addition leverages both the mechanical interlocking effect and the steel ductility. Despite the extra component, the connection remains straightforward to assemble, ensuring ease of execution. As illustrated in **Figure II.20**, this reinforcement significantly enhances structural behaviour, increasing the connection's deformability by 693% and strength by 67%, positioning the system within the lower right quadrant of the F_{max} vs. δ_{ult} correlation. This improvement is primarily attributed to mechanical interlocking rather than the steel intrinsic ductility, as evidenced by low extension values and the absence of deformation in the steel hasp, as shown in **Figure II.17**. The reinforced system shows a remarkable 3531% increase in energy absorption over the ECC_E connection, greatly enhancing energy dissipation and mechanical strength. This improvement boosts the system's durability, making it highly suitable for demanding applications.

The RC_$H_{steel}B_cE$_0° structure and connection combines a brittle material (concrete) with a ductile reinforcement (steel), enabling a continuous yet intricate assembly process. This configuration increases load capacity by 56% and reduces deformability by 36% compared to the ECC_H_{steel}E_0°, which highlights the ductility of the ECC material despite the aforementioned limitations. While the failure mode remains ductile, the energy dissipation of the RC_H_{steel}E_0° is 50% lower than that of the ECC_H_{steel}E_0°. The connection behaves similarly in both directions, making it suitable for multidirectional loading situations.

The CS_SC connection links tubular profiles using metal clamps, creating an easy-to-apply orthotropic connection. This setup may be a disadvantage in cases needing strength and deformability in all directions but can be advantageous when deformability is needed in a specific direction. The CS_SC system enhances the metallic element`s performance, particularly in the 0° orientation, as described in Sections 4.2 and 4.3 (**Figure II.13** and **Figure II.14**). The CS_SC_0° is positioned in the central region with moderate strength and deformability, while the SC_SC_180° lies in the lower right quadrant, showing high deformability but lower strength than the other connections. Failure occurs according to the deformability criterion, with the energy dissipation capacity concentrated in the central zone (**Figure II.20**(b)). This behaviour highlights the impact of orthotropic properties on connection performance in multi-loading scenarios. The KTP_ECC system protects the steel elements in the CS_SC connection, enhancing durability and making the connection isotropic. As shown in **Figure II.20**, the KTP_ECC system places the overall connection in the upper right quadrant,



(a)



(b)

Figure II.20: Correlation between (a) F_{max} vs δ_{ult} and (b) E_i vs δ_{ult}.

exhibiting high strength and deformability, making it the best-performing connection. The reinforcement significantly increases the maximum strength, particularly in the 90° orientation (+342%), while maintaining a high deformation capacity (+1.1%). In the other direction (0°), the increase in F_{max} and δ_{ult} are more linear, with improvements of 91% and 78%, respectively. Additionally, the CS_SC&KTP_ECC system also demonstrates improved energy dissipation capacity, with increases of 37% at 0° and 91% at 90°, optimizing material usage in the connection.

In sum, flexible structures and connectors with high deformation capacity and energy dissipation are ideal for dynamic environments, like marine settings, while rigid structures with moderate deformability are better suited for stable conditions with minimal external forces, requiring strength to withstand typical marine forces.

5.2. Connections construction challenges

The RC_$H_{steel}B_cE$ connections posed challenges due to the small wedge size for engaging the bar coupler, suggesting the need for larger edge dimensions. The CS_SC system demonstrated a lightweight and straightforward design, making it particularly suitable for underwater assembly. The application of the KPT layer proved practical, especially when conducted onshore. However, logistical challenges may emerge during the preparation and injection of ECC at sea, necessitating careful planning and resource allocation to ensure effective implementation in marine environments. The ECC_E and the ECC_$H_{steel}E$ connections did not present any relevant difficulties in assembly.

6 CONCLUSIONS

This research investigated the development and characterization of innovative structural connections for MFAR modular construction. The literature is scarce on the description of technical solutions and specifications or standards for these structural elements, which are assuming a relevant role in modern marine structures. The experimental program was devised to extract the fundamental structural performance and validate the conceptual designs developed, considering mainly construction feasibility, load bearing capacity, deformability and energy dissipation capacity. The approaches followed may be of great value for future development of alternative structural connections for modular construction. The resulting nonlinear behaviours experimentally obtained are essential to further support advanced structural analysis of complex shape MFARs made of multiple units, where

connections may be materialized by the designs developed or others following similar approaches. In general, the results obtained allowed to reach different levels of structural performance in terms of strength and energy dissipation capacity, which may comply with different application requirements and structural demands. In particular, and for the specific case of the connection systems developed and characterized, the main findings were:

- The non-linear behaviours exhibited by all connections indicate the complex and synergistic interaction between the utilized materials and the adopted connection types, relevant for ductile structural responses.

- The CS_SC&KTPsECC design was distinguished by superior load-bearing capacity (>146.55 kN) and energy dissipation ability (>2195.62 kNm.mrad), making it particularly suitable for highly dynamic marine environments such as coastal zones and open sea areas. The CS_SC&KTPsECC connection showed significant improvements compared to the CS_SC connection, with a 91% (0°) and 342% (90°) increase in load-bearing capacity, and a 37% (0°) and 91% (90°) increase in energy dissipation.

- The incorporation of high-performance concrete in the connection design substantially improves connection performance. Unlike conventional concrete, which fractures in a brittle manner, ECC deforms significantly before breaking. Its ductility provides higher energy dissipation capacity, contributing to improved performance in dynamic loading conditions. ECC generates fewer cracks during the load cycle, making it more resistant to wear over time.

- The RC_$H_{steel}B_cE$ design exhibited similar load-bearing capacity and deformability when compared to the CS_SC system, but with a significantly lower energy dissipation ability (-88%). These systems are more suited to stable and sheltered maritime conditions such as deeper seabed, lagoons, and estuaries.

- RC_$H_{steel}B_cE$_0° led to an increase in load bearing capacity (+56%) but a significant reduction in energy dissipation (-50%) compared to ECC_$H_{steel}E$_0°. While RC_$H_{steel}B_cE$_0° exhibited a 56% increase in load-bearing capacity, its reduced energy dissipation (-50%) suggests that the steel locking mechanism was not activated, as evidenced in the M-$\mu\varepsilon$ curves. Similarly, the ECC_$H_{steel}E$_0° design, despite having a non-attached steel locking mechanism, provides better energy dissipation due to the superior ductility of the ECC material. The stresses are redistributed throughout the material, as its microstructure effectively controls crack formation

and prevents brittle failure, thanks to the fibrous bridging mechanism. This behaviour aligns with the energy conservation law and fracture mechanics principles, which highlight the material's ability to dissipate energy through controlled microcracking and deformation without abrupt failure.

- The ECC_H_{steel}E system, with the steel hasp on the connection zone, outperformed the purely adhesive solution (ECC_E) by increasing deformability by 693% and load bearing capacity by 67%, as opposed to the ECC_E connection which typically showed brittle failure due to the surface detachment of the ECC matrix in the bonded area.

The combination of the advanced and durable materials used resulted in a wide range of structural performance levels, which may be properly selected during the MFAR global structural design. These findings may support further developments and improvements of tailored connection designs suited to alternative applications. Besides artificial reefs, also modular energy islands, modular wind or wave and tidal platforms for energy converters may rely on the joining of several units. Further studies should focus on the dynamic performance and the long-term and durability behaviours, as well as on design standards and experimental characterization. The subsequent steps should focus on real scenario exposure conditions and loads, for subsequent characterization and testing in the lab for durability and residual capacity quantification.

ACKNOWLEDGEMENTS

The first, third and fourth authors would thank the PhD grant SFRH/BD/137220/2018, SFRH/BD/144201/2019 and SFRH/BD/129583/2017 provided by Fundação para a Ciência e Tecnologia (FCT) and co-supported by European Social Fund (FSE) through the Programa Operacional Regional Norte. The authors also thank to the research project ‘‘NEXT-SEA: Next Generation Monitoring of Coastal Systems in a Scenario of Global Change”, NORTE-01-0145-FEDER-000032, financed by Comissão de Coordenação e Desenvolvimento Regional do Norte (CCDR-N) and Fundo Europeu de Desenvolvimento Regional (FEDER). We also thanks to Hilti® Portugal for providing the HIT RE 500 V4.

REFERENCES

[1] Bracho-Villavicencio C, Matthews-Cascon H, Rossi S. Artificial reefs around the world: A review of the state of the art and a meta-analysis of its effectiveness for the restoration of marine ecosystems. Environments 2023;10:121. https://doi.org/10.3390/environments10070121.

[2] López I, Tinoco H, Aragonés L, García-Barba J. The multifunctional artificial reef and its role in the defence of the Mediterranean coast. Sci Total Environ 2016;550:910–923. https://doi.org/10.1016/j.scitotenv.2016.01.180.

[3] Ding R, Liu CR, Zhang HC, Xu DL, Shi QJ, Yan DL, et al. Experimental investigation on characteristic change of a scale-extendable chain-type floating structure. Ocean Eng 2020;213. https://doi.org/10.1016/j.oceaneng.2020.107778.

[4] Fabi G, Scarcella G, Spagnolo A, Baines AS, Charbonnel E, Goutayer JJ, Haddad N, Altan L, Michel T. Practical guidelines for the use of artificial reefs in the Mediterranean and the Black Sea. Rome: Studies and Reviews, General Fisheries Commission for the Mediterranean; 2015.

[5] Silva J, Rosental I, Love M. Overview and trends of ecological and socioeconomic research on artificial reefs. Mar Environ Res 2019;145:81–96. https://doi.org/10.1016/j.marenvres.2019.01.010.

[6] Vivier B, Dauvin JC, Navon M, Rusig AM, Mussio I, Orvain F, et al. Marine artificial reefs: A meta-analysis of their design, objectives and effectiveness. Glob Ecol Conserv 2021;27. https://doi.org/10.1016/j.gecco.2021.e01538.

[7] Maslov D, Cruz F, Pinheiro M, Miranda T, Valente IB, Ferreira V, Pereira E. Functional conception of biomimetic artificial reefs using parametric design and modular construction. J Mar Sci Eng 2024;12:1682. https://doi.org/10.3390/jmse12091682.

[8] Shehab BA, Ekmekyapar T. Joint behaviour of through steel beam-to-composite column connections: Experimental study. Mar Struct 2021;76:102921. https://doi.org/10.1016/j.marstruc.2020.102921.

[9] Nadeem G, Safiee NA, Bakar NA, Karim IA, Nasir NAM. Connection design in modular steel construction: A review. Structures 2021;33:3239–3256. https://doi.org/10.1016/j.istruc.2021.06.060.

[10] Clamagirand E. Modular artificial reefs, 2001.

[11] Zhao H, Xu D, Zhang H, Shi Q. A flexible connector design for multi-modular floating structures. In: Proceedings of the ASME 37th International Conference on Ocean, Offshore and Arctic Engineering (OMAE 2018); 2018. p. 1–7. https://doi.org/10.1115/OMAE2018-78661.

[12] Shi QJ, Xu DL, Zhang HC, Zhao H, Wu YS. Optimized stiffness combination of a flexible-base hinged connector for very large floating structures. Mar Struct 2018;60:151–164. https://doi.org/10.1016/j.marstruc.2018.03.014.

[13] Jiang D, Tan KH, Dai J, Ang KK, Nguyen HP. Behavior of concrete modular multi-purpose floating structures. Ocean Eng 2021;229:108971. https://doi.org/10.1016/j.oceaneng.2021.108971.

[14] ReefSystems. Modular Sealife System. 2024.

[15] Reef Lab Design. Available from: https://www.reefdesignlab.com (accessed February 10, 2019).

[16] Belhassen Y, Rousseau M, Tynyakov J, Shashar N. Evaluating the attractiveness and effectiveness of artificial coral reefs as a recreational ecosystem service. J Environ Manage 2017;203:448–456. https://doi.org/10.1016/j.jenvman.2017.08.020.

[17] An W, Wang Y, Chen B, Duan M, Zhang X. Analysis of the reliability of subsea clamp connector based on multiple response surface methodology. J Mar Sci Eng 2023;11:1378. https://doi.org/10.3390/jmse11071378.

[18] Noferesti H, Razmkhah MH, Gerami M. Laboratory and ultra-low cycle fatigue evaluation of the seismic performance of BFP connection with different amounts of pre-tension in bolts. J Constr Steel Res 2024;212:108295. https://doi.org/10.1016/j.jcsr.2023.108295.

[19] Wang P, Zhang L, Wang L. Influence of temperature on the bolt loads and variation in a bolted flange for subsea pipeline connection. Math Probl Eng 2021;2021:5636941. https://doi.org/10.1155/2021/5636941.

[20] Jiang D, Tan KH, Wang CM, Dai J. Research and development in connector systems for very large floating structures. Ocean Eng 2021;232:109150. https://doi.org/10.1016/j.oceaneng.2021.109150.

[21] Jiang SC, Wang Z, Zhao XL. Structural performance of prestressed grouted pile-to-sleeve connections. Procedia Eng 2011;14:304–311. https://doi.org/10.1016/j.proeng.2011.07.037.

[22] Soon C, Ng L, Chou LM. Artificial reefs as a reef restoration strategy in sediment-affected environments: Insights from long-term monitoring. Aquat Conserv Mar Freshw Ecosyst 2017;27:976–985. https://doi.org/10.1002/aqc.2755.

[23] OSPAR Commission. OSPAR guidelines on artificial reefs in relation to living marine resources. London, UK: OSPAR Commission; 2013.

[24] Arguillarena A, Margallo M, Urtiaga A, Irabien A. Life-cycle assessment as a tool to evaluate the environmental impact of hot-dip galvanisation. J Clean Prod 2021;290:125676. https://doi.org/10.1016/j.jclepro.2020.125676.

[25] Lee MO, Otake S, Kim JK. Transition of artificial reefs (ARs) research and its prospects. Ocean Coast Manag 2018;154:55–65. https://doi.org/10.1016/j.ocecoaman.2018.01.010.

[26] Tej P, Kour M, Pokorny P. Evaluation of the impact of corrosion of hot-dip galvanized reinforcement on bond strength with concrete: A review. Constr Build Mater 2017;132:271–289. https://doi.org/10.1016/j.conbuildmat.2016.11.096.

[27] Cruz F, Pereira E, Valente IB, Tiago M, Maslov D, Pinheiro M. Structural design of an innovative multifunctional artificial reef. Oceans 2018 MTS/IEEE Charleston, IEEE; 2018, p. 1–7. https://doi.org/10.1109/OCEANS.2018.8604587.

[28] Coral Reef Arks. Coral Reef Arks. 2024. Available from: https://coralarks.org/projects.php. (accessed October 24, 2024).

[29] K Subsea Group. Subsea solutions. 2024. Available from: https://www.ksubsea-group.com/. (accessed October 25, 2024).

[30] Linden B. Tamar Artificial Reef. 2024. Available from: https://submersed.wordpress.com/. (accessed October 25, 2024).

[31] OceanBrick Group. Ocean Brick System (OBS). 2015. Available from: http://www.oceanbricks.com/.

[32] Cruz F, Pereira E, Lima M, Johnson J, Duarte D, Valente IB, et al. Experimental characterization of the scour of innovative artificial reef prototypes using hydraulic flume and photogrammetry. OCEANS 2019 MTS/IEEE Marseille, IEEE; 2019, p. 1–10. https://doi.org/10.1109/OCEANSE.2019.8867581.

[33] Maslov D, Pereira E, Duarte D, Miranda T, Ferreira V, Tieppo M, et al. Numerical analysis of the flow field and cross section design implications in a multifunctional artificial reef. Ocean Eng 2023;272:113817. https://doi.org/10.1016/j.oceaneng.2023.113817.

[34] European Committee for Standardization (CEN). EN 1993-1-8: Eurocode 3: Design of steel structures—Part 1-8: Design of joints. Brussels, Belgium: CEN; 2005.

[35] Gonçalves J. Mixed galvanized steel and concrete systems for the construction of marine and offshore structures [MSc thesis]. Guimarães, Portugal: University of Minho; 2021.

[36] European Committee for Standardization (CEN). EN 1992-4: Eurocode 2: Design of concrete structures—Part 4: Design of fastenings for use in concrete. Brussels, Belgium: CEN; 2018.

[37] Hilti. Hilti Corporation 2023.

[38] European Committee for Standardization (CEN). EN 1992-1-1: Eurocode 2: Design of concrete structures—Part 1-1: General rules and rules for buildings. Brussels, Belgium: CEN; 2004.

[39] European Committee for Standardization (CEN). NP EN 206-1: Concrete—Part 1: Specification, performance, production and conformity. Brussels, Belgium: CEN; 2005.

[40] American Galvanizers Association. Hot-dip galvanizing: Preparing the HDG surface. 2023. Available from: https://galvanizeit.org/duplex-systems-galvanize-it-seminar/preparing-the-hdg-surface. (accessed April 14, 2023).

[41] European Committee for Standardization (CEN). EN 12350-2: Testing fresh concrete—Part 2: Slump test. Brussels, Belgium: CEN; 2009.

[42] British Standards Institution (BSI). BS EN 12350-8: Testing fresh concrete—Part 8: Self-compacting concrete—Slump-flow test. London, UK: BSI; 2019.

[43] European Committee for Standardization (CEN). EN 12390-13: Testing hardened concrete—Part 13: Determination of secant modulus of elasticity in compression. Brussels, Belgium: CEN; 2013.

[44] European Committee for Standardization (CEN). EN 12390-3: Testing hardened concrete—Part 3: Compressive strength of test specimens. Brussels, Belgium: CEN; 2009.

[45] Yokota H, Rokugo K, Sakata N. JSCE recommendations for design and construction of high performance fiber reinforced cement composite with multiple fine cracks. In: High Performance Fiber Reinforced Cement Composites. Vol. 2. Tokyo, Japan: Springer; 2008.

[46] International Organization for Standardization (ISO). ISO 6892-1: Metallic materials—Tensile testing—Part 1: Method of test at room temperature. Geneva, Switzerland: ISO; 2009.

[47] Lopes L. Contribuições para o conhecimento do comportamento de ancoragens de pré-esforço por aderência [PhD thesis]. Caparica, Portugal: NOVA School of Science and Technology, NOVA University Lisbon; 2022.

PAPER III

EXPERIMENTAL CHARACTERIZATION OF BOND BETWEEN CONCRETE AND HDG STEEL TUBES FOR MIXED STEEL-CONCRETE STRUCTURES

REFERENCE: Cruz F, Valente IB, Almeida J, Neves A, Pereira E. Experimental characterization of bond between concrete and HDG steel tubes for mixed steel-concrete structures. Mater Struct 2024;57:89. https://doi.org/10.1617/s11527-024-02352-8. Impact factor: 4.0

ABSTRACT: Bond between concrete and reinforcement material is crucial for the structural behaviour and design of reinforced concrete or mixed steel-concrete structures. When considering applications in harsh environments, such as severe marine exposure or submerged conditions, hot-dip galvanized (HDG) steel seems to be a promising solution, as part of new mixed steel-concrete structural systems. Although it is essential to guarantee an effective composite response, the interaction and bond behaviour between materials is not yet sufficiently well understood.

This experimental investigation aimed to study the bond behaviour between concrete and HDG steel tubes, including the influence of adopting concrete pin connectors by creating holes in the tube profile, and also the influence of the galvanic surface state. The impact of bond length on the bond behaviour of the galvanized steel tube embedded in different concrete mixtures was analysed. Pushout tests were conducted to obtain the load end *versus* slip responses, as well as the failure modes.

The results showed that the embedment lengths and the concrete compositions had no relevant effect on the overall shape of the pushout experimental responses, with the exception of the specimens that include the concrete pin connector. However, both variables clearly influenced the bond stress, dissipated energy during pushout until failure, and residual pushout force. The addition of the concrete pin significantly improved the adherence mechanism, while the contamination of the galvanic surface showed to significantly reduce the bond strength.

Keywords: HDG steel; Concrete; Plain tubes; Bond behaviour; Pushout tests.

1 INTRODUCTION

Coastal and offshore marine structures are exposed to severe exposure conditions and, consequently, present durability problems due to physical, chemical and microbiological deterioration [1–3]. This reduces its service life and increases the maintenance costs [4,5].

Corrosion is a major cause of structural degradation and the main cause of structural failure [6–8]. Although this cannot be completely eliminated, the use of suitable protection systems, such as cathodic protection or corrosion inhibitors may limit corrosion and minimize durability problems [9, 10]. Nevertheless, these are expensive and may not always be applied due to its potentially environmental negative impact [11]. In particular, some inhibitors may cause significant deterioration in the mechanical properties of concrete. On the other hand, the use of coating products on steel presents itself as a protective method since it can prevent the direct contact of steel with oxygen, carbon dioxide, chlorides and moisture [12,13]. In this context, the use of a hybrid structure combining concrete and hot-dip galvanized (HDG) steel is regarded as a promising solution [6,9,14,15]. Concrete and HDG steel, in the form of tube profiles, may be used in marine constructions such as floating or submerged structures including artificial reef structures [2], submarine pipelines, offshore wind turbine towers and bridge piers, some in the form of concrete-encased steel elements or concrete-filled steel tubular (CFST) members [16,17].

The coating also guarantees the preservation of the mechanical properties of steel and does not require periodic maintenance, even in the harshest environments. However, despite all the advantages, it influences the bond behaviour between the steel and concrete [6,9,12,18,19].

The bond stress-slip relationship characterizes the steel-concrete interface behaviour and may be obtained experimentally using direct pushout or pullout tests, and indirectly through flexural tests [9,8].

The bond behaviour between galvanized steel and concrete is determined by the chemical bond strength between steel and the cement (chemical adherence) and depends on the relative displacement between the two surfaces (friction) and interlocking mechanisms (mechanical adherence).

Corrosion and galvanization can significantly influence the chemical bond between steel reinforcement and concrete, namely due to the reaction between galvanized coating and the cement paste, as well as the influence of corrosion on bond behaviour over time. Previous studies revealed inconclusive results [6,9,18,20–22]. According to several authors, the galvanized steel surface is activated when in contact with fresh concrete due to its alkaline nature [22,23]. During the curing process, the zinc coating corrodes until passivation occurs. At this early stage, rapid corrosion of the coating may result in the removal of a significant amount of this layer, thus resulting in poor protection. Simultaneously, as a result of the cathodic reaction, hydrogen production occurs, which increases the porosity of the concrete and consequently decreases the chemical bond between the materials [9,23–25]. Sanz et al (2017) found that the corrosion depth did not impact the maximum shear stress, suggesting consistent adherence in all specimens. Yet, the corrosion depth does influence residual stress, revealing a detectable dilatant behaviour. In contrast, according to Yeomans (2004), zinc corrosion products have the ability to migrate from the surface of galvanized reinforcement to the concrete matrix, reducing the likelihood of concrete corrosion-induced damage. Also, galvanized steel may be exposed to chloride ion concentrations at least 4-5 times higher than steel and remain passivated at a lower pH than regular steel [23]. The combination of these two factors is commonly accepted as the basis for the superior performance of galvanized reinforcement compared to uncoated steel. Ortolan et al., (2017) indicates that mixtures with a lower water/cement ratio, and therefore with greater strength, favour the use of galvanized steel [25].

While conventional galvanization of reinforcing steel extends the service life of reinforced concrete structures and has a clearly superior carbonation resistance, recent investigations show that it may result in decreased bond between steel and concrete, with negative consequences for the bearing capacity of structures [9]. On the other hand, some authors claim that its influence is negligible [26] and further studies are therefore required to investigate in detail the bond behaviour between HDG steel and concrete [27]. Thus, this experimental research aimed at characterizing the influence of the

bond length, the concrete mixture, the pin connector and the surface contamination on the HDG steel – concrete bond behaviour by direct pushout tests.

2 EXPERIMENTAL PROGRAM

In order to study the bond between HDG steel and concrete, an experimental program was devised, based on pushout tests, to evaluate the influence of the bond length (LB) and the concrete mixture (MXX). The experimental program was composed of 40 tests divided into four groups (I, II, III and IV) according to the concrete mixture developed. For each, three different series, according to the LB, were considered.

The chosen LBs were evaluated using expressions 6.9-4 to 6.9-6 of CEB-FIP model code 90 [28]. For that, the design bond stress considered the concrete tensile strength, smooth surface of the reinforcement bar, bad adherence with the concrete matrix and the tube diameter. The bond length required to anchor the tensile force installed in the tube was calculated assuming constant tension in the tube loaded end section and the mechanical properties of the steel used, leading to an LB equal to 1281.11 mm (considering C30/37). Note that, when considering the experimental bond stress obtained by Sanz et al (2017), the LB would be 176.72 mm. Therefore, to have debonding failure during testing, three LB values (50, 75 and 150 mm), smaller than the effective bond length and compatible with the concrete cube dimensions, were adopted. The following nomenclature was adopted for the specimens: MXX_LBYY_ZZ; where XX identifies the concrete mixture number, YY identifies the bond length in millimetres and ZZ designates the number of the specimen tested adopting the same testing conditions (**Table III.1**).

To understand the influence of concrete strength and cement content on the bonding properties, the three tested concrete compositions represented common low to medium strength concretes. An additional series of tests was included in group III with the suffix designation H40, suggesting “hole of 40mm”, in order to study the concrete pin on the bond behaviour. In this case the LB of 100 mm was adopted. These holes allowed the continuity between the inner and outer regions of the tube, which may be of interest for mixed concrete–HDG steel construction systems.

A total of 32 concrete cylinders were tested to characterize its mechanical properties at 7 and 28 days after casting. Moreover, 4 steel samples were extracted from the HDG steel in order to assess its mechanical properties.

It should also be noted that the specimens of group IV were constructed by reusing the tubes tested in group I and were not cleaned, in order to evaluate the importance of a clean HDG surface on the results compared with group III.

Table III.1: Variables and specimens tested in the experimental program.

Concrete	LB [mm]	Nº of specimens	Series
M01	50	3	M01_LB50_01 to 03
	75	3	M01_LB75_01 to 03
	100	4	M01_LB100_01 to 04
M02	50	3	M02_LB50_01 to 03
	75	3	M02_LB75_01 to 03
	100	3	M02_LB100_01 to 03
M03	50	3	M03_LB50_01 to 03
	75	3	M03_LB75_01 to 03
	100	3	M03_LB100_01 to 03
	100	3	M03_LB100_H40_01 to 03
M04 ("reused" tubes)	50	3	M04_LB50_01 to 03
	75	3	M04_LB75_01 to 03
	100	3	M04_LB100_01 to 03

2.1. Materials

Concrete composition requirements included a good workability in the fresh state to guarantee the appropriate filling of the moulds, characteristics that promote the durability of the structural systems, and strength and deformability properties in the hardened state comparable to the most common ones in the type of applications studied. One of the initial consequences of these requirements is the need to use small size aggregates, which allow concrete to flow without any constraint, particularly in M03_LB100_H40. The concrete compositions developed using the modified equations proposed by Andreasen & Andersen [29] are shown in **Table III.2**.

Table III.2: Concrete composition.

Materials	Mixture 1 [kg/m³]	Mixture 2 [kg/m³]	Mixture 3 & 4 [kg/m³]
CEM II/A-L 42,5R	230.0	350.0	450.0
Limestone filler	108.0	0.0	0.0
Fine sand 0/2	338.8	335.0	294.5
Fine sand 0/4	853.0	845.0	750.0
Gravel aggregate 6/14	637.2	625.0	558.0
Superlasticizer MasterEase 3530	1.6	1.6	1.6
Plasticizer MasterPozzolith 476N	1.6	1.6	1.6
Water	157.2	157.0	201.8
w/c	0.684	0.449	0.449

2.2. Geometry and preparation of the specimens

The test specimens consisted of concrete cubes of 150×150×150 mm³, where HDG steel tubes with a total length of 200 mm were embedded, at LB of 50 mm, 75 mm or 100 mm. In order to accurately guarantee these LB, circular pieces of polystyrene foam with different thicknesses were placed under the tubes before casting. To guarantee the correct positioning of the tubes, steel frames were attached to the moulds (**Figure III.1**). Casting was carried out cautiously, to avoid HDG steel tube surface contamination with products that could alter the bond behaviour. After two days, the concrete cylinders and the pushout specimens were placed in a climatic chamber at 58±2% of relative humidity (RH) and 20±1°C of temperature (T). Prior to the tests, the foam was removed and the air gap was measured. Before assembling the specimens, the HDG steel tubes were cleaned following the recommendation of the American Galvanizers Association [30], to remove organic contaminants resulting from handling, cutting and transportation processes. For this, a mild alkaline solution with ten parts water and one part of alkaline cleaner was used.



Figure III.1: Specimen's preparation.

2.3. Testing methods

2.3.1. Concrete properties

The fresh properties of the concrete mixtures were evaluated by performing the slump test with the Abrams cone, following the European Standard EN 12350-2 [31]. The compressive behaviour was characterized by means of uniaxial compression tests in cylinders with 150 mm diameter and 300 mm in height [32]. Young's modulus (E_{cm}) and compressive strength (f_{cm}) of concrete were assessed according to EN 12390-13 [33] and EN 12390-3 [34].

Table III.3 shows the average results obtained for concrete characterization. In general, the mixtures showed good consistency and workability with no segregation, i.e. the separation of the liquid from the solid phase.

Mixture M01, M02, M03 and M04 may be characterized by a strength class C12/15, C20/25, C30/37 and C35/45, respectively [35].

Table III.3: Slump flow and mechanical properties of concrete mixtures 1 to 4.

	Slump class	$E_{cm,7d}$ **[GPa]**	$f_{cm,7d}$ **[MPa]**	$E_{cm,28d}$ **[GPa]**	$f_{cm,28d}$ **[MPa]**
M01	S1	23.57 [0.30%]	16.99 [2,23%]	22.70 [6.16%]	20.44 [2.88%]
M02	S4	26.24 [3,54%]	26.11 [11.12%]	28.10 [1.44%]	31.17 [4.66%]
M03	S4	28.85 [0.07%]	34.38 [1.12%]	28.20 [2.25%]	37.89 [0.91%]
M04	S4	26.97 [1.32%]	36.81 [0.90%]	28.03 [0.92%]	43.27 [1.22%]

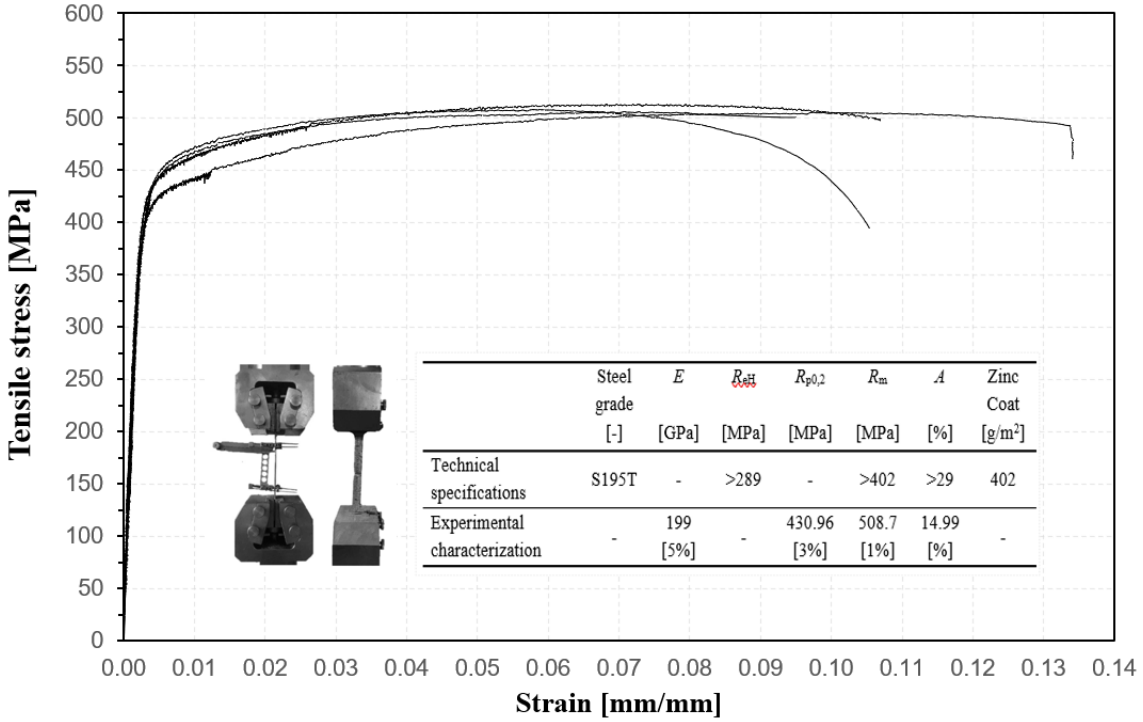
2.3.2. HDG steel properties

According to the manufacturer, the HDG steel tubes belong to the light series with a mean external diameter of 88.61 mm (CoV=0.04%) and a mean average thickness of 3.08 mm (CoV=0.86%).

According to EN 10255, it corresponds to steel with a yield strength exceeding 195 MPa, ultimate tensile strength between 320 and 520 MPa, and an ultimate tensile strain exceeding 20%.

In order to characterize the mechanical properties of the HDG steel, four uniaxial tensile tests were performed based on ISO 6892-1 [36]. The applied tensile load and the strain in the longitudinal axis at middle height were measured. The modulus of elasticity (E), the elongation (A), the tensile strength (Rm) and the upper yield strength (R_{eH}) or proof strength (R_p) were obtained.

Note that, according to the manufacturer, R_{eH} is equal to 289 MPa. However, since the experimental responses obtained in tension do not clearly exhibit a yielding plateau, the proof strength corresponding to 0.2% of strain ($R_{p0,2}$) was obtained instead. **Figure III.2** presents the steel uniaxial stress-strain curves and properties. The tested steel showed typical behaviour and rupture of the material.



	Steel grade [-]	E [GPa]	R_{eH} [MPa]	$R_{p0,2}$ [MPa]	R_m [MPa]	A [%]	Zinc Coat [g/m²]
Technical specifications	S195T	-	>289	-	>402	>29	402
Experimental characterization	-	199 [5%]	-	430.96 [3%]	508.7 [1%]	14.99 [%]	-

Figure III.2: HDG steel uniaxial stress-strain curves and properties.

2.3.3. Pushout tests

Considering the configurations and dimensions found in the literature [7,10,18,37], a concrete prism with 150 mm was adopted, in order to reduce the material waste and weight of the specimen. Supportive numerical analysis [38] were carried out to check the test configuration and ensure that the tensile strength of the surrounding concrete was not exceed by the circumferential stresses generated when the pushout force is transferred from the tube (action) to the block (reaction). The results showed that the stress distribution was satisfactory to the debonding phenomenon.

Figure III.3 shows the test setup adopted on the experimental program. The test consisted on subjecting the steel tubes to a uniaxial compressive force. The specimen was positioned on a rigid metal piece connected to a steel reaction frame. An angular spherical bearing was used at the loading section to provide stability and facilitate initial system adjustment. The specimens were tested at a loading rate of 2 μm/s until a constant residual force was reached, based on previous studies [17,18, 24,27,37]. A servo-hydraulic equipment with 100 kN (± 0.12 kN; 0.05% F.S.) maximum load capacity was used. A linear variable differential transducer (LVDT1) with a stoke of ±10 mm (linearity error of 0.24% F.S.) was used to control the test. LVDT 2, 3 and 4, positioned 120° from each other, with a

stoke of ±10 mm were used to measure the relative displacement between the tube and the concrete at the loaded end section. LVDT 5 with a stoke of ±5 mm was used at the at the free end section.

Although the bond shear stress (τ) presents an uneven distribution following a nonlinear shape along the anchorage length, an average shear stress was assumed for evaluation and comparison purposes, following the approach typically adopted in the design codes. Thus, τ_{max} was computed as shown in **Eq. (III.1)**.

$$\tau_{max} = \frac{F_{l,max}}{\pi \times D \times \left(LB - S_{l,max}\right)} \qquad \textbf{(III.1)}$$

where $F_{l,max}$ is the maximum pushout load, D is the outer diameter of the steel tube, LB is the bond length, and $s_{l,max}$ is the displacement of the tube at the loaded end section corresponding to $F_{l,max}$.

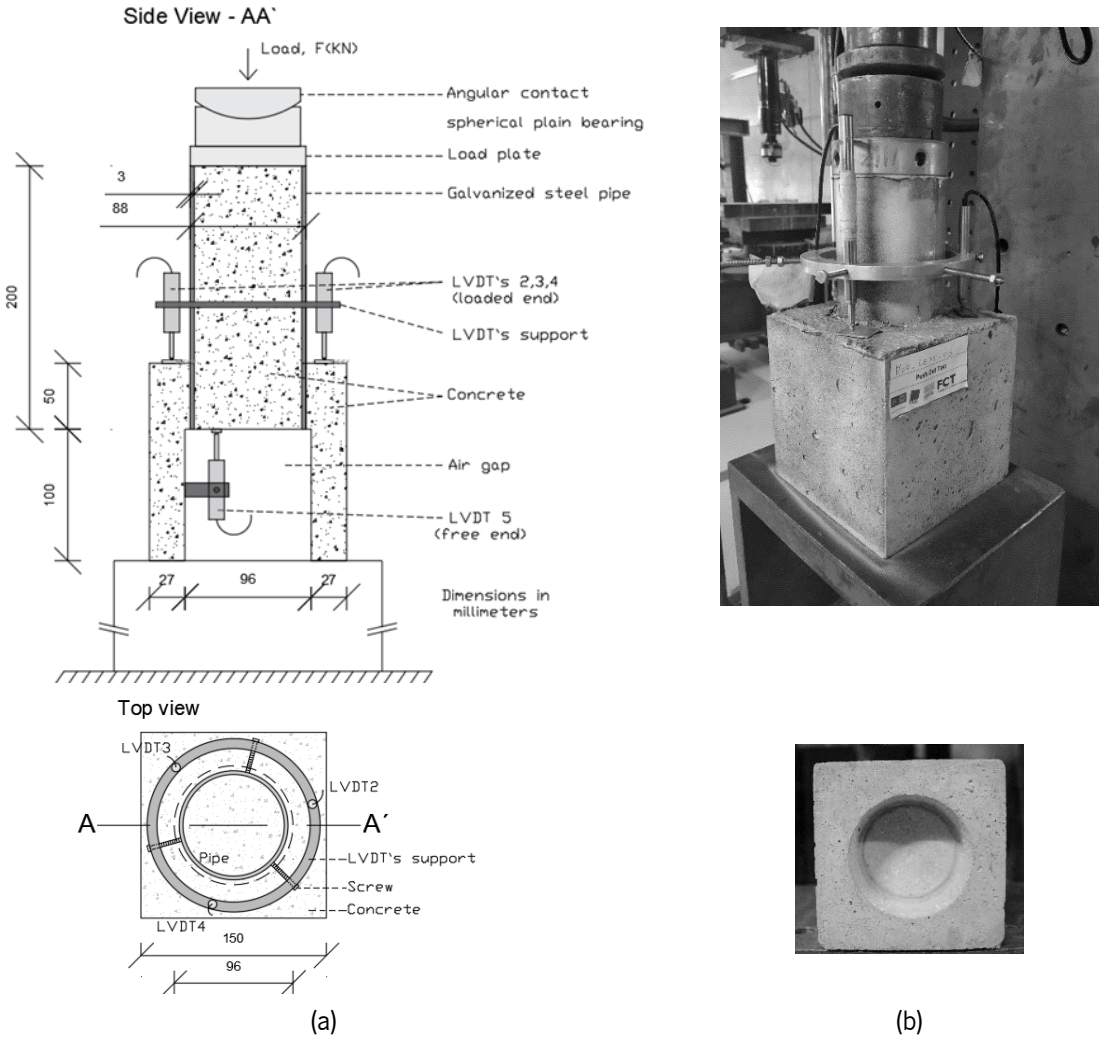
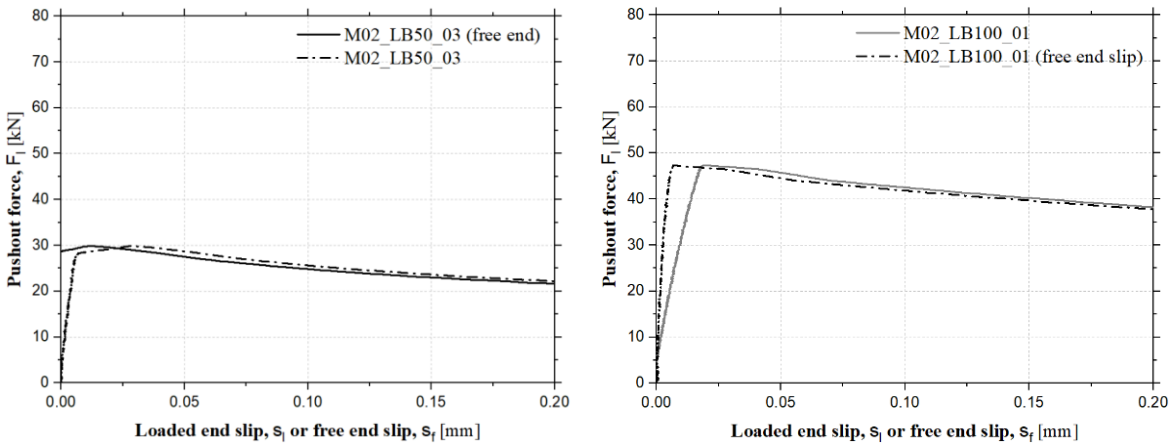


Figure III.3: Experimental setup and instrumentation adopted for pushout tests.

3 RESULTS AND DISCUSSION

3.1. Bond behaviour

Figure III.4 presents the amplification of the initial part of the typical experimental curve in terms of pushout force (F_l) versus loaded end slip (s_l) and free end slip (s_f). The loaded end slip curve allowed to discern the starting of the tube slip. In contrast, the sliding of the free end was initiated only at the final stage of the debonding experimental responses. **Figure III.5** shows the experimental responses obtained in terms of (F_l-s_l), at the loaded end zone. F_l was measured by the load cell of the actuator, and the s_l was obtained by averaging the measurements taken from the three LVDTs 2, 3 and 4.



(a) (b)

Figure III.4: Typical responses in terms of F_l-s_l and F_l-s_f: (a) M02_LB50_01 and (b) M02_LB100_01.

The experimental responses obtained are divided according to mixtures. In general, the F_l-s_l experimental responses exhibit a very similar global behaviour for all specimens. The responses are essentially marked by three distinct phases, regardless of the type of concrete used and the LB adopted. Initially an elastic behaviour phase is observed (pre-peak branch), due to the contribution of the chemical bond between concrete and the surface of the HDG steel, which results in the perfect bond between the two materials involved. The system shows a high initial stiffness, with a progressive increase of the load capacity for a very low s_l, until the peak pushout force is reached. After this first phase, the specimens exhibit a nonlinear F_l-s_l experimental response, that is characterized by a very fast reduction of the load carrying capacity and the loss of stiffness due to bond degradation (post-peak branch). It should also be noted that the transition between the pre-peak phase and the post-peak softening phase happens smoothly due to the progressive propagation of the detachment crack

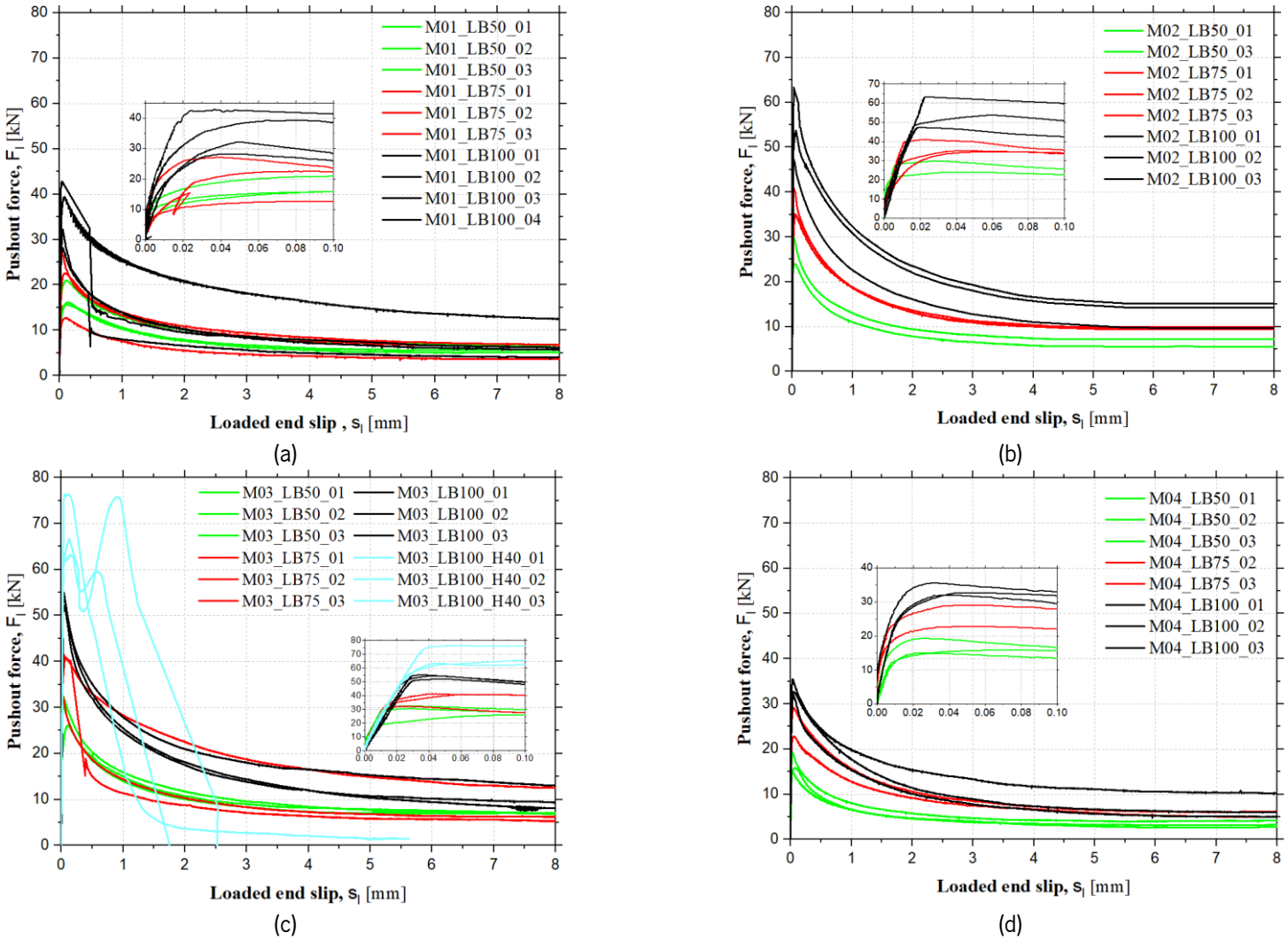


Figure III.5: F_l-s_l experimental responses: (a) M01, (b) M02, (c) M03 and (d) M04.

that breaks the chemical bond, and due to the remaining physical contact between materials. In the post-peak phase, the bond behaviour is governed by friction, which is typical in smooth surfaces. The descending shape of the F_l-s_l post-peak response reflects the gradual degradation of the interface, which leads to the reduction of the load bearing capacity. As the loaded end slip increases and damage at the interface progresses due to friction, the force reduction tends to smooth, and a residual force plateau is reached. Overall, despite slight variations between different experimental responses, the results are quite consistent and show well defined shapes. Note that tests that experienced problems during testing, were disregarded and not considered for the average results

Table III.4 summarizes the main experimental results obtained. The typical failure mode (FM) and the concrete compressive strength at 28 days ($f_{cm,28d}$) for each group series are also shown. $F_{l,max}$ represents the maximum pushout force, $s_{l,max}$ is the loaded end slip at maximum pushout force, $s_{f,max}$ is the free end slip at maximum pushout force and τ_{max} is the maximum average shear stress at the interface between the HDG steel tube and the concrete surface. The parameter F_r is the residual pushout force, defined as the pushout force obtained when s_l reaches 8 mm. G_f represents the energy dissipated during the pushout test until failure, and is obtained by computing the area under the F_l -s_l experimental curve until a s_l of 8 mm is reached. $F_r/F_{l,max}$ is the ratio between F_r and $F_{l,max}$.

The normalized shear strength ($\bar{\tau}_{max}$), and the normalized energy dissipated during pushout testing until failure ($\bar{G}_f$) were computed according to **Eq. (III.2)** and **Eq. (III.3)**, respectively. The average concrete tensile strength (f_{ctm}) was estimated according to Eurocode 2 [35] and CEB-FIP Model Code [28], following **Eq. (III.4)**.

$$\bar{\tau}_{max} = \frac{F_{l,max}}{f_{ctm} \times \pi \times D \times (LB - S_{l,max})} \quad \textbf{(III.2)}$$

$$\bar{G}_f = \frac{G_f}{f_{ctm} \times \pi \times D \times \left(LB - S_{l,max}\right) \times 8} \quad \textbf{(III.3)}$$

$$f_{ctm} = 0.3 \times f_{ck}{}^{\left(\frac{2}{3}\right)} \quad \textbf{(III.4)}$$

In a first observation to **Table III.4**, it appears that the value of CoV is more consistent and homogeneous for $F_{l,max}$ e τ_{max}, varying between 2% and 16%, which are considered good for the type of test performed. With regard to the remaining variables, there is greater variability of results and disparity between them. For example, in the case of F_r, the minimum and maximum CoV were 2% and 45%, respectively. The remaining variables follow a similar pattern.

Table III.4: Main pushout experimental results obtained for each mixture and series (average values).

Mixture	Series	$f_{cm,28d}$ [MPa]	$F_{l,max}$ [kN]	$s_{l,max}$ [mm]	$s_{l,max}$ [mm]	τ_{max} [MPa]	F_r [kN]	G_f [kN.mm]	$F_r/F_{l,max}$ [%]	$\overline{\tau}_{máx}$ [-]	$\overline{G}_f$ [-]	FM
M01	M01_LB50	20.44 [3%]	17.63 (13%)	0.11 (11%)	n.a	1.19 (12%)	5.81 (12%)	62.86 (13%)	33.06 (6%)	0.74 (12%)	0.33 (11%)	$D^{1,2,3}$
	M01_LB75		24.83 (9%)	0.07 (23%)	n.a	1.15 (6%)	6.46 (5%)	77.15 (3%)	26.11 (5%)	0.71 (6%)	0.28 (0%)	$D^{1,2,3}$
	M01_LB100		35.67 (16%)	0.05 (25%)	n.a	1.24 (14%)	7.14 (45%)	89.78 (41%)	19.78 (37%)	0.77 (14%)	0.25 (40%)	$D^{1,3,4}$ DC^{2}
M02	M02_LB50	31.17 [5%]	26.91 (11%)	0.04 (21%)	0.04 (71%)	1.76 (11%)	6.37 (13%)	60.21 (26%)	23.61 (2%)	0.72 (10%)	0.20 (25%)	$D^{1,2,3}$
	M02_LB75		36.92 (8%)	0.04 (38%)	0.04 (25%)	1.61 (8%)	9.65 (2%)	104.35 (1%)	26.29 (7%)	0.62 (1%)	0.23 (0%)	$D^{1,2,3}$
	M02_LB100		54.76 (12%)	0.03 (55%)	0.02 (47%)	1.88 (11%)	12.98 (18%)	151.13 (23%)	23.58 (10%)	0.77 (11%)	0.27 (15%)	$D^{1,2,3}$
M03	M03_LB50	37.89 [1%]	29.73 (9%)	0.05 (63%)	0.06 (69%)	2.05 (7%)	7.00 (2%)	81.51 (4%)	23.78 (11%)	0.71 (7%)	0.24 (5%)	$D^{1,2,3}$
	M03_LB75		38.20 (11%)	0.04 (31%)	0.05 (42%)	1.79 (12%)	8.18 (42%)	100.22 (38%)	21.29 (37%)	0.62 (12%)	0.20 (39%)	$D^{1,2}$ DC^{3}
	M03_LB100		55.88 (2%)	0.04 (13%)	0.05 (68%)	1.94 (1%)	10.13 (21%)	137.22 (11%)	18.81 (20%)	0.67 (1%)	0.21 (11%)	$D^{1,2,3}$
	M03_LB100_H40		71.86 (8%)	-	-	2.81 (9%)	-	89.41 (25%)	-	0.88 (9%)	-	$S^{1,2,3}$
M04 (reused tubes)	M04_LB50	43.27 [1%]	16.66 (11%)	0.04 (53%)	0.02 (45%)	1.12 (7%)	3.39 (18%)	38.56 (11%)	20.28 (10%)	0.35 (7%)	0.10 (7%)	$D^{1,2,3}$
	M04_LB75		25.94 (12%)	0.05 (4%)	0.04 (48%)	1.20 (9%)	5.61 (10%)	71.55 (8%)	21.65 (1%)	0.37 (9%)	0.13 (5%)	$D^{nd,2,3}$
	M04_LB100		33.38 (5%)	0.04 (17%)	0.04 (18%)	1.16 (2%)	7.08 (31%)	89.48 (20%)	20.94 (27%)	0.36 (2%)	0.12 (17%)	$D^{1,2,3}$

Notes: the values between parentheses are the coefficients of variation (% CoV);. The upper number next to the type of FM specified the specimen with that FM.

However, and despite the CoV values being higher than desirable, they are considered acceptable and normal since some of the mechanisms related to these variables present a fragile and sensitive behaviour.

Furthermore, despite all the care taken during the production of the specimens, it is important to mention that the heterogeneity of the concrete and the geometric imperfections may also have influenced this variability. In general, based on the results presented in **Table III.4**, there is an evident effect of the concrete mixture on the bond response values obtained. Comparing the mixtures (M01 to M03), the higher $f_{cm,28d}$ (M03 > M02 > M01) resulted in higher $F_{l,max}$, τ_{max} and F_r. Nevertheless, the order of magnitude of $\overline{\tau}_{máx}$ and $\overline{G}_f$ were similar between groups. It was possible to identify a polynomial trend in the relationship between the compressive strength of the concrete and the bond shear stress established at the interface. The influence on LB on the bond behaviour is less pronounced for the range of LB studied. Increasing LB led to higher $F_{l,max}$ in all three mixtures, as expected due to the larger contact area of the bonding interface. The same was observed for F_r and G_f. The τ and $\overline{\tau}$ values showed to be consistent among specimens of the same series, as well as among series of the same group, for all groups. In addition, the $F_r/F_{l,max}$ ratio was consistent and values of the same order of magnitude were observed for all specimens. An average value of 23.27% was found, with a maximum of 33.06% and a minimum of 18.81%.

The clearly different results obtained for M04 when comparing to M03 show that contaminated surface do not lead to the same results. Possible causes may be the previous contact of the bond surface with cement paste, which may produce a reaction that promotes better chemical bonding the first time it occurs. When the tubes are reused, part of this effect may be lost, because the main mechanism that contributes to the bond strength is the chemical bond between the fresh concrete and the galvanized coating. The reuse of the tubes may therefore result in a weaker and less uniform bond between the materials. The results of M04 are important to show that transport and handling of HDG steel during construction must be done with care, as recommended by the associations of HDG [30], in order to fully preserve the original interface properties. **Figure III.6** shows the F_r-s_l responses computed for all specimens tested, considering each bond length and concrete composition. The average responses were obtained by averaging the pushout force obtained at each loaded end slip for all specimens of the same LB and concrete strength. In general, test specimens from different groups with the same LB presented very similar F_r-s_l initial stiffnesses and overall response. Despite this, the type of concrete showed to clearly influence the load carrying capacity. Therefore, the maximum shear stress is the

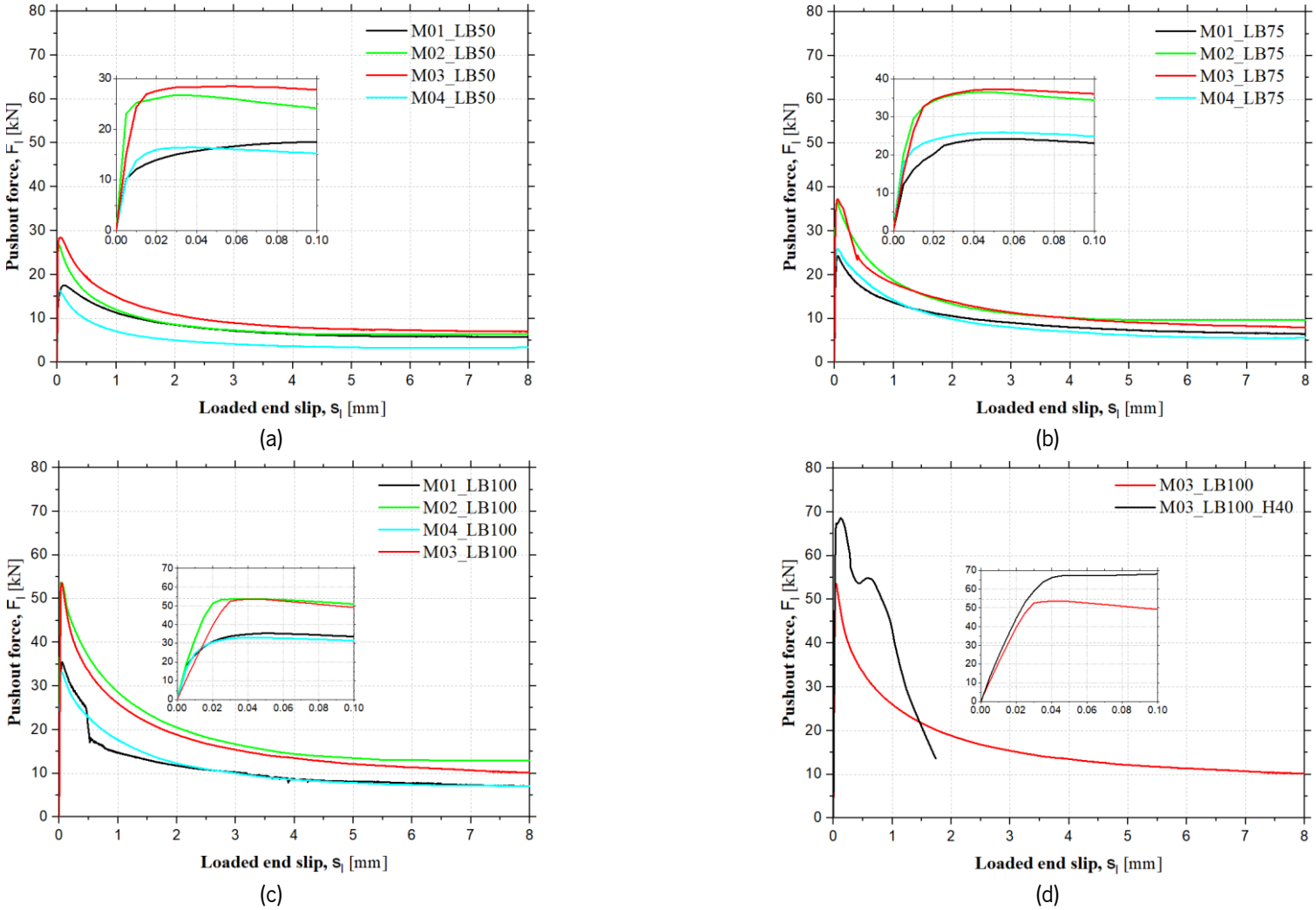


Figure III.6: Average pushout force versus loaded end slip (*Fl-sl*) responses computed for all specimens tested: (a) LB50, (b) LB75, (c) LB100 and (d) LB100 vs LB100_H40.

most affected variable when concrete strength and cement content are increased. The concrete pin adopted in the LB100_H40 specimens influenced the shape and magnitude of the values obtained in the experimental response, especially in the post-peak phase, and softening was not gradual as in the other cases (**Figure III.6**d).

3.2. Failure modes

Figure III.7 shows representative images of the most frequently FM. In general, three different failure modes were observed:

- D - pushout debonding failure at the concrete to HDG steel tube interface, which consists on the full development of a tunnel crack at the interface between both materials and the slipping of the steel tube with respect to the concrete block. This was the most common failure mode, which indicates an appropriate concrete substrate behaviour and the objective characterization of the bond behaviour. After removing the HDG steel tubes from the concrete substrates, homogeneous cement bonding films were visible at the surface of the tubes, as well as friction marks (**Figure III.7**(a));
- DC –formation of a thin crack in the concrete block during pushout debonding failure, visible after $F_{l,max}$ is reached (**Figure III.7**(b)). Given the reduced crack opening, a colour line adjacent to the crack was used to better identify the crack path. The surrounding concrete was not able to accommodate the tensile stresses generated during the push-out test, possibly influenced by a small vertical misalignment of the tube. Specimens M01_LB100_02 and M03_LB75_03 cracket during testing, and a sudden decrease in the F_l was observed. Despite that, the experimental F_l-s_l responses showed a similar overall shape when compared to the specimens with debonding failure (D). Note that M04_LB75_01 showed a crack even before testing, probably caused by any accidental impact. A homogeneous cement bonding films were also visible at the steel surface.
- S – premature failure of the concrete block by splitting (**Figure III.7**(c)). This failure mode was observed for the specimens M04_LB100_H40 and occurs due to excessive radial tensile stresses originated by the pushout load transfer from the HDG steel tube to the concrete block, which results in cracks in the transverse and longitudinal directions. The pushout behaviour is determined by the characteristics of concrete block itself and not by the bond properties, therefore the $F_{l,max}$ is underestimated. In this case, the obtained experimental responses were

quite different. After reaching a maximum load value, which was higher than in the specimens of the same type without holes, the concrete cubes suffered splitting failure, resulting in an abrupt drop in the load carrying capacity to 0 kN. The size of the concrete cubes would have to be substantially increased in order to avoid premature failure of the concrete block and allow full mobilization of the maximum bond strength. This means that, although a higher bond strength was obtained, the values could be even higher if the concrete blocks remained intact.



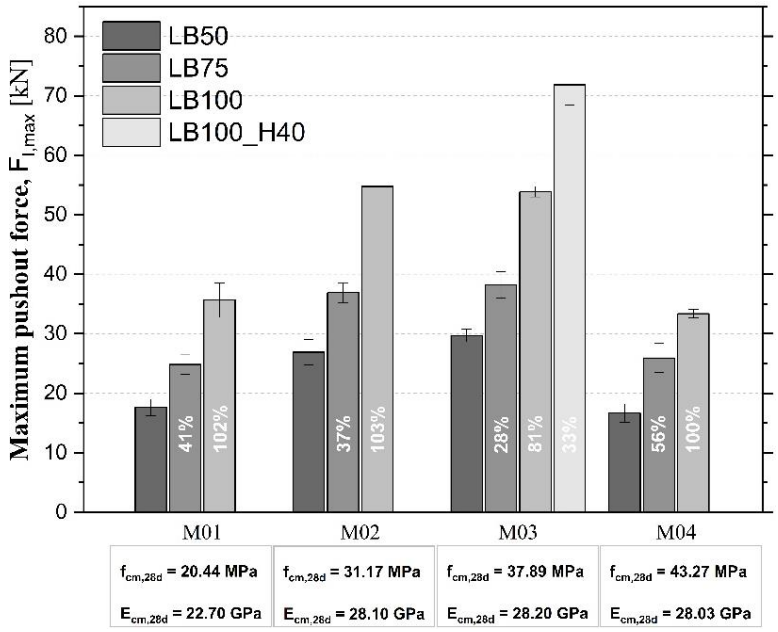
(a) (b) (c)

Figure III.7: Failure modes: (a) D, (b) DC and (c) S.

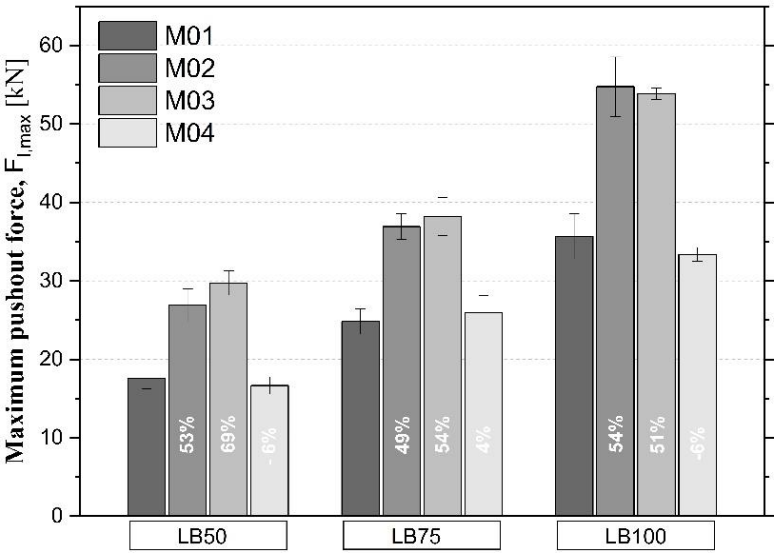
3.3. Maximum pushout force ($F_{l,max}$)

Figure III.8 shows the average results obtained in terms of $F_{l,max}$ with respect to concrete strength (**Figure III.8**(a)) and the bond length (**Figure III.8**(b)). The values within the bars represent the percentage increase compared to the first bar's value. LB100_H40 was compared to LB100.

For M01, $F_{l,max}$ increased by +41% when comparing LB50 and LB75, and +102% when LB50 and LB100 are compared. In the case of M02, when comparing LB50 to LB75 and LB50 to LB100, the increase was +37% and +103%, respectively. For M03, the increase was about +28% and +81% when comparing LB50 to LB75 and LB50 to LB100, respectively. Furthermore, the specimens LB100_H40 experienced an increase of +33% when compared to LB100. Regarding M04, the increase was +56% and +100% for the same bond lengths comparison. In summary, it was found that for the different series the maximum pull-out force, $F_{l,max}$, was approximately proportional to the bond length.



(a)



(b)

Figure III.8: Influence of the concrete strength, M01 to M04 (a), and LB (b), on the average value of $F_{l,max}$ within each series.

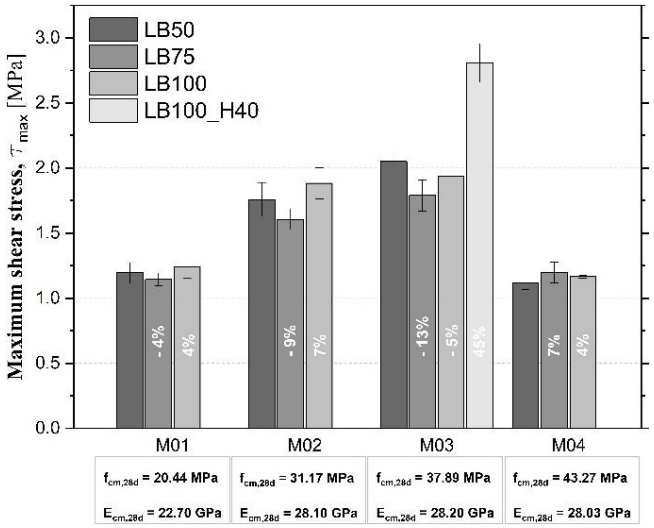
Figure III.8(b) shows that the parameters obtained in the tests were also clearly influenced by the concrete mixture and the cement content. For LB50, with respect to M01 a variation of $F_{l,max}$ of +53%, + 69% and -6% for mixtures M02, M03 and M04, respectively, was obtained. In the case of LB75, the variation of $F_{l,max}$ was +49%, +54% and +4%. For LB100, a variation of +54%, +51% and -6% was found. Summarizing, for all the three LB a significant increase in $F_{l,max}$ was found when M01 and M02 are compared. Between M02 and M03 this increase was less significant. In the case of M04, the values were very similar to those of M01.

3.4. Maximum shear stress (τ_{max})

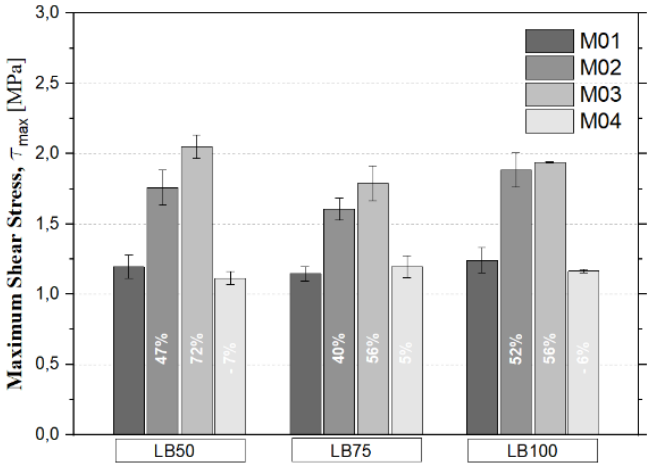
Despite slight variations, the τ_{max} and the $\bar{\tau}_{max}$ values for the various LB of the same concrete mixture were quite similar and consistent, as shown in **Figure III.9**(a). The average value of τ_{max} referring to the average obtained from all LBs of the same concrete mixture were also computed. In the case of M01, τ_{max} averaged 1.19±0.04 MPa (±3%). Comparing LB75 and LB100 to LB50, variations were -4% and +4%, respectively. For M02, τ_{max} averaged 1.75±0.11 MPa (±6%), with variations of -9% and +7%. For M03, the averaged of τ_{max} was 1.93±0.11 MPa (±6%), with variations of -13% and -5%. Comparing LB100 to LB100_H40, a significant increase of +45% in τ_{max} was observed, suggesting improved adherence promoted by the concrete pin. In M04, the average value of τ_{max} was 1.16±0.03 MPa (±3%), with variations of +7% and +4%. τ_{max} occurred at loaded end slips between 0.04 mm (most common) and 0.11 mm. In terms of $\bar{\tau}_{max}$, a mean value of 0.74±0.02 (±3%), 0.70±0.06 (±9%), 0.67±0.04 (±6%) and 0.36±0.01 (±3%) was found for the specimens of M01, M02, M03 and M04, respectively (**Figure III.9**(c). The τ_{max} experimentally obtained for a particular LB would require a higher LB in order to meet the maximum `theoretical` value. The relations between LB, f_{cm} and τ_{max} indicating that the LBs adopted are lower than the effective LB (**Figure III.9**(e) and (f)).

The concrete strength influenced the τ_{max}, regardless of the LB. An average variation of 53.8% was found considering M01 to M03, with a maximum of +72% (**Figure III.9**(b)). Despite the variations noted, the τ_{max} showed increasing values for the specimens of mixtures M03 > M02 > M03, which corresponded to the increase in the concrete compressive strength ($f_{cm,M03} > f_{cm,M02} > f_{cm,M01}$). The increasing of f_{cm} results in a polynomial increase in the experimental bond stress, although the theoretical values show linear increase.

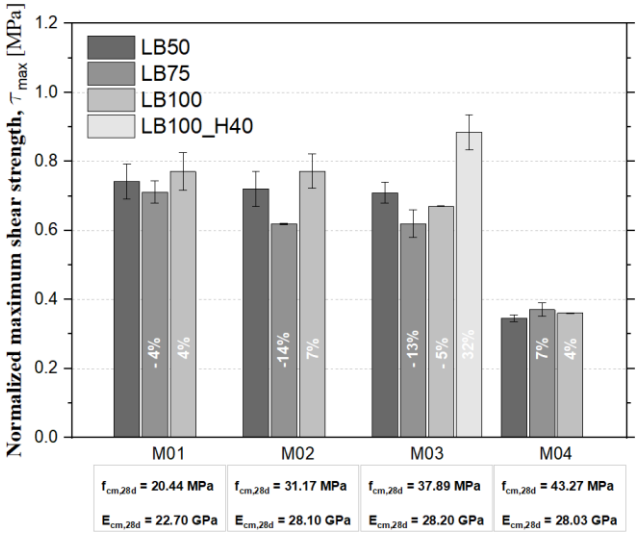
M04 presented identical values of τ_{max} to those of M01 showing that the surface contamination significantly reduced the bond stress in around -39.5% (M04 to M03), equivalent to a reduction in the concrete's compressive strength of 53% (**Figure III.9**(e) and (f)). Considering the mechanical parameters of the concrete mixtures presented in **Table III.3**, it was found that the mixture M02 was superior to M01 both in terms of compressive strength (52%) and modulus of elasticity (+24%). M03 was superior in 113% and +23% and, M04 in +85% and +24% in terms of $f_{cm,28d}$ and $E_{cm,28d}$, respectively.


LB50
LB75
LB100
LB100_H40
Maximum shear stress, τ_{max} [MPa]
3.0
2.5
2.0
1.5
1.0
0.5
0.0
- 4%
4%
- 9%
7%
- 13%
- 5%
45%
7%
4%
M01
M02
M03
M04
$f_{cm,28d}$ = 20.44 MPa
$E_{cm,28d}$ = 22.70 GPa
$f_{cm,28d}$ = 31.17 MPa
$E_{cm,28d}$ = 28.10 GPa
$f_{cm,28d}$ = 37.89 MPa
$E_{cm,28d}$ = 28.20 GPa
$f_{cm,28d}$ = 43.27 MPa
$E_{cm,28d}$ = 28.03 GPa

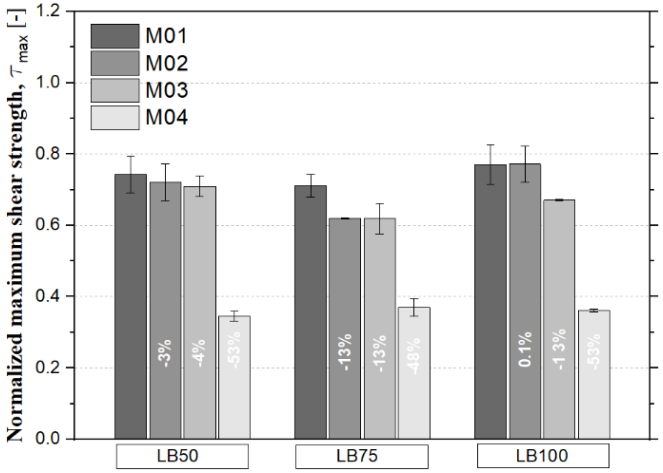
(a)


M01
M02
M03
M04
Maximum Shear Stress, τ_{max} [MPa]
3,0
2,5
2,0
1,5
1,0
0,5
0,0
47%
72%
- 7%
40%
56%
5%
52%
56%
- 6%
LB50
LB75
LB100

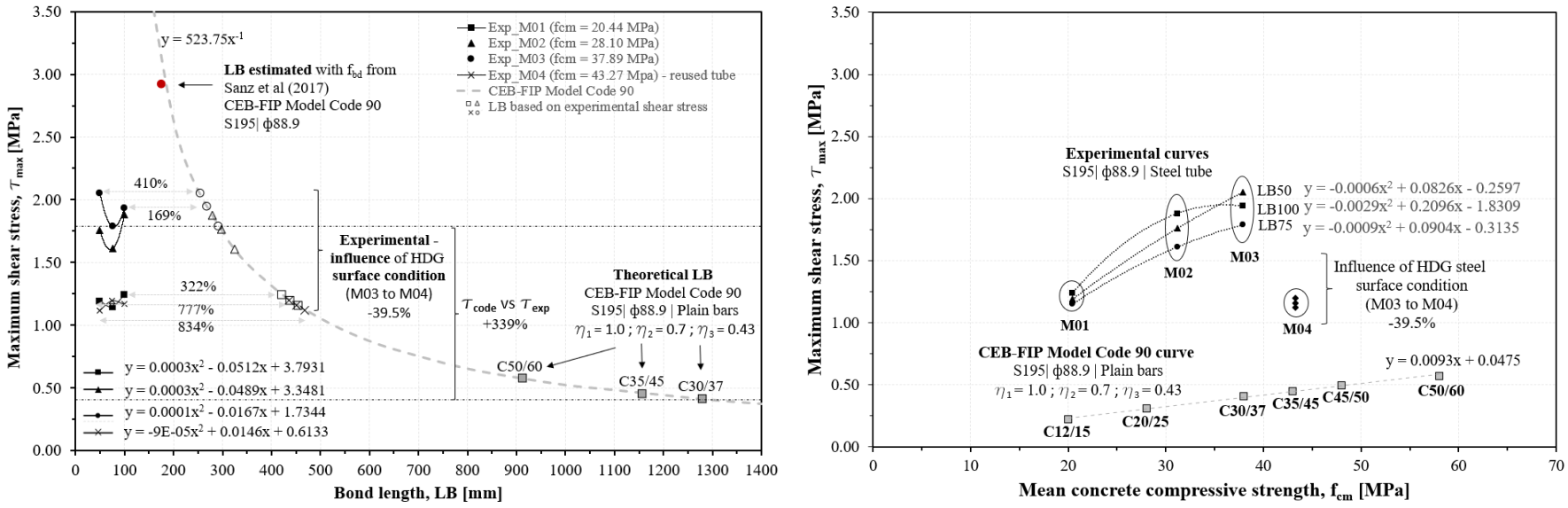
(b)


LB50
LB75
LB100
LB100_H40
Normalized maximum shear strength, τ_{max} [MPa]
1.2
1.0
0.8
0.6
0.4
0.2
0.0
- 4%
4%
-14%
7%
- 13%
- 5%
32%
7%
4%
M01
M02
M03
M04
$f_{cm,28d}$ = 20.44 MPa
$E_{cm,28d}$ = 22.70 GPa
$f_{cm,28d}$ = 31.17 MPa
$E_{cm,28d}$ = 28.10 GPa
$f_{cm,28d}$ = 37.89 MPa
$E_{cm,28d}$ = 28.20 GPa
$f_{cm,28d}$ = 43.27 MPa
$E_{cm,28d}$ = 28.03 GPa

(c)


M01
M02
M03
M04
Normalized maximum shear strength, τ_{max} [-]
1.2
1.0
0.8
0.6
0.4
0.2
0.0
-3%
-4%
-53%
-13%
-13%
-48%
0.1%
-1 3%
-53%
LB50
LB75
LB100

(d)



(e) (f)

Figure III.9: Influence of the f_{cm} and LB, on the average values of τ_{max} (a, b, e, f), and $\bar{\tau}_{max}$ (b, d), within each series.

Concretes with a higher resistance result in a better chemical bond strength in a polynomial relationship. Although this trend was observed between M01, M02 and M03, the same did not occur between M04 (reused tube) and M01. In this case, the values of $F_{l,max}$ and τ_{max} were very similar despite its superiority in the f_{cm}. However, looking at the homogenized variables, it appears that the values obtained for M04 are about half of those mixtures, and this difference cannot be neglected (**Figure III.9**(d)). Independently of LB and contrary to what happened for τ_{max}, the specimens of M01 resulted in $\bar{\tau}_{max}$ values higher than those obtained for M04, which highlights the importance of normalizations of the variables. Despite small variations, the values of $\bar{\tau}_{max}$ are all approximate.

3.5. Energy dissipated (G_f)

The total energy is clearly influenced by both LB (**Figure III.10**(a)) and the concrete mixture (**Figure III.10**(b)).

In the case of the mixture M01, there was a +23% and +43% variation between LB50 and LB75 and between LB50 and LB100, respectively. In mixture M02 the variation was +73% and +151%. In the case of M03, the variation was +23% and +69%. In mixture M04 there was a variation of +86% and +132%.

The LB value was found to have greater influence on total energy in mixtures M02 and M04 and less influence in mixtures M01 and M03. In the case of LB100_H40, the specimen presented a fragile rupture and as a consequence the total energy was affected. Although the type of concrete influences the total energy, it should be noted that the variations were smaller than those found on the influence of anchorage length. In general, apart from LB50, the specimens for mixture M02 had a higher total energy. Regarding to normalized energy, it appears that the values were similar between all groups, with a mean value of 0.245 (**Figure III.10**(c) and (d)).

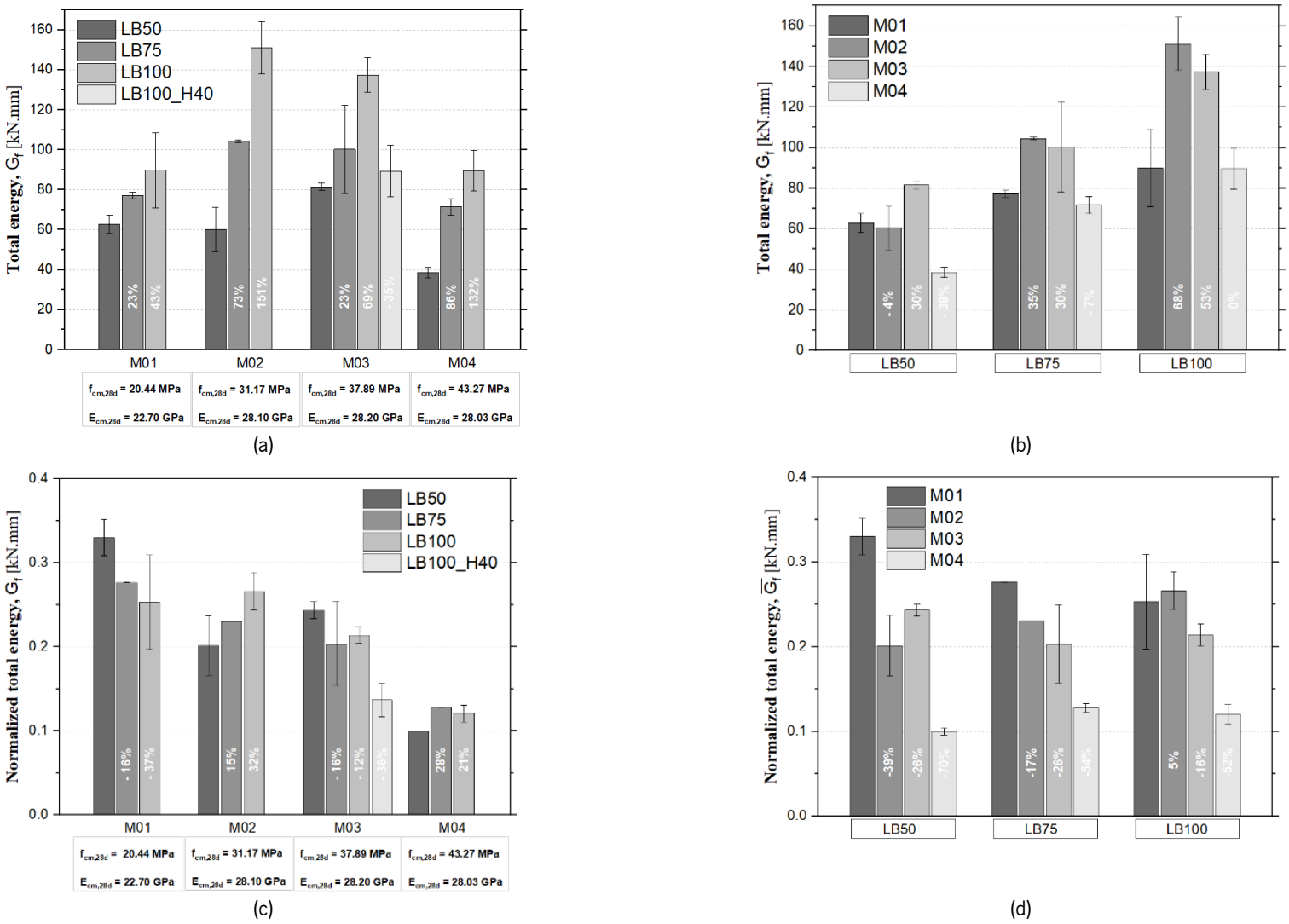


Figure III.10: Influence of the type of concrete and LB, on the average values of the energy dissipated during pushout testing, G_f (a, b), and $\bar{G}_f$ (c,d), within each series.

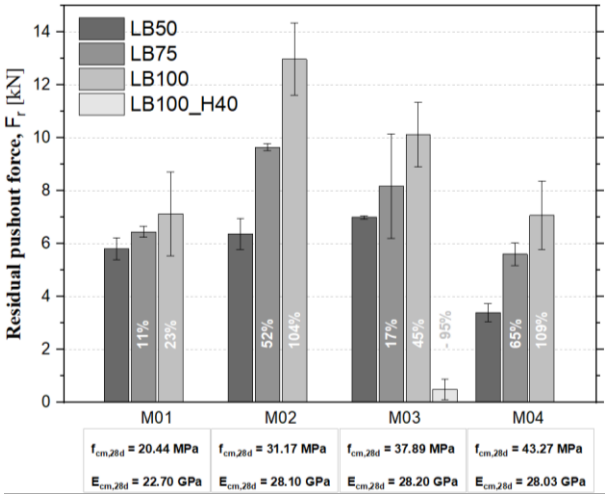
3.6. Residual force (F_r)

Figure III.11 shows that the residual force increases with increasing LB, regardless of the concrete mixture. The results also show a greater increase in residual strength for higher strength concrete, except for M04. While in the M01 mixture the increase between LB50 and LB75 was +11% and between LB50 and LB100 was +23%, in the case of mixtures M02 and M04 the increments were more than double. In M02 there was an increase of +52% and +104% and in the case of M04 a variation of +65% and +109% was observed. For M03, a variation of +17% and +45% was found. Note that the F_r obtained for the series LB100_H40 was near 0 kN, which was expected considering the brittle type of rupture observed.

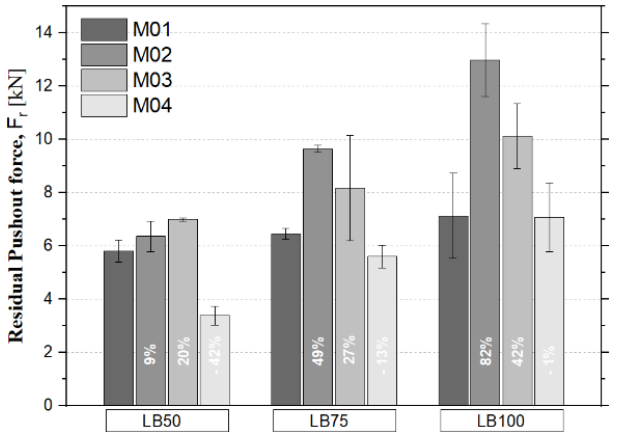
The highest residual strength values were obtained for the M02 with a value of 12.98 kN for the series LB100. The lowest values correspond to the M04, series LB50, with a value of 3.39 kN.

In addition, the $F_r/F_{l,max}$ ratio was consistent and the values present the same order of magnitude for all specimens. Thus, considering all the specimens, an average value of $F_r/F_{l,max}$ equal to +23.3% was found, with a maximum of 33.1% and a minimum of 18.8%.

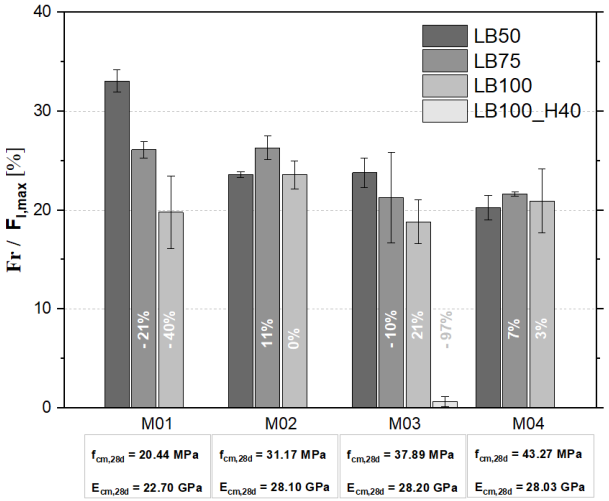
According to the literature, the three main mechanisms that influence bond strength are [23]: (i) the coating itself, (ii) the chemical reaction between zinc and the wet cement paste and (iii) the retarding effect of corrosion products that result from the reaction of zinc with the wet cement paste on cement hydration. As noted, the chemical component is an important mechanism that can actively influence the bond strength. The alkaline environment of the fresh concrete activates the galvanized steel surface, and zinc layer corrodes until passivation occurs. Since only one type of coating was used in this work for four different concrete mixtures, it is natural that different reaction products are formed. Thus, this may justify the variations observed for test specimens of different mixtures but with the same LB. Indeed, the concrete mixture seems to provide more influence on the results than the anchorage length.



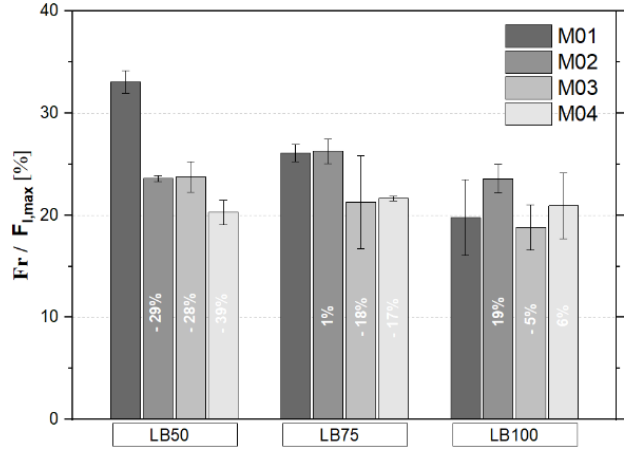
(a)



(b)



(c)



(d)

Figure III.11: Influence of the type of concrete, M01 to M04, and of LB, on the average values of F_r, (a, b) and $F_r/F_{l,max}$ (c,d), within each series.

It is important to emphasize the importance and care that must be taken when working with composite systems made of concrete and galvanized steel in order to prevent involuntarily contamination of the galvanized surface Although not intentionally, the existence of contaminating products such as oils and their variants resulting from the handling, transportation and application on site of this type of material can cause a decrease in the adherence between the materials, as stated by the American Galvanizers Association, that also educates on how to deal and decontaminate possible contaminated surfaces.

4 CONCLUSIONS AND FUTURE WORKS

This sub-chapter summarized the results obtained in an experimental program composed by 40 pushout tests performed in concrete cubes reinforced with HDG steel tubes, 32 cylinders to characterize concrete mixtures and 4 steel specimens to characterize the mechanical properties. The results obtained led to the following main conclusions:

- The behaviour of all the tested specimens was consistent and similar to those obtained by Sanz et al (2017): the curves showed a positive initial steep slope, as a result of the high stiffness of the system due to the strong bond between the two materials, raising up to $F_{l,max}$ and then progressively descend to a residual stress plateau.
- LB and concrete mixture did not significantly influence the shape of the curve F_l-s_l, however both influenced the values obtained of $F_{l,max}$, G_f and F_r.
- Higher f_{cm} led to a higher τ_{max} in a polynomial relationship;
- The τ_{max} experimentally obtained for a particular LB would require a higher LB in order to meet the maximum `theoretical` value, depending on the concrete strength. The relations between LB, f_{cm} and τ_{max} indicating that the LBs adopted were significantly lower than the effective LB;
- The importance of a clean HDG surface, in contrast to a contaminated surface, is clear on the results as the later reduces bonding in -39.5%, which may be equivalent to a reduction in the concrete's strength of 53%.
- The failure mode observed was consistent. Debonding (D), debonding with crack (DC) and splitting (S) were observed. Debonding phenomenon was the main FM, as expected.

- The contribution of the concrete pin achieved through the pipe hole improved the adhesion between materials. It should be noted, however, that the global failure mode was not the desired one and that the adherence bond stress could be even higher than that obtained.
- The test specimens and the methodology adopted proved to be adequate to fully characterize the bond behaviour between HDG steel tube and concrete.

Finally, the present study represents a first step for an extended investigation to study the effect of seawater on bond behaviour over time for marine applications. Some of the aspects to be considered include environmental factors' effect or the corrosion mechanism in bond behaviour (durability). Microstructural analysis with chemical assessment of the HDG coating–concrete interface could also help to clarify some of the bond mechanisms established during curing and corrosion process. Investigate the constitutive model of bond-slip and include it in analytical and numerical models.

Acknowledgements

The financial supports of Fundação para a Ciência e Tecnologia (FCT) co-supported by European Social Fund (FSE) [grant number SFRH/BD/137220/2018]; and of Comissão de Coordenação e Desenvolvimento Regional do Norte (CCDR-N) and Fundo Europeu de Desenvolvimento Regional (FEDER) within the research project ‘‘NEXTSEA” [grant number NORTE-01-0145-FEDER-000032] are gratefully acknowledged.

Conflict of interest

The authors declare that they have no conflict of interest.

References

[1] Liu PC. Damage to concrete structures in a marine environment. Mater Struct 1991;24(4):302–307. https://doi.org/10.1007/BF02472086.

[2] Cruz F, Pereira E, Valente IB, Tiago M, Maslov D, Pinheiro M. Structural design of an innovative multifunctional artificial reef. Oceans 2018 MTS/IEEE Charleston, IEEE; 2018, p. 1–7. https://doi.org/10.1109/OCEANS.2018.8604587.

[3] Ragab AM, Elgammal MA, Hodhod OAG, Ahmed TES. Evaluation of field concrete deterioration under real conditions of seawater attack. Constr Build Mater 2016;119:130–144. https://doi.org/10.1016/j.conbuildmat.2016.05.014.

[4] Shi X, Xie N, Fortune K, Gong J. Durability of steel reinforced concrete in chloride environments: An overview. Constr Build Mater 2012;30:125–138. https://doi.org/10.1016/j.conbuildmat.2011.12.038.

[5] González JA, Vazquez AJ, Jauregui G, Andrade C. Effect of four coating structures on corrosion kinetic of galvanized reinforcement in concrete. Mater Struct 1984;17(6):409–414. https://doi.org/10.1007/BF02473980.

[6] Figueira RB, Silva CJR. Corrosion of hot-dip galvanized steel reinforcement. Corros Prot Mater 2014;33(3):51–61.

[7] Coccia S, Imperatore S, Rinaldi Z. Influence of corrosion on the bond strength of steel rebars in concrete. Mater Struct 2016;49(1–2):537–551. https://doi.org/10.1617/s11527-014-0518-x.

[8] Baltazar-Zamora MA, et al. Corrosion behaviour of galvanized steel embedded in concrete exposed to soil type MH contaminated with chlorides. Front Mater 2019;6:257. https://doi.org/10.3389/fmats.2019.00257.

[9] Tej P, Kour M, Pokorny P. Evaluation of the impact of corrosion of hot-dip galvanized reinforcement on bond strength with concrete: A review. Constr Build Mater 2017;132:271–289. https://doi.org/10.1016/j.conbuildmat.2016.11.096.

[10] Rivera-Corral JO, Fajardo G, Arliguie G, Orozco-Cruz R, Deby F, Valdez P. Corrosion behaviour of steel reinforcement bars embedded in concrete exposed to chlorides: Effect of surface finish. Constr Build Mater 2017;147:815–826. https://doi.org/10.1016/j.conbuildmat.2017.04.186.

[11] Hellio C, Yebra DM, editors. Advances in marine antifouling coatings and technologies. Amsterdam: Elsevier; 2009.

[12] Sena-Cruz J, Cunha VMCF, Camões A, Barros JAO, Cruz P. Modelling of bond between galvanized steel rebars and concrete. In: Proceedings of the Congresso de Métodos Numéricos em Engenharia 2009; 2009. p. 1–15.

[13] Yu Z, Hu J, Meng H. A review of recent developments in coating systems for hot-dip galvanized steel. Front Mater 2020;7:74. https://doi.org/10.3389/fmats.2020.00074.

[14] Yeomans SR. Galvanized reinforcement in bridge and coastal construction. In: Proceedings of the 20th Congress of IABSE; New York City, NY, USA; 2019. p. 1592–1598.

[15] Arguillarena A, Margallo M, Urtiaga A, Irabien A. Life-cycle assessment as a tool to evaluate the environmental impact of hot-dip galvanisation. J Clean Prod 2021;290:125676. https://doi.org/10.1016/j.jclepro.2020.125676.

[16] Wang F, Cheng Z, Shen J. Flexural fatigue behaviour of butt-welded circular concrete-filled double skin steel tube (CFDST): Experimental study and numerical modelling. Mar Struct 2023;88:103380. https://doi.org/10.1016/j.marstruc.2022.103380.

[17] Tao Z, Song TY, Uy B, Han LH. Bond behaviour in concrete-filled steel tubes. J Constr Steel Res 2016;120:81–93. https://doi.org/10.1016/j.jcsr.2015.12.030.

[18] Chen Z, Zhou J, Ban M, Wang X. Residual bond behaviour of steel reinforced recycled aggregate concrete after exposure to elevated temperatures. Front Mater 2020;7:142. https://doi.org/10.3389/fmats.2020.00142.

[19] Hamad BS, Mike JA. Bond strength of hot-dip galvanized reinforcement in normal strength concrete structures. Constr Build Mater 2005;19:275–283. https://doi.org/10.1016/j.conbuildmat.2004.07.008.

[20] Tittarelli F, Bellezze T. Investigation of the major reduction reaction occurring during the passivation of galvanized steel rebars. Corros Sci 2010;52(3):978–983. https://doi.org/10.1016/j.corsci.2009.11.021.

[21] Maeda M, Li X, Ooi A, Tada E, Nishikata A. Passivation mechanism of galvanized steel rebar in fresh concrete. ISIJ Int 2020;60(2):337–345. https://doi.org/10.2355/isijinternational.ISIJINT-2019-396.

[22] Blanco MT, Andrade C, Macias A. SEM study of the corrosion products of galvanized reinforcements immersed in solutions in the pH range 12.6 to 13.6. Br Corros J 1984;19(1):41–48. https://doi.org/10.1179/000705984798273524.

[23] Yeomans SR. Galvanized steel reinforcement in concrete. Amsterdam, The Netherlands: Elsevier; 2004.

[24] Pokorný P, Pernicová R, Tej P, Kolísko J. Changes of bond strength properties of hot-dip galvanized plain bars with cement paste after 1 year of curing. Constr Build Mater 2019;226:920–931. https://doi.org/10.1016/j.conbuildmat.2019.07.147.

[25] de K Ortolan V, Hilgert T, Howland JJ, Silva L, Titikian BF. Comparative assessment of corrosion of concrete reinforced with unprotected steel and hot-dip galvanized steel. Rev Constr 2017;16(2):238–248. https://doi.org/10.7764/RDLC.16.2.238.

[26] Molina FJL, Cruz MA, Alonso A, Montes EH, Cecilio L. Galvanized steel in concrete: More durable structures maintaining the bond length. J Mater Civ Eng 2017;29(8):04017070. https://doi.org/10.1061/(ASCE)MT.1943-5533.0001903.

[27] Sun G, Yang K. Bond-slip behaviour between multi-partition steel tubes and concrete. Mater Struct 2023;56(3):74. https://doi.org/10.1617/s11527-023-02155-3.

[28] Comité Euro-International du Béton. CEB-FIP Model Code 1990. Bulletin d'Information No. 213/214. Lausanne, Switzerland: CEB; 1993.

[29] Andreasen AHM, Andersen J. Ueber die Beziehung zwischen Kornabstufung und Zwischenraum in Produkten aus losen Körnern (mit einigen Experimenten). Kolloid Z 1930;50(3):217–228. https://doi.org/10.1007/BF01422986.

[30] American Galvanizers Association. Hot-dip galvanizing: Preparing the HDG surface. Centennial, CO, USA: American Galvanizers Association; 2023. Available from: https://galvanizeit.org/duplex-systems-galvanize-it-seminar/preparing-the-hdg-surface. (accessed Apr. 14, 2023).

[31] European Committee for Standardization (CEN). EN 12350-2: Testing fresh concrete—Part 2: Slump test. Brussels, Belgium: CEN; 2009.

[32] European Committee for Standardization (CEN). EN 12390-1: Testing hardened concrete—Part 1: Shape, dimensions and other requirements for specimens and moulds. Brussels, Belgium: CEN; 2012.

[33] European Committee for Standardization (CEN). EN 12390-13: Testing hardened concrete—Part 13: Determination of secant modulus of elasticity in compression. Brussels, Belgium: CEN; 2013.

[34] European Committee for Standardization (CEN). EN 12390-3: Testing hardened concrete—Part 3: Compressive strength of test specimens. Brussels, Belgium: CEN; 2009.

[35] European Committee for Standardization (CEN). EN 1992-1-1: Eurocode 2: Design of concrete structures—Part 1-1: General rules and rules for buildings. Brussels, Belgium: CEN; 2004.

[36] International Organization for Standardization (ISO). ISO 6892-1: Metallic materials—Tensile testing—Part 1: Method of test at room temperature. Geneva, Switzerland: ISO; 2009.

[37] Sanz B, Planas J, Sancho JM. Study of the loss of bond in reinforced concrete specimens with accelerated corrosion by means of push-out tests. Constr Build Mater 2018;160:598–609. https://doi.org/10.1016/j.conbuildmat.2017.11.093.

[38] Gonçalves JA. Mixed galvanized steel and concrete systems for the construction of marine and offshore structures [MSc thesis]. Guimarães, Portugal: University of Minho; 2021

.

PAPER IV

LONG-TERM BEHAVIOUR OF BOND BETWEEN HDG STEEL AND CONCRETE FOR MIXED STEEL-CONCRETE MARINE STRUCTURES

REFERENCE: Cruz F, Valente IB, Miranda T, Pereira, EB. Long-term effect of seawater on bond performance between HDG steel and concrete for hybrid concrete-steel marine constructions [Submitted].

ABSTRACT: The use of hot-dip galvanized (HDG) steel in combination with concrete is often explored for its cost-effectiveness and corrosion resistance in marine environments. However, the primary challenge lies in understanding its long-term bond strength, as the interaction between concrete and HDG steel has been poorly studied and is not yet fully understood, particularly under prolonged seawater exposure. This study explores the long-term bond behaviour between concrete and HDG steel tubes under varying environmental conditions, including seawater immersion and a controlled atmospheric environment. The influence of bond length, exposure time, and environmental conditions on bond strength was assessed through direct pushout tests at different ages (28, 90, 180 and 500 days). Microstructural analyses based on Field-Emission Scanning Electron Microscope with microanalysis X-ray system Energy Dispersive Spectrometer (FEG-SEM/EDS) were conducted to examine the interface's morphology and chemical composition.

Visual inspections, carbonation, and chloride content were also assessed. The results revealed that specimens exposed to seawater showed a reduction in bond strength compared to those in an atmospheric environment. However, over time, specimens in seawater exhibited a gradual increase in bond strength, suggesting that prolonged exposure to seawater may initially reduce bond strength but later improves it, as corrosion products develop and enhance the bond.

KEYWORDS: Concrete/hot-dip galvanized steel structures; Long-term bond behaviour; Seawater exposure; Atmospheric exposure; Microstructural analysis; Pushout tests.

1 INTRODUCTION

Marine constructions, with their diverse designs and functionalities, are vital to global infrastructure, enabling the utilization and exploitation of marine resources. Structures such as offshore wind farms, energy islands, overseas bridges, underwater museums, and artificial reefs operate in highly aggressive environments [1], where factors like saltwater exposure, humidity, temperature variations, biofouling, and chloride penetration accelerate material degradation and corrosion [2,3]. These conditions pose significant challenges to the longevity and structural integrity of marine infrastructure [4].

Concrete and steel structural systems, particularly reinforced concrete and steel-concrete composite structures, have been widely adopted in marine construction due to their combination of superior strength, ductility, and durability [5,6] However, these structures are prone to deterioration primarily due to chloride ion penetration, which leads to the corrosion of steel elements [7] compromising structural integrity and increase maintenance costs [8]. These challenges highlight the importance of employing materials and protective methods to limit corrosion and minimize durability problems [9]. In this context, the use of cathodic protection, corrosion inhibitors or coating products on steel represents a promising approach to protective measures [1,10,11]. Among these solutions, hot-dip galvanizing (HDG) is often explored for its cost-effectiveness and corrosion resistance in harsh environments, as the zinc coating provides sacrificial protection to the steel, delaying the onset of corrosion and enhancing durability in marine environments [8,12–14].

Despite the advantages, the bond behaviour between concrete and HDG steel remains a subject of debate [12,15,16]. Several studies have been developed concerning early-age chemical

interactions that occur when zinc coatings come into contact with the highly alkaline environment of fresh concrete [16]. It has been stated that during the concreting process, zinc reacts with the calcium ions from the concrete, forming a passivating layer composed of zinc oxide (ZnO), zinc hydroxide ($Zn(OH)_2$), and CHZ-calcium hydroxyzincate ($Ca[Zn(OH)_3]_2{\cdot}2H_2O$), while also releasing hydrogen. This phenomenon gives rise to concerns regarding the potential increase in porosity of the concrete, which could result in a reduction in the bond strength [16,17]. Other authors state that porosity of the cement paste (caused by hydrogen evolution) could be filled by zinc corrosion products such as CHZ and that this phenomenon positively affects the bond strength of HDG steel reinforcement in concrete [12,18,19]. Pokorný et al. [16] examined the impact of HDG steel corrosion on the porosity evolution of cement paste at the interfacial transition zone (ITZ) over different exposure periods (6, 120 and 365 days) in distilled water. Their study confirmed that fresh cement paste actively corrodes HDG steel, increasing ITZ porosity due to hydrogen evolution. After one year, submerged samples exhibited higher porosity than semi-submerged ones, as continuous water supply sustained the cathodic corrosion reaction. The corrosion process formed interconnected channels within the cement paste, weakening the bond strength, while zinc corrosion products only partially filled these pores. Additionally, the presence of CHZ crystals, which lack bonding properties, further reduced adhesion. Regardless of exposure time, galvanized rebars exhibited lower bond strength than uncoated steel, with minimal change after four months of curing. Similar conclusions were drawn from standardized pull-out tests on smooth galvanized samples, which consistently exhibited lower bond strength than uncoated steel [16]. Beyond chemical interactions, other factors influencing bond performance have been identified. Concrete composition and higher strength improve the bond between HDG steel and concrete [1,20] while surface contamination can reduce bond strength by 39.5% [20]. Interlocking mechanisms, like pin connectors, enhance bond [20], and HDG coating thickness influences corrosion product formation [11,21–23].

Although long-term bond performance has occasionally been explored in studies on marine environments, research on this topic remains scarce, particularly about HDG steel tubes. Kazemi et al. [24,25] indicated that steel reinforcement may experience a reduction in bond strength of up to 10% after 250 days in a seawater environment, and that GFRP reinforcement may experience a reduction of up to 20% in bond strength in such an environment. Similarly, BFRP bars in seawater sea-sand concrete show a bond degradation of up to 20.6% after 120 days [26].

Andrade et al. [27] performed long-term tests and concluded that galvanized rebars maintain their bond strength after exposure to seawater for up to 10 years, outperforming bare rebars. Ismail et al. [15] evaluated the corrosion resistance of galvanized steel and dual-phase reinforcements in concrete, particularly in corrosive environments. The specimens were immersed in a 5% NaCl solution for 100 days, and the study assessed corrosion performance, microstructural changes, and the physical and mechanical properties of the steels. The galvanized steel showed some depletion of zinc layer and higher corrosion rate due to the presence of eutectoid carbide. Rivera-Corral et al. [28] investigated the corrosion behaviour of ordinary, dual-phase, and galvanized steel rebars embedded in concrete under chloride exposure using wetting and drying cycles for 2.6 years. The study monitored the evolution of corrosion potential (E_{corr}) and polarization resistance (Rp), revealing that HDG rebars formed a passivating zinc oxide layer, reducing corrosion rates compared to uncoated rebars. However, this protection diminished over time as the zinc coating degraded. Additionally, HDG rebars exhibited less concrete cracking and spalling, highlighting their superior performance in mitigating concrete damage in aggressive environments. More recent studies have sought to understand the role of chloride-induced corrosion on HDG-concrete bonding. Fonsêca & Meira [17] examined the influence of chloride-induced corrosion on the bond strength between HDG steel and concrete that had been immersed for periods between 8 and 38 days. The research suggests that, when tested at 28 days without corrosion acceleration, the initial corrosion of galvanized steel does not affect its bond to concrete. It seems probable that the increase in porosity, resulting from hydrogen evolution is offset by the filling of concrete pores with zinc corrosion products, which improves the bond. Under accelerated chloride, HDG steel shows superior bond strength compared to non-galvanized steel, suggesting enhanced durability in chloride-rich environments like seawater. The bond strength of the specimens with galvanized steel initially increases with corrosion due to pore-filling by corrosion products, stabilizes, and then decreases as the degree of corrosion increases. In fact, corrosion influences the bond strength. The results were in accordance with others works [29] that have not observed significant differences on bond strength between galvanized and non-galvanized steel. Pokorný et al. [11] investigated the corrosion behaviour and bond strength of HDG prestressing steel reinforcement in normal-strength concrete. The study specifically examined the impact of hydrogen evolution during the corrosion process on the bond strength between the reinforcement and concrete, as well as analysing the porosity changes at the interfacial transition zone (ITZ) due to hydrogen-induced corrosion. The authors of the study conclude that the corrosion of the HDG coating under hydrogen

evolution in concrete results in a reduction of the bond strength of the reinforcement. Furthermore, image analysis after 28 days revealed minimal filling of hydrogen-generated pores by zinc corrosion products. The study also demonstrates that water immersion may promote further hydrogen evolution, which can influence the durability and bond strength of the material by continuing the corrosion cycle.

While previous research has mainly focused on the early-age interactions between HDG steel and concrete, the long-term effects, particularly under marine exposure, remain poorly understood. This knowledge gap is significant given the influence of bond performance on structural performance and durability. To address this, the present study investigates the long-term bond behaviour between concrete and HDG steel tubes under different environmental conditions, supporting their application in steel– concrete composite systems for multifunctional modular artificial reefs [30–32]. Specifically, it examines the effects of bond length, exposure time, and exposure environment, including seawater immersion (simulating high-salinity conditions) and a controlled atmosphere. Bond strength was assessed through direct push-out tests, while microstructural analyses (FEG-SEM/EDS), visual inspections, carbonation, and chloride penetration tests were conducted to evaluate interface properties.

2 EXPERIMENTAL PROGRAM

The experimental program was based on the use of pushout tests to study the influence of the environmental exposure conditions on the bond behaviour between concrete and galvanized steel with smooth surface. The specimens were subjected to two different exposure conditions: (i) climatic chamber (CC) with controlled climatic conditions (relative humidity RH = 55% and temperature T = 18°C) and (ii) seawater (SW) immersion in a tank. The first exposure environment represents the control, and the second represents the marine environment. The seawater was collected from the Atlantic Ocean, at Póvoa do Varzim, in the Northwest of Portugal, and transferred to a tank on the Structures Laboratory of the Civil Engineering Department at the University of Minho. Various periods of exposure were studied in each environment, with a maximum exposure time of 500 days.

In general, the pushout testing program was composed of 63 tests divided into two categories of exposure conditions and distributed by four groups according to the age of the specimens after

casting (I – 28 days; II - 90 days; III – 190 days; IV – 500 days). Out of these 63 samples, 36 were placed in the climatic chamber and 27 in the seawater tank 28 days after casting. In each group, three different series, according to the bond lengths, were tested: (i) 50 mm, (ii) 75 mm and (iii) 100 mm. The nomenclature adopted to designate the specimens was EC_A_LBY_i, where "EC" represents the exposure condition (CC - climatic chamber; SW - seawater), "A" represents the age at which the test was performed, "Y" is the bond length in millimetres (50, 75 or 100) and "i" is the number of the specimen in the series (1, 2, 3) as shown in **Table IV.1**.

In addition, 22 concrete cylinders were subjected to the same exposure conditions and tested to characterize the mechanical properties, at 7 days after casting and at each of the testing ages of the pushout specimens. The mechanical properties of steel had already been characterized in previous works [20].

Two concrete beams with galvanized steel tubes embedded were also built and exposed to the same conditions, in order to evaluate the morphology and chemical composition at the cross-section and in the interface transition zone (ITZ) between materials over time.

Table IV.1: Variables and specimens tested.

Exposure conditions	Testing age [days]	Bond length, LB [mm]	Number of specimens	Series
Climatic chamber	28d	50	3	CC_28d_LB50_01 to 03
		75	3	CC_28d_LB75_01 to 03
		100	3	CC_28d_LB100_01 to 04
Climatic chamber or Seawater immersion	90d	50	3	CC_90d_LB50_01 to 03
			3	SW_90d_LB50_01 to 03
		75	3	CC_90d_LB75_01 to 03
			3	SW_90d_LB75_01 to 03
		100	3	CC_90d_LB100_01 to 03
			3	SW_90d_LB100_01 to 03
Climatic chamber or Seawater immersion	190d	50	3	CC_190d_LB50_01 to 03
			3	SW_190d_LB50_01 to 03
		75	3	CC_190d_LB75_01 to 03
			3	SW_190d_LB75_01 to 03
		100	3	CC_190d_LB100_01 to 03
			3	SW_190d_LB100_01 to 03
Climatic chamber or Seawater immersion	500d	50	3	CC_500d_LB50_01 to 03
			3	SW_500d_LB50_01 to 03
		75	3	CC_500d_LB75_01 to 03
			3	SW_500d_LB75_01 to 03
		100	3	CC_500d_LB100_01 to 03
			3	SW_500d_LB100_01 to 03

2.1. Materials

The materials involved in this investigation were concrete and HDG steel tube profiles (S195T), with a diameter of 88.9 mm, a thickness of 3.2 mm and a zinc coating of 400 g/m^2. The concrete composition was prescribed in accordance with NP EN 1992-1-1:2010 [33] and NP EN 206-1 [34] considering the requirements for marine constructions. The characteristics of concrete were the following: concrete strength class – C30/37; maximum aggregate size – 14 mm; cement class – CEM II 42.5 R; exposure class – XC4 (P); chloride content class – 0.40 and consistency class – S3, according to NP EN 1992-1-1:2010 [33].

2.2. Geometry and preparation of specimens

The pushout specimens were composed of concrete cubes with dimensions of 150×150×150 mm^3 serving as substrate, and HDG steel tubes embedded in those cubes with a total length of 200 mm and embedment lengths of 50 mm, 75 mm and 100 mm.

Prior to the assembly of the specimens, the HDG steel tubes were cleaned according to the recommendation of the American Galvanizers Association, (AGA) to remove organic contaminants (e.g., oil, dust), resulting from handling, cutting and transportation work. Thus, a mild alkaline solution with ten parts of water and one part of alkaline cleaner was used (**Figure IV.1** – Image 1).

Circular polystyrene foam pieces of varying heights (50, 75, and 100 mm) were placed under the tubes and glued to create an air gap and ensure the desired bond length (**Figure IV.1** – Image 2). A system of stud nuts and bolts was integrated into the moulds to ensure the tubes' correct positioning and verticality during concreting (**Figure IV.1** – Image 3). Thus, the tube was positioned in the centre and two bubble level as well as a ruler were used to ensure the correct positioning (**Figure IV.1** – Image 3). The procedure was carefully repeat for all specimens. It should also be noted that each formwork allowed the adjustment of 6 samples, and at the end of its assembly it was wrapped in plastic film to protect it from laboratory dirt, until the day of concreting (**Figure IV.1** – Image 4). Lastly, the moulds were placed in the outdoor concreting area and the specimens were concreted (**Figure IV.1** – Image 5). During this phase, the concrete was conveniently vibrated and at the top surface was finished manually using a trowel. After the casting, the specimens were sprayed with water and covered with plastic film.



Figure IV.1: Specimens preparations: (1) cleaning the steel tubes; (2) overview of the moulds and materials and detail of the foam-steel union; (3) adjustment and levelling of the tube in the mould; (4) mould positioned for casting and (5/6) demoulding of the specimens.

After demoulding (**Figure IV.1** – Image 5 and 6), the specimens were cured in a climatic chamber with controlled climatic conditions (HR = 55% and T = 18°C). As previously referred, some of the specimens were prepared to be immersed in the seawater tank at 28 days after casting. This task of preparation required several steps: (i) the protection of the concrete base and the free end of the galvanized steel tube with suitable waterproofing paint, (ii) the application of silicon on the edge between the concrete top surface and the steel tube and (iii) the waterproofing of the concrete top surface with epoxy. The silicon, applied on the edge between the concrete top surface and the steel tube to ensure that no additional bonding mechanism, was formed due to the epoxy. Although the epoxy used works better as a waterproofing barrier, it was not used in the concrete base, as its application could result in unwanted irregularities in the area that acts as support for the pushout tests. The concrete beam with the embedded excentric tube was also protected with epoxy at the free ends.

A monitoring system was developed to monitor the seawater parameters over time, namely the temperature, salinity, pH and oxidation reduction potential (ORP), as shown in **Figure IV.2**. The salinity was obtained through the measurement of conductivity. The system was built based on Arduino mega, suitable probes and its components. The data was collected onto a MicroSD card, and a data control via SMS was programmed to be sent once a week using a GSM/GPRS/GPS SIM module. Before the specimens were subjected to the monotonic tests, some procedures were carried out, such as the removal of silicone and the foam. In addition, seawater samples from the tank were taken for physical and chemical laboratorial analysis at the dates of testing. Thus, measurements of salinity, pH and ORP were validated, and the organic matter and dissolved elements (calcium, magnesium, sodium, potassium, strontium, fluoride, boron, sulphate, bicarbonates) were monitored. Chemical compounds such as sodium chloride (NaCl), magnesium chloride ($MgCl_2$), sodium sulphate (Na_2SO_4), calcium chloride (C_aCl_2), potassium chloride (KCl), sodium bicarbonate ($NaHCO_3$), boric acid (H_3BO_3) and strontium chloride ($SrCl_2$) were also estimated.

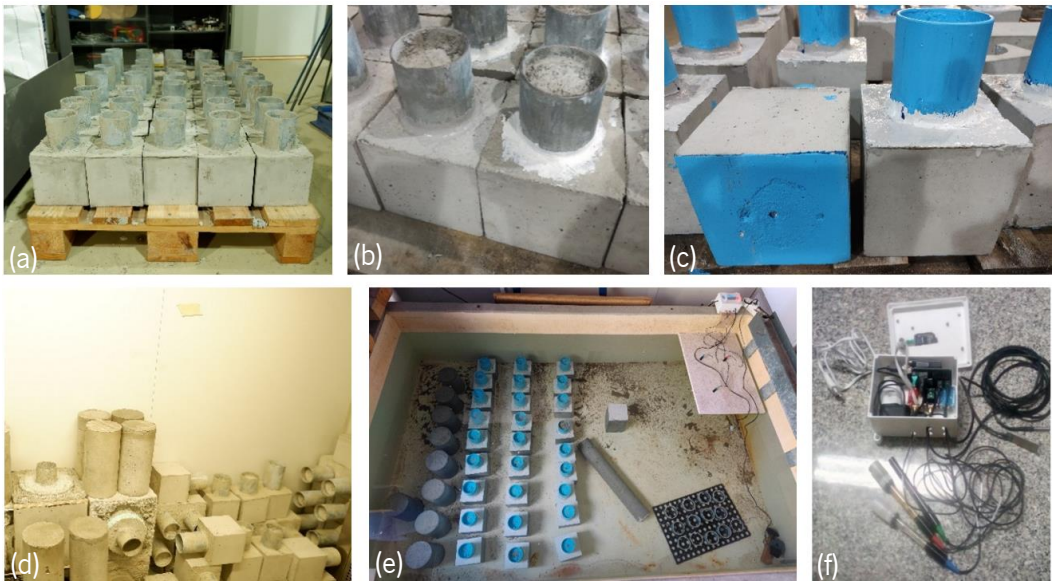


Figure IV.2: Preparation of the specimens for exposure in the climatic chamber and immersion in the seawater tank: (a) specimens after demoulding; (b,c) details of the silicone application and waterproofing measures; (d) specimens in the climatic chamber; (e) specimens immerse in the seawater tank and (f) seawater monitoring system.

2.3. Testing methods

2.3.1. Materials tests

The fresh properties of the concrete mixtures were evaluated by performing the slump test with the Abrams cone, following the recommendations of European Standard EN 12350-2 [35]. The results showed an S3 concrete. Moreover, the mixture provided by the supplier showed no segregation.

The compressive behaviour of the four mixtures was characterized by means of uniaxial compression tests in cylinders with 150 mm diameter and 300 mm in height [36–38].

Table IV.2 shows the mechanical properties of the concrete in the fresh and hardened state obtained from the uniaxial compression tests at 7, 28, 90, 190 and 500 days of concrete age.

Four uniaxial tensile tests were performed based on the recommendations of ISO 6892-1 [39] to characterize the mechanical properties of the HDG steel. **Table IV.3** shows the obtained average results. The tested steel showed typical behaviour and rupture of the material.

Table IV.2: Results obtained in concrete characterization at 7, 28, 90, 190 and 500 days.

Slump test			S3				
Exposure condition			**7 days**	**28 days**	**90 days**	**190 days**	**500 days**
CC (HR=55% T=18°C)	E_{cm}	**[GPa]**	27.69 [1.58%]	29.20 [4.73%]	31.29 [5.12%]	28.72 [5.41%]	29.13 [2.76%]
	f_{cm}	**[MPa]**	26.21 [11.39%]	34.47 [5.09%]	38.52 [5.35%]	40.15 [3.06%]	40.09 [2.38%]
SW	E_{cm}	**[GPa]**	-	-	28.67 [5.70%]	29.74 [3.48%]	36.56 [2.36%]
	f_{cm}	**[MPa]**	-	-	34.77 [3.25%]	40.31 [4.91%]	41.16 [3.55%]

Table IV.3: Steel characteristics.

	Steel grade	***E***	R_{eH}	$R_{p0,2}$	R_m	***A***	**Zinc Coat**
	[-]	[GPa]	[MPa]	[MPa]	[MPa]	[%]	[g/m²]
Technical specifications	S195T	-	>289	-	>402	>29	402
Experimental characterization	-	199 [5%]	-	430.96 [3%]	508.7 [1%]	14.99 [%]	-

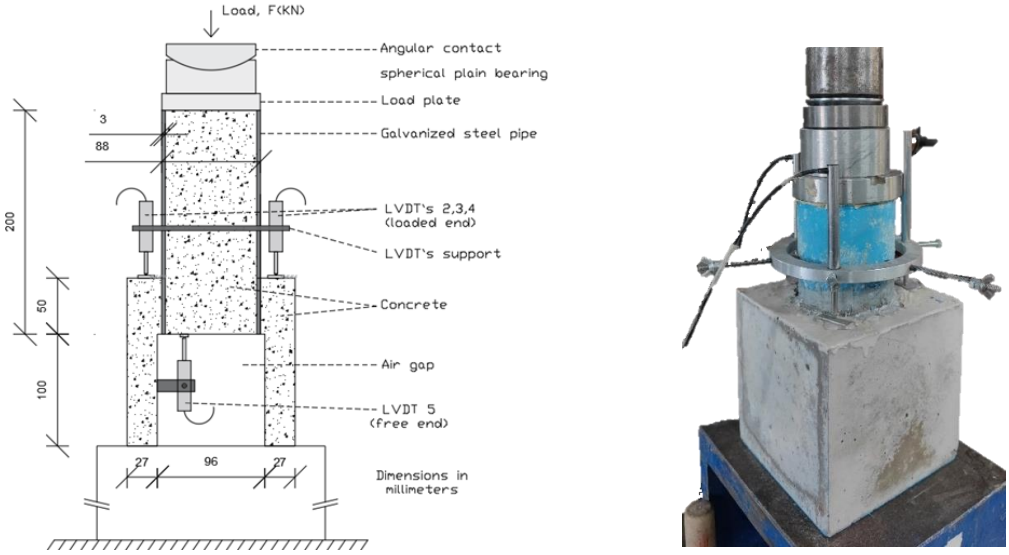
R_{eH} represents the upper yield strength if yielding is observed, and $R_{p0,2}$ represents the upper yield strength when the tensile response does not show an evident yielding plateau. R_m is the tensile strength and A is the maximum elongation.

2.3.2. Pushout tests

The pushout test followed the experimental setup and protocol described by Cruz et al., (2024) [20]. **Figure IV.3** shows the testing configuration as well as the instrumentation adopted. The test consisted of applying a uniaxial compressive force on the steel tubes, in the longitudinal direction of the specimen. The specimen was placed on a rigid steel reaction frame. A plate and an angular contact spherical plain bearing were used between the actuator and the HDG steel tube loading section to provide even load distribution and facilitate initial adjustment. The specimens were tested monotonically by external displacement control on the actuator, at an imposed displacement rate of 2 μm/s until a constant residual pushout force was reached [20]. For this purpose, a servo-hydraulic equipment, model CIL-DE-100KN-63-36-200 (version 443) with 100 kN (± 0.12 kN; 0.05% F.S.) maximum load cell capacity was used. A linear variable differential transducer (LVDT1) with a stroke of ±10 mm was used to control the test. LVDT 2, 3 and 4, with a stroke of ±10 mm were used to measure the relative displacement between the galvanized steel tube and the concrete at the loaded end section. These were positioned 120° from each other to obtain the relative mean displacements at three representative points of the section. Similarly, the relative displacement

was measured at the free end section by using LVDT5 with a stroke of ±5 mm. Although the bond shear stress (τ) presents an uneven distribution along the anchorage length, following a nonlinear shape, an average shear stress was assumed for evaluation and comparison purposes, in accordance with the approach typically adopted in design codes, as shown in **Eq. ((IV. 1)**. $F_{l,max}$ is the maximum pushout load, D is the outer diameter of the steel tube, LB is the bond length of the system, and $s_{l,max}$ is the displacement of the tube at the loaded end section corresponding to $F_{l,max}$.

$$\tau_{max} = \frac{F_{l,max}}{\pi \times D \times \left(LB - S_{l,max}\right)} \quad \textbf{(IV. 1)}$$



(a) (b)

Figure IV.3: Experimental setup and instrumentation adopted for pushout tests: (a) global scheme; (b) perspective image of the specimen during testing.

2.3.3. Chlorite and carbonation tests

After the pushout tests, the steel tube was removed from the concrete block and carbonation, and chloride tests were carried out on the specimens exposed to CC and SW exposure conditions. The carbonation test consisted of spraying an aqueous solution of 1% phenolphthalein in 70% of ethanol directly onto the inner surface of the specimen. If the concrete surface is not carbonated (pH higher than 9.2), the concrete exhibits a pink coloration. On the other hand, when the surface presents itself colourless, this indicates that the concrete is carbonated (pH lower than 9.2).

In the case of the chlorite test, the measurement of the depth of penetration was carried out through a colorimetric process. A silver nitrate solution ($AgNO_3$ 0.1N) was sprayed directly onto the inner surface of the specimen. If chloride penetration has occurred, a line with a dark grey colour is formed. It should be noted that this test allows the evaluation of free chlorides on the surface.

2.3.4. FEG-SEM/EDS micrographs properties of the CS and ITZ

The morphology and chemical composition of the cross-section (CS) and concrete-HDG steel interface transition zone (ITZ) were analysed using an ultra-high-resolution Field-Emission Scanning Electron Microscope with microanalysis X-ray system Energy Dispersive Spectrometer (FEG-SEM/EDS) system (FEI Nova 200 and EDAX Pegasus X4M) with a resolution of 1.0 nm at 15 kV under high vacuum conditions.

The samples were obtained by cutting the reinforced concrete beams with HDG steel tubes into slices, followed by core drilling to extract cylindrical specimens (18 mm diameter and 18 mm height), including CS and ITZ between concrete and HDG steel (**Figure IV.4**). The cross-sectional samples were polished prior to examination, while those for ITZ analysis were left unpolished to preserve the crystal formations and covered with an ultrathin coating of gold deposited by sputter coating.



Figure IV.4: Preparation of the samples for FEG/SEM (EDS) analysis.

3 RESULTS AND DISCUSSION

3.1. Bond behaviour

Figure IV.5 presents the experimental response, considering the pushout force and the loaded end slip, at the loaded end zone (F_l-s_l). The applied axial force (F_l) was measured by the load cell installed in the actuator, and the loaded end slip (s_l) was calculated by averaging the readings from

the three LVDTs mounted on the ring attached to the HDG steel tube at the loaded end. The results obtained are divided according to the exposure (CC and SW) and aging conditions (28, 90, 190 and 500 days).

In general, the F_l-s_l experimental responses show a similar behaviour for all specimens, regardless of the environmental exposure condition, time of exposition and LB adopted. Despite slight variations, the load-slip curves present a similar evolution and well-defined shape.

The curves obtained can be divided into three distinct phases. The first branch is a phase of elastic behaviour and high stiffness, with a progressive increase of the load capacity for very low slip s_l, until reaching the peak force. This part is governed mainly by the perfect chemical bond formed between the materials after the concreting and curing processes. The second phase corresponds to the post peak response which is governed by a nonlinear F_l-s_l behaviour, evidencing a reduction of load carrying capacity and the loss of stiffness due to bond degradation. As shown in **Figure IV.5**, in most cases, the transition between pre and post peak occurs smoothly due to progressive breaking of the chemical bond and the remaining physical contact between materials. Also, the F_l-s_l post-peak response shows a descending form that reflects the progressive degradation of the interface. The force reduction tends to smooth out and a residual force plateau is reached (third branch). However, it should be noted that certain specimens with LB equal to 100 mm did not exhibit a smooth transition between pre- and post-peak response, showing an abrupt loss of load capacity with cracking of the concrete block.

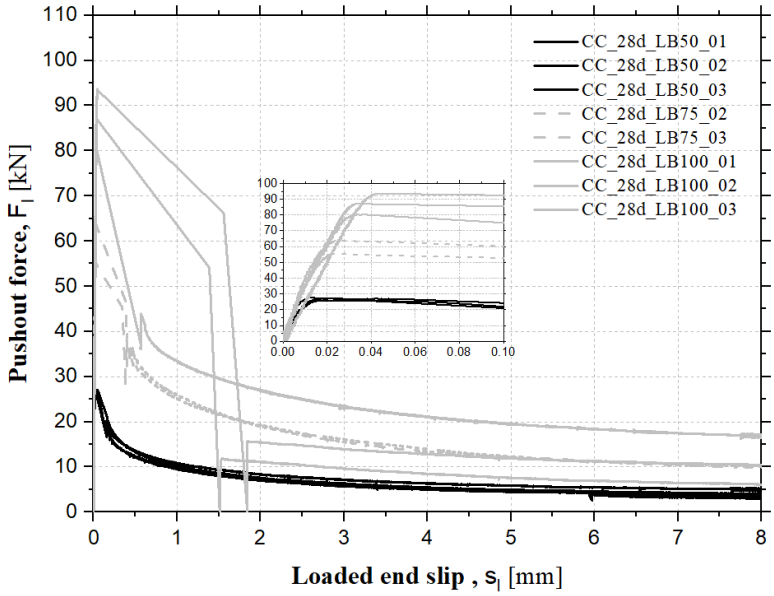


Figure IV.5: Curves of the pushout force versus relative vertical displacement at 28 days.

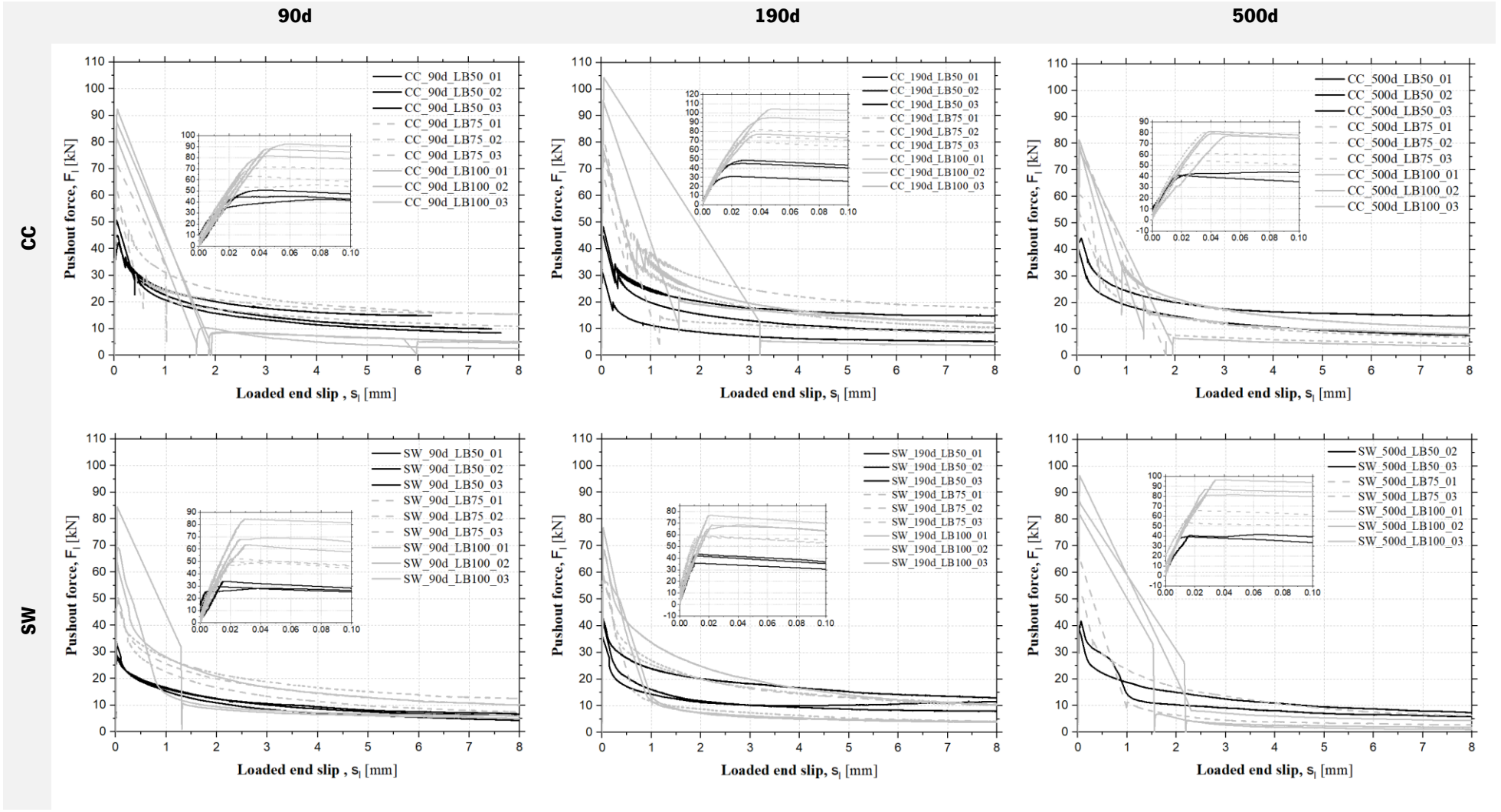


Figure IV.6: Curves of the pushout force versus relative vertical displacement for each.

The main results obtained from the experimental program are summarized in **Table IV.4**. The results correspond to the average values obtained for the specimen tested under the same conditions. The typical failure mode (FM) and the concrete compressive strength at all ages ($f_{cm,days}$) are also shown. The main variables calculated from the tests are $F_{l,max}$, the maximum pushout force, $s_{l,max}$, the loaded end slip at maximum pushout force, $s_{f,max}$, the free end slip at maximum pushout force and τ_{max}, the average maximum shear strength at the interface between the galvanized steel tube and the concrete surface. F_r is the residual pushout force corresponding to a value of s_l equal to 8 mm; G_f represents the energy dissipated and is obtained by computing the area under the F_l vs s_l experimental response until a s_l of 8 mm is reached; $F_r/F_{l,max}$ is the ratio between residual pushout force (F_r) and the maximum pushout force ($F_{l,max}$). FM represents the failure mode observed in the test. In addition, the concrete compressive (f_{cm}) and tensile (f_{ctm}) strengths were used to compute the normalized shear strength ($\overline{\tau}_{\max}$), and the normalized energy dissipated during pushout testing until failure ($\overline{G}_f$) **Eq. IV.2** and **Eq. IV.3**, respectively. According to **Eq. IV.4** and the recommendations given in NP EN 1992-1-1:2010 [30] as well as the outcomes of the compression tests, the value of f_{ctm} was calculated. It should be noted that tests with cracking prior to testing or issues during testing were ignored and not taken into account to compute the average results.

$$\bar{\tau}_{max} = \frac{F_{l,max}}{f_{ctm,28} \times \pi \times D \times (LB - S_{l,max})} \quad \textbf{IV.2}$$

$$\bar{G}_f = \frac{G_f}{f_{ctm,28} \times \pi \times D \times \left(LB - S_{l,max}\right) \times 8} \quad \textbf{IV.3}$$

$$f_{ctm,28} = 0.3 \times f_{ck}{}^{(\frac{2}{3})} \quad \textbf{IV.4}$$

Table IV.4 shows that the low CoV value for $F_{l,max}$ e τ_{max} seems to reflect more consistent and homogeneous results, ranging from 2% to 18%, which are considered good for the type of test carried out. The remaining variables present higher variation in the results. Although higher than ideal, they are still regarded as acceptable for the type of test performed since the mechanisms linked to those variables are unstable.

Table IV.4: Main pushout experimental results obtained for each group and series (average values).

Exposure condition	Tested age	Series	$f_{cm,days}$ [MPa]	$F_{l,max}$ [kN]	$s_{l,max}$ [mm]	$s_{r,max}$ [mm]	τ_{max} [MPa]	F_r [kN]	G_r [kN.mm]	$F_r/F_{l,max}$ [%]	$\bar{\tau}_{máx}$ [-]	$\bar{G}_f$ [-]	FM
Climatic Chamber "CC"	I (28 days)	CC_28d__LB50	34.47 [5%]	26.91 (3%)	0.02 (27%)	0.02 (32%)	1.81 (2%)	4.10 (9%)	56.83 (8%)	15.30 (12%)	0.68 (2%)	0.18 (8%)	$D^{1,2,3}$
		CC_28d__LB75		59.69 (7%)	0.02 (2%)	0.02 (17%)	2.71 (7%)	10.04 (1%)	148.30 (1%)	16.91 (8%)	1.02 76%)	0.32 (1%)	$D^{1,2,3}$
		CC_28d__LB100		87.03 (6%)	0.04 (13%)	0.02 (16%)	3.04 (14%)	11.14 (40%)	207.57 (12%)	13.06 (45%)	1.14 (6%)	0.34 (12%)	$D^{1}DC^{2,3}$
	II (90 days)	CC_90d__LB50	38.52 [6%]	45.98 (8%)	0.06 (25%)	0.06 (23%)	2.95 (6%)	13.27 (18%)	135.24 (12%)	28.68 (13%)	1.01 (6%)	0.37 (13%)	$D^{1,2,3}$
		CC_90d__LB75		63.43 (7%)	0.05 (15%)	0.05 (11%)	2.81 (5%)	11.66 (20%)	178.30 (8%)	18.42 (25%)	0.96 (5%)	0.34 (10%)	$D^{1,2}DC^{3}$
		CC_90d__LB100		87.23 (5%)	0.05 (14%)	0.03 (48%)	3.04 (5%)	4.10 (28%)	140.38 (11%)	4.64 (24%)	1.04 (5%)	0.21 (12%)	$DC^{1,2,3}$
	III (190 days)	CC_190d__LB50	40.15 [3%]	41.43 (18%)	0.03 (13%)	0.02 (78%)	2.75 (15%)	12.55 (43%)	113.79 (35%)	28.72 (30%)	0.90 (17%)	0.31 (35%)	$D^{1,2,3}$
		CC_190d__LB75		74.6 (4%)	0.04 (15%)	0.02 (40%)	3.34 (4%)	9.21 (12%)	172.56 (12%)	12.47 (17%)	1.10 (4%)	0.32 (12%)	$D^{1,2,3}$
		CC_190d__LB100		92.09 (12%)	0.05 (10%)	0.02 (65%)	3.25 (12%)	9.36 (43%)	200.28 (8%)	10.75 (49%)	1.07 (12%)	0.29 (9%)	$D^{2}DC^{1,3}$
	IV (500 days)	CC_500d__LB50	40.09 [2.38%]	42.58 (4%)	0.05 (64%)	0.06 (61%)	2.80 (5%)	11.29 (33%)	129.82 (18%)	26.22 (30%)	0.92 (5%)	0.35 (19%)	$D^{1,2}$
		CC_500d__LB75		65.30 (15%)	0.03 (10%)	0.03 (4%)	2.85 (13%)	7.32 (42%)	125.50 (15%)	11.86 (50%)	0.94 (13%)	0.23 (16%)	$D^{1,2}DC^{3}$
		CC_500d__LB100		79.14 (2%)	0.04 (14%)	0.02 (13%)	2.94 (2%)	7.34 (40%)	139.84 (15%)	9.22 (40%)	0.97 (2%)	0.21 (15%)	$D^{1}DC^{2,3}$
Submerged in Seawater "SW"	II (90 days)	SW_90d__LB50	34.77 [3%]	34.69 (17%)	0.02 (60%)	0.02 (70%)	2.00 (8%)	5.64 (18%)	83.17 (7%)	16.87 (30%)	0.74 (8%)	0.25 (7%)	$D^{1,2,3}$
		SW_90d__LB75		50.57 (3%)	0.03 (43%)	0.02 (39%)	2.23 (1%)	10.19 (22%)	141.49 (11%)	20.26 (24%)	0.83 (1%)	0.29 (13%)	$D^{1,2,3}$
		SW_90d__LB100		72.41 (12%)	0.04 (19%)	0.01 (27%).	2.48 (12%)	6.99 (31%)	131.58 (16%)	10.10 (41%)	0.93 (12%)	0.21 (16%)	$D^{1}DC^{2,3}$
	III (190 days	SW_190d__LB50	40.31 [5%]	40.34 (8%)	0.01 (13%)	0.01 (49%)	2.68 (8%)	10.82 (20%)	113.34 (22%)	27.04 (22%)	0.88 (8%)	0.31 (22%)	$D^{1,2,3}$

		SW_190d__LB75		58.68 (1%)	0.01 (8%)	0.01 (24%)	2.64 (2%)	8.49 (36%)	123.70 (27%)	14.50 (36%)	0.87 (2%)	0.23 (26%)	$D^{1,2,3}$
		SW_190d__LB100		71.24 (5%)	0.03 (30%)	0.01 (85%)	2.51 (5%)	6.04 (49%)	114.28 (35%)	8.61 (53%)	0.83 (5%)	0.17 (35%)	$D^{1,2,3}$
	IV (500 days)	**SW_500d__LB50**	41.16 [3.55%]	40.45 (3%)	0.04 (64%)	0.03 (87%)	2.75 (4%)	6.63 (11%)	95.45 (8%)	16.45 (14%)	0.89 (4%)	0.26 (7%)	$D^{2,3}$
		SW_500d__LB75		59.43 (10%)	0.02 (15%)	0.01 (7%)	2.66 (10%)	4.51 (36%)	96.08 (22%)	7.96 (45%)	0.86 (10%)	0.17 (22%)	$D^{1,3}$
		SW_500d__LB100		88.28 (7%)	0.04 (25%)	0.02 (31%)	2.86 (3%)	2.40 (61%)	143.29 (15%)	2.64 (54%)	0.92 (3%)	0.19 (11%)	$DC^{1,2,3}$

Notes: the values between parentheses are the corresponding coefficients of variation (% CoV); FM - failure mode: D – Pushout debonding failure at the concrete and galvanized steel tube interface which consist in the slipping of the steel tube from the concrete cube; DC - pushout debonding failure at the concrete and galvanized steel tube interface with the development of thin cracks in the concrete cube only after $F_{i,max}$; The values superscript is the n° of specimens with the specified FM.

Concrete heterogeneity as well as geometric imperfections may have also influenced the results. In **Table IV.4**, it is evident the influence of the environmental exposure conditions on the results since the specimens exposed to SW present a reduction in the values obtained for all analysed variables when comparing with CC. also shows that the environmental exposure conditions influenced the results, since the specimens exposed to SW showed a reduction in the values obtained for all analysed variables when comparing with CC.

For the specimens exposed to the CC, the analysed parameters did not exhibit a consistent trend with increasing exposure time, indicating that exposure duration does not have a significant effect on their evolution. However, in the specimens exposed to SW, there is a gradual and consistent increase in the value of τ_{max} and $\overline{\tau}_{máx}$ with the increasing exposure time. It should also be noted that the compressive strength of concrete also increases during time. On the other hand, the values of F_r and $F_r/F_{l,max}$ seem to decrease over time.

The value of LB adopted also seems to slightly influence the bond behaviour. The increase of LB was associated to the increase of $F_{l,max}$ which was expected since the contact area of the bonding interface is also larger. In general, the values of τ_{max} and $\overline{\tau}_{máx}$, obtained were consistent between samples of the same series, as well as among series of the same group. The order of magnitude of $\overline{G}_f$ was similar between groups and categories.

Figure IV.7 presents the average pushout force versus loaded end slip (F_l-s_l) responses for all specimens tested according to the same exposure condition and bond length. The responses were obtained by averaging the pushout force (F_l) obtained at each loaded end slip (s_l) for all specimens of the same series. The results show that the test specimens from different groups with the same LB presented approximately similar initial stiffness.

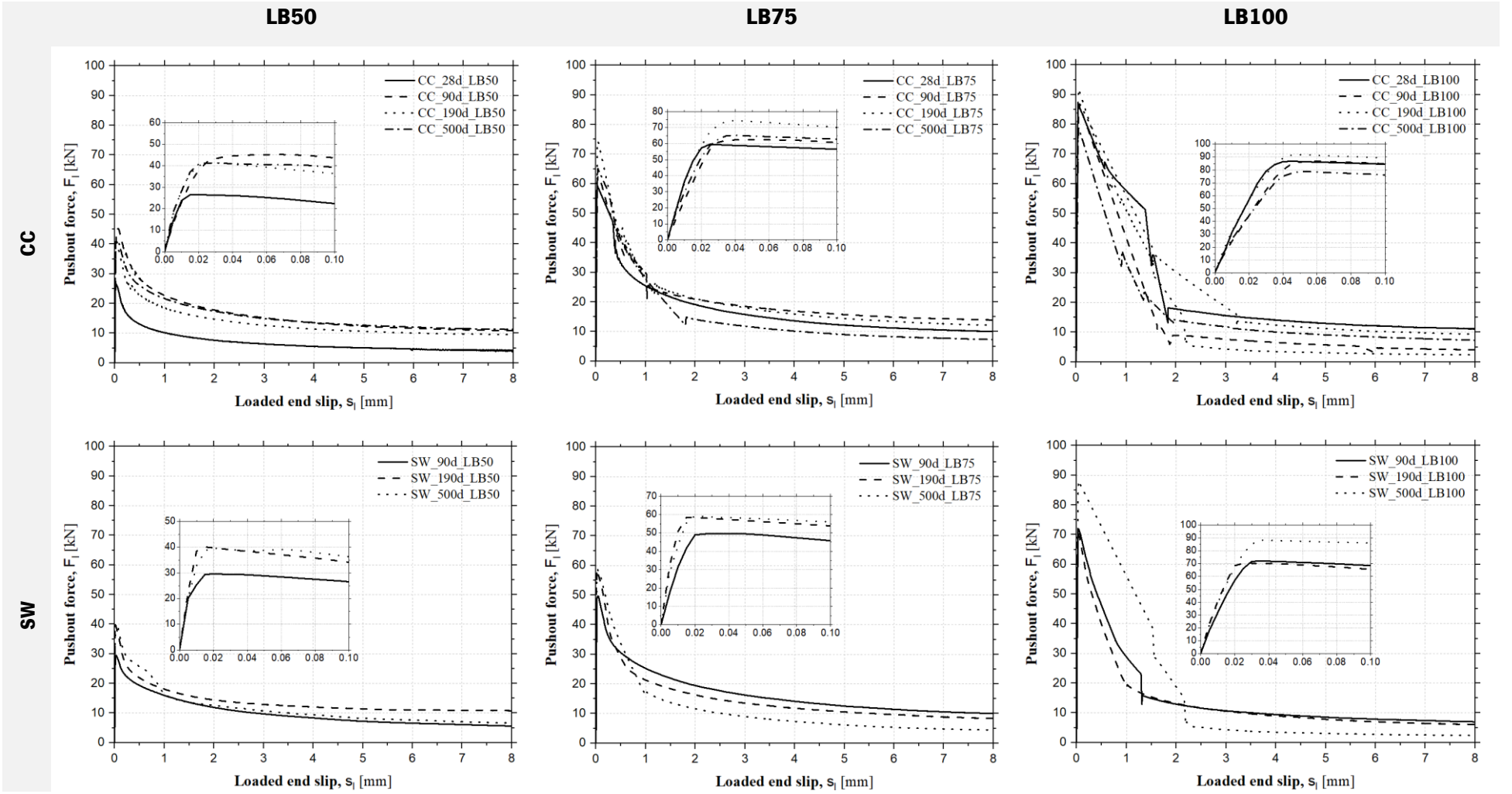


Figure IV.7: Average pushout force versus loaded end slip (F_l-s_l) responses computed for all specimens tested.

The exposure conditions do not seem to influence the initial stiffness of the experimental response, although clearly influencing the load carrying capacity and, therefore, the maximum shear stress at the contact interface. After peak the push-out force shows an asymptotic decay in all specimens till the residual force, F_r is reached.

3.2. Failure modes and surface visual inspection

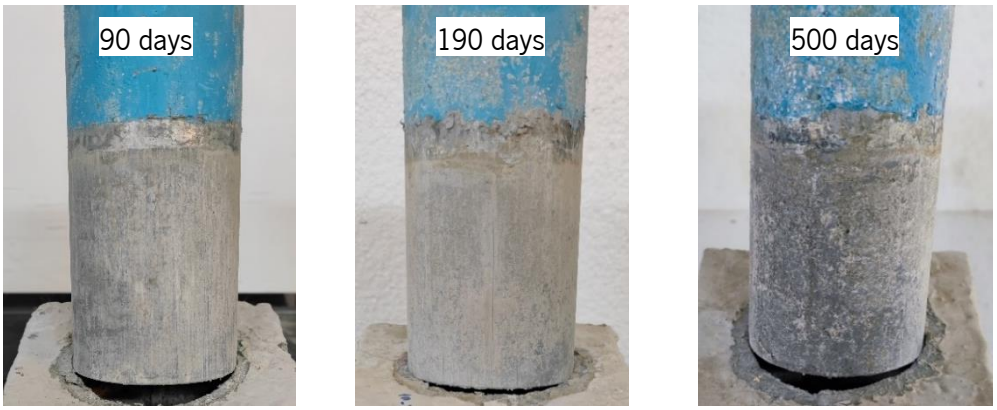
Figure IV.8 shows representative images of the obtained failure modes (FM). Two different failure modes were observed: (D) pushout debonding at the concrete to steel tube interface, which manifested itself as the full development of a tunnel crack at the interface between the two materials and the slipping of the steel tube with respect to the concrete block; (DC) pushout debonding with the formation of a thin crack in the concrete block, suggesting a reduced confinement by the concrete cube. D failure mode was prevalent, which shows that the concrete substrate exhibited appropriate behaviour. DC failure remained ductile and was more frequent in specimens with LB100, where a notable and sudden decline in the push-out force was observed.

After removing the HDG steel tubes from the concrete substrates, cement bonding films were visible at the surface of the tubes, as shown in **Figure IV.8**. **Figure IV.9** provides a more detailed illustration of the cement-based bonding films on the specimens exposed to SW for varying periods of time. It was observed that the specimens exposed to SW and CC show differences at the interface level. While the specimens kept in the climatic chamber maintain a very similar bonding film, the specimens submerged in seawater present a “thicker” bonding film, as the exposure time increases, denoting some signs of corrosion caused by the chlorides in the specimens with 500 days of exposure, as shown in **Figure IV.9c**.



(a) (b)

Figure IV.8: Typical FM: (a) pushout debonding failure, (b) pushout debonding failure with crack.



(a) (b) (c)

Figure IV.9: Detail of the steel ITZ in the specimen's exposure to SW with different exposition times.

3.3. Effect of exposure time on maximum shear stress

Figure IV.10 shows the effect of exposure time on maximum shear stress for each LB and exposure condition. In general, and despite the differences expressed in **Figure IV.10**, the values obtained show essentially similar results, regardless of the condition and time of exposure and LB. The greatest difference concerns the CC_28d_LB50 series, with an average value of 1.81 MPa. Apart from this value, the average values obtained for the specimens exposed to CC varied between 2.71 MPa and 3.34 MPa (+23%). In the case of SW, the average was between 2.00 MPa and 2.86 MPa (+43%). The maximum shear stress was reached for a loaded end slip (s_l) between 0.02 mm and 0.06 mm. No trend (positive or negative) was found for the τ_{max} in the specimens kept in the climatic chamber (CC) (**Figure IV.10**a,c). On the other hand, **Figure IV.10**b confirms the gradual increase of τ_{max} with the increase of the exposure time for the specimens exposed to seawater (SW), showing a variation from 1% to 38%. As reported in the state of the art, this suggests that corrosion products may gradually fill the concrete porosity over time. This effect counteracts the possible increase in concrete porosity at the contact surface due to the production of hydrogen, which is promoted by the cathodic reaction between zinc and cement paste at an early stage. Concrete strength increase over time may also contribute to the increase of τ_{max} over time (**Figure IV.10**d).

3.4. Effect of exposure condition over time on maximum shear stress

Figure IV.11 shows the impact of the environmental exposure conditions by comparing specimens with the same LB and different exposure times. As shown, the impact of saline environments on bond strength is evident, with specimens subjected to seawater always exhibiting a lower τ_{max} value. In general, the specimens exposed to SW show an average decrease of -14.3% with respect to the control unit. In most cases, the decrease is notable, with values ranging from -20% to -32%. It is also noted that the samples with 500 days of exposure show a smaller decrease of maximum shear stress, with values varying between -4% and -8%. Regarding the normalized shear strength, and despite small variations, the values of $\bar{\tau}_{max}$ are essentially comparable. The average decrease in the control unit was - 12.6%. The mean values for the specimens of CC_28d, CC_90d, CC_190d and CC_500d were 0.95 ± 0.19, 1.0 ± 0.03, 1.03 ± 0.09 and 0.94 ± 0.02, respectively. In the case of SW_90d, SW_190d and SW_500d, an average value of 0.84 ± 0.07, 0.86 ± 0.02 and 0.89 ± 0.03 was obtained, respectively.

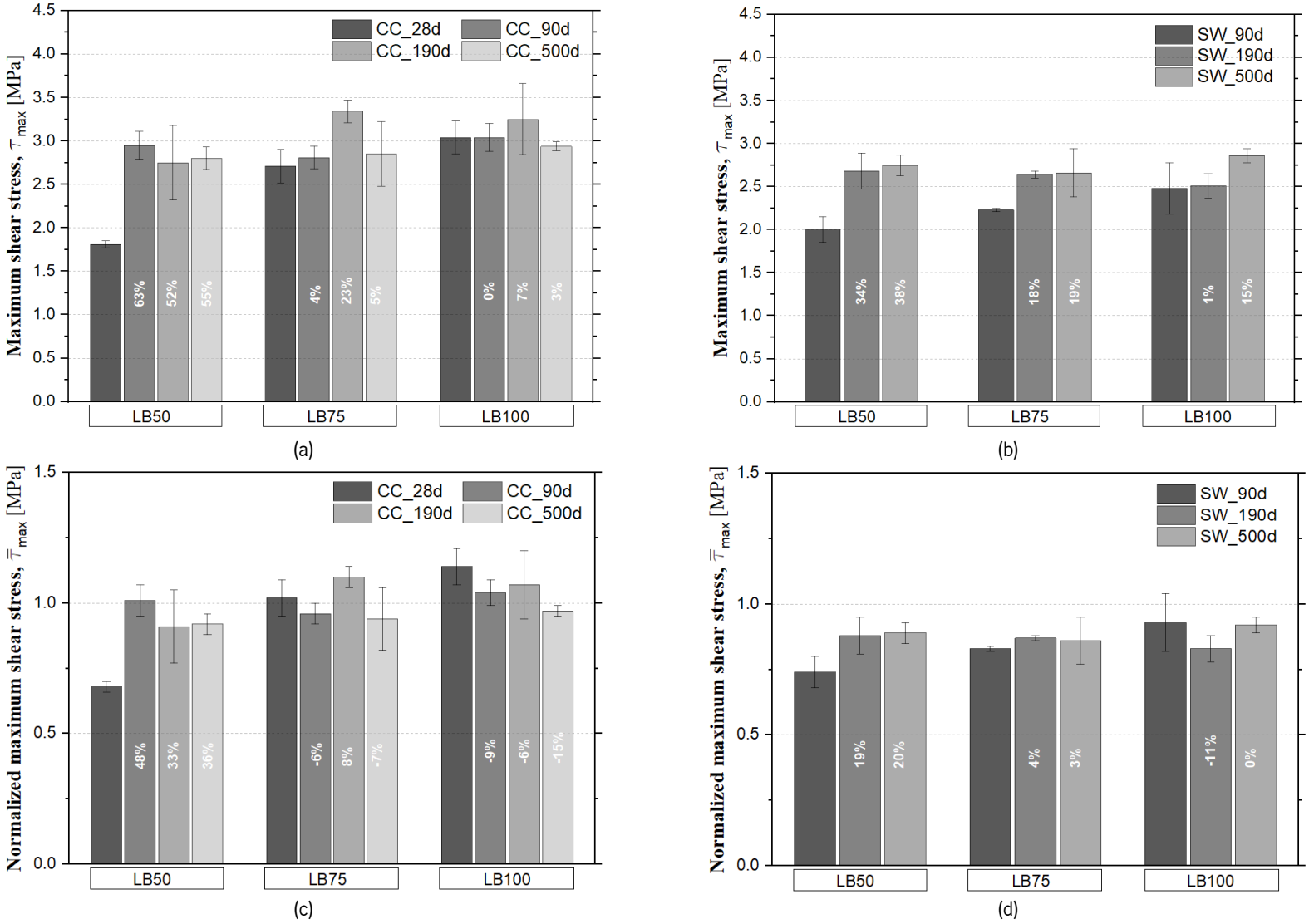


Figure IV.10: Influence of the bond length, LB on the average values of the τ_{max} (a, b) and $\bar{\tau}_{max}$ (b, d), within the exposure condition (CC or SW).

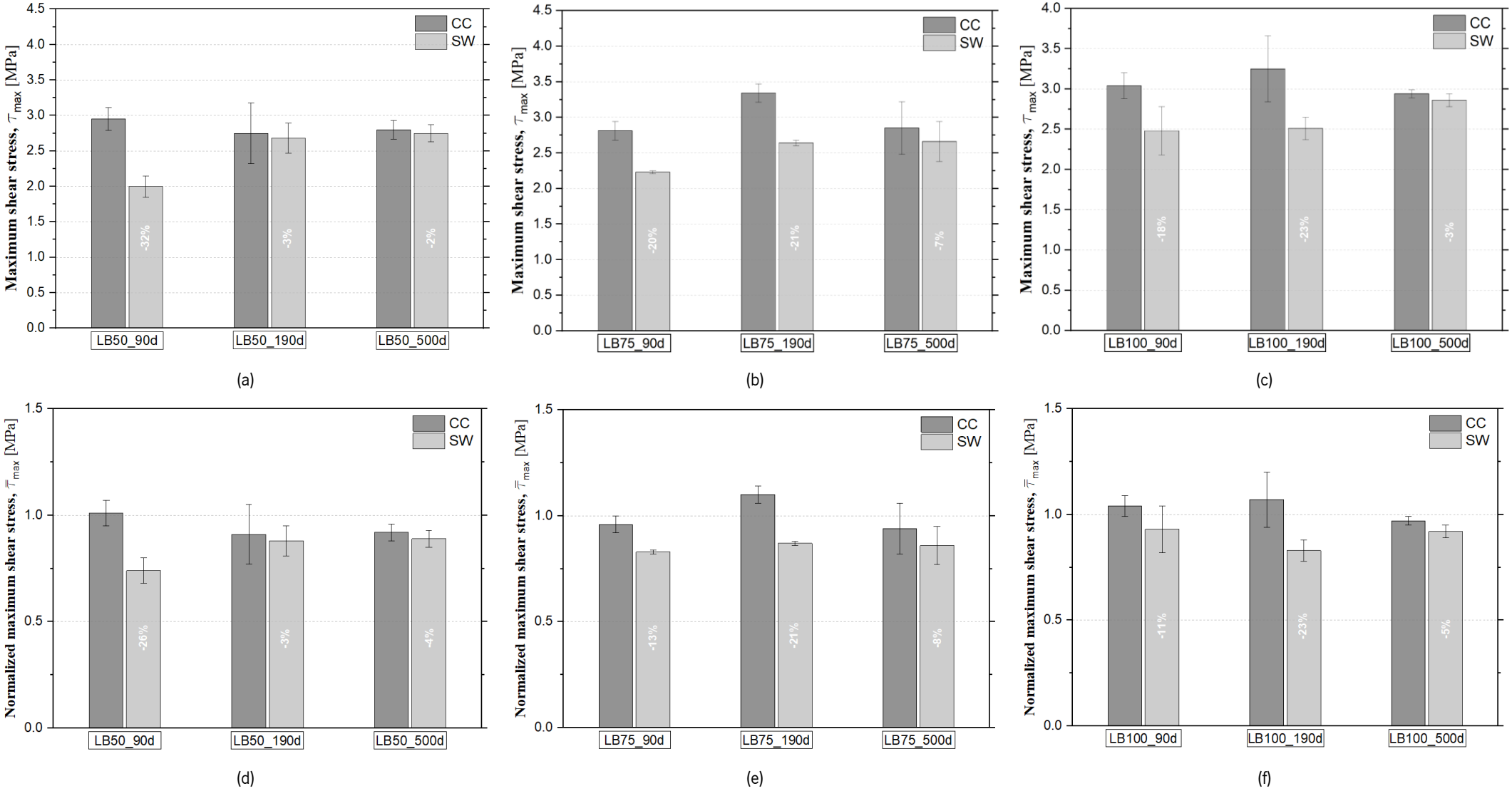


Figure IV.11: Influence of exposure conditions (CC and SW) and exposure times (90, 190 and 500 days) on the average values of (a) maximum shear strength and (b) normalized maximum shear strength within each LB.

3.5. Chlorite and carbonation

Table IV.5, **Figure IV.12** and **Figure IV.13** present the results of the carbonation and chloride content tests for all specimens. As observed, at 28 days, the specimens did not exhibit either carbonation or chlorite depths. At 90 days, the carbonation is visible in the specimens exposed to both exposure conditions. The mean depth of carbonation was found to be 5.96 mm and 3.87 mm for specimens subjected to CC and SW, respectively. No penetration of chlorides was observed. Regarding 190 days, no penetration of chlorides was observed. However, only the specimens from the climatic chamber exhibited evidence of carbonation, with an average depth of 7.64 mm. At 500 days the specimens exposed to CC show carbonatation depths of about 10.59 mm, while those exposed to SW showed no observable carbonation. Chlorites penetrated the entire thickness of the sample, which is consistent with the condition of the interface in the SW_500d samples (**Figure IV.8**c).

Table IV.5: Average results of depth of carbonatation and chlorites at 7, 28, 90, 190 and 500 days.

Exposure Condition	Test		28 days	90 days	190 days	500 days
CC	Carbonatation	[mm]	0	5.96	7.64	10.59
	Chlorites	[mm]	0	0	0	0
SW	Carbonatation	[mm]	-	3.87	0	0
	Chlorites	[mm]	-	0	0	30.55



Figure IV.12: Representative test of carbonation and chlorites on the pushout specimens CC_28d.

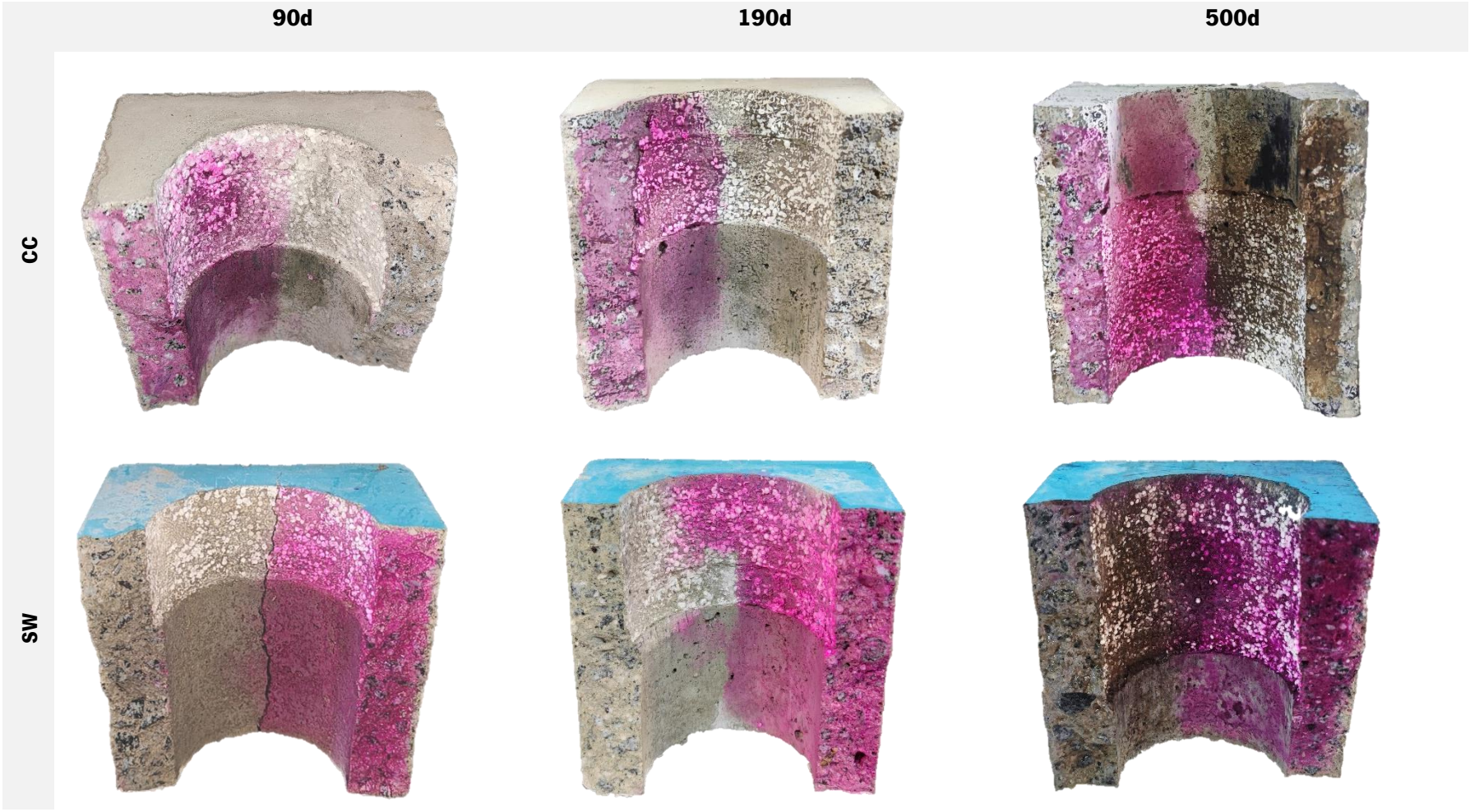


Figure IV.13: Representative pushout specimens for carbonation and chlorites tests according exposure condition (CC and SW) and age (90, 190 and 500 days).

These findings corroborate that chloride penetration at 500 days may have in fact affected the bonding behaviour and the formation of corrosion products at the interface potentially enhancing bond behaviour, may have in fact occurred.

3.6. Morphology and chemical analysis of the ITZ and CS

Figure IV.14 to **Figure IV.16** presents the SEM images and the chemical elements detected by EDS at the cross-section (CS) and interface transition zone (ITZ).

3.6.1. Cross-section

The SEM images allowed the verification of the coating thickness and the identification of the materials involved. The elements identified in the CS analysis were consistent across all materials, irrespective of the age of the material under analysis and the exposure conditions, as shown in **Figure IV.14**. The predominant elements in steel were iron (F >93%), in the galvanized coating was zinc (Zn >92.6%), and in the concrete were oxygen (O), calcium (Ca), iron (Fe), silicon (Si), aluminium (Al), and potassium (K). It is also noteworthy to state that the black areas, which contain a high percentage of carbon and oxygen, correspond to the epoxy used to prevent fragmentation of the interface during coring.

3.6.2. HDG steel ITZ

Figure IV.15 presents the SEM images of the concrete - galvanized steel interface for both exposure conditions over time.

- At the **90 days**, both SEM images (CC and SW) exhibited crystalline formations that resembled compact tabulated crystals ($Z1_{CC}$, $Z2_{SW}$, and $Z4_{SW}$) with similar elemental compositions. The predominant presence of oxygen (O), zinc (Zn), and calcium (Ca) in these regions with the plate morphology suggests the possible initial formation of compounds associated with the early stages of zinc corrosion, namely zinc oxide (ZnO), zinc hydroxide ($Zn(OH)_2$), and calcium hydroxyzincate ($Ca[Zn(OH)_3]_2 \cdot 2H_2O$). $Z1_{SW}$ exhibits a high proportion of zinc and oxygen, suggesting a composition dominated by zinc oxides (ZnO) and zinc hydroxides ($Zn(OH)_2$). The presence of calcium (6.3%) and silicon (3.2%) indicates a potential interaction with the concrete, which may result in the formation of calcium hydroxyzincates ($Ca[Zn(OH)_3]_2 \cdot 2H_2O$).

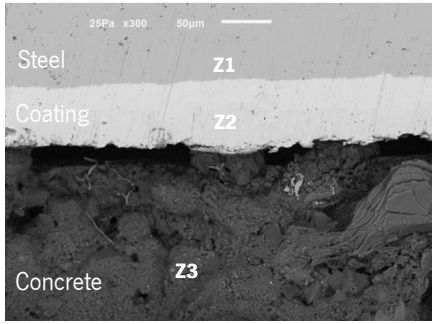
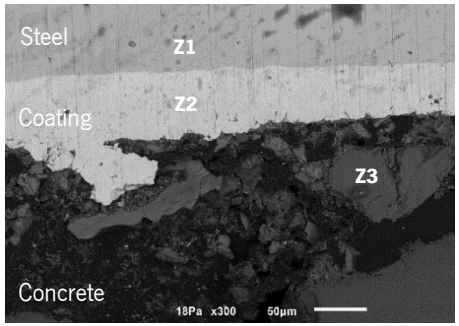
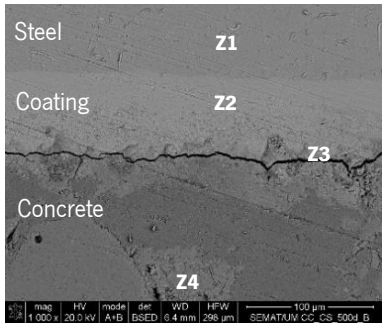
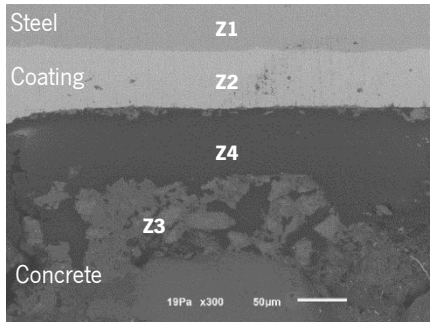
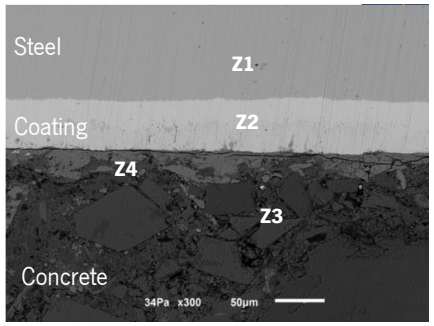
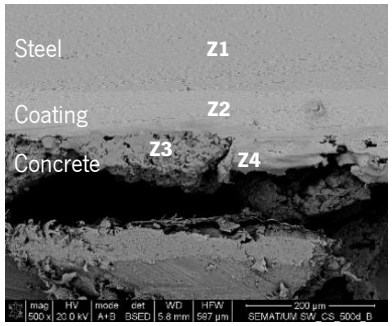
	90 days	190 days	500 days
CC			
	Z1: Fe (96.4%), Zn (2.7%), O (0.9%) **Z2: Zn (90.5%)**, Fe (7.1 %), O (1.8%), Si (0.7%) **Z3: O (44.1%)**, **Ca (17.5%), Fe (10.2%), Zn (10.0%), Si (9.2%),** Al (3.9%), K (2.4%), Mg (1.3%), S (0.7%)	**Z1: Fe (93%)**, Zn (5.2%), O (1%), Si (0.8%) **Z2: Zn (92.6%)**, Fe (4.2 %), O (2.2%), Si (1.%) **Z3: O (43.1%)**, **Ca (19.3%), Fe (10.4%), Si (9.7%), Zn (9.5%),** Al (3.1%), K (2.9%), Mg (1.4%), S (0.6%)	**Z1: Fe (100%)** **Z2: Zn (95.47%)**, Fe (4.63%) **Z3: Zn (39.4%), O (24.4%), C (19.7%), Ca (14.1%)**, Si (1.8%), Al (0.6%) **Z4: O (44.2), Si (26.7%)**, **Al (11.1%)**, **Na (6.1%)**, **Au (5.3%)**, C (3.3%), Ca (2.6%), K (0.7%)
SW			
	Z1: Fe (92.9%), Zn (5.3%), O (1.2%), Si (0.6%) **Z2: Zn (92.1%)**, Fe (4.5%), O (2.4%), Si (1%) **Z3: O (50.9), Ca (26.6%), Si (10.2%),** Fe (4.2%), Zn (3.7%), Al (2.9%), Mg (0.9%), S (0.6%) **Z4: O (51.3%), Zn (21.1%), Fe (17.7%)**, Si (6.4%), Ca (3.5%)	**Z1: Fe (92.4%)**, Zn (3.2%), C (2.4%) , O (1.1%), Si (0.9%), **Z2: Zn (83%), Fe (10%),** C (2.9%), O (2.6%), Si (1.2%), Ca (0.3%) **Z3: O (40.8%)**, **C (27.1%), Si (21.7%), Ca (3.0%),** Fe (2.8%), Zn (2.8%), Al (1%), K (0.7%), Cl (0.2%) **Z4: O (36.5%), Zn (35.8%), Ca (8.6%), C (7.4%), Fe (5%)**, Si (3.8%), Al (1.4%), K (0.8%), Mg (0.7%)	**Z1: Fe (100%)** **Z2: Zn (93.32%)**, Fe (6.68%) **Z3:Zn (67.5%), C (15.6%), O (10.6%), Ca (5.3%)**, Si (0.8%) **Z4: O (41.3), Si (20.1%)**, **C (19.7%)**, **Ca (15.1%)**, Al (2.0%), Na (0.8%), Mg (0.5%), K (0.4%)

Figure IV.14: Cross-section SEM images for both exposure condition over time.

$Z3_{sw}$ in Z_{cc} exhibits acicular formations, which are typical of compounds that grow in an alkaline environment, such as zinc oxide and zinc hydroxide. These formations have a high proportion of zinc and oxygen, confirming the formation of zinc-rich corrosion products. The traces of sodium and calcium suggest the possible presence of mixed zinc and calcium hydroxides. The $Z5_{sw}$ sample was found to contain a high proportion of oxygen and calcium, indicating a strong presence of calcium carbonates ($CaCO_3$) and calcium hydroxides ($Ca(OH)_2$). These are typical of interactions with the cement paste. The presence of silicon and aluminium suggests the formation of calcium silicates and possible aluminates, resulting from cement hydration.

- At **190 days**, in Z1 ($Z1_{cc}$ and $Z1_{sw}$), a tabular morphology is observed with a predominance of O (>40%), Zn (>35%), and Ca (>12%), which is similar to the observations made at 90 days. The high concentrations of oxygen and zinc suggest the presence of zinc oxides or hydroxides, $Zn(OH)_2$ or ZnO), which are formed as corrosion products of the galvanized coating when it comes into contact with the alkaline environment of the concrete.

The presence of carbon and calcium suggests possible interactions with the concrete, which may result in the formation of compounds such as calcium carbonate and calcium hydroxyzincates. The presence of traces of carbon (C) and silica (Si) suggests contributions from the concrete matrix or secondary reaction products. The Z2 region ($Z2_{cc}$ and $Z2_{sw}$) has been found to contain high concentrations of O and Ca, suggesting the formation of calcium hydroxides (portlandite) or calcium-containing compounds associated with corrosion products. The correlation between these compounds and Si indicates the possible formation of silicate-based compounds. The moderate zinc content (8.0%) suggests that reactions between the galvanized coating and calcium compounds in the concrete may have led to the formation of mixed compounds, such as calcium zinc hydroxycarbonate, potentially with increased environmental contamination (chlorides and sulphates). The presence of S and Cl may indicate the formation of sulphates and chlorides, possibly due to exposure to seawater, which suggests an initial interaction between zinc and chlorides. The elevated levels of zinc and oxygen in $Z3_{cc}$ imply a heightened formation of zinc oxides.

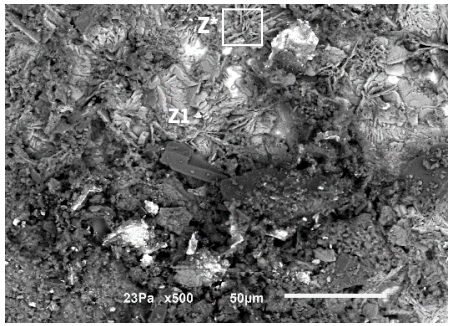
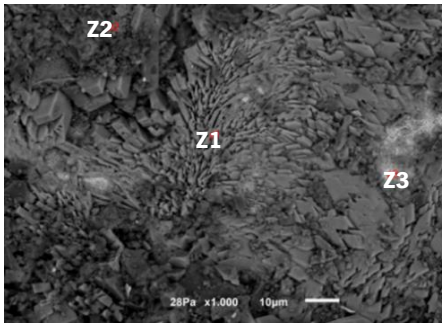
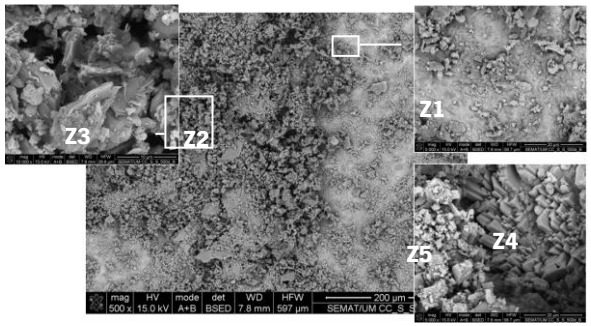
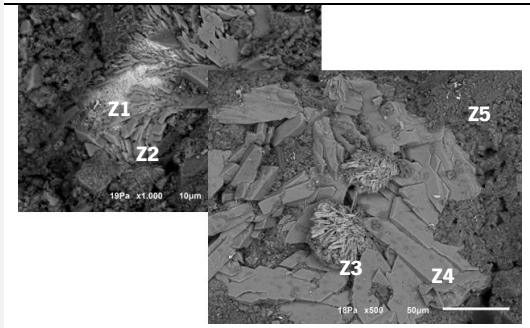
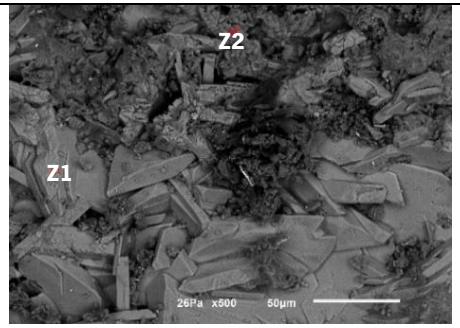
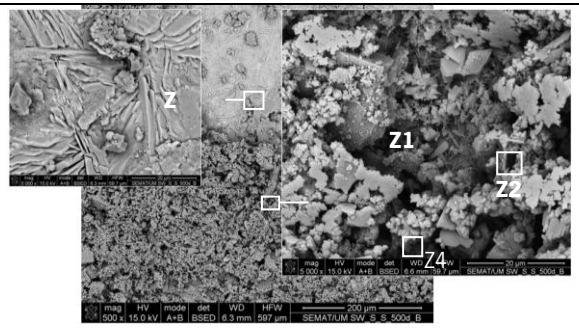
	90d	190d	500d
CC			
	$Z1_{cc}$: O (42%), Zn (33.4%), Ca (19.3%), Si (2.9%), Fe (1.4%), Al (1%) Z_{cc}*: nd	**$Z1_{cc}$: O (42.1%), Zn (35.2%), Ca (12.3%);** C (4.2%), Na (3.4%), Si (2.1%), Al (0.7%) **$Z2_{cc}$: O (48.4%), Ca (23.1%), C (9.6%), Si (7.4%), Zn (6.0%)**, Al (2.0%), S (1.3%), Fe (0.9%), K (0.7%), Mg (0.7%) **$Z3_{cc}$: Zn (58.6%), O (25.9%), C (6.7%),** Ca (4.3%), Si (2.9%), Al (1.2%), K (0.4%)	**$Z1_{cc}$: Zn (57.3%), O (17.7%), Ca (9.8%);** C (6.9%), Si (6.1%), Al (2.1%) **$Z2_{cc}$: O (32.5%), Si (23%), Ca (17.7%), Zn (7.5%), C (6.8%), Al (5.2%),** Fe (4.6%), K (2.1%), Mg (0.6%) **$Z3_{cc}$: Ca (44.8%), O (26.3%), Si (13.4%), Zn (6.4%), C (5.2%),** Fe (2.1%), Al (1.1%), K (0.6%), **$Z4_{cc}$: Zn (46.2%)**, **O (31.8%), Ca (12.9%), C (5.2%),** Si (2.9%), Al (0.6%), K (0.4%), **$Z5_{cc}$: O (26.9%), Si (25.8%), Ca (15.4%), Zn (11%), C (8.7%), Fe (5.3%),** Al (4.7%), K (2.3%)
SW			
	$Z1_{sw}$: Zn (60.9%), O (26.8%), Ca (6.3%), Si (3.2%), Al (1.9%), K (1%) **$Z2_{sw}$: O (43.3%), Zn (34.3%), Ca (14.6%),** Na (3.5%), Si (3.1%), Al (1.2%) **$Z3_{sw}$: Zn (55%), O (33.6%), Na (5.7%)**, Ca (3.8%), Si (1.3%), Al (0.6%) **$Z4_{sw}$: O (43.2%), Zn (36.8%), Ca (12.2%), Na (6.2%)**, Si (1.5%) **$Z5_{sw}$: O (51.8%), Ca (28.9%), Si (8.2%)**, Zn (4.3%), Al (2.7%), Fe (2.2%), S (1%), Mg (0.9%)	**$Z1_{sw}$: O (41.2%), Zn (37.8%), Ca (13.8%);** C (4.4%), Si (2.2%), Al (0.%) **$Z2_{sw}$: O (49.7%), Ca (25.3%), Si (8.6%), Zn (8.0%)**, Al (2.6%), Fe (1.9%), S (1.3%), Mg (1%) Cl (0.9%), K (0.6%)	**$Z1_{sw}$: Si (41.6%), O (38.6%), C (12.4%), Ca (6.9%);** Al (0.5%) **$Z2_{sw}$: Ca (40.8%), O (20.8%), Zn (12.6%), Si (12.5%), C (5.9%),** Fe (4.5%), Al (2.4%), Mg (0..6%) **$Z3_{sw}$: O (44.1%), Ca (22.5%), C (13.7%), Si (5.5%), Mg (5.1%),** Zn (4.8%), Al (1.9%), Fe (1.8%), K (0.7%) **$Z4_{sw}$: Zn (46.2%)**, **O (31.8%), Ca (12.9%), C (5.2%),** Si (2.9%), Al (0.6%), K (0.4%), **$Z5_{sw}$: O (26.9%), Si (25.8%), Ca (15.4%), Zn (11%), C (8.7%), Fe (5.3%),** Al (4.7%), K (2.3%)

Figure IV.15: HDG steel ITZ SEM images for both exposure condition over time.

- At **500 days**, $Z1_{CC}$, $Z4_{CC}$, and $Z4_{SW}$ exhibit a high concentration of Zn and O, suggesting the presence of zinc oxide and zinc hydroxides. The presence of Ca and C may indicate the formation of carbonates, and a morphology with an irregular surface featuring visible crystals or dendrites is observed.

In $Z2_{CC}$, $Z5_{CC}$, and $Z5_{SW}$, the presence of crystalline or granular deposits with a high concentration of O and Si suggests the presence of silicates. The presence of Ca, Zn, and C may indicate the formation of carbonates and complex oxides. With high concentrations of Ca and O, $Z3_{CC}$ and $Z2_{SW}$, suggesting the presence of calcium carbonate ($CaCO_3$) and calcium hydroxide ($Ca(OH)_2$). The former presents a tabular morphology, while the latter exhibits a nanorod structure. The presence of Zn, Si, and Fe may indicate the formation of silicates and complex oxides, related to the interaction with the cementitious matrix of the concrete. In $Z3_{SW}$, the prevalence of O and Ca is also documented, although calcium is present in smaller quantities, suggesting a possible greater presence of oxides, such as calcium hydroxide (Ca(OH)2) or zinc oxides (ZnO). Carbon is also higher, which may indicate greater formation of carbonates (CaCO3 and $ZnCO_3$), possibly due to exposure to seawater and reactions with dissolved CO_2. $Z1_{SW}$ suggests the presence of silicates due to the high content of Si and O, while the presence of C and Ca may indicate calcium carbonate, possibly due to seawater exposure.

3.6.3. ITZ at the concrete side

Figure IV.16 presents the concrete ITZ SEM images for both exposure condition over time.

- At **90 days** the CC sample exhibited crystalline formations on the interface surface of the concrete. These formations were primarily composed of oxygen (O), zinc (Zn), and calcium (Ca) ($Z1_{CC}$ and $Z3_{CC}$) suggesting the formation of corrosion products, including zinc oxide (ZnO), zinc hydroxide ($Zn(OH)_2$), and calcium hydroxyzincate ($Ca[Zn(OH)_3]_2{\cdot}2H_2O$) with the migration of calcium ions from the concrete to the interface. Additionally, the high concentration of O might be associated with oxidation processes. $Z2_{CC}$ indicates the predominance of iron (Fe), possibly due to the localized transfer of the zinc layer during interface detachment. In the sample exposed to SW, a high concentration of O and Ca is observed in $Z1_{SW}$ and $Z2_{SW}$, which may suggest the presence of calcium hydroxide ($Ca(OH)_2$) and possibly calcium carbonate ($CaCO_3$). The presence of S may indicate the formation of sulphates due to exposure to seawater.

- At **190 days**, the composition of the concrete surface in CC remains similar to that at 90 days, with the presence of Zn and Ca again indicating the formation of corrosion products ($Z1_{cc}$), while a slight increase in carbon (C) suggests the ongoing carbonation of the concrete. The high concentration of O (50%) and Ca (21%), along with significant amounts of silicon (Si - 9.7%) and C (8.9%) at $Z2_{cc}$, suggests the presence of calcium hydroxide ($Ca(OH)_2$) and possibly calcium carbonate ($CaCO_3$) due to carbonation. The presence of Zn indicates that zinc corrosion is still active. The SW sample zone, $Z1_{sw}$, preserves the same composition at 90 days, with observed morphological formations of ZnO nanorods.

- At **500 days**, the CC sample exhibited a predominance of Si and O, accompanied by significant amounts of Ca and C. This observation suggests a greater influence of the concrete aggregates, indicating the potential formation of silicates and calcium carbonation with zinc corrosion products ($Z1_{cc}$, $Z4_{cc}$, $Z5_{cc}$).

The high concentration of Ca and O confirms the formation of corrosion products ($Z2_{cc}$, $Z3_{cc}$), suggesting the presence of calcium hydroxide ($Ca(OH)_2$) and/or calcium carbonate ($CaCO_3$). The high concentration of Si and O suggests the influence of the concrete aggregates. The presence of Mg may indicate the possible presence of dolomite or interaction with cement.

The specimens exposed to SW also demonstrate elevated concentrations of zinc, oxygen and calcium, indicative of corrosion products namely calcium hydroxyzincate resulting from the cathodic reaction between the concrete and the zinc layer ($Z2_{sw}$). The prevalence of oxygen (39.8%) and magnesium (29.6%), accompanied by substantial amounts of zinc (20.5%) and carbon (8.3%), in $Z1_{sw}$ and $Z3_{sw}$, further support the hypothesis that corrosion products were formed. The elevated concentrations of silicon (Si) and aluminium (Al) imply the presence of silica (SiO2) and alumina (Al_2O_3) from the concrete aggregates, while the presence of carbon (C) indicates carbonation ($Z4_{sw}$). The presence of gold (Au) and palladium (Pd) corresponds to the use of conductive coatings in the preparation ($Z6_{cc}$, $Z5_{sw}$).

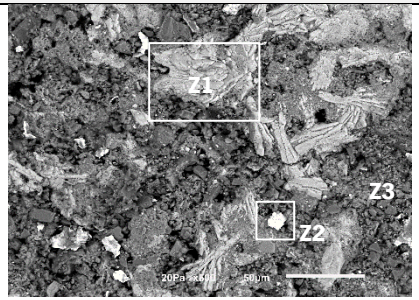
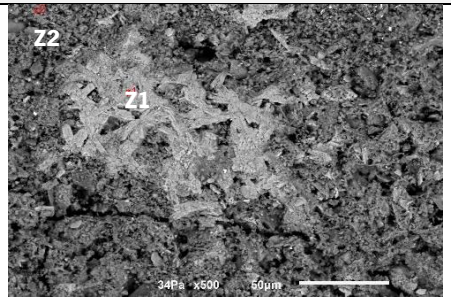
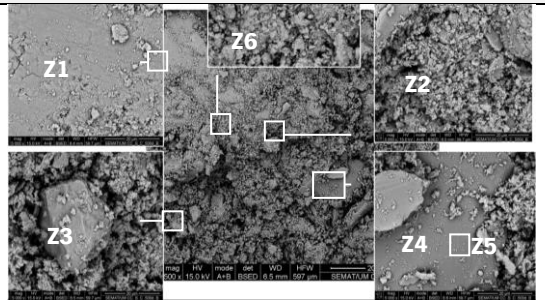
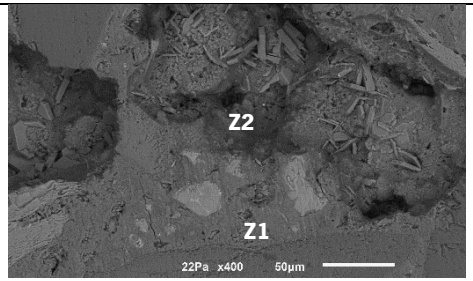
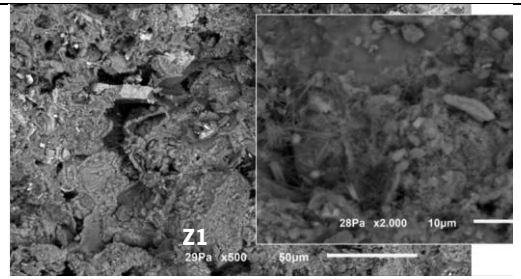
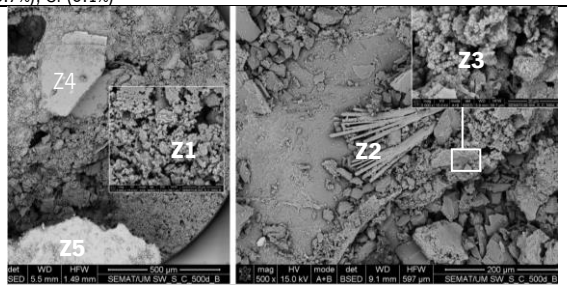
	90d	190d	500d
CC			
	$Z1_{cc}$: O (43.4), Zn (37.9%), Ca (13.2%), Na (3.0%), Si (1.7%), Al (0.6%), K (0.3%) **$Z2_{cc}$: Fe (72.5%)**, Zn (13.4%), Si (5%), Ca (4%), Zn (3%), Al (1.5%), K (0.7%) **$Z3_{cc}$: O (48.6), Zn (20.5%), Ca (18.5%)**, Fe (3.7%), Al (3.2%), K (2.1%), Na (1.4%), Zn (1%), Mg (0.5%), S (0.5%)	**$Z1_{cc}$: O (43.6%), Zn (31.4%), Ca (12.1%),** C (5%), Na (3.0%), Si (2.9%), Al (1.2%), K (0.4%), Mg (0.3%), S (0.3%) **$Z2_{sw}$: O (50%), Ca (21%), Si (9.7%) C (8.9%),** Zn (4.3%), Al (2.6%), K (1.1%), Fe (0.9%), Na (0.8%), S (0.5%), Mg (0.3%)	**$Z1_{cc}$: Si (29.5%), O (21.6%), Ca (18.4%), C (17.7%), Zn (8.6%),** Fe (2.63%), Al. (1.6%) **$Z2_{cc}$: Ca (41.9%), O (33.0%), Si (11.1%), C (10.5%),** Al (3.4%) **$Z3_{cc}$: Ca (36.1%), O (30.7%), C (10.4%), Fe (7.3%), Si (7.0%), Al (6.7%),** Mg (1.8%) **$Z4_{cc}$: Si (59.3%), O (22.3%), C (15.3%), Ca (3.19%)** **$Z5_{cc}$: O (31.3%), Si (22.8%), C (13.9%), Fe (11.9%), Al (7.3%), Ca (5.8%),** K (4.2%), Mg (3.3%) **$Z6_{cc}$: Au (60.62%), Zn (22.1%), Pd (5.6%), C** (3.6%), O (4.3%), Ca (3.7%), Si (0.1%)
SW			
	$Z1_{sw}$: O (49.2%), **Ca (44.6%),** Si (4.6%), K (0.9%), Al (0.7%) **$Z2_{sw}$: O (55.1%)**, **Ca (27.7%),** Si (9.8%), Al (2.5%), Fe (2%), S (1.1%), Mg (1%), K (0.8%),	**$Z1_{sw}$: O (56.4), Ca (16.2%), Si (12%), Al (5.6%),** S (3.6%), C (3.4%), Na (1.8%), K (0.8%), Mg (0.2%)	**$Z1_{sw}$: O (27.8%), Zn (19.4%), Si (18.4%), Mg (12.4%), C (10.3%), Al (7.1%),** Ca (4.1%), Al (0.7%) **$Z2_{sw}$: Zn (46.6%), O (26.1%), Ca (12.9%), Si (7.9%), C (5.8%),** Al (0.58%) **$Z3_{sw}$: O (29.8%), Mg (29.6%), Zn (20.5%), C (8.3%), Si (6.6%),** Ca (3.7%), Al (1.5%), **$Z4_{sw}$: Si (26.9%), O (26.3%), Al (18.1%), C (17.2%), K (8.7%),** Ca (2.7%) **$Z5_{sw}$: Au (64.5%), Zn (11.6%), Pd (6.7), Ca (6.7%), O (5.4%),** C (3.8%), Si (1.3%)

Figure IV.16: Concrete ITZ SEM micrographs for both exposure condition over-time.

4 CONCLUSIONS

This work describes the results of an experimental program developed to study the bond behaviour between concrete and galvanized steel tubes with smooth surface. Specimens were prepared and tested over time after being exposed to 2 different conditions: CC - climatic chamber and SW - seawater. For that, different specimens were built, namely (i) 63 pushout specimens; (ii) 18 samples for FEG-SEM/EDS analysis; and (iii) 20 cylinders to characterize concrete mixtures at 7, 28, 90, 190 and 500 days of age. The main goal was to study the influence of (i) the exposure conditions over time and (ii) the bond length (LB = 50, 75 and 100 mm) on the bond behaviour. Base on the results obtained, the following main conclusions are drawn:

1. The behaviour of the tested specimens was consistent and similar to what has been previously reported in the literature. The experimental responses were characterized by a positive initial steep slope, due to the strong bond between materials, reaching $F_{l,max}$ and followed by a gradual softening to a residual stress plateau. The transition occurs smoothly, except for the LB100 specimens which showed an abrupt loss of load bearing capacity.
2. The F_l-s_l experimental responses obtained showed an essentially similar behaviour for all specimens, regardless of the environmental exposure condition, time of exposure and LB adopted.
3. The mechanical performance variables in the SW specimens showed a slight decrease when compared with CC ones, which highlights the initial bond degradation due to seawater exposure. An average decrease of -14.3% was obtained for $\tau_{max,}$ with a maximum of -32%.
4. The specimens exposed to SW showed a gradual and consistent increase in the value of τ_{max} and $\bar{\tau}_{máx}$ with prolonged exposure time. This suggests that the migration of zinc corrosion products may be filling the concrete pores that were potentially formed during the cathodic reaction between zinc and the cement paste at an early stage.
5. No clear trend was observed for the evolution of the mechanical performance variables obtained for CC specimens over time. The exposure time does not seem to significantly influence the evolution of the analysed parameters in the specimens exposed to CC, even up to 500 days.
6. The values of F_r and $F_r/F_{l,max}$ seem to decrease overtime and the order of magnitude of $\overline{G}_f$ was similar among all specimens' groups and categories.

7. The failure modes observed were consistent among all test specimens with the same bond length (LB). A homogeneous cement bonding film was visible at the interface, and the SW specimens showed a "thicker" film as well as some signs of corrosion, namely at 500 days.
8. The FEG-SEM/EDS analysis allowed to identify several crystalline phases commonly mentioned in the literature as zinc corrosion products, which typically occur when galvanized steel comes into contact with the alkaline environment of fresh concrete, such as zinc oxide (ZnO), zinc hydroxide (Zn(OH)2), calcium zincate ($Ca[Zn(OH)_3]_2.2H_2O$), and may have affected the bond between concrete and steel either in a positive way by filling the pores or negatively, by causing physical separation at the interface, as suggested by other researches [16].
9. The presence of these crystals suggests the formation of an initial passivation layer, but it can also indicate ongoing corrosion under prolonged exposure, especially at interfaces with water or saline environments. The presence of S and Mg suggests the formation of sulphates and corrosion products due to the contact with seawater.

Future studies should include X-ray diffraction (XRD) to distinguish crystalline phases like $CaZn_2(OH)_6 \cdot 2H_2O$ and explore longer exposure periods, also with standard steel specimens to assess bond strength variation and compare results with galvanized steel specimens.

ACKNOWLEDGEMENTS

This work is financed by national funds through FCT – Foundation for Science and Technology, under Grant agreement SFRH/BD/137220/2018 attributed to the 1st author. This work was partly financed by FCT/MCTES through national funds (PIDDAC) under the R&D Unit Institute for Sustainability and Innovation in Structural Engineering (ISISE), under Reference UIDB/04029/2020 (https://doi.org/10.54499/UIDB/04029/2020), and under the Associate Laboratory Advanced Production and Intelligent Systems ARISE under Reference LA/P/0112/2020. This work was partially funded by the research projects ''NEXTSEA: Next Generation Monitoring of Coastal Systems in a Scenario of Global Change", NORTE-01-0145-FEDER-000032; and "R2UTechnologies - modular systems", PRR C644876810-00000019, funded by Plano de Recuperação e Resiliência.

REFERENCES

[1] Afshar A, Jahandari S, Rasekh H, Shariati M, Afshar A, Shokrgozar A. Corrosion resistance evaluation of rebars with various primers and coatings in concrete modified with different additives. Constr Build Mater 2020;262:120034. https://doi.org/10.1016/j.conbuildmat.2020.120034.

[2] Liu PC. Damage to concrete structures in a marine environment. Mater Struct 1991;24(4):302–307. https://doi.org/10.1007/BF02472086.

[3] Ragab AM, Elgammal MA, Hodhod OAG, Ahmed TES. Evaluation of field concrete deterioration under real conditions of seawater attack. Constr Build Mater 2016;119:130–144. https://doi.org/10.1016/j.conbuildmat.2016.05.014.

[4] Shi X, Xie N, Fortune K, Gong J. Durability of steel reinforced concrete in chloride environments: An overview. Constr Build Mater 2012;30:125–138. https://doi.org/10.1016/j.conbuildmat.2011.12.038.

[5] Melchers RE, Chaves IA. Durable steel-reinforced concrete structures for marine environments. 2021.

[6] Wang F, Cheng Z, Shen J. Flexural fatigue behavior of butt-welded circular concrete-filled double skin steel tube (CFDST): Experimental study and numerical modelling. Mar Struct 2023;88:103380. https://doi.org/10.1016/j.marstruc.2022.103380.

[7] Yi Y, Zhu D, Guo S, Zhang Z, Shi C. A review on the deterioration and approaches to enhance the durability of concrete in the marine environment. Cem Concr Compos 2020;113:103695. https://doi.org/10.1016/j.cemconcomp.2020.103695.

[8] Figueira RB, Silva CJR. Corrosion of hot-dip galvanized steel reinforcement. Corros Prot Mater 2014;33(3):51–61.

[9] Yu Z, Hu J, Meng H. A review of recent developments in coating systems for hot-dip galvanized steel. Front Mater 2020;7:74. https://doi.org/10.3389/fmats.2020.00074.

[10] Persson D, Thierry D, Karlsson O. Corrosion and corrosion products of hot dipped galvanized steel during long term atmospheric exposure at different sites world-wide. Corros Sci 2017;126:152–165. https://doi.org/10.1016/j.corsci.2017.06.025.

[11] Pokorný P, Chobotský T, Prodanovic N, Steinerová V, Hurtig K. Bond strength and corrosion protection properties of hot-dip galvanized prestressing reinforcement in normal-strength concrete. J Compos Sci 2024;8(10):407. https://doi.org/10.3390/jcs8100407.

[12] Tej P, Kour M, Pokorný P. Evaluation of the impact of corrosion of hot-dip galvanized reinforcement on bond strength with concrete: A review. Constr Build Mater 2017;132:271–289. https://doi.org/10.1016/j.conbuildmat.2016.11.096.

[13] Yeomans SR. Galvanized reinforcement in bridge and coastal construction. In: Proceedings of the 20th Congress of IABSE; New York City, NY, USA; 2019. p. 1592–1598.

[14] Arguillarena A, Margallo M, Urtiaga A, Irabien A. Life-cycle assessment as a tool to evaluate the environmental impact of hot-dip galvanisation. J Clean Prod 2021;290:125676. https://doi.org/10.1016/j.jclepro.2020.125676.

[15] Ismail M, Muhammad B, Hamzah E, Keong TC. Corrosion behaviour of dual-phase and galvanized steels in concrete. Anti-Corros Methods Mater 2012;59(4):174–181. https://doi.org/10.1108/00035591211224672.

[16] Pokorný P, Pernicová R, Tej P, Kolísko J. Changes of bond strength properties of hot-dip galvanized plain bars with cement paste after 1 year of curing. Constr Build Mater 2019;226:920–931. https://doi.org/10.1016/j.conbuildmat.2019.07.147.

[17] da Fonsêca MSDAB, Meira GR. Accelerated chloride-induced corrosion of hot-dipped galvanized reinforcements and its influence on bond strength to concrete. Constr Build Mater 2024;426:136123. https://doi.org/10.1016/j.conbuildmat.2024.136123.

[18] Yeomans SR. Galvanized steel reinforcement in concrete. Amsterdam, The Netherlands: Elsevier; 2004.

[19] Fratesi R, Moriconi G, Coppola L. The influence of steel galvanization on rebars behaviour in concrete. In: Page CL, Treadaway KWJ, Bamforth PB, editors. Corrosion of reinforcement in concrete construction. Cambridge, UK: Royal Society of Chemistry; 1996. p. 630–641.

[20] Cruz F, Valente IB, Almeida J, Neves A, Pereira E. Experimental characterization of bond between concrete and HDG steel tubes for mixed steel-concrete structures. Mater Struct 2024;57:89. https://doi.org/10.1617/s11527-024-02352-8.

[21] Andrade MC, Macias A. Galvanized reinforcements in concrete. In: Surface Coatings—2. Dordrecht, The Netherlands: Springer; 1988. p. 137–182.

[22] Bellezze T, Malavolta M, Quaranta A, Ruffini N, Roventi G. Corrosion behaviour in concrete of three differently galvanized steel bars. Cem Concr Compos 2006;28(3):246–255. https://doi.org/10.1016/j.cemconcomp.2006.01.011.

[23] Korkeakoulu T. Service life of hot-dip galvanised reinforcement bars in carbonated and chloride-contaminated concrete [MSc thesis]. Espoo, Finland: Helsinki University of Technology; 2009.

[24] Kazemi H, Yekrangnia M, Shakiba M, Bazli M, Vatani Oskouei A. Bond-slip behaviour between GFRP/steel bars and seawater concrete after exposure to environmental conditions. Eng Struct 2022;268:114796. https://doi.org/10.1016/j.engstruct.2022.114796.

[25] Kazemi H, Yekrangnia M, Shakiba M, Bazli M, Vatani Oskouei A. Bond durability between anchored GFRP bar and seawater concrete under offshore environmental conditions. Mater Struct 2023;56(3):72. https://doi.org/10.1617/s11527-023-02153-5.

[26] Zhou R, Zhou F, Du Y, Liao B, Feng G, Zhu D. Effect of seawater on bond performance between BFRP bars and seawater sea-sand concrete. Constr Build Mater 2024;415:135050. https://doi.org/10.1016/j.conbuildmat.2024.135050.

[27] Andrade C, Arteaga A, Lopez-Hombrados C, Vazquez A. Tests on bond of galvanized rebar and concrete cured in seawater. J Mater Civ Eng 2001;13(5):319–324.

[28] Rivera-Corral JO, Fajardo G, Arliguie G, Orozco-Cruz R, Deby F, Valdez P. Corrosion behavior of steel reinforcement bars embedded in concrete exposed to chlorides: Effect of surface finish. Constr Build Mater 2017;147:815–826. https://doi.org/10.1016/j.conbuildmat.2017.04.186.

[29] Yeomans SR. Comparative studies of galvanized and epoxy coated steel reinforcement in concrete. Melbourne, Australia: BHP Research; 1991.

[30] Cruz F, Valente IB, Maslov D, Miranda T, Pereira EB. Engineering-driven approach for the structural design of geometrically complex modular artificial reefs. Appl Sci 2025;15:5907. https://doi.org/10.3390/app15115907.

[31] Cruz F, Valente IB, Miranda T, Pereira EB. Construction and characterization of a structural unit for modular artificial reefs. Structures 2025;81:110154. https://doi.org/10.1016/j.istruc.2025.110154.

[32] Cruz F, Valente IB, Monteiro F, Maslov D, Miranda T, Pereira EB. Development and characterization of structural connections for modular artificial reefs. Ocean Eng 2025;320:120311. https://doi.org/10.1016/j.oceaneng.2025.120311.

[33] European Committee for Standardization (CEN). EN 1992-1-1: Eurocode 2: Design of concrete structures—Part 1-1: General rules and rules for buildings. Brussels, Belgium: CEN; 2004.

[34] European Committee for Standardization (CEN). NP EN 206-1: Concrete—Part 1: Specification, performance, production and conformity. Brussels, Belgium: CEN; 2005.

[35] European Committee for Standardization (CEN). EN 12350-2: Testing fresh concrete—Part 2: Slump test. Brussels, Belgium: CEN; 2009.

[36] European Committee for Standardization (CEN). EN 12390-1: Testing hardened concrete—Part 1: Shape, dimensions and other requirements for specimens and moulds. Brussels, Belgium: CEN; 2012.

[37] European Committee for Standardization (CEN). EN 12390-13: Testing hardened concrete—Part 13: Determination of secant modulus of elasticity in compression. Brussels, Belgium: CEN; 2013.

[38] European Committee for Standardization (CEN). EN 12390-3: Testing hardened concrete—Part 3: Compressive strength of test specimens. Brussels, Belgium: CEN; 2009.

[39] International Organization for Standardization (ISO). ISO 6892-1: Metallic materials—Tensile testing—Part 1: Method of test at room temperature. Geneva, Switzerland: ISO; 2009.

ANNEX A – SEAWATER PARAMETERS

Table IV.6 presents the seawater parameters obtained from physical-chemical analysis carried out in the laboratory at the different phases of the adherence tests. As can be seen, the salinity of the water extracted directly from the sea is higher than the seawater present in the tank. Furthermore, a small decrease in dissolved elements and salts present in the water is generally observed over time.

Figure IV.17 shows the continuous measurement of the seawater parameters measured by the built monitoring system, namely in terms of salinity, temperature, pH, TDS and ORP. In general, it seems that the values obtained by the monitoring system are consistent with those obtained from laboratory analyses. It is also observed that the temperature, salinity and TDS curves have the same shape, denoting a decrease in salinity and TDS values with the decrease in temperature. The pH value, although uniform and constant, increases slightly with decreasing temperature and salinity. Nevertheless, it is possible to conclude that the seawater did not undergo significant changes that would compromise the pushout durability tests.

Table IV.6: Parameters of seawater according to the pushout test dates.

	Unit	Sea*	0 day	90 days	190 days	500 days
pH POW.002/Potenciometria	-	7.2	7.7	8.2	8.1	8.3
Electric conductivity (25°C) POW.003/ Conductimetry	dS/m	57.6	45.5	47.3	42.8	50.2
Salinity POW.026/Conductimetry and calculation	g/L	38.5	29.7	31.0	27.8	33.0
Total dissolved solids POW.018 / Gravimetry	g/L	46.1	36.4	37.9	34.3	40.2
Redox potential MI nç 146 (09.06.2010)	mV	-39.5	-77.7	-88.6	-79.9	-87.0
Organic matter POW.023/catarometry and calculus	%	<1.00	<1.00	<1.00	<1.00	<1.00
Chloride POW.007/ Spectrometry	mg/L	18226	18299	15614	17193	14032
Calcium POW.001/ICP-OES	mg/L	359	474	289	272	215
Magnesium POW.001/ICP-OES	mg/L	1220	1600	1131	1068	1004
Sodium POW.001/ICP-OES	mg/L	9489	10020	8878	7887	7000
Potassium POW.001/ICP-OES	mg/L	508	1189	404	463	370
Strontium POW.001/ICP-OES	mg/L	4.78	nd	4.73	2.99	nd
Fluoride POW.017/ICP-OES	mg/L	0.78	nd	1	<0.5	nd
Boron POW.001/ICP-OES	mg/L	1.17	4.03	1.46	1.67	1.39
Sulfate POW.001/ICP-OES	mg/L	2457	3823	2579	3167	2217
Bicarbonates POW.008/Volumetria	mg/L	953.4	144.0	873.9	289.1	284.3
Sodium chloride (NaCl)	mg/L	24121	25471	22568	20049	17794
Magnesium chloride (MgCl)	mg/L	4779	6268	4431	4184	3933
Sodium sulphate (Na_2SO_4)	mg/L	3633	5652	3814	4682	3278
Calcium chloride (CaCl)	mg/L	995	1312	801	753	595
Potassium chloride (KCl)	mg/L	969	2267	770	883	706
Sodium bicarbonate ($NaHCO_3$)	mg/L	1313	198	1203	398	391
Boric acid (H_3BO_3)	mg/L	6.7	23	8.4	9.6	7.9
Strontium chloride ($SrCl_2$)	mg/L	8.6	nd	8.6	5.4	nd

*seawater collected directly from the sea to analyse; 0 day means the day before placement of the samples.

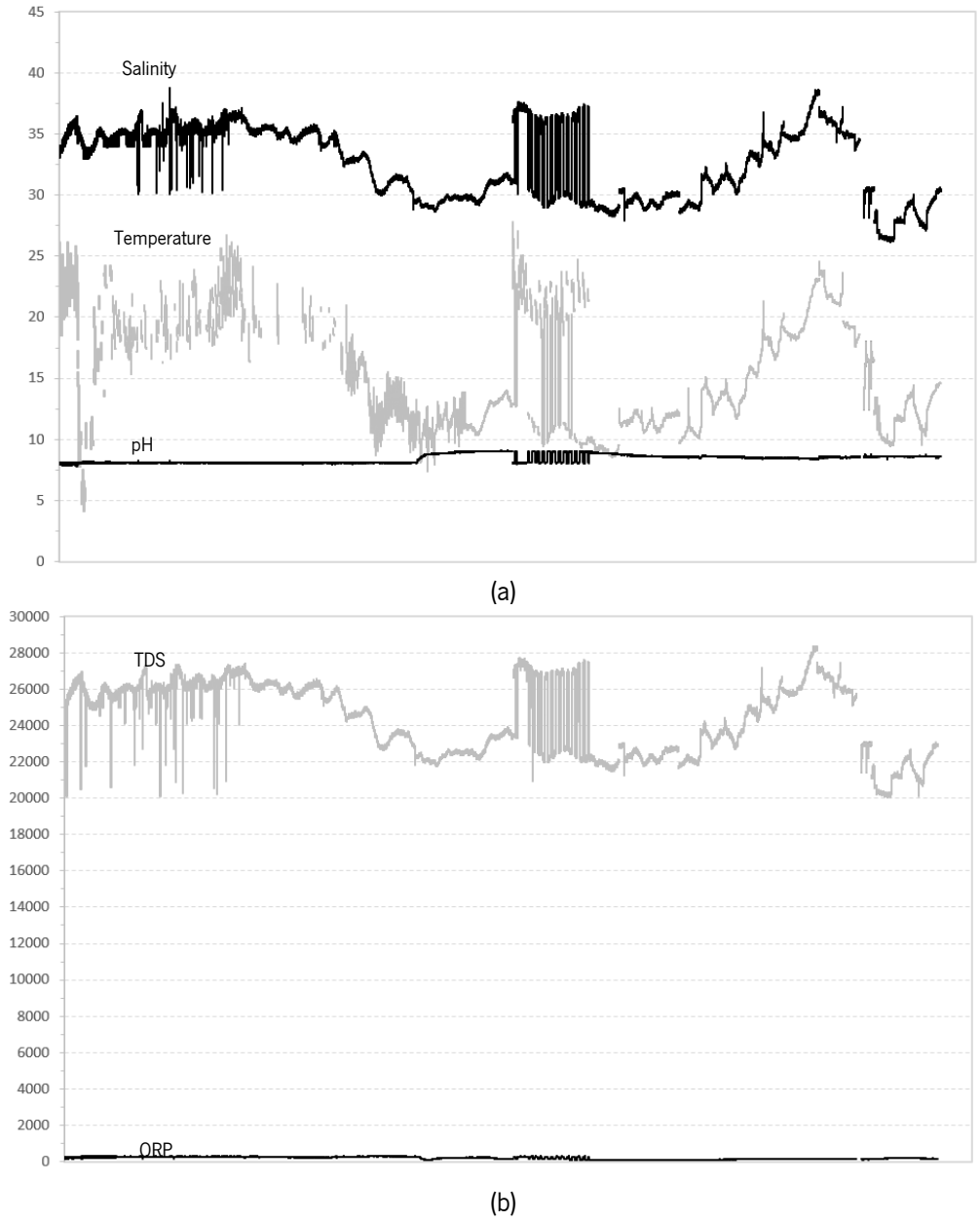


Figure IV.17: Continuous measurements of seawater parameters from the built monitoring system: (a) seawater temperature, pH and salinity and (b) Total Dissolved Solids (TDS) and Oxydation Reduction Potential.

PAPER V

CONSTRUCTION AND CHARACTERIZATION OF STRUCTURAL UNIT FOR MODULAR ARTIFICIAL REEFS

REFERENCE: Cruz F, Valente IB, Miranda T, Pereira EB. Construction and characterization of a structural unit for modular artificial reefs. Structures 2025;81:110154. https://doi.org/10.1016/j.istruc.2025.110154. Impact factor: 4.3

ABSTRACT: In recent years, the development of artificial reefs has gained significant importance, driven by the need to preserve marine ecosystems and promote the sustainability of human activities. These structures increasingly incorporate complex geometries to enhance their functionality and ecological integration, requiring advanced modelling approaches, more flexible and innovative construction methods.

Given the need to address this increasing complexity, this study focuses on the construction and experimental characterization of a modular artificial reef unit using two alternative structural systems: reinforced concrete (RC) and engineered cementitious composite (ECC). The module development involved the use of 3D-printed moulds to optimize fabrication and reduce costs. Full-scale structural tests, including bending tests, were conducted to evaluate stiffness, strength, ductility, and failure modes of the modules.

The results indicate that the RC unit exhibited superior structural performance, with higher load capacity, greater deformation, and higher initial stiffness compared to the ECC unit. The failure modes differed between the systems, with the RC unit failing due to cracking of the central bulb and failure of the reinforcement lashing, while the ECC unit failed due to separation of one of the loaded limbs. This study also highlights the feasibility of 3D printing for cost-effective and sustainable mould production.

KEYWORDS: Modular multifunctional artificial reef; 3D-printed moulds; Reinforced concrete; Engineered cementitious composite; Experimental structural performance.

1 INTRODUCTION

The construction of artificial reefs has undergone significant evolution over the past decades, driven by the need to restore degraded marine ecosystems and the search for sustainable solutions that promote biodiversity [1–7]. Initially, these reefs were often made from materials of opportunity such as rocks, tires, and obsolete metal structures [8–10]. However, many of these materials proved to be unsuitable due to their potential for pollution and rapid degradation in the marine environment [11]. With advancements in technology and a better understanding of the interactions between artificial structures and the marine environment, significant progress has been made in the development of artificial reefs with more large, complex shapes and more durable materials [12,13]. The design of these structures has been optimized to maximize biological colonization and provide shelter for various marine species [14]. This progress has been driven by technological advancements, including recent developments in smart materials and engineered/strain-hardening cementitious composites (ECC/SHCC) [15–17], as well as innovative parametric tools and advanced manufacturing processes. Conventional subtractive and formative manufacturing methods, which involve casting into moulds or removing material through machining, have evolved to shape more complex forms, though they still have limitations in flexibility [15]. Additive manufacturing (AM), including 3D printing, has been a game changer in recent years, establishing itself as a revolutionary technology in artificial reef production [15–17]. It enables the creation of parameterized and complex geometries with greater precision and efficiency [15]. AM offers significant advantages, including customization, adaptability, mass production with reduced material waste, shorter production times, and competitive costs. Additionally, the ability to fabricate structures with optimized topologies enhances the functionality of artificial reefs [15–17].

Various construction techniques have been employed for artificial reef fabrication, as illustrated in **Figure V.1**. Traditional wood and steel formwork methods have been widely used but offer limited flexibility in shaping complex geometries. Manufactured glass fibre reinforced polymer (GFRP) moulds provide enhanced durability and customization, while silicon moulds allow for more intricate designs. Recent advancements include the use of 3D printing technologies. 3D printed concrete has become a widely used and innovative technique in artificial reef construction, providing greater design freedom and improved structural integration with the marine environment [15,17,18]. Additionally, printing with alternative materials such as plastic [15] clay [13] and sand [19] has also been explored for artificial reef fabrication [18]. For more complex structural systems where direct 3D printing might not be feasible, this technology enables the production of 3D printed moulds for intricate geometries.

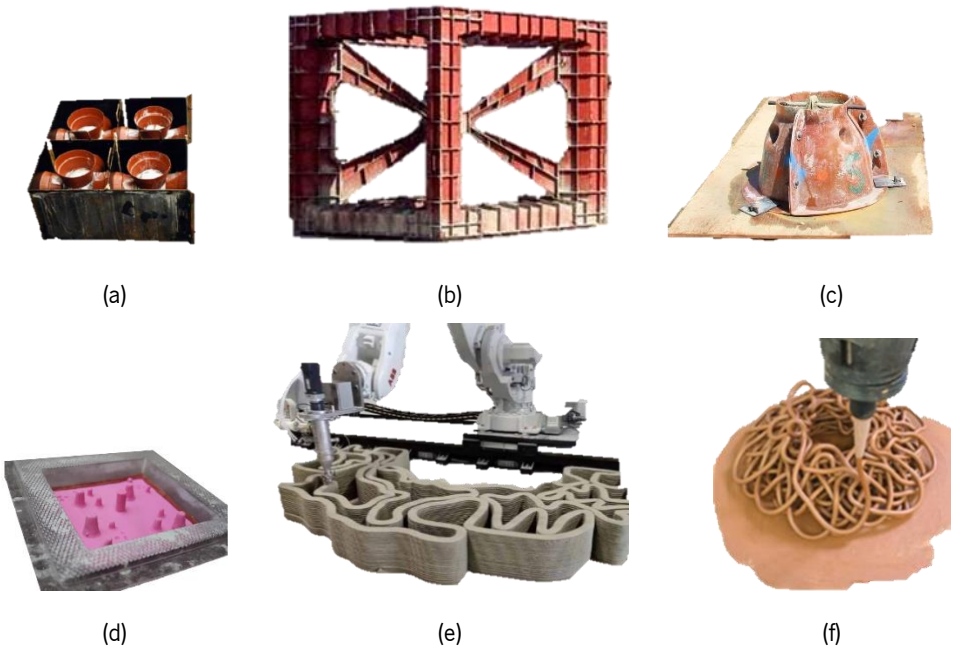


Figure V.1: Construction techniques used for artificial reefs constructions: (a) traditional wood formwork [20], (b) steel formwork [21], (c) manufactured GFRP moulds [22], (d) silicon moulds [23], (e) concrete 3D printer [24] and (f) clay 3D printer [13].

Despite significant advancements in the design and fabrication of artificial reefs, the structural characterization of these modules remains largely unexplored. Most studies focus on ecological and flow field performance [3,25–31], while research on the mechanical behaviour of reef structures is not documented. The absence of standardized mechanical characterization protocols makes it challenging to assess their structural behaviour. Given that artificial reefs must withstand harsh marine conditions, including wave action, currents, and potential impact loads, evaluating their mechanical properties is essential for ensuring their static and dynamic stability and longevity.

In this context, the present study aims to construct a full-scale module for a modular artificial reef using low-cost moulds using 3D printing, followed by its structural characterization. To achieve this, an experimental program was planned, based on mechanical tests, including bending tests and material characterization. The proposed research seeks to contribute to the development of more efficient and sustainable construction solutions for artificial reefs.

2 MODULAR ARTIFICIAL REEF STRUCTURE

2.1. Materials

In light of the challenges faced for the development of artificial reefs and the construction of scalable structures in marine environments, a MMFAR structure was developed, comprising individual modules and a connection system (**Figure V.2**) The development of the MMFAR prototype builds upon a broader research program conducted by the authors. The geometrical concept was established through functional and hydrodynamic studies, which addressed the influence of site conditions, habitat requirements, and flow–structure interactions [35,36]. Complementary research addressed the structural design [37,38], the development and characterization of connection systems [39], and mechanical interfacial behaviour between different materials [40].

In order to ensure optimal conditions for transportation and deployment, a maximum weight of 150 kg was established for each unit, fitting inside a cube with approximately 650 mm side. The limb exhibits a variable cross-section, ranging from approximately 150 mm at the connection end to approximately 196.5 mm at the junction with the central bulb with approximately 300 mm of radius [37]. Besides the requirements of geometric design, which should mimic the complex natural shapes, alternative structural systems for the module were explored (i) RC - reinforced concrete unit with a central galvanized rebar along each limb of the unit; (ii) CS - composite steel and concrete unit with perforated galvanized steel tube, following the geometric centroid of each limb; (iii) ECC - engineered cementitious composite unit, along with a connection system tailored to ensure mechanical stability and straightforward underwater assembly (**Figure V.2**).

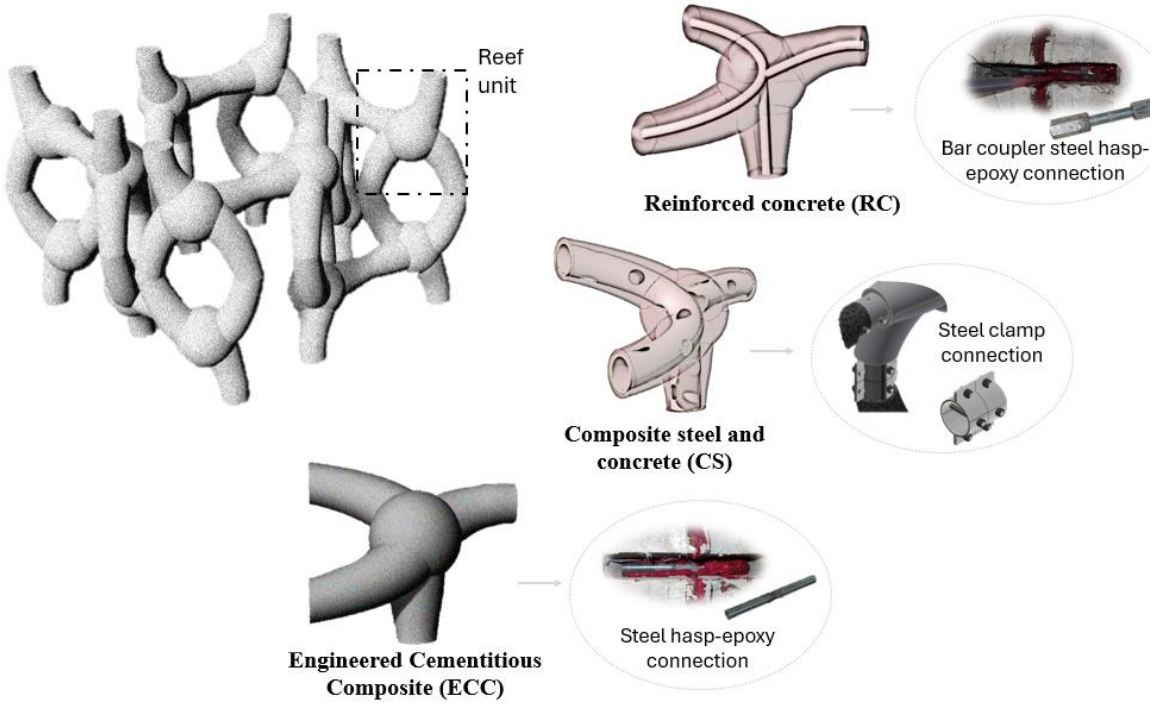


Figure V.2: MMFAR with possible construction systems.

The design process was based on analytical and numerical analysis mostly supported by the recommendation of DNV-RP-C205 and API (actions and hydrodynamic coefficients) [41,42], ISO 19903:2006 (load cases and loads combinations) [43], NP-EN 206-1 (concrete specification) [44], Eurocode 2 [45] and Eurocode 4 [46]. The design of the metallic connector and fastenings-adhesive connector were based on EN 1993-1-8:2011 [47] and EN 1992-4:2018 [48], respectively.

2.2. Materials

The materials involved in the scope of the present investigation were (i) concrete; (ii) ECC and (iii) threaded rod DIN 976-1, 8.8 Zn, M16. The concrete and ECC composition follow the quantities given in **Table V.1** and **Table V.2**.

Table V.1: Materials composition for 1 m^3 of concrete.

Cement II AL 42,5R	Fine sand 0/2	Fine sand 0/4	Coarse sand 6/14	Water	SP 3530	PL 476N
450 kg	294.5 kg	750.0 kg	558.0 kg	201.8 kg	1.6 kg	1.6 kg

Table V.2: Materials composition for 1 m³ of ECC.

Cement II AL 42,5R	Fly ash	Silica sand[1]	Limsetone filler	Water	SP Sika 5501	VMA	PVA fibres[2]
461.0 kg	691 kg	161.4 kg	161.1 kg	342.2 kg	26.1 kg	1.25 kg	26.0 kg

[1] silica sand under 500 μm maximum aggregate size; [2] fibres with 8 mm length and 40 μm diameter.

The fresh characteristics of the concrete were evaluated using the Abrams cone, following EN 12350-2 [49]. The ECC workability and consistency were determined through the mini slump test in accordance with BS EN 12350-8 [50]. The compressive mechanical properties of both concrete and ECC were accessed through uniaxial compression tests conducted on cylinders. EN 12390-13 [51] and EN 12390-3 [52] were used to determine the Young's modulus (E_{cm}) and compressive strength (f_{cm}). The tensile properties of the ECC were obtained from direct tensile test conducted on dogbone shaped specimens, adhering to the guidelines outlined by the Japan Society of Civil Engineers [53]. **Table V.3** presents the average results obtained from the experimental characterization of concrete and ECC. Both materials show an adequate behaviour in the fresh and in the hardened state. The nominal tensile characteristics of the threaded rod steel are Young's modulus of 210 GPa, yield strength of 640 MPa and tensile strength of 800 MPa, with a zinc coating of 35.34 g/m²).

Table V.3: Results of the mechanical properties of the concrete and ECC.

	Slump class	E_{cm} [GPa]	f_{cm} [MPa]	E_{tm} [GPa]	f_{ctm} [MPa]	***Strength class***
Concrete	S3	28.72 (5.42%)	40.15 (3.06%)	28.72 (5.42%)	40.15 (3.06%)	C30/37
ECC	280[1]/173[2]	9.04 (6.36%)	30.27 (2.36%)	20.08 (13.31%)	2.28 (9.60%)	-

[1] mini slump without fibres; [2] mini slump test with fibres; 3estimated according to Eurocode 2; [4]typical reference value

2.3. Fabrication of the reef module prototypes

The fabrication of the artificial reef module used a printed reusable mould that is more economical than those produced by machining or by the mould industry. Small-scale prototypes were produced to evaluate the processes and technology for mould execution, construction and demoulding. **Figure V.3** shows the prototypes built at scales 1:13, 1:3.6 and 1:1.



Figure V.3: Reef modules prototypes constructed with different scales: 1:13 (left), 1:3.6 (centre) and real scale 1:1 (right).

In the first phase, acrylonitrile butadiene styrene plastic modules were produced at a scale of 1:13, using a small 3D printer. With the aim of producing modules in cement matrix, silicone moulds with negative form were produced. They were injected and demoulded, validating their use (**Figure V.4**). However, the main disadvantage was the amount of silicone required, and the environmental and economic costs involved in producing larger units.

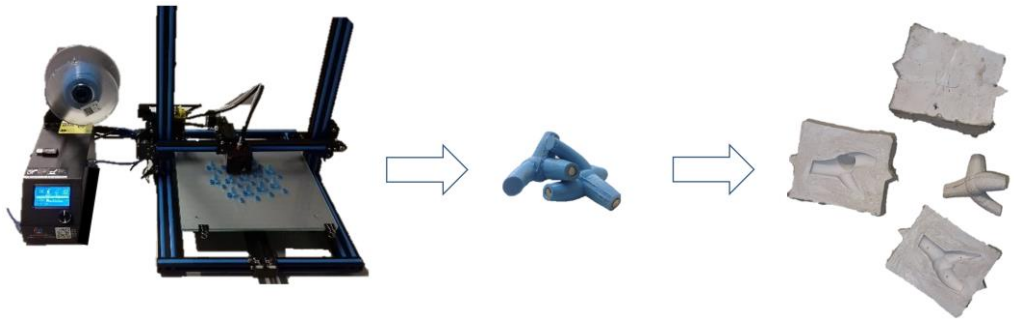


Figure V.4: Production of the smallest-scale unit reef prototype in cement paste at 1:13 scale.

Using 3D technology, a mould was printed in acrylonitrile butadiene styrene material at a 1:3.6 scale to evaluate the demoulding process and the real printing time (**Figure V.5**). The mould was an assemblage of 4 individual pieces forming a solid structure. The mould proved to serve the purpose, and the demoulding occurred without any problems. However, the printing time and the amount of material used were considered excessive, if large-scale parts are to be produced. Although requiring adjustments in terms of material reduction and consequent printing time, 3D printing technology proved to be capable and quite promising for producing the real mould.



Figure V.5: Production of the small-scale unit reef prototype in cement paste at 1:3.6 scale.

Figure V.6 illustrates the production process of the real-scale prototype. The macro-scale mould was subdivided into 16 parts, each approximately 3 mm thick, forming a mould with a thin shell structure. The parts were assembled using screwed tabs. Prior to casting, internal joint lines were sealed with tape, the interior of the mould was coated with *Vaseline*, reinforcements were inserted, and three ends were closed with polystyrene and glue. Subsequently, the mould was transferred to a cubic wood box with approximately 650 millimetres side, which was filled with fine sand to support and balance the weight of the cement matrix from the concreting. The concrete and ECC mixtures were prepared in the laboratory and carefully poured from the end of the mould facing upward and compacted using a vibrating device applied from the same end, ensuring uniform distribution and consolidation throughout the entire volume. The pouring was conducted in layers to avoid air entrapment, and the vibration was applied gradually across each layer to achieve full compaction without segregation. Two days later, the specimens were demoulded and stored indoors under controlled conditions until testing.



Figure V.6: Prototype construction phases: 3D printing, assembling, concreting, demoulding.

2.4. Numerical modelling of the reef structure and of the units

A numerical model was developed to evaluate the structural response of a MMFAR positioned at a depth of 20 m in the Marine Protected Area of Esposende, Portugal. The system consisted of 16 interlinked macro modules assembled into a 2 × 2 m arrangement, resulting in a bottom projection area of approximately 4.81 m^2 and a volume of 1.76 m^3 [35]. The finite element method structural analysis was performed using a linear static analysis in a three-dimensional finite element environment. In this process, the original 3D geometry was idealized by transforming the solid elements into beam elements connected by nodes (**Figure V.7**). The connections between modules were modelled as rigid joints to represent continuous monolithic behaviour, while the base was

assigned with pinned supports to replicate real support condition. Material properties adopted were the ones previously found for the concrete and the steel used in the fabrication [35].

The model incorporated self-weight, buoyancy, and hydrodynamic forces arising from waves, tidal currents, and marine growth as detailed by Cruz et., all [37] (**Figure V.7**). Hydrodynamic loading was determined using Stokes wave theory to estimate local fluid kinematics, combined with the Morison equation to obtain distributed drag and inertia forces along each structural member. Coefficients for drag (Cd) and inertia (Cm) followed API recommendations [41,42], while marine growth effects were simulated with an additional layer 0.1 m thick, in accordance with DNV-RP-C205 [37]. The adopted current profile assumed velocities of 1.2 m/s from the water surface to mid-depth and 0.3 m/s from mid-depth to the seabed [37].

Two critical loading scenarios were examined: (i) an extreme storm condition, defined by a significant wave height of 9 m and a period of 14.6 s (Ultimate Limit State – ULS), and (ii) an abnormal extreme event with a significant wave height of 15.61 m and a period of 20 s (Accidental Limit State – ALS) [37]. The load combinations followed ISO 19903:2006 recommendations [37], and the crest wave phase was selected for analysis as it corresponds to the most demanding horizontal loading on the structure.

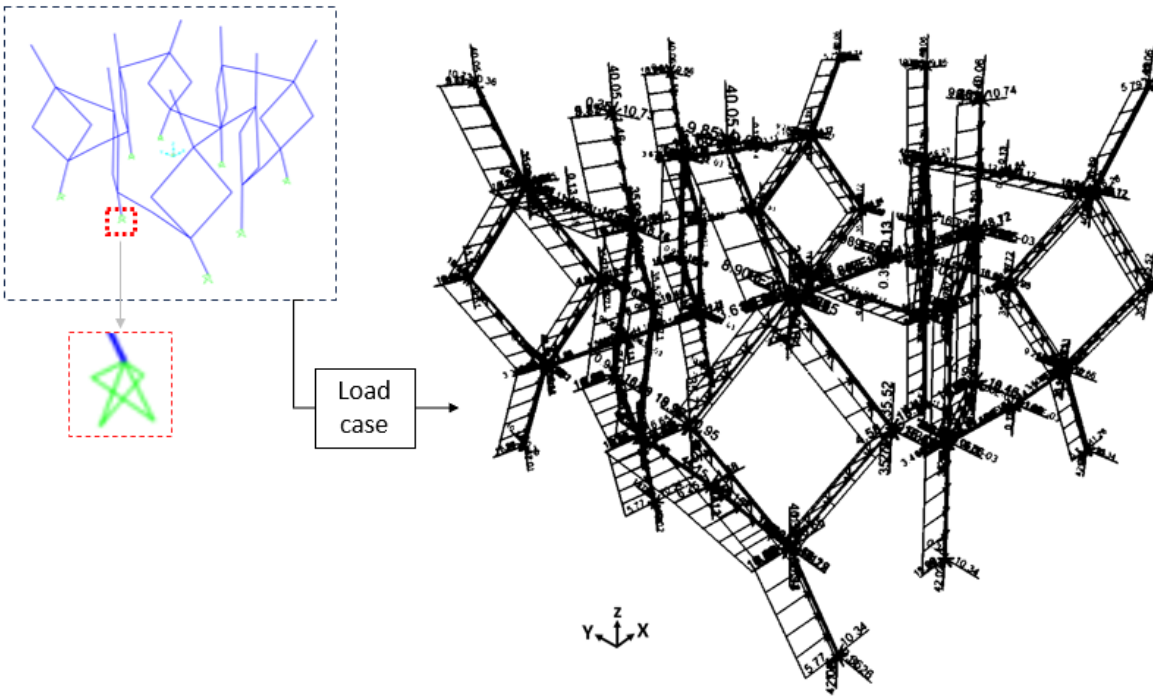


Figure V.7: MMFAR numerical model, defined with beam elements.

To predict the structural behaviour of the MMFAR module and prepare the experimental prototypes, a numerical model of a module was developed. This model is used to evaluate the stress distribution acting on the unit when it is included in the global structure, while maintaining compatibility with a feasible experimental configuration. Taking into account the geometric constraint of the unit in the overall configuration, translational displacements in the X, Y and Z directions at the joint node have been constrained while maintaining rotational freedom. This reflects the rotational capacity of the joint systems with the greatest potential for practical application [39]. External loading was simulated using a unitary force applied at the centre of gravity of the module, as shown in **Figure V.8**.

This unitary force can be increased until there is a match between the imposed stresses and the stresses that result from the most severe loading conditions on the MMFAR numerical model.

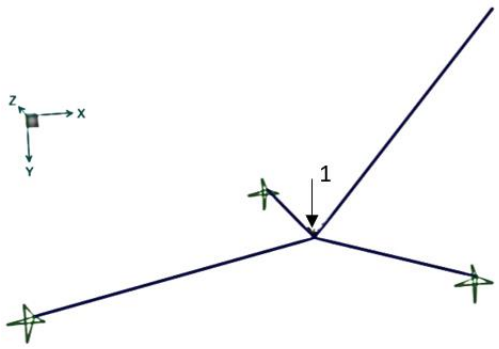


Figure V.8: Numerical model of reef module with unitary load to support experimental test setup.

2.5. Testing of prototypes

An experimental program with bending tests was carried out to study the structural behaviour of the real scale reef modules. The main objective was to understand the general functioning of the artificial reef modules and obtain information on their (i) stiffness, (ii) strength, (iii) ductility behaviour and (iv) failure modes in order to analyse the structural requirements and safety.

Two full-scale reef modules were constructed for testing, adopting the two alternative structural systems: (i) reinforced concrete (RC) and (ii) engineered cementitious composite (ECC). Each prototype was cast in a single batch, with the mixtures being prepared in the laboratory to ensure uniformity. Additionally, four concrete and four ECC cylinders were prepared for compression testing, while four dogbone-shaped ECC specimens were prepared for tensile mechanical characterization.

The curing conditions and testing age of all specimens were consistent with those of the reef modules to ensure comparable mechanical properties.

Figure V.9 presents the test configuration and the instrumentation adopted in the experimental program following the scheme of Fig. 8. The module was positioned on metallic reaction points, which were supported and linked to a steel reaction frame. Cyclic tests were conducted using a configuration in which the structure was supported at three points and a central point load was applied at mid-span. The direct distance between supports and the applied load was equal to 325 mm. The tests were carried out with a servo-controlled equipment under displacement control in the actuator at a speed of 10 μm/s and with a data acquisition of 10 Hz. The test protocol involved successive loading and unloading cycles, with imposed vertical displacements in the actuator of 0.5 mm, 1 mm, 1.5 mm, 2 mm, 3 mm, 5 mm, 10 mm, 20 mm and 100 mm. The force (F) was applied in the centre of the specimens and monitored through a load cell with a maximum measuring capacity of 500 kN (±0.12 kN; 0.05% F.S.). Three linear variable differential transducers (LVDT1 to LVDT3), with a stoke of ±10 mm (linearity error of 0.24% F.S.), were used to record the vertical deflection in each limb. These were spaced around 3 cm from the limit of the spherical centre. The vertical displacement was measured by using one LVDT with a stroke of ±50 mm (linearity error of 0.24% F.S.) placed at the bottom part and aligned with the loading axis, to record the vertical deflection. Furthermore, a DSLR camera was positioned at the bottom, to carry out sequential photographic recordings of 3 photos per minute to monitor the development of the cracks and the progress of rupture. Prior to the test, the specimens were painted with a white colour to better monitor the development of cracks during the test.



Figure V.9: General test configuration and instrumentation of the artificial reef module, perspective view.

3 RESULTS AND DISCUSSION

3.1. Numerical modelling

The analysis of the global model allows the identification of critical sections in the structural module. As illustrated in **Figure V.10** and detailed in Annex A, the maximum bending moments M^{2-2} and M^{3-3}, aligned with local axes 2 and 3 of a frame element respectively, occur in the centroid core of the module. This region is therefore identified as the primary critical section in terms of bending demand. Additionally, maximum axial forces (N) are found in the vertical support element, torsional moments (T) are concentrated in the vertical connector to a second-level unit, and shear forces (V) are most significant in the horizontal element linking adjacent modules. These observations collectively define the critical stress paths within the structure.

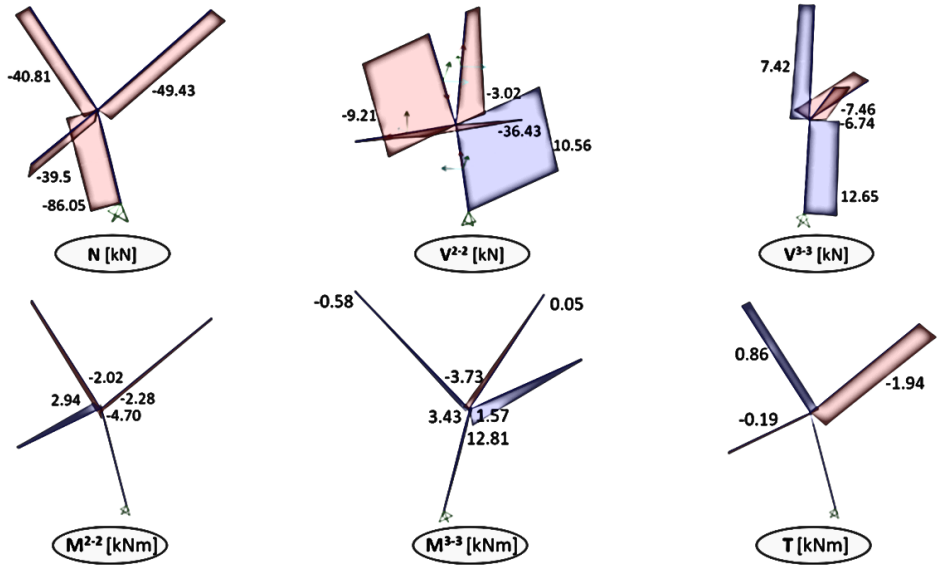


Figure V.10: Identification of maximum internal forces in MMFAR for abnormal extreme condition.

In parallel, the simplified model was used to understand the local behaviour of an isolated module under a unitary load, as shown in **Figure V.11**. The scheme promotes the highest bending moments in the central zone, while generating uniform shear forces along the leg. This model, with the unitary load, produced a maximum bending moment of 0.1717 kNm, in contrast with the 12.81 kNm obtained in the global analysis. The resulting load factor of 74.6 quantifies the amplification necessary to represent the global effects in the simplified model. The term load factor in this context refers to the ratio between the effects observed in the entire structure when the limit state analysis was performed, and the effects observed in the isolated module when subjected to the unit load (1 kN). This factor not only reflects the influence of the surrounding structural system on the local module but also reinforces the importance of correctly identifying and scaling the critical sections for design or

optimisation purposes. The central core, being the zone where the highest flexural demands occur, emerges as the most structurally sensitive region, requiring particular attention in reinforcement and detailing. In the case of an extreme storm condition ($H_{S,maxstorm}$ = 9 m; T = 14.6 s), which corresponds to the Ultimate Limit State (ULS), the analysis resulted in a maximum design bending moment of 5.47 kNm, associated with a ratio of 31.85.

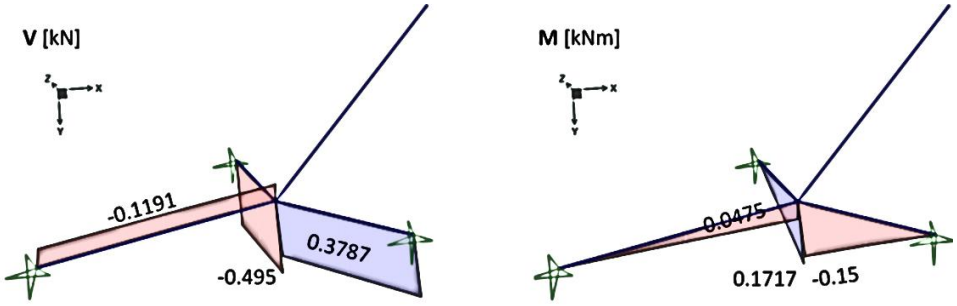


Figure V.11: Shear force and bending moment distribution in the reef module for unitary load.

3.2. Experimental response of the units

Figure V.12 presents the experimental curve in terms of force (F) versus vertical displacement (δ). The applied force (F) was measured by the load cell installed in the actuator, and the vertical displacement (δ) was obtained by the measurements taken from three LVDTs.

In the specimens tested, the F-δ experimental responses of RC and ECC specimens demonstrate a similar global behaviour. Generally, the experimental responses indicate four distinct phases. Initially, there is a phase of elastic behaviour characterized by high stiffness, followed by a degradation phase marked by a lower stiffness due to cracking of the cement-based materials (concrete and ECC), until reaching the maximum load. At this stage, the RC unit shows more noticeable degradation and recovery of load, while the ECC specimen displays a smoother load increase. This difference is likely due to the presence and distribution of PVA fibres within the ECC's cementitious matrix, which enhances stress dissipation and crack control prior to peak load. Subsequently, an abrupt reduction of the load capacity and stiffness occurs due to the reduction of the effective cross section in critical sections (first cracks zones).

In the case of the RC specimen, an additional critical crack develops at the central bulb, possibly due to an insufficient bond length at the mooring point, where the central reinforcing bars converge (post-

peak branch). From then on, the experimental response is mainly characterized by a residual force and progressive deformation, until the rupture of the system.

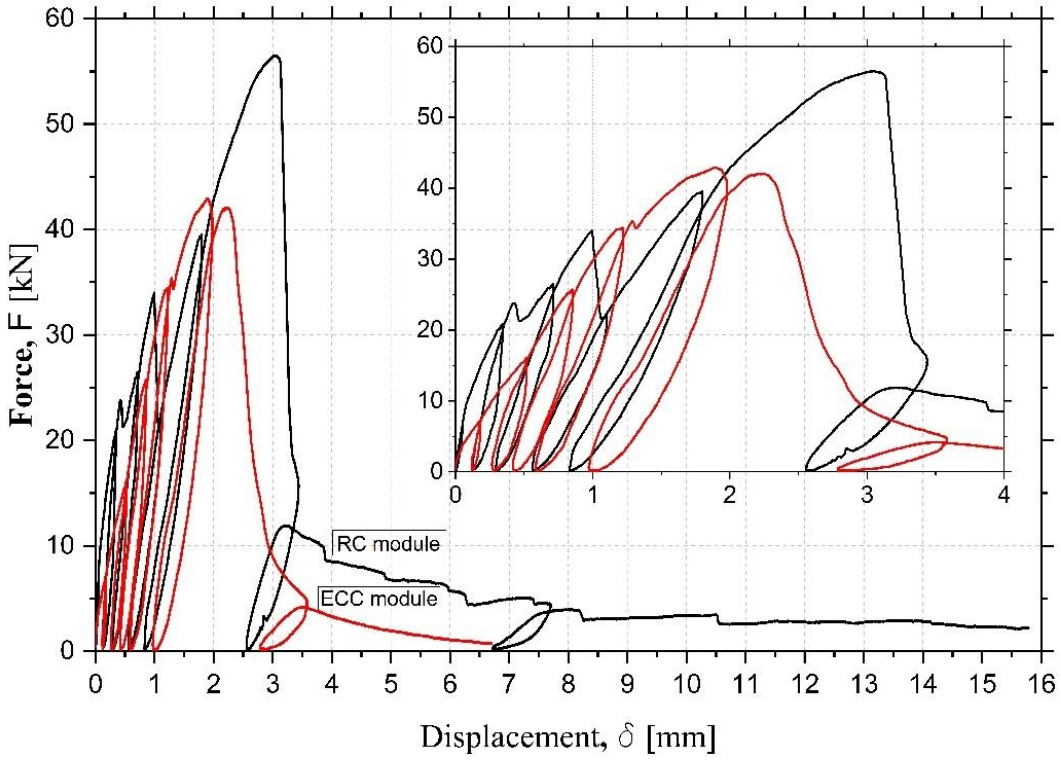


Figure V.12: Experimental responses obtained in terms of load force versus displacement at mid-span.

Table V.4 summarizes the main experimental results obtained for both specimens. F_{max} represents the maximum force, δ_{Fmax} is the displacement at maximum force, δ_{ult} is the ultimate displacement and K_i represent the deflection hardening stiffness and K_i' deflection reloading stiffness as shown in **Figure V.13**. The maximum load capacity is superior for the RC unit (+31.6%) and shows a higher range in terms of deformation, indicating greater ductility of the structural system (+120.4%). The residual force, F_r, obtained for the RC module is 180.8% higher than that of the ECC module. The ECC unit presents higher initial stiffness than the RC module. A decrease in stiffness values is also observed in both structural systems, highlighting the level of damage imposed in both modules.

Table V.4: Main results obtained from the experimental tests.

Name	F_{max} [kN]	δ_{max} [mm]	F_r [kN]	δ_{ult} [mm]	F_{max}/F_r [-]	K_1	K_2 $K_{2'}$	K_3 $K_{3'}$	K_4 $K_{4'}$	K_5 $K_{5'}$	K_6 $K_{6'}$ [kNm/mm]	K_7	K_8	K_9
ECC	42.98	2.90	0.78	8.73	0.02	212.95	31.17 95.01	25.72 71.47	34.53 50.09	49.42 46.82	15.72 38.63	-42.13	6.03	-1.07
RC	56.54	4.49	2.20	19.25	0.04	110.56	43.62 83.37	12.34 55.80	30.32 37.05	26.67 35.53	16.78	-178.02	20.29	-1.48
RC vs ECC	31.6%	54.7%	180.8%	120.4%	113.4%	-	-	-	-	-	-	-	-	-

*RC also has K_{11} = 4.37 and K_{12} = -0.15

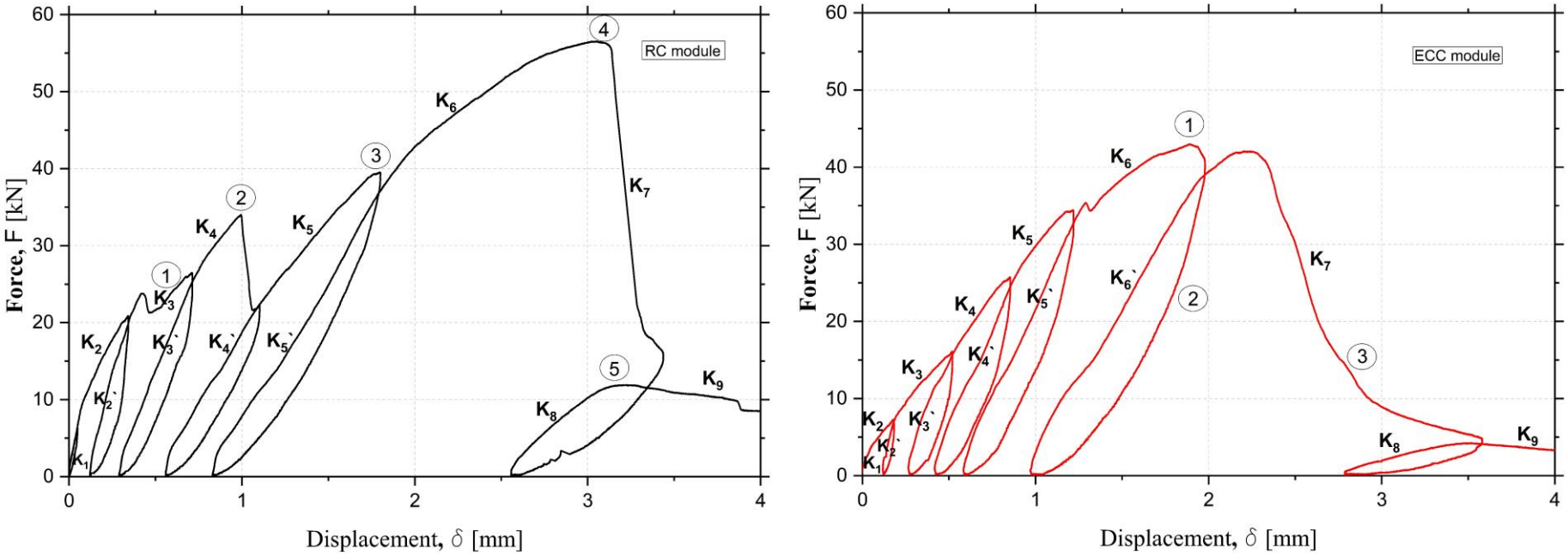
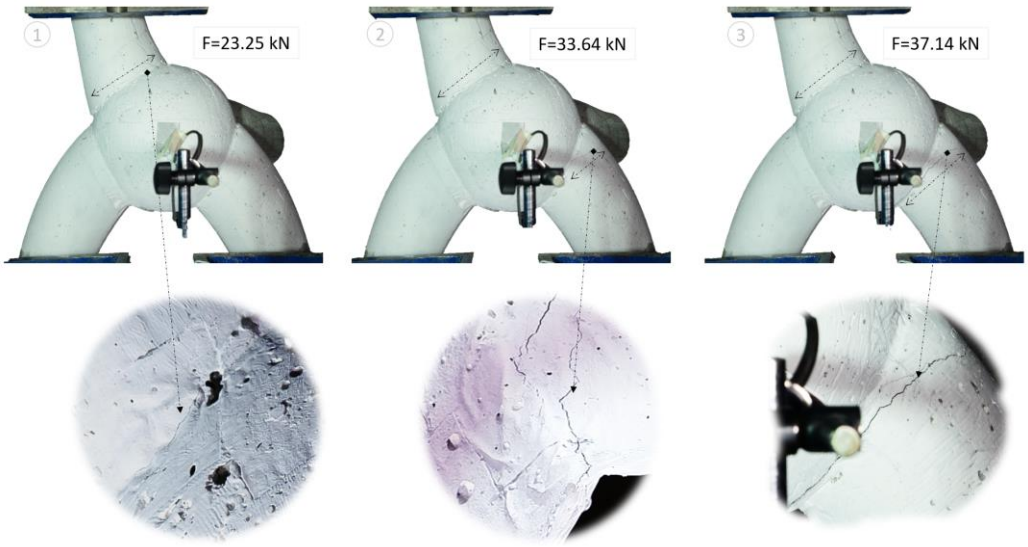


Figure V.13: Representation of the Ki and Ki′ in the experimental response of (a) RC module and (b) ECC module.

3.3. Failure modes

Figure V.14 and **Figure V.15** identify the critical phases that characterize the evolution of damage and the eventual rupture in both systems. As can be seen, the RC and ECC specimens exhibit distinct failure modes, which are reflected in both the cracking patterns and the underlying mechanisms, as detailed below.

In the case of the RCs unit, there is cracking of concrete at the bottom part and the failure results from the progressive opening of these cracks. Initially, the specimen shows, on one of its limbs, a small transversal crack in the tensile zone near the central bulb (see Phase ①, **Figure V.14**). Seconds later, a new crack was visible on another limb, initially more marked on one side but quickly spreading across the transversal section (sections ② and ③, **Figure V.14**). As the load applied increases, a transverse crack forms in the central bulb, which progressively increases until the specimen physically ruptures into two halves (see Phase ④, ⑤ and ⑥, **Figure V.14**). As can be seen, the specimen breaks in the central area, mainly due to the separation between the steel rebars, denoting an insufficient lashing length (⑦, **Figure V.14**). It should be noted that although there are several critical areas, the weakest component is the lashing between the reinforcing elements.



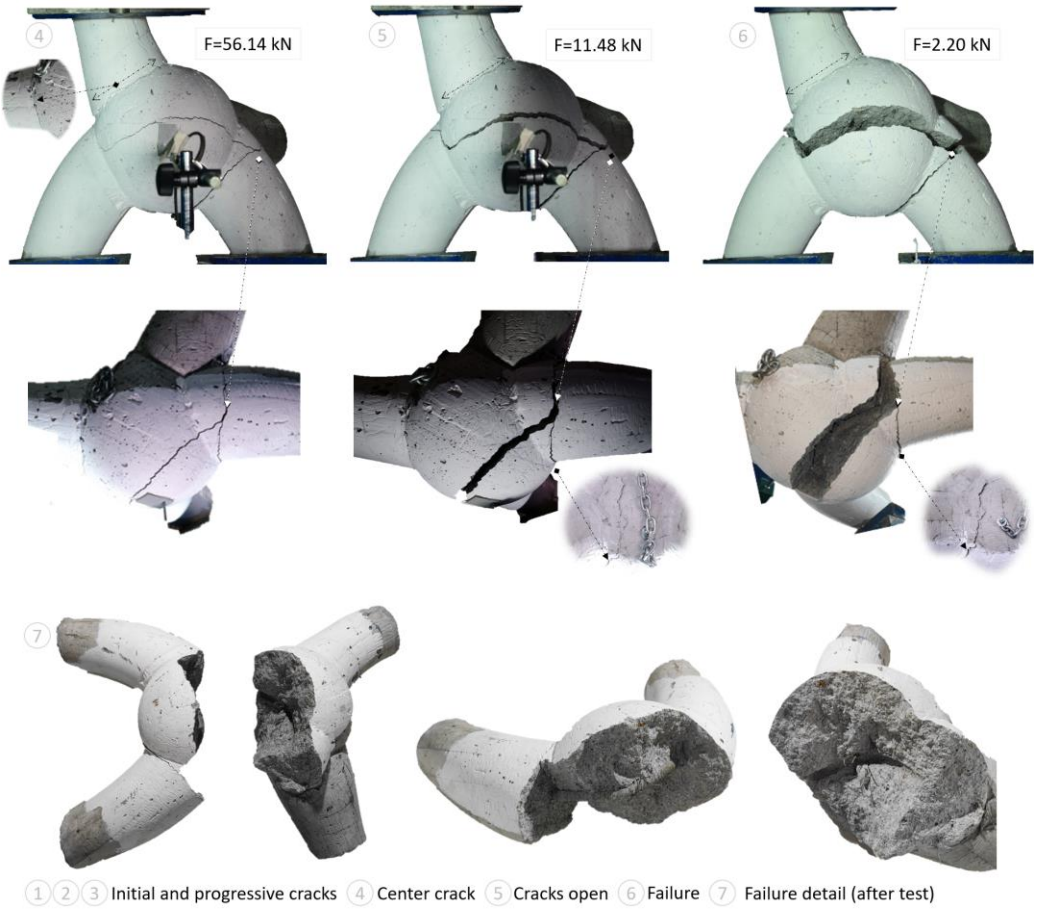


Figure V.14: Failure mode of the RCs reef module.

In the ECC unit, the initial cracks appear simultaneously in two limbs, similarly to what was observed for the RC unit. Furthermore, on the lower right branch of the unit, multiple cracks can be seen parallel to the initial crack (Phase ①, **Figure V.15**). At this location, as the load increases, the crack spreads along the height of the cross-section, indicating a possible failure point (Phase ②, **Figure V.15**) which would later be confirmed (Phase ③, **Figure V.15**). As can be seen, the unit broke due to the dismemberment of one of the three limbs, rendering the unit unusable (Phase ④ and ⑤, **Figure V.15**). The greater loading on this branch may be related to the fact that the load is applied to the geometric centre and not to the centre of mass.

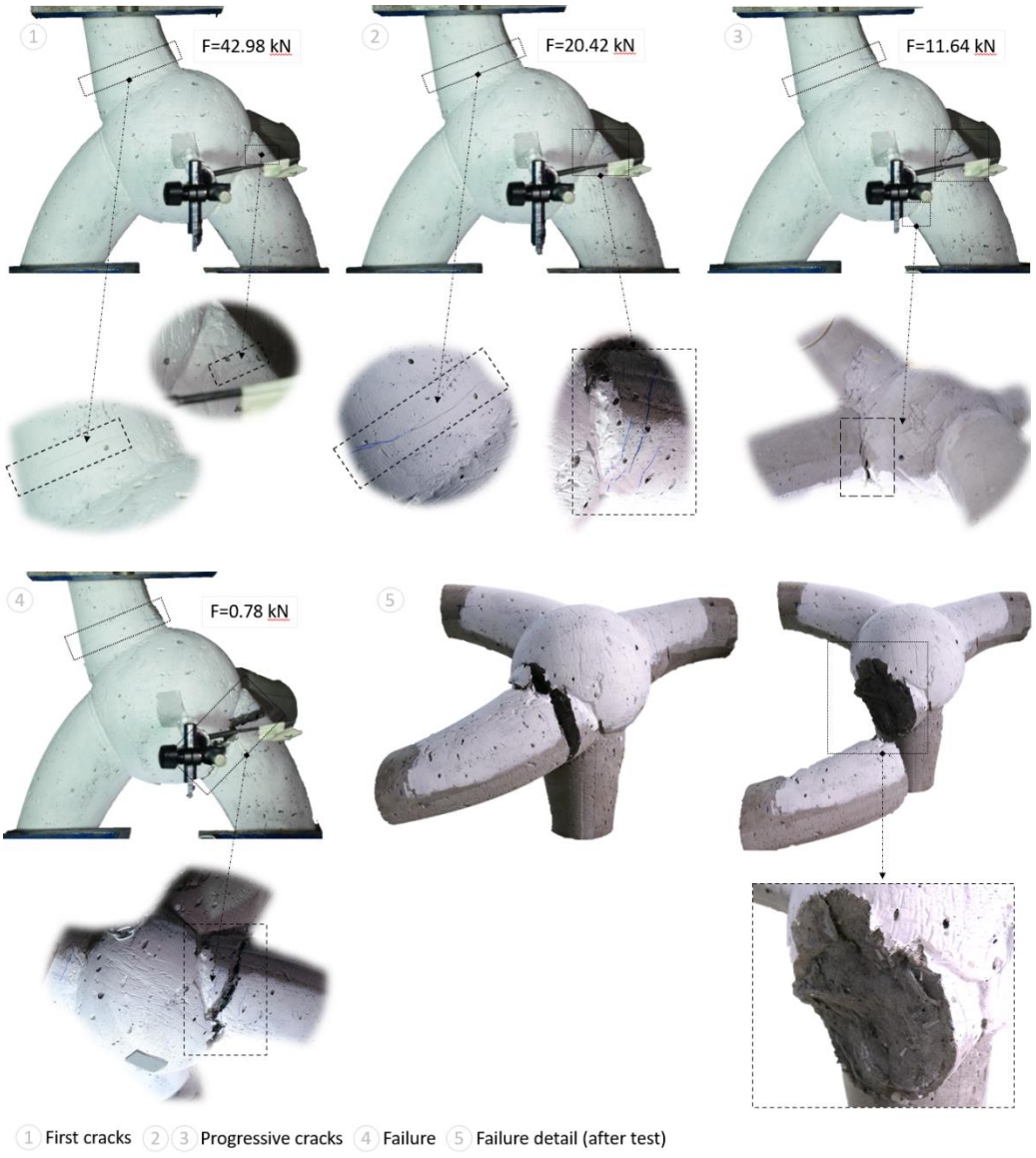


Figure V.15: Failure mode of the ECC reef module.

3.4. Structural requirements and safety modes

From The analysis of the load factor and the experimental response suggests that both structural systems perform adequately for the serviceability limit state (SLS) and ultimate limit state (ULS) (**Figure V.16**). It was demonstrated that both modules exhibited high-capacity reserves, with the ECC module demonstrating 34% and the reinforced concrete (RC) module demonstrating 78%. The findings suggest that both systems possess the capacity to withstand the forces calculated for the SLS and ULS, thereby ensuring a substantial safety margin. However, when the accidental limit state (ALS) is taken into consideration, it was found that the modules did not meet the required safety criterion. The discrepancy between the maximum experimental forces and the calculated forces for ALS resulted in

a 32% disparity for the ECC module and a 74% disparity for the RC module. The values obtained from this analysis indicate that neither of the structural systems will be able to resist the ALS. This suggests the necessity for adjustments or structural reinforcements in order to ensure safety under accidental conditions.

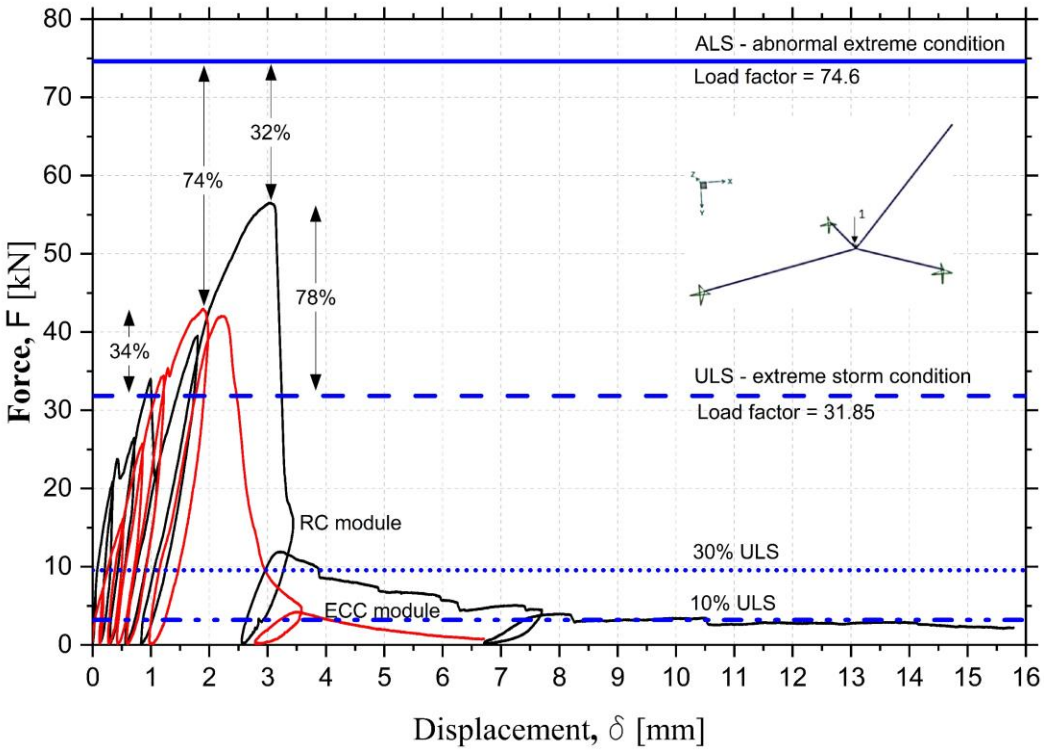


Figure V.16: Load factor considering the experimental responses.

4 CONCLUSIONS

In this research the development of a reef unit for MMFAR was explored utilizing two alternative structural systems. The study included the integration of 3D printing technology in both the construction of the moulds and the structural testing of artificial reef modules. The results obtained support the following main conclusions:

(1) **Impact of 3D printing on mould production efficiency** – The substantial cost reduction (-98%) and manufacturing time savings (-27%) achieved with 3D printing are primarily linked to the elimination of intermediate manufacturing steps, such as the CNC machining of foam cores and the manual lamination of fiberglass moulds. The direct additive manufacturing process also enables complex geometries to be produced without the geometric simplifications often required in traditional mould fabrication, reducing the need for post-processing.

(2) **Geometric flexibility and performance optimisation** – The ability to fabricate intricate module geometries allows for optimized hydrodynamic flow patterns and increased surface complexity, which are essential for marine biodiversity colonization.

(3) **Structural system performance** – The RC unit exhibited higher maximum load capacity (+31.56%), greater deformation (+120.44%), and higher stiffness (+180.33%) than the ECC unit, which can be attributed to the combined effect of steel reinforcement's ductility and its superior ability to restrain crack propagation under increasing loads. The ECC unit, while more effective in controlling cracking for lower deformations due to fibre reinforcement, showed a lower peak load capacity due to its reduced reinforcement ratio and lower stiffness in bending-dominated loading scenarios.

(4) **Failure mode mechanisms** – The splitting failure observed in the RC unit is related to insufficient bond length, which caused stress concentrations in the central bulb region. This led to crack propagation along the longitudinal axis of the limb and bulb. In contrast, the ECC unit's failure, dominated by the limb rupture, is consistent with the material's strain-hardening behaviour, which delayed cracking but ultimately led to the localization of deformations in a single critical cross-section.

(5) **Safety margin across limit states** – The adequate performance for SLS and ULS indicates that both units can handle operational and extreme storm conditions without structural instability. However, the inability to meet ALS safety requirements reveals a limitation under abnormal extreme wave events. At these load levels, bending moments and shear forces in limb-bulb junctions exceed both concrete tensile strength and reinforcement anchorage capacity, leading to brittle-type failures.

In order to further validate the findings and improve the reliability of the results, it is essential to expand the scope of testing by incorporating additional structural experiments, such as shear and fatigue tests. This will enable a more comprehensive assessment of the load factors under a broader range of conditions. Future work should include a greater number of tests of the same type, as well as durability tests in real and laboratory conditions with total submersion of the specimens in seawater.

ACKNOWLEDGEMENTS

This work is financed by national funds through FCT – Foundation for Science and Technology, under grant agreement SFRH/BD/137220/2018 attributed to the 1st. This work was partly financed by FCT/MCTES through national funds (PIDDAC) under the R&D Unit Institute for Sustainability and Innovation in Structural Engineering (ISISE), under reference UIDB/04029/2020 (doi.org/10.54499/UIDB/04029/2020), and under the Associate Laboratory Advanced Production and Intelligent Systems ARISE under reference LA/P/0112/2020. This work was partially funded by the research projects ‘‘NEXT-SEA: Next Generation Monitoring of Coastal Systems in a Scenario of Global Change”, NORTE-01-0145-FEDER-000032; “ASTRIIS – Atlantic Sustainability Through Remote and In-situ Integrated Solutions", POCI-01-0247-FEDER-046092, financed by FEDER funds; and “R2UTechnologies - modular systems”, PRR C644876810-00000019, funded by Plano de Recuperação e Resiliência.

REFERENCES

[1] Ng K, Phillips MR, Calado H, Borges P, Veloso-Gomes F. Seeking harmony in coastal development for small islands: Exploring multifunctional artificial reefs for São Miguel Island, the Azores. Appl Geogr 2013;44:99–111. https://doi.org/10.1016/j.apgeog.2013.07.013.

[2] López I, Tinoco H, Aragonés L, García-barba J. The multifunctional artificial reef and its role in the defence of the Mediterranean coast. Sci Total Environ 2016;550:910–23. https://doi.org/10.1016/j.scitotenv.2016.01.180.

[3] Dafforn KA, Glasby TM, Airoldi L, Rivero NK, Mayer-pinto M, Johnston EL, et al. Marine urbanization: an ecological framework for designing multifunctional artificial structures. Front Ecol Environ 2015;13:82–90. https://doi.org/10.1890/140050.

[4] Lee MO, Otake S, Kim JK. Transition of artificial reefs (ARs) research and its prospects. Ocean Coast Manag 2018;154:55–65. https://doi.org/10.1016/j.ocecoaman.2018.01.010.

[5] H.O. Pörtner, Roberts DC, Masson-Delmotte V, P. Zhai MT, Poloczanska E, Mintenbeck K, et al. The Ocean and Cryosphere in a Changing Climate. 2019.

[6] Bracho-Villavicencio C, Matthews-Cascon H, Rossi S. Artificial reefs around the world: A review of the state of the art and a meta-analysis of its effectiveness for the restoration of marine

ecosystems. Environments 2023;10:121. https://doi.org/10.3390/environments10070121.

[7] Bohnsack JA, Sutherland DL. Artificial reef research: a review with recommendations for future priorities. Bull Mar Sci 1985;37:11–39.

[8] OSPAR Commission. Assessment of construction or placement of artificial reefs. Biodiversi. London: 2009.

[9] Fabi G, Giuseppe Scarcella, Alessandra Spagnolo SAB, Charbonnel E, Goutayer JJ, Haddad N, And AL, et al. Pratical guidelines for the use of artificial reefs in the Mediterranean and the Black sea. Rome: 2015.

[10] Florisson JH, Rowland AJ, Matthews AC, Tweedley JR, Campbell L. The application, needs, costs and benefits of Habitat Enhancement Structures in Western Australia and cost-effective monitoring methods. 2018.

[11] Great Barrier Reef Marine Park Authority. Guidelines for the Management of Artificial Reefs in Great Barrier Reef Marine Park 2011:1–6.

[12] Bao H, Nikolaeva A, Xia J. Evolution Trends and Future Prospects in Artificial Marine Reef Research: A 28-Year Bibliometric Analysis. Sustain 2025;17:184. https://doi.org/https://doi.org/10.3390/su17010184.

[13] Berman O, Weizman M, Oren A, Neri R, Parnas H, Shashar N, et al. Design and application of a novel 3D printing method for bio-inspired artificial reefs. Ecol Eng 2023;188:106892. https://doi.org/10.1016/j.ecoleng.2023.106892.

[14] Carral L, Alvarez-feal JC, Tarrio-saavedra J. Social interest in developing a green modular artificial reef structure in concrete for the ecosystems of the Galician rías. J Clean Prod 2018;172:1881–98. https://doi.org/10.1016/j.jclepro.2017.11.252.

[15] Xu L, Yu J, Huang B, Lao J, Wu H. Green and low-carbon matrices for Engineered / Strain-Hardening Cementitious Composites (ECC/SHCC): Toward sustainable and resilient infrastructure. J Clean Prod 2025;496:144968. https://doi.org/10.1016/j.jclepro.2025.144968.

[16] Li Q, Zhao S, Huang B, Xu L, Xu S. Simultaneous enhancement of ductility and sustainability of high-strength Strain-Hardening Cementitious Composites (SHCC) using recycled fine aggregates. J Clean Prod 2024;470:143357.

https://doi.org/10.1016/j.jclepro.2024.143357.

[17] Zhu J, Weng K, Liu W, Huang B, Peng K, Zhu J. Thin-Walled Structures Thin-layer Ultra-High-Strength Engineered Cementitious Composites (UHS-ECC) reinforced with small-diameter FRP bars for structural strengthening. Thin-Walled Struct 2024;205:112592. https://doi.org/10.1016/j.tws.2024.112592.

[18] Matus IV, Alves JL, Vaz-pires P. Artificial reefs through additive manufacturing: a review of their design, purposes and fabrication process for marine restoration and management. Rapid Prototyp J 2024;11:87–122. https://doi.org/10.1108/RPJ-07-2023-0222.

[19] Pham LT, Huang JY. 3D printed artificial coral reefs: design and manufacture. Low-Carbon Mater Green Constr 2024;4. https://doi.org/10.1007/s44242-024-00056-4.

[20] Yoris-nobile AI, Slebi-acevedo CJ, Lizasoain-arteaga E, Indacoechea-vega I, Blanco-fernandez E, Castro-fresno D, et al. Artificial reefs built by 3D printing: Systematisation in the design, material selection and fabrication. Constr Build Mater 2023;362. https://doi.org/10.1016/j.conbuildmat.2022.129766.

[21] Kuang W, Pavlenko P, Guo H, Tian K, Liu H. Utilization of machine-made sand waste in 3D-printed ecological concrete for artificial reefs. Case Stud Constr Mater 2025;22:e04494. https://doi.org/10.1016/j.cscm.2025.e04494.

[22] Lescinski J, Kramer A. Boskalis Horizons: Revolutionary ReefVival 2017. https://magazine.boskalis.com/issue05/revolutionary-reefvival (accessed March 11, 2025).

[23] Santos J, Weber M, Veloso Gomes F. Concepção, Construção, Implantação e Monitorização de Recifes Artificiais de Betão com Incorporação de Lamas Orgânicas. J Integr Coast Zo Manag 2010;10:23–48.

[24] Haejoo Group. Haejoo Group Projects n.d. https://haejoo.com/category/projects/ (accessed March 20, 2025).

[25] Reef Ball Fundation. Reef Ball Fundation n.d. www.reefball.org (accessed January 10, 2019).

[26] Dunn K, Haeusler MH, Zavoleas Y, Bishop M, Dafforn K, Sedano F, et al. Recycled Sustainable 3D Printing Materials for Marine Environments, 2020, p. 583–91. https://doi.org/10.5151/proceedings-ecaadesigradi2019_641.

[27] PRINTERA. PRINTERA n.d. https://printera3d.com/projects/aquatic/florida-oceanographic-society/ (accessed March 27, 2025).

[28] Vogler V. A New Framework for Artificial Coral Reef Design. J Digit Landsc Archit 2022;2022:524–37. https://doi.org/10.14627/537724050.

[29] Vogler V. A framework for artificial coral reef design: Integrating computational modelling and high precision monitoring strategies for artificial coral reefs – an Ecosystem-aware design approach in times of climate change. Bauhaus-Universität Weimar, 2021.

[30] Vivier B, Dauvin JC, Navon M, Rusig AM, Mussio I, Orvain F, et al. Marine artificial reefs, a meta-analysis of their design, objectives and effectiveness. Glob Ecol Conserv 2021;27:e01538. https://doi.org/10.1016/j.gecco.2021.e01538.

[31] Reeds KA, Smith JA, Suthers IM, Johnston EL. An ecological halo surrounding a large offshore artificial reef: Sediments, infauna, and fish foraging. Mar Environ Res 2018;141:30–8. https://doi.org/10.1016/j.marenvres.2018.07.011.

[32] Silva J, Rosental I, Love M. Overview and trends of ecological and socioeconomic research on artificial reefs. Mar Environ Res 2019;145:81–96. https://doi.org/10.1016/j.marenvres.2019.01.010.

[33] Carral L, Lamas MI, Barros JJC, López I, Carballo R. Proposed Conceptual Framework to Design Artificial Reefs Based on Particular Ecosystem Ecology Traits. Biology (Basel) 2022;11:1–20. https://doi.org/https://doi.org/10.3390/biology11050680.

[34] Carral L, Alvarez-Feal C, Jesús Rodríguez-Guerreiro M, Vargas A, Arean N, Carballo R. Methodology for positioning a group of green artificial reef based on a database management system, applied in the estuary of Ares-Betanzos (Nw Iberian Peninsula). J Clean Prod 2019;233:1047–60. https://doi.org/10.1016/j.jclepro.2019.06.092.

[35] Maslov D, Cruz F, Pinheiro M, Miranda T, Valente IB, Ferreira V, et al. Functional Conception of Biomimetic Artificial Reefs Using Parametric Design and Modular Construction. J Mar Sci Eng 2024. https://doi.org/https://doi.org/10.3390/jmse12091682.

[36] Maslov D, Pereira E, Duarte D, Miranda T, Ferreira V, Tieppo M, et al. Numerical analysis of the flow field and cross section design implications in a multifunctional artificial reef. Ocean Eng 2023;272. https://doi.org/10.1016/j.oceaneng.2023.113817.

[37] Cruz F, Valente IB, Maslov D, Miranda T, Pereira EB. Engineering-Driven Approach for the Structural Design of Geometrically Complex Modular Artificial Reefs. Appl Sci 2025;15:31. https://doi.org/https://doi.org/10.3390/app15115907.

[38] Cruz F, Pereira E, Valente IB, Tiago M, Maslov D, Pinheiro M. Structural design of an innovative multifunctional artificial reef. Oceans 2018 MTS/IEEE Charleston, IEEE; 2018, p. 1–7. https://doi.org/10.1109/OCEANS.2018.8604587.

[39] Cruz F, Valente IB, Monteiro F, Maslov D, Miranda T, Pereira EB. Development and characterization of structural connections for modular artificial reefs. Ocean Eng 2025;320. https://doi.org/10.1016/j.oceaneng.2025.120311.

[40] Cruz F, Valente I, Almeida J, Neves A, Pereira E. Experimental characterization of bond between concrete and HDG steel tubes for mixed steel - concrete structures. Mater Struct 2024. https://doi.org/10.1617/s11527-024-02352-8.

[41] DET NORSKE VERITAS (DNV). Recommended practise DNV-RP-C205: environmental conditions and environmental loads 2010:124.

[42] API RP 2A-WSD. Recommended Practice for Planning, Designing and Constructing Fixed Offshore Platforms — Working Stress Design 2003:242.

[43] International Organization for Standardization (ISO). BS EN ISO 19903:2006 Petroleum and natural gas industries — Fixed concrete offshore structures. BSI Stand Publ 2006;3.

[44] NP EN 206-1. Concrete-Part 1: Specification, Performance, Production and Conformity. NP EN 206-1, Brussels, Belgium: 2005, p. 1–29.

[45] EN 1992-1-1. Eurocode 2: Design of concrete structures - Part 1-1: General rules and rules for buildings. Eur Stand 2004:225.

[46] EN 1994-1-1. Eurocode 4: Design of composite steel and concrete structures - Part 1-1: General rules and rules for buildings 2007:1–9.

[47] EN 1993-1-8. Eurocode 3: Design of steel structures - Part 1-8: Design of joints 2011;1:135.

[48] EN 1992-4. Eurocode 2 - Design of concrete structures - Part 4: Design of fastenings for use in concrete 2013.

[49] EN 12350-2. Testing Fresh Concrete-Part 2: Slump-Test 2009:8.

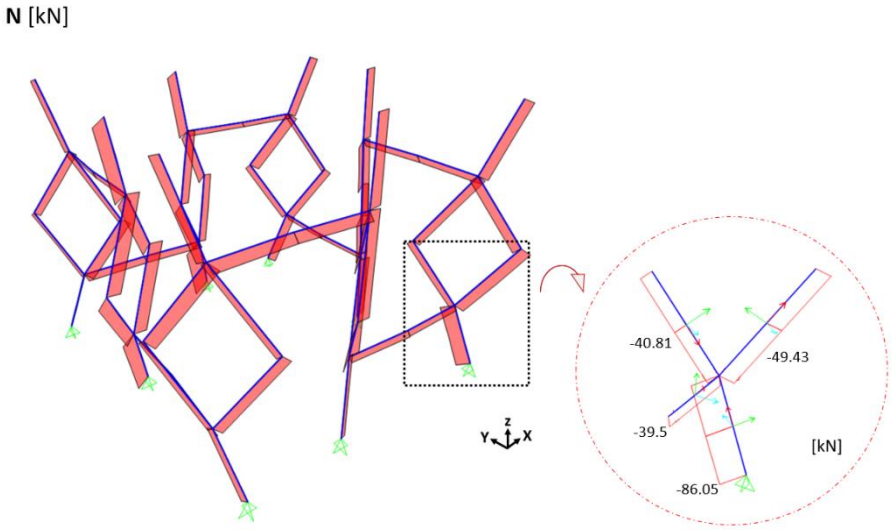
[50] European Standard. BS EN 12350-8. Testing fresh concrete - Part 8: Self-compacting concrete - Slump-flow test 2019:19.

[51] EN 12390-13. Testing hardened concrete Part 13: Determination of secant modulus of elasticity in compression. Eur Stand 2013:14.

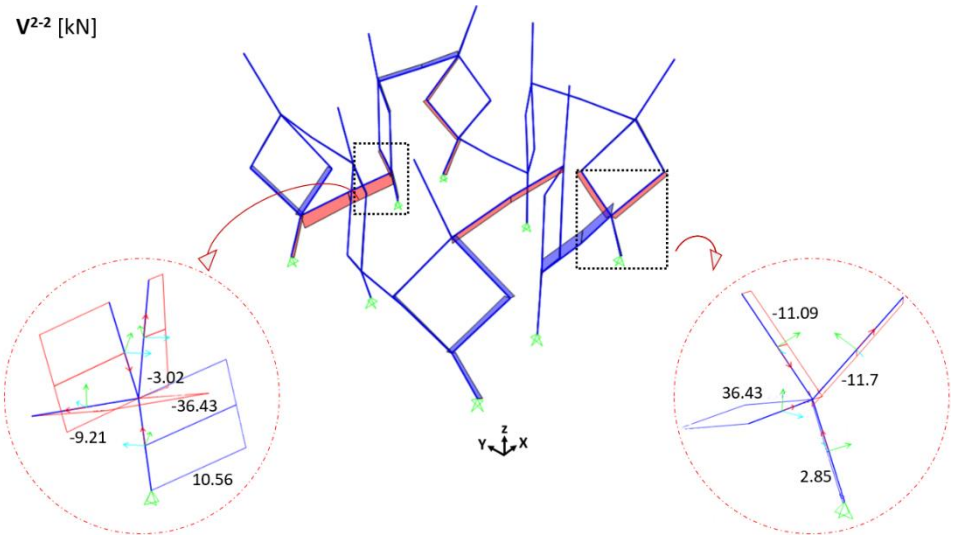
[52] EN 12390-3. Testing Hardened Concrete-Part 3: Compressive Strength of Test Specimens. Eur Stand 2009:21.

[53] Yokota H, Rokugo K, Sakata N. JSCE recommendations for design and construction of high performance fiber reinforced cement composite with multiple fine cracks. High Perform. Fiber Reinf. Cem. Compos., vol. 2, Springer Tokyo, Japan; 2008.

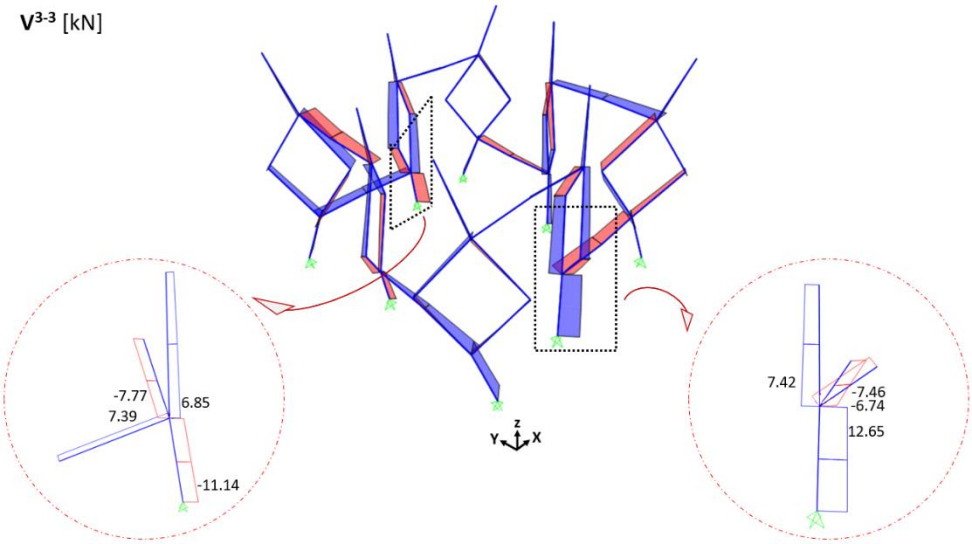
Annex A – MMFAR forces and moment distribution



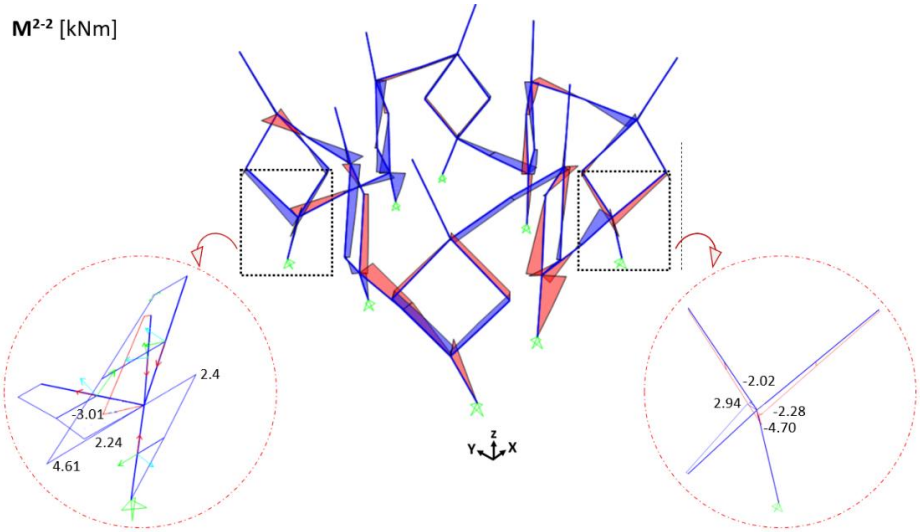
V^{2-2} [kN]



V^{3-3} [kN]



M^{2-2} [kNm]



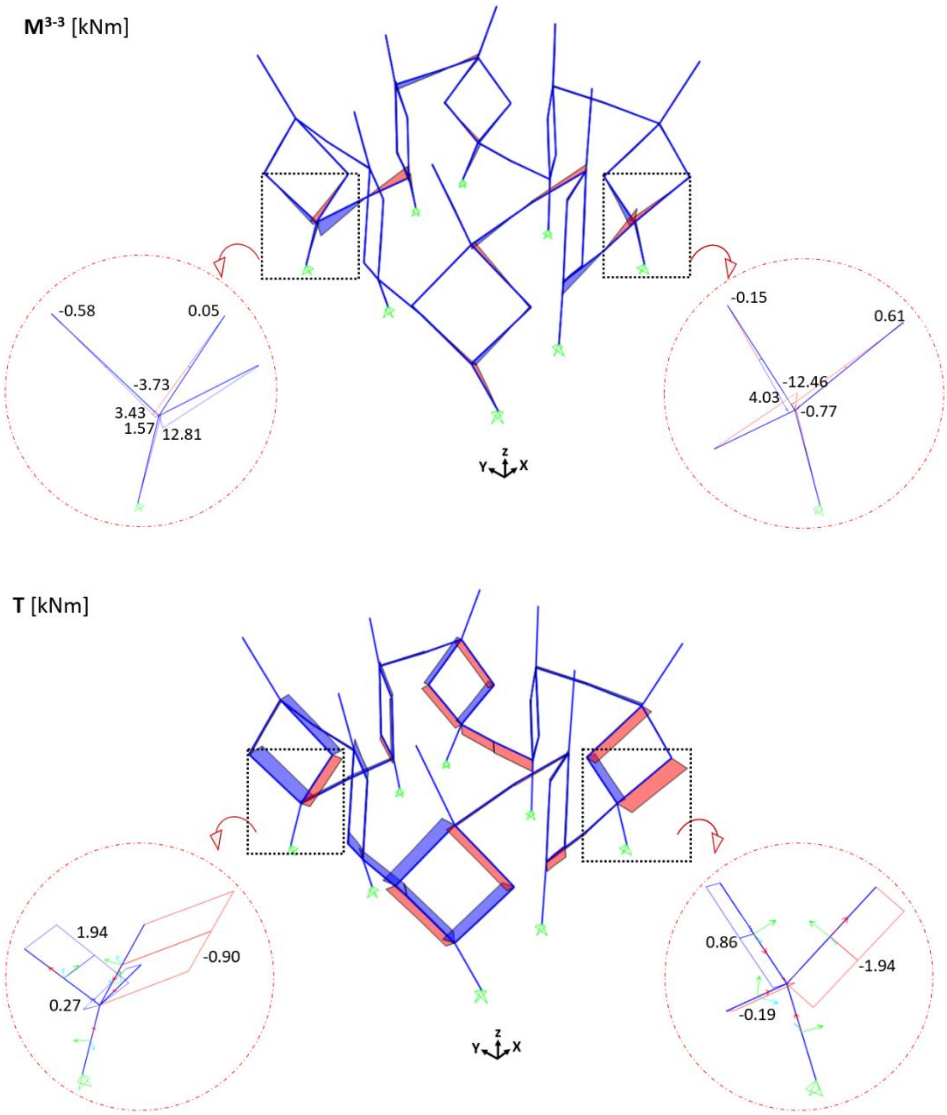


Figure V. 17: Forces and moment distribution in MMFAR for an extreme scenario in terms of axial force (N), shear force (V), bending moment (M) and torsional moment (T).

PAPER VI

EXPERIMENTAL CHARACTERIZATION OF THE SCOUR OF INNOVATIVE ARTIFICIAL REEF PROTOTYPES USING HYDRAULIC FLUME AND PHOTOGRAMMETRY

REFERENCE: Cruz F, Pereira E, Lima M, Johnson J, Duarte D, Valente IB, et al. Experimental characterization of the scour of innovative artificial reef prototypes using hydraulic flume and photogrammetry. OCEANS 2019 MTS/IEEE Marseille, IEEE; 2019, p. 1–10. https://doi.org/10.1109/OCEANSE.2019.8867581.

ABSTRACT: This paper describes an experimental study of an innovative Multifunctional Artificial Reef geometry, as part of the decision framework for its planning, design, construction, and installation. The aim is to experimentally assess the scour phenomenon and the hydrodynamic behaviour of a small-scale multifunctional artificial reef prototype (PMFAR) in a non-cohesive bed of sediment. Hydraulic flume tests and a photogrammetry survey were conducted. An Acoustic Doppler Velocimeter was used to measure flow velocities both upstream and downstream of the PMFAR to quantify the impact of the PMFAR on the hydrodynamic flow field. A non-invasive experimental method was developed, allowing information to be obtained on the scour cavity located around the structure

and thus to characterize this phenomenon. This proved to be interesting and an important approach in support of the decision framework for the development and design of these innovative structures.

KEYWORDS: Small-scale multifunctional artificial reef prototype; Hydraulic tests; Scour; Hydrodynamic; Photogrammetry.

1 INTRODUCTION

Due to an increased awareness on the importance of carefully balancing marine resources, there is a new demand for multidisciplinary, innovative solutions that promote and stimulate survival and growth of habitats, as well as the sustainability of human activities. Coastal and offshore structures, such as platforms, wind farms and multifunctional artificial reefs (MFAR), are some examples of such solutions. MFARs present several advantages related to rehabilitation of marine ecosystems, coastal protection, support of recreational and sports activities and aquatic environmental monitoring [1].

During the design process of any marine structures, it is essential to evaluate aspects such as the hydrodynamic behaviour and scour phenomenon [2]. The measurement of velocity fields along the water column allows the quantification of the impact of a structure on its environment. Scour, a specific term for the more general term erosion, is one of the major causes of instability and consequent failure of marine structures. It is a complex phenomenon that results from the interaction between the three-dimensional flow around a structure and the sediment bed. Local erosion, or scour, may occur due to the interactions between the structure and currents, waves, tides, or a combination of these actions [3-4]. It is important to minimize erosion and scouring effects of artificial reefs as these can lead to an overall sinking or overturning of the designed structure.

Hydraulic flume testing allows for simplified environmental scenarios to be recreated in a laboratory space. This becomes important when it is desirable to control one or more critical variables, which might not be possible in situ. In 2015, Ha et al. [5] conducted tests in a hydraulic flume to access the resettling rates of sediment around an artificial reef. In this study, a mesh grid was laid under the artificial reef in an attempt to stabilize the surrounding sediment. It was found that less sediment transportation occurred in cases where the grid was in place. This study highlighted how variations in the structural design of a reef can lead to significant changes in sediment transportation [5]. Another test, conducted in 1994, used a hydraulic flume to characterize the local scour to understand the sinking phenomenon experienced by cylindrical artificial reefs placed in sandy environments [6].

These tests used a hydraulic flume to characterize the local scour in order to understand the sinking phenomenon experienced by artificial reefs placed in sandy environments. In this study, two definitions of scour were used, clear water scour, where sediment is removed from the scour hole and is not replaced, and live bed scour, where the sediment is removed and replaced continuously [7]. The channel used was 10 m long, 0.7 m wide, and 0.9 m deep and with a sand grain size of 0.035 mm. Throughout the testing, scouring led to an overall sinking and rotation of the structure. The formation of a sand dune behind the structure was also noted. This study established a relationship between scour hole depth and water flow velocities, where faster velocities led to deeper scour hole depths. Furthermore, in a different study, it was found that the shape and material of the artificial reef reflected different sinking rates, with cylindrical reefs sinking at a faster rate than cubic block reefs [8].

A significant challenge in this field involves the prediction of the erosion cavity's maximum depth, through adjustments of mathematical laws against laboratory tests and real observations [3]. Unfortunately, the capability to predict maximum scour depth is lacking for many situations [3]. Many researchers have attempted to understand and evaluate the process of scour around bridge piers. Typically, the investigations have been made through either laboratory model studies or field investigations, with some disparities between them. For example, the values obtained through laboratory tests tend to be larger than values obtained in the field. One possible reason is that most of the design estimates for scour depths were based on a limited range of experiments and/or did not consider the numerous factors affecting the scour process. In recent years, the preferred methods used to predict equilibrium scour depth at complex piers are the Auckland method [9], the FDOT method [10] and the HEC-18 method [11-12].

In addition to analytical forecasting methods, this phenomenon can be studied through experimental research or numerical simulation. Experimentally, a paraffin mould and petroleum mixture is typically used to measure the depths of excavation [4]. Alternatively, due to the popularity of digital photography and the successive advances in equipment and image processing, photogrammetry has been increasingly used to demonstrate physical interactions between objects and environments through the recording, measuring and interpretation of images and patterns.

The aim of this research was to experimentally assess the local scour phenomenon and hydrodynamic behaviour of MFAR prototypes as part of the decision framework for the planning, design, construction and installation. To achieve this, hydraulic flume tests and photogrammetry surveys were used. This

approach proved to be interesting and valuable in supporting the decision framework for the development and design of these innovative structures.

2 PHYSICAL PRINCIPLES OF SCOUR

Any water flowing over unstable sediment beds, in a maritime or river environment, can cause erosion. This erosion is classified as global if it occurs even in the absence of an obstacle, and local if it occurs due to the local existence of an obstacle. Thus, local erosion or scour can be defined as the loss of sediment due to scour around hydraulic structures such as columns, piers, bridge abutments or other support elements [3–4].

The mass of water that contacts an object (oncoming flow) tends to move downstream, due to the pressure differential between the surface of the water and the bottom. At the top, higher velocities are associated with higher flow pressures against the pier, and at the bottom, where friction is felt more strongly, velocity tends to be lower [4]. This property, inherent to the influence of bottom friction in the flow, is often referred to as the bed-boundary layer [4]. In the case of piers, there is a downward flow moving downstream, and horseshoe vortices form immediately upstream of the pier [3–4]. These two features, in the case of unidirectional currents, serve as the main mechanism of localized erosion. On the downstream face of the structure, the existence of vortices (Lee-wake vortices) influences the erosion phenomenon, as it increases with the presence of more complex flow regimes, as in the case with currents, waves or a combination of the two. The presence of these mechanisms, as well as, the significant increase of velocity around the submerged object, leads to the increase of bed-shear stress near the bottom. Above this critical shear value, depending on the particle size, the sediments are transported downstream in areas where the shear stress is sufficient. For situations where the bed-shear stress is below the critical value, the transport of solid matter occurs only in the surroundings of the structure, with a higher incidence downstream. Therefore, the foundation sediment that is removed from the abutments cannot be compensated with material coming from upstream, generating an erosion cavity that jeopardizes the stability of the structure. Eventually, the erosion hole reaches a state of equilibrium, since the force of the horseshoe-shaped vortex tends to decrease with increasing erosion depth [3].

Scour may occur for two distinct sediment transport conditions [3,12–13]: (i) clear-water scour and (ii) live-bed scour. In the first, there is no movement of the bed material upstream of the hydraulic

structure and is typical of localized erosion usually reproduced in the laboratory. When bed-shear stress is less than or equal to the critical bed-shear stress local sediment begins to move. In the second condition, there is the transportation of bottom material upstream of the hydraulic structure, this phenomenon is cyclical in nature. When the bed-shear stress is higher than the critical bed-shear stress the entire bottom is mobilized with locally higher stresses. It should also be noted that in the first case the depth of the scour cavity reaches the maximum value for a longer period of time and is about 10% higher than the second case [3].

The factors that affect the local scour depth magnitudes of bridge piers are [13] the approach velocity of the flow, the flow water depth, the shape and width of the structure, the length of the structure element if oblique in relation to the flow, the granular size and distribution of sediments from the bed material [2–5,12]. The geometric scale is an important parameter and must be properly chosen, respecting the relationship between the sediment and hydraulic structure dimensions [3]. Sometimes incompatibilities may occur between the dimensions of the study prototype and the dimensions of the available hydraulic channel. Usually, a solution is adopted based on a scaled relationship between the sediment and structure (whichever is considered more important) [3]. The depth of the scour cavity depends on the sand diameter and its granulometric distribution. A sand is uniform if it has a sediment geometric standard deviation (σ_D) less than 1.4 [14] or 1.5 [15]. In the presence of a non-uniform granulometry, transportation of smaller particles occurs, thus influencing the evolution of the erosive process. It is recommended to use sand with σ_D similar to the actual environment in which it will be deployed [3].

3 RESEARCH PROCEDURES

An experimental method, composed of four tests, was carried out using a hydraulic flume to perform an initial assessment and analysis the hydrodynamic effects and to identify the scour mechanism of a MFAR prototype in sandy environments (**Table VI.1**). The tests were performed for steady flow conditions.

Table VI.1: Tests performed, running time and experiments measurements.

Tests	Maximum running time corresponding to scour survey	Measurement files	
		Downstream @17	Upstream @9
Test A	2h27min	VPA30 VPA033 (fixed) VPA034`	VPA032 VPA034
Test B	4h02min	VPA039 VPA043 (fixed) VPA044	VPA041 VPA045
Test C	4h40min	VPA 061 (fixed)	
Test D	9h	VPA068 (fixed) VPA070	VPA071

3.1. Experimental installation

The hydraulic flume, located in the Laboratory of Hydraulics and Water Resources of the Department of Civil Engineering of University of Minho, measured 14 m in length, of which 10 m provided the testing area. This testing area had a cross section with a width of 30 cm and a height of 45 cm.

The longitudinal slope varied between - 1/200 and 1/50, had been used a slope of 1/500. The channel allowed the transportation of a maximum water flow of 150 m^3/h, monitored through a magnetic flow meter (resolution class: 0.3). Within this flume, a sandbox was constructed measuring 2.5 m long, 10 cm high and with a width equal to that of the channel. There was a small ramp (1.5 m long) leading up to the sandbox at an angle of 5° to the horizontal. The ramp and platform were made of acrylic glass.

3.2. Hydraulic structure and sediments

The hydraulic structure tested was composed of individual units connected to each other to form a three-dimensional object. Initially, the small-scale prototype of the modular artificial reef was built using a 3D printer, based on a parametric model. This model previously designed [1,16], was printed adopting a 1:20 scale of the final design (**Figure VI.1**) Each unit measured approximately 5 cm in length. The structure elements in contact with the bed of sediments were vertical and had an oval shape. The diameter of these elements was approximately 1 cm. Thin pieces of metal were inserted after production in order to maintain the 1:20 weight ratio. A non-cohesive sediment was used as

represent natural sand. This sand had a median diameter of 0.328 mm (D_{50}), a density of 2440 kg/m^3 and a σ_D equal to 1.89.

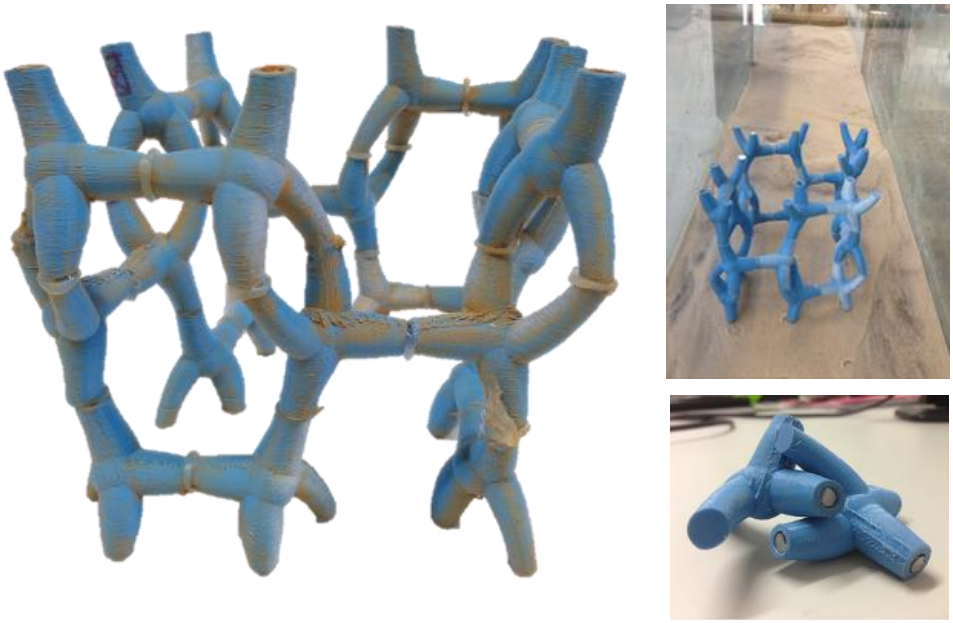


Figure VI.1: Assembled small-scale prototype of the modular artificial reef with the dimensions of 15×15×15 cm and individual prototype units of 5 cm.

3.3. Test procedures

Considering the requirements for scour, namely for clear-water scour, it was essential to define the relationships between flow, water height and flow velocity. A water depth of 25 cm (above the sandbox) was selected in order to allow complete submersion of the structure. The water flow velocity was calculated using the relation between the water flow velocity (U) and critical average velocity (U_c). The critical average velocity (maximum average velocity of the flow which does not cause sediment transport) with a value of 27 cm/s was calculated using the **Eq. (VI.1)** [13]:

$$U_c = \frac{\sqrt{\Psi_c \times (s-1) \times D_{50} \times h^{\frac{1}{3}}}}{0.041 \times D_{50}{}^{\frac{1}{6}}} \quad \text{[m/s];} \qquad \textbf{(VI.1)}$$

where U_c represents critical average velocity, ψ_c is the Shields coefficient, s is the density of the bottom material, h is the water flow height, D_{50} average sediment diameter.

Local scour occurs in the presence of an obstacle for $U/U_c > 0.5$. When $U/U_c > 0.9$ generalized scour occurs, and the obstacle's effect is camouflaged by natural movement of the bottom layer of sediment. In this regard, a U/U_c of 0.6 was selected, representing water flow velocity of 16.2 cm/s. A water

volumetric flow rate of 43.74 m^3/h was maintained. The tests ran between 2h:27min and 4h:30min, to allow time for scour to develop.

Once the relationship between flow rate and water height was established, the sand was levelled and the channel test section was filled slowly, to raise the water level without causing sediment transport. After reaching the desired water height, the structure was placed in the defined area. After the onset of the local scour phenomenon and the stipulated time for the duration of the test, the flume was drained and the sand dried. Subsequently, the final shape of the sandy bottom surface was documented using a photogrammetry technique.

During this experiment an Acoustic Doppler Velocimeter (ADV) by *Sontek Triton* was used to measure flow velocity fields upstream and downstream of the MFAR prototype (vertical and horizontal). The measurements of the water flow profiles were taken in three stages:

a. stage 1, involved the measurements of the flow velocities in the vertical plane of the upstream (@9) and downstream zone @17) without the PMFAR (**Figure VI.2**(a));

b. stage 2, PMFAR was put into place, and measurements were immediately taken downstream from the PMFAR. The velocity was measured at a fixed point to serve as the control while scouring process occurred;

c. stage 3, involved measurements of the flow velocities in the vertical plane of the downstream and upstream zone in the presence of the PMFAR (**Figure VI.2**(b) and (c));

In stages 1 and 3, the measurement sensor was submerged to a vertical distance from the bottom (S_d) of 4 cm at a horizontal distance from the PMFAR installation point (L_d) of 30 cm. The ADV collected data at a sampling rate of 3 seconds for 5 minutes. Every 5 minutes, the sensor was raised by an additional 1 cm. For each sample, the average value obtained from 30 measurements was used. This data was recorded on the data logger and downloaded onto a computer for interpretation. **Figure VI.2** shows the ADV testing locations for each of the tests. In stage 2, the sensor was placed at a S_d of 10 cm and a L_d of 30 cm.

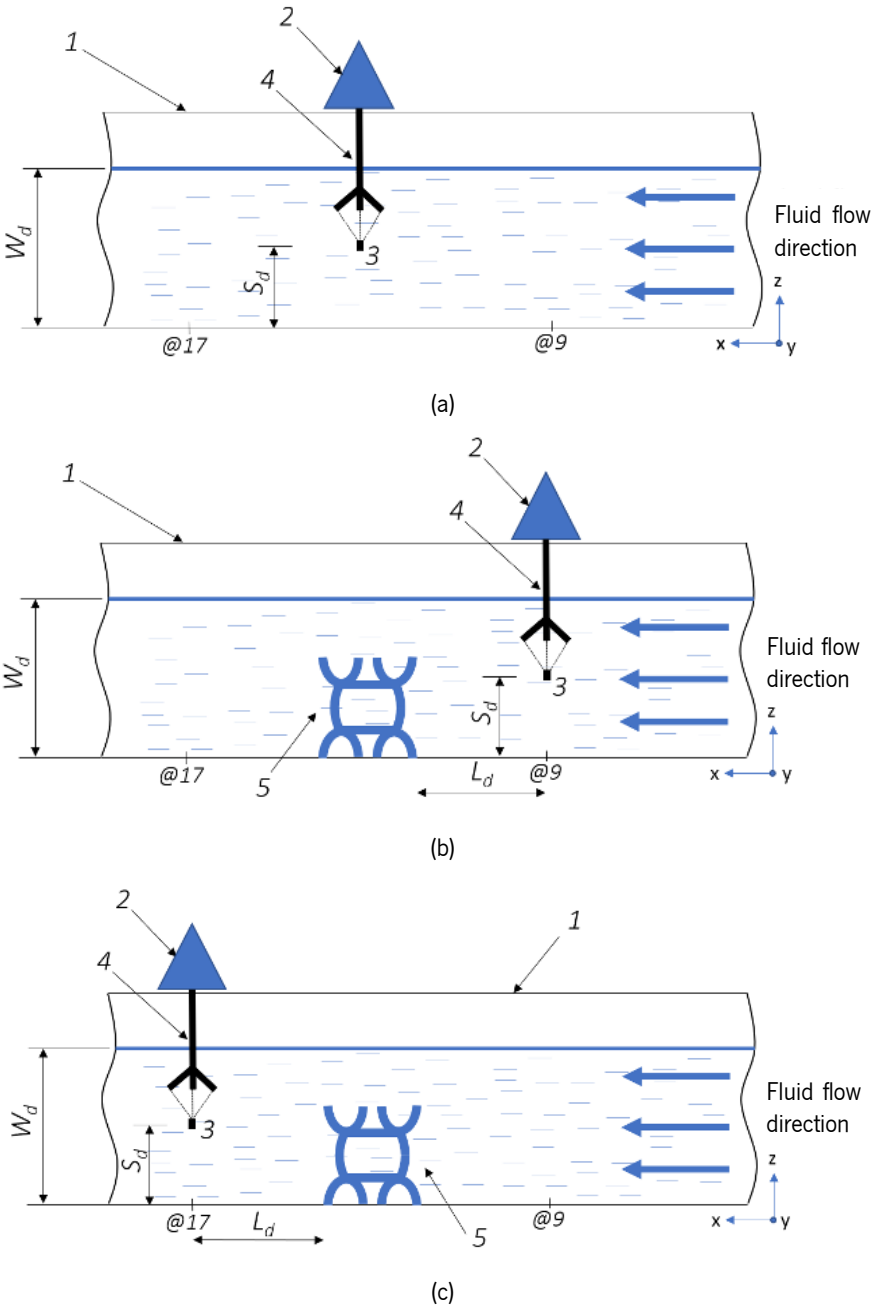


Figure VI.2: ADV testing locations for the two stages of testing: (a) without the structure, stage 1, (b) before structure, stage 3 and (c) after structure, stage 3. Note: (1) is the flow chamber, (2) is the holder of the measurement sensor above the flow chamber, (3) is the sensor, (4) is the sensor holding pole, (5) is the PMFAR. W_d is the water depth in the chamber (W_d=25cm), S_d is the sensor depth, and L_d is the distance between the artificial reef and the sensor (L_d=30cm).

The photogrammetric survey of the resulting scouring patterns was carried out using high resolution photography. These photos were taken from a position 90° from the horizontal plane, 40 cm above the sand. The photos were taken every 5 cm, ensuring at least 60-80% overlap between consecutive pictures. It was important to capture each area at least three times in different photographs [17].

Control points were places along the testing area to serve as reference locations used when reconstructing the 3D image. The higher number of control points used, the more accurate the final product would be. For this system, reference tape was placed every 10 cm along the outside of the glass. A small camera stand was constructed to allow a Nikon D800E, 36.3 MP resolution, camera to glide along the top of the hydraulic chamber. An ISO 250 and TIF format were chosen to maximize resolution. These photographs were later processed using *Agisoft's Photoscan* software. This software compares all the features of the photographs and generates a 3D model in the form of point clouds or a three-dimensional mesh. These results were used to generate a 3D model with sand texture, a digital elevation model (DEM), orthomosaic model (DOM) and a general contour map with an equidistance between lines of 0.002 m (**Figure VI.1**). These models could be overlaid on the photographs to generate an orthomosaic image of resulting sediment patterns after each of the tests were run. In this way, it was possible to document the erosion and the scour patterns around the structures

4 RESULTS AND DISCUSSION

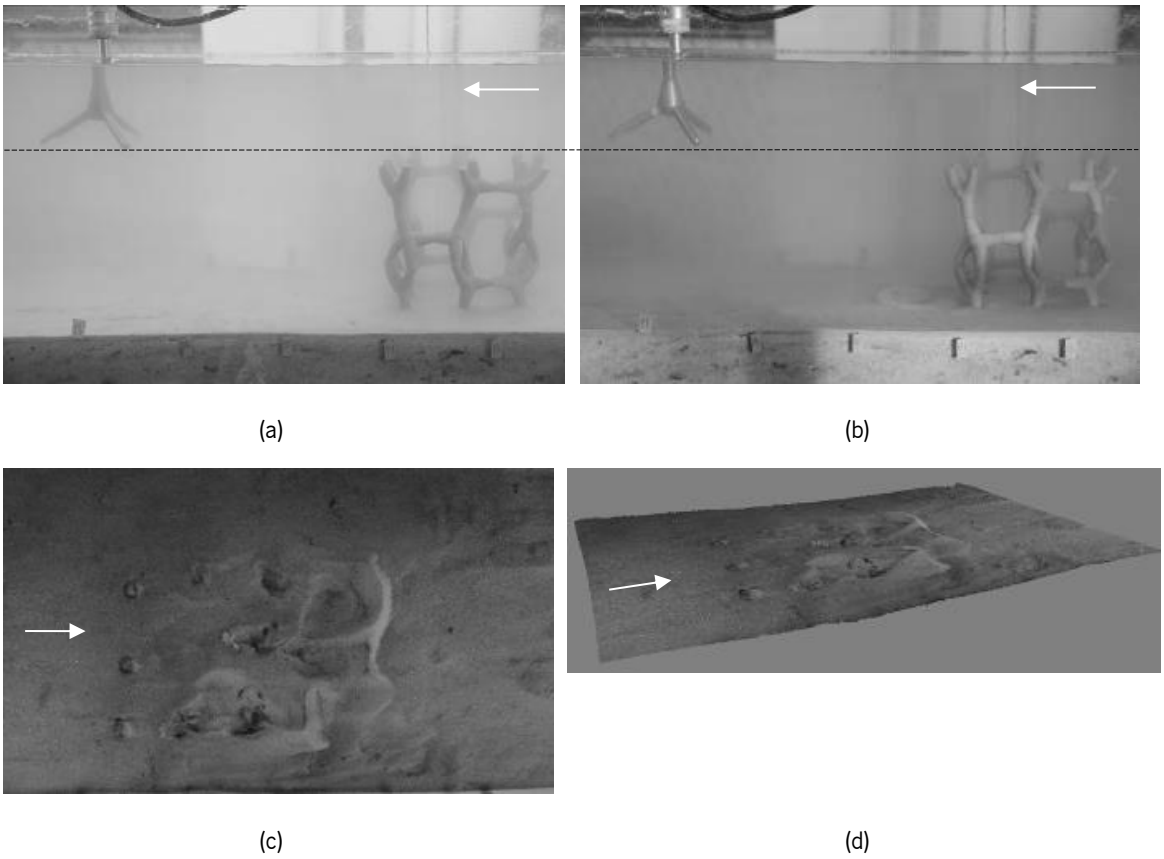
4.1. Scour cavity configuration

The following results were obtained through photogrammetric surveys performed at the conclusion of each test, in order to characterize the configuration of the scour cavity. In all images, white arrows indicate the direction of water flow.

Local scour phenomenon was clearly seen, namely around each vertical support element of the PMFAR structure in contact with the bed of sediments. In general, the structure sunk slightly and three asymmetric dunes were observed downstream, typical of the process of scouring and deposition and explained by structure asymmetry. However, despite small variations between the models, a clear and consistent trend was observed: the sediment was transported from upstream to downstream, for tests A, B and D.

The results of leaving the sandbox drain valve closed overnight, allowing the sand to remain fully saturated, can be seen in test C. Test C is an example with minimal sediment transportation around the PMFAR. The formation of the dunes typically resulting from deposition of sediments downstream of the structure cannot be verified.

In tests A, B and D, where the valve was open and the sand was able to dry overnight, the final dune structures could be clearly seen. Although less pronounced than in tests B and D, test A presented the same pattern (**Figure VI.3**).



(a) (b)

(c) (d)

Figure VI.3: Test A: (a) start, (b) final, (c) 2D photography and (d) reconstructed digital 3D model. Note: due some technical problems it was not possible to accurately reconstruct the digital models.

As shown in **Figure VI.4**, test B, the PMFAR sinks longitudinally (xx) with upstream rotation, and evenly transversally (yy). The maximum excavation was -0.022 m and the maximum sediment deposition zone was +0.011 m. In this DEM model, negative values indicate areas of accretion and positive values indicate areas of erosion. The distance between the columns upstream of the PMFAR and the furthest sediment deposition zone (L) was 0.235 m.

As shown in **Figure VI.5**, test C, the PMFAR sinks longitudinally (xx) with downstream rotation, and evenly transversally (yy). The maximum excavation was -0.004 m and the maximum sediment deposition zone was + 0.002 m. The distance between the columns upstream of the PMFAR and the farthest sediment deposition zone (L) was 0.233 m.

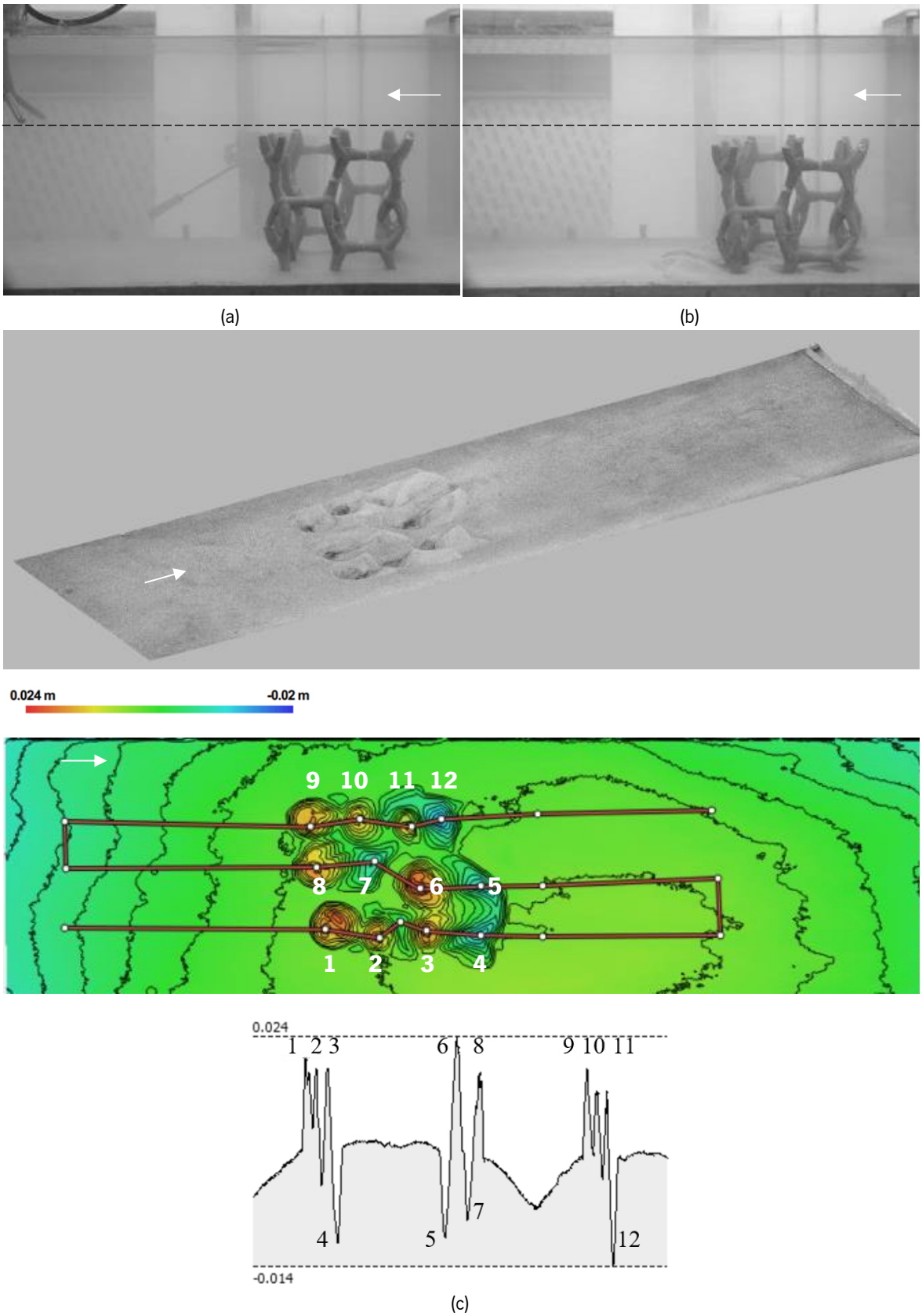


Figure VI.4: Test B: (a) time-lapse: start, (b) time-lapse: final and (c) reconstructed digital 3D model, digital elevation model and elevation map in meters. Note: the image of the DEM model is viewed from the bottom plane (excavation zones: 1, 2, 3, 6, 8, 9, 10 and 11; deposition zones: 4, 5, 7 and 12).

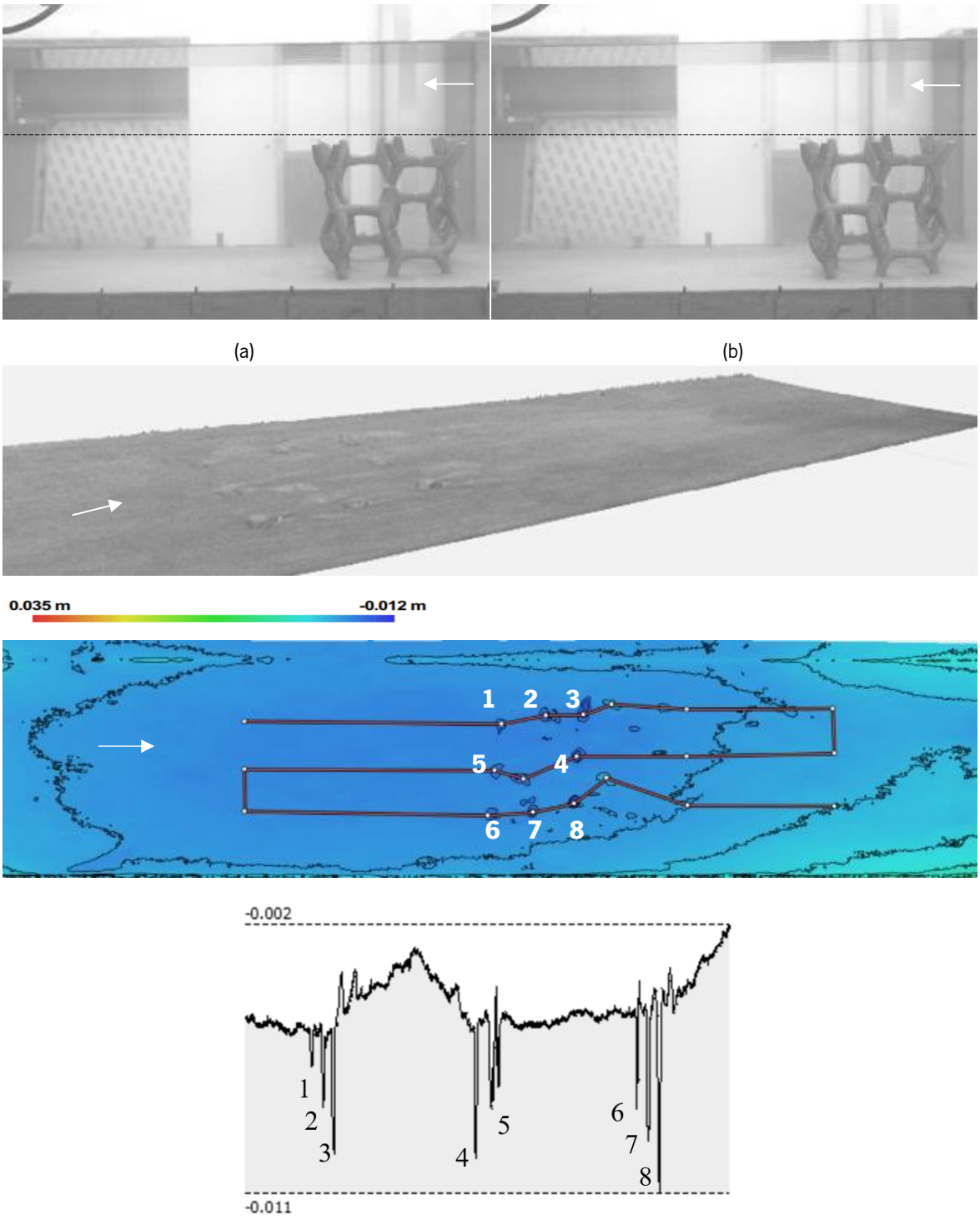


Figure VI.5: Test C: (a) time lapse-start, (b) time lapse-final and (c) reconstructed digital 3D model, digital elevation model and elevation map in meters.

As shown in **Figure VI.6**, test D, the PMFAR sinks longitudinally (xx) with upstream rotation, and transversely (yy). The maximum excavation was -0.019 m and the maximum sediment deposition zone was + 0.025 m. The distance between the columns upstream of the PMFAR and the furthest sediment deposition zone (L) was 0.256 m.

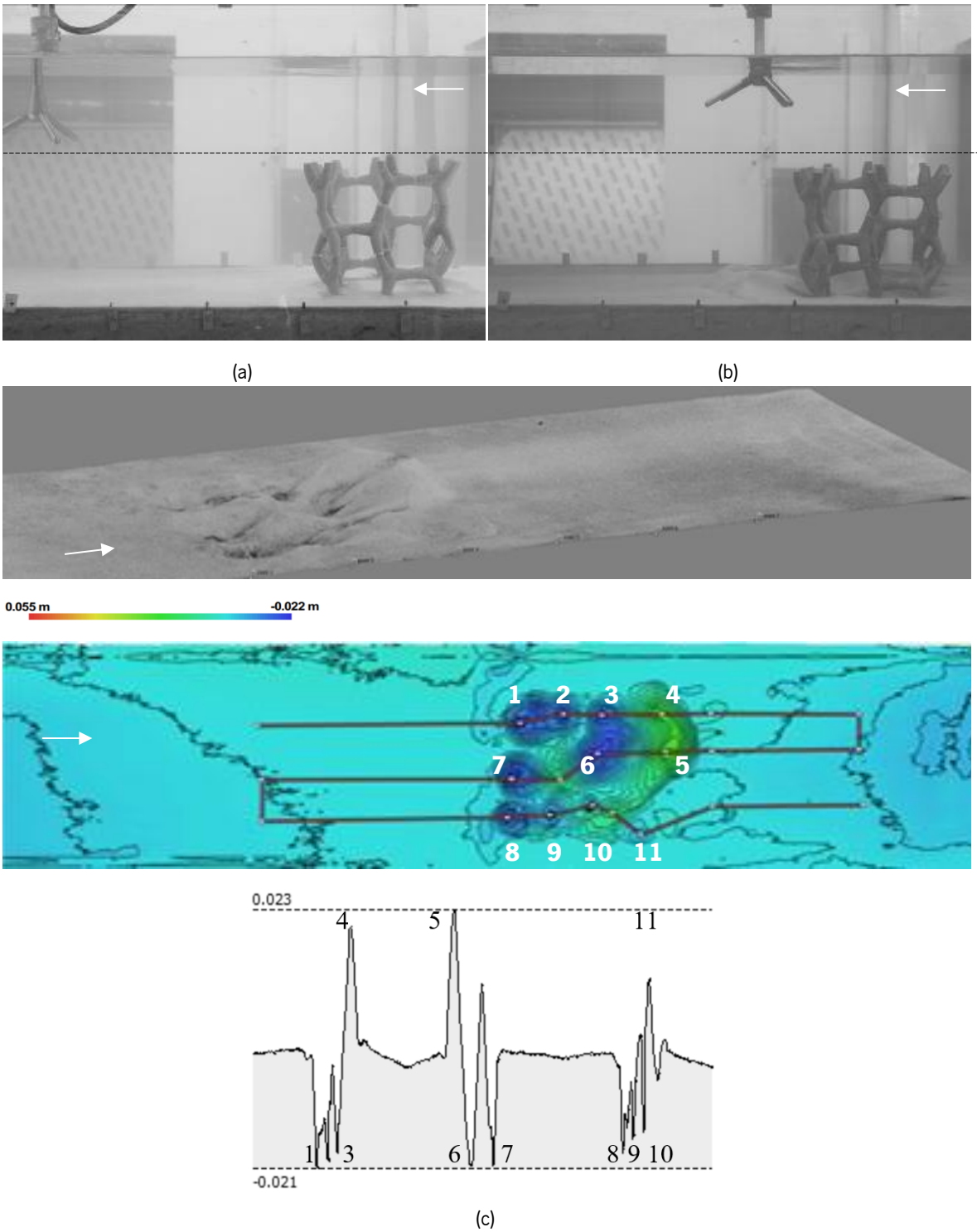


Figure VI.6: Test D: (a) time-lapse: start, (b) time-lapse: final and (c) reconstructed digital 3D model, digital elevation model and elevation map in meters.

4.2. Velocity profile measurements

The velocity magnitude is practically equal to the velocity in the x-direction. Therefore, the velocity magnitude as well as the velocities in the y-direction and z-direction are presented and discussed.

1) Measurements without PMFAR (stage 1)

The next series of measurements were conducted to quantify the variations in flow velocities without the presence of the PMFAR. **Figure VI.7** shows the results of the velocity magnitude profiles along the water column as well as the average velocities in the y- and z directions both upstream and downstream of the predicted position for the PMFAR. In general, the velocity profiles were similar in both sections, as expected for fully developed flow.

At the upstream position (@9) two different tests were conducted, VPA032 and VPA041, which correspond to tests A and B, respectively. The velocity magnitude was maintained at around 18 cm/s with a slight decrease to around 17 cm/s near the bottom. Average velocities in the y-direction were fairly consistent, around 1 cm/s with a slight decrease near the bottom. A very slight velocity increase at a depth of 5-6 cm was observed. The z-direction average velocities in VPA032 were very low, and reached a negative value around 8 cm depth, then slightly increased near the bottom. The z-direction average velocities in VPA041 were held steady at around 0.4 cm/s and decreased to 0 at the bottom.

At the downstream position (@17) two different tests were conducted, VPA030 and VPA039, which correspond to tests A and B, respectively. The velocity magnitude for all tests ranged between approximately 19 cm/s and 17 cm/s, and decreased near the bottom. Y direction average velocities for both tests hovered around 1 cm/s. Z direction flow measured just slightly above zero, and in the case of VPA039, registered as a negative flow at the very bottom.

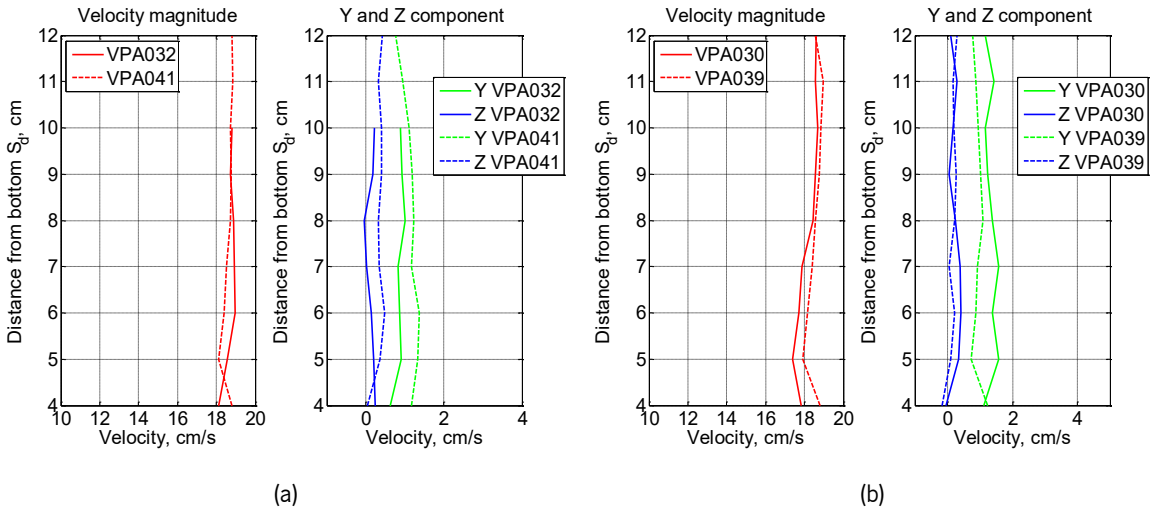


Figure VI.7: Velocity magnitude profiles and average velocity in the y and z-direction without PMFAR (a) upstream, position@9 and (b) downstream position@17.

2) Measurements with PMFAR (stage 3)

The next series of measurements were obtained to quantify the variations in flow velocities with the presence of the PMFAR. **Figure VI.8** shows the results of the velocity magnitude profiles along the water column as well as the average velocities in the y- and z-directions both upstream and downstream of the PMFAR position.

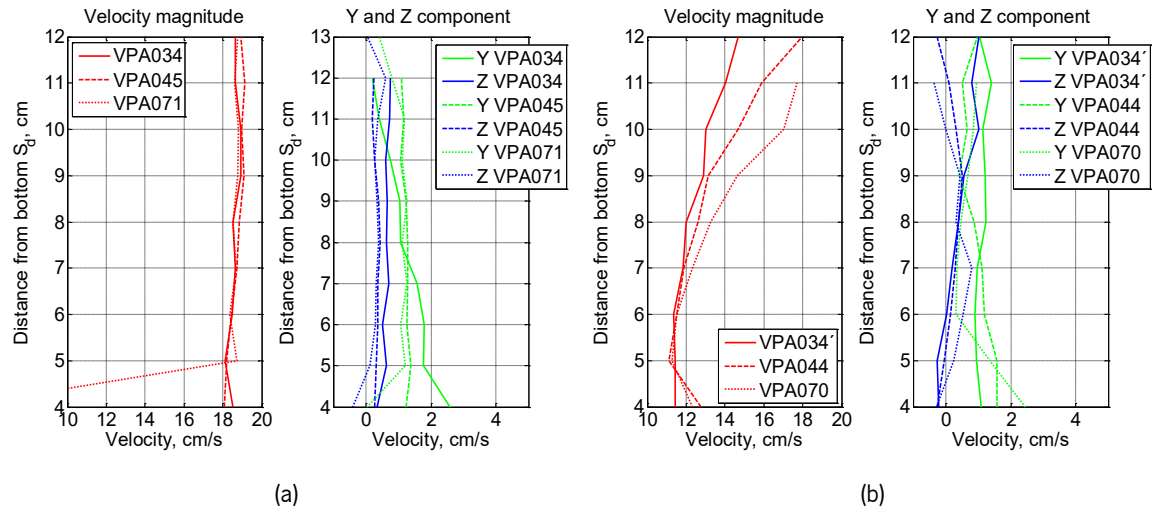


Figure VI.8: Velocity magnitude profiles and average velocity in the y and z-direction with PMFAR: (a) upstream, position@9 and (b) downstream position@17.

At the upstream position (@9) three different tests were conducted, VPA034, VPA045, and VPA071, corresponding to tests A, B and D, respectively. As expected, in all three tests, the velocity magnitude profiles along the water column maintained fairly consistent values between 18 cm/s and 19 cm/s between the depths of 12 cm and 4 cm (PMFAR zone). The velocity values were similar to measurements performed without PMFAR since there was no interaction between the PMFAR and flow at this location. In the case of VPA071, there was a rapid decrease in velocity to 5 cm/s between the depths of 5 cm and 4 cm.

Y-direction average flow velocities varied between the three tests. In the case of VPA034, flow velocities steadily increased with depth, experiencing a flow velocity just about 0 at a depth of 12 cm, and a flow velocity near 2.5 cm/s at a depth of 4 cm. In the case of VPA045, y-direction average flow velocities maintained a consistent value just about 1 cm/s between the depths of 12 cm and 4 cm. VPA071 experienced an increase in y-direction flow velocities between the depths of 13 cm and 11 cm, at which point the velocities plateaued at just about 1 cm/s between 11 cm and 5 cm depth and then quickly fell to near 0 at a depth of 4 cm. However, all results obtained with the ADV measuring volume closer to the bottom, at smaller distances than 4 cm, should be regarded with great caution due to the interference effects produced by the proximity to the bottom.

The z-direction average flow velocities were about the same in all three tests, slightly fluctuating between 0 and 1 cm/s. In the case of VPA071, the z-direction flow velocity rapidly decreased below the depth of 5 cm to achieve a negative flow velocity of -0.3 cm/s at 4 cm depth.

At the downstream position (@17) three different tests were conducted, VPA034', VPA044, VPA070, which correspond to tests A, B and D, respectively.

The velocity magnitude decreased with depth in all three tests. As expected, at the boundary between the free water surface and the top of the structure (10 cm), the velocities were higher, similar to the value obtained in the free water surface upstream region. In VPA034', the velocity magnitude ranged between 15 cm/s to around 11 cm/s whereas the velocities magnitude in VPA044 and VPA070 ranged from 17.5 cm/s to 11 cm/s.

Y-direction average flow had slightly different characteristics in each of the three tests. For VPA034', velocity hovered near 1 cm/s across all depths with a slight increase to around 1.3 cm/s near 11 cm depth. In VPA044, y-direction average velocity decreased between depths of 12 cm and 9 cm, and

then steadily increased from 0.3 cm/s to 1.5 cm/s near the bottom. Finally, VPA070 showed a decrease from 1 cm/s to 0.2 cm/s between the depths of 11 cm and 7 cm, a slight plateau between 7 cm and 6 cm, and then a steady increase to around 2.3 cm/s at the bottom.

Z-direction average flow in VPA034' steadily decreased from 1 cm/s to -0.2 cm/s with depth. In VPA044 z-direction flow velocity saw a slight increase from -0.2 cm/s to 0.5 cm/s between the depths of 12 cm and 9 cm, and then a steady decrease back to -0.2 cm/s until the bottom. Similarly, VPA070 z-direction flow velocity showed a slight increase in velocities between depths 11 cm to 7 cm (-0.2 cm/s to 0.8 cm/s) and then a steady decrease from 7 cm to the bottom, returning to the velocity -0.2 cm/s.

3) Time test series (stage 2)

The next series of measurements were conducted to quantify the variations in flow velocities in the presence of the PMFAR while the scour process occurred (**Figure VI.9**). The tests were VPA033, VPA043, VPA061 and VPA068, which correspond to tests A, B, C and D, respectively.
The velocity magnitude maintained a fairly consistent value, fluctuating between 10 cm/s and 15 cm/s for all tests except VPA033. VPA033 experienced similar flow velocities until just over an hour into the test, at which point the flow velocities started fluctuating between 20 cm/s and 6 cm/s until the end of the test.

Y-direction average flow for tests VPA033 and VPA043 experienced slight fluctuations centered around a flow velocity of 1 cm/s throughout the duration of the tests. Test C, VPA061, experienced the highest flow velocities of all of the tests, which fluctuated between 2 cm/s and 1.5 cm/s throughout the test. Finally, test D, VPA068 experienced y-direction flow velocities which ranged from 2 cm/s at the start of the test, to just below 1 cm/s at the end. The flow velocities decreased from 2 cm/s to 1 cm/s within the first 1000 seconds of the test, and then continued to fluctuate around 1 cm/s until the completion of the test.

Z-direction average flow velocities were similar across all tests except VPA033. For these tests, the flow velocities slightly fluctuated between 0 and 1 cm/s, always maintaining positive values. In the case of VPA033, the z-direction flow velocity fluctuated between 0 and 2.5 cm/s reaching a maximum value twice at around 7000 and 9500 seconds.

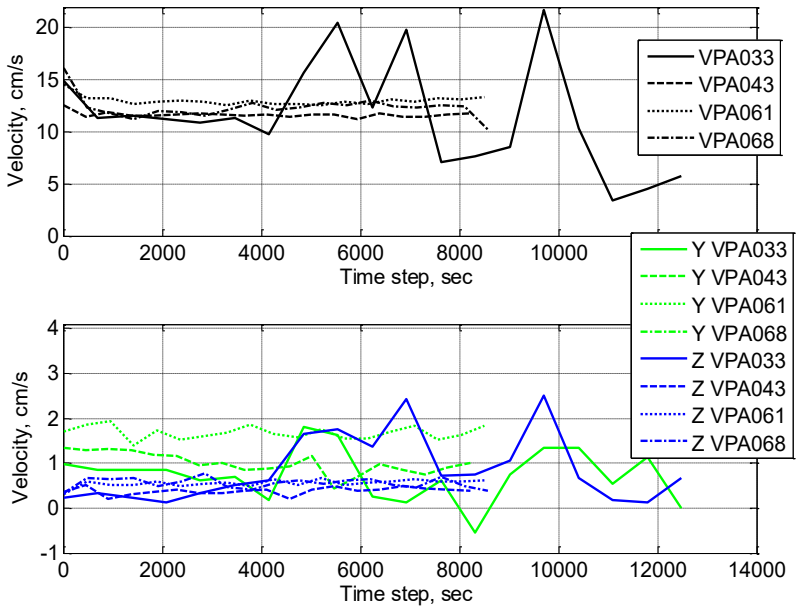


Figure VI.9: Velocity magnitude (above) and average velocity in the y and z-direction (below) time series data with PMFAR at downstream position@17 during the scour process for all tests.

5 DISCUSSION

Ideally, the grain size used during testing should reflect the natural grain size associated with the installation area, matching the ratio of the MFAR to PMFAR (20:1). However, this was not possible to reach. If an average grain size diameter of the installation area is assumed to be 0.3 mm, then a sand of 0.01 mm should be used [129]. According to the Wentworth scale, sediment with a diameter of 0.01 mm is classified as "medium silt" and would have affected the transportation and settlement properties of the sediment [130], so it would no longer represent the naturally occurring interactions for the installation area. Therefore, and due to material availability and physical limitations of the testing facilities, a sand with mean diameter of 0.328 mm was selected and used during testing. Although these conditions may not be ideal, eventually this data may serve to calibrate numerical models which can then be extrapolated to real scale and real environments.

The scour patterns were analysed through photogrammetric surveys performed at the end of each test. In general, the structure sinks slightly and three asymmetric dunes, explained by structure asymmetry, were observed downstream. This result raises two concerns. First, it is necessary to determine if the erosion would be excessive enough to result in the sinking of the MFAR enough to neutralize the benefits of its installation. The second issue concerns the risk of instability and overturning of the MFAR, potentially damaging the structure or the flora and fauna that surrounds it.

In response to these problems, the structure of the MFAR may need to be constructed over a baseplate, thereby minimizing erosion and the possible risk of overturning. The possible scour of such baseplate should also be investigated.

The influence of other test factors on the experimental results, such as the degree of saturation of sand prior to testing, were highlighted during the analysis of these models. The saturation levels of the sand affected the subsequent profiles taken during the photogrammetric surveys. In cases where the release valve of the hydraulic chamber was not opened, and the test area was left saturated in water overnight, there was a negative impact on preservation of the erosion and scouring profiles the following day.

Equipment limitations meant that the complete vertical mean velocity profiles could not be collected. Nevertheless, the resulting blind zone did not inhibit the analysis of the results. However, in future experiments, either a deeper tank or a different ADV could be used to minimize this blind zone. Additionally, further consideration concerning the frequency of acquisition of the ADV data may be required, namely for the study of turbulence, which would require faster sampling frequencies.

When studying the water flow velocity without the PMFAR, either from position (@9) or (@17), there were no significant fluctuations in velocities within the water column. There was a slight decrease in all velocities right before the bottom, which was expected due to the loss of energy caused by friction with the sand. Velocities in the y- and z-direction were much lower (near 0) than when compared with the x- direction (≈18 cm/s). Statistically speaking, the x- and z-direction data had a very low coefficient of variation (close to 0) when compared to the y-direction. The absence of significant differences in velocities between position (@17) and (@9) was expected, as there is nothing to interfere with the water flow, except the boundary conditions. Furthermore, this confirmed that the transition ramp and sand bottom apparatus did not significantly disturb the testing flow conditions.

Once the PMFAR was introduced, a difference in values between these two positions would be expected. At position (@9), x- and z-direction velocities were fairly consistent throughout the water column as seen in the previous case (without PMFAR). The y-directional flow velocities varied between the three tests, making it very difficult to analyse trends in flow velocities in the y-direction, therefore being statistically insignificant for this study.

At position @17 (downstream), measurements revealed the impact of the PMFAR on flow direction velocities. The obtained results suggest that flow velocity decreases with the increasing depth due to the presence of the PMFAR. This verified that dissipation of energy in the system occurred in and around the PMFAR, causing a decrease of the flow velocity downstream of the structure

6 CONCLUSIONS

In this experiment, the hydrodynamic effects of a modular artificial reef and the phenomenon of local scour in a non-cohesive sediment were evaluated. A non-invasive experimental method was developed that allowed to collect information about the scour pattern located around the structure. In general, the tests evaluated and validated the developed test protocol in its effectiveness to the study of innovative geometries of artificial reefs, which is essential in the preliminary phase of their development. In addition, these tests also served to illustrate the current impact of the MFAR on sediment transport and water flow.

In all cases, the PMFAR experienced sand erosion around the front of the structure and sand deposition near the back. This highlights the concern involving the possible rotation and the sinking of the PMFAR, which could be perhaps mitigated in the future through the use of a baseplate or geogrid.

Photogrammetry proved to be an alternative survey technique which provides high density information and accurately records the real shape of the sand bottoms, its irregularities, deformations and damage, resulting in excellent cost/benefit ratios. The resulting elevation maps also allow precise and quantitative assessments of the volumes of sand transported, as well as, the slopes of the dunes and elevation of the ripples, among other important parameters to characterize erosion and local scour.

The results obtained and observed can thus contribute to a better understanding of complex situations, such as the development of modular artificial reefs with irregular and complex geometry when placed in unstable sediment beds of non-cohesive nature. When the full-sized MFAR is installed off the coast, an analysis of typical wave characteristics must be conducted to ensure MFAR will not either sink too deep or topple over in high energy conditions. Furthermore, actual physical parameters of the area of installation should be used during testing to verify structural stability of the design is maintained. In addition, advanced methodology may allow the extension of hydraulic tests to consider the following additional aspects:

i. Include advanced techniques such as optical methods that allow the visualization and analysis of particle motion in fluids - PIV (particle image velocimetry).
ii. Study the evolution of erosion and local scour phenomena for different intervals of time.
iii. Analyse sediment beds with different grain size.
iv. Evaluate the overturning potential considering the real environment conditions.
v. Study the effect of elements that attenuate the local scour, for example the addition of a base plate, geogrid, etc.
vi. Perform numerical simulations to study the local scour and thus complement the experimental work.
vii. Study the influence of the structure orientation and other geometries on the results.

ACKNOWLEDGEMENTS

The study presented in this paper is a part of the research project "NEXT-SEA: Next Generation Monitoring of Coastal Systems in a Scenario of Global Change", financed by FEDER funds in the scope of the Next-sea project (NORTE-01-0145-FEDER-000032). The authors also like to thank Sr. João Rui Mendes de Oliveira, technician of the Laboratory of Hydraulics and Water Resources - Azurém, for his laboratory support. The first and eighth authors wish also to acknowledge the PhD grants SFRH/BD/137220/2018 and SFRH/BD/129583/2017, respectively, provided by FCT.

REFERENCES

[1] Cruz F, Pereira E, Valente IB, Tiago M, Maslov D, Pinheiro M. Structural design of an innovative multifunctional artificial reef. Oceans 2018 MTS/IEEE Charleston, IEEE; 2018, p. 1–7. https://doi.org/10.1109/OCEANS.2018.8604587.

[2] Gautam P, Eldho TI, Mazumder BS, Behera MR. Experimental study of flow and turbulence characteristics around simple and complex piers using PIV. Exp Therm Fluid Sci 2019;100:193–206.

[3] Lima MMCL. Estudo experimental da erosão localizada na proximidade de pilares de pontes. Rev Eng Civ 2008;33:41–52.

[4] Ferradosa TF, Taveira-Pinto F, Simons R. Sedimentos mistos e dispostos por camadas – Scour

around marine foundations in mixed layered sediments. In: 7as Jornadas de Hidráulica, Recursos Hídricos e Ambiente; 2012; Porto, Portugal. p. 22–30.

[5] Ha YS, Yun DH, Singh Pradhan AM, Pradhan B, Kim YT. Study on the settlement reduction of artificial reef. In: Proceedings of the 2015 World Congress on Advances in Structural Engineering and Mechanics (ASEM15); 2015 Aug 25–29; Incheon, Republic of Korea.

[6] Kimura H, Ingsrisawang V, Ban M. A study on local scour of cylindrical artificial fish reefs. J Fish Eng 1994;31(1):33–40.

[7] Chabert J, Engeldinger P. Study of scour around bridge piers. Chatou, France: Laboratoire National d'Hydraulique; 1956.

[8] Sungthong S. Evaluation of artificial reef installed in Rayong, Thailand, 1978–1987. In: Workshop on Artificial Reefs Development and Management; 1988 Sep 13–18; Penang, Malaysia.

[9] Coleman SE. Clearwater local scour at complex piers. J Hydraul Eng 2005;131(4):330–334.

[10] Sheppard DM, Renna R. Florida bridge scour manual. Tallahassee, FL: Florida Department of Transportation; 2010.

[11] Arneson LA, Zevenbergen LW, Lagasse PF, Clopper PE. Evaluating scour at bridges (HEC-18). Technical Report FHWA HIF-12-003. Washington, DC: Federal Highway Administration; 2012.

[12] Castiblanco MEM. Experimental study of local scour around complex bridge piers [PhD thesis]. Porto, Portugal: Faculdade de Engenharia da Universidade do Porto (FEUP); 2016.

[13] Richardson EV, Davies SR. Evaluating scour at bridges. 4th ed. Hydraulic Engineering Circular No. 18 (HEC-18), FHWA-NHI-01-001. Washington, DC: U.S. Department of Transportation, Federal Highway Administration; 2001.

[14] Dey S, Raikar RV. Characteristics of horseshoe vortex in developing scour holes at piers. J Hydraul Eng 2007;133(4):399–413.

[15] Couto LT, Cardoso AH. Erosões localizadas junto de encontros e pilares de pontes. Parte I – Caracterização da situação de referência (in Portuguese). Recursos Hídricos 2001;22(1):65–74.

[16] Maslov D, Pereira E, Miranda T, Valente M, Cruz F, Pinheiro M. Innovative monitoring strategies

for multifunctional artificial reefs. OCEANS 2018 MTS/IEEE Charleston. 2018:1–8. https://doi.org/10.1109/OCEANS.2018.8604656.

[17] Agisoft LLC. PhotoScan user manual: Professional edition, version 1.4. St. Petersburg, Russia: Agisoft LLC; 2018. Available from: http://www.agisoft.com/pdf/photoscan-pro_1_4_en.pdf (accessed 1 October 2018).

[18] Li B, Granja HM, Farrell EJ, Ellis JT, Sherman DJ. Aeolian saltation at Esposende Beach, Portugal. J Coast Res 2009;SI 56:327–331.

[19] Wentworth CK. A scale of grade and class terms for clastic sediments. J Geol 1922;30(5):377–392.